

Lecture Notes in Civil Engineering

Sondipon Adhikari

Anjan Dutta

Satyabrata Choudhury *Editors*

Advances in Structural Technologies

Select Proceedings of CoAST 2019

 Springer

Lecture Notes in Civil Engineering

Volume 81

Series Editors

Marco di Prisco, Politecnico di Milano, Milano, Italy

Sheng-Hong Chen, School of Water Resources and Hydropower Engineering,
Wuhan University, Wuhan, China

Ioannis Vayas, Institute of Steel Structures, National Technical University of
Athens, Athens, Greece

Sanjay Kumar Shukla, School of Engineering, Edith Cowan University, Joondalup,
WA, Australia

Anuj Sharma, Iowa State University, Ames, IA, USA

Nagesh Kumar, Department of Civil Engineering, Indian Institute of Science
Bangalore, Bengaluru, Karnataka, India

Chien Ming Wang, School of Civil Engineering, The University of Queensland,
Brisbane, QLD, Australia

Lecture Notes in Civil Engineering (LNCE) publishes the latest developments in Civil Engineering—quickly, informally and in top quality. Though original research reported in proceedings and post-proceedings represents the core of LNCE, edited volumes of exceptionally high quality and interest may also be considered for publication. Volumes published in LNCE embrace all aspects and subfields of, as well as new challenges in, Civil Engineering. Topics in the series include:

- Construction and Structural Mechanics
- Building Materials
- Concrete, Steel and Timber Structures
- Geotechnical Engineering
- Earthquake Engineering
- Coastal Engineering
- Ocean and Offshore Engineering; Ships and Floating Structures
- Hydraulics, Hydrology and Water Resources Engineering
- Environmental Engineering and Sustainability
- Structural Health and Monitoring
- Surveying and Geographical Information Systems
- Indoor Environments
- Transportation and Traffic
- Risk Analysis
- Safety and Security

To submit a proposal or request further information, please contact the appropriate Springer Editor:

- Mr. Pierpaolo Riva at pierpaolo.riva@springer.com (Europe and Americas);
- Ms. Swati Meherishi at swati.meherishi@springer.com (Asia—except China, and Australia, New Zealand);
- Dr. Mengchu Huang at mengchu.huang@springer.com (China).

All books in the series now indexed by Scopus and EI Compendex database!

More information about this series at <http://www.springer.com/series/15087>

Sondipon Adhikari · Anjan Dutta ·
Satyabrata Choudhury
Editors

Advances in Structural Technologies

Select Proceedings of CoAST 2019

 Springer

Editors

Sondipon Adhikari
Swansea University
Wales, UK

Anjan Dutta
Indian Institute of Technology Guwahati
Guwahati, Assam, India

Satyabrata Choudhury
National Institute of Technology Silchar
Silchar, Assam, India

ISSN 2366-2557 ISSN 2366-2565 (electronic)
Lecture Notes in Civil Engineering
ISBN 978-981-15-5234-2 ISBN 978-981-15-5235-9 (eBook)
<https://doi.org/10.1007/978-981-15-5235-9>

© Springer Nature Singapore Pte Ltd. 2021

This work is subject to copyright. All rights are reserved by the Publisher, whether the whole or part of the material is concerned, specifically the rights of translation, reprinting, reuse of illustrations, recitation, broadcasting, reproduction on microfilms or in any other physical way, and transmission or information storage and retrieval, electronic adaptation, computer software, or by similar or dissimilar methodology now known or hereafter developed.

The use of general descriptive names, registered names, trademarks, service marks, etc. in this publication does not imply, even in the absence of a specific statement, that such names are exempt from the relevant protective laws and regulations and therefore free for general use.

The publisher, the authors and the editors are safe to assume that the advice and information in this book are believed to be true and accurate at the date of publication. Neither the publisher nor the authors or the editors give a warranty, expressed or implied, with respect to the material contained herein or for any errors or omissions that may have been made. The publisher remains neutral with regard to jurisdictional claims in published maps and institutional affiliations.

This Springer imprint is published by the registered company Springer Nature Singapore Pte Ltd. The registered company address is: 152 Beach Road, #21-01/04 Gateway East, Singapore 189721, Singapore

Preface

National Conference on Advances in Structural Technologies (CoAST-2019) held during 1–3 February, 2019, was aimed towards a national level forum for profound discussions with shared interest on novel research and developments in the entire domain of structural engineering. Academicians, researchers, consultants, practicing engineers working in government/private sectors from all over India were sincerely encouraged to participate in this national conference. CoAST-2019 was also a good opportunity for many to visit the North-Eastern part of India.

Wide ranges of topics/themes associated with Structural Engineering were considered in CoAST-2019, like: Solid Mechanics, Computational Mechanics and Modelling, Composite Structures, Emerging Structural Materials, Structural Health Monitoring, Vibration Control, Probabilistic Structural Mechanics, etc. Most of the topics have been represented in the selected papers.

CoAST-2019 was the first national level conference in the domain of Structural Engineering organized by National Institute of Technology (NIT) Silchar. NIT Silchar, an Institute of National Importance under the NIT Act, was established in 1967, as Regional Engineering College (REC) Silchar, in Assam. In year 2004, it was upgraded to the status of an NIT.

I am thankful to Prof. Sivaji Bandyopadhyay, Director, NIT Silchar and Prof. Parthasarathi Choudhury, Head, Civil Engineering Department, NIT Silchar, for their encouragement in various steps of the Conference. It is thankfully acknowledged that the Conference was funded by TEQIP-III.

We are thankful to the following keynote speakers: Prof. Biswajit Bhattacharjee (IIT Delhi), Prof. Nirjhar Dhang (IIT Kharagpur), Prof. Siddhartha Ghosh (IIT Bombay), Prof. Balaji Raghavan (INSA, Rennes, France), Dr. Debiprasad Ghosh (DGM, L&T).

I wish to convey thanks to my colleagues, some of whom I mention here: Prof. A. I. Laskar, Dr. Nirmalendu Debnath, Dr. B. K. Roy, Dr. Arjun Sil, Pallab Das, Dr. Subhrajit Dutta, Dr. M. L. V. Prasad Raju, Dr. Debjit Bhowmick, Dr. Sudip Dey, Dr. Nitsh A. and others.

Such a big event could not have been organized without the help of our students force. I wish to mention the names of research scholars like, Sourav Das, Durga Mibang, Kamalesh Bhowmick, Subham Ghosh, Mrinal Kanti Sen, Sandeep Das, Pritam Hait, especially. And last but not the least, the contributions of our PG students: some names which I remember are: Navendu Nimare, Suman Banerjee, Anneta A. Joseph, Sitesh Mohapatra, Charla Venkatesh, Bharti Mishal, Mayuri Borah, Nazeel Sabha, Sudipta Malakar, etc.

We are thankful to Springer Publications for their consent in publishing a SCOPUS indexed proceedings of the selected papers of CoAST-2019. Springer has not only added extra flavour to the conference, but also encouraged contributors of papers.

I am thankful to Prof. Sondipon Adhikari, Swansea University and Prof. Anjan Dutta, IIT Guwahati for their editorial works and guidance. Thanks due to our reviewers and finally to our participants who made the conference a success.

Hope this proceedings will throw new light to the researchers and motivate them further in research.

Satyabrata Choudhury
Chairman CoAST-2019
Professor in Civil Engineering
NIT Silchar
Silchar, India

Contents

Seismic Control and Performance of Passive Hybrid Damper Under Near-Field Earthquakes	1
Swabarna Roy, Swagato Das, and Purnachandra Saha	
Wall Effects on Terminal Velocity of Test Fuel Bundle in the Fuel Test Loop of High Flux Research Reactor	15
G. Verma, S. Sengupta, S. Mammen, P. Mukherjee, and P. V. Varde	
Comparison of Seismic Performance of Composite (RCS) Frame with RC Frame Using Pushover Analysis	31
Manoranjan Singh Oinam and S. S. Ningthoukhongjam	
Investigating Load Withstand by L-Shape Concrete Cube, RCC Slab and to Safeguard Reinforcement of RCC Slab in Saltwater Environment Using Cathodic Protection	45
C. F. Rajemahadik, M. M. Kulkarni, R. S. Durge, A. R. Kamble, S. B. Babar, and P. A. Bansode	
Performance Evaluation of Two-Way RC Slab Subjected to Blast Loading Using Finite Element Analysis	57
Kasturi Bhuyan, Kiran Kumar Jujjavarapu, and Hrishikesh Sharma	
Development of Fragility Curves for Different Types of RC Frame Structures	71
Neeva Ahanthem and S. S. Ningthoukhongjam	
Smart Lightweight MR Damper for the Enhancement of Seismic Mitigation	89
C. Daniel, G. Hemalatha, L. Sarala, D. Tensing, and S. Sundar Manoharan	
Rheological Behavior of Geopolymer Mortar with Fly Ash, Slag and Their Blending	99
Biswajit Roy and Aminul Islam Laskar	

Effect of Pile Spacing and Raft Thickness on the Behaviour of Piled-Raft Foundation—A Parametric Study Using FEM	111
Mukul Kalita, Utpal Kumar Nath, and Palash Jyoti Hazarika	
Removal of VOCs and Improvement of Indoor Air Quality Using Activated Carbon Air Filter	123
Sujon Mondal, Soham De, and Purnachandra Saha	
A Comparative Study of Normal and Self-compacting Concrete	133
Deep Tripathi, Rakesh Kumar, P. K. Mehta, and Amrendra Singh	
Evaluating Toughness as a Parameter to Determine the Fatigue Life of Wollastonite Microfiber Reinforced High Flow Pavement Quality Concrete	145
Shashi Kant Sharma and K. P. Marisarla Chaitanya	
Response of Single and Multilayered Flexible Base for Static and Earthquake Loading Under Framed RC Structure	169
Gaurav D. Dhadse, G. D. Ramtekkar, and Govardhan Bhat	
Analysis of Moment and Torsion in Skew Plates Using ABAQUS	185
Anjani Kumar Shukla, Vishal Koruthu Philip, and P. R. Maiti	
Behavior of Liquid Storage Tank Under Multidirectional Excitation	203
Sourabh Vern, Mahendra Kumar Shrimali, Shiv Dayal Bharti, and Tushar Kanti Datta	
Osdag: A Software for Structural Steel Design Using IS 800:2007	219
Siddhartha Ghosh, Danish Ansari, Ajmal Babu Mahasrankintakam, Dharma Teja Nuli, Reshma Konjari, M. Swathi, and Subhrajit Dutta	
Experimental and Analytical Investigations on Two-Way Flexural Capacity of Biaxial Voided Slab	233
R. Sagadevan and B. N. Rao	
A Comparative Study of Seismic Response of Structure Isolated with Triple Friction Pendulum Bearing and Single Friction Pendulum Bearing Under Different Hazard Levels of Earthquake	249
Ankit Sodha, Sandip Vasanwala, Devesh Soni, and Shailendra Kumar	
Assessment of Important Parameters for Seismic Analysis and Design of Confined Masonry Buildings: A Review	261
Bonisha Borah, Vaibhav Singhal, and Hemant B. Kaushik	
Design and Performance Criteria for Fire-Resistant Design of Structures—An Overview	277
Nitant Upasani, Mansi Bansal, Ashirbad Satapathy, Sanket Rawat, and G. Muthukumar	

Wear Behavior of Marble Dust Filled Aluminum Metal Matrix Structural Composite 295
 Hariom Tripathi and Sandeep Kashyap

Quantifying Uncertainty in Structural Responses of Polymer Sandwich Composites: A Comparative Analysis of Neural Networks . . . 305
 R. R. Kumar, T. Mukhopadhyay, K. M. Pandey, and S. Dey

Buckling Analysis of Braced Frames under Axial and Lateral Loadings: The Effect of Bracing Location 317
 Narayan and Krishna Kant Pathak

A Study on Moment–Curvature Relationships for REINFORCED CONCRETE BEAMS with Varying Fire Loading Conditions 335
 Ankit Borgohain and Sriman Kumar Bhattacharyya

Effect of Slab Thickness on Period of the Vibration of Reinforced Concrete Building 353
 Prabhat Kumar Soni, S. K. Dubey, and Prakash Sangamnerkar

Sampling-Based Techniques for Finite Element Model Updating in Bayesian Framework Using Commercial Software 363
 Ayan Das and Nirmalendu Debnath

Stochastic Structural Optimization of Multiple Tuned Mass Damper (MTMD) System with Uncertain Bounded Parameters 381
 Kamallesh Bhowmik and Nirmalendu Debnath

Hearth Monitoring of Blast Furnace Using Finite Element Analysis and Artificial Intelligence 393
 Debi Prasad Ghosh, Bhaskar Sengupta, and Shyam Krishna Maitra

Fatigue Resistance of Recycled Steel Fibers (Discarded Vehicle Tyre Steel Fibers) Concrete Pavement 407
 M. V. Mohod and K. N. Kadam

About the Editors

Prof. Sondipon Adhikari is the chair of Aerospace Engineering in the College of Engineering of Swansea University (from April 2007) and a Fellow of the Royal Aeronautical Society (from April 2017). In 2010 he received the Wolfson Research Merit Award from the Royal Society (UK academy of sciences). He was an Engineering and Physical Science Research Council (EPSRC) Advanced Research Fellow (2004-09) and winner of the Philip Leverhulme Prize (2007) in Engineering (given to an outstanding scholar under the age of 35). He received his Ph.D. in 2001 as a Jawaharlal Nehru Memorial Trust scholar at the Trinity College from the University of Cambridge. He was a lecturer at the Bristol University (2003–07) and a Junior Research Fellow at Fitzwilliam College, Cambridge (2001–03). From 2015, he has been a Distinguished Visiting Professor at the University of Johannesburg. He was a visiting Professor at Carleton University (Canada, 2006) and a visiting scientist at the Los Alamos National Laboratory (USA, 2006). In 2008, he was an official visitor to the Cambridge University Engineering Department and a visiting Fellow of Fitzwilliam College, Cambridge. In January 2016, he was a visiting Professor at the University of Paris East.

Professor Adhikari's research stands on three fundamental footings - structural dynamics, probabilistic methods and computational mechanics. Specific research areas include uncertainty quantification in computational mechanics, dynamics of complex systems, inverse problems for linear and non-linear dynamics, vibration energy harvesting, wind turbines and dynamics of nanoscale systems. He has obtained more than £2.5M of competitive research funding as a principal investigator, published 5 books, 286 peer-reviewed journal papers (Scopus h-index = 51) and more than 185 conference papers in these areas. He was the recipient of the Jawaharlal Nehru Memorial Trust (London) scholarship at the Trinity College, Cambridge (1997). In 1999, he had won the best student paper prize (John Winbolt Prize) from the Cambridge University, for a single-authored paper in the AIAA Journal. In 2001, he had won the second prize from the Acoustical Society of America, for the best student paper/presentation in the 141st Meeting in Chicago. Later that year he received the junior research fellowship (in science and engineering) from Fitzwilliam College, Cambridge. Professor Adhikari received the

EPSRC advanced research fellowship award in 2004. He was a member of the winning project team in the EPSRC Ideas factory Workshop (January 2006) on Scientific Uncertainty and Decision-Making (awarded £338,591). Prof. Adhikari had won three highly competitive Newton Fellowships, two Marie Curie International Fellowships and the Newton-Bhabha award.

Prof. Adhikari has been an Associate Editor for the Shock and Vibration Journal between 2006–2011. He is a technical reviewer for over 120 international journals, 20 conferences and 15 funding bodies. He is a member of the American Institute of Aeronautics and Astronautics (AIAA) Nondeterministic Approaches Technical Committee (NDA-TC) and Uncertainty Quantification and Model Validation (UQMV) technical division of the Society for Experimental Mechanics (SEM). Professor Adhikari is a member of the Engineering and Physical Sciences Research Council (EPSRC) peer-review college. He has been a research grant reviewer for Nuffield foundation, NRF (National Research Foundation), South Africa, US Department of Energy and Science and Technology, book reviewer for Wiley, Elsevier/Butterworth-Heinemann Publishers and Royal Aeronautical Society.

Prof. Anjan Dutta is HAG Professor in the Department of Civil Engineering, IIT Guwahati, India. He had his Bachelor degree from REC Silchar, Master's degree in Structural Engg from IIT Madras and Ph.D. from IIT Delhi. He worked as Lecturer at REC Silchar, as assistant professor and associate professor at IIT Guwahati, and is presently a professor in the same institute.

He has 59 publications in international referred journals, many papers in international and national conferences. His research interests are: Finite Element method, Bridge Engineering, Optimization, Structural Control, Health Monitoring, Structural Retrofitting. He was a Gold medalist of Gauhati University (B.E.), received Commendation certificate from IRC and was felicitated as Eminent Engineer by Institute of Engineers (India). He has a patent on "Elastomeric Seismic Isolation with High Damping Capacity and Manufacturing Method Thereof". Based on this patent philosophy, a two-storey Masonry building supported on isolators has been constructed in Tawang, Arunachal Pradesh, India. This is the first prototype building in the world on Fibre Reinforced Elastomeric Isolators. He has guided 11 Ph.D. scholars, and is currently supervising another half a dozen scholars. He has completed 9 sponsored research projects. He has published one book chapter. Prof. Dutta has contributed a large number of consultancy services to many prestigious projects. He is member of various committees and has rendered services to IIT Guwahati, in various capacities like Dean (Institute Works), Head of the Department, etc.

Prof. Satyabrata Choudhury is working as a Professor in the Department of Civil Engineering, NIT Silchar, India. He has been a faculty of this institute since 1983, first as Lecturer and then as Assistant Professor, and now as Professor. Prof. Choudhury obtained his bachelor's degree in Civil Engineering from REC Silchar (Now NIT Silchar), India. He obtained his master's degree in Structural Engineering from IIT Kharagpur, and Ph.D. in Earthquake Engineering from IIT

Roorkee. He has served in various administrative positions in the institute including: Head of the Department, Dean (P&D), Coordinator of various activities.

He has received various awards including President of India's prize, Dr. Jai Krishna Gold medal (two times), Institution prize (IEI), etc.

His area of research is Performance-based seismic design. He has 17 papers in international peer reviewed journals, 6 papers in national journal and number of papers in international and national conferences. He has supervised about 50 M. Tech. dissertations, produced two Ph.D. and working with another 10 Ph.D. scholars. He has evolved a new design methodology named as Unified performance-based design (UPBD) which accommodates both drift and performance level as target design objectives. This method also provides member sizes.

Seismic Control and Performance of Passive Hybrid Damper Under Near-Field Earthquakes



Swabarna Roy, Swagato Das, and Purnachandra Saha

Abstract In structural engineering aspect, the inherent structural property of the building is not sufficient to control the structural response when it comes to strong earthquakes. The common control strategy used by researchers makes use of energy dissipating devices that absorb the energy imparted to the structure due to earthquake and dissipate the energy by their hysteresis nature. In this study, seismic response of a G + 4 storey building installed with a hybrid damper has been investigated. The hybrid damper system comprises of Viscous Fluid Damper (VFD) and Shape Memory Alloy (SMA). The performance of the building under near-field earthquakes, Tabas, Kobe, and Gebze earthquakes has been evaluated. The dampers have been installed at the base of the superstructure. SMA exhibits a good self-centering capability and is known for its superior super-elasticity properties. It is capable of dissipating energy through its hysteresis nature while maintaining a low level of residual displacement. VFD dissipates energy through the movement of fluid inside it, which minimizes both stress and displacement the structure due to seismic effect. The time history analysis result shows the effectiveness of hybrid damper for controlling the seismic forces acting on the structure. In this present study, there is a significant reduction in base shear and displacement by about 16% and 8% by using Hybrid damper when compared to VFD and SMA dampers. A comparative study is made showing the effect of the Hybrid damper in reducing the seismic responses for the selected near-field earthquakes.

Keywords Shape memory alloy · Viscous fluid damper · Hybrid damper · Near-field earthquakes · Passive energy dissipation devices

S. Roy (✉) · P. Saha
School of Civil Engineering, KIIT Deemed to be University, Bhubaneswar, Odisha, India
e-mail: swabarnaroy0210@gmail.com

P. Saha
e-mail: dr.purnasaha@gmail.com

S. Das
Department of Civil Engineering, C. V. Raman Global University, Bhubaneswar, Odisha, India
e-mail: swagatodas83@gmail.com

1 Introduction

In recent years the use of base isolators for seismic protection of structures has attracted the interest of many researchers. During an earthquake, a finite quantity of energy in the form of vibration is stuck directly at the base of the structure, so the technique of isolating the base has been adopted to preserve the stability of the structure. The flexibility of the connection or dampers between the substructure to superstructure produces enough counter-response to the ground excitation remaining the structure sustainable. The performance of the base isolation system depends upon the capacity by which the system's fundamental frequency can be shifted to a value lower than that of the unmodified structure and its capacity to dissipate energy [1].

With the advancement in technologies, there is an increasingly important role of passive energy dissipation system for seismic protection of structures. The passive dampers when installed on a structure functions by absorbing a part of the input seismic energy and hence, minimizing the amount of energy needed to be dissipated by the primary structural members, thus reducing possible structural damages. The passive dampers are mainly categorized into rate-independent devices and rate-dependent devices [2]. The mechanical response of rate-dependent devices depends on the relative velocity between the ends of the device. For example, viscoelastic fluid dampers (VFD) are rate dependent devices which have dynamic behavior characterized by their ability to lower stiffness values within a range of given frequencies and have a negligible influence on the fundamental natural frequency. Shape Memory Alloys (SMA) dampers are rate-independent devices whose mechanical responses depend on displacement occurring between both the ends of the device and describes by nonlinear hysteretic models. SMAs exhibit several unique properties such as recovery to original shape after large deformation due to the effect of heating (shape memory effect) or due to the object being loaded (super-elasticity) [3]. Re-centering, high damping capacity, minimal maintenance, high fatigue resistance, and durability are the characteristics which make SMAs an effective damping device or a base isolator [4, 5]. In case of SMA, a hysteretic cycle is obtained which reduces the transmission of energy to the structure by the help of a hysteretic cycle, which dissipates energy within its own area [6].

In this study, a G + 4 storey building has been modeled and the performance of the building under near-field earthquakes taking into consideration the Tabas earthquake, Kobe earthquake, and Gebze earthquake. The present study aims to compare the performance of isolation system when the individual dampers, VFD and SMA, and Hybrid damper, combination of both VFD and SMA, are installed at the base of the structure.

Table 1 Details of the near-fault earthquakes considered for study

Earthquake	Distance (km)	PGA (g)	Magnitude	Year
Tabas (Boshrooyeh station)	17	0.8	7.4	1978
Kobe (Kakogawa station)	22.5	0.8	6.9	1995
Gebze (Yarimca station)	22.7	0.3–0.4	7.4	1999

2 Near-Field Earthquakes

The earthquakes occurring on the earth's surface close to the fault are referred to as near-field earthquakes. The distance ranges from 10–60 km around the fault [6]. These earthquakes have long-pulse periods and high accelerations. During fault rupture, a part of the wave is transferred to the site location, and if the site is in the same direction, they get closer to each other, thus generating a large pulse which dampens with time length during which waves gets to the structure. But in case of the site being located in the opposite direction to that of the occurred fault, the distance between the site and the waves increases incrementally, and hence longer time is required for the waves to reach the structure [7]. Due to this long period of oscillation, which may sometimes be too close to the natural oscillation, the structure tends towards resonance condition. This condition causes more structural damages and more fragile behavior of the structure. Table 1 below shows details of some near-fault earthquakes considered in the present research study.

3 Shape Memory Alloy (SMA)

Seismic Isolation system using Shape Memory Alloy or SMA has attracted good attention as a smart material and has been used effectively in passive protection of structures [8]. Shape memory effect and super-elasticity are two unique properties of SMA, in which the former refers to the property by which the SMA retains the predefined shape and returns back to it when agitated and the latter refers to the property by which SMA undergoes large inelastic deformations and recovers its own shape upon unloading [9]. The schematic diagram of an SMA damper is shown in Fig. 1. When under excitation, the SMA dampers generate a controlled force which makes the main structure safe against earthquake. The schematic diagram of the working of SMA damper is shown in Fig. 2. The SMA dampers follow the passive control concept by which it absorbs major part of input energy due to seismic activity, or undergoes major damage, keeping the structural members in the elastic limit or makes sure that the structure undergoes minimal damage.

No external power source is required for a passive control system and structural control using SMAs makes use of its damping property to reduce the structural response and subsequent structural damage subject to severe vibration or loading [9]. The hysteresis loop for the SMA Damper is shown in Fig. 3. The hysteresis loop for

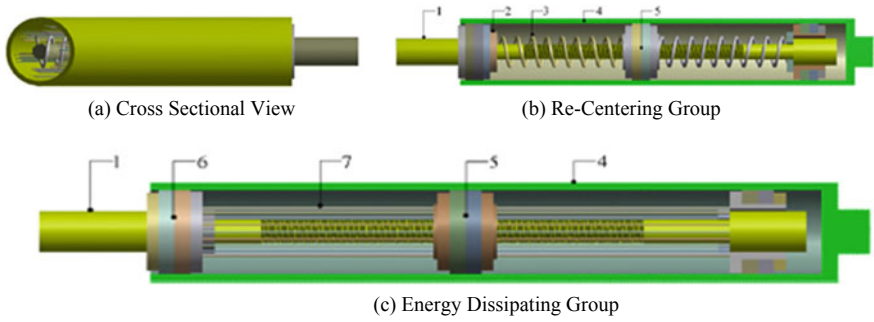


Fig. 1 Schematic detailed figure of SMA Damper showing (1) Internal Shaft, (2) Shim Plate, (3) Pre-Compressed Spring, (4) External Tube, (5) Middle Anchor, (6) Side Anchor, and (7) SMA wires [10]

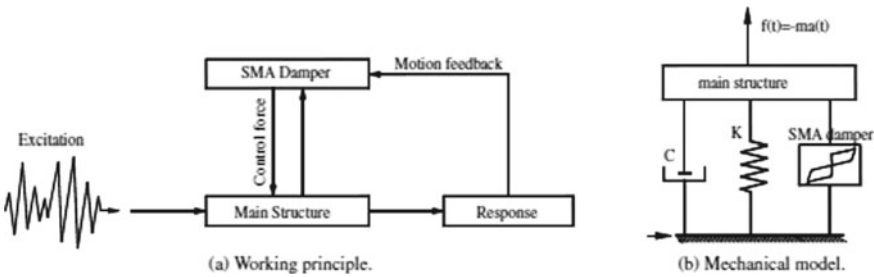


Fig. 2 Schematic diagram of performance evaluation passive structure [10]

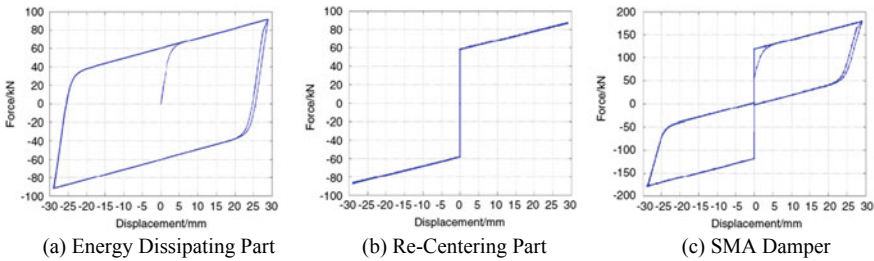


Fig. 3 Hysteresis loop for SMA Damper as presented using Bouc-Wen model [10]

energy dissipation and re-centering has been shown in Fig. 3a and b, respectively. The combination of the behavior of both these functional groups represents the hysteresis loop for SMA damper which is represented in Fig. 3c. Thus, the graph shows both self-centering capability and maximum energy-dissipating capacity. As discussed, SMA damper, being highly nonlinear material, is difficult to model based on some fixed rules. However, the mathematical model for hysteresis loop of SMA damper is effective for a damper control structure [10].

The energy dissipating device restoring force is shown as [11]:

$$F_{\text{restore}} = \alpha K_0 x + (1 - \alpha) K_0 Z_s \quad (1)$$

where x is the displacement or the elastic part, α indicates the ratio between post-yielding to pre-yielding stiffness, K_0 is the linear stiffness, and Z_s is the hysteresis part of the isolator displacement. The maximum displacement in the austenite phase is denoted by a and b , and is the displacement responsible for martensitic transformation. In order to linearize the complex nonlinear equation of the hysteresis curve, a linearized equation is introduced which minimizes the residual error of the nonlinear and linear terms of governing equation of motion. The simplified linearized version of Z_s is given as Eq. 2 [12, 13]:

$$Z_s = [1 - \text{sgn}\{\text{sgn}(|x_s| - a) + 1\}]x_s + \frac{\{\text{sgn}(|x_s| - a) + 1\}}{2} \left[\frac{\{\text{sgn}(x_s) + \text{sgn}(\dot{x}_s)\}}{2} (b - a) + a \text{sgn}(x_s) \right] \quad (2)$$

where $\text{sgn}(x_s)$ is signum function:

$$\text{sgn}(x) = \begin{cases} 1 & \text{if } x_s > 0 \\ 0 & \text{if } x_s = 0 \\ -1 & \text{if } x_s < 0 \end{cases}$$

4 Viscous Fluid Damper (VFD)

The implementation of Viscous fluid damper (VFD) has been recently adapted for seismic protection of buildings. A Viscous fluid damper comprises of piston within a damper housing which is filled with silicon oil acting as a fluid [2]. The piston consists of numerous small orifices through which the movement of fluid occurs from one part of the piston to the other part. The schematic cross-sectional figure of VFD is shown in Fig. 4. When the piston rod is stroked, the fluid is pressurized to flow through the orifices. This creates a pressure differential across the piston head which produces very large forces, thus resisting the relative motion of the damper [14, 15]. The fluid flows at a higher velocity thus resulting in the generation of friction force between fluid particles and piston head. This force is responsible for energy dissipation in the form of heat. This damping force reduces both stress and displacement in the structure. In a viscous fluid damper, the resistive control force is:

$$f = C_d |\dot{x}b|^\lambda \text{sgn}(\dot{x}b) \quad (3)$$

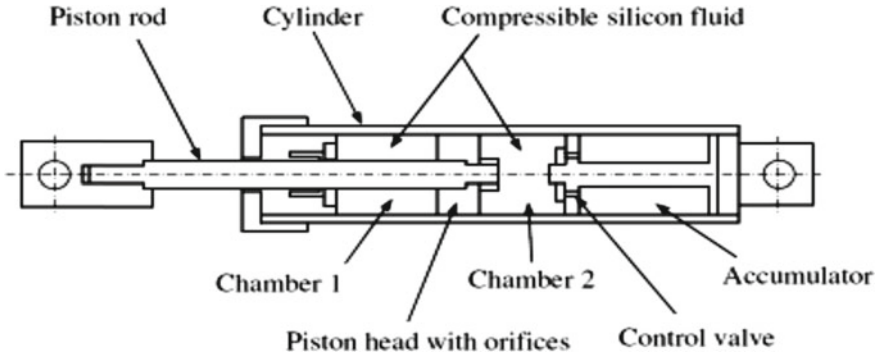
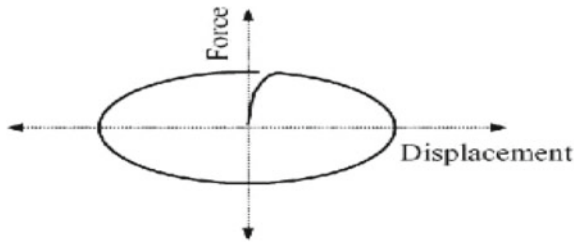


Fig. 4 Schematic cross-sectional figure of VFD [14]

Fig. 5 Force Displacement relation in case of VFD [14]



In the above equation, f indicates damping force, C_d indicates damping coefficient with units of force per velocity, $\dot{x}b$ indicates velocity across both the ends of damper, λ indicates velocity exponent whose value ranges between 0.4 and 1.4. The force–displacement relation of VFD is shown in Fig. 5. The performance of passive VFD depends upon its velocity exponent (λ) and damping coefficient (C_d).

5 Numerical Study

A G + 4 model R.C.C. framed structure was analyzed using MATLAB [16] for the three earthquakes to study the performance of the hybrid control system. The building is a 3 * 3 bay-framed structure with a ground-level height of 5.2 m, storey height of 3.1 m, and bay distance of 5 m as shown in Fig. 6. The time history analysis is performed using the State Space Method on the equations of motion in order to obtain the structural response of the building [17].

The equation of motion for SDOF system may be written as (Eq. 4) [18, 19]

$$M\ddot{X}(t) + C\dot{X}(t) + KX(t) = -M\ddot{U}_g + F_E(t) \quad (4)$$

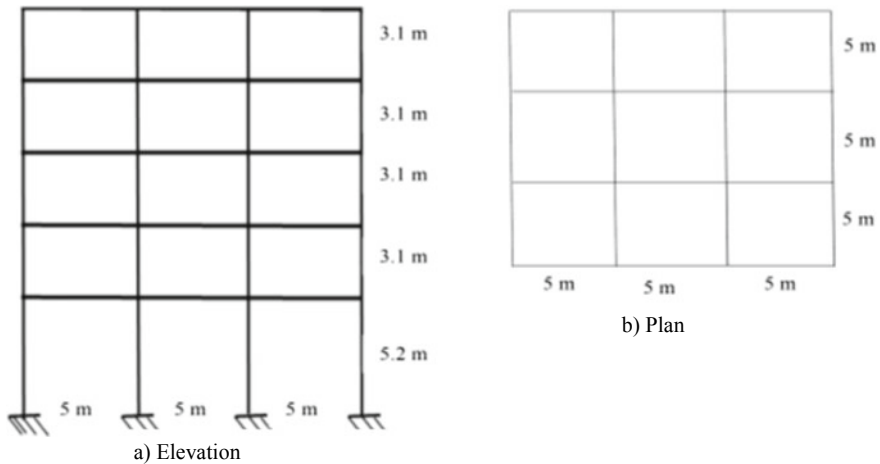


Fig. 6 The Basic Structural Frame of G + 4 building (a) Elevation and (b) Plan

where, $F_E(t)$ the external force, M indicates the mass matrix, C indicates the damping ratio matrix, K indicates the stiffness matrix, \ddot{U}_g is ground acceleration, $X(t)$, $\dot{X}(t)$, and $\ddot{X}(t)$ are displacement, velocity, and acceleration, respectively.

State Space Equation has been employed for smart base isolation structural problem and is given by Eq. 5.

$$\dot{x}(t) = Ax(t) + Bu(t) + E\ddot{U}_g(t) \quad (5)$$

where $u(t) = f_d(t)$ is the time-varying control device force, x consists of the states, and A , B , and E are the system matrices defined as

$$A = \begin{bmatrix} 0 & I \\ -M^{-1}K & -M^{-1}C \end{bmatrix}, B = \begin{bmatrix} 0 \\ M^{-1}\Lambda \end{bmatrix}, E = -\begin{bmatrix} 0 \\ \Gamma \end{bmatrix}$$

where Λ and Γ are the location of the device and the earthquake influence vector, respectively.

Time history analysis is performed using near-field earthquakes taking into consideration the three earthquake ground motions namely Tabas (1978), Kobe (1995), and Gebze (1999) earthquake to obtain the uncontrolled and controlled structural responses of the building. The time history of the earthquakes for a time period of 60 s is shown in Fig. 7. Passive damper SMA and VFD and Hybrid are installed at the base of the structure. The effectiveness of the Hybrid Damper is investigated against individual dampers. Time history analysis is performed for the uncontrolled and controlled responses under the earthquakes. The lumped masses (m_i), storey stiffness (k_i), and damping ratio (ξ_i) for every storey of the superstructure have been considered identical for the sake of simplicity. The mass ratio (ξ) (i.e., ratio between isolator mass to the total superstructure-isolation system mass) is taken as 2% and

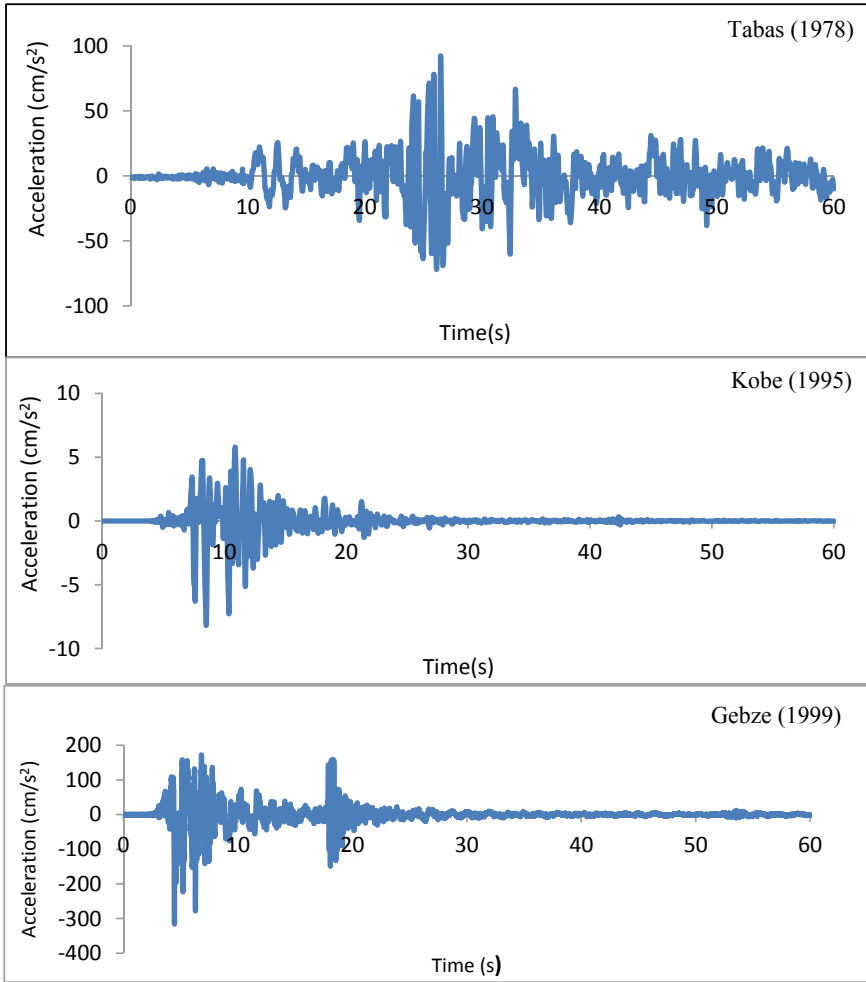


Fig. 7 Time History of Tabas (1978), Kobe (1995), Gebze (1999), respectively

the structural time period (T) is 0.55 s. The superstructure damping (ξ_b) assumed is of viscous type and taken as 5% [9]. α_s is the constant determining the ratio of pre-transformation to post transformation stiffness caused during the load deformation behavior of SMA which has been considered as 0.1. Maximum displacement in the austenite phase is represented by a and b and is the displacement responsible for martensitic transform which has been obtained from experiments conducted by Shinozuka et al. [12], and has been taken as 0.005 and 0.05, respectively. The time period (T_b) for the damper was taken as 2 s. The value of C_d considered for VFD damper is 1500. The parameters considered for the SMA damper force–deformation hysteresis loop has been shown in Table 2 [20].

Table 2 Structural parameters and SMA parameters considered for design

Structural parameters	SMA parameters
$T = 0.55 \text{ s}$	$T_b = 2 \text{ s}$
$\xi = 2\%$	$\xi_b = 5\%$
	$\alpha_s = 0.10$
	$a = 0.005$
	$b = 0.05$

6 Results and Discussions

The time history analysis has been performed in order to calculate the structural responses of the structure for the three specified near-field earthquake ground motions. The three specified near-field earthquakes are: (1) 1978 Tabas (Boshrooyeh station) with PGA (peak ground acceleration) equals to 0.8 g having a hypocentral distance of 17 km; (2) 1995 Kobe (Kakogawa station) with PGA value equals to 0.8 g and hypocentral distance 22.5 km; (3) 1999 Gebze (Yarimca station) with PGA value equals to 0.3–0.4 and the hypocentral distance of 22.7 km.

From the earthquake data, a comparison has been carried out between base shear and displacement for uncontrolled structure and structure fitted with dampers. The time variation of the displacement response of the earthquakes for a damping ratio of 1.5% for VFD and 2% for SMA and Hybrid damper combination of SMA and VFD are shown in Fig. 8. In this figure, the displacement response of the structure has been compared for both uncontrolled structure and structure individually incorporated with SMA, VFD, and next by Hybrid of SMA and VFD. From the figures, it can be observed that when the model was applied to the Tabas earthquake, the reduction in displacement by Hybrid damper is 4% more than that of VFD and 8% more than that of SMA. Then in case of Kobe earthquake acceleration, the reduced value of displacement by Hybrid damper is about 2% and 7% more than that of VFD and SMA. While considering the Gebze earthquake acceleration data, the Hybrid damper reduces displacement by about 4% more than of VFD and 7% more than of SMA. Thus, the control system has helped to reduce the structural displacement thus preventing damage to the structure.

The base shear of the structure has been compared for the uncontrolled and SMA, VFD, and Hybrid damper incorporated structure and shown in Fig. 9. From the figure, it can be observed that the model when incorporated with a Hybrid damper under Tabas earthquake motion data reduces the base shear response by 11% more than that of VFD and 16% more than that of SMA. In case of Kobe earthquake acceleration, the Hybrid damper reduces the base shear responses by about 10% and 13% more than that of VFD and SMA. Further, under Gebze earthquake motion the Hybrid damper is effective in reducing the base shear response by 4% more than VFD and 7% more than SMA. Thus, the hybrid damper is successful in absorbing the input seismic energy and dissipating the same more effectively than VFD and SMA, thus protecting the main structure from damage. As a whole, considering all the three earthquake

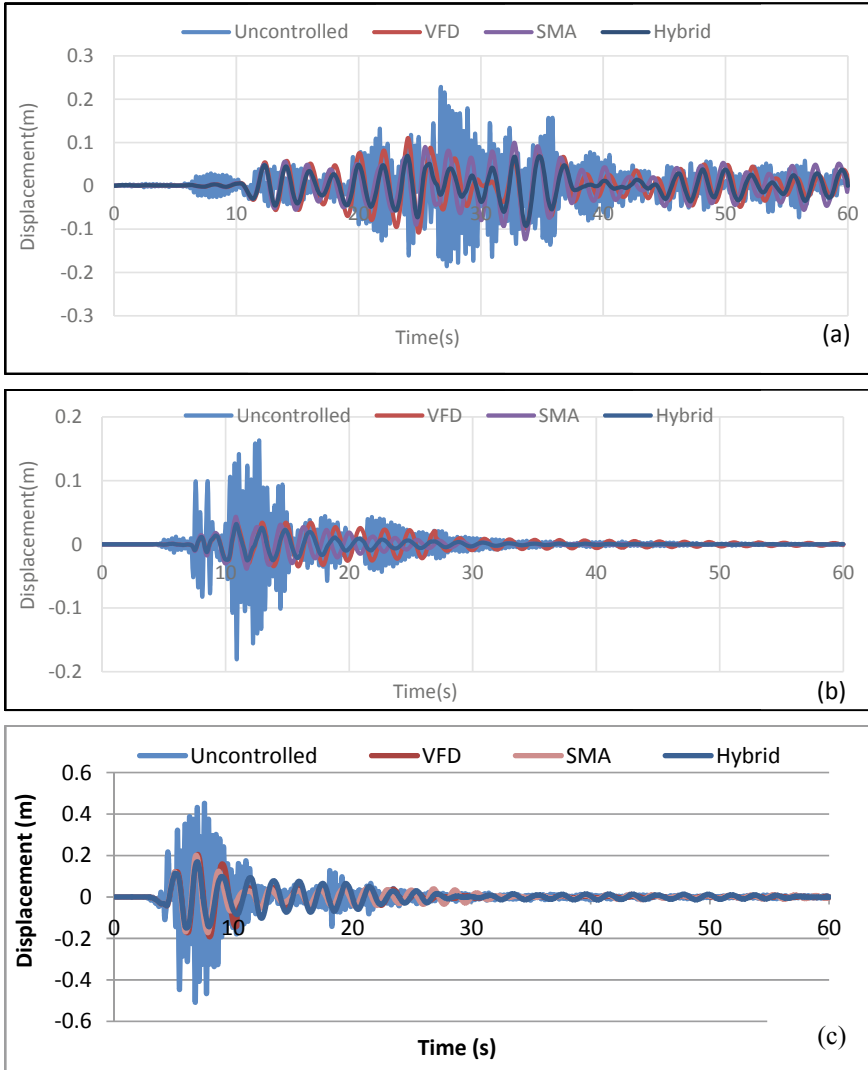


Fig. 8 Uncontrolled and displacement controlled by the dampers for **a** Tabas (1978), **b** Kobe (1995), **c** Gebze Earthquake (1999)

motions, we can say that maximum reduction in displacement and base shear using Hybrid damper is obtained as 8% and 16%, respectively, when compared to VFD and SMA. With the application of Hybrid damper both the displacement and base shear has been controlled and the damage to the structure due to long duration, near-field earthquakes can be prevented. Thus, the structural responses of the structure have been reduced, hence proving the effectiveness of the Hybrid damper.

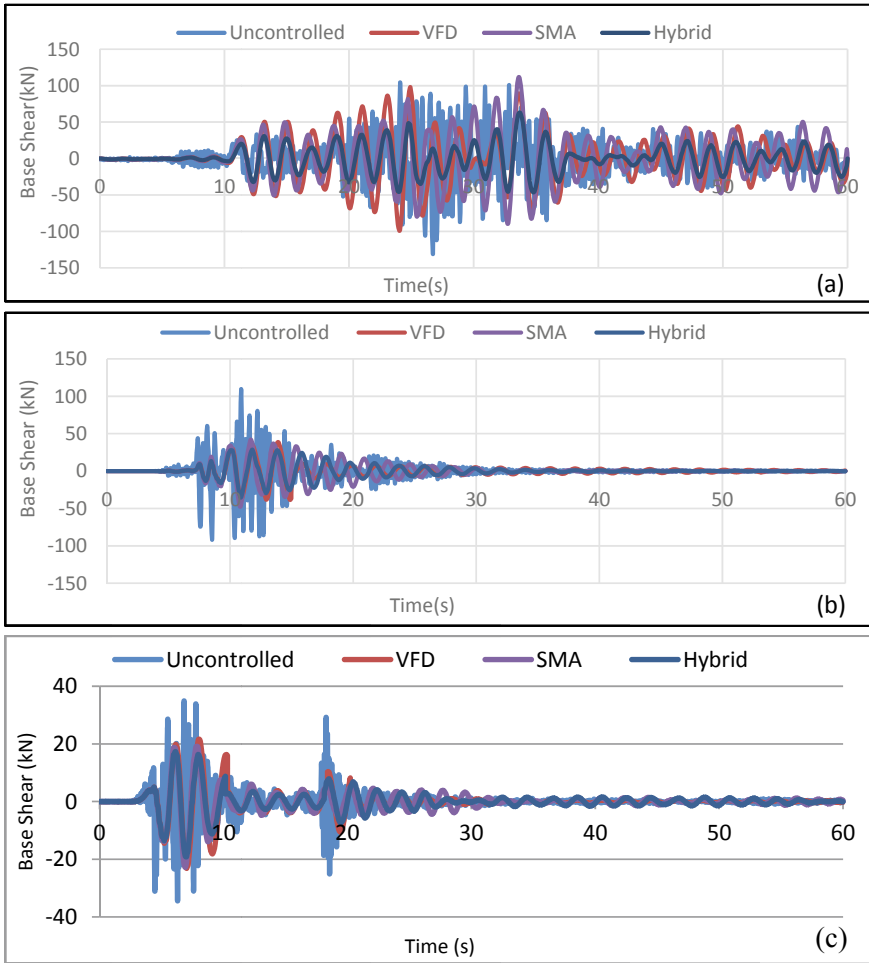


Fig. 9 Uncontrolled and controlled base shear responses by the dampers for **a** Tabas (1978), **b** Kobe (1995), **c** Gebze Earthquake (1999)

7 Conclusion

In this paper, a G + 4 building has been modeled and an attempt is made to compare the effectiveness of Hybrid damper which comprises of VFD and SMA combined. The performance of the building is under three near-field earthquakes, Tabas, Kobe, and Gebze are investigated. Based on the investigation, the performance of Hybrid damper is found to be better than the performance of individual VFD and SMA, in regard to seismic response control of the building. The hybrid damper is found to be robust as it works on the combined principle of energy dissipation property from

VFD and re-centering ability from SMA. The following conclusions are drawn from the research paper:

1. Generally, the near-field earthquake causes higher structural damage but with the application of a Hybrid damper, the G + 4 structure was seismically controlled, hence showing good dampening performance and damage reduction.
2. Higher reduction in seismic response of building can be obtained by the installation of a Hybrid damper in the base of the building than that of VFD and SMA installed individually at the base.
3. Reduction in seismic response displacement of the building using Hybrid Damper is obtained as about 4% more than that of VFD alone and 8% more than that of SMA alone.
4. The reduction in the shear response of base using hybrid damper has been observed to be about 11% more than that of VFD and 16% more than that of SMA for all the three earthquakes, hence showing that hybrid damper is better in mitigating floor displacement and base shear.

References

1. Ibrahim RA (2008) Recent advances in nonlinear passive vibration isolators. *J Sound Vib* 314:371–452
2. Castaldo P (2014) Passive energy dissipation devices. In: *Integrated seismic design of structure and control systems*. Springer, Switzerland, pp 21–62
3. Sepulveda J, Boroschek R, Herrera R (2008) Steel beam-column connection using copper-based shape memory alloy dampers. *J Constr Steel Res* 64:429–435
4. Motahari SA, Ghassemieh M, Abolmaali SA (2007) Implementation of shape memory alloys dampers for passive control of structures subjected to seismic excitations. *J Constr Steel Res* 63:1570–1579
5. Des Roches R, Mc Cormick J, Delemont MA (2004) Cyclical properties of superelastic shape memory alloys. *ASCE J Struct Eng* 130(1):38–46
6. Heydari M, Mousavi M. The comparison of seismic effects of near-field and far-field earthquakes on relative displacement of seven-storey concrete building with shear wall. *Int Res J Environ Sci (Iran)*
7. Taheri JS, Anderson JG (1988) The 1978 Tabas, Iran earthquake: An interpretation of the strong motion records. *Bull Seismol Soc Am* 78(1):142–171
8. Ozbulut E, Hurlbauss S (2010) Evaluation of the performance of a sliding-type base isolation system with a NiTi shape memory alloy device considering temperature effects. *Eng Struct* 32:238–249
9. Song G, Li HN (2006) Applications of shape memory alloys in civil structures. *Eng Struct* 28:1266–1274
10. Ma H, Yam MCH (2011) Modelling of a self-centring damper and its application in structural control. *J Constr Steel Res* 67: 656–666 (Elsevier)
11. Ikhrouane F, Rodellar J (ed) (2007) *Systems with hysteresis: analysis, identification and control using the Bouc–Wen model*. Wiley, Chichester (England, Hoboken, NJ)
12. Shinozuka M, Chaudhuri SR, Mishra SM (2015) Shape-Memory-Alloy supplemented Lead Rubber Bearing (SMA-LRB) for seismic isolation. *J Sound Vib* 41:34–45
13. Yan X, Nie J (2000) Response of SMA super elastic systems under random excitation. *J Sound Vib* 238(5):893–901

14. Kumar PS, Naidu MV, Mohan SM, Reddy SS (2016) Application of fluid viscous dampers in multi-story buildings. *Int J Innov Res Sci Eng Technol* 5(9):17064–17069
15. Marko J, Thambiratnam D, Perera N (2006) Study of viscoelastic and friction damper configurations in the seismic mitigation of medium-rise structures. *J Mech Mater Struct* 1(6):1001–1039
16. MATLAB. The Math Works Inc. Natick Massachusetts (2010)
17. Saha P, Jangid RS (2009) Seismic control of benchmark cable stayed bridge using passive hybrid systems. *IES J Part A Civ Struct Eng* 2(1):1–16
18. Chopra AK. *Dynamics of structures—theory and applications to earthquake engineering*. Prentice Hall
19. Elnashai AS, Sarno LD (2008) *Fundamentals of earthquake engineering*. Wiley
20. Roy S, Das S, Saha P (2018) Seismic response control of a building using passive hybrid damper. In: *Structural engineering convention-2018*. Jadavpur University Press, Jadavpur University, Kolkata

Wall Effects on Terminal Velocity of Test Fuel Bundle in the Fuel Test Loop of High Flux Research Reactor



G. Verma, S. Sengupta, S. Mammen, P. Mukherjee, and P. V. Varde

Abstract Fuel Test Loop (FTL) is a self-contained independent experimental loop which is designed for testing of nuclear fuel materials under simulated power reactor conditions in the High Flux Research Reactor being developed at BARC. It is a high-pressure loop with maximum operating pressure up to 17.5 MPa and maximum operating temperature up to 330 °C. The In-Pool Test Section of the FTL consists of a series of concentric tubes with different thicknesses and functionality. The test fuel bundle resides within the innermost Fuel Tube which is further enclosed within an internally insulated Pressure Tube which acts as a pressure boundary enclosure to the test fuel bundles. The present work deals with the investigation of wall effects on the terminal velocity of test fuel bundles falling under gravity within the In-Pool Test Section. While loading/unloading of the test fuel bundle, accidentally the fuel bundle may fall under the influence of gravity within the fluid filled Fuel Tube. The minimum gap between the fuel bundle and the fuel tube is 2 mm. Thus, the wall effects on the velocity of the falling fuel cannot be neglected. The purpose of the present work is to estimate this wall effects on the terminal velocity of the falling fuel in terms of Drag Coefficient. This involves, initially estimating drag characteristics and terminal velocities with wall effects for different geometries, and finally predicting the overall characteristics with the test fuel bundle as the geometry

G. Verma (✉) · S. Sengupta · S. Mammen · P. Mukherjee
Research Reactor Design and Projects Division, Bhabha Atomic Research Centre, Mumbai
400085, India
e-mail: gaurav91verma@gmail.com

S. Sengupta
e-mail: samsen@barc.gov.in

S. Mammen
e-mail: mshaji@barc.gov.in

P. Mukherjee
e-mail: pradipm@barc.gov.in

P. V. Varde
Research Reactor Services Division, Bhabha Atomic Research Centre, Mumbai 400085, India
e-mail: varde@barc.gov.in

of interest. To fulfill this objective, an analytical methodology is established which has been validated through a commercial code.

Keywords Terminal velocity · Test fuel bundle · Wall effect · Drag coefficient

Nomenclature

C_D	Drag coefficient
Re	Reynolds Number
f	Velocity ratio or wall factor
U_t	Terminal velocity in confined medium
$U_{t\infty}$	Terminal velocity in infinite medium
d_p	Diameter of sphere
ρ_p	Density of sphere
D	Fall Tube Diameter
ρ_f	Fluid Density
μ	Fluid Viscosity
λ	Sphere-to-tube diameter
d_s	Diameter of sphere with volume equal to that of nonspherical particle
L	Length of the Cylinder
V	Volume of the object
d_A	Projected Area Diameter
A_p	Projected Area
k	Volumetric Shape Factor
φ	Sphericity
A_v	Surface area of a sphere having the same volume as of the particle
m_p	Mass of the particle
g	Gravitational acceleration
d_c	Cylinder diameter
Ga	Galileo Number
Ga'	Modified Galileo Number
E	Aspect ratio of the nonspherical particle
Re _T	Reynolds Number in the Newtonian Regime
Re _L	Reynolds Number in the Stokes and Transitional flow regime
T_1, T_2	Weighting Factor

1 Introduction

The FTL in the proposed High Flux Research Reactor (HFRR) is a high-temperature and high-pressure experimental loop to perform testing of nuclear fuel of power reactors under similar conditions. The maximum operating pressure and temperature

of the FTL is 17.5 MPa and 330 °C, respectively. The FTL consists of two sections, the In-Pool Test Section and Out-of-Pool Section. The In-Pool test section provides a pressure boundary enclosure to the test fuel bundles and also a separation between test section high-temperature/pressure water with the pool water. It is designed such that it maintains its mechanical strength and structural integrity over the lifetime of the reactor. The Out-of-Pool section consists of various process systems (such as Main Loop System, Purification and Sampling System, Pressurizer System, Jacket Coolant System, etc.), piping, and equipment necessary to maintain the required temperature, pressure, and flow conditions inside the In-Pool test section.

The In-Pool Test Section of the FTL consists of a series encapsulation of four concentric tubes (Fuel Tube, Pressure Tube, Inner Jacket Tube, and Outer Jacket Tube) with different thickness and functionality. The present work investigates wall effects on the terminal velocity of test fuel bundles accidentally falling under gravity within the 4.5 m long fuel tube of the In-Pool Test Section while loading/unloading of the test fuel bundle. Since minimum gap between the falling fuel bundle and the fuel tube is very small, the wall effects on the falling fuel velocity need to be established. The present work estimates this wall effects on the terminal velocity of the falling fuel in terms of Drag Coefficient. For this, drag characteristics and terminal velocities with wall effects for different geometries are estimated which is further utilized to estimate these characteristics for the geometry of interest using an established analytical methodology which is subsequently validated with fluid–solid interaction coupled techniques through a commercial code (ESI CFD-ACE+).

2 Analytical Methodology

According to Gabitto and Tsouris [1], an object falling in an infinite fluid medium under the influence of gravity will accelerate until the gravitational force is exactly balanced by the resistance force that includes buoyancy and drag. This constant velocity, hence achieved is termed as “terminal velocity”. Correlations are developed by various researchers (Clift et al. [2], Kahn and Richardson [3], and Haider [4]) that relates drag coefficient (C_D) and the Reynolds Number (Re) for objects of spherical shape falling at their terminal velocities in an infinite medium. Further, there have been literature suggesting the retarding effects of the nearby wall on an object settling in a liquid. Most of these investigations have involved a single sphere settling in cylindrical/triangular/rectangular ducts in either Newtonian or Non-Newtonian fluids [5–7]. However, not much literature is available for complex geometries falling in a confined flow passage under the influence of gravity.

To introduce the wall effects on the motion of a sphere falling axially in a cylindrical tube filled with a stagnant fluid, as per Arsenijevic et al. [8], velocity ratio (f) or the wall factor is defined as

$$f = \frac{U_t}{U_{t\infty}} = (1 - 1.12\lambda^{1.26})^{0.7} \quad (1)$$

where U_t is the terminal velocity of the falling sphere (diameter d_p and density ρ_p) settling along the axis of a tube of diameter, D , in a fluid medium of density (ρ_f) and viscosity (μ), whereas $U_{t\infty}$ denotes the unbounded velocity of the same sphere in the same liquid in the absence of walls. λ denote the ratio of the sphere-to-tube diameter (d_p/D). Other widely used correlations in the turbulent flow regime are those of Newton [9], as shown in Eq. (2) and of De Felice [10], as presented in Eq. (3).

$$f = (1 - \lambda^2)(1 - 0.5\lambda^2)^{0.5} \quad 0.11 \leq \lambda \leq 0.83 \quad (2)$$

$$f = \left(\frac{1 - \lambda}{1 - 0.33\lambda} \right)^{0.85} \quad (3)$$

For nonspherical particles (such as cylinders), Chhabra [11], correlated the wall factor as

$$f = 1 - 1.33(d_s/D) \quad (L/D) < 10 \quad (4)$$

$$f = 1 - 3.58(d_s/D) \quad (L/D) > 10 \quad (5)$$

where d_s is the diameter of a sphere with volume equal to that of a nonspherical particle and D is the fall tube diameter through which the cylinder is falling. The length of the cylinder is taken as L .

In order to calculate the terminal velocity of the cylindrical object, various empirical relations have been proposed. One such factor is the ‘‘volumetric shape factor’’ defined by Heywood [12] as

$$k = \frac{V}{d_A^3} \quad (6)$$

where, V is the volume of the object and $d_A = (4A_p/\pi)^{0.5}$ is the projected area diameter, which is calculated as the diameter of a sphere with the equal projected area as that of the particle, and A_p is the projected area of the object.

The degree of sphericity is given by Wadell [13] as

$$\phi = \frac{A_V}{A} \quad (7)$$

where A_V is the surface area of a sphere having the same volume as that of the particle, and A is the actual surface area of the particle. The sphericity of a true sphere is equal to 1.

For spherical objects, a number of C_D -vs- Re correlations are available depending on the Reynolds number range. In the present study, a two termed correlation developed by Cheng [14], is used to estimate the drag coefficient. According to this relation

$$C_D = \frac{24}{Re}(1 + 0.27Re)^{0.43} + 0.47[1 - \exp(-0.04Re^{0.38})] \quad (8)$$

The first term is for $Re < 100$ and is an extension of Stokes law. The second term estimates drag coefficients for high values of Reynolds number.

Drag coefficient of a nonspherical object explained by Haider and Levenspiel [15], as a relation between C_D -vs- Re in the form

$$C_D = \frac{24}{Re} [1 + \exp(2.3288 - 6.4581\varphi + 2.4486\varphi^2) Re^{(0.0964+0.5565\varphi)}] + \frac{73.69Re \exp(-5.0748\varphi)}{Re + 5.378 \exp(6.2122\varphi)} \quad (9)$$

which predicts higher accuracy up to a $\varphi > 0.67$.

Terminal velocity for any object can be given as

$$U_t = \sqrt{\frac{2m_p g (\rho_p - \rho_f)}{\rho_f \rho_p A_p C_D}} \quad (10)$$

where U_t is the terminal velocity, C_D is the drag coefficient based on projected area, m_p is the object mass, ρ_p is the object density, ρ_f is the density of the surrounding fluid, A_p is the projected area of the object in the direction of the motion, and g is the gravitational acceleration.

For cylinders, Coulson and Richardson [16], developed k as

$$k = (\pi/4)^{2.5} (d_c/L)^{0.5} \quad (11)$$

Reynolds number is calculated for nonspherical particles using Galileo Number (Ga) number using Heywood's [12], method as

$$Ga = 4kd_A^3 \rho_f g (\rho_p - \rho_f) / (\pi \mu^2) \quad (12)$$

where μ is the fluid viscosity. Haider and Levenspiel [15] developed a correlation for modified Galileo number (Ga') as

$$Ga' = C_D Re^2 = \pi d_c^3 \rho_f g (\rho_p - \rho_f) / (2\mu^2) \quad (13)$$

Reynolds numbers within the Stokes and transitional flow regimes can be calculated using the following set of equations:

$$\text{Log}_{10}(\text{Re}_L) = a_0 + a_1w + a_2w^2 + a_3w^3, \quad (14)$$

where

$$w = \text{Log}_{10} \left[(\text{Ga}')^{1/3} \right], \quad (15)$$

$$a_0 = -0.81824 - 0.55689/E, \quad (16)$$

$$a_1 = 2.41227 + 1.54674/E - 0.53872/E^2, \quad (17)$$

$$a_2 = -0.2056 - 1.34714/E - 0.65696/E^2, \quad (18)$$

$$a_3 = 0.82343 - 0.40625a_0 - 0.5625a_1 - 0.75a_2, \quad (19)$$

where E is the aspect ratio (L/d_c). The procedure presented here allows for the explicit calculation of the Reynolds numbers in the Stokes and transitional flow regimes for which Ga' extends up to 200,000. For the estimation of Reynolds number in the Newton flow regimes (Re_T) as a function of the ratio of object-to-water densities and of the cylinder aspect ratio.

$$\text{Re}_T = (\rho_p/\rho_f)^{0.06} E^{0.04} \text{Ga}'^{0.5} \quad \text{for } (\text{Ga}' > 100,000) \quad (20)$$

Gabbito and Tsouris [1] provides the following equation for all the flow regimes and for aspect ratio $E > 1$.

$$\text{Re} = \text{Re}_L T_1 + \text{Re}_T T_2, \quad \text{for } (0.01 < \text{Ga}' < 10^8) \quad (21)$$

where

$$T_1 = 1 \quad \text{for } \text{Ga}' < 2 \times 10^3, \quad (22)$$

$$T_1 = (\text{Ga}^*)^3, \quad \text{for } 2 \times 10^3 < \text{Ga}' < 2 \times 10^5 \quad (23)$$

And

$$T_1 = 0 \quad \text{for } \text{Ga}' > 2 \times 10^5 \quad (24)$$

Table 1 Comparison of drag coefficients and terminal velocity between analytical and numerical procedures for the sphere in an infinite medium

Methodology	Drag coefficient (C_D)	Terminal velocity (U_t)
Analytical (Cheng model)	0.3505	1.067 m/s
Numerical simulation	0.3354	1.08 m/s
Error (%)	4.3	-1.21

where

$$Ga^* = (2 \times 10^5 - Ga') / (2 \times 10^5 - 2 \times 10^3), \quad (25)$$

And

$$T_2 = 1 - T_1 \quad (26)$$

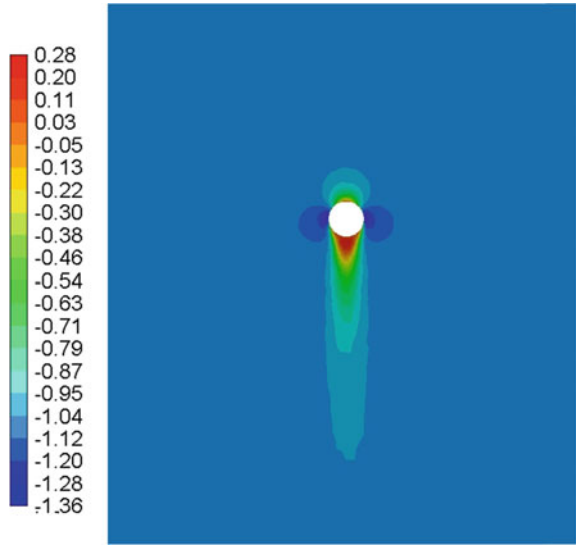
3 Benchmarking

In an effort to validate the modeling procedure and analyses, the drag coefficient of a spherical object free-falling in an unbounded medium is estimated through numerical simulation and is compared with the analytical results available in the literature. For this purpose, an Aluminum sphere of 10 mm diameter is allowed to free-fall in a cylindrical tank of 200 mm diameter and 400 mm length such that wall effects are negligible. Cheng correlation Eq. (8), is used to estimate the drag coefficient and is compared with the numerical simulation results in Table 1. Figure 1 displays the flow velocity contour across the sphere at terminal velocity. The velocity contour observed through numerical simulation provides an idea about the distance of the boundary from the falling object. Generally, higher velocity contours are observed in case when the object is falling in an unbounded medium as seen in Fig. 1. However, this trend shifts toward the decreasing velocity contour in the presence of a boundary in the vicinity. Further, the velocity contour predicts the distribution and velocity in close vicinity to the falling object.

4 Results and Discussion

In order to investigate the wall effects on terminal velocity and drag forces for the test fuel bundle (19 cylindrical pin geometry-Aluminum dummy), multiple analytical and numerical case studies are performed for cylindrical geometry by varying the nearness of the wall.

Fig. 1 Flow velocity contour across the sphere at terminal velocity in an infinite medium



4.1 Wall Effects on Terminal Velocity and Drag Coefficients of Cylinder

A number of case studies are performed, in which an Aluminum solid cylinder of dimensions comparable to that of test fuel bundle with an aspect ratio (E) of 4.615 is allowed to fall under the influence of gravity in a fall tube filled with water. In order to study the wall effects, a reduced fall tube diameter (D) is chosen for each case study. The observations are presented below.

Ratio of cylinder diameter to fall tube diameter ($d_c/D = 0.05$). In this case study, the drag coefficient and terminal velocity of the falling cylinder is estimated such that the wall effects of the fall tube diameter are negligible. Both analytical and numerical procedures are employed in this case study and its results are compared in Table 2. Equations presented by Gabitto and Tsouris [1], are used for analytical determination of the results. The analytical terminal velocity is observed to be 4.33 m/s, whereas the numerical results imply a value of 4.18 m/s having an error of 3.46%. Similarly, drag coefficients observed through analytical and numerical methods are 0.789 and 0.846, respectively, with an error of 7.17%. This suggests that both the analytical and

Table 2 Comparison of the drag coefficients and terminal velocities between analytical and numerical procedures for a cylinder in an infinite medium

Methodology	Drag coefficient (C_D)	Terminal velocity (U_T)
Analytical (Gabbito & Tsouris)	0.789	4.33 m/s
Numerical simulation	0.8456	4.18 m/s
Error (%)	-7.17	3.46

numerical results are in good agreement. Figure 2 displays the flow velocity contour across the cylinder at terminal velocity.

Ratio of cylinder diameter to fall tube diameter ($d_c/D = 0.1$). In this case study, the drag coefficient and terminal velocity of the falling cylinder is estimated for the reduced diameter of the fall tube in order to understand the influence of wall effects on the characteristics of the falling cylinder. Different analytical models and numerical procedures are employed in this case study and its results are presented in Table 3. It is important to note that not many models are available in the literature for predicting the wall effects on the free fall of cylindrical objects (only Chhabra [11]), Newton [9], and De Felice [10] models which are for spherical objects are used for comparison. As can be seen from Table 3, the velocities predicted by the analytical model are lower (especially Chhabra) in comparison to our numerical prediction. This can be explained on the basis of changing orientation during the drop through the fall tube. For all the numerical case studies, it is assumed that the principal axis of the cylinder is parallel to that of the fall tube. However, there has been no mention as such of the falling orientation in the literature by Chhabra. Since fall orientation plays a key role in changing the drag because of the higher resistance caused by increased surface area, therefore, lower velocity is predicted by Chhabra.

Ratio of cylinder diameter to fall tube diameter ($d_c/D = 0.167$). In this case study, the fall tube diameter is reduced even further in order to understand the influence of wall effects on the characteristics of the falling cylinder. Results from different analytical models and numerical methods are tabulated and are presented in Table 3.

Fig. 2 Flow velocity contour across the cylinder at terminal velocity in an infinite medium

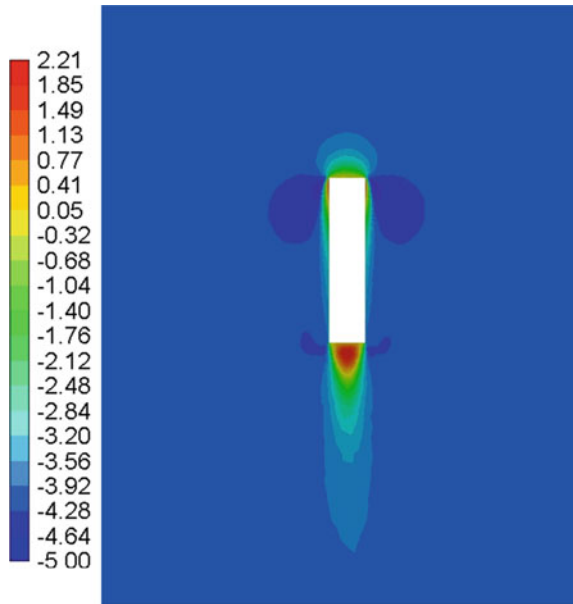


Table 3 Comparison of the drag coefficients and wall factor between analytical and numerical procedures for various cylinder diameter to fall tube diameter ratios (for cylinder diameter, $d_c = 65$ mm)

Sr. No	D (mm)	d_c/D	Methodology	Terminal velocity (U_T) (m/s)	Wall factor (f)
1	650	0.1	Chhabra model ^a	3.23	0.7465
			Newton model ^b	4.13	0.954
			De Felice model ^b	3.82	0.883
			Numerical simulation	4.14	0.99
2	390	0.167	Chhabra model ^a	2.5	0.578
			Newton model ^b	3.79	0.876
			De Felice model ^b	3.43	0.794
			Numerical simulation	3.99	0.954
3	260	0.25	Chhabra model ^a	1.58	0.366
			Newton model ^b	3.15	0.728
			De Felice model ^b	2.89	0.668
			Numerical simulation	3.86	0.923
4	130	0.5	De Felice model ^b	0.442	0.102
			Numerical simulation	2.95	0.706
5	117	0.556	Numerical simulation	2.63	0.629
6	104	0.625	Numerical simulation	2.21	0.528
7	91	0.714	Numerical simulation	1.585	0.379
8	78	0.833	Numerical simulation	0.83	0.198
9	71.5	0.91	Numerical simulation	0.335	0.08
10	68.25	0.952	Numerical simulation	0.115	0.0275

Note ^aAnalytical model for cylindrical particle; ^bAnalytical model for spherical particle

As explained in 4.1.2, Chhabra model continues to estimate lower values of the wall factor and the terminal velocity in comparison to that of the numerical values.

Ratio of cylinder diameter to fall tube diameter ($d_c/D = 0.25$). The ratio of cylinder diameter to fall tube diameter is further increased to 0.25 with increased wall effects on the fall object characteristics. Results obtained from different analytical models and numerical methods are compared in Table 3. The terminal velocity and wall factor values obtained from Chhabra are much lower than the numerical values.

Ratio of cylinder diameter to fall tube diameter ($d_c/D = 0.5$). The ratio of cylinder diameter to fall tube diameter is now increased to 0.5. Results obtained from different analytical models and numerical methods are compared in Table 3. For these diameter ratios, Chhabra and Newton model are not applicable. Further, the De Felice model predicts a much lower value of the wall factor and the terminal velocity compared to the numerical results.

Ratio of cylinder diameter to fall tube diameter ($d_c/D = 0.556$). Beyond this ratio of cylinder diameter to fall tube diameter, results from analytical models cease to exist as no literature is available for prediction of wall factor and terminal velocity for these diameter ratios which was the primary objective of the present investigation on wall effects of falling objects. Results obtained from the numerical method are presented in Table 3.

Ratio of cylinder diameter to fall tube diameter ($d_c/D = 0.625$). The ratio of cylinder diameter to fall tube diameter is further increased to 0.625 with increased wall effects on the fall object characteristics. Results obtained from the numerical method are presented in Table 3. The terminal velocity and wall factor values obtained are 2.21 m/s and 0.528, respectively.

Ratio of cylinder diameter to fall tube diameter ($d_c/D = 0.714$). In this case study, the terminal velocity and wall factor of the falling cylinder is estimated for $d_c/D = 0.714$. Numerical results for this case study are presented in Table 3. The terminal velocity and wall factor values obtained are 1.585 m/s and 0.379, respectively. It can be seen from these results that with the decreasing fall tube diameter, the wall effects are significantly affecting the characteristics of the falling cylinder.

Ratio of cylinder diameter to fall tube diameter ($d_c/D = 0.833$). As the fall tube diameter is approaching the cylinder diameter, the wall effects on the terminal velocity reduction are gaining more significance. In this case study, terminal velocity and the wall factor of the falling cylinder is estimated for an increased d_c/D of 0.833 through numerical analysis. The terminal velocity and wall factor values obtained are 0.83 m/s and 0.198, respectively, as shown in Table 3.

Ratio of cylinder diameter to fall tube diameter ($d_c/D = 0.91$). The ratio of cylinder diameter to fall tube diameter is further increased to 0.91. Results obtained from the numerical method are provided in Table 3. The terminal velocity and wall factor values are reduced to 0.335 m/s and 0.08, respectively.

Ratio of cylinder diameter to fall tube diameter ($d_c/D = 0.952$). In this last case study for a cylindrical object falling freely in a fall tube, terminal velocity and wall factor is estimated for $d_c/D = 0.952$. Numerical results for this case study are presented in Table 3. The terminal velocity and wall factor values obtained are 0.115 m/s and 0.0275, respectively. It is observed that there has been a considerable reduction of the terminal velocity and the wall factor when compared to case study 4.1.1, where the cylinder was falling freely in an unbounded or infinite medium.

Figures 3 and 4 display the variation of terminal velocity and wall factor with respect to the diameter ratio (d_c/D). Both terminal velocity and wall factor follow the same trend as wall factor (f) is directly proportional to the terminal velocity (Eq. 1). It can be seen from Figs. 3 and 4 that the available analytical models do not predict the terminal velocity and wall factor for higher diameter ratios. At lower diameter ratio values, the error between the results of the analytical values and numerical values is large. This difference is explained in terms of the orientation of the falling objects. Therefore, in the absence of appropriate analytical models, the results obtained from numerical simulations are employed for future uses.

Fig. 3 Variation of terminal velocity with respect to the diameter ratio

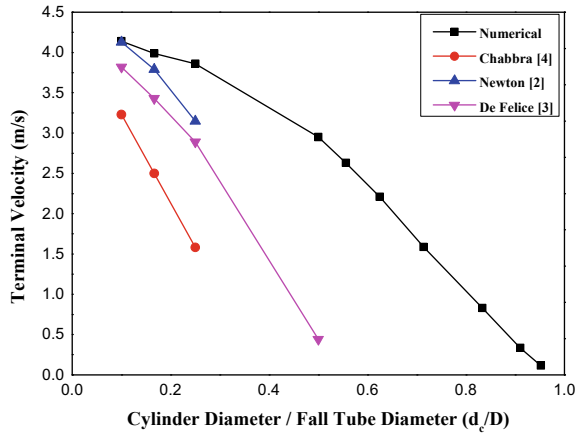
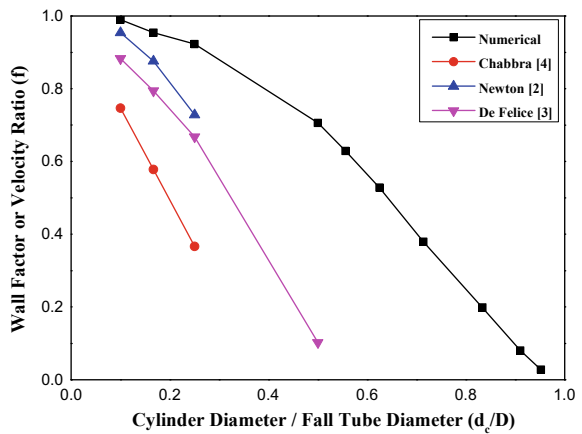


Fig. 4 Variation of wall factor with respect to the diameter ratio



4.2 Wall Effects on Terminal Velocity and Drag Coefficients of Fuel Bundle

The following case studies estimate the terminal velocity, drag coefficients, and the wall factor for the gravity-influenced fall of the fuel bundles.

Ratio of cylinder diameter to fall tube diameter ($d/D = 0.05$). In this case study, the drag coefficient and terminal velocity of the falling fuel bundle is estimated with a large fall tube diameter when compared to the fuel diameter. Both analytical and numerical procedures are employed in this case study and its results are compared in Table 4. The analytical terminal velocity is observed to be 3.45 m/s, whereas the numerical results imply a value of 3.31 m/s having an error of 4.05%. However, drag coefficients observed through analytical and numerical methods are 0.789 and 1.73, respectively, with a large error estimate of 119.2%. This suggests that the analytical

Table 4 Comparison of the drag coefficient and terminal velocity for analytical and numerical procedures for fuel geometry in infinite medium ($d/D = 0.05$)

Methodology	Drag coefficient (C_D)	Terminal velocity (U_t)
Analytical	0.789	3.45 m/s
Numerical simulation	1.73	3.31 m/s
Error (%)	-119.2	4.05

expressions in the literature available ineffectively estimates drag coefficients for complex geometries like that of the test fuel bundle. Also, compared to the solid cylinder with a similar dimension and aspect ratio, the terminal velocity obtained is lower. This attribute can be explained in terms of the higher surface area of the fuel bundle in comparison to that of the solid cylinder. Figure 5 displays the flow velocity contour across the cylinder at terminal velocity.

Ratio of cylinder diameter to fall tube diameter ($d/D=0.94$). In this case study, the terminal velocity and wall factor of the falling fuel bundle is estimated for the reduced diameter of the fall tube in order to understand the influence of wall effects on the characteristics of the falling cylinder. The dimensions used are comparable to the dimensions in the actual geometry of the FTL. Figure 6 shows the flow velocity contour across the fuel bundle for a diameter ratio of 0.94. Because of the higher diameter ratio, no analytical model is available in the literature for the prediction of results for this case study. As can be seen from Table 5, the velocities predicted by the numerical procedure are higher in comparison to the numerical prediction of the solid cylinder with similar diameter ratios. In solid cylinders, the presence of the fall

Fig. 5 Flow velocity contour across the fuel bundle at terminal velocity in an infinite medium

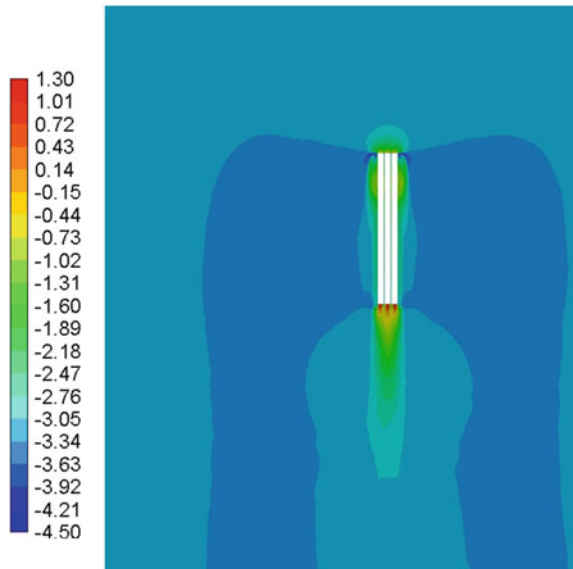


Fig. 6 Flow velocity contour across the fuel bundle at terminal velocity for diameter ratio of 0.94

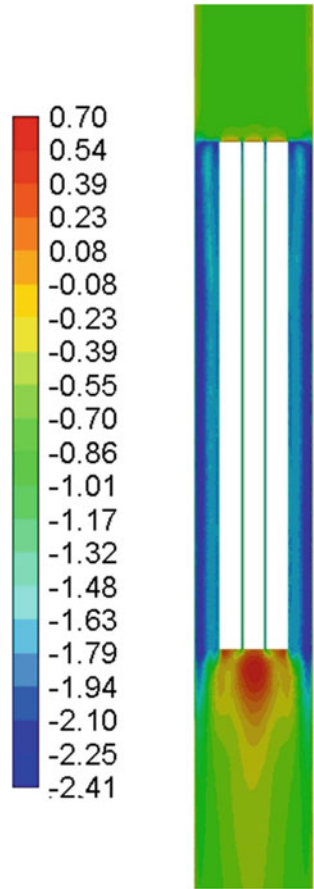


Table 5 Comparison of the drag coefficients and terminal velocity between analytical and numerical procedures for fuel geometry ($d/D = 0.94$)

Methodology	Wall factor (f)	Terminal velocity (U_t)
Numerical simulation	0.229	0.76 m/s

tube wall in the vicinity considerably reduces the terminal velocity, however, such is not the case with fuel having comparable dimensions. With the presence of an open area between the pins (for cooling purposes), the influence of the fall tube wall diminishes.

5 Conclusions

In the present work, the investigation of wall effects on the terminal velocity of test fuel bundles falling under gravity within the In-Pool Test Section of the FTL was carried out both analytically and numerically. In order to achieve this, multiple case studies estimating drag characteristics and terminal velocities with wall effects were performed on a comparable dimension cylinder having similar diameter and aspect ratio. It was observed that at higher diameter ratios, the reduction in the terminal velocity and the wall factor was very large attributing to considerable influence of the wall in the vicinity. Further, in the absence of analytical models in the literature for higher values of the diameter ratio, results obtained through numerical simulations could not be compared. Subsequently, the estimation of terminal velocity, drag coefficient, and wall factor was carried out. It was observed that the velocities predicted are higher in comparison to the prediction of the same characteristics of the solid cylinder with similar diameter ratios. As in solid cylinders, the presence of a fall tube wall in the vicinity considerably reduces the terminal velocity, however, such is not the case with fuel having comparable dimensions. With the presence of an open area between the pins (for cooling purposes), the influence of the fall tube wall diminishes.

References

1. Gabitto J, Tsouris C (2008) Drag coefficient and settling velocity for particles of cylindrical shape jointed plates. *Powder Technol* 183:314–322. <https://doi.org/10.1016/j.powtec.2007.07.031>
2. Clift R, Grace JR, Weber ME (1978) Bubbles, drops and particles. Academic Press, New York
3. Kahn AR, Richardson JF (1987) The resistance to motion of a solid sphere in a fluid. *Chem Eng Commun* 62–135. <https://doi.org/10.1080/00986448708912056>
4. Haider AM (1987) M.S. Project, Oregon State University
5. Miyamura A, Iwasaki S, Ishii T (1981) Experimental wall correction factors of single solid spheres in triangular and square cylinders, and parallel plates. *Int J Multiph Flow* 7(1):41–46. [https://doi.org/10.1016/0301-9322\(81\)90013-6](https://doi.org/10.1016/0301-9322(81)90013-6)
6. Machac I, Lecjaks Z (1995) Wall effects for a sphere falling through a non-newtonian fluid in a rectangular duct. *Chem Eng Sci* 50:143–148. [https://doi.org/10.1016/0009-2509\(94\)00211-9](https://doi.org/10.1016/0009-2509(94)00211-9)
7. Balaramakrishna PV, Chhabra RP (1992) Sedimentation of a sphere along the axis of a long square duct filled with non-Newtonian liquids. *Can J Chem Eng* 70:803–807. <https://doi.org/10.1002/cjce.5450700427>
8. Lj AZ, Grbavcic ZB, Garic-Grulovic RV, Boskovic-Vragolovic NM (2010) Wall effects on the velocities of a single sphere settling in a stagnant and counter-current fluid and rising in a co-current fluid. *Powder Technol* 203:237–242. <https://doi.org/10.1016/j.powtec.2010.05.013>
9. Newton I (1687) *Philosophiæ Naturalis Principia Mathematica*, Lib. II, Prop. XXXIX, Theor. XXXI. Cambridge University Press, Cambridge
10. De- R (1996) Experimental wall: a relationship for the wall effect on the settling velocity of a sphere at any flow regime. *Int J Multiph Flow* 22:527–533. [https://doi.org/10.1016/0301-9322\(96\)00004-3](https://doi.org/10.1016/0301-9322(96)00004-3)

11. Chhabra RP (1995) Wall effects on free-settling velocity of non-spherical particles in viscous media in cylindrical tubes. *Powder Technol* 85:83–90. [https://doi.org/10.1016/0032-5910\(95\)03012-X](https://doi.org/10.1016/0032-5910(95)03012-X)
12. Heywood H (1962) Uniform and non-uniform motion of particles in fluids. In: *Proceedings of the symposium on interaction fluids and particles*, Institution of Chemical Engineers, London, pp 1–8
13. Wadell H (1934) The coefficient of resistance as a function of Reynolds number for solids of various shapes. *J Franklin Inst* 217:459–490. [https://doi.org/10.1016/S0016-0032\(34\)90508-1](https://doi.org/10.1016/S0016-0032(34)90508-1)
14. Cheng NS (2009) Comparison of formulas for drag coefficient and settling velocity of spherical particles. *Powder Technol* 189(3):395–398. <https://doi.org/10.1016/j.powtec.2008.07.06>
15. Haider A, Levenspiel O (1989) Drag coefficient and terminal velocity of spherical and non-spherical particles. *Powder Technol* 58:63–70. [https://doi.org/10.1016/0032-5910\(89\)80008-7](https://doi.org/10.1016/0032-5910(89)80008-7)
16. Coulson JM, Richardson JF (1977) *Chemical engineering*, vol 2, Pergamon Press, Oxford (Chapter 4)

Comparison of Seismic Performance of Composite (RCS) Frame with RC Frame Using Pushover Analysis



Manoranjan Singh Oinam and S. S. Ningthoukhongjam

Abstract In this paper, comparison of seismic performance has been investigated between RCS (Reinforced Concrete column-Steel beam) composite frame and RCC (Reinforced cement concrete) frame using SAP2000 software. Nonlinear static analysis (pushover) is employed for evaluation of the seismic performance of both RCS and RC frames. Both the RCS and RC frames are similar in geometry, as well as sectional members used except the beams in RCS frame are replaced by steel member of the equivalent flexural capacity of beams in RC frame. Seismic performances of both RCS and RC frames in terms of base shear, spectral displacement, etc., are investigated. It has been observed that the RCS frame is more cost-effective than the RC frame of equivalent seismic performance.

Keywords CS frame · Pushover analysis · Performance point · Pushover curves

1 Introduction

Reinforced concrete has been used as a major construction material for building frames. In the past few decades, numerous researches, [1–4] started working on the optimum combination of steel and concrete in the construction of the building which then introduced Reinforced Concrete-Steel (RCS) frames to the engineering society. RCS composite moment resisting frames consist of Reinforced Concrete (RC) columns and Steel (S) beams. RCS frames have many advantages than traditional RC or steel frame from structural, economical and construction points of views. From the construction viewpoint, RCS frames are easy in construction since the erection of steel beam is simple as compared to casting of RCC beam which includes formwork, reinforcement detailing, casting of concrete, etc. Further, erection of steel beam requires much less time than the casting of RCC beam since the casting of RCC

M. Singh Oinam (✉) · S. S. Ningthoukhongjam
Department of Civil Engineering, Manipur Institute of Technology, Imphal, India
e-mail: oinammanoranjan@gmail.com

S. S. Ningthoukhongjam
e-mail: sukunao@gmail.com

beams requires curing times in terms of weeks. From the structural point of view, the lateral stiffness of RCS frame is greater than that of equivalent strength of RCC or steel frame since the weight of the building is reduced in RCS frame due to the use of composite floor slabs which are lighter in weight than RCC floor slabs. Hence, all the member sections, foundation size, inertial forces, etc., in RCS frame will be reduced which will minimize the cost of the building construction. Another advantage of RCS frame is that there is a provision for providing long-span (column free) steel beams due to lighter weight of composite floors. Further, these composite systems have the ability to accommodate various innovative construction techniques which can lower the overall cost and expedite the process of erecting buildings.

Many researchers have started working on RCS frames. For example, Mirghaderi et al. [1], proposed a new moment connection between the steel beam and reinforced concrete column. In the proposed connection, the parallel beams passing through the column are welded to the cover plate at the joint area near the concrete column. Rathod et al. [2] performed a comparative study on RCC, steel and composite high rise building (G + 11) using parameters like displacement, storey drift, Performance point, and base shear. The study concluded that composite sections are more preferable than RCC for high rise building in terms of lighter and speedy construction. Prakarsh et al. [3] performed a comparative study of analysis and design of RC and steel structures using ETABS. Storey drifts of steel structures are found comparatively more than RC structures (greater weight) within the permissible limit. Cholekar et al. [4] conducted a comparative study of RCC and Composite buildings having mass irregularity. It is observed that the mass irregularity can affect all the parameters of storey drift, base shear, dead weight, shear force, and joint displacement during an earthquake. Thus, RCS composite may become the favourable option for medium to high rise building frames. Most of the research works on RCS structure focuses on the connection between the reinforced concrete column and steel beam. Experimental studies have shown that RCS joints have excellent strength and stiffness (Sheikh et al. [5]). The connection joint between the steel beam and reinforced concrete column can be assumed rigid as proven by Eysa Salajegheh and Hooman Habib Agahi [6]. It has been seen that the research works on RCS frames has been carried out in determining the behaviour of steel beam and RC column, lighter and speedy construction time; however, as per the author's knowledge, cost analysis of RCS frame with equivalent RC frame has not been performed.

In this paper, a residential of G + 3 multistorey RCC building located at Nagamapal area, Imphal, Manipur, is studied for Pushover Analysis using SAP2000. The same building is remodelled in SAP2000 software by replacing the beam members with I-section structural steel so as to model a composite RCS building and studied by pushover analysis. The connection joint between the steel beam and reinforced concrete column is assumed to be rigid as suggested by Eysa Salajegheh and Hooman Habib Agahi [6]. The basic loading on both types of structure is considered equal. The structural steel for the beam is selected so as to have equivalent flexural strength as that of the RCC beam so that seismic performance and cost comparison can be investigated between the two structures.

2 Methodology

Nonlinear static analysis known as pushover analysis has been adopted for the analysis of both RCC and RCS frames in this paper. In pushover analysis, a structure is subjected to gravity loading and a monotonic lateral load pattern which is constantly increasing over elastic and inelastic behaviour until the target displacement is attained. It can be executed as force-controlled (used when the load is known, for instance, gravity loading) or displacement-controlled (used when specified drifts are known). A curve is obtained between base shear and roof displacement in pushover analysis which is known as the capacity curve (Fig. 1) [7].

Pushover analysis has been the preferred method for seismic performance evaluation of structures by the major rehabilitation guidelines and codes because it is conceptually and computationally simple. Pushover analysis allows tracing the sequence of yielding and failure on member and structural level, as well as the progress of overall capacity curve of the structure. Federal Emergency Management Agency (FEMA) and Applied Technical Council (ATC) formulated and put forward the nonlinear static pushover analysis in their seismic rehabilitation programme and guidelines.

Figure 2 above describes the typical force–deformation relation. The points A, B, C, D, and E in the above diagram denote the force-deflection behaviour of the hinges. Also, shown in are the hinge states of IO (Immediate Occupancy), LS (Life Safety), and CD (Collapse Prevention). The force–deflection curve between A and B indicates the elastic state, B and C indicates the plastic state, and beyond E indicates the collapse. In SAP2000, the colour bands given below are used to identify those points in order to understand the plastic hinges formed in each stage.

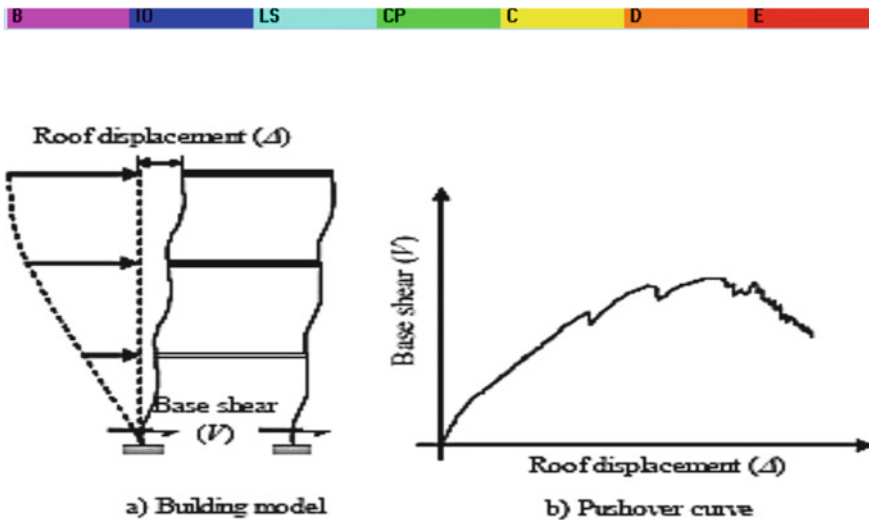
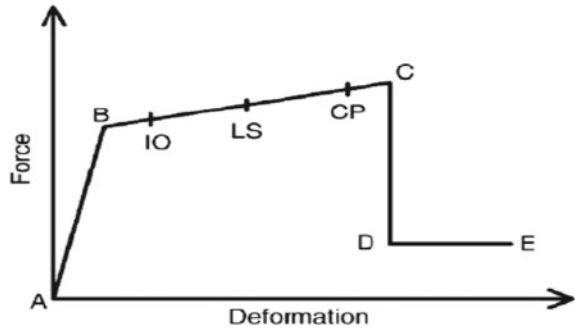


Fig. 1 Pushover analysis

Fig. 2 Different stages of plastic hinge [7]



3 Structural Frame Modelling

An idealized G + 3 RCC building has been considered for investigation using Pushover analysis in SAP2000 software. The building is four storeys high. The bay lengths are 3.5 m in both the directions as shown in Fig. 3. The plan dimension is 14 m × 10.5 m. The same building is converted in SAP2000 software by replacing the beam members with I-section structural steel so as to model a composite RCS building. The structural steel for the beam of RCS building is selected so as to have equivalent flexural strength as that of the RCC beam such that seismic performance and cost comparison can be conducted between the two structures. The structural data of both RCS and RCC building is given in Tables 1 and 2. The basic loading on both types of structure is kept equal.

Fig. 3 Plan layout of the proposed building

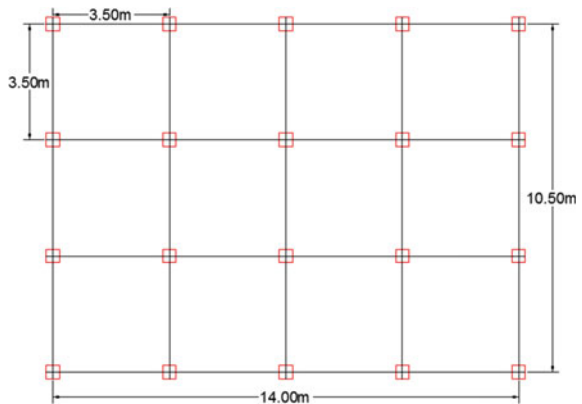


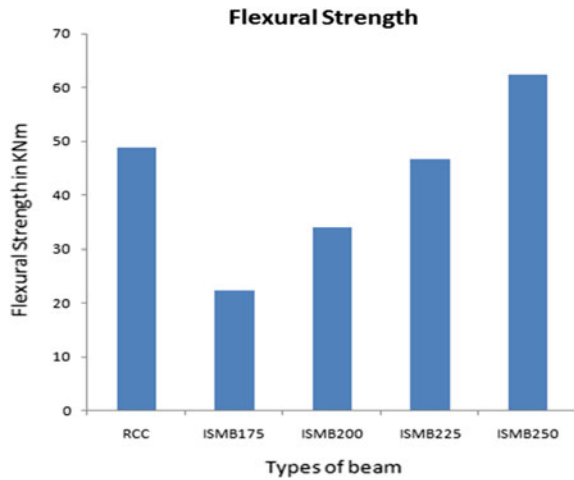
Table 1 Structural data for RCC building

Plan dimension	14 m × 10.5 m
Total height of building	12.5 m
Height of each storey	3.5 m for ground floor, 3 m for above ground floors
Beam	0.35 × 0.3 m
columns	0.35 × 0.35
Thickness of slab	130 mm
Live load (as per IS: 875 part-2 1987)	2.5 kN/m ² (for typical floors), 1.5 kN/m ² (roof)
Seismic zone	V
Importance factor	1
Soil condition	Medium soil (assumed)
Response reduction factor	5
Depth of foundation	1.5 m
Grade of concrete	M20
Grade of steel	Fe500
Damping ratio	5%

Table 2 Structural data for RCS building

Description	RCS
Plan dimension	14 m × 10.5 m
Total height of building	12.5 m
Height of each storey	3.5 m for ground floor, 3 m for above ground floors
Beam	ISMB 225 (I-section)
Columns	0.35 × 0.35
Thickness of slab	120 mm
Live load (as per IS: 875 part-2 1987)	2.5 kN/m ² (for typical floors), 1.5 kN/m ² (roof)
Seismic zone	V
Importance factor	1
Soil condition	Medium soil (assumed)
Response reduction factor	5
Depth of foundation	1.5 m
Grade of concrete	M20
Grade of steel	Fe500
Damping ratio	5%

Fig. 4 Flexural strength of beams



3.1 Flexural Strength of Beams

Since the flexural strength of the ISMB225 is nearest to the flexural strength of the existing RCC beam, the RCS frame is modelled by replacing the RCC beam with the steel beam of ISMB225 structural steel. The connection joint between the steel beam and reinforced concrete column is assumed rigid. The basic loading on both types of structure is kept equal. The structural steel for the beam is selected so as to have identical strength as that of the RCC building such that a cost comparison can be made between the two structures (Fig. 4).

3.2 Material Properties

The material used for RC construction is reinforced concrete with M-20 grade concrete and Fe-500 grade reinforcing steel. The structural steel used for steel beam is I-section ISMB 225. The Stress–Strain relationship used is as per IS 456:2000 and IS 800-2007. The basic material properties used are as follows:

- Modulus of Elasticity of steel, $E_s = 210000$ MPa
- Modulus of Elasticity of concrete, $E_c = 24890$ MPa
- Characteristic strength of concrete, $f_{ck} = 20$ MPa
- Yield stress for reinforcing steel, $f_y = 500$ MPa
- Yield stress for structural steel, $f_y = 250$ MPa

3.3 Structural Data for RCC Building

3.4 Structural Data for Composite RCS Building

4 Building Analysis

The general finite element package SAP 2000 (Version.19) has been adopted for the analyses. A three-dimensional model of each structure has been modelled to undertake the nonlinear analysis. Beams and columns are modelled as nonlinear frame elements with lumped plasticity at the start and the end of each element. The following hinge properties are provided for modelling nonlinear frame elements in SAP2000 i.e., P-M2-P3 hinges for columns with plastic rotation (in radians) of IO as 0.01, LS as 0.025, and CP as 0.05; and M3 hinges for beams with plastic rotation of IO as 0.002, LS as 0.0076, and CP as 0.008 as per FEMA 356. Both the building frames that is the existing RCC building and the RCS composite building are analyzed first by considering linear static analysis for defining gravity load case and then a lateral pushover analysis was performed in a displacement control manner (Fig. 5).

Fig. 5 3D model of the proposed building developed in SAP2000

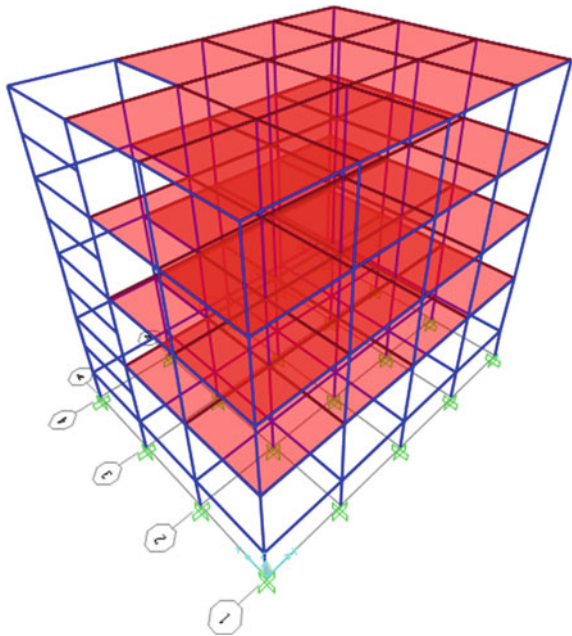


Table 3 Base shear and displacement

Building	Target displacement (m)	Elastic base shear (KN)	Inelastic base shear (KN)
RCC building	0.052	900.64	2283.016
RCS building	0.066	803.56	2111.209

5 Result and Discussion

The results from the pushover analysis of the two buildings are as follows.

5.1 Base Shear and Displacement

From Table 3, the target displacement is more in RCS frame than the RCC frame. The base shear of RCS having structural beam ISMB 225 is more than the base shear of RCC building. In case of RCC building, the inelastic base shear is 2.53 times of the elastic base shear which suggests that the building is seismically safe and has good resistance against earthquake. Similarly, in case of RCS building, the inelastic base shear is 2.62 times the elastic base shear which also shows that the building has good resistance against earthquake. The base shear of RCS building is less than RCC building owing to reduced dead load in case of RCS frame. The RCC building has more stiffness as compared to RCS building which results in less roof displacement than RCS building (as shown in Table 3).

5.2 Demand-Capacity Curve (Pushover Curve)

Figure 6 and Fig. 7 below show the capacity curve of RCC and RCS composite structure, respectively. The curve initially follows linear state and then starts to deviate from linearity as the beams and the columns undergo inelastic actions. When the buildings are pushed well into the inelastic range, the curves become linear again but with a smaller slope. For a target displacement of 0.052 m for the RCC building, the base shear of the whole structure is 2283.016 KN. For RCS composite building, for a target displacement of 0.066 m, the base shear is 2111.209 KN.

From the Figs. 4 and 5, it is obvious that the performance point (intersection of capacity and demand curve) of the RCS building is nearer to the yield point of the capacity curve as compared to the performance point of RCC building. This suggests that the RCS building has more reserve strength and stiffness left after being pushed into the inelastic range.

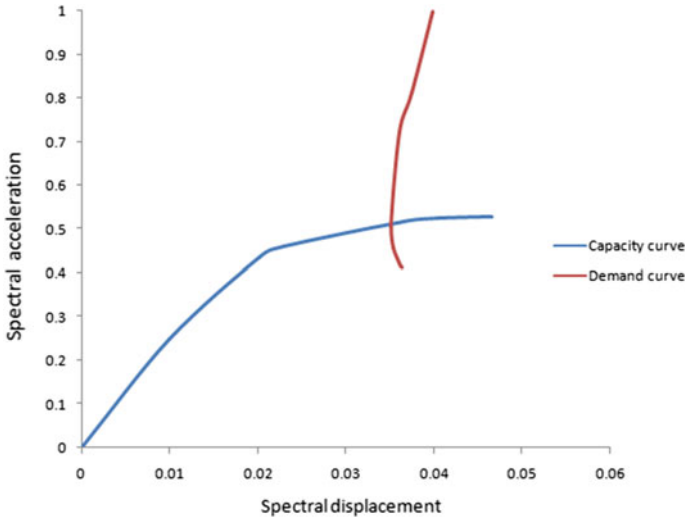


Fig. 6 Performance point for RCC

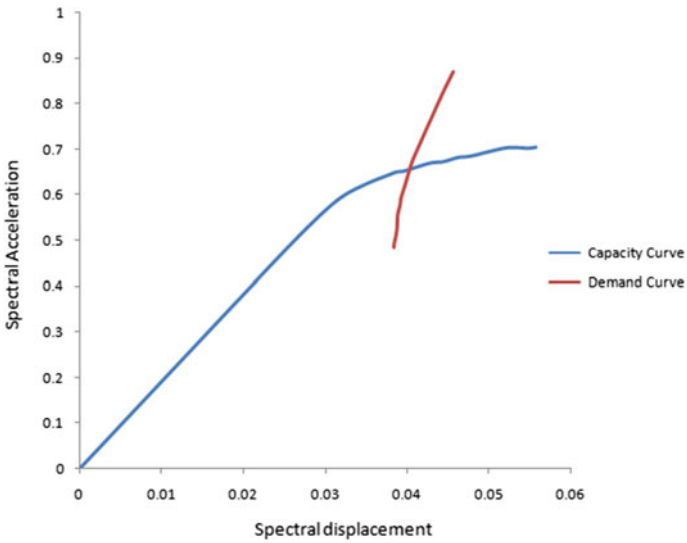


Fig. 7 Performance point for RCS frames

5.3 Plastic Hinge Mechanism

Tables 4 and 5 shows the hinge state details at each step of the analysis of RCC and RCS composite building, respectively. In case of RCC building, it can be seen that for the performance point taken as step 7 (which actually lies between steps 6

Table 4 Hinge states in each step of pushover analysis (RCC building)

Load case	Step	Displacement	Base force	A to B	B to IO	IO to LS	LS to CP	C to D	D to E	Beyond E	Total hinges
Text	Unitless	m	KN	Unitless	Unitless	Unitless	Unitless	Unitless	Unitless		Unitless
Push	0	0	0	518	0	0	0	0	0	0	518
Push	1	0.010042	690.787	517	1	0	0	0	0	0	518
Push	2	0.037359	1991.882	402	116	0	0	0	0	0	518
Push	3	0.041176	2130.258	388	130	0	0	0	0	0	518
Push	4	0.041878	2145.976	386	132	0	0	0	0	0	518
Push	5	0.042539	2152.968	386	132	0	0	0	0	0	518
Push	6	0.044385	2186.871	384	134	0	0	0	0	0	518
Push	7	0.054268	2304.052	372	146	0	0	0	0	0	518
Push	8	0.058626	2338.478	367	151	0	0	0	0	0	518

Table 5 Hinge states in each steps of pushover analysis (RCS building)

Load case Text	Step	Displacement m	Base force KN	A to B	B to IO	IO to LS	LS to CP	C to D	D to E	Beyond E	Total hinges
	Unitless			Unitless	Unitless	Unitless	Unitless	Unitless	Unitless	Unitless	Unitless
Push	0	0	0	518	0	0	0	0	0	0	518
Push	1	0.045444	1564.575	517	1	0	0	0	0	0	518
Push	2	0.056061	1905.015	498	20	0	0	0	0	0	518
Push	3	0.082424	2429.758	462	56	0	0	0	0	0	518
Push	4	0.086652	2475.934	449	57	12	0	0	0	0	518
Push	5	0.087597	2481.267	448	56	14	0	0	0	0	518
Push	6	0.095461	2550.996	432	66	20	0	0	0	0	518
Push	7	0.096152	2554.887	428	70	20	0	0	0	0	518
Push	8	0.097963	2567.984	421	77	20	0	0	0	0	518
Push	9	0.099484	2571.526	418	80	20	0	0	0	0	518
Push	10	0.099484	2574.543	417	81	20	0	0	0	0	518
Push	11	0.100496	2578.182	416	82	20	0	0	0	0	518
Push	12	0.101506	2580.016	416	82	20	0	0	0	0	518

and 7), 71.8% of the hinges lie within B and only 28% of hinges lie between B and IO. Hence, the damage will be limited. As for the RCS building, at the performance point taken as step 3, 89.1% of the hinges lie within B and 10.8% of the hinges lie between B and IO. Hence the damage level, in case of RCS building, will be more limited than RCC building.

Figures 8 and 9 show the hinge states during various stages in the course of the analysis.

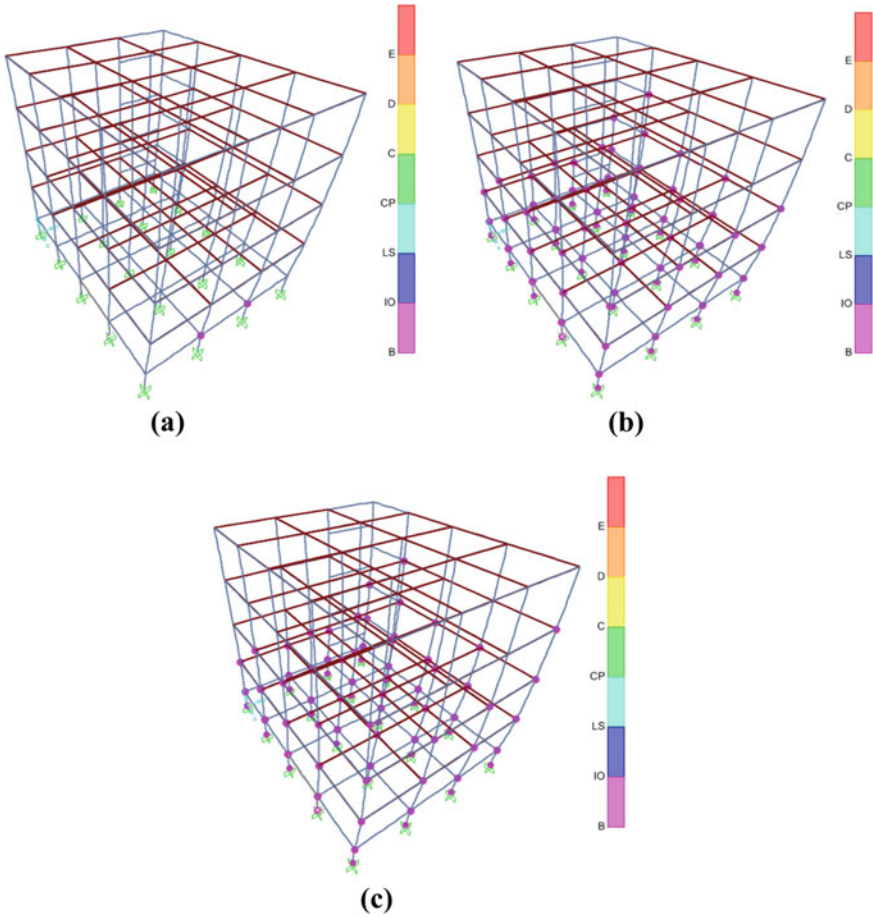


Fig. 8 a Hinge state in the structure model of RCC frame at step 2. b Hinge state in the structure model of RCC frame at step 5. c Hinge state in the structure model of RCC frame at step 8

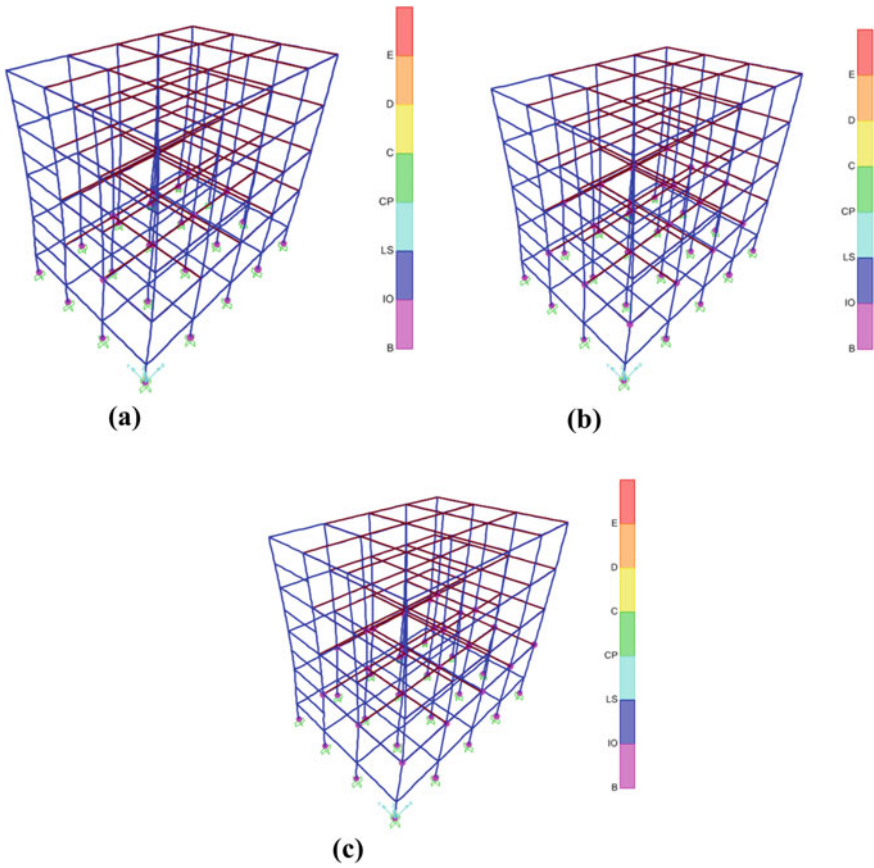


Fig. 9 **a** Hinge state in the structure model of RCS frame at step 2. **b** Hinge state in the structure model of RCS frame at step 5. **c** Hinge state in the structure model of RCS frame at step 8

5.4 Cost Analysis

From the cost analysis of both the buildings that is RCS and RCC building, the following result has been obtained. The cost analysis excludes the cost of formwork and the loading cost of structural steel in RCS building and other miscellaneous costs.

Building	Cost in rupees
RCC	20,02,441
RCS composite	15,45,203
Difference	4,57,238

6 Conclusions

Comparison of seismic performances between RCC and RCS frames has been investigated using SAP2000 software. Nonlinear static analysis and pushover method is employed for the evaluation of the seismic performance of both the frames. Based on the analysis the following conclusions are drawn:

- The base shear of RCS composite building is observed to be less than that of RCC building since lightweight composite floors are used in RCS frames. Lightweight and inherent ductility characteristics of the RCS building gives better seismic performances than RCC building during an earthquake.
- RCS building possesses more reserve strength than RCC building since the performance point of RCS building occurs near the yield point in the capacity curve than that of RCC building.
- RCS composite structures are found to be more economical than RCC structure since all the member sections, foundation size, inertial forces, etc., in RCS frame will be reduced due to lighter seismic weight which will minimize the cost of the building construction.
- The construction time for RCS building is less than that of RCC building since the erection of steel beams and composite floor slabs require much less time as compared to that of RCC beam and slabs.

References

1. Mirghaderi SR, Eghbali NB, Ahmadi MM (2016) Moment connection between continuous steel beams and reinforced concrete column under cyclic loading. *J Constr Steel Res* 118:105–119
2. Rathod AV, Ishtiyaque M (2017) Pushover analysis of building structure. *Int J Innov Res Sci Eng Technol* 6(3)
3. Sangave P, Madur N, Waghware S (2015) Comparative study of analysis and design of RC and steel structures. *Int J Sci Eng Res* 6(2):256
4. Cholekar SB, Basavalingappa SM (2015) Comparative analysis of multistoried RCC and Composite building due to mass irregularity. *IRJET* 2(4)
5. Sheikh TM (1987) Moment connection between steel beam and concrete columns. Bureau of Engineering Research, University of Texas, Austin
6. Salajegheh E, Habib H (2008) Performance based design of RCS frames. In: 14th world conference on earthquake engineering, Beijing, China
7. FEMA 440 (2005) Improvement of nonlinear static seismic analysis procedures. Department of Homeland Security Federal Emergency Management Agency, Washington

Investigating Load Withstand by L-Shape Concrete Cube, RCC Slab and to Safeguard Reinforcement of RCC Slab in Saltwater Environment Using Cathodic Protection



C. F. Rajemahadik, M. M. Kulkarni, R. S. Durge, A. R. Kamble, S. B. Babar, and P. A. Bansode

Abstract Structures constructed in reinforced cement concrete (RCC) are currently at risk when exposed to saltwater conditions. Eventually, RCC structure fails after the corrosion of reinforcement, reducing strength and its life. The investigation focuses on load-carrying capacity of slab specimen (RCC) and shear strength of L-shape concrete cubes after exposure to saltwater. The concrete of M20 mix was prepared using 53 grade cement to cast L-shape concrete cubes and reinforced slab specimen having 10 mm bar diameter. The size of RCC slab was $300 \times 300 \times 100$ mm and L-shape cubes were prepared after cut of $90 \times 150 \times 60$ mm in regular concrete cube with M-20 mix. After casting and curing of L-Shape cube and slabs, these specimens are exposed to 0.1 M NaCl water for curing. The L-Shape cubes after regular curing gave 12.21 MPa at 7 days and 19.11 MPa at 28 days of shear strength. Furthermore, shear strength increased from 13.42 MPa at 7 days to 21.07 MPa at 28 days after curing in 0.1 M NaCl water for 30 h. A D.C. power supply was used to accelerate the corrosion of steel in the slab at 0.02 mA/mm^2 . Slab specimens tested for 30 h were as follows: slab reinforcement as anode (P1), slab coated with sodium silicate and reinforcement as anode (P2) and slabs reinforcement as cathode (P3) in 0.1 M NaCl water with iron plate as anode. The failure loads of slabs were 41.75 kN for P1, 75.35 kN for P2 and 78.5 kN for P3 type. This study indicates L-shaped cubes after curing in NaCl environment can increase shear strength. In addition, cathodic protection to reinforcement in slab increases load-carrying capacity, ultimately increasing the life of RCC specimen.

Keywords Salt-water · L-Shape cubes · Loading capacity · Cathodic protection

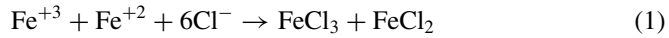
C. F. Rajemahadik (✉) · R. S. Durge · S. B. Babar · P. A. Bansode
Department of Civil Engineering, Sanjay Ghodawat Polytechnic, Kolhapur, India
e-mail: crajemahadik@gmail.com

M. M. Kulkarni
School of Technology, Sanjay Ghodawat University, Kolhapur, India

A. R. Kamble
School of Engineering, MIT-ADT University, Pune, India

1 Introduction

Recently, corrosion of reinforcement in RCC structure and shear strength has boosted many researchers [1]. In the state of corrosion of reinforcement, steel turns to a passive state in an alkaline environment. Chloride breaks passive state, after its attack on steel, boosting corrosion [2]. Chlorides accelerate, rate of corrosion with an increase in concentration, as shown in reactions (1) given below.



After reaction (1), chlorides separates and stays suspended, free to react again with reinforcement (2) [3].



Thus, corrosion caused due to chlorides can affect RCC structures adversely, hampering stability and reducing its life span [3]. This leads to structural deterioration pouncing safety and economic concern for owners and its stakeholders [4]. The present scenario concentrates more on considering saltwater environment for the stability of RCC structures. Another vital parameter for concrete is shear strength, a major parameter to overcome strength or failure capacity [5]. Among all parameters shear in concrete is analyzed for the past 100 years [6]. Protection of reinforcement structural members and observing the shear failure of concrete is a task to look forward too. In addition, more focus is required to concentrate on the shear strength of the RCC structure. The observations of such parameters mentioned above are a vital task, as these may depend on site and environmental conditions [7]. Furthermore, reinforcement of corrosion needs protection or proper maintenance, if RCC structures constructed in the vicinity of saltwater environment. The corrosion of reinforcement in structure can be controlled using the electrochemical method known as cathodic protection (CP). This technique has proved best for saltwater conditions on-site, also known as impressed current method [8]. In this method, an electrical potential is provided to protect reinforcement (metal) in structure to resist corrosion [9]. Moreover, cathodic polarized current is bifurcated as current cathodic protection (ICCP), with an external supply of power defined as sacrificial anode cathodic protection (SACP), which has separate anode [10]. In addition, basic method to control corrosion using cathodic protection is divided as impressed current systems (ICS) and sacrificial anodes [11]. This paper focuses on the shear strength of concrete using L-Shaped cubes and applying cathodic protection to reinforcement in concrete slab specimens using anode to learn the effect on load withstanding capacity in saltwater environment.

2 Materials and Methods

2.1 Materials

Cement: The ordinary portland cement (OPC) of Ultratech company of 53 Grade was purchased. Cement was tested for fineness, normal consistency and setting time. Table 1, gives the physical properties of cement.

Fine aggregate (Sand): The natural sand was tested for fineness modulus, specific gravity and water absorption satisfying IS-383-1970 [13], as shown in Table 2.

Water: Water used was potable from municipal supply satisfying IS-456:2000 [14], for a mix of concrete.

Coarse aggregate: Natural crushed stones are purchased from locally available quarries of size 20 mm, which are used as coarse aggregates (Table 3).

Other materials:

Steel Rods—Mahalaxmi TMT 10 mm diameter of length-25 cm

Wooden Block—90 mm × 150 mm × 60 mm

Plywood size—900 mm × 900 mm (slab base)

Slab Cover—25 mm

Electric Wires sustaining up to 3 amperes

Iron flats of size 150 mm × 150 mm

Table 1 Physical properties of cement

Sr. no	Physical test	Results obtained	IS 12269: 2013 [12]
1	Fineness (retained on 90 μm sieve) (%)	7.9%	10 max
2	Normal consistency (%)	31%	—
3	Vicat time of setting (min)		
	Initial	39	30 min
	Final	517	600 min

Table 2 Physical test on river Sand

Sr. no	Type of test	As per IS code	IS code	Result obtained
1	Fineness modulus	2.60–2.90	IS:383-1970	2.79
2	Specific gravity	2.63–2.67	IS:383-1970	2.68
3	Water absorption			2.5%

Table 3 Basic properties of coarse aggregate

Properties	As per IS code	IS code	Result obtained
Specific gravity	2.7–3.0	IS:2386-1963 [15]	2.94
Fineness modulus	5.5–8.0	IS:383-1970 [13]	6.81
Water absorption	Less than 10%	IS:2386-1963 [15]	9.43%

Chemicals: Chemicals required such as NaCl and sodium silicate for experimentation were procured from Thomas Baker.

2.2 Concrete Mix Design

The nominal mix proportion of concrete was 1:1.5:3 with water-cement ratio of 0.20 based on the above-listed material properties shown in Table 4.

Steps for casting of specimens

- Measuring all ingredients of concrete for the mix.
- Mixing of concrete ingredients.
- Proper compaction and finishing of concrete is processed.
- Curing of specimens for 7 and 28 days is carried out.

Casting of L-Shape concrete cube

- Cubes were casted using M20 nominal mix in a mould (150 * 150 * 150) (Fig. 1a). This method is simple and easy to operate and can be performed on a compressive testing machine [16].
- A wooden block was placed in the cube mould (60 * 90 * 150 mm) and concrete was poured with tamping (Fig. 1b).
- After 24 h, demoulding of L-shaped (Fig. 1c) concrete block was done and immersed in curing tank.

Preparation of Slab specimen

- Preparing mould for slab specimen of size 300 mm x 300 mm × 100 mm was prepared in plywood as base and side panels of fibreglass (Fig. 2b).

Table 4 Quantities of ingredients of concrete mix

Cement	Fine aggregate	Coarse aggregate	Water
373.33 kg/m ³	553.170 kg/m ³	1120 kg/m ³	18.66 kg/m ³

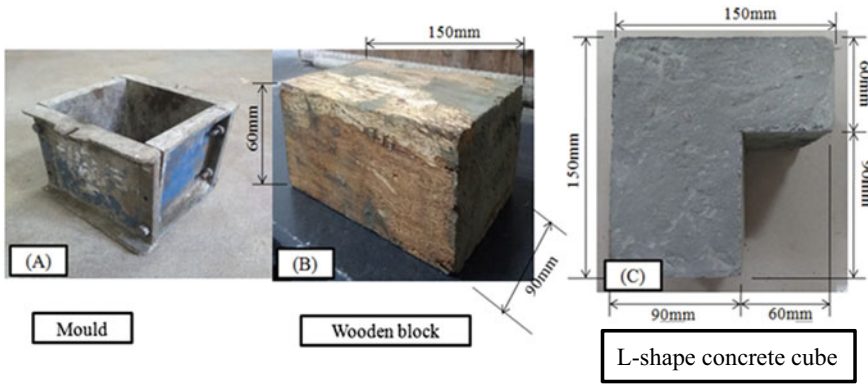


Fig. 1 Details of L-shaped concrete cube

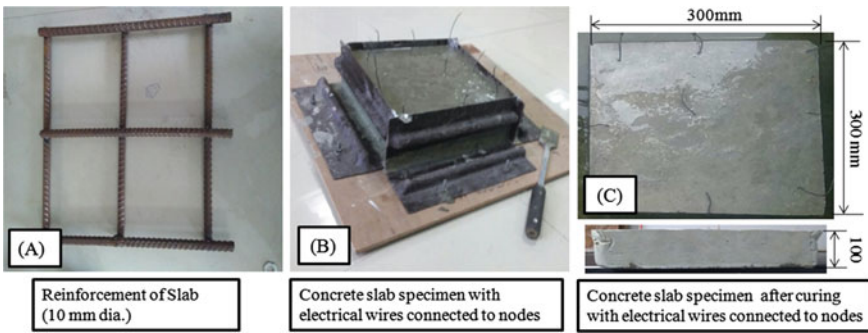


Fig. 2 Details of slab specimen used in the experiment

- Reinforcement of 10 mm dia. for slab in the grid was tied with the help of steel wire of 1 mm diameter (Fig. 2a).
- Electrical weirs were tied to each node of reinforcement in the grid.
- Slab specimen was casted using M20 nominal mix in the constructed mould (Fig. 2b).
- After the initial and final setting time, slab specimen were demoulded and allowed to surface dry, and kept for curing in the tank (Fig. 2c).

Curing: After casting and surface drying of L-shaped concrete cubes and reinforced slab specimens, specimens were immersed in curing tank for 7 and 28 days, respectively. Figure 3 shows slab specimen with wires and L-shaped cubes kept in the tank for curing.

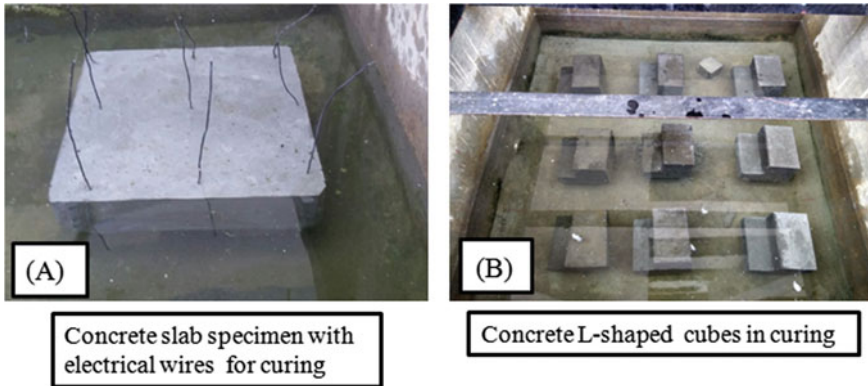


Fig. 3 Curing of RCC slab specimen and L-Shaped concrete cube

2.3 *Experimental Setup*

Slabs were casted using cement, fine aggregate, coarse aggregate and water. A mix design of M-20 grade with mix proportion of 1:1.5:3 was considered. Manually mixed concrete was placed in respective moulds of the slab. The reinforcement was introduced during the casting practice of slab with proper cover. Electrical wires connected with nodes of reinforcements in slab specimen and were covered properly. Then, slab specimens were demoulded after 24 h. Further, slab specimens were kept in curing tanks for 7 and 28 days. After curing, slabs are dried and again immersed in 0.1 M NaCl water tank having 6 litres volume, maintaining water level at half of the slab thickness [17]. A cover of 1 cm was provided at bottom of slabs and in between tank's inner surface. Water filled in tank contained 0.1 M of NaCl mimicking saltwater conditions [17, 18]. Wires from nodes were connected to the D.C. power supply of range 0–3 A and 0–30 V to anode and cathode of the specimen (Fig. 4c), according to cases (P1, P2, and P3). A current density of 0.02 mA/mm^2 was maintained for 30 h in saltwater conditions for all experiments on slab specimens. Three of the cases are studied as (1) P1—reinforcement of slab as anode connected with the external cathode, (2) P2—reinforcement of sodium silicate coated slab as anode, connected with external cathode (3) P3—reinforcement of slab as cathode, connected with the external anode (cathodic protection). The external cathode in Case P1 and P2 is iron electrode acting as cathode connected below slab to maintain circuit for corrosion. After 30 h, slab specimens were allowed to dry completely to check for load carrying capacity (Fig. 4a). A steel frame supported slab specimen for the plain and suspended position. The load was applied on the slab under UTM (Fig. 4a).

The loading arrangement for direct shear for L-shaped cubes and failure load for slab specimens was demonstrated using a universal testing machine as shown in Fig. 5, respectively. For the shear test of L-shaped cubes, $85 \times 10 \times 150 \text{ mm}$ size plate is placed on the left side portion of 90 mm face. Mild steel bar of 12 mm diameter is placed over mild steel plate. The centre 12 mm bar is adjusted to coincide with



Fig. 4 Experimental set up for compression and cathodic protection

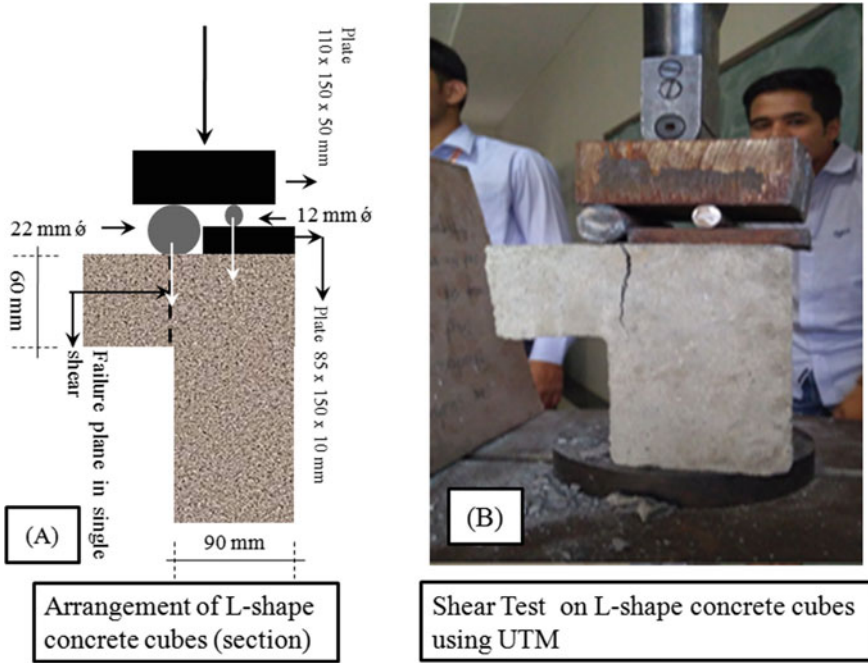


Fig. 5 Experimental set up of L-shaped concrete cubes for shear testing

centre of 90 mm length of concrete section. The centre of 22 mm bar placed exactly over the failure plane of concrete section as shown in Fig. 5. The load was applied on a 110 × 50 mm plate, which forms shear plane below the centre of 22 mm diameter bar. Similarly, a steel support was provided to slab specimens with 25 mm cover at the edges. The load was applied to check the failure of slab specimens experimented in different conditions.

3 Results and Discussion

L-shaped cubes: Experiment analysis to check for effect of 0.1 M NaCl on shear strength on L-shape concrete cubes as shown in Fig. 6. Concrete mix of M-20 was used for cubes specimens. During test of shear on L-shapes cube specimens, reveled cubes placed for curing in 0.1 M NaCl concentration of water for 30 h, resulted in 9.90% more shear strength than normal water for 7 days specimen. In addition, 10.25% of excess shear strength was observed compared to normal water cured specimen of 28 days [19].

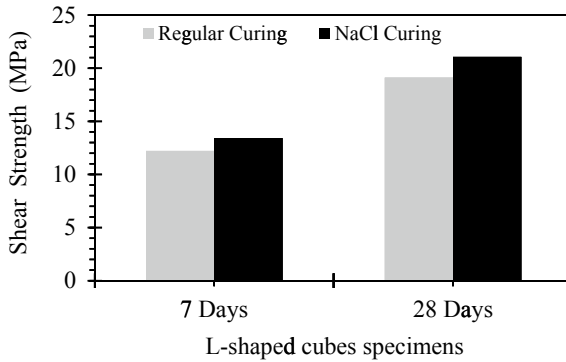


Fig. 6 Shear load failure of cubes after 30 h of curing in 0.1 M NaCl solution

Slab specimens: Three types of slab specimens were tested against failure load in a universal testing machine. Among them, P1- slab specimen casted and kept in 0.1 M NaCl with reinforcement of slab as anode at 0.02 mA/mm^2 in water for 30 h after curing and drying cycle. Similarly, P2- slab specimen with 0.02 mA/mm^2 of current density to reinforcement and coated with sodium silicate with 1:3 ratio to water. Solution coating was applied in three layers to slab specimens. In addition, P3- slab specimen, where reinforcement worked as cathode and anode as iron plate is provided at the bottom of the slab surface [20]. During the experiments of 30 h the current density of 0.02 mA/mm^2 was applied to reinforcement of slab specimens (P1, P2 and P3). P3 slab specimen failed at load of 78.5 kN, followed by P2, coated with sodium silicate resisted 75.35 kN of load and P1 specimen, in which reinforcement of slab was treated as anode connected to iron plate as cathode in saltwater environment failed at 41.75 kN (Fig. 7).

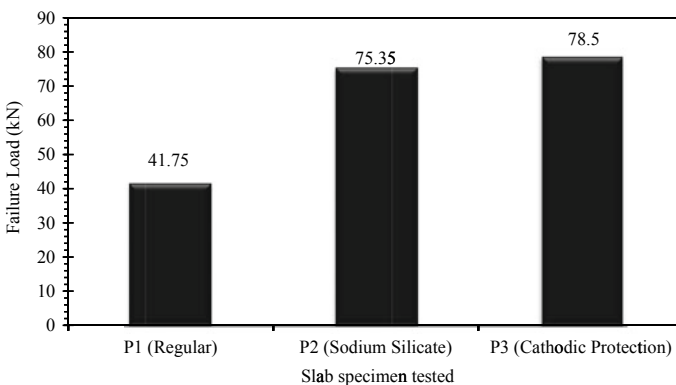


Fig. 7 Load carrying capacity of slab specimens in different condition

4 Conclusions

Experimental analysis for concrete and RCC structures showed that the shear in concrete increases but failure may be possible for RCC structures like slab. Cathodic protection to reinforcement in RCC structure could gain good strength to structure. The experiment showed a rise in strength to 46.81% with cathodic protection to reinforcement, 44.60% of rise with sodium silicate coating on slab, compared to slab reinforcement as anode at similar current density. In addition, structures in saltwater conditions could improve shear strength complimenting, combining the technique of cathodic protected reinforcement. L-Shaped cubes tested for shear increased strength by 10.25% after 28 days for M20 concrete mix. NaCl may help to reduce the rapid strength degradation of concrete in this condition. Cathodic protection method may overpass the economy, this could be overcome by renewable energy sources such as solar or wind power. A study in the combination of shear and cathodic protection of reinforcement in RCC members could lead in the extension of the life of the structure.

References

1. Woo-Yong J, Young-Soo Y, Young-Moo S (2003) Predicting the remaining service life of land concrete by steel corrosion. *Cem Concr Res* 33:663–677
2. Söylev TA, Richardson MG (2008) Corrosion inhibitors for steel in concrete: state-of-the-art report. *Constr Build Mater* 22:609–622
3. Medeiros MHF, Helene P (2009) Surface treatment of reinforced concrete in marine environment: influence on chloride diffusion coefficient and capillary water absorption. *Constr Build Mater* 23:1476–1484
4. Ghods P, Isgor OB, Pour-Ghaz M (2007) A practical method for calculating the corrosion rate of uniformly depassivated reinforcing bars in concrete. *Mater Corros* 58:265–272
5. Aman M, Amr E (2008) Importance of shear assessment of concrete structures detailed to different capacity design requirements. *Eng Struct* 30:1590–1604
6. Evan CB, Frank JV, Michael PC (2006) Simplified modified compression field theory for calculating shear strength of reinforced concrete elements. *ACI Struct J* 103:614–624
7. Suhag P, Vikas K, Patel HK, Patel VR, Pandya II (2017) Prediction of ultimate shear strength of moderate deep concrete beam including size effect. *Int Res J Eng Technol* 04:813–818
8. Xu J, Wu Y (2009) Current distribution in reinforced concrete cathodic protection system with conductive mortar overlay anode. *Constr Build Mater* 23:2220–2226
9. Marcassoli P, Bonetti A, Lazzari L, Ormellesse M (2015) Modeling of potential distribution of subsea pipeline under cathodic protection by finite element method. *Mater Corros* 66:619–626
10. Montoya R, Nagel V, Galván JC, Bastidas JM (2013) Influence of irregularities in the electrolyte on the cathodic protection of steel: a numerical and experimental study. *Mater Corros* 64:1055–1065
11. MATCOR and CP Masters (2018). www.matcor.com/impressed-current-cathodic-protection. Assessed 01 Dec 2018.
12. IS 12269 (2013) Ordinary Portland Cement, 53 grade—specification. Bureau of Indian Standards, New Delhi
13. IS-383 (1970) Indian Standard for specification for coarse and fine aggregates from natural sources for concrete. Bureau of India Standard, New Delhi
14. IS 456 (2000) Plain and reinforced concrete—code of practice. Bureau of Indian Standards, New Delhi

15. IS:2386 (1963) Methods of test for aggregates for concrete (part III) specific gravity, density, voids, absorption and bulking. Bureau of Indian Standards, New Delhi
16. Senthil K, Baskar K (2015) Shear strength of concrete with E-waste plastic. *Proc Inst Civ Eng Constr Mater* 168:53–56
17. Saraswathya V, Ha-Won S (2007) Improving the durability of concrete by using inhibitors. *Build Environ* 42:464–472
18. Rodrigo de Almeida Souza LRA, Farias de Medeiros MH, Pereira E, Brandão Capraro AP (2017) Electrochemical chloride extraction: efficiency and impact on concrete containing 1% of NaCl. *Constr Build Mater* 145:435–444
19. Nanak PJ, Pamnani A, Kachwala A (2015) Shear strength of M30 grade self compacting concrete with different water based curing techniques. *Int J Adv Eng Technol Manag Appl Sci* 2:6–14
20. Fajardo G, Escadeillas G, Arliguie G (2006) Electrochemical chloride extraction (ECE) from steel-reinforced concrete specimens contaminated by “artificial” sea-water. *Corros Sci* 48:110–125

Performance Evaluation of Two-Way RC Slab Subjected to Blast Loading Using Finite Element Analysis



Kasturi Bhuyan , Kiran Kumar Jujjavarapu, and Hrishikesh Sharma

Abstract Recently, blast and impact have gained more importance in research work owing to the fact that these high-intensity events can completely destroy any structure, causing tremendous casualties and property loss. Therefore, for any structure to withstand such extreme events, it is important to consider the effect of blast and impact loading in their design. Research works on response and damage analysis of reinforced concrete structural components such as slabs, columns, beams and walls subjected to blast and impact are limited in the literature and are essential for assessing its vulnerability. The current work investigates the performance of two-way reinforced concrete (RC) slabs subjected to blast loading. To simulate the field blast tests on different slabs, initially, a numerical model is established in a finite element preprocessor (HyperMesh). Later on, with the help of a commercial simulation software package (LS-DYNA), the numerical analysis is carried out. The developed numerical model is validated with the results of an experimental work done on an RC slab subjected to air blast from previous research. The results of the developed model are found in close agreement with actual experimental results. The numerical parameters of the validated model are used to develop a probabilistic model to investigate the blast response of the slab designed in current work. The probabilistic model developed in this research is able to capture the damage phenomena and also capable enough to reproduce the dynamic response.

Keywords RC slab · Blast loading · LS-DYNA · Numerical modeling · Maximum central deflection

K. Bhuyan (✉) · K. K. Jujjavarapu · H. Sharma
Indian Institute of Technology Guwahati, Guwahati, India
e-mail: b.kasturi@iitg.ac.in

K. K. Jujjavarapu
e-mail: kiranjujvarapu@gmail.com

H. Sharma
e-mail: shrishi@iitg.ac.in

1 Introduction

Blast-resistant design was earlier considered for only limited and significant structures which were supposed to be subjected to blast loading events such as military construction and nuclear power plant. With the increasing terrorist attacks causing loss of life and economy, it has now become necessary to include blast-resistant designs for civilian structures as well. A blast triggers the deterioration of individual structural components which may lead to the progressive collapse of the entire structure. The damages to buildings include failure of external and internal structural elements, disintegration of walls and bursting of windows. The intensity of damage imparted to a building due to blast load depends on the weight of blast charge, stand-off distance, orientation and configuration of the building. Analyzing the structural response with all its complexities like material nonlinearities and time-dependent deformation under blast loading is of paramount importance.

Considering the ability of reinforced concrete to resist blast, it can be treated as a key material in the alleviation of blast effects. In general, concrete and steel behave differently under suddenly applied load. Hence, a reasonable failure assessment of structural components is of utmost importance in anticipating blast loading. Since RC slab is a major structural component, evaluation of blast resistance for the same is essential. The current work focuses on modeling the behavior of RC slabs under blast loading which also accounts for RC walls. The RC slab in the current work is a 2-way system with appropriate boundary conditions and is subjected to out of plane blast loading. Similar inference can also be drawn for RC wall members subjected to out of plane loading during blast events in addition to the in-plane vertical loading.

2 Literature Review

Many researchers conducted experimental studies on RC slabs subjected to blast loading. With the help of experimental results, the explosive charges' weight and stand-off distances required to impose a given damage level on RC slabs using a modified displacement-based methodology were predicted [1]. The results of an experimental investigation conducted on the blast resistance of concrete panels made of ultra-high-strength concrete (UHSC) in Woomera, South Australia, in May 2004, was presented and a finite element computer code was also developed to analyze concrete structures subjected to blast loading which was validated with the outcome from the experimental test [2]. A series of tests investigating the blast resistances of RC slabs was also conducted and an ANFO blast test using ANFO charge was performed on reinforced ultra-high-strength concrete panels. Rebar and short steel fibers provide sufficient ductility, confer outstanding energy absorption and negate the brittle characteristics of these materials. Ultra-high-performance slabs showed more resistance to blast as compared to conventional concrete slabs [3].

Incorporating random changes in the structural and blast loading properties, two loosely coupled SDOF systems were used to model one-way RC slab subjected to blast loading for analyzing its flexural and direct shear response. An experimental investigation indicated that reinforced concrete structures subjected to distribute the load of short duration may not behave plastically at mid-span and fail there, as large loading with short duration is more likely to cause a slab to fail by its shear failure mode while a relatively small amplitude load with a longer duration will result in flexural failure [4]. A three-dimensional numerical model of RC plate was simulated for concrete material spallation under various blast loading and structural conditions and was seen that with proper configuration of protective structure, it can sustain a specific level of the blast without global failure [5]. To simulate the dynamic response of a simply supported RC slab under blast loadings, one finite difference program was developed and the deformation of the slab was due to the duration time and peak value of blast loadings. The SDOF analysis is straightforward and suitable for use in a design office but the results can be substantially conservative [6].

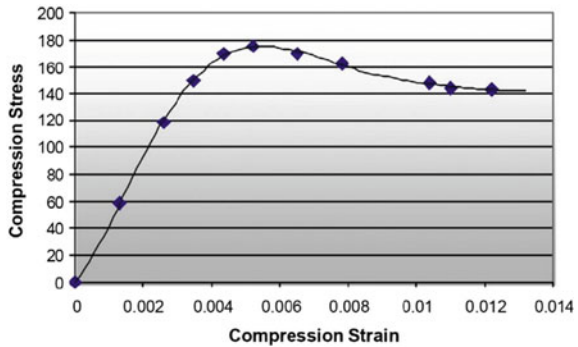
Research conducted on the damage modes of an RC slab under the air blast loadings by using the erosion technique in LS-DYNA was clearly showed [7]. Six one-way RC slabs of two groups were tested under real blast loads to address the scaling of the dynamic response [8]. The scaling used for the structure is geometrical, whereas that for the explosive charge is based on Hopkinson's law. The research concludes that the local damage on the concrete slabs with larger scale factors reduces when compared with that of slabs with smaller scale factors; and the normalized damage parameters of the slabs slightly increase with decreasing scale-down factor.

Dynamic response and the damage mechanism of the RC slab were analyzed under close-in explosion using LS-DYNA considering the strain rate effects, dynamic increasing factor and equation of state for concrete [9]. It was observed that the increase in the amount of the explosive can change the failure mode of the slab. A parametric study concluded that the damage degree increases when the explosive weight is increased or the explosive position is moved from the center to the boundary after simulating the blast response and damage assessment of a two-way RC slab under blast loading [10]. In an experimental study and numerical simulations on the dynamic performance of a UHPC slab in comparison to normal strength concrete slab under contact charge explosion, a significant reduction in concrete punching and spall damage in UHPC was observed as compared with the NRC slab. The feasibility and accuracy of the numerical model were validated by comparing numerical results with the experimental observations [11]. Figure 1 shows the schematic of the stress-strain response of UHPC.

Limitations associated with the modeling of blast loading using a single degree-of-freedom analysis cause the response to deviate from the actual behavior of concrete structures. Moreover, they do not account for the inherent uncertainty associated with the blast loading, geometric and material uncertainties of concrete structure, and the uncertainty in the interaction of blast loading with the concrete structure.

In this study, the probabilistic model for an RC slab subject to blast loading is developed. Since the testing of RC slabs with actual blast events is difficult, the probabilistic models are developed with the help of numerical simulation results.

Fig. 1 Stress–strain relationship of UHPC material [11]



The data obtained through numerical analysis is used for the regression analysis and the models are developed such that they fit best to the data. The developed model incorporates the multi-model response of the structure, interaction among different components and inherent uncertainty associated with modeling configuration and material properties.

3 Experimental Design for FE Simulation

For developing the probabilistic capacity model for any structural component at the ultimate limit state, a sufficient number of data regarding the ultimate deformation capacity is required from experiments. Due to the limitations of conducting actual blast experiments, FE simulation results are used to develop probabilistic capacity models. The ranges of variables of these developed models are selected in such a way that they should replicate the practical scenario. Blast loadings on these RC slabs are also designed with varying blast charge weight and stand-off distance. A sufficient number of data is required for minimizing the statistical uncertainty. Thus, the developed probabilistic model is valid only for the range of data used for developing the model. The ranges of geometric and material properties in the probabilistic model of the RC slab are established using the data from the literature and common design practices for ensuring contribution from both existing and new data of RC slabs. If all the variables in the experiments are randomly combined, the resulting model developed can be unrealistic. Thus, in order to generate the realistic data, the design variables are divided into primary variables and secondary variables. The variables which capture the basic design requirements are categorized into primary variables (shown in Table 1), and the rest of the variables derived from primary variables are categorized as derived variables or secondary variables as given in Table 2.

The entire experimental design is divided into the design of RC slabs and the design of blast pressure. The load variables are designed separately to create almost all the combinations of blast loading scenarios during a detonation. The ranges of

Table 1 Range of basic variables of RC slab

Variable	Symbol	Range
Slab length (m)	L	2–15
Slab thickness (m)	T	0.2–0.5
Longitudinal reinforcement ratio (%)	ρ_l	0.12–2.47
Transverse reinforcement ratio (%)	ρ_s	0.12–0.94
Compressive strength of concrete (MPa)	f_{ck}	20–55
Yield strength of longitudinal and transverse reinforcement (MPa)	f_y	415–550
Boundary condition of the slab	B_T	Four-side fixed condition
Blast Charge (kg-TNT)	Q	150.00–900.00
Stand-off distance (m)	R	1.00–12.00

Table 2 Expression and range of secondary variables of RC slabs

Variable	Symbol	Expression/Range
Diameter of the longitudinal bar (mm)	d_l	6, 8, 10, 12, 16, 20, 22, 25, 30
Diameter of the transverse bar (mm)	d_s	6, 8, 10, 12, 16, 20, 22, 25
Spacing of longitudinal bar	S_l	$(\frac{\pi}{4}d_l^2 \times 1000)/(\rho_l BD/100)$
Spacing of transverse bar	S_s	$(\frac{\pi}{4}d_s^2 \times 1000)/(\rho_s BD/100)$

blast charge (Q) and its stand-off distance (R) used in the current work are confined to a level of protection required to prevent a building from collapsing or minimize injuries and deaths. However, this research aims to contribute a low to medium level blast protection and so, a blast threat level from a bomb or any explosive which can be carried by luggage, automobile and van (FEMA 428) are accounted for. Considering the slab variables and load cases together in the experimental design, there could have been cases when some slabs experience the blast events to impractical scenarios. This is avoided by splitting the experimental design into basic and dependent variables and then performing a realistic combination of the RC slab parameters as well as blast loading parameters.

4 Numerical Model

The most acceptable modeling methods of RC structures are the smeared model, embedded model and discrete model. For performing the dynamic response of individual structural components, the discrete model is the best method [12]. In a discrete model, the concrete element and steel bar element are treated as different elements. A one-dimensional slide contact is provided between the concrete elements and reinforcement elements to simulate the longitudinal shear behavior, and the differences

in two material mechanical properties can be clearly shown, when the blast loadings affect the structure. The mechanical behaviors of the slab depend on the aspect ratio of length to width. When the aspect ratio is greater than 2, the slab can be considered as a one-direction bending-type structure and when less than 2, the mechanical behavior of the slab is two-way bending [13].

In LS-DYNA [14], mainly pure Lagrangian and Arbitrary Lagrangian Eulerian (ALE) [15] are the available numerical techniques for analyzing the structural response subjected to blast loadings. Though both methods provide accurate results, Lagrangian formulation can lead to erroneous results or termination when the simulation involves large angular distortion. Another shortcoming of this method is its applicability to blast problems involving large mass flow and limited fluid–structure interaction. A Eulerian analysis has a disadvantage over Lagrangian as the material moves from one element to the other and the use of advection algorithms are necessary for material flow, thus making it more complex and costlier. ALE formulation is developed by combining the Lagrangian and Eulerian formulation, for addressing both the structural and fluid dynamics of a detonation. This method rezones the nodes to an optimal position, unlike the Eulerian solver. ALE simulation is costlier compared to Lagrangian as most of the time is spent in calculating the material to be transported between the elements. ALE handles large distortion and preserves the ability to identify interfaces covering the shortcomings of Lagrangian and Eulerian methods. In the present investigation, an ALE formulation is used to simulate a two-way RC slab fixed on all sides subject to blast loading. A geometric model of the RC slab is made using HyperMesh [16], and analysis is done in the commercial FE program LS-DYNA [14].

4.1 Material Model

A rate-dependent material model is used for all the materials due to the sensitivity of material properties. Concrete is modeled as 3D-solid elements with the formulation of continuous surface cap model (CSCM) [17] available in the software LS-DYNA. This is a cap model with a smooth intersection between the shear yield surface and hardening cap; and this model contributes to erosion in concrete and also takes into account the strain rate dependency of the concrete strength. The reinforcement bars are modeled explicitly as one-dimensional elements with the formulation of an elastoplastic material as it accounts for strain rate dependency and also failure, based on plastic strain. The contact between the concrete and reinforcement is modeled using the Lagrangian coupling method. This method provides the coupling mechanism for steel and concrete interaction by allowing the coupling between edges of each part and saves the effort of matching the nodes of the reinforcement and the concrete which might be very difficult in some cases. Mesh refinement is done and convergence is achieved at 25 mm mesh size, and minimization of the hourglass energy is ensured.

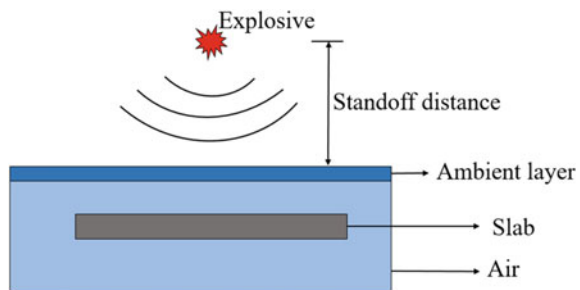
The boundary conditions of the RC slab modeled are the four-side fixed-boundary conditions. In order to simulate the exact practical condition, non-reflecting boundary is provided for air. And boundary conditions are applied directly to the eight sets of nodes in the slab rather than assigning only to the last set of nodes for a realistic bearing state.

4.2 Blast Loading

Whenever the explosion happens inside or outside of the structure, the pressure exerting on the slab is not uniformly distributed. It depends on the relative location between the charge and the slab, the direction of the shock wave motion and many aspects. At the same time, the slab will be subjected to more than one impact by the reflected pressure wave. From the software LS-DYNA, the pressure of the explosive, which is exerted on the slab, was determined and the pressure is calculated by considering Arbitrary Lagrangian Eulerian (ALE) formulation, to overcome the current limitations of the conventional approach. A hemispherical surface blast at the mid-height of the slab is simulated with a blast charge (Q) at a stand-off distance (R) as shown in Fig. 2. The blast load is simulated through an empirical pressure load history due to a conventional chemical explosion, directly applied to the nodes of a Lagrangian structure.

To overcome the limitations of the conventional approach in blast load simulations, in this approach, an Arbitrary Lagrangian Eulerian (ALE) formulation is used. A single element layer of ambient formulation makes up the exterior surface of the air domain which faces the blast. Its function is to receive information from the blast loading as provided by CONWEP formulation (Livermore Software Technology Corporation), which is then converted to thermodynamic state data and subsequently applied as a source to adjoining ALE air elements. The air mesh interacts with Lagrangian structural elements to apply the load on the elements. Meshed slab with air and ambient layer is given in Fig. 3.

Fig. 2 Schematic view of blast loading



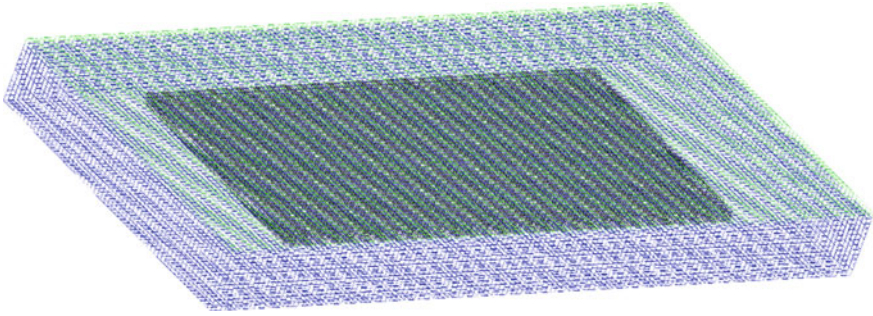


Fig. 3 FE model of RC slab along with air and ambient layer

5 Numerical Simulation

The numerical model is developed using LS-PrePost and then it is analyzed with the finite element software LS-DYNA. The software is a general purpose finite element software capable of simulating complex realistic problems. The codes' origin lies in a highly nonlinear, transient dynamic finite element analysis using the explicit time integration method. To analyze the capacity of the RC slab, the deformation is recorded at the ultimate limit state of the two-way RC slab. For the ultimate performance level, the values are recorded for the RC slab reaching the prescribed damage. The values of the RC slab which do not get damaged are also recorded. The FE model takes into account the strain rate effect, the multi-modal response and the interaction of the RC slab with different pressure fields during the blast loading. Figure 4 shows the FE model of an RC slab at different stages of evolution of blast loading.

5.1 Finite Element (FE) Validation

The FE model used in this research is validated with the experimental results of a two-way reinforced concrete plate tested under fully clamped two-way bending of blast load under shock tube analysis by Jacques Eric in Ottawa-Carleton Institute for Civil Engineering, University of Ottawa [18].

The clear dimensions of the validated slab are 2440 mm in both length (L) and width (B), and thickness of slab (t) is 75 mm. The clear span kept in both directions is 2032 mm. So, the aspect ratio of length to width is 1.0, which means that the slab is a two-way bending slab. The specimen is constructed with a 6.3 mm diameter un-deformed steel wire with a yield strength of 580 MPa at a yield strain of 0.002 mm/mm. The experimental slab was specified to have a 28-day compressive strength of 40 MPa, using 10 mm crushed limestone aggregate and a slump of

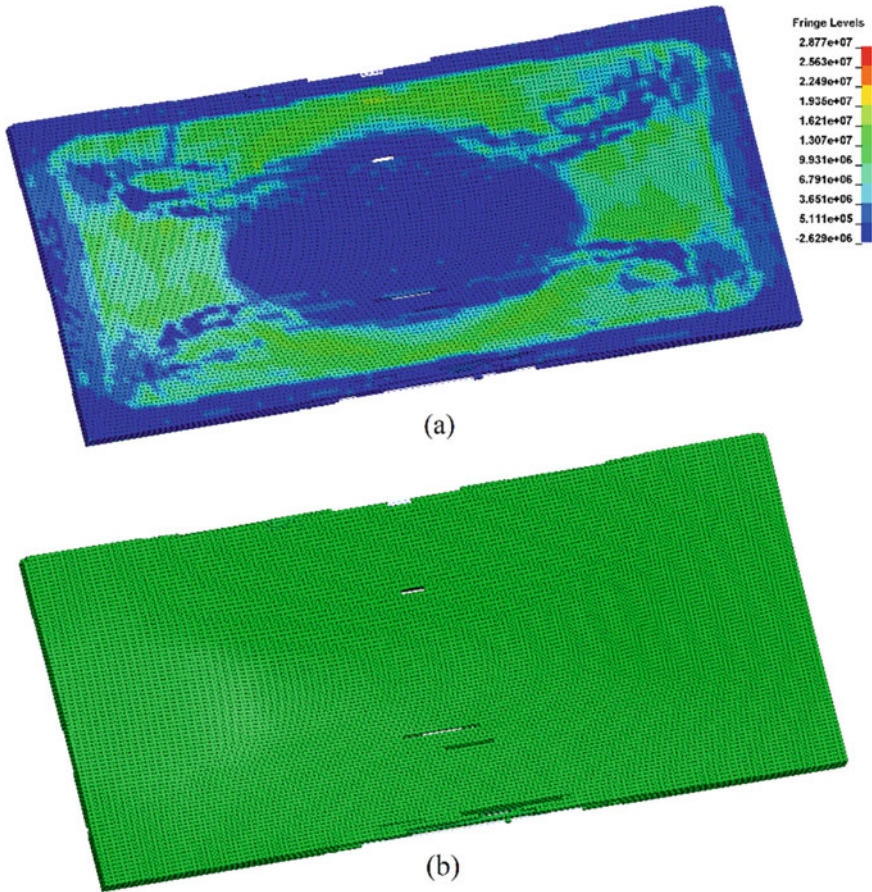


Fig. 4 FE model of an RC slab (a) at pressure transfer and (b) at damage state

100 mm. However, the concrete strength for the specimens at the time of testing was approximately 50–60 MPa.

The steel bars were laid out in two ways with two layers; the spacing between the two bars in both the directions is 240 mm. The mesh generation of the concrete and steel bar is 25 mm and one-dimensional slide contact between the concrete and steel bar nodes was established. During the experiment, the RC slab was subjected to a pressure of 355 MPa, and to simulate the exact pressure, corresponding blast charge and stand-off distance are determined and applied in LS-DYNA. ALE formulation is used for creating a realistic environment and practical scenario. CSCM [17] concrete material model is used for the concrete, and the steel bars are modeled with plastic kinematic material model and beam element formulation. The experimental result is shown in Fig. 5a, b exhibits the plastic strain developed in the RC slab with the help of LS-DYNA.

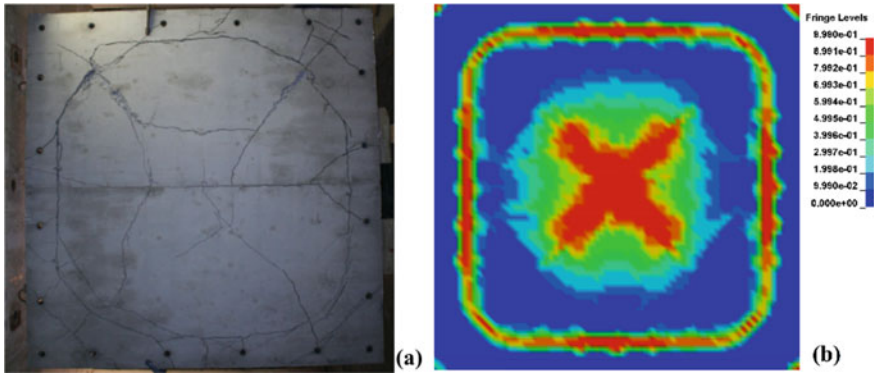


Fig. 5 (a) Two-way RC slab subjected to the blast load in the experiment [14] and (b) Plastic strain developed in the slab with FE analysis

In Fig. 6(a), pressure profile is compared for experimental, simulation as well as analytical purposes. Hand calculated and simulated pressure is almost close to 0.08 MPa whereas from experimental data, it is found to be 0.065 MPa. The maximum displacement of the RC slab in the experiment was 21.2 mm at 14.7 ms with cracking of the slab at the center. FE analysis shows a close similarity to the experimental results from Fig. 6(b). The maximum deflection of numerical analysis of RC is 14.7 mm at 14.9 ms with cracking at the center and some elements at the support. And from the analytical method, the value of deformation is 10.3 mm considering an SDOF (single degree of freedom) analysis. The result shows that the RC slab model performed well and gave deflection predictions that were close to the experimental values. Therefore, the modeling technique followed in this research is able to capture the damage mechanism. The close agreement which is obtained between the FE

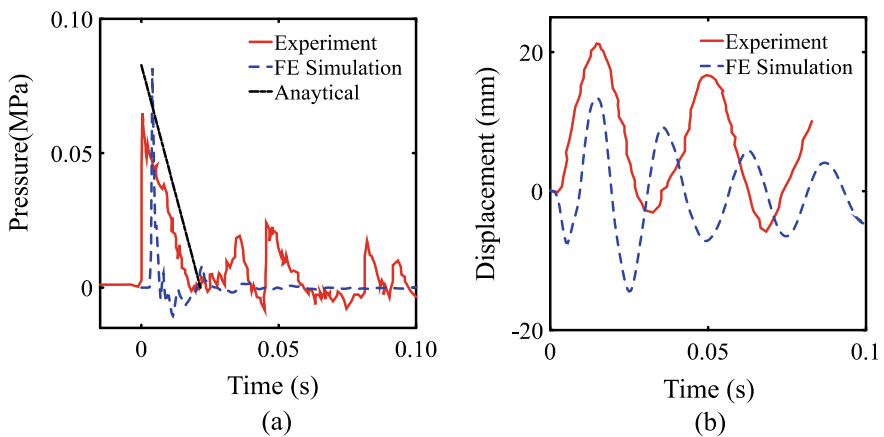


Fig. 6 Comparison of (a) pressure and (b) displacement profile for two-way RC slab

simulation and the experiment shows that the FE model yields a reliable prediction of dynamic response.

6 Probabilistic Capacity Model

Using the results in FE simulations, the probabilistic models are developed for estimating the probabilistic deformation capacity of a two-way RC slab subjected to blast loading under the ultimate performance level. The estimated probabilistic capacity models take into account the multi-modal response of the structure, the interaction among the different components and the inherent uncertainty associated with the modeling, configuration and material properties of the concrete structure.

The probabilistic models are constructed by adding correction terms to mechanical models. Because the data used for the model assessment come from FE simulations, it is assumed that there is no measurement error in the data. The following equation shows the model form where a transformation of the quantity of interest is written as the sum of (in order from left to right) a mechanical model, a correction term to account for the bias in the mechanical model and model error [19]. Following the general formulation for probabilistic models, the deformation capacity for the ultimate limit state is formulated as

$$\ln[P_i(x, \Theta_{P_i})] = \ln[p_i(x)] + \gamma_{P_i}(x, \theta_{P_i}) + \sigma_{P_i}e_{P_i} \quad (1)$$

where P_i is the probabilistic capacity of RC slab for i deformation; p_i is the mechanical capacity of the RC slab for i deformation; $\gamma_{P_i}(x, \theta_{P_i})$ is the correction term for the bias inherent in the mechanical model defined as

$$\gamma_{P_i}(x, \theta_{P_i}) = \sum_{j=1}^n \theta_{P_i,j} h_{P_i,j}(x) \quad (2)$$

where $h_{P_i,j}(X)$, $j = 1, \dots, n$ is an explanatory function (or regressors) defined as functions of x , $\theta_{P_i,j}$, $j = 1, \dots, n$ are the parameters associated with explanatory functions, $\sigma_{P_i}e_{P_i}$ is a model error, e_{P_i} is Gaussian error and $\Theta_{P_i} = \theta_{P_i}$ is the set of unknown model parameters in which $\theta_{P_i} = (\theta_{P_i,1}, K, \theta_{P_i,k})$.

6.1 Mechanical Model

For an RC slab under the ultimate performance level, an analytical model for deformation developed by Newmark is used in this research [20].

$$\frac{X_m}{X_E} = 1 + \frac{t_d}{\beta} \left(\frac{1}{2} - \frac{1}{3}\beta \right) \quad (3)$$

where $\beta = (r_u/P)$ is explained as the ratio of yield strength to the average applied load, and $X_E = (r_u/K_E)$ is the equivalent maximum elastoplastic deformation. For calculating the maximum deformation (X_m) from the Newmark equation, β is considered as 1; as capacity is independent of the load applied,

$$\frac{X_m}{X_E} = 1 + \frac{t_d}{6} \quad (4)$$

6.2 Model Correction

The model correction terms are used to capture the physical phenomena that are not accounted for in the case of the mechanical model. The first explanatory function h_1 accounts for the contribution of span moment and support moment of the structure (M_x/M_y). The second explanatory function, h_2 , accounts for the contribution of positive blast duration and natural period of structure (T_d/T_n). The following equation is proposed to estimate the probabilistic deformation (X_p) of a two-way RC slab subjected to blast loading, under ultimate performance level.

$$X_p = x_m \times e^{(0.000215h_1 + 0.009096h_2 + \sigma_x e_x)} \quad (5)$$

$$X_p = x_m \times e^{(0.000215 \frac{M_x}{M_y} + 0.009096 \frac{T_d}{T_n} + \sigma_x e_x)} \quad (6)$$

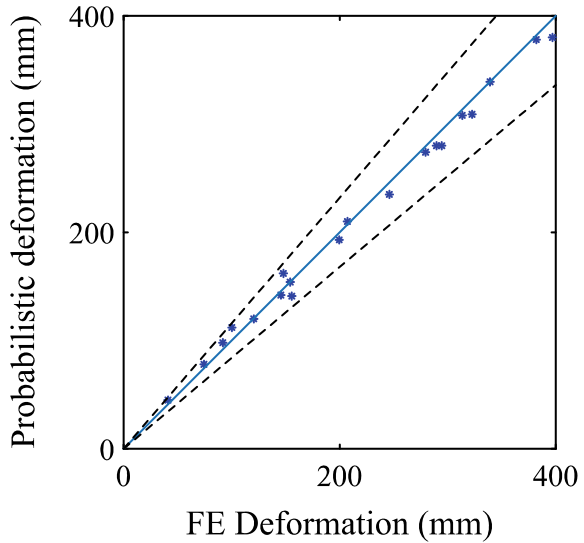
The standard deviation of the model is 8.13. Figure 7 shows the comparison between FE obtained results and predicted values of the probabilistic deformation capacity model. The median value is plotted for the probabilistic model. The proposed model is capable of predicting the deformation as most of the data set points lie within one standard error ($\pm\sigma_x$) bin as shown by dotted lines.

7 Conclusion

The developed probabilistic deformation capacity model is realistic, easy to use and also comforts in avoiding tedious FE simulations or experiments.

In the future, from this laid foundation, work can be focused on improvising the current proposed model for higher accuracies by increasing the number of data sets and also reducing the mesh size. In this current work, probabilistic capacity models are developed only for predicting the deformation, so developing models

Fig. 7 FE
Deformation—Probabilistic
deformation capacity of RC
slab



for the internal strain energy can be focused in the future which will be helpful for energy-based designs. As these models are valid only for prescribed boundary conditions, this work can further be expanded for other boundary conditions that are in practice. Developing this model for different performance levels such as crack limit state and post-blast scenario will also be considered in the future as the present model only accounts for the ultimate limit state performance level. Moreover, the performance-based capacity model of RC members can be developed, which leads to further improvement of current blast code provisions.

References

1. Silva PF, Lu B (2007) Improving the blast resistance capacity of RC slabs with innovative composite materials. *Compos B Eng* 38(5–6):523–534
2. Ngo T, Mendis P, Gupta A, Ramsay J (2007) Blast loading and blast effects on structures—an overview. *Elect J Struct Eng* 7(S1):76–91
3. Wu C, Oehlers DJ, Rebstroff M, Leach J, Whittaker AS (2009) Blast testing of ultra-high performance fibre and FRP-retrofitted concrete slabs. *Eng Struct* 31(9):2060–2069
4. Low HY, Hao H (2002) Reliability analysis of direct shear and flexural failure modes of RC slabs under explosive loading. *Eng Struct* 24(2):189–198
5. Xu K, Lu Y (2006) Numerical simulation study of spallation in reinforced concrete plates subjected to blast loading. *Comput Struct* 84(5–6):431–438
6. Jones J, Wu C, Oehlers DJ, Whittaker AS, Sun W, Marks S, Coppola R (2009) Finite difference analysis of simply supported RC slabs for blast loadings. *Eng Struct* 31(12):2825–2832
7. Tai YS, Chu TL, Hu HT, Wu JY (2011) Dynamic response of a reinforced concrete slab subjected to air blast load. *Theoret Appl Fract Mech* 56(3):140–147

8. Wang W, Zhang D, Lu F, Wang SC, Tang F (2012) Experimental study on scaling the explosion resistance of a one-way square reinforced concrete slab under a close-in blast loading. *Int J Impact Eng* 49:158–164
9. Zhao CF, Chen JY (2013) Damage mechanism and mode of square reinforced concrete slab subjected to blast loading. *Theoret Appl Fract Mech* 63:54–62
10. Jia H, Yu L, Wu G (2014) Damage assessment of two-way bending RC slabs subjected to blast loadings. *The Scientific World Journal*, 2014
11. Li J, Wu C, Hao H (2015) Investigation of ultra-high performance concrete slab and normal strength concrete slab under contact explosion. *Eng Struct* 102:395–408
12. Hentz S, Daudeville L, Donzé FV (2004) Identification and validation of a discrete element model for concrete. *J Eng Mech* 130(6):709–719
13. IS 456 (2000) Plain and reinforced concrete—code of practice. Indian Standard, ICS, 91.100.30, New Delhi
14. Livermore Software Technology Corporation (2003) *LSDYNA Keyword User's Manual*, Version 970. Livermore, CA
15. Olovsson L, Souli MH (2000) ALE and fluid-structure interaction capabilities in LS-DYNA. *ASME-PUBLICATIONS-PVP* 414(1):71–78
16. Altair Computing (2003). *HyperMesh Ver. 6.0 Basic Tutorial*, Altair Engineering Inc., 1820 E. Big Beaver, Troy, MI 48083
17. Schwer LE, Murray YD (2002) Continuous surface cap model for geomaterial modeling: a new LS-DYNA material type. In *Seventh International LSDYNA Users Conference*. Dearborn, Michigan, LSTC& ETA, pp. 16–35
18. Jacques E (2011) Blast retrofit of reinforced concrete walls and slabs. University of Ottawa (Canada)
19. Gardoni P, Der Kiureghian A, Mosalam KM (2002) Probabilistic capacity models and fragility estimates for reinforced concrete columns based on experimental observations. *J Eng Mech* 128(10):1024–1038
20. Brooks NB, Newmark NM (1953) The response of simple structures to dynamic loads. Technical Report, Office of Naval Research

Development of Fragility Curves for Different Types of RC Frame Structures



Neeva Ahanthem and S. S. Ningthoukhongjam

Abstract In this paper, seismic behaviors of different types of reinforced concrete (RC) frames conforming and non-conforming to strong column-weak beam (SCWB) design principles have been investigated using SAP2000. Nonlinear static (pushover) analysis has been employed to obtain the capacity curves of different RC frames. The fragility curves are then plotted from the capacity curves obtained from pushover analysis. The guidelines given in the HAZUS manual have been referred to for developing fragility curves. The performance points of RC frames conforming to SCWB design principles have been obtained at IO levels whereas those non-conforming to SCWB design principles have been obtained at LS levels. This shows that the damage of RC frames non-conforming to SCWB design principles will be severe than that of the RC frame conforming to SCWB design principles. Moreover, from the fragility curves, it has been observed that the RC frame non-conforming to SCWB design criteria frame has a higher probability of damage than that of the RC frame conforming to SCWB criteria at a particular value of spectral displacement.

Keywords Pushover analysis · Capacity spectrum · Performance point · Fragility curve · HAZUS methodology · Damage states

1 Introduction

The destruction caused by major earthquakes to mankind and its properties has been massive since time immemorial. During past earthquakes, many buildings had been collapsed due to the failure of vertical members. It has been found beneficial to disperse earthquake-induced energy by yielding the beams rather than the columns in building frames, since columns provide total strength and stability to the entire frame structure and their failure resulted in the global collapse of the structure. Hence,

N. Ahanthem (✉) · S. S. Ningthoukhongjam
Department of Civil Engineering, Manipur Institute of Technology, Imphal, India
e-mail: nivzthem@gmail.com

S. S. Ningthoukhongjam
e-mail: sukunao@gmail.com

it is desirable to control the formation of plastic hinges in columns to a possible extent while allowing the dissipation of most of the energy through the yielding of the beams. This is the concept of “strong-column weak-beam”. Seismic design codes such as ACI 318–14 [1] and IS 13920: 2016 [2] have requirements for capacity design in which the strength at the member level is at the top of the strength pyramid and then the structural level. As a result, the strength of the column ought to be higher than that of the beam. Some variations have been observed in some of the international seismic codes in the requirements of a strong-column weak-beam design concept. SCWB ratio (i.e., the ratio of the moment capacities at the end of the column to that of the beam meeting at a joint) recommended by ACI 318–14 [1] is 1.2, Eurocode 8 [3] recommends a ratio of 1.3, and that recommended by IS 13920: 2016 [2] is 1.4. Besides capacity-based design principle (SCWB), seismic vulnerability assessment of building structures is equally important for pre-earthquake disaster mitigation planning and post-earthquake recovery and retrofitting. The fragility curve is one of such extensively used tools for seismic vulnerability assessment of the structures. It is a statistical tool indicating the probability of surpassing a certain damage state as a function of an engineering demand parameter (spectral displacement at a given frequency) that denotes the ground motion. The fragility curve has been plotted using the capacity curve of the structure, whereas the capacity curve has been developed using Pushover (static-nonlinear) analysis in which the structure is subjected to a monotonic displacement-controlled lateral load pattern of constantly increasing magnitude until the structure totally collapses. Surana et al. [4] observed from the fragility analysis that the buildings conforming to strong column-weak beam design criterion lead to a substantial decrease in the probability of collapse. Bhandari et al. [5] studied the effect of column-to-beam moment capacity ratio (CBMCR) on the seismic performance of RC frames. It has been observed that an increase in CBMCR of the building frame decreases the probability of exceeding a given damage state for the same demand. Cagurangan [6] examined the effects of strong-column weak-beam (SCWB) ratios on tall reinforced concrete special moment frame structures. It has been found for all structures that the probability of collapse decreases as SCWB ratios increase. Haselton et al. [7] investigated the consequence of SCWB ratio on the seismic behavior as well as the probability of failure for two RC frames (4 storey and 12 storey). It has been observed that SCWB ratio depends on the height of the building for the same performance. SCWB ratios of 1.2 and 3 have been found adequate for 4-storey and 12-storey RC frame buildings, respectively. Kirchil et al. [8] investigated the effect due to the changes in the number of storeys of the building on fragility parameters using regression analysis. It has been observed that fragility parameters change significantly due to an increase in the number of storeys of the building. Mwafy et al. [9] observed that for the twelve RC buildings taken into consideration, a good correlation was obtained between the calculated “Dynamic Pushover” idealized envelopes of the dynamic analyses and the results obtained from static pushover analysis. Shinozuka et al. [10] investigated that similar fragility curves are obtained by both Pushover and Time-history analysis when minor damages occur in the structure; however, similar fragility curves obtained by these two methods are no longer applicable if major damages occur in the structure where nonlinear effects play a

crucial role. It has been observed from the above literature that many research works have been carried out on SCWB design principles; however, the quantification study on various SCWB ratios given by different seismic codes has not been performed as per author's knowledge. Thus in this paper, four hypothetical building frames are developed in such a way that one frame is non-conforming to SCWB criteria and the other three are conforming to SCWB criteria of seismic codes ACI 318–14 [1], Eurocode 8 [3], and IS 13920: 2016 [2], respectively. The seismic performance of the four building frames is investigated using Pushover analysis in FE-based software SAP2000. First, a brief description of the methodology used in the analysis is presented. Then, details of the structural models are discussed and the results of the analysis are presented in the form of capacity curves, performance point, and fragility curves.

2 Methodology

2.1 Pushover Analysis

Pushover analysis is a static nonlinear analysis where a structure is subjected to gravity loading and a monotonic lateral load pattern which is constantly increasing over elastic and inelastic behavior until an ultimate state is reached. It can be executed as force-controlled (used when the load is known, for instance, gravity loading) or displacement-controlled (used when specified drifts are known). A curve is obtained between the base shear and roof displacement in pushover analysis which is known as the capacity curve.

Since pushover analysis gives only the capacity curve of the structure, however, performance point of the structure is determined by the intersection of the capacity curve and the demand curve of the structure. Hence, the demand curve of the structure has to be determined separately which is carried out in relation to the maximum displacement induced by the earthquake either to the equivalent SDOF system or at the control node of the full structure. This maximum displacement has been known as the target displacement of the structure. The force–deformation curve for pushover analysis as per ATC 40 [11] and FEMA 273 [12] is shown in Fig. 1 where the points A, B, C, D, and E indicate the force–deflection behavior of the hinge and the points IO (Intermediate Occupancy), LS (Life Safety), and CP (Collapse Prevention) indicate the acceptance criteria of the hinge.

2.2 Capacity Spectrum Method (CSM)

The CSM [11] is an approximate procedure to analyze the seismic response of a structure with a nonlinear static analysis (pushover). The CSM helps to analyze the

Fig. 1 Force deformation for Pushover Analysis

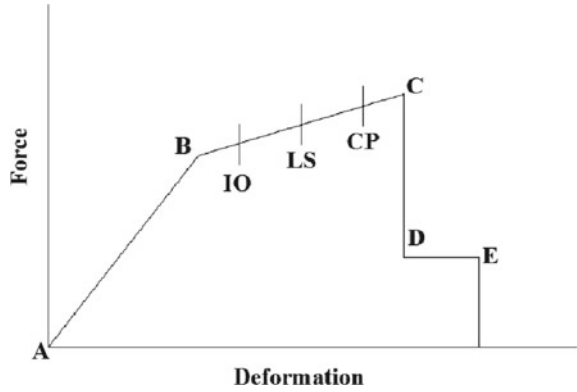
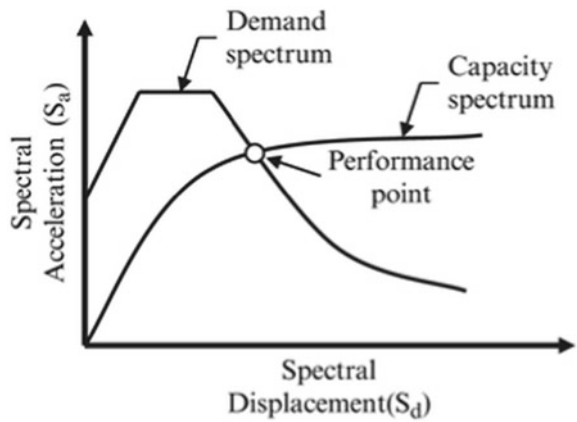


Fig. 2 Capacity Spectrum Method



seismic response of a structure in terms of forces and displacement, and permits to describe efficiently the seismic performance of structures. The pushover curve can be transformed into the “capacity spectrum” using the structure’s originally elastic dynamic properties (participation factor and modal mass coefficient). This capacity spectrum is represented in the Acceleration Displacement Response Spectrum format (ADRS), using spectral displacements (S_d) and spectral accelerations (S_a). The point at which the capacity curve intersects the demand curve represents the performance point, at which, capacity and demand are equal. By determining the performance point, practice engineers can develop an assessment of the spectral acceleration, displacement, and damage that possibly will occur for a particular structure responding to a certain earthquake (Fig. 2) [13].

2.3 HAZUS Methodology

The FEMA/NIBS earthquake loss estimation methodology, commonly known as HAZUS [14], is a complex collection of components that work together to estimate casualties, loss of function, and economic impacts on a region due to a scenario earthquake. The HAZUS technical manual offers the method for developing fragility curves for different kinds of structures. Building fragility curves are lognormal functions that describe the probability of reaching, or exceeding, structural and non-structural damage states, at given median estimates of spectral response, for example, spectral displacement. These curves take into account the variability and uncertainty associated with capacity curve properties, damage states, and ground shaking. Figure 3 [14] provides an example of fragility curves for the four damage states used in the FEMA/NIBS methodology and illustrates differences in damage-state probabilities for three levels of a spectral response corresponding to weak, medium, and strong earthquake ground shaking, respectively.

For a given damage state, a fragility curve is well described by the lognormal probability density function as per the HAZUS methodology

$$P[ds|S_d] = \phi \left[\frac{1}{\beta ds} \left(\frac{S_d}{S_{d,ds}} \right) \right] \tag{1}$$

where S_d is the spectral displacement defining the threshold of a particular damage state, $S_{d,ds}$ is the median value of spectral displacement at which the building reaches the threshold of damage states and can be calculated by various damage state models, βds is the standard deviation of the natural logarithm of spectral displacement for damage state, ds and ϕ is standard normal cumulative distribution function.

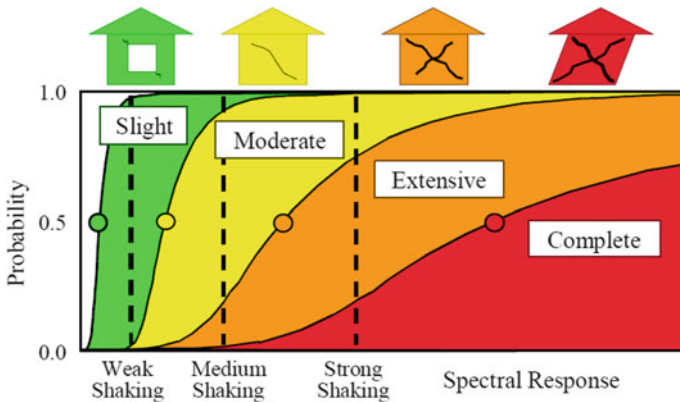


Fig. 3 Example Fragility Curves for Slight, Moderate, Extensive, and Complete Damage

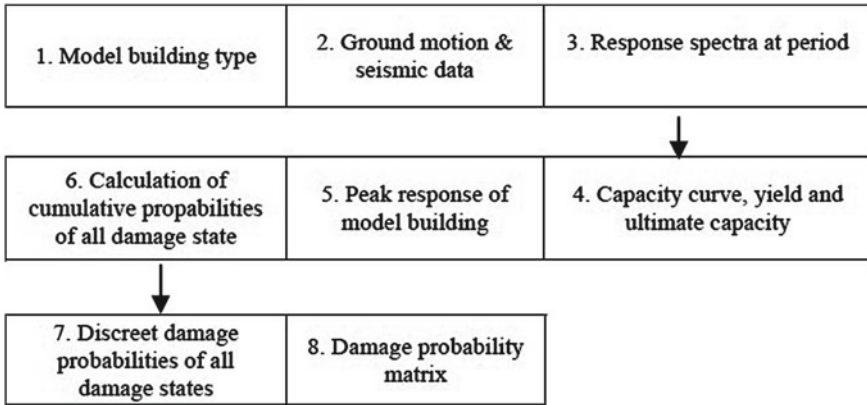


Fig. 4 Flow diagram of the HAZUS methodology

Table 1 Proposed damage state model

Damage states	Spectral displacement (m) ($S_{d,ds}$)
Slight	$0.7 S_{dy}$
Moderate	$1.5 S_{dy}$
Extensive	$0.5 (S_{dy} + S_{du})$
Complete	S_{du}

The methodology of the earthquake loss estimation method adopted by HAZUS has been shown in Fig. 4. This methodology consists of a total of seven steps starting from the input condition to the advancement of the Damage Probability Matrix.

In this paper, fragility curves have been obtained on the basis of capacity spectra which are obtained from pushover analysis. These capacity spectra are used to obtain the yield spectral displacement (S_{dy}) and ultimate spectral displacement (S_{du}). The values of the yield spectral displacement and ultimate spectral displacement have been used to obtain the values of medians at different damage states. The damage state model for the median value of spectral displacement ($S_{d,ds}$) proposed by Giovinazzi and Lagomarsino [15] has been used in this paper. The values of the median at the damage states are given in Table 1.

2.3.1 Development of Damage State Variability

The procedure given in FEMA, HAZUS-MH MR1 [14] for the development of damage state variability has been adopted in the present study. Lognormal standard deviation or beta describes the total variability of fragility curve damage states. The variability associated with the capacity curve (β_C), the variability associated with

Table 2 Variability Values used for two-storey model

Damage state	Kappa factor (κ)	Degradation values for		
		Damage (β_{Tds})	Capacity curve (β_C)	Total (β_{ds})
Slight	Minor degradation (0.9)	Moderate (0.4)	Moderate (0.3)	0.80
Moderate	Major degradation (0.5)	Moderate (0.4)	Moderate (0.3)	0.95
Extensive	Extreme degradation (0.1)	Moderate (0.4)	Moderate (0.3)	1.05
Complete	Extreme degradation (0.1)	Moderate (0.4)	Moderate (0.3)	1.05

demand spectrum (β_D) which is a key parameter in calculating damage state variability, and the variability associated with the discrete threshold of each damage state (β_{Tds}) are the three primary sources which contribute to the total variability of any given state. Owing to the dependence of demand spectrum with the capacity spectrum, their respective contributions to the total variability have been combined by the convolution process which is referred to as “CONV” in the Eq. (2) as per the HAZUS methodology. The third element β_{Tds} has been assumed mutually independent of the first two variability elements and is combined with the results of the CONV process using the square root of the sum of the squares (SRSS) method.

$$\beta_{ds} = \sqrt{(CONV[\beta_C, \beta_D])^2 + (\beta_{Tds})^2} \quad (2)$$

where β_{ds} is the lognormal standard deviation parameter that describes the total variability of damage state (ds); β_C is the lognormal standard deviation parameter that describes the variability of the capacity curve; β_D is the lognormal standard deviation parameter that describes the variability of the demand spectrum ($\beta_D = 0.45$ at short periods, $\beta_D = 0.5$ at longer periods); and β_{Tds} is the lognormal standard deviation parameter that describes the variability of the threshold of damage state (ds).

Sets of pre-calculated values of Damage-State Betas are mentioned in the HAZUS technical manual [14] (Tables 5 through 6.7). Hence, β_{ds} values can be taken directly from the tables considering appropriate values of degradation or Kappa factors (κ), β_C , and β_D values for different types of structures. Table 2 shows the variability values which are used for the two storeys considering the moderate cases of degradation without considering infill walls.

3 Structural Modeling

Four hypothetical G + 2 RC building frames have been considered in the present study. One building frame has been considered non-conforming to SCWB criteria of

Table 3 Structural data

Items		Dimensions	
		Column beam	
Strong column-weak beam	ACI 318–14	0.39 × 0.39 m	0.34 × 0.38 m
	Eurocode 8	0.42 × 0.42 m	0.35 × 0.40 m
	IS 13,920: 2016	0.46 × 0.46 m	0.36 × 0.44 m
Non-conforming to SCWB criteria		0.33 × 0.33 m	0.30 × 0.36 m
Size of the structure		13.11 × 10.06 m	
Floor height		3.04 m	
Thickness of slab		0.15 m	
Seismic zone		V	
Seismic zone factor		0.36	
Importance factor		1	
Response reduction factor		5	
Type of soil		Medium	

seismic codes with SCWB ratio approximately equal to 1, whereas the other three building frames have been considered conforming to SCWB criteria with SCWB ratios of 1.2, 1.3, and 1.4, respectively. The four RC building frames are taken as bare frames without infill walls for simplicity. The geometry of all the four RC frames are similar except different in member sizes. The sizes of the columns and beams are adopted as per SCWB ratio considering the limiting moment capacity of the members' section. Details of geometry for the RC frames are given in Table 3. All the frames have a common floor plan which is shown in Fig. 5 and floor slabs are modeled as a rigid diaphragm.

M20 grade of concrete and Fe500 grade of reinforcing steel have been used for the modeling of all the RC frames. Mander model (1988) [16] was used for the modeling of concrete, and the stress–strain model is shown in Fig. 6.

The shaded area shown in Fig. 6 represents the additional capacity provided by the confinement steel for storing strain energy. This area is limited to the energy capacity available in the area under the confinement steel stress–strain curve up to the ultimate steel strain, ϵ_u .

3D modeling of all the four RC building frames according to the requirements of Indian Standards (IS 456: 2000 [17], IS 1893 (Part1):2016 [18]) were developed in SAP2000 software. Beams and columns were modeled as nonlinear frame elements with lumped plasticity at the start and end of each member. The following hinge properties are provided for modeling nonlinear frame elements in SAP2000, i.e., P-M2-M3 hinges for columns with plastic rotation (in radians) of IO as 0.01, LS as 0.025, and CP as 0.05; and M3 hinges for beams with plastic rotation of IO as 0.002, LS as 0.0076, and CP as 0.008 as per FEMA 356 [19]. Live load intensity of 2.5kN/m² and floor finishes of 1kN/m² have been applied on each floor.

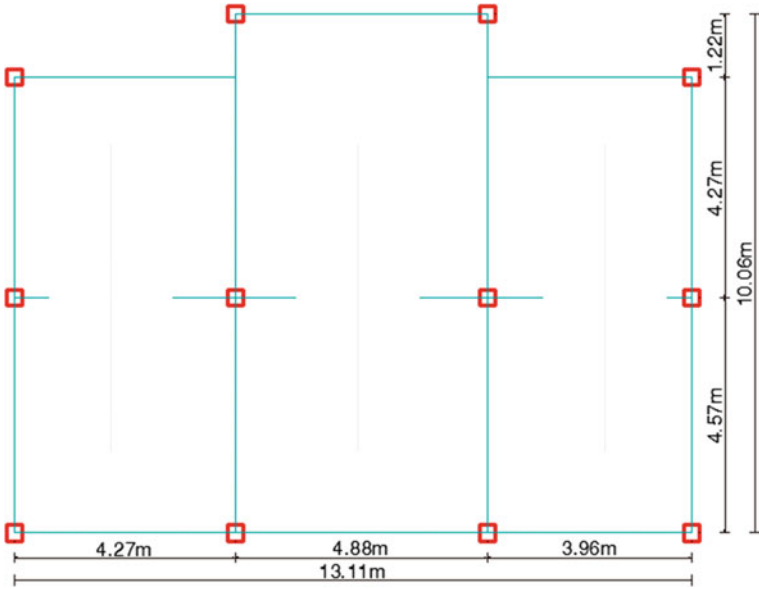


Fig. 5 Plan layout of both the structures

Fig. 6 Stress–strain model for monotonic loading of confined and unconfined concrete in compression

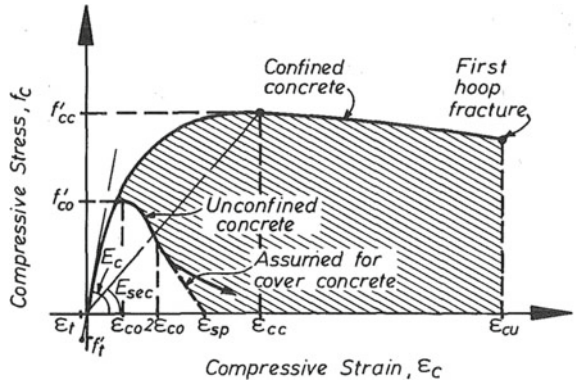


Table 4 Material properties

Modulus of elasticity of steel, E_s	210000 MPa
Modulus of elasticity of concrete, E_c	22360.68 MPa
Characteristic strength of concrete, f_{ck}	20 MPa
Yield stress of steel, f_y	500 MPa

4 Results and Discussions

4.1 Pushover Curve

Pushover curves (capacity curve) for the four RC frames have been shown in Fig. 7. It has been observed that the frame conforming to SCWB ratio 1.4 can resist more load at less deformation whereas the non-conforming frame with SCWB (~ratio 1.0) can resist less load at more deformation. The RC frames conforming to SCWB ratios of 1.4, 1.3, and 1.2 can resist more loads of 175, 150, and 137% at less deformation of 70, 75, and 87%, respectively, as compared to the RC frame non-conforming with SCWB (~ratio 1.0).

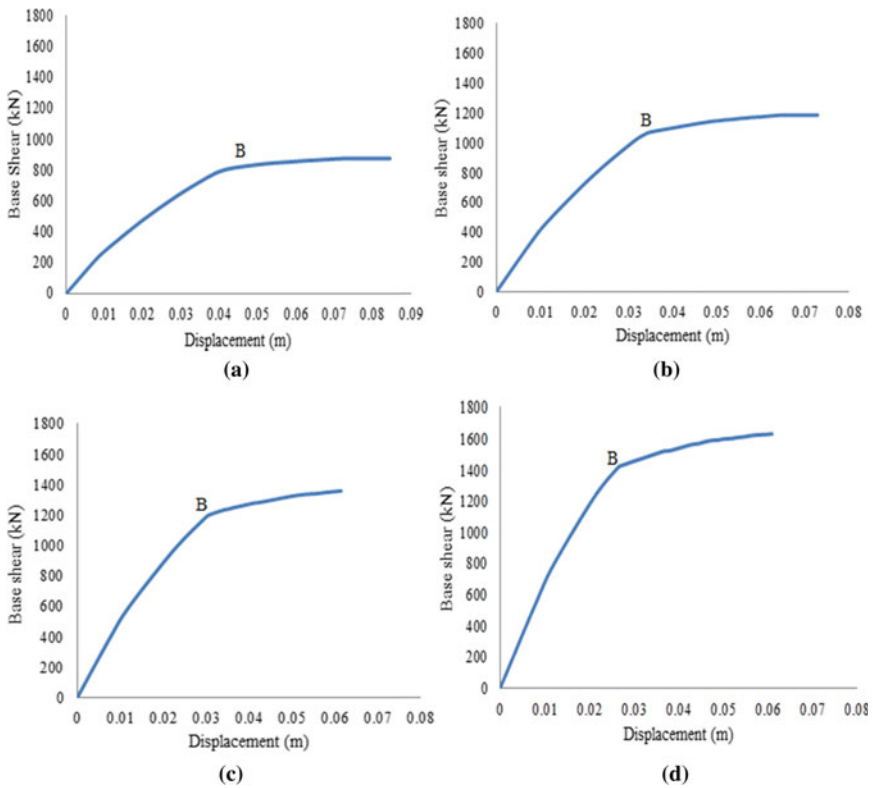


Fig. 7 Pushover curves for frames **a** non-conforming to SCWB criteria **b** SCWB ratio 1.2 **c** SCWB ratio 1.3 **d** SCWB ratio 1.4

4.2 Performance Point

The performance point in terms of base shear and displacement of all the four different frame structures based on the Capacity Spectrum Method are shown in Fig. 8a, b, c and d, respectively.

The performance point RC frames conforming to SCWB ratios of 1.4, 1.3, and 1.2 occur at higher base shear 180.72, 151.84, and 180.72% at less deformation of 69.81, 79.24, and 84.91%, respectively, as compared to the RC frame non-conforming to SCWB (~ratio 1.0). The occurrence of performance points at a greater value of base shear and a smaller value of displacement for a strong column-weak beam structure indicates good seismic performances.

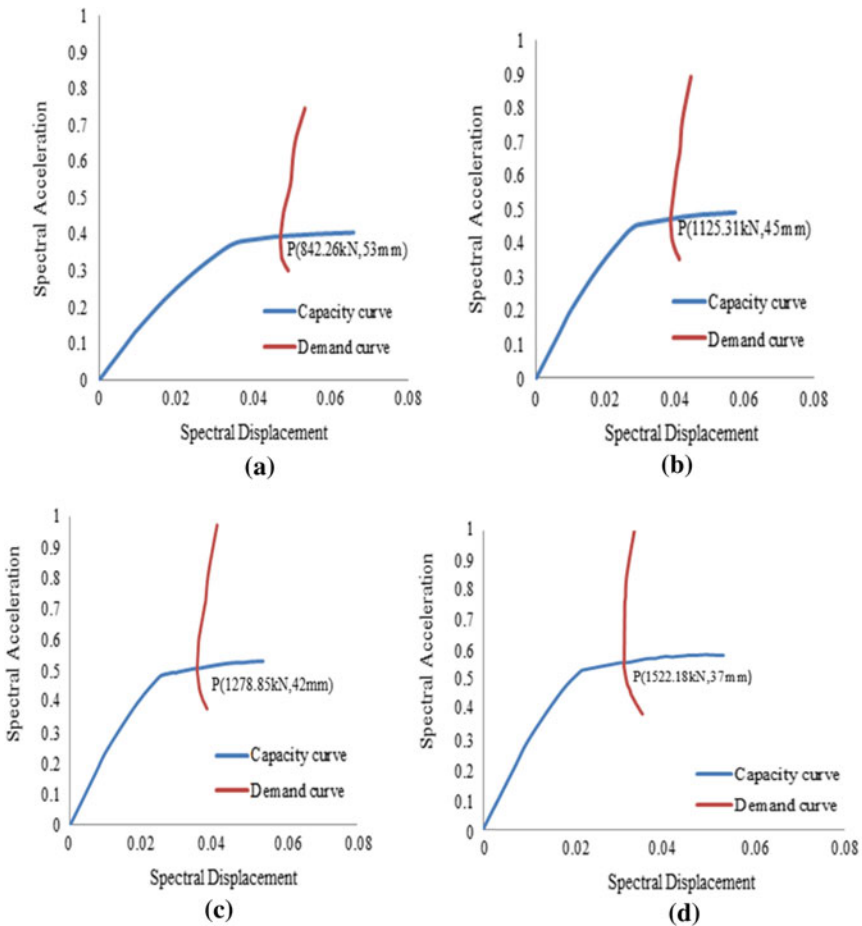


Fig. 8 Performance points for frames **a** non-conforming to SCWB criteria **b** SCWB ratio 1.2 **c** SCWB ratio 1.3 **d** SCWB ratios 1.4

4.3 Plastic Hinge Formation

Plastic hinges are formed at various levels of displacement for the four frame structures. The formations of hinges at the last step for the four RC frame structures are shown in Fig. 9a, b, c, and d.

In case of frame structure non-conforming to SCWB criteria, the hinge formation at the IO level is 16.8% and that at the LS level is 9.8%. In a frame structure with SCWB ratio 1.2, the hinge formation at the IO level is 23.4% and that at the LS level

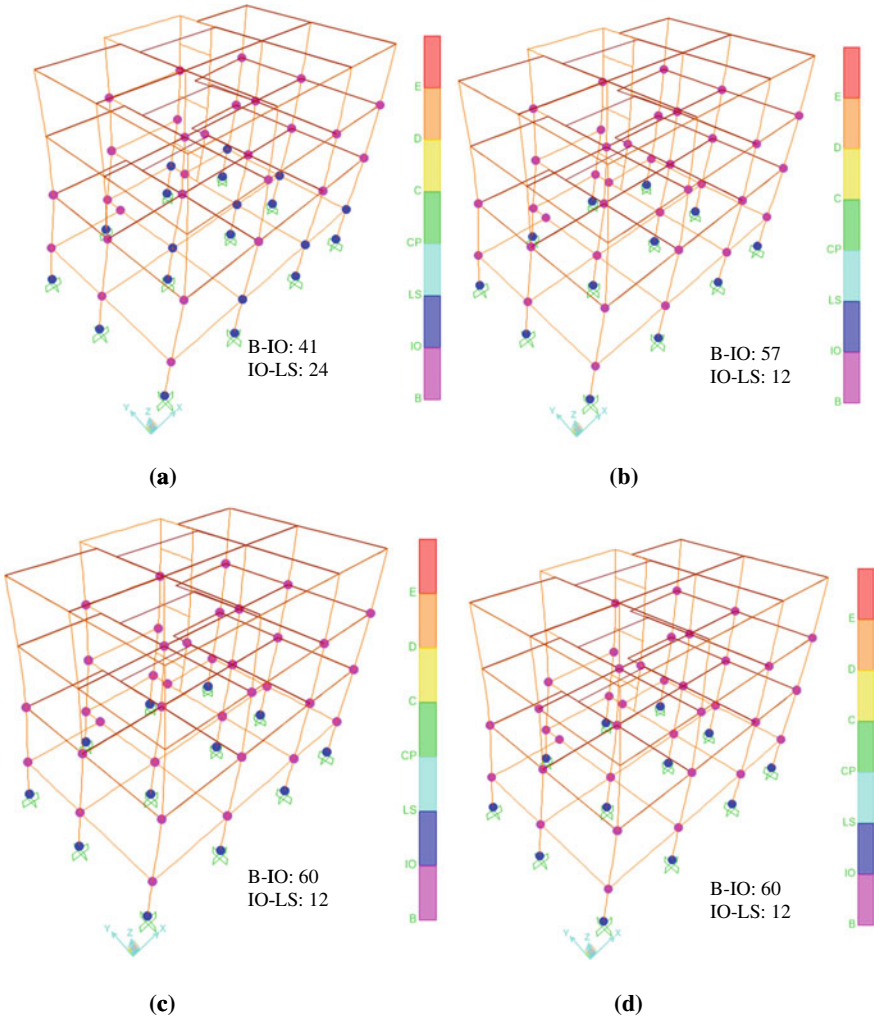
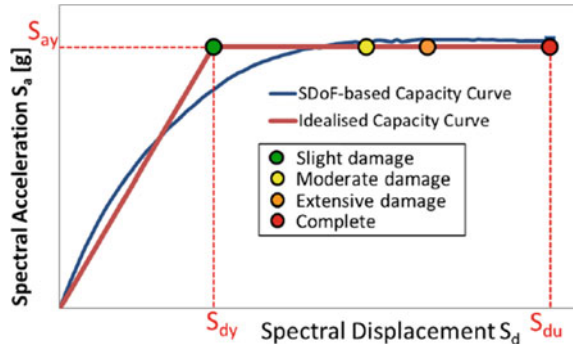


Fig. 9 Hinge formation at the last step for frames **a** non-conforming to SCWB criteria **b** SCWB ratio 1.2 **c** SCWB ratio 1.3 **d** SCWB ratio 1.4

Fig. 10 Simplified bilinear capacity curve



is 4.9%. In a frame structure with SCWB ratios 1.3 and 1.4, the hinge formation at the IO level is 24.6% and that at the LS level is 4.9% each. Therefore, in frame structures conforming to SCWB criteria, the damage of the structure is relatively limited and the structure retains a significant portion of its original stiffness and strength, while in the non-conforming to SCWB criteria frame structure, substantial damage occurs to the structure as well as it might lose a significant amount of its original stiffness but a substantial margin remains for additional lateral deformation before the collapse would occur.

4.4 Fragility Curve

The relations of damage states commonly used are expressed as a function of yield and ultimate top displacement. The global damage states are estimated from a simplified bilinear capacity curve as shown in Fig. 10.

Giovinazzi and Lagomarsino [15] provided the values of the median at the damage states as follows:

- Slight Damage = $0.7S_{dy}$.
- Moderate Damage = $1.5S_{dy}$.
- Extensive Damage = $0.5(S_{dy} + S_{du})$.
- Complete Damage = S_{du}

The fragility curves for the four RC frame structures have also been plotted as shown in Fig. 11a, b, c, and d based on the spectral displacement values that satisfy the damage states' level (slight, moderate, extensive, and complete) as per the HAZUS methodology. It is evident from the four curves that all the frame structures have higher probability (~0.9) of slight damage than the other damage states.

The comparison of the probability of damage is made at a spectral displacement of 12 cm as the curves of the damages do not overlap and are constant in all the fragility curves of the structures. From Fig. 12, it has been observed that the structure non-conforming to SCWB criteria has a higher probability of damage in all the damage states than the structure conforming to SCWB criteria.

Table 5 Material properties

Damage States	Non-conforming to SCWB criteria S_{dy} S_{du}	SCWB ratio of 1.2 S_{dy} S_{du}	SCWB ratio of 1.3 S_{dy} S_{du}	SCWB ratio of 1.4 S_{dy} S_{du}
	4.0cm 8.4cm	3.4cm 7.3cm	3.0cm 6.25cm	2.45cm 6.1cm
Slight	4.000cm	3.400cm	3.000cm	2.450cm
Moderate	6.000cm	5.100cm	4.500cm	3.675cm
Extensive	6.200cm	5.350cm	4.625cm	4.275cm
Complete	8.400cm	7.300cm	6.250cm	6.100cm

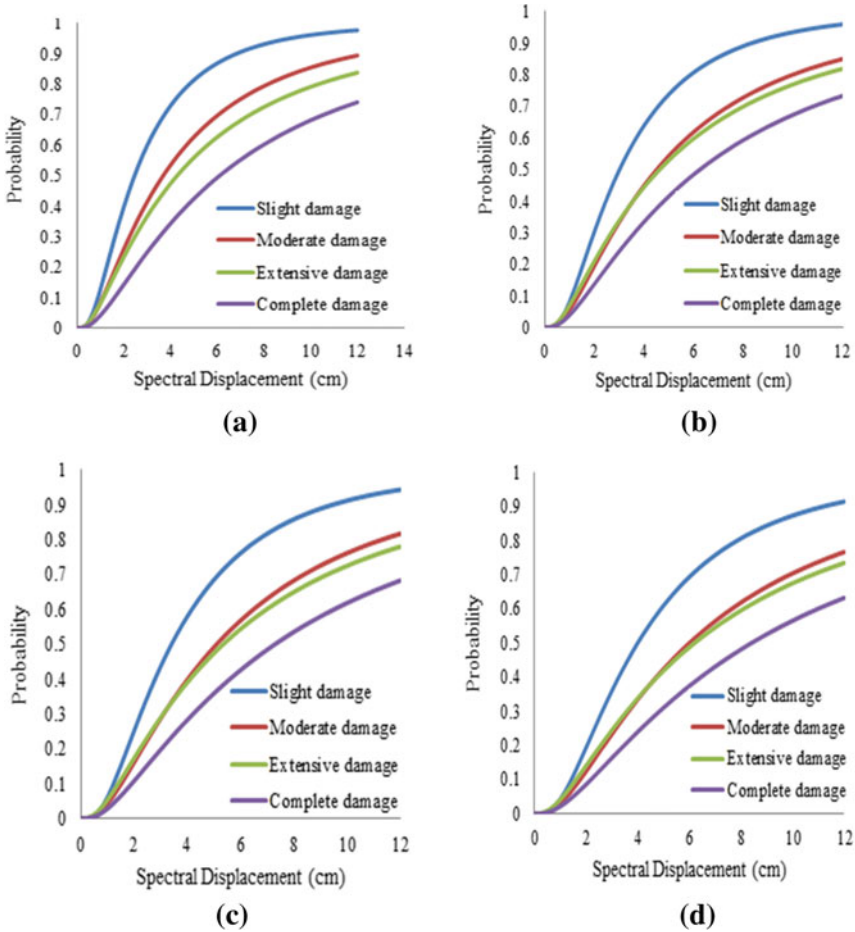


Fig. 11 Fragility curves for frames **a** non-conforming to SCWB criteria **b** SCWB ratio 1.2 **c** SCWB ratio 1.3 **d** SCWB ratio 1.4

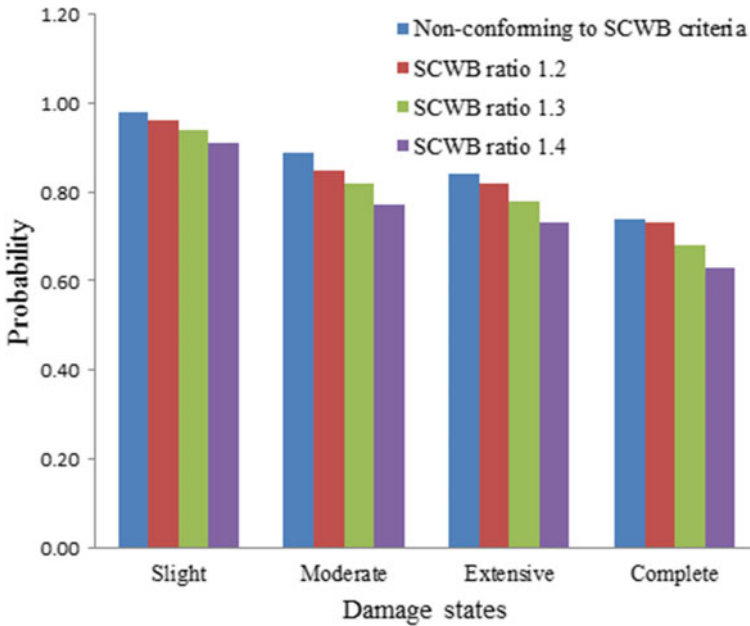


Fig. 12 Probability of damage at a spectral displacement of 12 cm

5 Conclusions

In this study, the performances of the four RC frame structures (one non-conforming and three conforming to SCWB criteria) have been investigated using pushover analysis. The frame structure non-conforming to SCWB criteria showed a substantial decrease in the failure capacity even though similar base shear coefficients with frame structures conforming to SCWB criteria were adopted. It has also been observed that the base shear and spectral acceleration at performance points were found to increase with an increase in SCWB ratio. Hence, the frame structure with SCWB ratio of 1.4 will show better seismic performance. Moreover, the formation of hinges at performance points is at the IO level for frame structures with SCWB ratio of 1.4, and that of SCWB ratio 1.2 and 1.3, the number of hinges formed is the highest at IO levels though a small number hinges are formed at the LS level. But for frame structure non-conforming to SCWB design criteria, the highest number of hinges is formed at LS levels. As a result, the frame structures conforming to SCWB criteria will show substantial damage of the structure elements. Further, the HAZUS methodology for the development of fragility curves has been discussed for the four RC frame structures. It has been observed that the frame structure non-conforming to SCWB criteria has a higher probability of damage in all the damage states than the structure conforming to SCWB criteria. SCWB ratio recommended by three seismic codes (ACI 318–14 [1], IS 13920: 2016 [2], and Eurocode 8 [3]) does not entirely pledge

to end hinging of columns even if the probability of exceeding a given damage state is reduced with increase in SCWB ratio.

From the results obtained, it can be concluded that the pushover analysis is relatively simple in procedure and less time consuming to explore the nonlinear behavior of the structure, and also the HAZUS methodology gives an idea to predict the damage level of the building corresponding to a particular value of spectral displacement.

Since Pushover Analysis is a static nonlinear procedure, the results generated using Pushover Analysis can be compared with the results obtained from nonlinear time history using the HAZUS methodology as a future scope for this study.

References

1. Commentary on Building Code Requirements for Structural Concrete (ACI 318R-14), American Concrete Institute (2014)
2. BIS, IS 13920 (2016) Ductile design and detailing of reinforced concrete structures subjected to seismic forces—code of practice. Bureau of Indian Standards, New Delhi
3. Eurocode 8 (2004) Design of structures for earthquake resistance- part 1: general rules, seismic actions and rules for buildings. European Committee for Standardization, Brussels
4. Surana M, Singh Y, Lang DH (2018) Effect of strong-column weak-beam design provision on the seismic fragility of RC frame buildings. *Int J Adv Struct Eng*. <https://doi.org/10.1007/s40091-018-0187-z>
5. Bhandari S, Shrestha HD (2017) Effect of column-to-beam moment capacity ratio on seismic performance of reinforced concrete moment resisting frames, Proceedings of IOE Graduate Conference, 2017 Vol 5, ISSN: 2350–8914 (Online), 2350–8906 (Print)
6. Cagurangan CK (2015) Effects of strong column weak beam ratios on collapse capacities of tall reinforced concrete moment frame structures. Ph.D. Thesis, University of California, Berkeley
7. Haselton CB, Liel AB, Deierlein GG, Dean BS, Chou JH (2011) Seismic collapse safety of reinforced concrete buildings. I: assessment of ductile moment frames. *J Struct Eng ASCE* 137:481–491
8. Kircil MS, Polat Z (2006) Fragility analysis of mid-rise RC frame buildings. *Eng Struct* 28:1335–1345
9. Mwafy AM, Elnashai AS (2001) Static pushover versus dynamic collapse analysis of RC buildings. *Eng Struct* 23:407–424
10. Shinozuka M, Feng MQ, Kim H-K, Kim S-H (2000) Nonlinear Static Procedure for Fragility Curve Development. *J Eng Mech* 126:1287–1295
11. ATC-40 (1996) Seismic Evaluation and Retrofit of Concrete Building, Volume 1 and 2, Report NO. SSC 96–01, Seismic Safety Commission, Redwood City
12. FEMA 273 (1997) Federal emergency management agency, NEHRP guidelines for the seismic rehabilitation of buildings, Washington DC, U.S.A., October
13. Manohar S, Madhekar S (2015) Seismic design of RC buildings: theory and Practice, Springer, pp 431
14. FEMA (2003) HAZUS-MH-MR 1 technical manual, federal emergency management agency, building seismic safety council, Washington, DC, USA
15. Giovinazzi S, Lagomarsino S (2006) Macro-seismic and mechanical models for the vulnerability and damage assessment of current building. *Bull Earthquake Eng* 30(7):415–443, September
16. Mander JB, Priestley MJN, Park R (1998) Theoretical stress-strain model for confined concrete. *J Struct Eng* 114(8):1804–1826
17. BIS, IS 456 (2000) Plain and reinforced concrete code of practice, Bureau of Indian Standards, Fourth revision

18. BIS, IS 1893 (Part 1) (2016) Criteria for earthquake resistant design of structures Part-1 general provisions and buildings, Bureau of Indian standards, Sixth revision
19. FEMA-356 (2000) Pre-standard and commentary for seismic rehabilitation of buildings, federal emergency management council. Washington DC, USA
20. FEMA 440 (2005) Improvement of nonlinear static seismic analysis procedures, department of homeland security federal emergency management agency, Washington
21. Vasavada M, Dr Patel VR (2016) Development of fragility curves for RC buildings using HAZUS method, IRJET, e-ISSN: 2395 -0056, p-ISSN: 2395-0072, vol 03, Iss 05th May
22. SAP User Manual (2000) version 15, Berkeley (CA. Computer and Structures Inc., USA)

Smart Lightweight MR Damper for the Enhancement of Seismic Mitigation



C. Daniel, G. Hemalatha, L. Sarala, D. Tensing, and S. Sundar Manoharan

Abstract Magnetorheological (MR) fluids with exceptional rheological properties are skilled in exhibiting quick performance to control vibrations during earthquakes. The significant damping properties of MR fluids were effectively controlled with the help of externally applied magnetic field and current. Currently, MR fluids with nano Fe_3O_4 iron particles are used in the preparation of MR fluid to reduce sedimentation. Fabrication of MR damper consists of nylon material to reduce the weight and resist high-temperature distortion. The weight of the proposed MR damper was about 445 g with the magnetic core. The MR fluid of proportions 30% (MRF30), 45% (MRF 45) and 60% (MRF 60) of iron particle is prepared, and the cyclic load test frequency is 0.5 Hz and amplitude, ± 5 mm. The maximum damping force was found to be 1.032 kN obtained from the MR fluid containing 60% Fe_3O_4 particles in magnatec oil. For variable frequency, the time history loading test was done with El Centro ground acceleration data where the maximum damping force for MRF 60 is 1.3 kN.

Keywords Damping force · MR damper · Cyclic load test · Nano Fe_3O_4 · Time history loading

1 Introduction

MR damper is a semi-active type of vibration mitigator, and it is filled with Magnetorheological fluid which can be precisely controlled by a magnetic field [1, 1–3]. MR fluid consists of micron-size iron particles with a carrier oil which can generate the chain formation in the presence of the magnetic field when current is applied to it. In recent years, the demand for MR damper devices has been intensifying more and more. There are three types of MR fluid modes available. Flow mode is used in

C. Daniel (✉) · G. Hemalatha · L. Sarala · D. Tensing
Department of Civil Engineering, Karunya Institute of Technology and Sciences, Coimbatore,
India
e-mail: danielckarunya@gmail.com

S. S. Manoharan
Pandit Deendayal Petroleum University, Gujarat, India

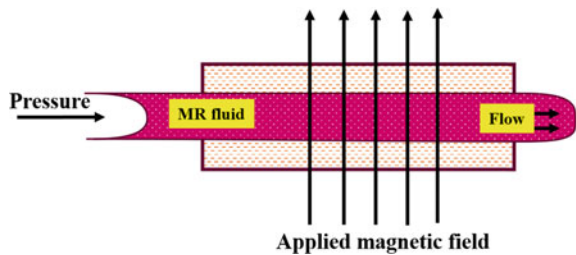
vehicle suspension, prosthetic leg, washing machine as a damper application. Whatever the passive damper used in present condition is not having this kind of features like change in damping force with requirement as flow mode [4–7]. Based on the working modes, different MR dampers exhibit different hysteretic behaviors. The aim of this paper is to design the lightweight MR damper for seismic application. The magnetic iron particle used in the proposed work is nano Fe_3O_4 synthesized from a waste product. The controllable damping force of the proposed MR dampers possessing lightweight is higher than that of the traditional MR dampers. Additionally, for shocks and vibration mitigation the flow mode MR damper with various MR fluids is investigated experimentally. Configuration of a flow mode MR damper for shock and vibration mitigation at various MR fluid proportions is experimentally investigated.

2 Valve Mode

In the valve mode, the smart fluid is placed between the two stationary poles. However, the fluid flow resistance is modified by controlling the magnetic field which acts perpendicular to the flow as shown in Fig. 1. Some of the devices making use of the flow mode of operation are dampers, shock absorbers, servo-valves and actuators [8].

MR fluid was successfully prepared by mixing the nano Fe_3O_4 of average particle size 12 nm in the carrier oil [9, 10]. In the present case, three different MR fluids was prepared by varying the percentage of iron particles used; 30, 45, 60% by weight of nano Fe_3O_4 was mixed with 70, 55, 40% magnatec. The whole mixture was stirred at room temperature using overhead stirrer for about 24 h as depicted in Fig. 2. The resultant MR fluid is further used for testing.

Fig. 1 Valve mode



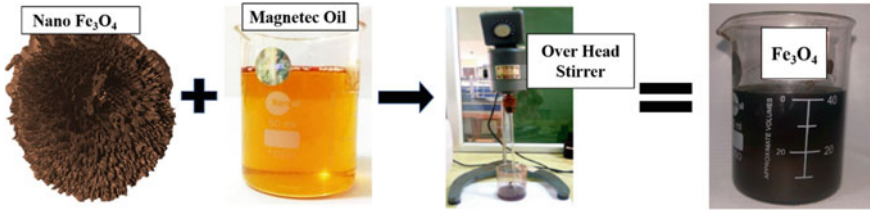
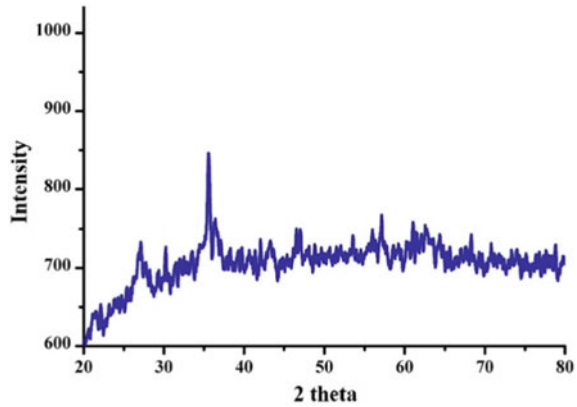


Fig. 2 Schematic representation for the synthesis of MR fluid

Fig.3 XRD pattern of a synthesized nano Fe₃O₄



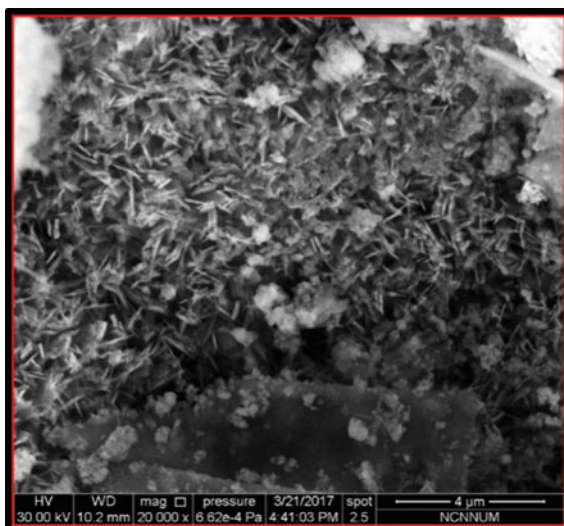
3 X-ray Diffraction Studies

Figure 3 depicts the X-ray diffraction pattern of synthesized nano Fe₃O₄ measured using Shimadzu equipment, Model XRD-6000, Tokyo, Japan. The particle size of the material was calculated using the famous Scherrer equation and was found to be 12 nm. The characteristic XRD plane (3 1 1) for Fe₃O₄ was found at 35.44°. Since it was the most intense plane, the average particle size was calculated from the FWHM value of the same plane.

4 Scanning Electron Microscopic Studies

The surface morphological study was carried out using the SEM instrument JSM-6390, JEOL, USA. Figure 4 shows the SEM micrograph of synthesized nano Fe₃O₄. From the figure, it is clear that the material shows a flake-like structure.

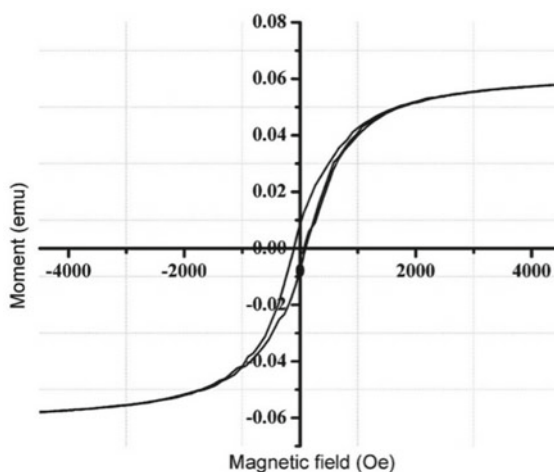
Fig. 4 SEM image of nano Fe_3O_4



5 Vibrating Sample Magnetometer

Since the material synthesized is magnetic, the magnetic measurement was done using a vibrating sample magnetometer at room temperature. Figure 5 depicts the magnetic hysteresis loop of nano Fe_3O_4 particles. The sample showed a magnetization of 59 emu/g and coercivity of 108G.

Fig. 5 Magnetic measurement of nano Fe_3O_4



6 MR Damper

The schematic representation of the proposed MR damper and dimensions are depicted in Fig. 6a. Figure 6b shows the image of the proposed MR damper fabricated by nylon material. The smart lightweight MR damper contains the damper outer housing, inner piston with rod and multiple annular gaps, outer magnetic cores, seal ring and cylinder cap. The outer cylinder and piston pole head, cylinder cap is fabricated by nylon rod material. The nylon material type 6 has high resistance toward resistance, vibration, brittleness, deterioration and abrasion. Nylon is easy to machining and high-temperature distortion. The nylon material has a specific gravity of 1.15 cm^3 , tensile strength of $93,079.22 \text{ kN/m}^2$, compressive strength of $110,316.11 \text{ kN/m}^2$ and deflection temperature range starts from 320° F . Nylon material is a tenacity fiber which has high durability. The conventional MR damper has a weight of 2500 g and the proposed MR damper has a weight of 445 g which is an 82% reduction in weight. The MR damper is featured by the four-shear forming layer in the piston pole head. The thickness of an annular inner gap is 1 mm . The magnetic field generation depends on the outer coil by which the current is varied from 0 to 1 A with the 0.25 A interval. On applying current, MR fluid that flows inside is magnetized, the yield stress of fluid increases and the circuit is closed. In general, it is proposed that controlling the current applied to the applied coil, the required damping force was generated by the MR damper.

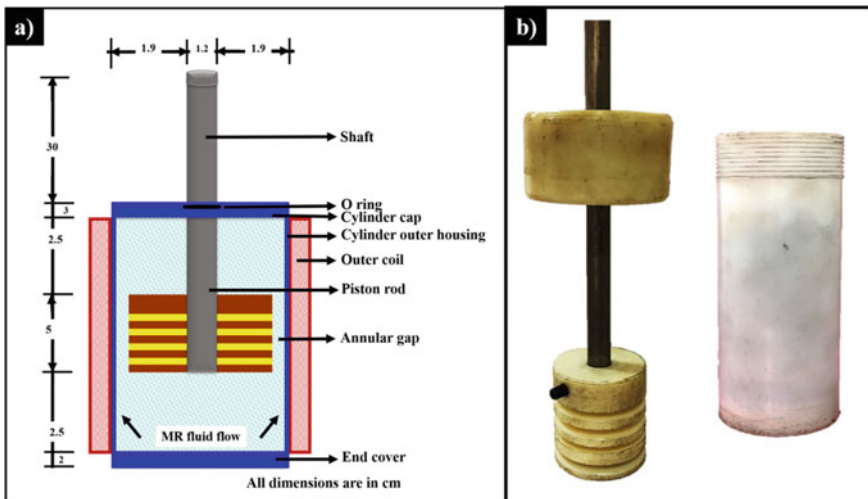


Fig. 6 a Main structural dimension of the proposed MR damper b fabricated lightweight MR damper

7 Experimental Investigation

The MR damper is tested by exciting the damper with amplitude ± 5 mm, current range 0A, 0.25A, 0.5A, 0.75A and 1A and frequency 0.5 Hz using MTS Universal testing machine as shown in Fig. 7. This vibration is similar to the cyclic load test. The resulting damping force of the proposed MR damper is measured by a data acquisition system, and an accelerometer is used to measure the movement of the Magnetorheological damper. The outer coil is connected to the DC power supply to produce power. The measured damping force with respect to displacement for MRF 30, MRF 45 and MRF 60 is represented in Figs. 8–10. The damping force obtained for MRF 30 at 0A was found to be 0.38kN, whereas at 1 A it was raised to 0.552 kN. 31% increase in damping force was observed for MRF 30 at 1 A than 0A. Similarly, for MRF 45 and MRF 60, the maximum damping force was observed at 1 A, and the result was found to be 0.8228 kN and 1.032 kN, respectively. 44% of damping force increased for MRF 60. The damping force obtained in the test is appropriate for vibration control.

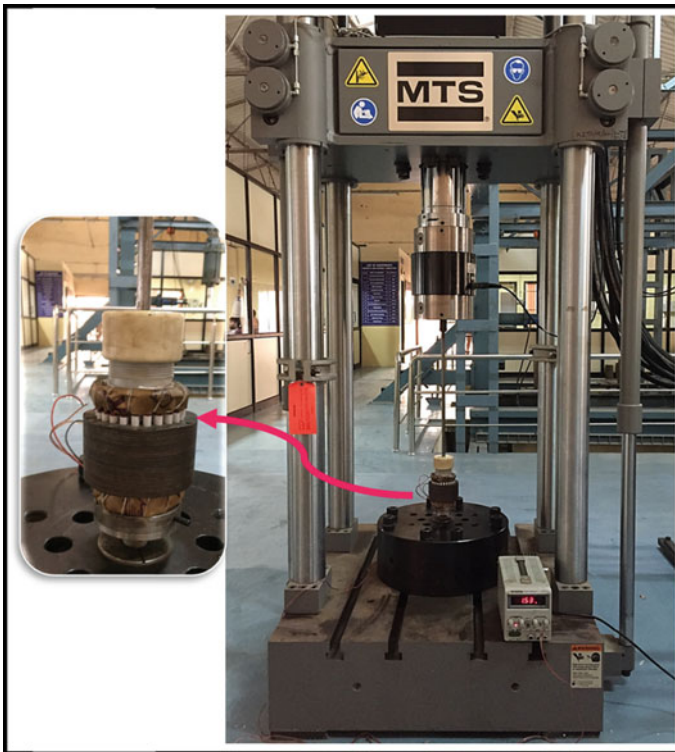


Fig. 7 Experimental setup of lightweight MR damper

Fig. 8 Responses of MR damper for MRF 30

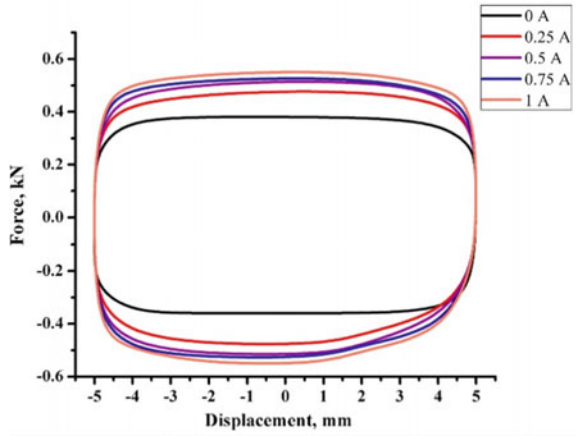


Fig. 9 Responses of MR damper for MRF 45

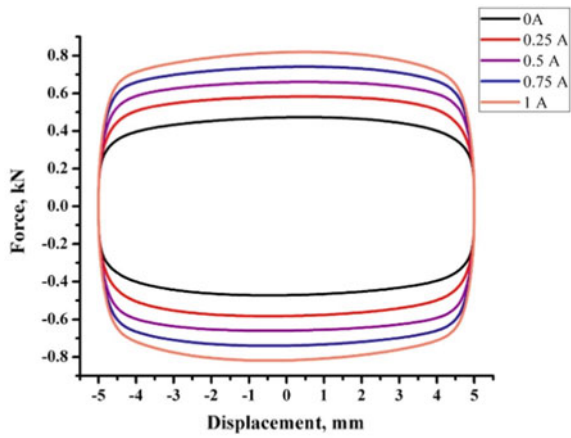
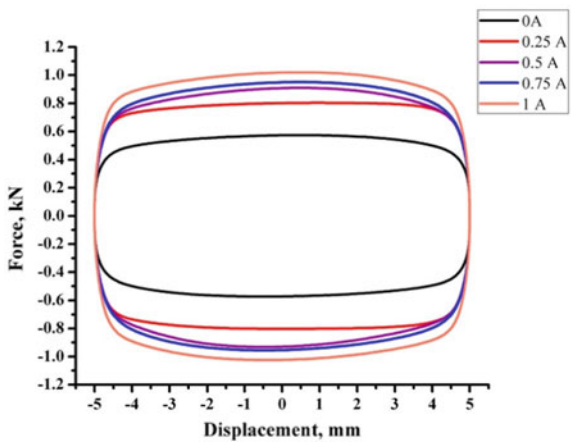


Fig. 10 Responses of MR damper for MRF 60



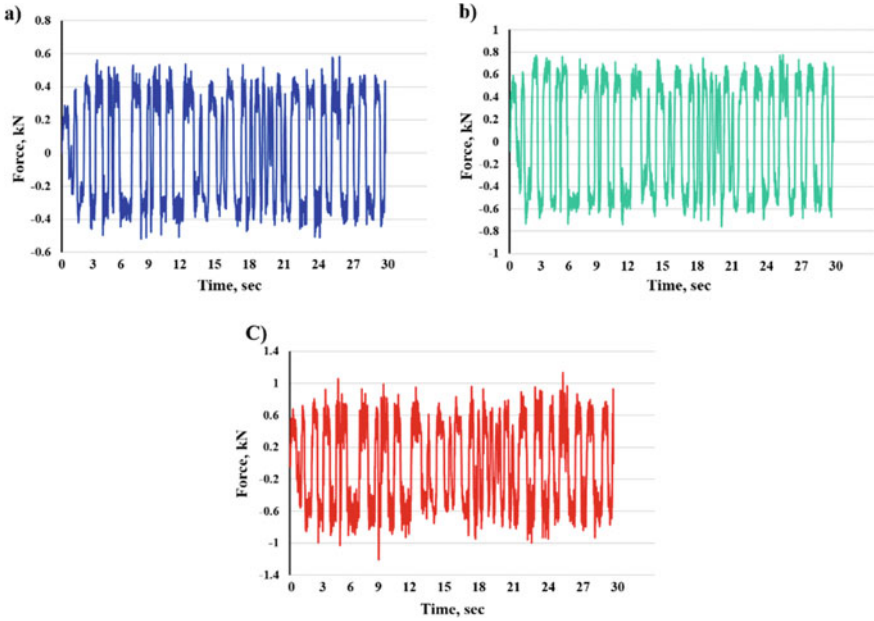


Fig. 11 a force versus time—MRF 30 b force versus time—MRF 45 c force versus time—MRF 60.

8 Time History Loading

The El Centro earthquake ground acceleration data was used to study the behavior of the MR damper under time history loading. Figure 11 plotted graph represents an increase in the percentage of iron particles which leads to an increase in damping force. When compared with the cyclic load test, time history loading has a 30.81 percentage increase in force due to the variable frequency. The maximum damping force obtained for MRF 60 is 1.353 kN at 1.

9 Conclusion

In the present work, the smart lightweight MR damper was successfully fabricated using lightweight nylon material. The conventional MR damper has a weight of 2500 g and the proposed MR damper has a weight of 445 g which is an 82% reduction in weight. The nano Fe₃O₄ was characterized by XRD and SEM analysis. The magnetic measurement of the smart material nano Fe₃O₄ was obtained by VSM at room temperature. Three different MR fluids prepared by varying the percentage of iron particles are presented in namely MRF 30, MRF 45 and MRF 60, respectively. Magnatec oil acts as the carrier fluid. Cyclic load test was carried out with a

frequency of 0.5 Hz and amplitude ± 5 mm for various input current ranges from 0-1A. The damping force was measured using MTS Universal testing machine, the maximum damping force was observed for the fluid MRF 60 at 1 A is 1.032 kN. For time history loading, MRF 60 has a maximum damping force of 1.32 kN.

Acknowledgements The authors thank Karunya Institute of Technology and Sciences, Coimbatore, Tamilnadu, India, for their constant support. We also extend our acknowledgement to the Department of Science and Technology (Grant No: DST/TSG/STS/2015/30-G).

References

1. Chauhan ND, Patel D (2018) Design Optimization of flow mode magnetorheological damper. *Appl Mech Mater* 877:403–408. (February 2018). <https://doi.org/10.4028/www.scientific.net/amm.877.403>
2. Goldasz J (2013) Study of a magnetorheological fluid damper with multiple annular flow gaps. *Int J Veh Des* 62(1):21. <https://doi.org/10.1504/ijvd.2013.051601>
3. Liao CR, Zhao DX, Xie L, Liu Q (2012) A design methodology for a magnetorheological fluid damper based on a multi-stage radial flow mode. *Smart Mater Struct* 21(8):085005. (July 13, 2012). <https://doi.org/10.1088/0964-1726/21/8/085005>
4. Jia Y (2012) Design and experimental research on the vehicle twin-tube magnetorheological fluids damper based on pressure driven flow mode. *J Mech Eng* 48(10):103. <https://doi.org/10.3901/jme.2012.10.103>
5. Yu J, Dong X, Sun S, Li W (2018) Hysteretic model of a rotary magnetorheological damper in helical flow mode. *Commun Comput Inf Sci*, 15–24. https://doi.org/10.1007/978-981-13-2384-3_2
6. Fu B, Liao C, Li Z, Xie L, Zhang P, Jian X (2017) Impact behavior of a high viscosity magnetorheological fluid-based energy absorber with a radial flow mode. *Smart Mater Struct* 26(2):025025. (January 24, 2017). <https://doi.org/10.1088/1361-665x/aa56f4>
7. Ciocanel C, Nguyen T, Elahinia M, Naganathan NG (2007) Squeeze-flow mode magnetorheological fluid mount. In: *Electrorheological Fluids and Magnetorheological Suspensions* (October 2007). https://doi.org/10.1142/9789812771209_0079
8. Kim K, Chen Z, Yu D, Rim C (2016) Design and experiments of a novel magneto-rheological damper featuring bifold flow mode. *Smart Mater Struct* 25(7):075004. (May 24, 2016). <https://doi.org/10.1088/0964-1726/25/7/075004>
9. Zeinali M, Mazlan SA, Choi S-B, Imaduddin F, Hamdan LH (2016) Influence of piston and magnetic coils on the field-dependent damping performance of a mixed-mode magnetorheological damper. *Smart Mater Struct* 25(5):055010. (March 30, 2016). <https://doi.org/10.1088/0964-1726/25/5/055010>
10. Daniel C, Magdalene A, Hemalatha G, Tensing D, Sundhar Manoharan S (2016) Experimental investigation on magnetorheological damper for seismic resistance of structures with nano Fe₃O₄ MR fluid. *Int J Appl Bio-Eng* 10(2):1–6. <https://doi.org/10.18000/ijabeg.10140>
11. Cruze D, Gladston H, Immanuel S, Loganathan S, Dharmaraj T, Manoharan Solomon S (2018) Experimental investigation on magnetorheological damper for RCC frames subjected to cyclic loading. *Adv Civil Eng Mater* 7(3):20170112. (June 14, 2018). <https://doi.org/10.1520/acem20170112>

Rheological Behavior of Geopolymer Mortar with Fly Ash, Slag and Their Blending



Biswajit Roy  and Aminul Islam Laskar

Abstract In the present paper, an attempt has been made to study the rheological behavior of geopolymer mortar made with fly ash, ground granulated blast furnace slag (slag) and their blending (1:1) as source materials. NaOH solution was used as an alkaline activator. The molar concentrations of the alkaline activator used in the present study were 4, 8, 12 and 14.5 M. For the preparation of mortar, the ratio of source material to sand was kept constant at 1:3. Three different ratios of activator to binder were considered in the present experimental investigation. Experiments were conducted by a rotational viscometer. It was observed that the degree of thixotropy of the slag-based geopolymer mortar reduces after the addition of fly ash. Down curve of geopolymer mortar followed the Bingham model with good accuracy with and without blending. Rheological parameters of slag-based mortar reduced significantly after blending with fly ash.

Keywords Rheology · Geopolymer · Fly ash · Slag · Yield stress · Plastic viscosity

1 Introduction

Single point workability tests are widely accepted tests and are empirical in nature that measure time or distance most of the times to determine the workability of fresh cementitious materials. Two-point tests, on the other hand, determine rheological parameters in terms of yield stress and plastic viscosity which are considered as fundamental properties [12, 18, 30, 31]. Fluid rheology methods are used to describe the flow behavior of mortar and concrete under applied shear stress. It is well established that non-Newtonian fluids such as cement mortar and cement concrete most often behave like a Bingham fluid with good accuracy [7, 12, 18, 27, 30, 31]. The

B. Roy (✉) · A. I. Laskar

Department of Civil Engineering, National Institute of Technology Silchar, Silchar, India 788010
e-mail: biswajit.1117@gmail.com

A. I. Laskar

e-mail: aminul.nits@gmail.com

© Springer Nature Singapore Pte Ltd. 2021

S. Adhikari et al. (eds.), *Advances in Structural Technologies*, Lecture Notes in Civil Engineering 81, https://doi.org/10.1007/978-981-15-5235-9_8

Bingham model is represented by the following equation:

$$\tau = \tau_0 + \mu \dot{\gamma} \quad (1)$$

where τ is the shear stress, τ_0 is the yield stress, μ is the plastic viscosity and $\dot{\gamma}$ is the shear strain rate. Yield stress gives initial resistance to flow, and plastic viscosity governs the flow after it is initiated. Yield stress is the manifestation of friction among solid particles, and plastic viscosity is the contribution of suspending liquid that results from viscous dissipation due to the movement of water and sheared material [12, 18–20].

The use of geopolymer binder in mortar and concrete is a field of recent research interest mainly due to its eco-friendly nature. Geopolymer binder has some advantages over Portland cement such as better resistance to chemical attack, better freeze–thaw resistance [1–4, 11, 26, 28], stronger aggregate–matrix interface formation [29] and better fire resistance [32]. The mineral binders containing amorphous siliceous material and alumina when activated with alkaline solutions undergo a reaction to form a geopolymer binder. The alkali activation of aluminosilicate minerals is a complex chemical process involving the dissolution of raw materials, transportation, orientation and polycondensation of the reaction products. Alkali activator used in the geopolymerization reaction is sodium hydroxide (NaOH), potassium hydroxide (KOH), mixture of sodium hydroxide and sodium silicate or mixture of potassium hydroxide and potassium silicate [10, 19, 20, 25].

A review of the literature reveals that there had been a lot of research on geopolymer concrete with different source materials and their blends for the determination of mechanical properties of geopolymer concrete [1–4, 11, 26, 28, 29, 32]. An attempt has also been made by researchers to investigate the rheological behavior of geopolymer concrete, mortar and paste; though such reported literature are not many. Palacios et al. [23] conducted rheological tests on slag-based geopolymer mortar and concluded that slag paste and mortar follow the Bingham model when NaOH solution is used as an activator. Criado et al. [8] investigated the rheological behavior of fly ash-based geopolymer paste with NaOH as an activator and observed that the Bingham model could be fitted to those pastes. Laskar and Bhattacharjee [20] conducted rheological tests on fly ash-based geopolymer concrete and concluded that thixotropy is present in fly ash-based geopolymer concrete. They observed that fly ash-based geopolymer concrete prepared with a mixture of sodium silicate and sodium hydroxide solution follows the Bingham equation, and yield stress and plastic viscosity are affected by the molar concentration of the alkaline activator. In another study, Laskar and Bhattacharjee [19] observed that in the presence of plasticizer and superplasticizer, rheological parameters of fly ash geopolymer concrete are affected badly when molar strength of alkali is more than 4.0 molar. Jang et al. [16] conducted a flow test on slag–fly ash blend pastes at different slag–fly ash ratios using a mixture of sodium hydroxide and sodium silicate as an activator. Kashani et al. [17] studied the interrelationship between surface chemistry and rheology in alkali-activated slag paste and concluded that alkali hydroxide activators cause a significant increase in

yield stress of an activated slag paste in comparison to silicate activators at an early stage, and all the activated slag exhibits shear thinning and thixotropic behavior.

Investigation on rheological behavior and factors affecting yield stress and plastic viscosity of geopolymer mortar incorporating a mixture of fly ash and slag is yet to be explored. An attempt has, therefore, been made in the present study to investigate the rheological behavior of geopolymer mortar with fly ash and slag as source materials. Effect of molar strength, and activator to binder ratio (R) on yield stress and plastic viscosity has also been studied.

2 Experimental Investigation

2.1 Mixture proportion and preparation

Mix designations and proportions of geopolymer mortars are shown in Table 1. In the table, “M” represents the molar strength of NaOH solution and “R” represents the activator to binder ratio by weight. The dry mass of binder and sand was mixed thoroughly in a laboratory mortar mixer for two minutes. Sodium hydroxide solution was added and mixed for three minutes. The required quantity of the mix was

Table 1 Mix designations and proportions (by weight)

Mix no	Fly ash	Slag	Sand	Molar strength	R
1	1	–	3	4 M	1.33
2	1	–	3	8 M	1.33
3	1	–	3	8 M	1.17
4	1	–	3	8 M	1
5	1	–	3	12 M	1.33
6	1	–	3	14.5 M	1.33
7	–	1	3	4 M	1.33
8	–	1	3	8 M	1.33
9	–	1	3	8 M	1.17
10	–	1	3	8 M	1
11	–	1	3	12 M	1.33
12	–	1	3	14.5 M	1.33
13	0.5	0.5	3	4 M	1.33
14	0.5	0.5	3	8 M	1.33
15	0.5	0.5	3	8 M	1.17
16	0.5	0.5	3	8 M	1
17	0.5	0.5	3	12 M	1.33
18	0.5	0.5	3	14.5	1.33

Table 2 Chemical composition of binders

Chemical Constituents	Fly ash (% by weight)	Slag (% by weight)
CaO	5	37
SiO ₂	52	38
Al ₂ O ₃	23	14
Fe ₂ O ₃	11	1
MgO	–	9

transferred in the cup of a viscometer with a spatula for rheological testing. Identical mixing procedure and mixing time were maintained for all the samples.

Fine aggregate. Locally available alluvial sand with water absorption of 1.5% and a specific gravity of 2.6 was used in this study. The sieve analysis, specific gravity, moisture content and water absorption were determined as per IS: 2386 [14]. Sand was stored inside the laboratory throughout the experimental investigation.

Fly ash. Fly ash conforming to ASTM Class F collected from National Thermal Power plant at Farakka (India) was used in this study. The specifications of the fly ash conform to IS: 3812 [15]. The chemical composition of fly ash used in this study is tabulated in Table 2. The specific gravity and loss on ignition are 2.10 and 0.90, respectively.

Slag. Commercially available ground granulated blast furnace slag (slag) was used as another source material. The specification of the slag conforms to IS: 12,089 [13]. The chemical composition of the slag is tabulated in Table 2. The specific gravity and loss on ignition are 2.80 and 1.41, respectively.

Alkaline activator. Sodium hydroxide palletes (98% purity and specific gravity = 2.13) were used in the preparation of different concentrations of activator solution. The alkali solution was prepared 24 h prior to the start of the experiment.

2.2 Rheological Measurement

Bohlin Visco 2000, a rate and temperature-controlled viscometer, was used to measure the rheological properties of the mortar mixes. The viscometer is attached to a computer and operated through software (Fig. 1). Samples subjected to stepwise increasing shear rate sequence (15 per sec–300 per sec in 1.5 min) followed by a stepwise decreasing shear rate sequence (300 per sec–15 per sec in the next 1.5 min) were used for all the mixtures. Stepwise decreasing shear rate (300 per sec–15 per sec in 1.5 min) was used for the determination of Bingham parameters. The stepwise decreasing shear rate sequence is the most commonly used method for measuring the rheological parameters of cement concrete [25]. Plug flow, if any, is corrected by



Fig. 1 Photograph of Visco 2000 used in the present study

the point elimination method [21]. Rheological parameters reported are the average of three respective readings.

2.3 Thixotropy

An important phenomenon that affects the rheological measurements of cement-based materials is thixotropy. Thixotropy will lead to error in test results in terms of yield stress and plastic viscosity if it is not properly addressed. Mewis [22] used the term thixotropy to describe an isothermal gel-sol transition due to mechanical agitation. Barnes et al. [5] described thixotropy as a decrease of the apparent viscosity under constant shear stress or shear rate, followed by a gradual recovery when the stress or shear rate is removed. The thixotropic sample experiences a reversible, time-dependent decrease in viscosity and represents a hysteresis loop when the torque is measured under a linear increase and then a decrease in rotational frequency [9]. In cement paste, thixotropy is governed by a combination of reversible coagulation, dispersion and re-coagulation of cement particles [6]. Researchers have suggested several approaches to investigate and measure thixotropy. The simplest approach,

developed by Mewis [22], is to measure torque under a linear increase and then a decrease in rotational frequency. The hysteresis loop, if obtained, indicates the presence of thixotropy, although the loops do not provide a good basis for quantitative assessment. In this study, a stepwise increasing shear rate sequence (15 per sec–300 per sec in 1.5 min) followed by a stepwise decreasing shear rate sequence (300 per sec–15 per sec in the next 1.5 min) was used for all the mixtures. The reason for using an increase and then a stepwise decrease in the shear rate and thus creating a hysteresis loop was mainly to investigate the degree of thixotropic presence, if any, in the mortar mix.

3 Results and Discussions

3.1 Fly Ash-Based Mortar

The typical flow curve of fly ash-based geopolymer mortar activated with different concentrations of NaOH solution (as per Table 1) is provided in Fig. 2. The down curve does not follow the up curve, and forms a loop. This is due to the thixotropic breakdown of the sheared material. The down curve of the plot is a straight line which indicates that the Bingham model can be fitted for fly ash-based geopolymer mortar.

Figure 3a, b shows the variation of rheological parameters with the variation of molar strength at constant activator to binder ratio (R). Yield stress decreases continuously till 12 M solution and then there is a slight increase at 14.5 M. This behavior is not in agreement with Laskar and Bhattacharjee [20]. Plastic viscosity, on the other hand, increases continuously with the increase in molar strength. NaOH is a viscous liquid and any increase in NaOH content makes the mixture more cohesive. An increase in plastic viscosity is also due to a decrease in water content at a higher molar solution.

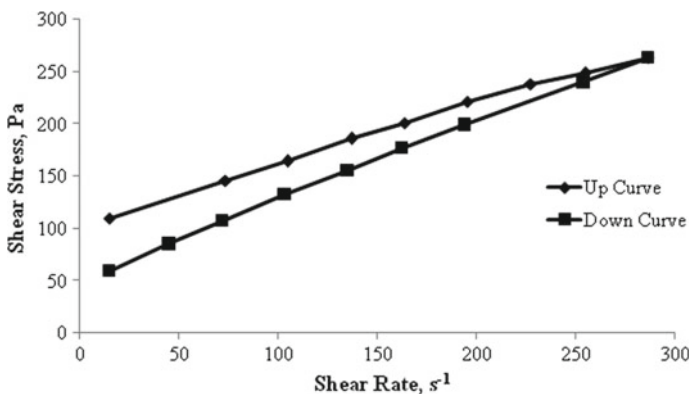


Fig. 2 Typical flow curve of fly ash-based geopolymer mortar ($M = 8$, $R = 1$)

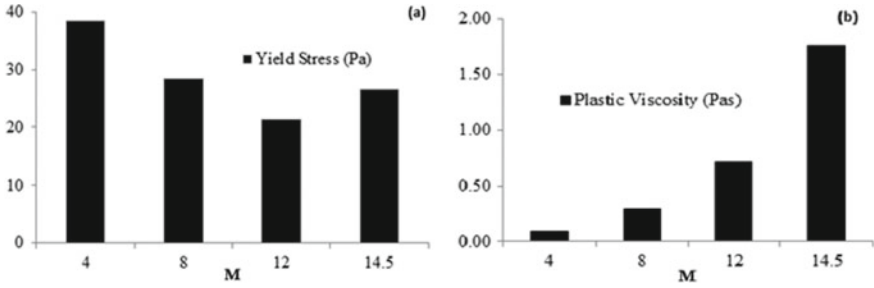


Fig. 3 Variation of a yield stress b plastic viscosity with molar strength for fly ash-based mortar

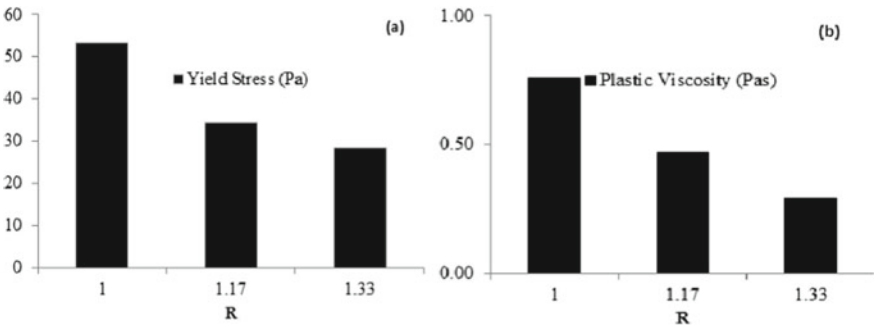


Fig. 4 Variation of a yield stress b plastic viscosity with alkali to binder ratio for fly ash-based mortar

Variation of yield stress and plastic viscosity with the variation of R at constant M is presented in Fig. 4a, b. There is a continuous decrease in both yield stress and plastic viscosity with the increase in R due to the introduction of more and more water content at higher R, thereby increasing workability.

3.2 Slag-Based Mortar

The typical flow curve of a slag-based geopolymer is provided in Fig. 5. It is evident that thixotropy is present in slag-based geopolymer mortar with NaOH as an activator and the Bingham model could be fitted with good accuracy to the down curve. For constant activator to binder ratio (R), both yield stress and plastic viscosity increase with the increase in molar strength (M) of NaOH solution (Fig. 6a, b). This behavior is in good agreement with Kashani et al. [17]. An increase in yield stress and plastic viscosity with an increase in M is due to a more cohesive mix at high molar strength and a decrease in water content. As seen in a fly ash-based geopolymer mortar, a

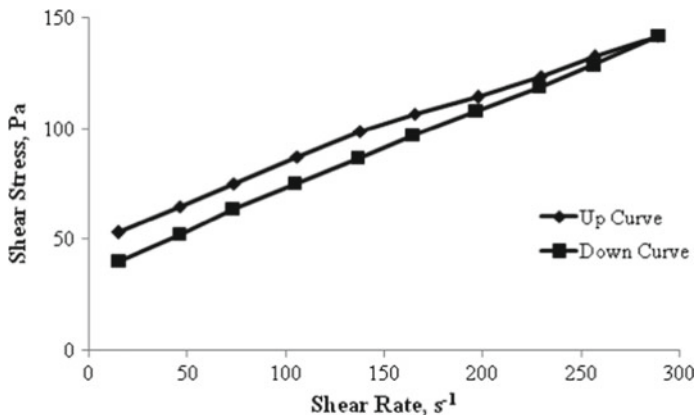


Fig. 5 Typical flow curve of slag-based geopolymer mortar ($M = 8, R = 1.33$)

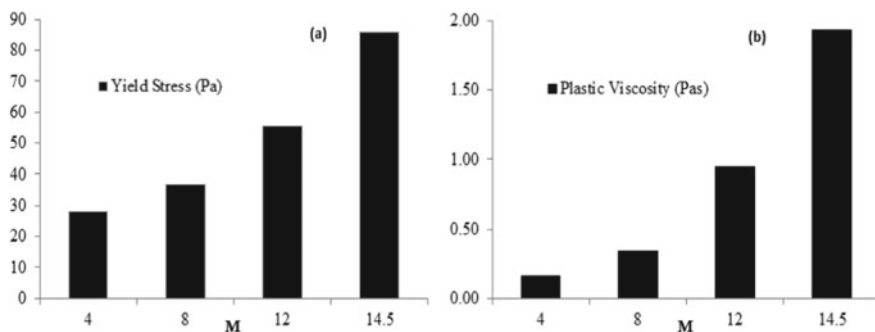


Fig. 6 Variation of a yield stress b plastic viscosity with molar strength for slag-based mortar

decrease in yield stress and plastic viscosity is observed with an increase in R at constant M (Fig. 7a, b).

3.3 Blending of Fly Ash and Slag

The typical flow curve of a blended mix is presented in Fig. 8. It may be observed that thixotropy is present in all the mixes and the down curve obeys Bingham’s equation. In the present study, the degree of thixotropy is assessed by evaluating the area enclosed under hysteretic loops of the flow curve [22]. The area of the hysteretic loop represents the amount of work done in breaking down the microstructure of the mortar. Energy required for the thixotropic breakdown of mortars having $M = 4$ and $R = 1.33$ is presented in Table 3. A comparison of thixotropy among slag-based mortar, fly ash-based mortar and mortar with a blending of fly ash and slag shows

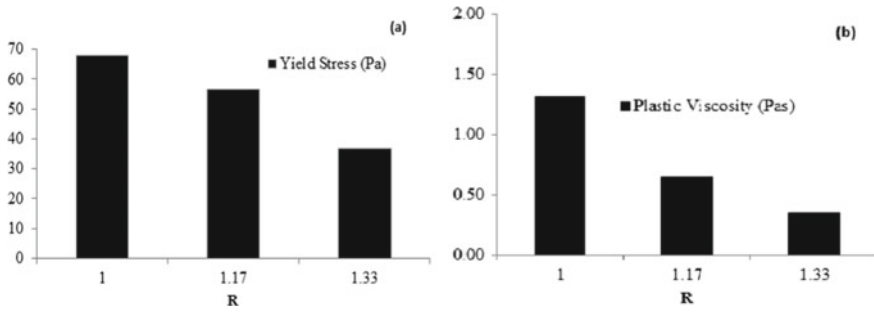


Fig. 7 Variation of a yield stress b plastic viscosity with alkali to binder ratio for slag-based mortar

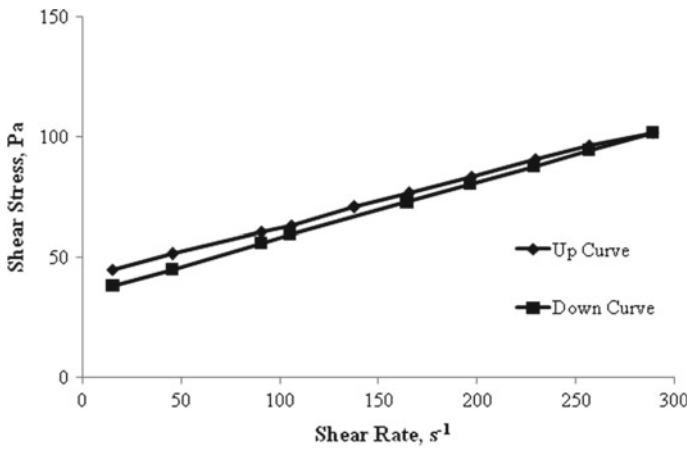


Fig. 8 Flow curve for blended mix (M = 8, R = 1.33)

Table 3 Thixotropic evaluation (M = 4, R = 1.33)

Mortar type	Work done (Pa·s ⁻¹)
Fly ash	897
Slag	964
Blend (Fly ash + Slag)	922

that degree of thixotropy is the highest in case of slag-based mortar and is the lowest in fly ash-based mortar.

A comparison of rheological parameters of blending with slag- and fly ash-based geopolymer mortar is shown in Figs. 9–10. It may be observed that both the rheological parameters of the slag-based geopolymer mortar decreased to a large extent after blending with fly ash. Values of yield stress and plastic viscosity of blended specimens are always greater than the values of rheological parameters with fly ash, and are less than the values of rheological parameters with slag. It is to be noticed

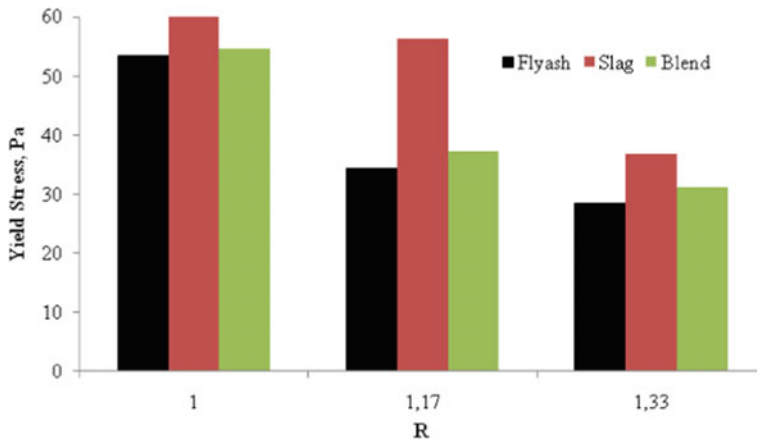


Fig. 9 Comparison of Yield Stress with fly ash, slag and blending

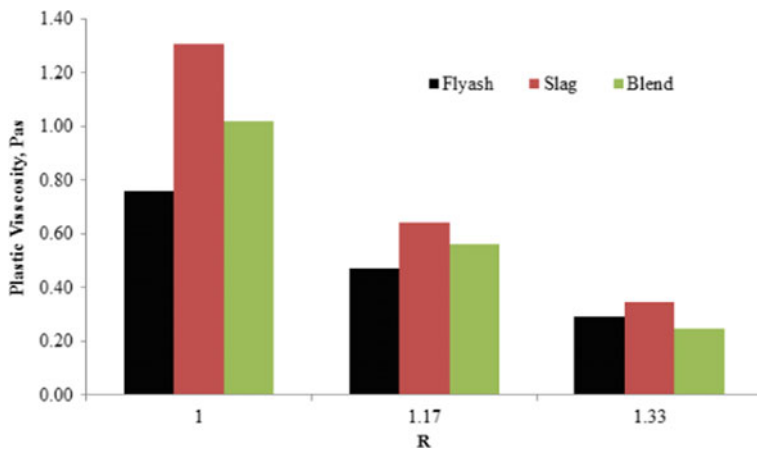


Fig. 10 Variation of plastic viscosity with fly ash, slag and blending

from Fig. 9 that values of yield stress for mortars incorporating fly ash and blended source materials are very close and there is no significant difference.

4 Conclusion

In the present study, the rheological behavior of fly ash- and slag-based mortar and their blending (1:1 by weight) were investigated at different molar concentrations of NaOH activator and at different R values. It may be concluded that thixotropy is present in geopolymer mortar with fly ash, slag and their blending when activated

with NaOH solution. The degree of thixotropy is the highest with slag and is the lowest with fly ash as the source material. The down curves in all the cases under investigation follow the Bingham equation with good accuracy. Values of rheological parameters such as yield stress and plastic viscosity of the slag-based geopolymer mortar are maximum and are reduced significantly after the addition of 50% fly ash.

References

1. Ariffin MAM, Bhutta MAR, Hussin MW, Tahir MM, Aziah N (2013) Sulfuric acid resistance of blended ash geopolymer concrete. *Const Build Mater* 43:80–86
2. Bakharev T, Sanjayan JG, Cheng Y-B (2003) Resistance of alkali-activated slag concrete to acid attack. *Cem Conc Res* 33:1607–1611
3. Bakharev T, Sanjayan JG, Cheng Y-B (2002) Sulfate attack on alkali-activated slag concrete. *Cem Conc Res* 32:211–216
4. Bakharev T, Sanjayan JG, Cheng Y-B (1999) Alkali activation of Australian slag cements. *Cem Conc Res* 29:113–120
5. Barnes HA, Hutton JF, Walters K (1989) *An introduction to rheology*. Rheol Ser 3, Elsevier, Amsterdam
6. Beaupre B (1994) *Rheology of high performance shotcrete*, Ph.D thesis, University of British Columbia, Vancouver, BC, Canada
7. Bouras R, Kaci A, Chaouche M (2012) Influence of viscosity modifying admixtures on the rheological behavior of cement and mortar pastes. *Korea-Australia Rheol J* 24:35–44
8. Criado M, Palomo A, Fernandez-Jimenez A, Banfill PFG (2009) Alkali activated fly ash: effect of admixtures on paste rheology. *Rheol Acta* 48:447–455
9. De Larrard F, Sztikar J-C, Hu C, Joly M (1993) Design of a rheometer for fluid concrete. In: *RILEM Workshop Special Concrete- Workability and Mixing*, pp 201–208
10. Duxson P, Fernandez-Jimenez A, Provis JL, Palomo A, van Deventer JSJ (2007) Geopolymer technology: the current state of art. *J Mater Sci* 42:2917–2933
11. Fernandez-Jimenez A, Palomo JG, Puertas F (1999) Alkali-activated slag mortars: mechanical strength behavior. *Cem Conc Res* 29:1313–1321
12. Ferraris CF, Brower LE (2001) Comparison of concrete rheometer: international tests at LCPC Nantes France. Report No. NISTIR 6819
13. IS: 12089 (1999) Specification for Granulated Slag For the Manufacture of Portland Slag Cement. Bureau of Indian Standards, Indian Standard Code of Practice, New Delhi, India
14. IS: 2386 (1999) Methods for Tests for Aggregates for Concrete. Bureau of Indian Standards, Indian Standard Code of Practice, New Delhi, India
15. IS: 3812 (1999) Specification for Fly Ash for Use as Pozzolana and Admixture. Bureau of Indian Standards, Indian Standard Code of Practice, New Delhi, India
16. Jang JG, Lee NK, Lee HK (2014) Fresh and hardened properties of alkali activated fly ash/slag pastes with superplasticizers. *Const Build Mater* 50:169–176
17. Kashani A, Provis JL, Qiao GG, van Deventer JSJ (2014) The interrelationship between surface chemistry and rheology in alkali activated slag paste. *Const Build Mater* 65:583–591
18. Koehler EP, Fowler DW (2004) Development of a portable rheometer for fresh Portland cement concrete. Report No. ICAR 105–3F, International Center for Aggregate Research, The University of Texas at Austin
19. Laskar AI, Bhattacharjee R (2013) Effect of plasticizer and super plasticizer on rheology of fly-ash-based geopolymer concrete. *ACI Mater J* 110:513–518
20. Laskar AI, Bhattacharjee R (2011) Rheology of fly ash based geopolymer concrete. *ACI Mater J* 108:536–542
21. Laskar AI, Talukdar S (2008) Design of a new rheometer for concrete, *J ASTM Int* 5

22. Mewis J (1979) Thixotropy- a general review. *J Non-Newtonian Fluid Mech* 6:1–20
23. Palacios M, Banfill PFG, Puertas F (2008) Rheology and setting of alkali activated slag pastes and mortars: effect of organic admixtures. *ACI Mater J* 105:140–148
24. Palomo A, Santiago A, Fernandez-Jimenez A, Sobrados I, Sanz J (2004) Alkaline activation of fly ashes: NMR study of the reaction products. *J Am Ceram Soc* 87:1141–1145
25. Palomo A, Grutzeck MW, Blanco MT (1999) Alkali-activated fly ashes: A cement for the future. *Cem. Conc. Res.* 29:1323–1329
26. Puertas F, Amat T, Fernandez-Jimenez A, Vazquez T (2003) Mechanical and durable behaviour of alkaline cement mortars reinforced with polypropylene fibres. *Cem Conc Res* 33:2031–2036
27. Sant G, Ferraris CF, Weiss J (2008) Rheological properties of cement pastes: a discussion of structure formation and mechanical property development. *Cem Conc Res* 38:1286–1296
28. Shi C, Krivenko PV, Roy D (2006) *Alkali-activated cements and concretes*. Taylor and Francis, USA and Canada
29. Shi C, Xie P (1998) Interface between cement paste and quartz sand in alkali-activated slag mortars. *Cem Conc Res* 28:887–896
30. Tattersall GH (1991) *Workability and quality control of concrete*. E & FN Spon, London
31. Tattersall GH, Banfill PFG (1983) *The rheology of fresh concrete*. Pitman Publishing, Marshfield, MA
32. Zhang HY, Kodur V, Qi SL, Cao L, Wu B (2014) Development of metakaoline-fly ash based geopolymers for fire resistance application. *Const Build Mater* 55:38–45

Effect of Pile Spacing and Raft Thickness on the Behaviour of Piled-Raft Foundation—A Parametric Study Using FEM



Mukul Kalita, Utpal Kumar Nath, and Palash Jyoti Hazarika

Abstract This paper presents a parametric study of piled-raft foundation under static loading in homogenous soft clay and loose sand. 3D finite element analyses have been carried out for conventional unpiled raft as well as piled rafts with 4 and 9 number of piles underneath the raft. A three-dimensional finite element package for soil and foundation is used for plane strain, linear elastic modelling of piled-raft system, and Mohr–Coulomb yield criterion is used to represent the two soil types as elastic-perfect plastic material. The loading parameters, length and diameter of circular piles, Poisson’s ratio and elastic moduli of raft, piles and soil are kept constant throughout the analyses. Focus is thereby on two parameters—pile spacing, i.e. S/D ratio and raft thickness. Variation in the peak values of settlements, bending moments, torsion, axial forces and shear forces are investigated in both raft and piles due to varying pile spacing and raft thickness in clay and sandy soil. The general conclusion of this study for providing a piled-raft foundation is to design a flexible/semi-flexible raft of optimum thickness and S/D ratio so that the deflections and force parameters on the raft and the piles are within permissible limits and the piles can effectively act as settlement reducers in addition to sharing of loads.

Keywords Piled raft · Soft clay · Loose sand · Finite element analyses · S/D ratio · Raft thickness

M. Kalita

Department of Civil Engineering, Assam Don Bosco University, Guwahati, India
e-mail: mukulkalita138@gmail.com

U. K. Nath (✉) · P. J. Hazarika

Department of Civil Engineering, Assam Engineering College, Guwahati, India
e-mail: ukn.ce@aec.ac.in

P. J. Hazarika

e-mail: pjhaz@rediffmail.com

© Springer Nature Singapore Pte Ltd. 2021

S. Adhikari et al. (eds.), *Advances in Structural Technologies*, Lecture Notes in Civil Engineering 81, https://doi.org/10.1007/978-981-15-5235-9_9

1 Introduction

In the past few decades, there has been an increasing recognition that the use of pile groups in conjunction with the raft can lead to considerable economy without compromising the safety and performance of the foundation. Such a foundation makes use of both the raft and the piles, and is referred to here as a piled raft. The use of piled-raft foundation has become popular in recent years, as the combined action of the raft and the piles can increase the bearing capacity, reduce settlements, and the piles can be arranged so as to reduce deflection in the raft. A piled-raft foundation is economical compared to the pile foundation because piles in this case do not have to penetrate the full depth of soil stratum but it can be terminated at higher elevations.

The main objective of the study is to investigate the influence of some of the factors such as pile spacing and thickness of raft on the behaviour of piled-raft foundation system. The scope of this work is to study the variation in the peak values of settlement, bending moments, torsional moments, shear forces and axial forces for a piled-raft foundation due to change in pile spacing and raft thickness in soft clay and loose sand, and to compare the results for the two types of soil considered for arriving at some general hypothetical conclusions.

2 Methodology

In this study, a 16 m × 16 m raft with 0.6 m diameter massive circular piles were analysed using a finite element software package 'Plaxis 3D Foundation'. A plane strain finite element model was used to model the piled-raft foundation. The raft and piles were assumed to be linearly elastic. The Mohr–Coulomb yield criterion was used to represent both the soil types—soft clay and loose sand, as elastic-perfect plastic material. A single layer homogenous isotropic soil with water table at a depth of 6 m from ground level was assumed for the study. Here an undrained condition was assumed and total stress analysis was carried out using plastic calculations. The soil was discretized as 15 noded triangular elements. The piles and raft were modelled using a plate element. The side skin friction in piles was taken into account by applying interface reduction factor R_{inter} . Sub-soil thickness is considered to a depth of 30 m from ground surface for both the soil types. A non-uniform vertical loading in the form of concentrated column loads has been imposed on the piled raft. Effect of lateral loading is pseudo-statically considered by making one half of the piled raft heavier compared to the other half. The various geometric and material properties of soil, raft, piles and interfaces are tabulated below (Tables 1, 2, 3 and 4).

The loading and geometric details of the model have been depicted in Fig. 1.

Table 1 Properties of the soil being used in the study

Soil type	Soft clay	Loose sand
Material model	Mohr–Coulomb	Mohr–Coulomb
Angle of friction (ϕ)	0°	28°
Stiffness (E_{ref}) (kN/m ²)	1.5×10^4	6×10^3
Cohesion (C_u) (kN/m ²)	30	1
Poisson’s ratio (ν)	0.35	0.30
Dilatancy angle (Ψ)	0°	1°
Saturated unit weight (γ_{sat}) (kN/m ³)	17	18 kN/m ³
Unsaturated unit weight (γ_d) (kN/m ³)	15	16 kN/m ³
Drainage condition	Undrained	Undrained
Permeability (m/day)	0.25	1
Depth of water table (m)	6	6

Table 2 Properties of the materials being used in the study

Material	Bored pile	Raft (floor)	Basement wall
Material model	Linear elastic	Linear isotropic	Linear isotropic
Material type	Non-porous	Non-porous	Non-porous
Stiffness (E_{ref}) (kN/m ²)	2.15×10^7	2.15×10^7	2.15×10^7
Poisson’s ratio (ν)	0.15	0.15	0.15
Unit weight (γ_{sat}) (kN/m ³)	25	25	25
Permeability (m/day)	0	0	0

Table 3 Properties of the soil–pile and soil–raft interface

Soil type	Soft clay	Loose sand
R_{inter}	0.8	0.9
Angle of friction (ϕ_i)	0	25.6°
Cohesion (C_i) (kN/m ²)	24	0.8

Table 4 Dimensions of the materials being used in the study

Material	Pile	Raft	Basement wall
Diameter, D	0.6 m	–	–
Thickness, d	–	0.8, 1.0, 1.2, 1.4, 1.6 m	0.5 m
Length, L	8, 10, 12, 14, 16 m	–	–
Number, N	0, 4, 9	–	–
Spacing, S	6 m	–	–
S/D ratio	10	–	–

3 Results and Discussions

3.1 Effect of Pile Spacing

It is observed that the maximum positive moment in raft decreases non-linearly with increase in pile spacing, for loose sand and soft clay, with pile diameter and raft thickness remaining constant. For a pile length of 10 m, there are almost 21 and 20% reduction in positive raft moment for clay and sand over a pile spacing increment from 4 to 12 m (Fig. 2).

Other parameters remaining same, the maximum negative moment in raft first decreases and then increases with increase in pile spacing from 4 to 12 m, for both the types of soil. For a pile length of 10 m, the maximum decrement in negative moments observed are almost 40 and 47% for clay and sand, respectively, when the pile spacing increases from 4 to 6 m (Fig. 3).

The maximum torsional moment in raft first decreases and then increases with increase in pile spacing from 4 to 12 m, for both the types of soil. For a pile length of 10 m, the maximum decrement in torsional moments observed are almost 39% and 34% for clay and sand, respectively, when the pile spacing increases from 4 m to 6 m (Fig. 4).

The maximum shear force in raft exhibits a significantly decreasing trend with increase in pile spacing, for both the types of soil. Over a pile spacing increment from 4 m to 12 m, there are almost 51% and 48% reduction in raft shear for clay and sand, respectively (Fig. 5).

The maximum vertical deflection of raft varies directly with the spacing of piles for both the types of soil. The maximum deflection in raft decreases by about 6% for clay and 11% for sand when the pile spacing is decreased from 12 to 4 m (Fig. 6).

Maximum pile axial force is found to be increasing uniformly with the increase in pile spacing. For a pile spacing increment from 4 to 12 m, increase in maximum pile axial values are

- Almost 10% for soft clay and
- Almost 14% for loose sand (Fig. 7).

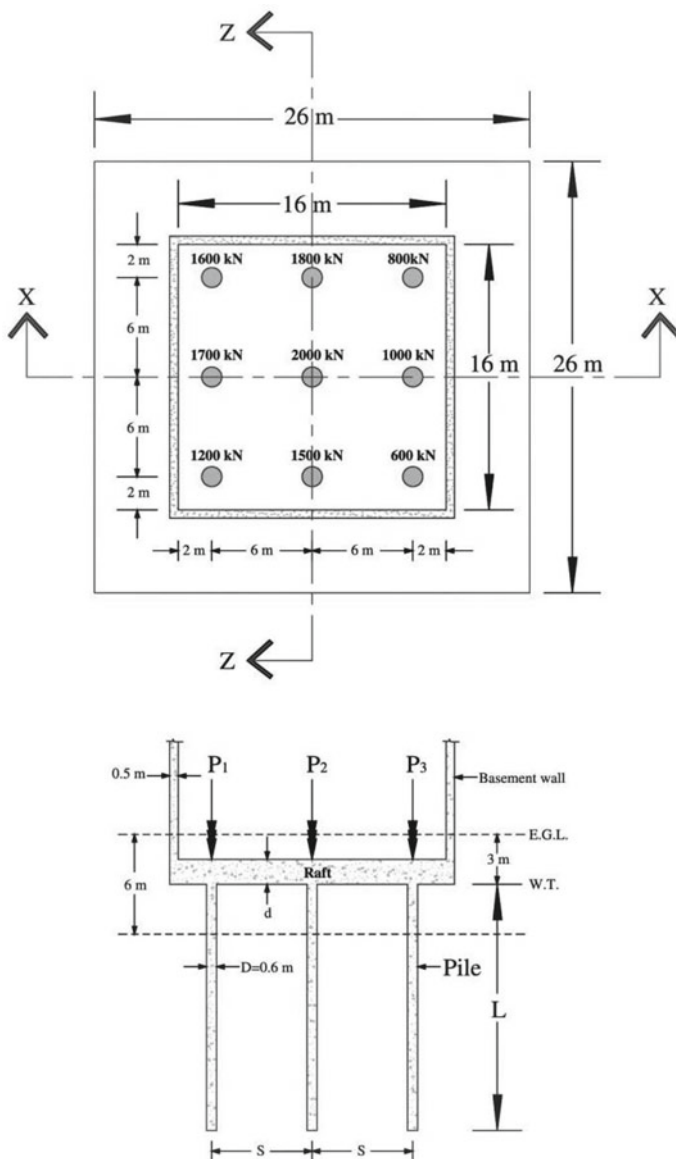


Fig. 1 Piled-raft configuration for analysis

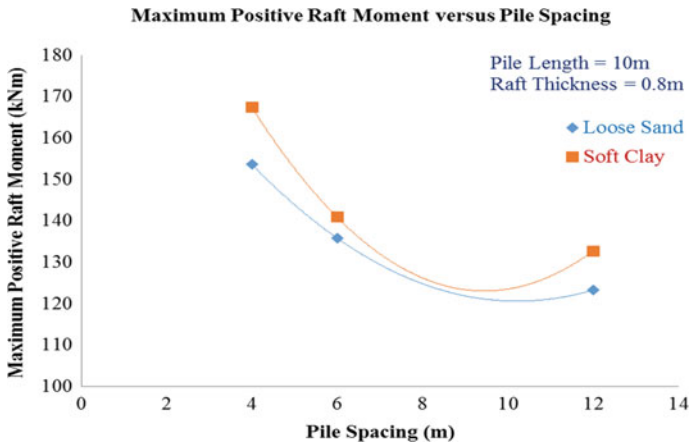


Fig. 2 Maximum positive raft moment versus pile spacing

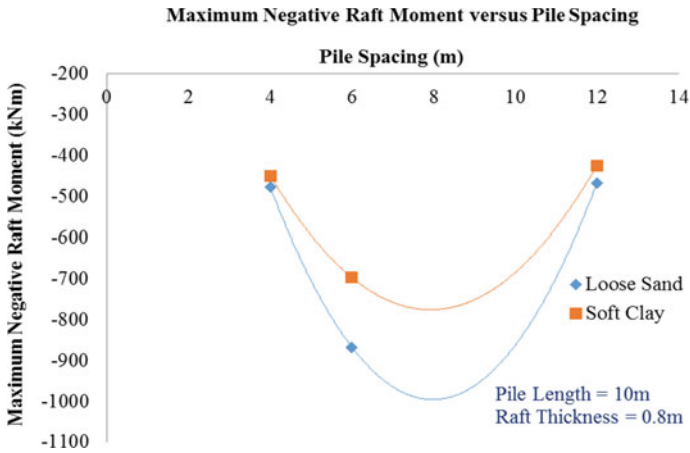


Fig. 3 Maximum negative raft moment versus pile spacing

The maximum settlement of piles varies directly with the spacing of piles. For both the types of soil, it is observed that the maximum vertical deflection of piles decreases with decrease in pile spacing from 12 to 4 m, the maximum reduction being 6% for clay and 11% for sand over that range of pile spacing decrement (Fig. 8).

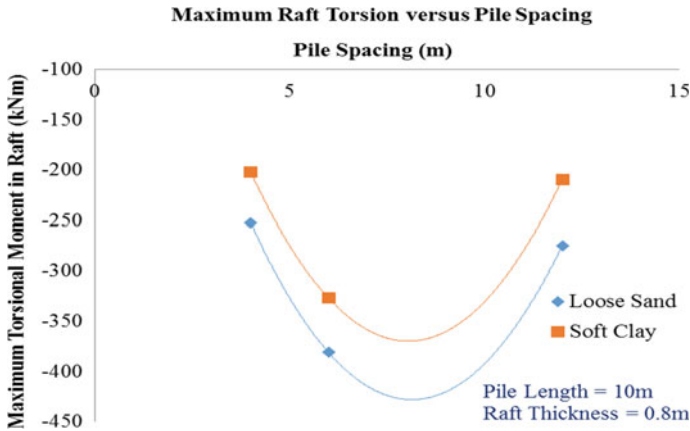


Fig. 4 Maximum raft torsion versus pile spacing

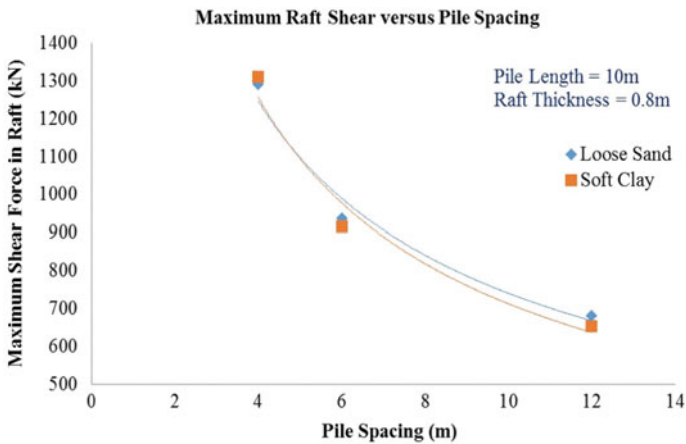


Fig. 5 Maximum raft shear versus pile spacing

3.2 Effect of Raft Thickness

Pile diameter, pile spacing and pile length remaining constant, the maximum positive moment in raft decreases significantly with increase in raft thickness, for loose sand and soft clay. The trend of decrease is almost uniform for both the types of soil. For a 9 pile group, there are almost 52 and 35% reduction in positive raft moment for clay and sand, respectively, when the raft thickness increases from 0.8 to 1.6 m (Fig. 9).

Other parameters remaining same the maximum negative bending moment in raft increases directly with increase in raft thickness, for both the types of soil. Over a

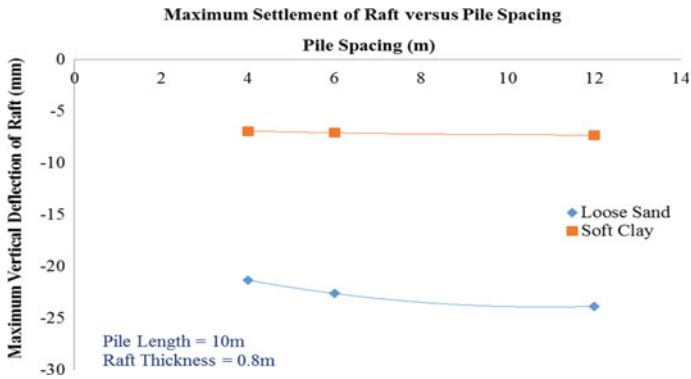


Fig. 6 Maximum settlement of raft versus pile spacing

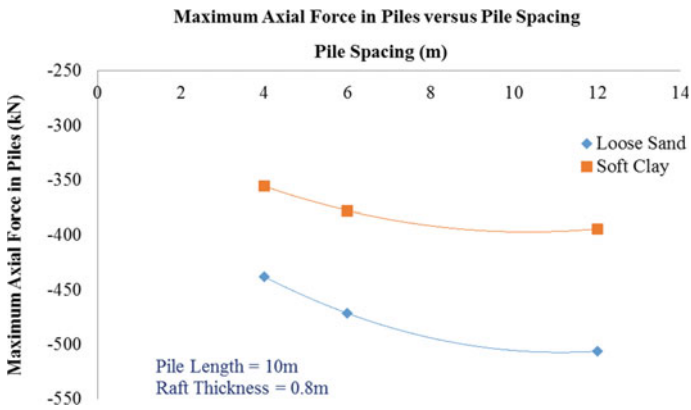


Fig. 7 Maximum axial force in piles versus pile spacing

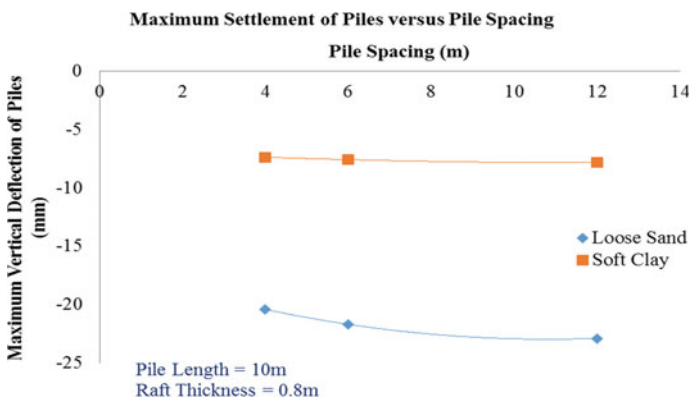


Fig. 8 Maximum settlement of piles versus pile spacing

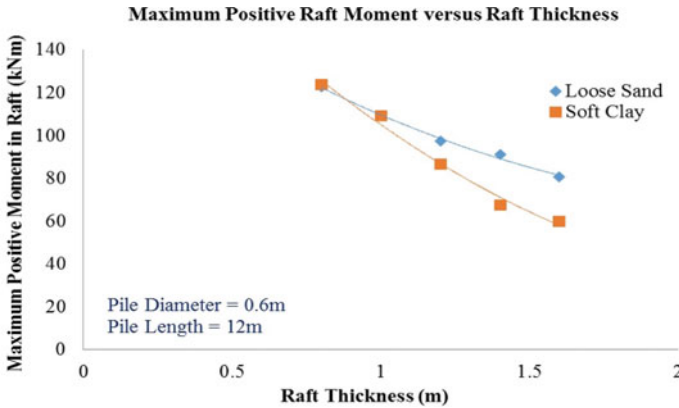


Fig. 9 Maximum positive raft moment versus raft thickness for a 9-piled raft

thickness increment from 0.8 to 1.6 m of raft, there are almost 40 and 36% increase in negative raft moment for clay and sand, respectively, for a 9-piled raft (Fig. 10).

The maximum shear force in raft shows an increasing trend with increase in raft thickness, for both the types of soil. As the raft thickness increases from 0.8 m to 1.6 m, the maximum raft shear increases by about 10% and 12% in clay and sand, respectively (Fig. 11).

The maximum torsional moment in raft increases directly with increase in raft thickness, for both the types of soil. Over a thickness increment from 0.8 m to 1.6 m of raft, there are almost 39% and 36% increment in raft torsion for clay and sand, respectively, for a 9-piled raft (Fig. 12).

The maximum settlement of raft varies directly with the thickness of raft. For both the types of soil, the maximum deflection in raft increases almost uniformly with

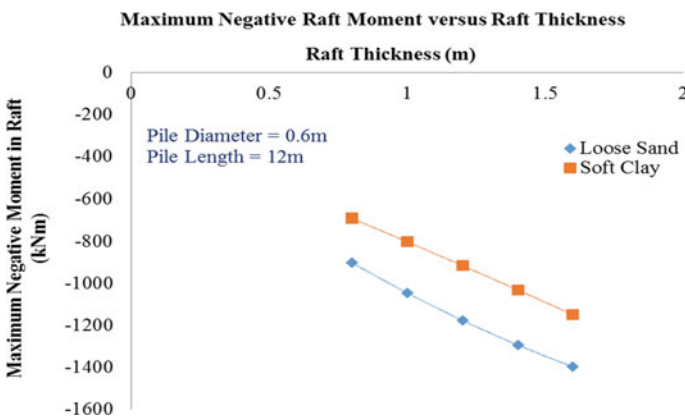


Fig. 10 Maximum negative raft moment versus raft thickness for a 9-piled raft

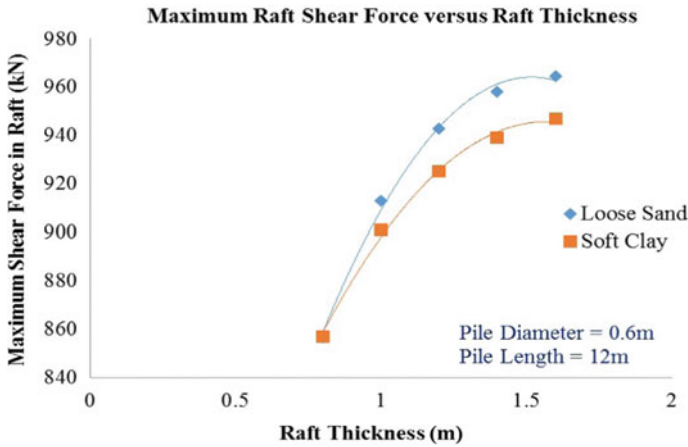


Fig. 11 Maximum raft shear force versus raft thickness for a 9-piled raft

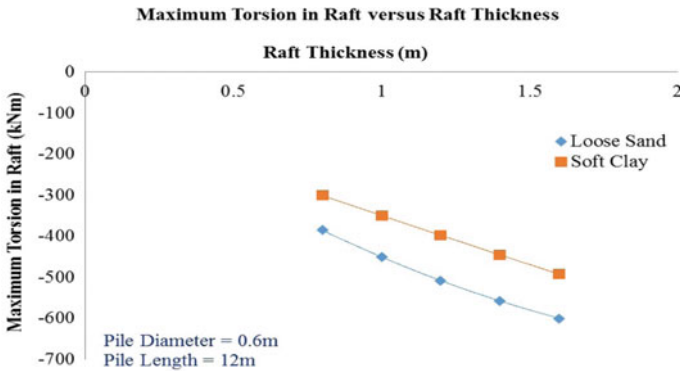


Fig. 12 Maximum torsion in raft versus raft thickness for a 9-piled raft

increase in raft thickness from 0.8 to 1.6 m, the maximum increment being 21% for soft clay and 28% for loose sand (Fig. 13).

A significant effect of raft thickness on axial forces in piles has been observed for both the types of soil. Maximum pile axial is seen to be increasing uniformly with increase in raft thickness. For a thickness increment from 0.8 to 1.6 m of raft, increase in maximum pile axial values are

- Almost 22% for soft clay and
- Almost 24% for loose sand (Fig. 14).

The maximum settlement of piles varies directly with the thickness of raft. For both the types of soil, it is observed that the maximum vertical deflection of piles

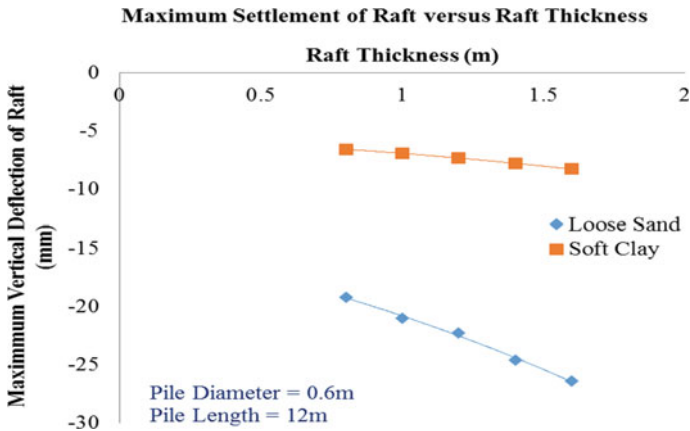


Fig. 13 Maximum settlement of raft versus raft thickness for a 9-piled raft

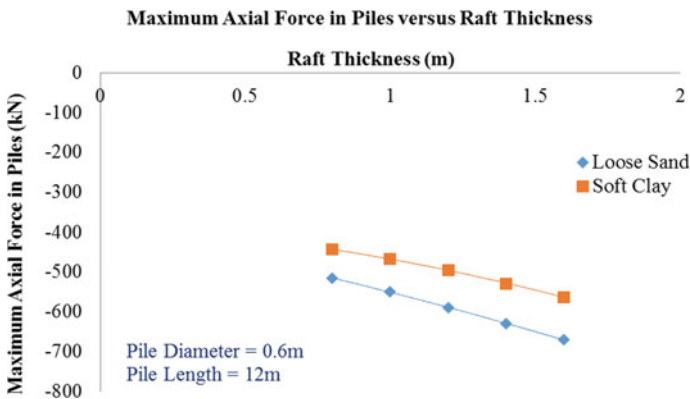


Fig. 14 Maximum axial force in piles versus raft thickness for a 9-piled raft

decreases significantly with decrease in raft thickness from 1.6 to 0.8 m, the maximum reduction being 17% for soft clay and 23% for loose sand (Fig. 15).

4 Conclusion

The general observations of this study can be summarised as follows.

The force parameters (axial forces, bending moments, torsional moments, shear forces, etc.) in raft reach their minimum value for an optimum spacing of piles beyond which the moments and forces in raft increase considerably. Increased pile spacing gives rise to increased vertical deflection in both the raft and the piles. The force

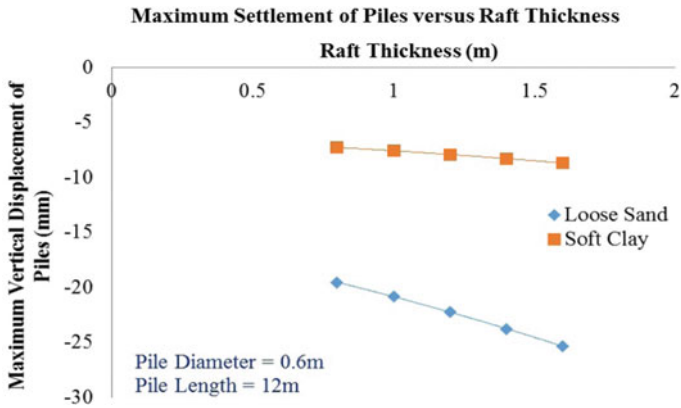



Fig. 15 Maximum settlement of piles versus raft thickness for a 9-piled raft

parameters are also considerably higher for a raft which is rigid and stiff compared to a flexible raft. Again these forces acting on the raft increase with increase in thickness of the raft. The piles supporting the raft basically reduce the vertical deflection of the system. The force parameters in piles also exhibit an increasing trend with increased raft thickness.

The most favourable solution to provide a piled raft system is to design a flexible/semi-flexible raft of optimum thickness so that the forces coming on the raft and the piles are not excessively high and the piles have adequate capacity to withstand the forces transferred to them. To get the most serviceable and economic design of a piled raft, optimization analyses have to be carried for determining the most favourable pile spacing that will give rise to optimum forces in the raft and the piles.

Removal of VOCs and Improvement of Indoor Air Quality Using Activated Carbon Air Filter



Sujon Mondal, Soham De, and Purnachandra Saha 

Abstract Volatile Organic Compound (VOC) is one of the most common air pollutants emitted from industries like Chemical, Petrochemical, as well as when plastics are burned. It is very harmful to our environment which affects climate change, the life cycle of plants, and the health of all living beings. So, it is necessary to control its emission for improvement of air quality which is beneficial to the indoor environment. The objective of the study is to review the performance of different activated carbon-based air filters. Various activated carbon-based techniques are the use of coconut shells, photocatalyst TiO_2 , Polystyrene foam, sorption-type, and granular activated carbon. Several aldehydes and ketones have been removed effectively using activated coconut shell. Removal of nitrogen oxide was possible by using TiO_2 -based activated carbon. It is observed from this study that activated carbon-based techniques are effective for the removal of VOCs and enhancing the indoor air quality.

Keywords VOCs · IAQ · Activated carbon filter · Coconut shell · Photocatalyst TiO_2 · Polystyrene foam

1 Introduction

Volatile organic component (VOC) is one of the most harmful contaminants present in the air. Its boiling point lies between 50 and 260 °C. It consists of several components such as Acetaldehyde, Acetone, Benzene, Carbon tetrachloride, Ethyl acetate, Ethylene glycol, Formaldehyde, Heptane, Hexane, and several others [1]. There are several detrimental effects that occur due to this such as serious health disorders

S. Mondal · S. De · P. Saha (✉)

School of Civil Engineering, KIIT Deemed to be University, Bhubaneswar, India

e-mail: dr.purnasaha@gmail.com

S. Mondal

e-mail: sujonmondal986@gmail.com

S. De

e-mail: sohamde053@gmail.com

© Springer Nature Singapore Pte Ltd. 2021

S. Adhikari et al. (eds.), *Advances in Structural Technologies*, Lecture Notes in Civil Engineering 81, https://doi.org/10.1007/978-981-15-5235-9_10

which include irritation of nose and eyes, damages in the liver, and badly affects the nervous system [2]. It not only affects the human body but also affects the change of climate, and the temperature of the earth also reduces the plant growth [2, 3]. This indirectly affects the indoor air quality (IAQ). IAQ is defined as the air quality in and around the building. There are several factors that affect the IAQ such as temperature, humidity, biological pollutants, air exchange rate, air movement, particle pollutants, and gaseous pollutants. One of the major factors that affects the IAQ is the gaseous pollutants [4, 5]. For improvement of this IAQ and also outdoor air quality there are several activated carbon-based filters that are used which might be shell-based such as coconut shell-based, pecan shell, and almond shell-based [6–8] or it might be activated charcoal, bamboo charcoal [9]. Other types of activated carbons are the granular activated carbon and the activated carbon fiber (AFC) [10, 11]. There are several techniques that are used for the filtration process such as oxidation, catalysis, regeneration, and reverse reactor process [2, 3, 12]. The main objective of the study is to study the different activated carbon-based filter and comparing their

- (1) Removal Efficiency and Specific Surface area.
- (2) Study the several filtration techniques that are available.

2 Different Techniques of Activated Carbon-Based Air Filter

Activated carbon-based air filter (ACBAF) is mainly used for the removal of different harmful contaminants and impurities in the air which include VOCs, CO₂, NO₂, SO₂, etc. This filtration process mainly differs based on the activated carbon used and processed [10]. There are two types of techniques, namely adsorption and filter based which are used to improve the indoor air quality. In the adsorption process, increasing surface area with more pore development should be used to improve the performance [2]. These types of techniques are mainly used for the purification of the indoor as well as outdoor air. Filter-based techniques mainly contain several activated carbon-based filters which purify the air using oxidation, catalysis, regeneration, and reverse reactor process [1].

2.1 Adsorption Type

Adsorption is a surface phenomenon in which solid surface attracts gas molecule or liquid solution. The adsorbing solid is called adsorbent (activated carbon) and the adsorbed particle is called adsorbate (air contaminants).

When gas or vapor comes in contact with solid particles, a portion of the gas-composition is absorbed by the solid. The contact-solid surface is called adsorbate. Many organic and inorganic contaminants are removed either from the gaseous or liquid solutions by the natural process of adsorption on the very porous medium solid

phase with large internal surfaces. Adsorbates can attach themselves onto the surfaces in two ways: (a) physisorption, (b) chemisorptions. In physisorption, adsorbents attach themselves to the solid medium by weak van der Waals force. But in case of chemisorptions, the adsorbates stick to the solid medium by forming (a) chemical bond between the adsorbates and the solid medium. The above-scripted steps of adsorption can be summarized as per the following: solute diffuses near the solid surface, diffuses into the pores of the particle, then moves through the pore wall and adsorbs to the pore wall surface. To increase the adsorption capacity of activated carbon a large specific surface is favored [13].

2.2 Adsorption Process

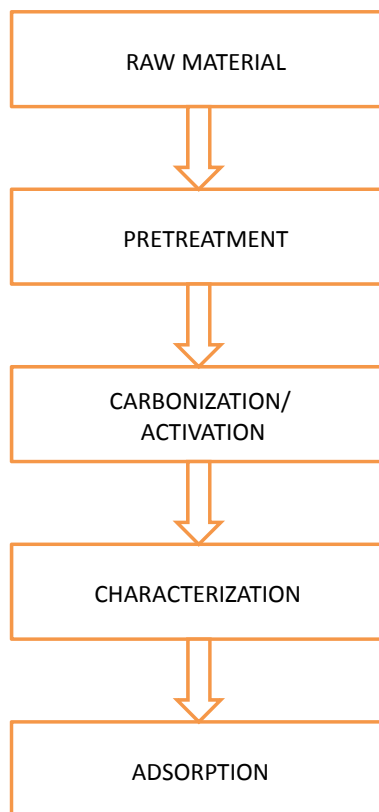
Activated carbons are mainly used as a filter material for removal of contaminant gases present in the air, porous carbon-based materials have high thermal and chemical stability as well as good adsorption capabilities [14]. Coconut shell, activated charcoals, commercial fibers of polymetaphenylene, fiber of Polyparaphenylene terephthalamide, bamboo carbon and anthracite activated carbon were used as raw materials for activated carbon. The samples were milled inside planetary ball mill for 30 h with the speed of 300 rpm to reduce the size. Hydrogen (H₂) was used as adsorbate gas. The granular coconut shell charcoals used were in the granulated form [15]. The average diameter of the fibers was around 10 μm(pm) [11].

Different types of carbonaceous materials with more concentration of carbon can be obtained from plants, mineral origins can be converted to activated carbon using different types of methods such as chemical and physical activation method. For this reason, a pretreatment was performed that involved cutting, removing all of the pulp and some of the fibers, and air-drying the remaining shell. For uniform quality in carbonization and activation, the water content of the shells was maintained between 13 and 16% [14] (Fig. 1).

2.2.1 Carbonization/Activation

Activated carbons can be produced by two different processes: one is Physical or gas activation process and other process is Chemical activation. The choice of activation method solely depends upon the material used which can have either a low- or high-density carbon [13]. After pretreatment, the samples were placed in a high-temperature kiln for carbonization by electric heating. During carbonization, heating rate of 10 °C/min is held for 2 h [16]. Five activation temperatures 600, 700, 800, 900, and 1000 °C have been investigated [14].

Fig. 1 VOC removal process



After carbonization, the samples were cooled to room temperature under N₂ flow (100 cm³/min) [16]. Carbon is oxidized usually with the help of carbon dioxide or steam at 800–1000 °C or and with low-temperature air flow, and carbonization of primary raw material is followed by the oxidation process [13].

Coconut Shell, Activated Charcoal, Bamboo Charcoal

The rapid development of industrial technologies increased the concentration of greenhouse gases such as VOCs, CO₂, NO₂, N₂, CH₄, and HFCs, and because of this increasing global warming, ocean water levels raise [14]. Porous carbon-based materials such as coconut shell, activated charcoal, bamboo charcoal, pecan shell, and almond shell-based activated carbon have high thermal and chemical stability as well as good adsorption capabilities for such harmful gases.

Phosphoric acid activated (almond shell) has the surface area of 1340 m²/g and absorption of 347 ppb. Coal based activated (coal) has the surface area 835 m²/g and absorption is 476 ppb whereas the steam-based activated (pecan shell) has a surface

of $917 \text{ m}^2/\text{g}$ and absorption of 506 ppb [7]. Coconut shell charcoal has least surface area of about $36.5 \text{ m}^2/\text{g}$. When it is chemically activated, surface area increases up to $1768.8 \text{ m}^2/\text{g}$ [6] and absorption of about 516 ppb [7]. But when modified or synthesis with TiO_2 nanoparticle removal/absorption, efficiency increase than the unmodified coconut shell based activated carbon [8]. The removal efficiency of the bamboo charcoal and activated carbon is 10% more than coconut shell based activated carbon [9].

Granular Activated Carbon Fiber of Polyparaphenylene Terephthalamide and Fibers of Polymetaphenylene Isophthalamide

Granular activated carbon is mainly used for the removal of harmful contaminants. It has a specific surface area of $900\text{--}1200 \text{ (m}^2/\text{g)}$ depending on the activation [10]. In case of activated carbon fiber which may be of different types of pitch-based activated, cellulose-based, pan-based ACFs [17]. The specific surface area varies $700\text{--}2500 \text{ (m}^2/\text{g)}$ and due to this the absorption of ACFs is more than that of the granular activated carbon. Some other derivatives of ACFs such as Nomex and Kevlar have also specific area more than $1000 \text{ (m}^2/\text{g)}$ [11]. But PAN has more surface area that is about $2400 \text{ m}^2/\text{g}$ [17]. Also the SO_2 retention capacity of $266 \text{ MgSO}_2/\text{g}$ which is more than the Nomex ($165.5 \text{ MgSO}_2/\text{g}$) and Kevlar ($192.5 \text{ MgSO}_2/\text{g}$) makes the PAN most efficient [11].

2.3 Filter Based

Filter means to remove unwanted impurities from air or liquid. Filtration is the process by which the air or liquid is getting filtered. Filtration can be done by several techniques such as using oxidation, catalysis, regeneration, and reverse reactor process. These techniques are mainly for the removal of impurities such as VOCs, NO_2 , and SO_2 . Filters mainly contain several activated carbons that are mentioned above such as ACF, charcoal-based activated carbon, and granular activated carbon (Fig. 2).



Fig. 2 Simple process of filtration

3 Different Types of Filtering Techniques

Thermal oxidation is one of the techniques used for VOC removal and other contaminants in the air. Generally, the temperature at which the oxidation takes place is 1300–1800 °C. The temperature also depends on the material used and the destruction and removal efficiency.

Higher removal efficiency value required more elevated temperature and also longer retention time within the reactor.

The process mainly proceeds with the inflow of the air which is injected in the filter then it is heated to a certain temperature. The thermal oxidizer is used for oxidation of the air so the VOC can be removed. Also, the heat is recovered either in the cyclic process or it is stored in the heat storage system [3].

Another major technique that is used is the catalysis for oxidation. The catalyst is mainly provided to increase the surface area for reaction and also for the reduction of the activation temperature. There are various processes by which the catalyst is used for the filtration process.

The first common step is that the injection of impure air heated to a temperature of about 303 °C. Then it is taken to the heat exchanger for further heating process and then is passed through the catalysis bed which is mainly honeycomb shaped that is coated with the catalyst and this lead to the catalytic oxidation. Another process in which the air is directly sent to the catalysis bed that is honeycomb shaped and coated with TiO_2 , and then this is subjected to UV light with the help of photocatalysis and helps in the removal of harmful contaminant. In other processes where the air and the catalyst are directly injected into the filter, the photocatalysis takes place due to absorption of the light energy of the catalyst particle where the temperature is also controlled according to the catalyst size. This reaction mainly takes place in the solid–gas phase where the optimal particle size is about 12 nm. In the other techniques used, the catalyst is in a fluidized bed and there is also photocatalysis taking place; at first the air is injected into the reactor where the fluidized base is present and it is subjected to UV light for the photocatalysis of the removal of the contaminant. The fluidized catalyst bed is mainly obtained by the impregnation of the silica gel with sol–gel which makes the bed more fluidized which improves the removal efficiency [18]. There are several other catalysts which are also used for the removal such as the Carbon Chem bituminous coal, envirotrol bituminous coal, and envirotrol coconut shell which are some of the add-on catalyst that is also used for the removal contaminants from the air [12].

The removal efficiency of these photocatalysis techniques is about 95%, where in the other techniques the efficiency is about 90%. Another technique that is generally used is the reverse reactor. At first, the VOC laden air enters the filter then it is dried and is taken to a pressure-regulated chamber then to adiabatically packed bed reactor where the filtration process takes place. The feed flow direction is periodically changed. The main problem with the reactor is that heat insulation which needs to be more than the packed bed. So in order to make it insulated it is vacuum jacketed. There are several factors that affect the performance of RFR: (a) Cycle period (b)

Table 1 Adsorption efficiency of different activated carbon materials

Material	Adsorption efficiency (%)
Coconut shell charcoal	51.6
Bamboo activated carbon	70.9
Bamboo charcoal	72.3
Phosphoric acid activated carbon	34.7
Charcoal based	47.6
Pecan shell	50.6

Table 2 Effective size of carbon

Material	Surface area (m ² /g)
Phosphoric acid activated carbon	1340
Granular activated carbon	1050
Charcoal based	835
Pecan shell	917
Activated carbon fiber	1600
Coconut shell charcoal	36.5

Gas velocity (c) Adiabatic temperature (d) Different component (e) Pressure, etc. The main advantage of the reactor is that no external heat/thermal energy is required for the reactor to function (Tables 1 and 2).

Regeneration is another technique which is also used for the filtration process. This process is carried out by the release of the N₂ gas from the cylinder, and it gets purified by the gas purifier which contains silica gel and mol. Sieves is mainly used for removal of moisture and hydrocarbon. Then it is bubbled through VOC to bottle the gas which is then passed to the chamber containing the shell on one side and activated carbon fiber wrapped Teflon on the other side and a device was used to maintain the bed temperature; also gas chromatography with FID was used for the test for purification. Now this AFC can be regenerated completely by electrical heating in the presence of the nitrogen gas which is the biggest advantage of this filter absorption of VOC or other contaminants does not decrease with the regeneration process [2] (Figs. 3 and 4).

4 Improvement of Indoor Air Quality (IAQ)

Indoor air quality is the air quality in and around the building. There are several efforts which have been made to improve the air quality. Exposure to poor air quality can lead to various long-term and short-term effects on human health. Some of the short-term effects are dizziness, headaches, irritation in eyes, nose, and throat. The long-term effects include lung cancer, heart disease, and respiratory diseases such as asthma and also may lead to damages to nerves, brain, and failure of other organs.

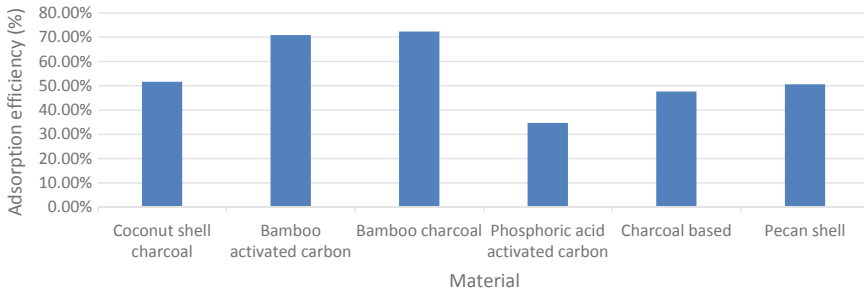


Fig. 3 Adsorption efficiency (%)

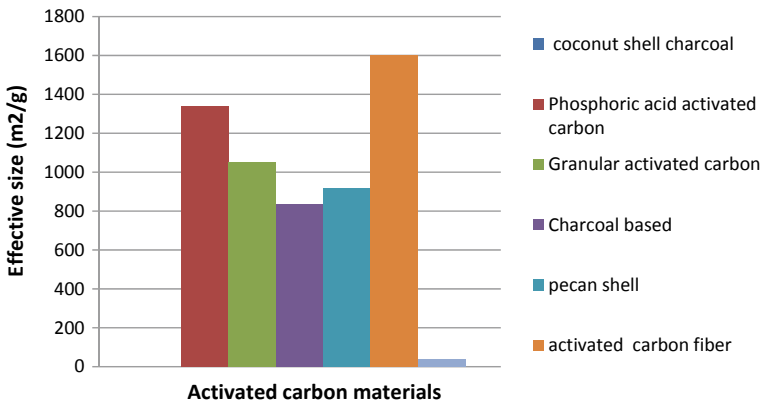


Fig. 4 Effective surface area (m²/g)

There are several parameters that affect the indoor air quality (IAQ) [19, 21]. Toxic pollutant emissions such as particulate matter (P₁₀ and PM_{2.5}), CO₂, VOC, SO₂, CO, Radon, O₃ are some of the parameters responsible for intoxicating IAQ [4, 13, 19]. Also some of the physical factors responsible for controlling IAQ are temperature, airflow rate/ventilation, and humidity [20]. Other biological factors may also affect IAQ such as allergens due to pollens, growth of fungi, insect and animal infestation, and virus spread by the birds [4, 19, 20]. The activated carbon air filter used in this paper mainly deals with the removal of VOC to improve the IAQ. The components of VOC which can be removed from indoor air using activated carbon air filter have been shown in Table 3.

Table 3 VOC removal efficiency of individual activated carbon

VOC	Activated carbon almond shell	Coal-based activated carbon	Steam-based activated pecan shell	Coconut shell charcoal	Coconut shell activated carbon
Bromo dichloromethane (%)	59.9	72.0	85.4	–	–
Benzene (%)	75.8	88.3	87.0	65	74
Carbon tetrachloride (%)	39.6	77.5	80.6	60	64
Trichloro ethan (%)	80.3	88.9	92.5		
Chlorofom (%)	52.1	74.9	77.9	48	63
Dichloro ethane (%)	39.6	75	82.7	–	–

5 Conclusion

Several studies have been made in the recent years for improvement of air quality which has halted the deterioration of IAQ. Different Techniques of activated carbon-based air filters have been discussed to improve the IAQ in this study. Adsorption base and commercially available filtering techniques using activated carbon are efficient methods of air purification. Based on the study, following observations can be made

1. Bamboo-Based Activated Carbons are easily available. They are highly chemically and thermally stable and have high pore density and can be produced in large quantity among all the activated carbon filters studied, and it has the highest adsorption efficiency of around 70% which improves the IAQ.
2. Activated Carbon Fibers are fibrous in nature and it not only contains micropores but also nanopores which also has high volumetric capacity making it an effective surface area more than other materials.
3. IAQ depends on many factors but in this study we have mainly focused on the removal of VOC. VOC has several components such as the Bromo dichloromethane, Benzene, Carbon tetrachloride, Trichloro ethan, Chlorofom, Dichloro ethane. Among all the activated carbon, steam-based activated pecan shell has the highest removal efficiency for the individual components except for benzene which is efficiently removed by coal-based activated carbon; this improves the IAQ.

References

1. Gallego E, Roca FJ, Perales JF, Guardino X (2013) Experimental evaluation of VOC removal efficiency of a coconut shell activated carbon filter for indoor air quality enhancement. *Build Environ* 67:14–25
2. Das D, Gaur V, Verma N (2004) Removal of volatile organic compound by activated carbon fiber. *Carbon* 42:2949–2962
3. Khan IF, Ghoshal KA (2000) Removal of Volatile Organic Compounds from polluted air. *J Loss Prev Process Ind* 13:527–545
4. Shrimandilkar PP (2013) Indoor air quality monitoring for human health. *Int J Mod Eng Res (IJMER)* 3(2):891–897
5. Patnaik A, Kumar V, Saha P (2018) Importance of indoor environmental quality in green buildings. In: *Environmental pollution. Water science and technology library*, vol 77. https://doi.org/10.1007/978-981-10-5792-2_5
6. Iqbalidin IMN, Khudzir IX, Azlan Mohd MI, Zaidi AG, Surani B, Zubri Z (2013) Properties of coconut shell activated carbon. *J Trop For Sci* 25(4):497–503
7. Bansode RR, Losso NJ, Marshall EW, Rao RM, Portier JR (2003) Adsorption of volatile organic compounds by pecan shell and almond shell-based granular activated carbons. *Bioresour Technol* 90:175–184
8. Hoang AL, Le Thuy LSC, Jongsoo J (2012) Photocatalytic degradation of methylene blue by a combination of TiO₂-anatase and coconut shell activated carbon. *Powder Technol* 225:167–175
9. Chuan CC, Ying PH, Wie CW, Jun HC, Yuan YW (2011) Efficiency of moso bamboo charcoal and activated carbon for adsorbing radioactive iodine. *Clean Soil Air Water* 39(2):103–108
10. Dwivedi P, Gaur V, Sharma A, Verma N (2004) Comparative study of removal of volatile organic compounds by cryogenic condensation and adsorption by activated carbon fiber. *Sep Purif Technol* 39:23–37
11. Muniz J, Marban G, Fuertes AB (2000) SO₂ retention over polyaryamide-based activated carbon fibers. *Environ Prog* 19(4) (Winter)
12. Dalai KA, Cundall TM, De M (2008) Direct oxidation of hydrogen sulphide to sulphur using impregnated activated carbon catalysts 86
13. Mohammad KA, Ansari R (2009) Activated charcoal: preparation, characterization and applications 1(4):859–864
14. Pei HH, Hao HC, Sheau HL (2015) Adsorption of carbon dioxide onto activated carbon prepared from coconut shells. *J Chem* 2015(Article ID 106590):10
15. Fatriansyah FJ, Matari T, Harjanto S (2018) The preparation of activated carbon from coconut shell charcoal by novel mechano-chemical activation 929:50–55
16. Yang K, Peng J, Srinivasakannan C, Zhang L, Xia H, Duan X (2010) Preparation of high surface area activated carbon from coconut shells using microwave heating. *Bioresour Technol* 101:6163–6169
17. Youa Y So, Parka HY, Parkb RC (2000) Preparation and properties of activated carbon fabric from acrylic fabric waste. *Carbon* 38:1453–1460
18. Peral J, Xavier DN, Ollis FD (1997) Heterogeneous photocatalysis for purification, decontamination and deodorization of air. *J Chem Technol Biotechnol* 70:117–140
19. Vannan VK, Haralappa P, Sundeep SS, Alpa DKA (2015) Enhancing indoor air quality—the air filter advantage. *Lung India* 32(5):473–479
20. Angell WJ, Grimsrud DT, Lee H (2005) Residential indoor air quality, ventilation, and building-related health effects: critical review of scientific literature
21. Josep AG, Piers M (2015) Green buildings and health. *Curr Environ Health Rep* 2(70):250–258

A Comparative Study of Normal and Self-compacting Concrete



Deep Tripathi, Rakesh Kumar, P. K. Mehta, and Amrendra Singh

Abstract In this paper, the experimental results of both Normal Concrete (NC) and Self-Compacting Concrete (SCC) are presented. Both the fresh and hardened properties were investigated. The SCC was developed by replacing 20% of Ordinary Portland Cement (OPC) by Fly ash (FA), so that the amount OPC is almost same in both NC and SCC. The workability of the mix increases with the inclusion of FA and the mix becomes cost-effective. For workability, the slump test was conducted on NC while for SCC, slump flow, T_{50} time, V-funnel, L-box, U-box and J-ring tests were conducted. The water/binder (w/b) ratio was kept constant for both the NC and SCC. For M25 grade concrete, cubes of size 100 mm, cylinders of size 100 mm \times 200 mm and beams of size 100 mm \times 100 mm \times 500 mm were cast to find the compressive, split tensile and flexural strengths, respectively. The samples were tested after curing in tap water for 7, 28, 56 and 90 days. The water absorption of both NC and SCC was also studied up to 90 days. The XRD analysis of both the concrete samples was also carried out to investigate the microstructural changes.

Keywords Self-compacting concrete · Fly ash · Ordinary portland cement · X-ray diffraction

D. Tripathi (✉) · R. Kumar · P. K. Mehta · A. Singh
CED, MNNIT Allahabad, Prayagraj, UP, India
e-mail: deep@mnnit.ac.in

R. Kumar
e-mail: rkpat@mnnit.ac.in

P. K. Mehta
e-mail: pradeep11@mnnit.ac.in

A. Singh
e-mail: amrendra@mnnit.ac.in

1 Introduction

All over the world, concrete plays a vital role in the field of construction. At present, NC is mostly used throughout the world; however, some problems are encountered during construction, viz. lacking of skilled labour, concreting in congested reinforcement areas, etc. To speed up the construction and to get a durable structure, a new type of concrete which was highly flowable and would not require any compaction, i.e. SCC was developed. Generally, the SCC needs more binder as compared to the NC and is being used successfully at construction sites. It differs from NC in the material proportion/composition. It is flowable under its own weight and is able to compact itself into congested reinforcement areas without the need for any additional vibration. SCC was first proposed in Japan by Prof. Okamura [1] to overcome the shortage of skilled labour. The SCC offers many advantages over NC which include—increased speed of construction, cost savings due to lower labour requirement, superior concreting, aesthetically pleasing finishes, improved structural durability due to better compaction, low noise levels at site and ability to pass through heavily congested reinforcement with relative ease. In SCC, cement consumption is less due to the addition of pozzolanic materials. This also helps in reducing the carbon-footprint besides consuming the industrial by-products like FA. SCC can be made with easily available pozzolanas and superplasticizers. The other difference lies in its design wherein the material proportions vary [2]. Incorporation of FA in SCC enhances the flowability, strength and durability with respect to the control mix. It is reported that by the inclusion of FA in the SCC, its fresh properties are improved and there is less heat of hydration which reduces the cracking of concrete [3]. Klug et al. [4] reported that for the same w/b ratio, the compressive strength is the same for both types of concrete, and split tensile strength of SCC is better than NC; however, the modulus of elasticity of NC is higher than SCC. At the same w/b ratio, the compressive strength of SCC is at least 10% higher than that of NC at the age of 28 days [5, 6]. Bertil Persson [7] reported that the creep, shrinkage and the modulus of elasticity of SCC are comparable with the NC. Ramanathan et al. [8] reported that 30% replacement of OPC by FA in SSC showed improvement in properties as compared to the other replacement levels. It is also reported that with increase in FA content, the loss in compressive strength and water absorption are decreased. Gaywala et al. [9] reported that the compressive, split tensile, flexural and pull out strengths of SCC were maximum at 15% addition of FA in the mix. By increasing FA in SCC, the water absorption is increased while it decreased with increase in the curing period [10]. It is found that for the production of sustainable SCC, FA is the most suitable pozzolana [11]. The replacement of OPC by FA in SCC improves the properties of fresh concrete, specially at 50–60% replacement level; the concrete exhibits lower viscosity and better passing ability. Further, it lowers the gain in compressive strength and superplasticizer dose. The improvements were significant up to 180 days [12]. Güneyisi et al. [13] reported that the inclusion of mineral admixtures enhanced significantly the permeability characteristics and the compressive strength in comparison to the NC. The self-compactability of SCC is improved

significantly and the doses of superplasticizer are reduced due to ball-bearing effect of FA [14]. The compressive strength of concrete is found to increase with a curing period with a considerable improvement after 56 days due to formation of additional C–S–H gel at later ages [15]. Siddique et al. [16] recommended FA inclusion up to 35%. The SCC made using FA and other ternary materials shows improvement due to refinement of microstructure and filling capacity of the pozzolanas [17]. Güneysi et al. [18] found that the incorporation of FA increased the slump flow diameter. The SCC made with or without FA fall in different categories of EFNARC specifications. The use of FA and Silica fume in SCC as part replacement of OPC is found to reduce the surface water absorption and sorptivity. The reduction in sorptivity is noticeable beyond 20% replacement level [19]. The SCC made using FA exhibits higher permeable voids and water absorption in comparison to the NC. A lower weight loss and chloride ion diffusion against acidic and chloride environment are reported in SCC made using high volume FA [20]. The properties of SCC made using FA are influenced by the superplasticizer dose. Further, the inclusion of FA improves the stability of SCC [21]. Güneysi et al. [22] proposed to use higher FA content in SCC. This enhances the flowability and durability besides reducing the superplasticizer dose. X-Ray Diffraction (XRD) method is one of the tools to identify the minerals and compounds present in the SCC. This also indicates about the strength and permeability of the specimens. The micro- and macro-level properties of concrete are enhanced on inclusion of pozzolanic materials (MK) [23].

In this study, M25 grade SCC and NC mix were prepared using 43 grade OPC. Slump flow, T_{50} time, V-funnel, L-box, U-box and J-ring experiments were performed on fresh SCC while for NC only slump was measured using Abram's cone apparatus. 100 mm cubes, 100 mm \times 200 mm cylinders and 100 mm \times 100 mm \times 500 mm beams of both NC and SCC were cast to determine the compressive, tensile and flexure strengths, respectively, after 7, 28, 56 and 90 days water curing.

2 Materials and Their Properties

The OPC (Brand- M P Birla) of grade 43 was used for this experimental programme. The cement test results were Normal consistency = 27%; Initial setting time = 45 min; Final setting time = 480 min; Specific gravity = 3.14; Compressive strength = 48.69 MPa (28 days). The test values satisfy the provisions of IS: 8112-1989 [24]. The natural river sand, i.e. fine aggregate of round shape was used (conforms to zone II, IS: 383-1987 [25]). Its bulk density and specific gravity were found to be 1680 kg/m³ and 2.65, respectively. The Coarse aggregates (CA) of size 10 mm and 20 mm having, Specific gravity = 2.66 and 2.7, respectively; Water absorption = 1.0% and 0.9%, respectively, conforming to IS 383-1987, were used [25]. The bulk density of 10 mm and 20 mm aggregates were 1590 kg/m³ and 1560 kg/m³, respectively. The fineness modulus of fine aggregate was 2.7, and its value for the coarse aggregates of sizes 10 mm and 20 mm was 6.7 and 7.2, respectively. Class F- FA (procured from NTPC Unchahar, U.P.) of grey colour having specific gravity

Table 1 Chemical properties of the binders

S. No.	Chemical Composition (%)	OPC	FA
1	Silicon dioxide (SiO ₂)	20.05	55.40
2	Calcium oxide (CaO)	61.95	4.19
3	Aluminium oxide (Al ₂ O ₃)	5.28	19.98
4	Iron oxide (Fe ₂ O ₃)	4.12	6.82
5	Magnesium oxide (MgO)	2.78	2.03
6	Potassium oxide (K ₂ O)	0.95	1.92
7	Sodium oxide (Na ₂ O)	0.24	0.61
8	Loss of ignition	3.12	2.41

Source OPC—M P Birla Cement Company; FA—NTPC, Unchahar, UP, India

2.13, confirming to IS 3812-2000 [26] was used. A polycarboxylic ether based Master Rheobuild 817RL superplasticizer having density approximately 1.08 was used. Tap fresh potable water was used in the mix design and curing of the specimens. The chemical properties of the binders are presented in Table 1.

3 Experimental Methodology

3.1 Mix Proportion

M25 grade NC and SCC were prepared, using a constant w/b ratio of 0.44. 20% of OPC was replaced by FA for mix design of SCC. The mix of NC was prepared as per the provisions contained in IS: 10262-2009 [27]. The SCC mix was designed as per the EFNARC specifications [28]. The final mix proportions of both NC and SCC are presented in Table 2.

Table 2 Mixture proportioning of both NC and SCC

S. no.	Materials	Quantity (kg/m ³)	
		NC	SCC
1.	Cement	345	356
2.	Fly ash	–	89
3.	Coarse aggregate	1234	750
4.	Fine aggregate	686	890
5.	Water	154	198
6.	Water/binder	0.44	0.44
7.	Superplasticizer	–	4.95

3.2 *Water Absorption Test*

Durability of the concrete is affected by water absorption because it is the indicator of permeability of concrete. Thus, it is important to find the absorption of concrete specimens. The water absorption test for all concrete mixes was carried out to determine the change in weight (%), as given by Eq. (1). A is the weight of concrete cube at 7, 28, 56 and 90 days curing and B is the weight after demoulding,

$$\text{Water Absorption (\%)} = \frac{A - B}{B} \times 100 \quad (1)$$

3.3 *Properties of NC and SCC*

For the determination of fresh state properties of NC only slump was measured, using Abram's cone apparatus, while for SCC slump flow, T₅₀ time, V-funnel, L-box, U-box and J-ring experiments were performed. The slump flow test is performed to check the flowability of SCC. The diameter of the SCC circle is measured in two orthogonal directions as per the provisions contained in EFNARC [28]. T₅₀ time is the time taken by concrete to reach 500 mm diameter. To check flowability/filling ability of the SCC, V-Funnel test is carried out. L-box, U-box and J-ring tests are performed to check passing ability of SCC.

The compressive strength of concrete cubes was determined using compression testing machine (capacity 2000 kN) with loading rate of approximately 140 kg/cm²/min, as per the provisions contained in IS: 516-1959 [29]. The cubes were tested after curing the specimen in tap water for 7, 28, 56 and 90 days. Split tensile strength was determined by casting and testing the cylinders of size 100 mm × 200 mm, as per the provisions of IS: 5816-1999 [30]. The Split tensile strength was determined after curing the specimen in tap water for 7, 28, 56 and 90 days. To determine the flexural strength, beams of size 100 mm × 100 mm × 500 mm were cast and tested, using two-point method on loading frame of capacity 500 kN at a loading rate of 180 kg/min, without any shock, as per the provisions contained in IS: 516-1959 [29]. The flexural strength was determined after curing the specimen in tap water for 7, 28, 56 and 90 days.

3.4 *XRD Analysis*

The behaviour of every material is related to its microstructure. Microstructure analysis is the best way to predict/interpret the performance of concrete because it controls the properties of concrete and its behaviour. XRD analysis is one of the methods to find the presence of mineral compounds in the concrete specimen.

Table 3 Test results of fresh SCC

S. no.	Tests	Result	EFNARC limits [28]	
			Min	Max
1.	Slump flow (mm)	690	650	800
2.	T ₅₀ time (s)	4.0	2	5
3.	V-funnel (s)	9.5	6	12
4.	L-box (h_2/h_1)	0.9	0.8	1.0
5.	U-box ($h_2 - h_1$)	28 mm	0	30 mm
6.	J-ring	10 mm	0	10 mm

4 Results and Discussions

4.1 Fresh Concrete Properties

The slump of NC was 100 mm. For SCC, slump flow, T₅₀ time, L-box, U-box and J-ring tests were performed. The results are shown in Table 3.

4.2 Hardened Concrete Properties

4.2.1 Compressive Strength

The compressive strength test results of both NC and SCC are presented in Fig. 1.

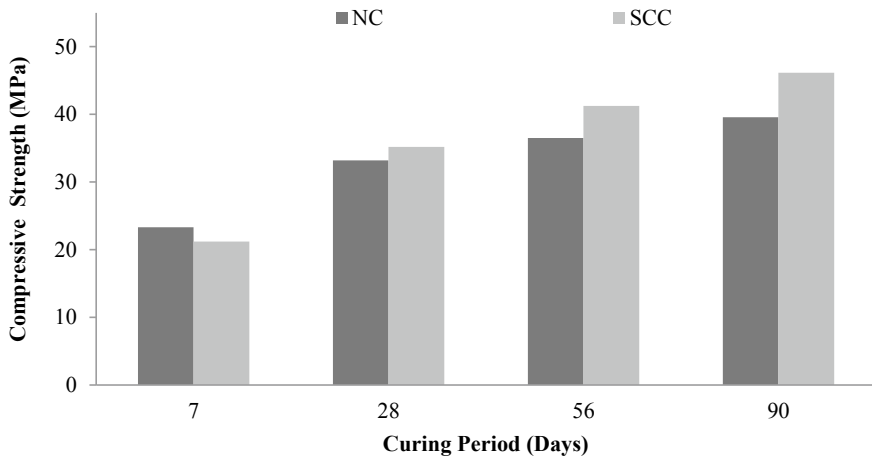


Fig. 1 Compressive strength of the specimen

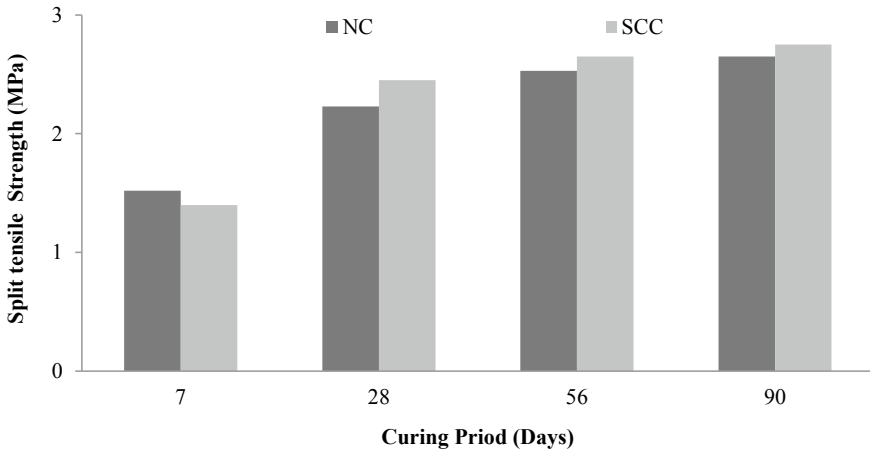


Fig. 2 Split tensile strength of the specimen

It is found that at early ages, the compressive strength of SCC is lower in comparison to NC but at later ages it is higher for SCC. At 7 days, the compressive strength of SCC is about 9.0% lower than the NC. However, after 28, 56 and 90 days, the compressive strength of SCC is found to be higher by 6.0, 12.8 and 16.5%, respectively. Several other researchers have also reported the same trend [5, 6]. The difference in compressive strength of both the mixes is found to increase with age. The strength gain may be attributed to the formation of additional C–S–H gel in FA mixed SCC and refined pore structure.

4.2.2 Split Tensile Strength

The results of the split tensile strength tests conducted on both NC and SCC are presented in Fig. 2.

At 7 days, the split tensile strength of SCC is found to be lower than the NC; however, beyond that it is higher for SCC. At 7 days, the split tensile strength of SCC is about 9.0% lower than the NC. However, after 28, 56 and 90 days, the tensile strength of SCC is found to be higher by 9.8, 4.7 and 3.7%, respectively. The same trend was observed by Klug et al. [4].

4.2.3 Flexural Strength

The results of the flexural strength tests conducted on both NC and SCC are presented in Fig. 3.

The flexural strength of SCC at early ages is lower than the NC; however, beyond that it is higher for SCC. At 7 days, the flexural strength of SCC is 5.4% lower than

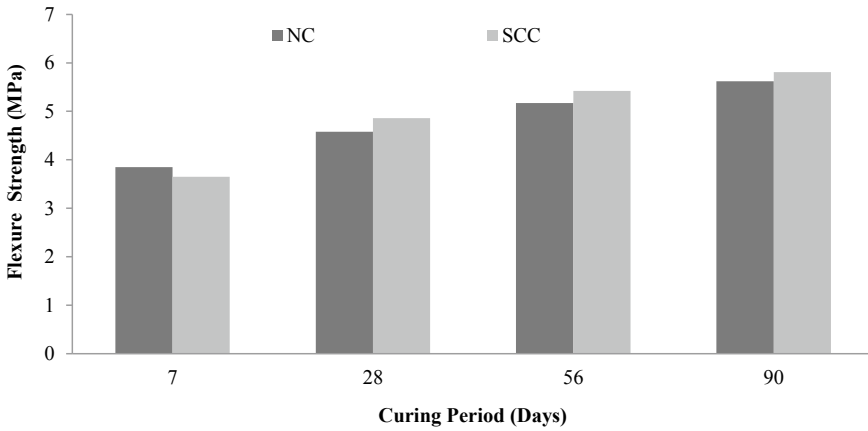


Fig. 3 Flexure strength of the specimen

the NC. However, after 28, 56 and 90 days, it is found to be higher in case of SCC by 5.8, 4.8 and 3.3%, respectively.

4.3 Water Absorption

The typical values of water absorption for both NC and SCC are shown in Fig. 4.

It is evident from Fig. 4 that water absorption of SCC is lower than the NC. However, with age it is found to decrease for both the concrete types. FA acts both as a filler material and material for generation of more gel which help in reduction

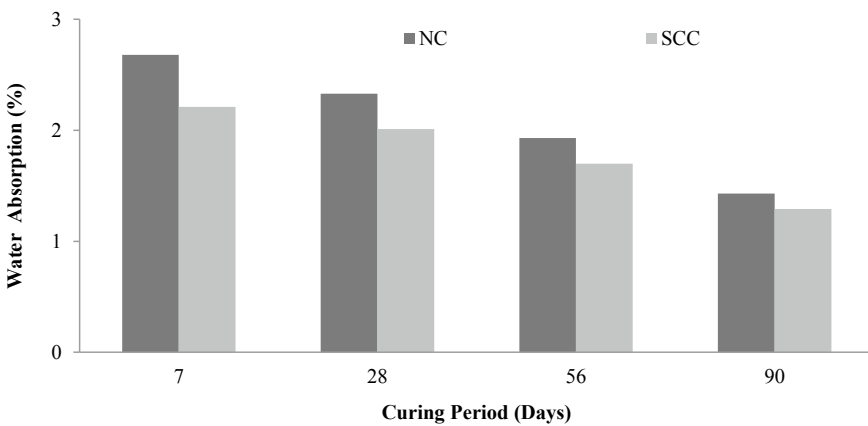


Fig. 4 Water absorption of the specimen

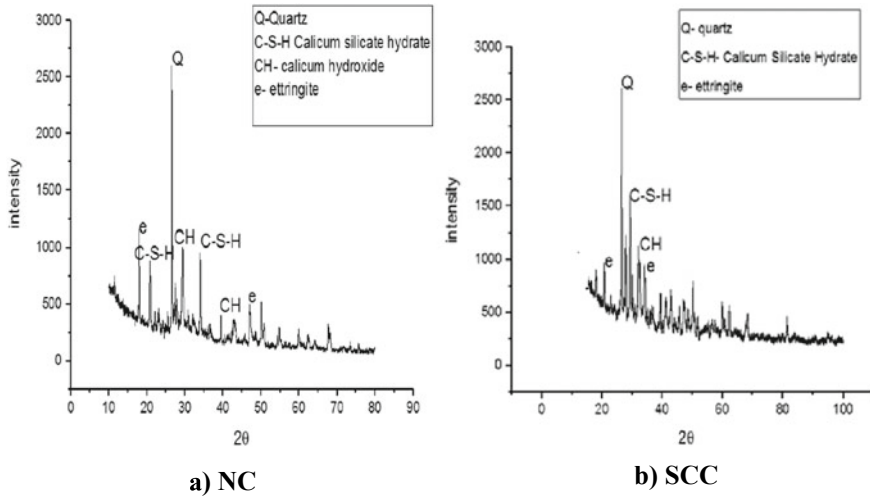


Fig. 5 XRD traces after 28 days curing **a** NC and **b** SCC

of water absorption. The water absorption of SCC is found to be lower by 17.5, 13.7, 11.9 and 9.7% than the corresponding values for NC samples at 7, 28, 56 and 90 days, respectively. The same trend was also observed by others [10].

4.4 XRD Analysis

XRD analysis of both the samples- NC and SCC- were carried out after 28 days curing. The typical XRD traces are presented in Fig. 5a, b. Some major crystalline phases identified include, Quartz (Q), Calcium Silicate Hydrate (C–S–H), Portlandite (CH) and Ettringite (e).

From the figures, it is clear that a higher peak of C–S–H gel is present in SCC than NC. This improves the durability and strength of SCC. More Ettringite is formed in NC in comparison to the SCC.

5 Conclusion

The following are concluded from the experimental study:

- The SCC is more workable than NC because of its flowable characteristics.
- At 7 days, all the strength parameters, viz. compressive, tensile and flexural are lower in case of SCC in comparison to the NC; however, beyond this age these are higher in case of SCC.

- At 7 days, the compressive, tensile and flexural strengths of SCC are lower by about 9.0, 9.0 and 6.0%, respectively, in comparison to the NC. However, after 28 days, the respective strengths are higher in case of SCC by 6.0, 9.8 and 5.4%, respectively. The respective changes at 56 days are 12.7, 4.8 and 4.7% while at 90 days these values are 16.5, 3.7 and 3.3%.
- The water absorption of SCC samples is lower in comparison to the NC sample. The respective values are 17.5, 13.7, 11.9 and 9.7% at 7, 28, 56 and 90 days.
- At the same w/b ratio, the SCC is superior.
- The microstructure is improved in case of SCC in comparison to the NC, as indicated by higher peaks of C–S–H gel in SCC. This along with the filler effect of FA improves the strength and durability of SCC.
- Less Ettringite is formed in SCC in comparison to the NC. This implies that the durability of SCC is superior to the NC.

References

1. Okamura H, Maekawa K, Ozawa K (1993) High-performance concrete. Gihodo Publishing
2. Okamura H, Ouchi M (2003) Self-compacting concrete. *J Adv Concr Technol* 1(1):5–15 (Japan)
3. Kurita M, Nomura T (1998) Highly-flowable steel fiber-reinforced concrete containing fly ash. Special Publication 178:159–176
4. Klug Y, Holschemacher K, Wallevik O, Nielsson (2003) Comparison of the hardened properties of self-compacting and normal vibrated concrete. Paper presented at 3rd RILEM symposium on self compacting concrete, Reykjavik
5. Bennek W (2007) SCC applied in the precast industry (ICCX) 24–24, 26, 27
6. Van Keulen DC (2000) Onderzoek Naar Eigenschappen Van Zelfverdichtend Beton. Rapport TUE/BCO/00.07, TU Delft, Apr 2000
7. Persson B (2001) A comparison between mechanical properties of self-compacting concrete and the corresponding properties of normal concrete. *Cem Concr Res* 31:193–198
8. Dhiyaneshwaran S, Ramanathan P, Baskar I, Venkatasubramani R (2013) Study on durability characteristics of self-compacting concrete with fly ash. *Jordan J Civ Eng* 7(3):342–352
9. Khatib JM (2008) Performance of self-compacting concrete containing fly ash. *Constr Build Mater* 22:1963–1971
10. Gaywala NR, Raijiwala DB (2011) Self compacting concrete: a concrete of next decade. *J Eng Res Stud* 2(4)
11. Mohammed MK, Dawson AR, Thom NH (2013) Production, microstructure and hydration of sustainable self-compacting concrete with different types of filler. *Constr Build Mater* 1(49):84–92
12. De Matos PR, Foiato M, Prudêncio LR Jr (2019) Ecological, fresh state and long-term mechanical properties of high-volume fly ash high-performance self-compacting concrete. *Constr Build Mater* 203:282–293
13. Güneyisi E, Gesoğlu M, Booya E, Mermerdaş K (2015) Strength and permeability properties of self-compacting concrete with cold bonded fly ash lightweight aggregate. *Constr Build Mater* 74:17–24
14. Puthipad N, Ouchi M, Rath S, Attachaiyawuth A (2016) Enhancement in self-compactability and stability in volume of entrained air in self-compacting concrete with high volume fly ash. *Constr Build Mater* 128:349–360
15. Mahalingam B, Nagamani K, Kannan LS, Mohammed Haneefa K, Bahurudeen A (2016) Assessment of hardened characteristics of raw fly ash blended self-compacting concrete. *Perspect Sci* 8:709–711

16. Siddique R (2011) Properties of self-compacting concrete containing class F fly ash. *Mater Des* 32(3):1501–1507
17. Da Silva PR, De Brito J (2015) Experimental study of the porosity and microstructure of self-compacting concrete (SCC) with binary and ternary mixes of fly ash and limestone filler. *Constr Build Mater* 86:101–112
18. Güneysi E, Gesoglu M, Al-Goody A, İpek S (2015) Fresh and rheological behavior of nano-silica and fly ash blended self-compacting concrete. *Constr Build Mater* 95:29–44
19. Leung HY, Kim J, Nadeem A, Jaganathan J, Anwar MP (2016) Sorptivity of self-compacting concrete containing fly ash and silica fume. *Constr Build Mater* 113:369–375
20. Dinakar P, Babu KG, Santhanam M (2008) Durability properties of high volume fly ash self compacting concretes. *Cem Concr Compos* 30(10):880–886
21. Ponikiewski T, Gołaszewski J (2014) The effect of high-calcium fly ash on selected properties of self-compacting concrete. *Arch Civ Mech Eng* 14(3):455–465
22. Begum SJ, Anjaneyulu PJD, Ratnam MKMV (2018) A study on effect of steel fiber in fly ash based self compacting concrete. *Int J* 5:95–99
23. Kavitha OR, Shanthi VM, Arulraj GP, Sivakumar P (2015) Fresh, micro-and macrolevel studies of metakaolin blended self-compacting concrete. *Appl Clay Sci* 114:370–374
24. IS: 8112-1989. Specification for 43 grade ordinary Portland cement. Bureau of Indian standards, New Delhi, India
25. IS: 383-1987. Specification for coarse and fine aggregate from natural sources for concrete. Bureau of Indian Standards, New Delhi, India
26. IS: 3812-2000. Specification for pulverized fuel ash, part 1: for use as pozzolana in cement. Cement mortar and concrete
27. IS: 10262-2009. Concrete mix proportioning—guidelines. Bureau of Indian Standards, New Delhi, India
28. EFNARC-2002. Guidelines for self-compacting concrete. Association House, London, UK, pp 32–34
29. IS: 516-1959. Methods of tests for strength of concrete
30. IS: 5816-1999. Splitting tensile strength of concrete-method of test

Evaluating Toughness as a Parameter to Determine the Fatigue Life of Wollastonite Microfiber Reinforced High Flow Pavement Quality Concrete



Shashi Kant Sharma and K. P. Marisarla Chaitanya

Abstract Rigid pavements are designed on the basis of flexural strength, since the concrete is brittle and supposed to show little strains post-peak stress. The stress ratio, which is the ratio of flexural stresses to flexural strength generally determines the fatigue life of the pavement. Under service load, pavements face a continuous reduction in flexural strength on account of propagating cracks, which causes fatigue damage. But the evolution of cracks in quasi-ductile concrete is different, which is somehow anticipated to depend upon the toughness of concrete. Toughness is the area under load deflection curve and indicates the energy possessed by concrete. Under repetitive loading, there is continuous reduction in strength of concrete but the total energy possessed by concrete should not vary. This paper, thus tries to find the relationship of fatigue life with stress ratio, and fatigue life with toughness and stress ratio together to check for the validity of stress ratio-fatigue life equation in case of quasi-ductile concrete. Equations have been generated for normal pavement quality concrete (PQC), flyash admixed and wollastonite microfiber reinforced PQC. Results proved that even though the toughness affects the formation of flexural stresses in any kind of concrete, stress ratio is singularly effective for finding out the fatigue life, since it reflects both toughness (through flexural stresses) and flexural strength. Quantitatively, WMF-reinforced concrete has very high fatigue life than normal PQC and flyash admixed PQC, respectively.

Keywords Rigid pavements · Fatigue life · Toughness · Flyash · Wollastonite microfiber

1 Introduction

Cement composites are mainly made up of three components: cement paste, cement mortar and cement concrete. All these composites have same deficiencies, i.e. weak tensile strength (brittleness) and limited deformation capacity in the presence of

S. K. Sharma (✉) · K. P. Marisarla Chaitanya
Department of Civil Engineering, NIT Jalandhar, Jalandhar 144011, India
e-mail: shashi.pec@gmail.com; sharmask@nitj.ac.in

cracking (lesser toughening strength). Once cracks are originated, these composites fail in a brittle manner with little warning due to limited deformation capacity. The interface between aggregates and cement paste, called as interfacial transition zone (ITZ) acts as a major weak zone for distribution of stresses. If weak, strains grow at a larger rate in this zone, which leads to crack formation and finally failure of concrete mix. When load is first applied to the cement concrete, areas of stress concentration develop at the tips of the initial flaws. With additional loading, microcracks form (or initially present) and grow in the frontal process zones ahead of the flaw tips. It is assumed that the initial flaw will extend into the microcracked region when the microcracking has reached a saturated level [18]. Afterwards, they coalesce and turn into macro-cracks. A reinforcing material is therefore required which may provide strength to the concrete before cracking, and cause delay in the propagation of cracks once they are formed. The need for special reinforcing is fulfilled by the introduction of fibers in concrete. With proper incorporation of fibers, the failure mode of cement composites can change from brittle to quasi-ductile [13–15]. For a thin sheet fiber reinforced cement concrete having initial flaw of approximately 60 μm , fibers with diameter $<30 \mu\text{m}$ will be deemed microfibers. Generally, microfibers are fine fibers with lengths less than 10 mm and diameters $<40 \mu\text{m}$ [1, 20]. Examples of microfibers are steel fibers, carbon fibers, PVA fibers, polypropylene fibers and wollastonite microfiber. Steel fibers have high yield strength (nearly 1100 MPa) and possess lesser bond strength with the concrete [2]. Wollastonite has found tremendous applicability in the improvement of repair works because of its better bonding with the concrete. Wollastonite is a naturally occurring, acicular, inert, white mineral (calcium meta silicate [B-CaO-SiO_2]) of high modulus of elasticity, which is less costly than steel and carbon microfibers [3]. Prices for wollastonite range from \$0.2/kg to \$0.37/kg depending on its size, which is substantially cheaper than that of steel (\$6.6/kg), carbon (\$11/kg) or glass (\$2/kg) fibers [3]. It is formed due to the interaction of limestone with silica in hot magmas. It is formed in the nature by the reaction of calcium carbonate CaCO_3 with silica SiO_2 in hot magmas. Wollastonite is mined commercially for use in refractory ceramics and as a filler in paints. The processed granular material is of high purity, inexpensive, and readily available.

Available in abundance along the Udaipur belt of Rajasthan state of the Indian union as a low-cost material, it may be ground to fine powder. Its composition of nearly equal proportions of lime and silica having fine particle size are favourable indicators for its admixing in concrete by partial replacement of cement. In itself, wollastonite does not possess binding properties like cement, but in the presence of microsilica, it improves the properties of admixed concrete by fine packing of inert material [16, 17].

Soliman and Nehdi [19] investigated the effect of incorporating wollastonite microfibers in ultra-high performance concrete (UHPC) on its early-age properties. Wollastonite microfibers were added at 0, 4, 8 and 12% as partial volume replacement for cement. Increasing the wollastonite microfibers content resulted in compressive strength comparable to or higher than that of the control mixture without microfibers. Wollastonite microfibers reduced shrinkage strains and increased cracking resistance

compared to that of the control mixture. Hence, these fibers could be used in pavements to enhance the factors which increase the fatigue life. But in the absence of proper quantitative results, it becomes subtle to testify the role of fibers in enhancing the fatigue life of pavements. Indian Roads Congress (IRC) 58 [7] codal provisions suggest the stress ratio of concrete as a parameter to determine the fatigue life of a normal PQC considering the fact that concrete is brittle. This makes flexural strength as the only property to be tested. But in the light of fibers' use in concrete, present study is envisaged to check the effect of both toughness and flexural strength in concrete. Toughness is the area under the load deflection curve and thus represents the energy possessed by the concrete which could be checked against the total energy consumed by the concrete during loading cycles. The use of high flow concrete could expedite the construction process and even find use in retrofitting concrete pavements. Hence high flow pavement quality concrete is tested in this study. Literature studies are mostly concentrated on finding out fatigue life of pavement with or without admixtures, but toughness has never been compared with stress ratio.

2 Materials and Mixes

Ordinary Portland cement (OPC) 43 grade conforming to Indian standard code IS 8112 [11] was used. Graded river sand conforming to Zone-II having fineness modulus of 3.23 and specific gravity of 2.58 was used as fine aggregate. Crushed graded coarse aggregates of 20 and 10 mm conforming to IS 383 [8] were used in the proportion of 60:40. The specific gravity of 20 mm and 10 mm aggregates were 2.62 and 2.58, respectively.

Fine amorphous wollastonite powder supplied by Rajwara Stonex Limited was used. It had a specific surface and specific gravity values of 827 m²/kg and 2.9, respectively. Densified 920D grade Microsilica supplied by India Private Limited was used. It had a specific surface and specific gravity value of 18000 m²/kg and 2.05. High water reducing poly carboxylate ether (PCE) based superplasticizer was used to introduce self-compacting workability conditions to the concrete.

3 Testing Program

3.1 Materials' Testing

Powder materials were tested for physical properties such as surface area, particle size distribution, specific gravity and chemical composition. The mixes were classified into binary and ternary mixes. Binary mixes were made by substituting cement with

Wollastonite/flyash in intervals of 10% up to maximum 30%. For ternary combinations, the mixes were prepared such that Wollastonite/flyash had same replacement levels as later and microsilica was added maximally up to 10% in addition for each mix, at intervals of 2.5%, respectively, thereby making 12 mixes. Pictorial (SEM image analysis) and quantitative analysis (XRD analysis shown in Table 1)

Table 1 Mix composition and X-ray diffraction data of pastes

Mix	Percentage of constituting material	% Ettringite	% CH	% CSH	% C ₃ A
C	100C	2.3	9.8	37.0	5.5
CW1	90C + 10W	2.5	10.0	39.9	5.8
CW2	80C + 20W	5.4	5.4	41.9	5.1
CW3	70C + 30W	10.2	4.2	39.8	6.3
CWS1	87.5C + 10W + 2.5S	6.2	2.0	39.3	5.7
CWS2	85C + 10W + 5S	9.0	4.1	40.0	5.9
CWS3	82.5C + 10W + 7.5S	2.0	2.1	40.5	5.9
CWS4	80C + 10W + 10S	7.1	5.8	43.2	5.7
CWS5	77.5C + 20W + 2.5S	2.9	5.6	46.2	6.3
CWS6	75C + 20W + 5S	4.9	4.4	47.4	6.4
CWS7	72.5C + 20W + 7.5S	5.8	2.9	50.2	6.0
CWS8	70C + 20W + 10S	4.4	2.5	55.4	6.2
CWS9	67.5C + 30W + 2.5S	2.8	8.6	40.7	5.4
CWS10	65C + 30W + 5S	7.5	5.6	44.1	4.7
CWS11	62.5C + 30W + 7.5S	5.3	5.8	45.9	6.0
CWS12	60C + 30W + 10S	4.9	6.1	46.3	5.5
CF1	90C + 10F	2.8	8.9	38.7	5.8
CF2	80C + 20F	2.7	6.4	40.2	6.5
CF3	70C + 30F	3.2	2.8	42.4	6.7
CFS1	87.5C + 10F + 2.5S	2.5	10	39.4	5.8
CFS2	85C + 10F + 5S	2.9	10.6	40.1	5.8
CFS3	82.5C + 10F + 7.5S	3.6	7.7	41.3	6.2
CFS4	80C + 10F + 10S	4.1	4.6	45.9	6.2
CFS5	77.5C + 20F + 2.5S	2.8	7.2	41.4	5.9
CFS6	75C + 20F + 5S	2.9	8.6	42.2	6.0
CFS7	70C + 20F + 7.5S	3.4	6.2	46.6	6.1
CFS8	72.5C + 20F + 10S	3.0	5.6	46.9	6.1
CFS9	67.5C + 30F + 2.5S	2.4	6.3	44	5.8
CFS10	65C + 30F + 5S	3.4	4.1	45.1	6.6
CFS11	60C + 30F + 7.5S	3.1	4.5	47.4	7.1
CFS12	62.5C + 30F + 10S	2.8	6.0	50.4	6.9

of hydrated compounds obtained from paste mixes were performed after 7 days and 14 days of hydration, respectively.

3.2 Wet Concrete Testing

The testing program of wet concrete aims at sequentially finding out the workability related ambiguities with the use of admixtures and wollastonite microfiber in self-compacting concrete. For this, one control concrete mix of modulus of rupture 4.5 kg/cm^2 was designed as per IRC 44 [6] (shown in Table 2) and 15 cement substituted trial mixes were sought from it. Flow trials were conducted to achieve SCC by changing the binder content of the control concrete mix (by admixing); then correspondingly changing the fine aggregate to coarse aggregate ratio along with superplasticizer content at a constant water to cementitious material ratio of 0.35. Superplasticizer was added to fulfil the water demand for creating self-compacting conditions. Table 3 shows the trial methodology to obtain SCC.

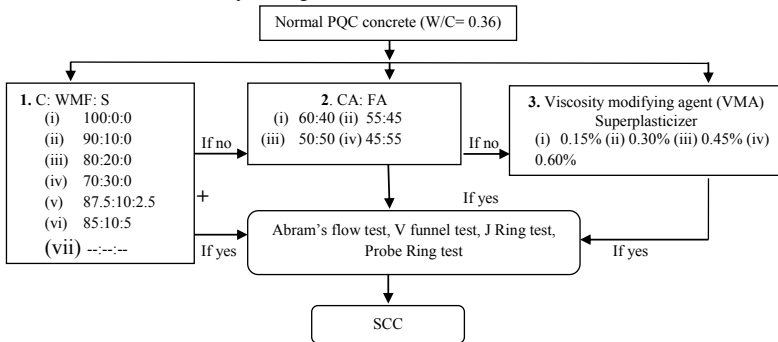
Abrams flow, V funnel, J ring and probe ring tests were conducted on the SCC trial mixes (Fig. 1) as per the guidelines of EFNARC [4, 5], whereas control concrete failed in these tests. Concrete volume of 6 litres was used for Abrams flow test and J

Table 2 Mix design of normal PQC

Mix design for normal M-40 concrete used to derive SCC for retrofitting as per IRC 44					
Cement	Sand	Coarse aggregates		Water	Nominal MSA = 16 mm
450	711	1057		165	Superplasticizer 0.3% ~ 1.23 lt/cu m
1	1.58	2.35		0.36	
		20 mm	10 mm		CA:FA = 60:40
		740	317		C.A:- 20 mm:10 mm = 70:30

Assuming that 20% cement reduction takes place on addition of superplasticizer

Table 3 Schematic method of yielding SCC from normal PQC



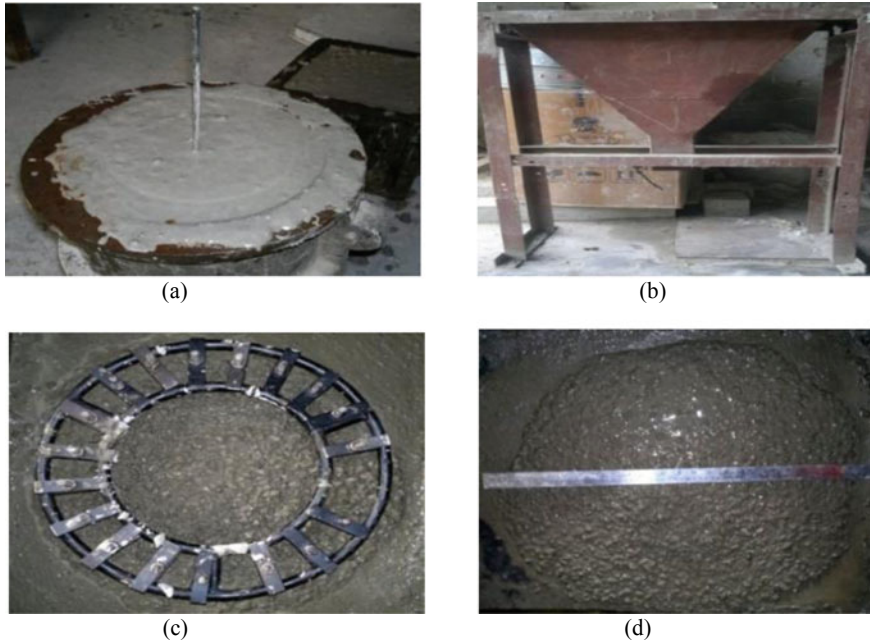


Fig. 1 Workability tests of concrete mixes. **a** Probe ring. **b** V funnel. **c** J Ring and **d** Abram's flow test

ring test, whereas 12 litres of concrete volume was used for V funnel test. Probe ring test was conducted by pouring concrete in cylindrical moulds ($150\phi \times 300$ mm).

3.3 Dry Concrete Testing

Flexural strength test was conducted on beams of size $500 \times 100 \times 100$ mm³ as per IS 516 [9] guidelines respectively. Later on plate load test was conducted on five pavement prototypes constructed with these mixes, i.e. CF3, CW3, CFS6 and CWS6. The prototypes were constructed with about 6 ton of concrete (DLC 100 mm + PQC 300 mm) each, and contained a contraction joint, with dowel bars of 38 mm for load transference. Figure 2 shows the loading points as well as the locations where the dial gauges were set up to find the deflections in the pavement. Location 1, 3, 2 and 4 correspond to corner, centre, left and right edge locations at which loads would be applied. Dial gauges at location 1, 2, 3 and 4 were installed to observe the deflections on the loading side, whereas dial gauges 5, 6 and 7 were installed to find out the deflections on the adjacent side of loading. The test was performed under deflection controlled condition and performed as per IS: 1888 [10]. Also due to the difference in stiffness of loading points different loading profile was obtained for each loading

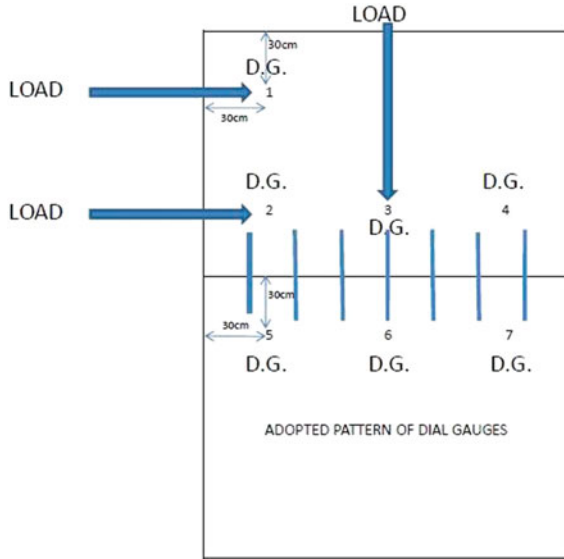


Fig. 2 Schematic layout of plate load test conducted in the laboratory

location. Plate load test performed on normal concrete and CWS6 has been shown in Fig. 3a, b.

The model as well as prototype consisted of two panels laid in the direction of traffic flow, having a contraction joint in between. The panel size was $1800 \times 1800 \times 300 \text{ mm}^3$, dowel bars of $\phi 35$ and 500 mm length were embedded as wire elements in the model, and a dry lean concrete (DLC) layer of 100 mm thickness was sandwiched between PQC slab and properly compacted subgrade layer.

Figure 4a shows one panel of PQC with the dowel bars embedded within, and dry lean concrete layer introduced beneath the PQC slab. The loading pattern at the edge of the slab is being shown in Fig. 4b which is in the form of a circular ring having diameter of 45 cm spaced at a distance of 30 cm from both the edges of the panel.

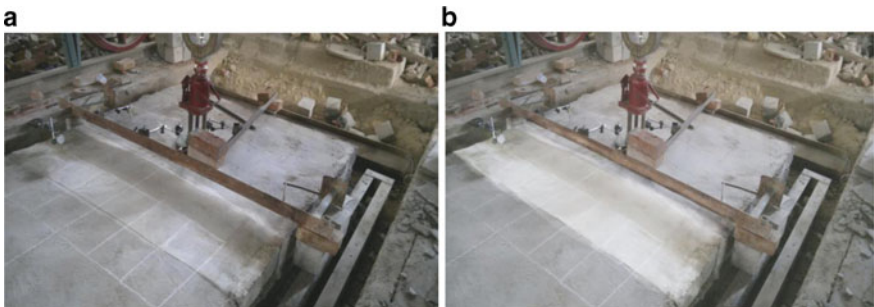


Fig. 3 Plate load test on a non-retrofitted and b FRSCC retrofitted PQC

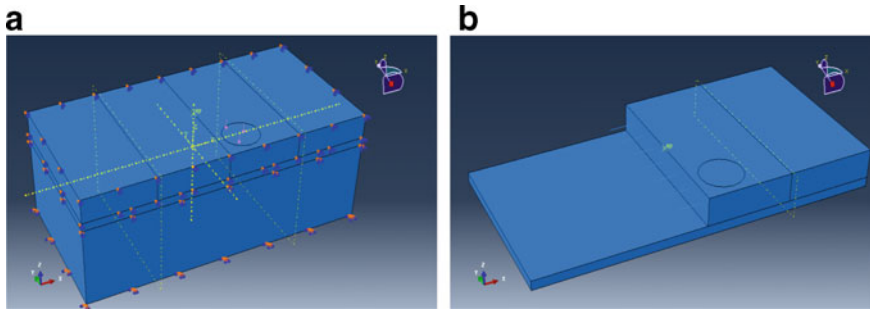


Fig. 4 **a** Full model of PQC. **b** Model showing the DLC, one panel of PQC and dowel bars

The loading was applied by means of circular bearing plate made of steel having 25.4 mm thickness. The FEM model was designed having same geometric scale on ABAQUS and was subjected to similar loading profile. Boundary conditions to the model were assigned on the basis of the actual working of rigid pavement. The top and bottom face of the slab were fixed against the movement in two horizontal directions. The bottom face of PQC was also restricted in the same manner to allow the bending of the slab. This restriction will produce tensile stresses at critical zones and compressive stresses in their vicinity, thereby producing cracks in the pavement. The top and bottom face of the DLC was free to move in vertical direction, and along the transverse direction but restricted in the vehicular direction. The top face of the subgrade was free to move in all directions but its bottom face was restricted in the vertical direction to simulate infinite subgrade behaviour. The division lines in the panel show the area earmarked for different mesh spacing. The half area where load was applied was provided with lesser mesh spacing (50 mm inter nodal distance) for ease in converging to the solution, whereas the half panel area away from load was given larger mesh spacing (100 mm).

Validation of the model was done for all five types of concrete on the basis of Chi Square test which analysed the goodness of fit between deflections of model and prototype at 5% significance level. It was assumed that the model will get validated for other prototypes too taking into consideration similar properties of constituents in the five prototype mixes. This also saved huge amount of time and cost to be incurred in constructing all the prototypes. After validation, the model was run for 10000 loading cycles of 20 KN at all the loading locations so as to create a conditioned pavement under use. The model was then run with cyclic loading with a frequency of 0.01 Hz (864 axles load per day) with load-time variation using Fourier function at the edges of the pavement near the transverse joint. Each concrete mix was checked for 1.5% areal strains (using nodal displacement in both directions) at the critical node present on the bottom face of the slab. This value of strain has been chosen on the basis that quasi-ductile concrete shows up to 0.75% ultimate axial strains under compressive loading and areal strains are the summation of axial strain in the longitudinal and transverse direction, respectively. It was assumed that cracks will fully propagate to the upper-most region of slab when the strains have achieved this

level in the lower layer. Load cycles of 20 KN and 22.5 KN were applied in such a way that the strains were checked each time after 50, 100, 200, 400, 800, 1600, 3200, 6400, 12800, 25600, 51200, 102400, 204800, 509600, 1019200, 3057600, 611520, 1223040 and 2446080 cycles, until 1.5% strains were observed. Strains beyond were calculated by extrapolating the curve.

4 Observations and Results

4.1 Powdery Material

4.1.1 Physical Composition of Powdery Materials

Particle size analysis has been shown in Fig. 5. Microsilica was finest among all considered powdery materials followed by WMF, flyash and cement, respectively. The peak of WMF lies exactly in between the peaks of microsilica and OPC. This interpretation clearly infers that WMF used was median size to both microsilica and OPC and hence, an excellent interlocking within these particles is anticipated physically. It is also clearly depicted that OPC used for the study exhibits particle sizes comparable to flyash as revealed by the presence of secondary peak in Fig. 5. Peak patterns analysis suggests that flyash and OPC have nearly same size range but prolonged post-peak profile of flyash indicates that there are numerous fractions of flyash which are even larger in size than OPC particles.

The degree of fineness of microsilica, WMF and flyash with respect to OPC are 60, 2.8 and 1.3, respectively. Results strongly hinted that microsilica would be prominently proactive in comparison to the rest as it has inherent ability to contribute strength development through its least surface area.

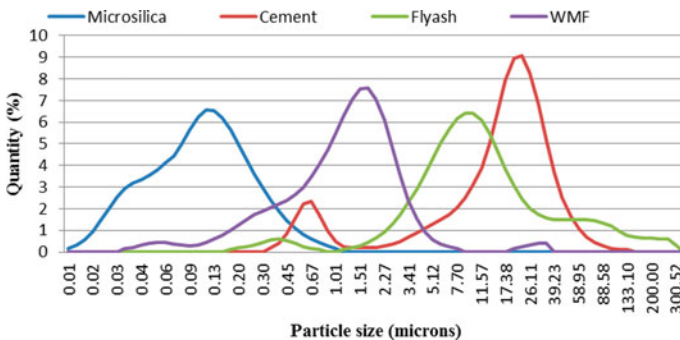


Fig. 5 Particle size variation for various materials

Table 4 Chemical properties of cementitious materials including OPC

Compound	Cement	Flyash	WMF	Silica fume
SiO ₂	20.2	35	48	92.9
Al ₂ O ₃	5.2	26	1.4	0.9
Fe ₂ O ₃	3	8.7	0.6	0.72
MgO	1.51	5	0.2	0.57
SO ₃	2.2	3	–	0.16
Na ₂ O	0.08	1.5	–	0.32
Chloride	0.014	0.005	–	0.037
Loss on ignition	4.3	5	4	2.6
CaO	62.9	15.3	45.9	1.4
K ₂ O	0.6	0.5	–	0.4

4.1.2 Chemical Composition of Powdery Materials

Table 4 shows the quantitative results of the amount of oxides present in cement and other admixtures found through X-Ray fluorescence spectrometer test conducted in accordance with IS: 12803 [12]. Following are the few observations drawn from the study of chemical compositions:

1. Flyash used in the present study contains appreciable amount of silica and highest amount of alumina when compared to the rest of the materials.
2. WMF shares equal amounts of lime and silica, and traces of alumina. Their presence indicates that WMF has tendency for self-cementation and moderate rate of reaction. But by virtue of its crystalline nature, WMF is more inert and serves as excellent pore filler.
3. Microsilica mainly consists of silica and rest other oxides are in meagre amount. In its amorphous state, fine microsilica possesses higher surface areas because of which it has greater infilling capacity and reactivity too. Thus, it is apt for reduction of CH and ettringite considerably.

4.2 Concrete

4.2.1 Workability of Concrete Mixes

Table 5 shows the achieved mix designs for different concrete mixes having different paste compositions. Some mixes were qualified for SCC whereas rest were just able to achieve high workability and lacked in one or other property of an SCC. The table shows the minimum CA:FA ratio required for achieving the workability parameters, which are shown besides them along with the superplasticizer content needed in purview. Since the paper aims to focus on fatigue life and its parameters so workability results have not been explained.

Table 5 Observations from the workability tests conducted on trial concrete mixes

Mix	CA:FA	Abram’s flow (600–750) mm	V Funnel time (6–12 s)	V Funnel after 5 min (9–15 s)	J Ring difference (0–10 mm)	Probe ring penetration (0–7 mm)	Super plasticizer C.M.) % by weight of cement
C	60:40	360	17	24	24	2	0.30
CW1	55:45	560	10	12	21	3	0.45
CW2	50:50	580	8	10	19	5	0.45
CW3	50:50	540	12	12	21	4	0.6
CWS1	55:45	580	9	11	15	3	0.45
CWS2	50:50	630	8	10	9	5	0.45
CWS3	50:50	620	9	10	10	4	0.45
CWS4	50:50	605	10	11	13	3	0.45
CWS5	50:50	646	7	11	11	5	0.45
CWS6	50:50	660	7	9	5	7	0.6
CWS7	50:50	620	8	11	8	5	0.6
CWS8	50:50	590	9	14	10	4	0.6
CWS9	50:50	570	10	12	14	5	0.6
CWS10	45:55	630	7	9	12	3	0.6
CWS11	45:55	575	9	13	17	2	0.45
CWS12	45:55	530	13	18	22	2	0.45

4.2.2 Flexural Strength

Flexural strength depends equally on mortar strength and mortar-aggregate interface strength. On admixing, WMF improves the interfacial transition zone (ITZ) considerably. The flexural strength of concrete mixes after 28 and 90 days of curing has been shown in Figs. 6 and 7, respectively. The rate of improvement is more profound

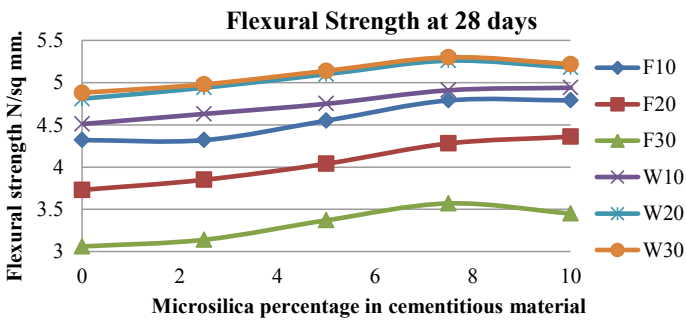


Fig. 6 Flexural tensile strength of concrete mixes after 28 days curing

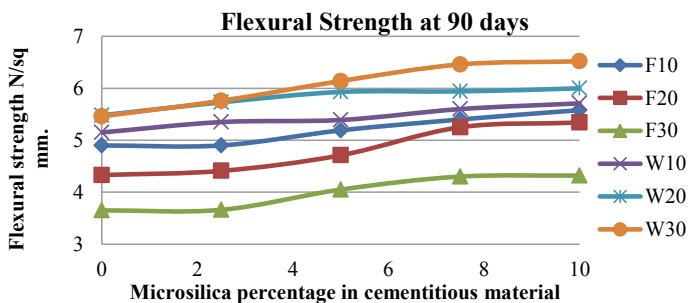


Fig. 7 Flexural tensile strength of concrete mixes after 90 days curing

for higher part replacement of cement by WMF, i.e. up to 30% (4.88 MPa against 4.87 MPa of reference concrete at 28 days). Beyond this replacement level, no significant improvement was observed as more WMF did not find more surface area of concrete matrix to reinforce. Surprisingly, admixing of flyash reduced the flexural strength of concrete mixes even after long durations. This may be due to the fact that bigger sized flyash particles could not induce effective pore size refinement in the concrete. Even flyash has least tendency to reduce ettringite in the interfacial transition zone. Though, it was effective in reducing the calcium hydroxide content in this zone but it could not fill up the deficiency in strength caused by replacement of cement with flyash.

Microsilica increases flexural strength in both flyash and WMF admixed concrete mixes (Figs. 6 and 7) at a much larger rate per unit mass than the other two admixtures. Prolonged curing shows significant improvement in flexural strength of concrete but the concrete mix containing 30% flyash and 10% microsilica did not show any improvement in the flexural strength with respect to corresponding mix at 7.5% microsilica (Fig. 7). This is attributed to the self-desiccation caused by the presence of excessive amount of microsilica than that required. Similar trend for strength gain with curing duration due to microsilica has been observed in WMF ternary mixes but it was found that percentage increase in flexural strength with microsilica addition is lesser in this case. The percentage improvement in flexural strength with time (28–90 days) ranged from 10 to 20% generally in all binary mixes in comparison to ternary mixes (10–25%). Ternary mixes of Wollastonite microfiber showed generally higher modulus of rupture value than normal concrete mix at all durations, except CWS1 and CWS2. This indicates that 20–30% WMF with any content range of microsilica will definitely improve flexural strength of concrete. This proves that grain size refinement of WMF in the mortar as well as the mortar-aggregate interface plays a major role than just pore size refinement of flyash in holding the concrete matrix together under bending stresses. Here the complementary effect provided by microsilica further improves the interface and mortar. As discussed in modulus of elasticity, even though stiffness at interface was higher for flyash-microsilica mixes, which improved stress distribution, but the holding together of aggregate and mortar at interface under bending tensile stresses is better for WMF-microsilica mixes.

Overall, the flexural strength decreases by 22.5% and 3.2% in binary flyash and WMF mixes, respectively, with respect to reference concrete mix after 90 days curing. Whereas it decreases by 14.1% in ternary flyash-microsilica mixes. An increase of 6.1% was observed in ternary WMF-microsilica mixes.

4.2.3 Compressive Toughness

Figure 8 shows that for binary mixes, as Flyash content increases the compressive toughness decreases (toughness for CF10 > CF20 > CF30) whereas mix CW20 has highest toughness followed by CW30 and CW10. Also, if microsilica is added to flyash mixes then there is approximately linear increase in toughness. Same results are not seen in WMF-microsilica ternary mixes. Ternary mix containing 10% WMF with microsilica showed linear increase in toughness whereas that containing 30% WMF showed a linear decrease beyond 2.5% microsilica addition. Only mix CWS5-CWS8 containing 20% WMF showed nonlinear relationship with increasing amounts of microsilica such that toughness was highest for 7.5% microsilica and beyond that reduced to large extent. The decrease in toughness due to flyash addition is obvious as flyash reduces the modulus of elasticity and even increases the brittleness of concrete post cracking. WMF addition in concrete though decreased the modulus of elasticity to some extent but the binding of concrete by WMF due to its inherent nature, as well as its fiber reinforcement provided post crack ductility to concrete, thereby bringing the toughness value to 47.15 MPa in comparison to reference concrete’s 40.91 MPa. With addition of microsilica, the ductility provided by WMF at interfaces got highly reduced as microsilica got adsorbed over the surface of WMF to reduce the fiber concrete interaction, thereby reducing the toughness abruptly for higher WMF contents, i.e. $\geq 20\%$. Hence, a continuous reduction in compressive toughness has been observed right away from 2.5% microsilica addition in mixes corresponding to 30% WMF i.e. from mix CWS9-CWS12, whereas similar trend has been observed from 7.5% microsilica addition for mixes containing 20% WMF i.e. from CWS7-CWS8. Addition of microsilica, obviously increased the toughness for flyash-microsilica mixes on account of increase in stiffness or modulus of elasticity.

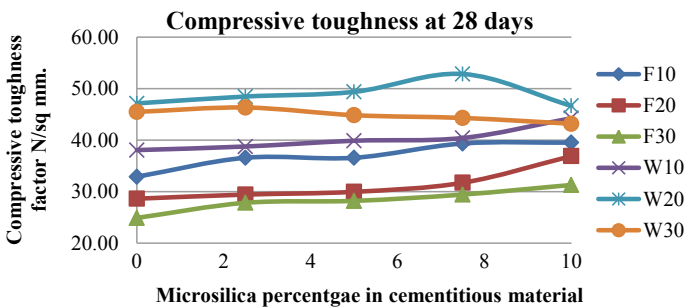


Fig. 8 Compressive toughness factor of concrete mixes after 28 days curing

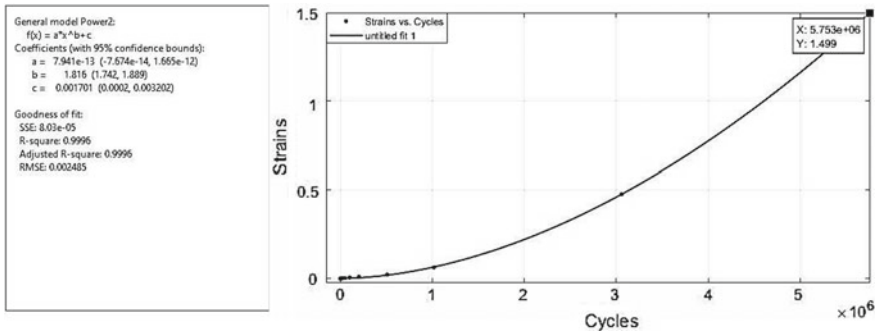


Fig. 9 Extrapolated strains-cycles curve representing cycles at 1.5% areal strains

Overall, the compressive toughness factor decreases by 29.5% and 19.1% in binary flyash and ternary flyash-microsilica mixes, respectively, with respect to reference concrete mix after 28 days curing. Whereas it increases by 6.5% and 9.9% in binary WMF and ternary WMF-microsilica mixes, respectively.

4.2.4 Fatigue Life from Pavement Models

After application of load cycles, a curve was obtained in which areal strains regress upon the cycles. Using this curve, the value of cycles corresponding to 1.5% areal strains was evaluated. Figure 9 shows the extrapolated regression curve of areal strains on cycles for normal concrete at 22.5 KN. Similarly, cycle values were obtained for all concrete mixes.

Table 6 shows the toughness and flexural strength of concrete mixes. It also shows the flexural stresses produced just after the application of conditioning load of 10000 cycles on the concrete slab. All these three parameters have been shown in conjunction with the fatigue life of the pavement corresponding to 20 KN and 22.5 KN loading.

Statistical curve fitting analysis was performed at 95% confidence interval for all the concrete mixes to find five types of relationships: between (a) stress ratio and toughness; (b) flexural stresses and toughness; (c) fatigue life and both stress ratio and toughness; (d) fatigue life and toughness; and (e) fatigue life and stress ratio. Regression equations provided in Table 7 serve as results obtained from the analysis. Corresponding curves are provided in Figs. 10, 11, 12, 13, 14 and 15. It was apparent from Eqs. 5–12 that fatigue life depends mostly upon stress ratio irrespective of toughness, load intensity or type of concrete mix. The overall relationship between fatigue life and stress ratio in Eq. 6 was not so appreciable and it was observed that the curve was having three zones corresponding to three stress ratios: 0.35–0.5, 0.5–0.65 and >0.65. So relationships at these values were also checked. To verify the role of toughness along with stress ratio, relationships were checked for them too. It was found that toughness along with stress ratio has weaker correlation with fatigue life

Table 6 Toughness, flexural strength, flexural stresses and cycles for various PQC

Mix	Toughness factor (N/mm ²)	Toughness (Nmm)	Flexural strength	Stress at 20 KN	Stress ratio at 20 KN	Cycles	Stress at 22.5 KN	Stress ratio at 22.5 KN	Cycles
C	40.91	812828	4.866	2.079	0.427	54929243	2.285	0.470	5753000
CF1	32.91	653866	4.316	2.340	0.542	174922	2.602	0.603	48284
CF2	28.64	569086	3.728	2.774	0.744	2949	3.079	0.826	947
CF3	24.91	494903	3.061	3.035	0.991	249	3.219	1.052	131
CFS1	36.59	726989	4.316	2.063	0.478	2844939	2.300	0.533	294930
CFS2	36.59	726989	4.552	2.050	0.450	24720433	2.320	0.510	469392
CFS3	39.36	782096	4.787	1.868	0.390	125723225	2.116	0.442	35839292
CFS4	39.52	785275	4.787	1.854	0.387	139292249	2.180	0.455	21483225
CFS5	29.44	584982	3.846	2.674	0.695	6583	2.850	0.741	3531
CFS6	29.97	595580	4.042	2.682	0.664	10483	2.901	0.718	5839
CFS7	31.73	630551	4.277	2.440	0.570	89472	2.744	0.642	16949
CFS8	36.91	653347	4.356	2.426	0.557	100292	2.648	0.608	39021
CFS9	27.84	553190	3.139	2.853	0.909	684	3.116	0.993	195
CFS10	28.21	560608	3.375	2.810	0.833	929	3.145	0.932	530
CFS11	29.44	584982	3.571	2.621	0.734	4832	3.000	0.840	738
CFS12	31.31	622073	3.453	2.490	0.721	5473	2.696	0.781	1634
CW1	38.08	916662	4.513	2.180	0.483	2057282	2.496	0.553	113293
CW2	47.15	936819	4.807	2.140	0.445	27959305	2.393	0.498	893753
CW3	45.49	903967	4.876	2.200	0.451	24294902	2.479	0.509	583853
CWS1	38.77	895038	4.630	2.213	0.478	28433593	2.551	0.551	119382
CWS2	39.89	912693	4.748	2.194	0.462	11273939	2.550	0.537	268374

(continued)

Table 6 (continued)

Mix	Toughness factor (N/mm ²)	Toughness (Nmm)	Flexural strength	Stress at 20 KN	Stress ratio at 20 KN	Cycles	Stress at 22.5 KN	Stress ratio at 22.5 KN	Cycles
CWS3	40.43	883291	4.905	2.242	0.457	18254829	2.609	0.532	295382
CWS4	44.27	879593	4.944	2.250	0.455	21493005	2.551	0.516	424492
CWS5	48.48	963313	4.944	2.065	0.418	68382022	2.360	0.477	3184322
CWS6	49.39	981329	5.101	2.025	0.397	124949206	2.280	0.447	28429493
CWS7	52.85	1050212	5.258	1.900	0.361	170403026	2.130	0.405	96849335
CWS8	46.67	927281	5.18	2.150	0.415	74739202	2.413	0.466	8583929
CWS9	46.35	920923	4.983	2.159	0.433	40002949	2.433	0.488	1295939
CWS10	44.85	891250	5.14	2.227	0.433	38892042	2.519	0.490	1294943
CWS11	44.32	880652	5.297	2.250	0.425	55020482	2.545	0.480	2335949
CWS12	43.2	858398	5.219	2.313	0.443	31073994	2.611	0.500	759249

Table 7 Regression equations of fatigue life on stress ratio and toughness

Eq. No.	Correlating variables	Coefficients (with 95% confidence bounds)	Goodness of fit
1.	Flexural stress versus toughness for normal/flyash mixes at 20 KN $f(x) = a * x^b + c$	$a = 7.061e+06 (-2.397e+08, 2.539e+08)$ $b = -1.125 (-3.927, 1.677)$ $c = 0.3432 (-4.848, 5.535)$	SSE: 0.2073 R-square: 0.8919 RMSE: 0.1263
2.	Flexural stress versus toughness for normal/flyash mixes at 22.5 KN $f(x) = a * x^b + c$	$a = -0.00128 (-0.02975, 0.02719)$ $b = 0.6073 (-0.8712, 2.086)$ $c = 7.001 (-3.594, 17.59)$	SSE: 0.06187 R-square: 0.9725 RMSE: 0.06899
3.	Flexural stress versus toughness for WMF mixes at 20 KN $f(x) = p1 * x + p2$	$p1 = -2.134e-06 (-2.234e-06, -2.035e-06)$ $p2 = 4.131 (4.04, 4.222)$	SSE: 0.0009034 R-square: 0.994 RMSE: 0.008336
4.	Flexural stress versus toughness for WMF mixes at 22.5 KN $f(x) = p1 * x + p2$	$p1 = -2.625e-06 (-3.004e-06, -2.246e-06)$ $p2 = 4.876 (4.527, 5.226)$	SSE: 0.01321 R-square: 0.9451 RMSE: 0.03188
5.	Fatigue life versus stress ratio and toughness (overall) $f(x, y) = p00 + p10 * x + p01 * y + p20 * x^2 + p11 * x * y + p30 * x^3 + p21 * x^2 * y$	$p00 = 3.481e+08 (-5.765e+08, 1.273e+09)$ $p10 = -1.661e+09 (-5.435e+09, 2.113e+09)$ $p01 = 943.1 (132.3, 1754)$ $p20 = 3.129e+09 (-1.488e+09, 7.747e+09)$ $p11 = -3325 (-6257, -391.6)$ $p30 = -1.939e+09 (-3.507e+09, -3.698e+08)$ $p21 = 2618 (-30.11, 5265)$	SSE: 1.165e+16 R-square: 0.8695 RMSE: 1.455e+07
6.	Fatigue life versus stress ratio (overall) $f(x) = a * x^b + c$	$a = 5.506e+04 (5488, 1.046e+05)$ $b = -8.104 (-9.027, -7.182)$ $c = -6.362e+06 (-1.086e+07, -1.869e+06)$	SSE: 6.483e+15 R-square: 0.9274 RMSE: 1.048e+07
7.	Fatigue life versus stress ratio and toughness at SR 0.35–0.5 $f(x, y) = p00 + p10 * x + p01 * y + p20 * x^2 + p11 * x * y$	$p00 = 2.711e+09 (2.225e+09, 3.197e+09)$ $p10 = -1.013e+10 (-1.192e+10, -8.35e+09)$ $p01 = -376.2 (-692.4, -59.9)$ $p20 = 9.24e+09 (7.491e+09, 1.099e+10)$ $p11 = 847.3 (116.7, 1578)$	SSE: 8.904e+14 R-square: 0.986 RMSE: 5.852e+06

(continued)

Table 7 (continued)

Eq. No.	Correlating variables	Coefficients (with 95% confidence bounds)	Goodness of fit
8.	Fatigue life versus stress ratio for SR 0.35–0.5 $f(x) = a1 * e^{-\left\{\frac{(x - b1)}{c1}\right\}^2}$	a1 = 1.715e+08 (1.636e+08, 1.794e+08) b1 = 0.3561 (0.3511, 0.3611) c1 = 0.06573 (0.06208, 0.06938)	SSE: 2.936e+14 R-square: 0.9954 RMSE: 3.238e+06
9.	Fatigue life versus stress ratio and toughness at SR 0.5–0.65 $f(x, y) = p00 + p10 * x + p01 * y + p20 * x^2 + p11 * x * y$	p00 = 7.507e+06 (-7.081e+06, 2.209e+07) p10 = -3.386e+07 (-7.562e+07, 7.891e+06) p01 = 10.41 (1.497, 19.33) p20 = 3.759e+07 (9.588e+06, 6.558e+07) p11 = -19.18 (-35.58, -2.778)	SSE: 2.051e+10 R-square: 0.97 RMSE: 4.529e+04
10.	Fatigue life versus stress ratio for SR 0.5–0.65 $f(x) = a * x^b$	a = 7.359 (-1.954, 16.67) b = -16.63 (-18.52, -14.73)	SSE: 1.266e+10 R-square: 0.9815 RMSE: 3.12e+04
11.	Fatigue life versus stress ratio and toughness at SR > 0.65 $f(x, y) = p00 + p10 * x + p01 * y + p20 * x^2 + p11 * x * y$	p00 = 1.728e+05 (2.777e+04, 3.178e+05) p10 = -3.351e+05 (-5.628e+05, -1.074e+05) p01 = -0.0782 (-0.2628, 0.1064) p20 = 1.534e+05 (8.104e+04, 2.258e+05) p11 = 0.09553 (-0.1202, 0.3112)	SSE: 8.567e+06 R-square: 0.9374 RMSE: 882.5
12.	Fatigue life versus Stress ratio for SR 0.65–1.5 $f(x) = a1 * e^{-\left\{\frac{(x - b1)}{c1}\right\}^2}$	a1 = 1.012e+05 (-4.936e+05, 6.96e+05) b1 = 0.2834 (-0.5933, 1.16) c1 = 0.2527 (-0.004975, 0.5103)	SSE: 2.449e+06 R-square: 0.9821 RMSE: 434

with respect to just stress ratio alone. There was medium-ranged correlation (0.6–0.8) between fatigue life and toughness which was discarded, yet it indicated that toughness has some effect on fatigue life. This indication was proved true when a good correlation between flexural stress and toughness was found at both load intensities and for all types of mixes in Eqs. 1–4. This is due to the fact that the cracks are formed only when the concrete elements are strained beyond a certain limit. The higher the limit, the higher energy concrete will absorb to crack. When cracks are fully developed at the bottom face of the PQC, they start propagating upwards. Cracks also widen during this time in the bottom face in both longitudinal and transverse directions. The post-peak stress energy held by concrete in bottom layer enables it to get strained up to higher limits without widening the cracks further which hinders the propagation of cracks vertically, thereby relieving the flexural stresses along the

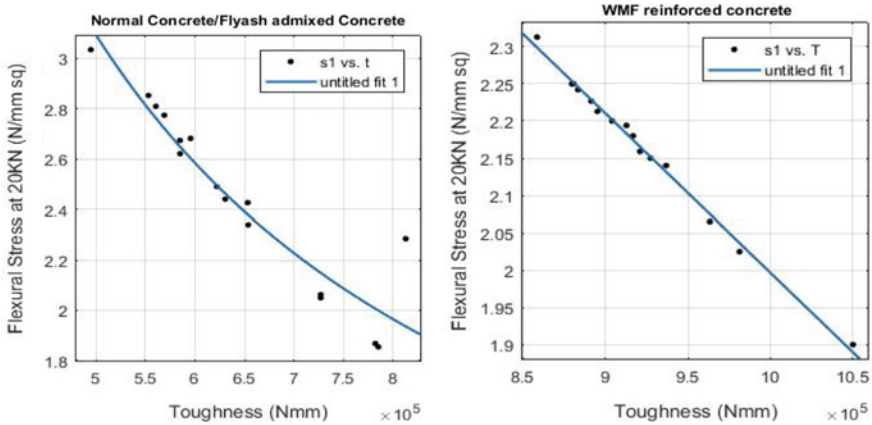


Fig. 10 Flexural stresses at 20 KN for **a** normal PQC/Flyash admixed PQC, **b** WMF-reinforced PQC

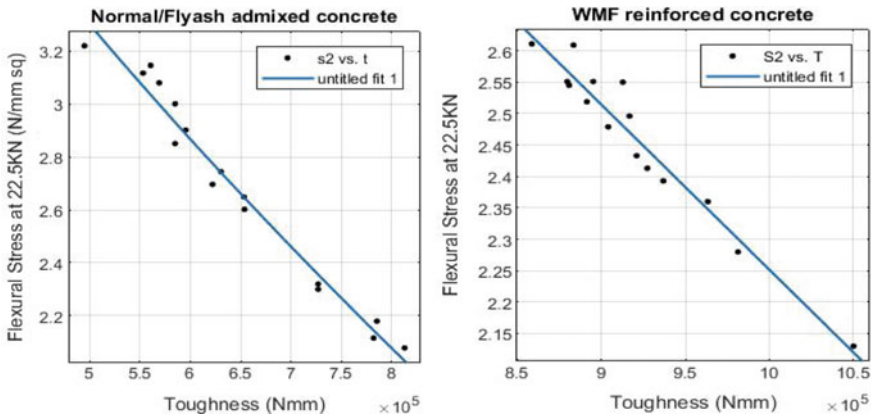


Fig. 11 Flexural stresses at 22.5 KN for **a** normal PQC/Flyash admixed PQC, **b** WMF-reinforced PQC

vertical direction. The stiffness of concrete in upper layers which is also a parameter of toughness in turn relieves the stresses of bottom layer. Highly stiff normal concrete thus has higher toughness and lesser flexural stresses in comparison to weakly stiff flyash admixed concrete mixes (Table 6). Hence, more is the toughness lesser will be the flexural stresses produced in the pavement. This is also apparent from Table 6 which showed lesser flexural stresses associated with highly Tough WMF-reinforced mixes.

Medium-ranged correlation ($R^2 = 0.6-0.8$) exists between stress ratio and toughness which explains the role of flexural strength in stress ratio values. High flexural

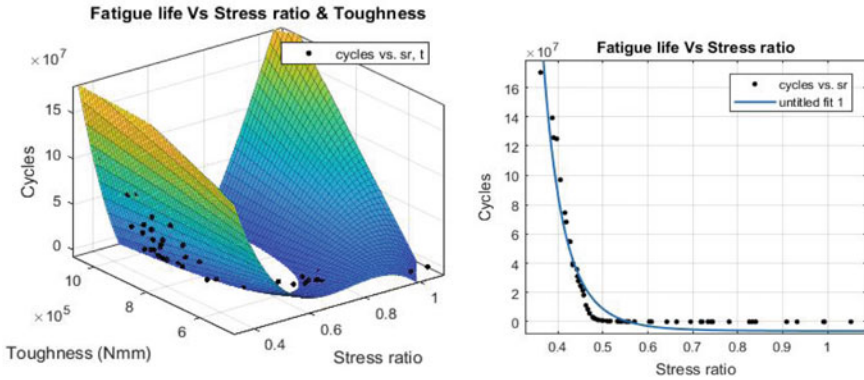


Fig. 12 Fatigue life versus a stress ratio and toughness, b stress ratio

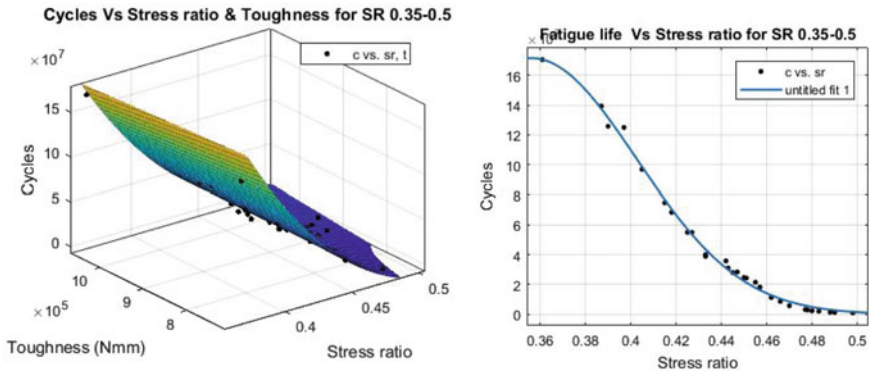


Fig. 13 Fatigue life versus a stress ratio and toughness, b stress ratio, at SR 0.35–0.5

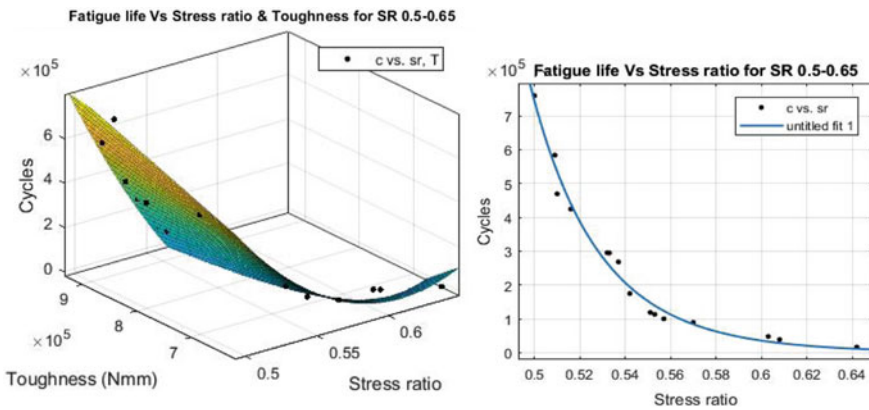


Fig. 14 Fatigue life versus a stress ratio and Toughness, b stress ratio, at SR 0.5–0.65

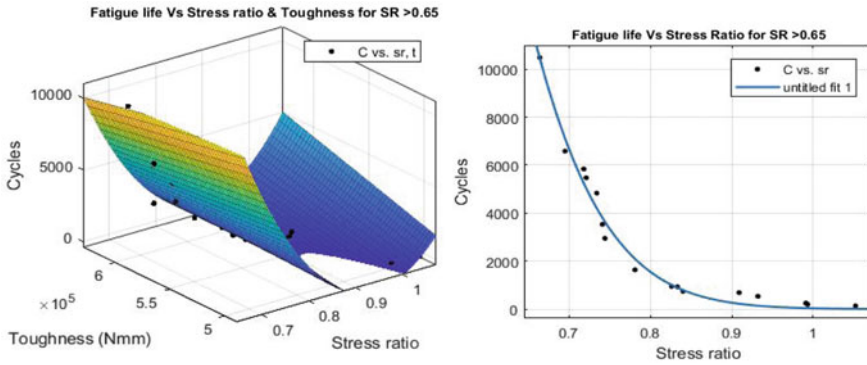


Fig. 15 Fatigue life versus **a** stress ratio and toughness, **b** stress ratio, at SR > 0.65

strength may or may not indicate a high toughness value since it also depends upon stiffness as well as ductile nature of concrete post ultimate stress.

Hence, while calculating the fatigue life on basis of stress ratio, i.e. flexural stresses upon flexural strength, the toughness factor is introduced indirectly by the flexural stresses. Thus, the stress ratio is singularly capable enough to regress the value of fatigue life. Regarding the life of concrete, it could be said that overall WMF-reinforced concrete has very high fatigue life in comparison to both normal and flyash admixed concrete. At 20 KN load, maximum fatigue life values of WMF-reinforced, flyash admixed, and normal concrete mixes are 170, 139.3 and 54.9 million, respectively, whereas these are 96.8, 57.8 and 5.75 million, respectively, at 22.5 KN load. Though overall flyash admixed concrete is a poor performer and showed very low fatigue life on account of high flexural stresses and low flexural strength.

5 Conclusion

Following points could be read as the conclusion on the basis of this study:

1. On an average fatigue life of WMF-reinforced rigid pavements is very high. Its peak fatigue life value is 3.1 times at 20 KN to 16.8 times at 22.5 KN in comparison to normal PQC. Similarly, it varies from 1.22 times at 20 KN to 1.67 times at 22.5 KN in comparison to flyash admixed PQC. Wollastonite microfiber reinforced concrete is beneficial not only because of the fact that they exhibit higher flexural strength but also higher toughness.
2. Since, WMF-reinforced concrete exhibited high flow, hence it would not be wrong to say that high fatigue life could be achieved with the use of high flow fiber reinforced concretes.

3. Flyash admixed concrete pavements have on an average very low fatigue life than normal PQC.
4. Stresses developing in the lower most layer of concrete are relieved either by the stiffness of layers above or due to the post-peak stress energy possessed by the concrete which strains the concrete without fracture. In either way, it is the toughness that plays the role because both stiffness and post-peak stress energy are components of toughness. Yet, it is obvious that higher flexural strength will ensure high fatigue life as more cycles will be consumed to fracture the concrete. Higher toughness reduces the crack propagation in concrete by relieving the stresses and thus indirectly affects the stress ratio of concrete.
5. Stress ratio remains a sufficient parameter in order to evaluate the fatigue life of a pavement.
6. Fatigue life equation could be a consolidated equation for all types of loads and for all types of concrete, since it depends only upon stress ratio. For a given value of stress ratio, it could be similar for different concrete types or different load types.

References

1. Banthia N, Sheng J (1996) Fracture toughness of microfiber reinforced cement composites. *Cem Concr Compos* 18(4):251–269 (Elsevier)
2. Banthia N, Trottier JF (1994) Concrete reinforced with deformed steel fibers, part I: bond-slip mechanisms. *ACI Mat J* 91(5):435–446
3. Clark P (1998) Future of automotive body materials: steel, aluminum & polymer corporation. Massachusetts Institute of Technology. <http://readpdf.net/file/future-steel-vehicle.html>
4. EFNARC (2002) Specification and guidelines for self-compacting concrete. EFNARC, Association House, 99 West Street, Farnham, Surrey, UK
5. EFNARC (2005) The European guidelines for self-compacting concrete: specification, 557 production and use. EFNARC. www.efca.info or www.efnarc.org
6. IRC 44 (2008) Tentative guidelines for cement concrete mix design for pavements. Indian Roads Congress, New Delhi, India
7. IRC 58 (2015) Guidelines for the design of plain jointed rigid pavements for highways. Indian Roads Congress, New Delhi, India
8. IS 383 (1970) Indian standard methods of tests for gradation of coarse aggregates. Bureau of Indian Standards, New Delhi, India
9. IS 516 (1959) Indian standard methods of tests for strength of concrete. Bureau of Indian Standards, New Delhi, India
10. IS: 1888 (1982) Indian standard methods of load tests on soils. Bureau of Indian Standards, New Delhi, India
11. IS 8112 (2013) Ordinary portland cement 43 grade specification. Bureau of Indian Standards, New Delhi, India
12. IS 12803 (1989) Methods of analysis of hydraulic cement by X-ray fluorescence spectrometer. Bureau of Indian Standards, New Delhi, India
13. Leung CKY (1992) Fracture-based two-way debonding model for discontinuous fibers in elastic matrix. *J Eng Mech* 118(11):2298–2318 (ASCE)
14. Li VC, Leung CKY (1992) Tensile failure modes of random discontinuous fiber reinforced brittle matrix composites. *J Eng Mech* 118(11):2246–2264 (ASCE)

15. Li VC, Wu HC (1992) Conditions for pseudo strain-hardening in fiber reinforced brittle matrix composites. *Appl Mech Rev* 45(8):390–398
16. Low NMP, Beaudoin JJ (1992) Mechanical properties of high performance cement binders reinforced with Wollastonite micro-fibres. *Cem Concr Res* 22(5):981–989
17. Low NMP, Beaudoin JJ (1993) The effect of Wollastonite micro-fibre aspect ratio on reinforcement of portland cement-based binders. *Cem Concr Res* 23:1467–1479
18. Nelson PK, Li VC, Kamada T (2002) Fracture toughness of microfiber reinforced cement composites. *J Mater Civ Eng* 14(5):384–391
19. Soliman AM, Nehdi ML (2012) Effect of natural Wollastonite microfibers on early-age behavior of UHPC. *J Mater Civ Eng* 24(7):816–824
20. Wu HC (2001) Discussion on mechanical properties of steel microfiber reinforced cement pastes and mortars. *J Mater Civ Eng* 13(3):240–241

Response of Single and Multilayered Flexible Base for Static and Earthquake Loading Under Framed RC Structure



Gaurav D. Dhadse , G. D. Ramtekkar, and Govardhan Bhat 

Abstract As it is well known that, if the effect of Soil–Structure Interaction (SSI) is to be assessed, then structure must be placed on physical soil mass with actual properties to get the perfect behavior of soil and structure rather than Winkler’s Spring Model. In case of non-interaction analysis problem, the structure is to be placed on non-yielding support; hence, it is assumed that there will be zero displacement beneath the footing or displacement is considered less than the permissible limits as stated by standards. However, the actual condition is totally different and settlement due to soil properties can be seen by naked eyes. In non-interaction analysis, the footings are design based on Safe Bearing Capacity (SBC) of soil, but as per literature review and SSI analysis done in this paper, it is observed that the footing deformation is more than permissible value and stress value just below the footing is also higher than SBC. To demonstrate the actual nature of the ground response, a multi-storey frame is analyzed with four different cases. The SSI system modeling is done using finite element method ANSYS Software program. The portal frame is modeled as elastic (linear), whereas the ground is modeled as both elastic–plastic (linear elastic and non-linear). The study gives insight into the variation of deformation and stress intensities in soil mass while considering linear and non-linear behavior of ground. In the analysis of soil, the deformation in soil mass is plotted along with depth and discussed, whereas stresses are plotted along the width with a variation for different types of soil and different loadings. Thus, after complete analysis, it is observed that both the stresses and deformations are out of permissible limit after considering the actual stiffness of soil.

Keywords SSI · Finite element method · Stress · Vertical deformation · Linear and non-linear soil mass

G. D. Dhadse (✉) · G. D. Ramtekkar · G. Bhat
National Institute of Technology, Raipur, C.G., India
e-mail: gddhadse@yahoo.com

1 Introduction

In order to understand the effect of Soil–Structure Interaction over general fix support condition, the structure must be placed on soil mass and then allow the structure to behave accordingly, to the support condition applied by soil mass. The amount of soil mass required to be taken while modeling is decided by shear wave velocity criteria and direct method is used for the analysis of the SSI problem. Also, about 90% of researchers did their work considering soil mass as linear and single-layered [1] and none of them provide a solid reason for providing the extent of soil mass in modeling. So here, in this paper, the above-mentioned gaps in the study are fulfilled with the help of analysis of four models considering both single-layered and multilayered as well as linear and non-linear soil mass as given below [2]. Output of all analysis shows the amount of deformations as well as stress intensity in soil. Paper further converges on the importance of stiffness of soil over safe bearing capacity. In this paper, four models are considered, which are as follows:

1. Single-layered soil + frame structure model (Gravity loading)
2. Single-layered soil + frame structure model (Gravity loading + Lateral loading)
3. Multilayered soil + frame structure model (Gravity loading)
4. Multilayered soil + frame structure model (Gravity loading + Lateral loading).

Thus, SSI analysis is carried out for all above-mentioned models considering elastic and elastoplastic soil mass [3, 4]. Also for the analysis, finite element modeling of a frame structure, isolated footing, and semi-infinite soil mass is done in ANSYS 11.0. The basic aim of this paper is to check the behavior of soil mass and understanding the settlements and stress distribution patterns in the soil mass.

2 Models Under Investigations

2.1 Limitations and Introduction to Model

- a. Structure and soil are modeled as plane strain with unit thickness and element is considering Plane 82 (two degrees of freedom per node).
- b. The interface between soil and structure is considered as a tie, i.e., structure and soil are tied together.

In the present problem, a 3 bay \times 3 storey RCC space frame resting on homogeneous soil mass with elastic and elastoplastic properties and subjected to gravity and combined gravity + lateral loading with single-layered and multilayered soil mass is analyzed. The problem under consideration is symmetric about both axes in terms of material, geometry, and loading. The superstructure of the proposed model is depicted in Fig. 1.

To investigate the interaction behavior, the interaction analyses are carried out for the following two cases considering all frames of structure as the plane frame.

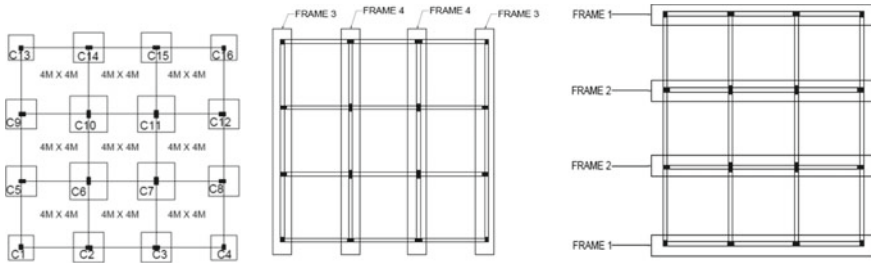


Fig. 1 Plan showing columns and footings

- Case-1:** The interaction analysis of plane frame isolated footing–soil system considering the columns supported on individual column footings and resting on soil media (Elastic Analysis). (IAE).
- Case-2:** The interaction analysis of plane frame isolated footing–soil system considering the columns supported on individual column footings and resting on soil media (Elastoplastic Analysis). (IAEP) [5–7].

Where,
 IAE—Interaction Analysis Elastic.
 IAEP—Interaction Analysis ElastoPlastic.

The frame and foundation are considered to be elastic and soil mass is considered as both elastic and elastoplastic. The geometric and material properties of proposed models are given in Table 1 (Single-layered) and Table 2 (Multilayered). And, the elevation of Frame 1, Frame 2, Frame 3, Frame 4, and plan of all beams are shown in Fig. 2a, 2b, and 2c, 2d, respectively.

Thus, a significant depth is generally taken as the depth at which the vertical stress is 1/5th of load intensity. In this case, vertical stress is calculated from Boussinesq’s Equation. Also, the depth of soil mass is calculated from shear wave velocity criteria [8–10].

3 Loads

3.1 Gravity Loads

Loads are calculated by usual way, i.e., for the slab, Live Load = 3 kN/m², Floor Finish = 1.25 kN/m², and after this factored it and distributed on beams as per IS 456–2000 [11]. For beams, loads of walls are calculated and factored.

As far as the dead load is concerned, ANSYS 11 calculated dead weight of members from mass density and acceleration due to gravity; hence, these properties are required while assigning. Table 3 shows the factored UDL intensities on all beams [11].

Table 1 Geometric and material properties of frame, footing, and soil mass (Single-layered)

Component	Description	Data
Frame	Number of stories	3
	Number of bays in the X direction	3
	Number of bays in the Y direction	3
	Floor to floor height	3.0 m
	Plinth height	1.0 m
	Bay width in the X direction	4.0 m
	Bay width in the Y direction	4.0 m
	Beam dimensions	(0.23 × 0.3) m
	Columns C1, C13, C4, C16 (A)	(0.23 × 0.3) m
	Columns C2, C14, C3, C15, C5, C9, C8, C12 (B)	(0.38 × 0.23) m
	Columns C6, C10, C7, C11 (C)	(0.23 × 0.45) m
	Thickness of all slabs	0.15 m
Isolated footing	Footing under Columns C1, C13, C4, C16 (F1)	1.5 m × 1.5 m × 0.35 m
	Footing under Columns C2, C14, C3, C15, C5, C9, C8, C12 (F2)	1.8 m × 1.8 m × 0.4 m
	Footing under Columns C6, C10, C7, C11 (F3)	2.2 m × 2.2 m × 0.5 m
Concrete	Modulus of elasticity of concrete for (M20)	22,360 × 10 ⁶ N/m ²
	Poisson's ratio of concrete	0.15
Soil mass (Medium-hard clay)	Extent of Soil Mass ^a	30.0 m × 15.0 m
	Modulus of elasticity of soil	100 × 10 ⁶ N/m ²
	Poisson's ratio of soil	0.2
	Cohesion	50 × 10 ³ N/m ²

^aExtent of soil mass depend upon a significant depth, which is defined as the depth up to which the stress increment due to applied loads can produce a significant settlement and shear stress

3.2 Lateral Loads

Gravity loading is the same as Sect. 3.1 of the first model and lateral loading is calculated according to IS 1893-2002 [12] for Seismic Zone III and ordinary moment resting frame. Thus, the distribution of base shear, i.e., lateral load intensity on each floor of the frame is given in Table 4 and gravity loading is given in Table 3.

4 Finite Element Modeling

The interaction analysis of the problem is carried out using ANSYS software (Version 11.0). The finite element discretization of the problem is shown in Fig. 3.

Table 2 Geometric and material properties of frame, footing, and soil mass (Multilayered)

Component	Description	Data
Frame	Same data for Frame as given in Table 1	
Isolated footing	Same data for isolated footings as given in Table 1	
Concrete	Same data for concrete as given in Table 1	
Soil mass	Total Extent ^a	60.0 m × 58.34 m
First layer (Firm clays or stiff clays or medium hard clay)	Depth	13.65 m
	Modulus of elasticity of soil	$100 \times 10^6 \text{ N/m}^2$
	Poisson's ratio of soil	0.30
	Cohesion	$50 \times 10^3 \text{ N/m}^2$
	Frictional angle	19^0
Second layer (Silty sand)	Depth	27.20 m
	Modulus of elasticity of soil	$120 \times 10^6 \text{ N/m}^2$
	Poisson's ratio of soil	0.25
	Cohesion	$30 \times 10^3 \text{ N/m}^2$
	Frictional angle	21^0
Third layer (Dense sand and gravel)	Depth	17.49 m
	Modulus of elasticity of soil	$170 \times 10^6 \text{ N/m}^2$
	Poisson's ratio of soil	0.20
	Cohesion	$20 \times 10^3 \text{ N/m}^2$
	Frictional angle	25^0

^aExtent of soil mass depend upon a significant depth, which is defined as the depth up to which the stress increment due to applied loads can produce a significant settlement and shear stress

The frame structure, footing, and soil mass are discretized with 8-noded plane stress element (PLANE 82) for case 1 and case 2 with two degrees of freedom per node (U_x and U_y). It provides more accurate results for mixed automatic meshes and can tolerate irregular shapes without as much loss of accuracy. The 8-node elements have compatible displacement shapes and are well suited to model curved boundaries. The element may be used as a plane strain element or as an axisymmetric element. The element has plasticity, creep, swelling, stress stiffening, large deflection, and large strain capabilities [13] (Fig. 4).

It is assumed that various member joints are perfectly rigid. The vertical displacements in soil mass are restrained at the bottom boundary, whereas horizontal displacements are restrained at vertical boundaries. The soil mass is idealized as an isotropic, homogeneous, and half-space model. For Case 2, elastic-plastic behavior of the ground is modeled using Drucker-Prager criterion in ANSYS' 11. The input consists of only three constants:

- The cohesion value (must be >0)
- The angle of internal friction
- The dilatancy angle.

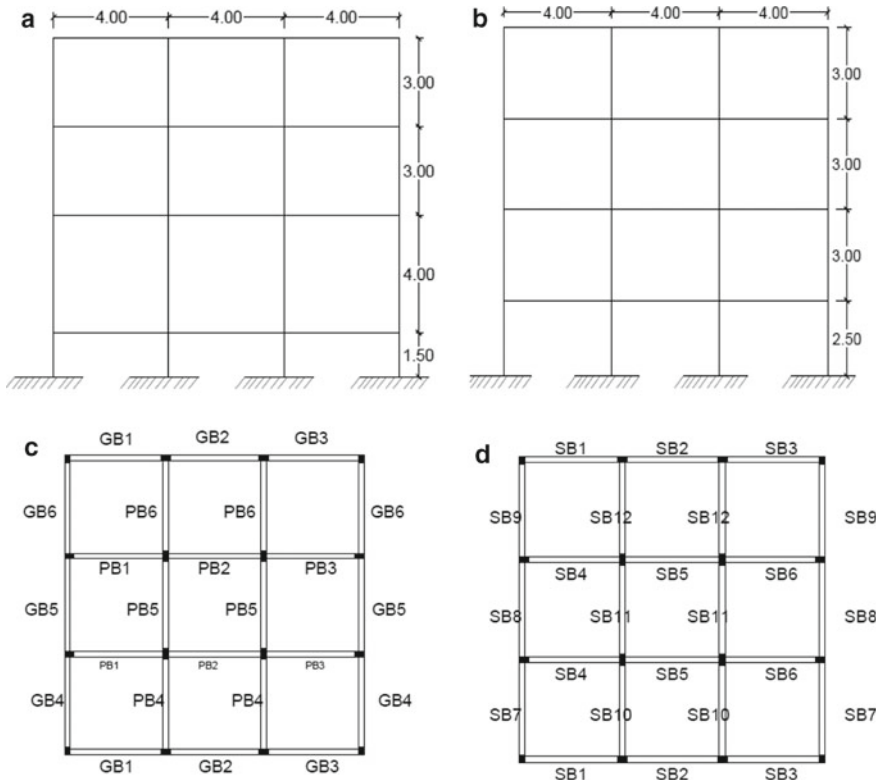


Fig. 2 a Elevation of Frame 1 and Frame 3. b Elevation of Frame 2 and Frame 4. c Plan showing Ground beams and Plinth beams. d Plan showing Slab beam for first, second, and terrace floor

Table 3 Factored UDL intensities on beams

Structural component	UDL intensities (N/m)
Ground beams	25,530
Plinth beams	9315
First and second floors	
Outer slab beams	34,630
Inner slab beams	41,315
Terrace floor	
Outer slab beams	22,900
Inner slab beams	38,900

Table 4 Lateral load intensity on each floor

Floor	load intensities (N)/frame
Terrace floor	60,170
Second floor	46,095
First floor	20,870
Ground-level floor	525

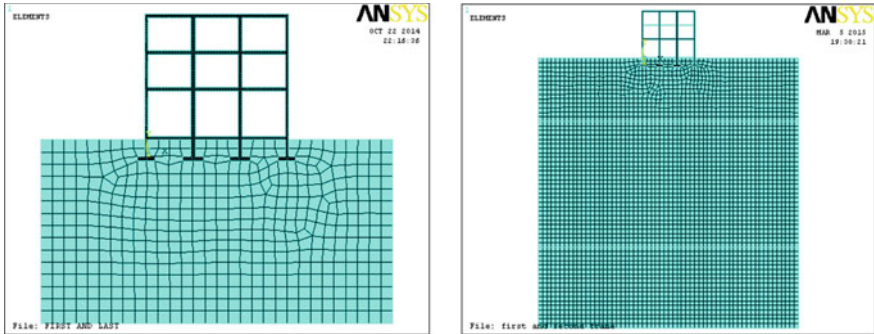


Fig. 3 Finite element discretization of frame-footing-soil system (Single-layered and Multilayered)

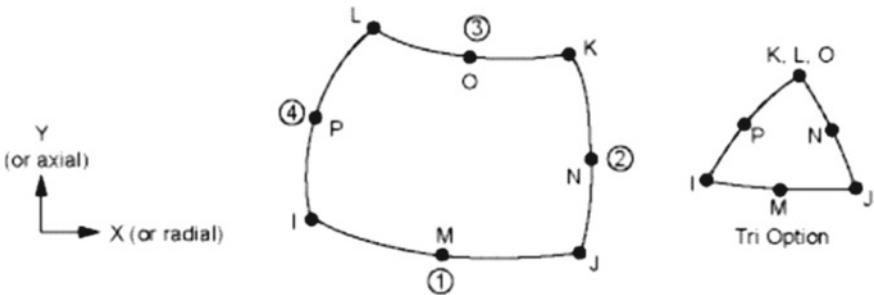


Fig. 4 PLANE 82 element geometry

The interface characteristics between the isolated footing and soil are represented by TARGE169 and CONTA172 elements. The element size for frame and footings are taken as 100 mm × 100 mm. The soil mass is discretized with 1000 mm × 1000 mm finer meshes in close vicinity of footing where stresses are of a higher order [13].

5 Analysis of Soil Mass

In soil mass analysis, the displacement, as well as stress approach, is used. And, this part of the study discussed the response of soil mass for elastic and plastic soil properties, due to frame structure over it. Thus, soil mass for the same models mentioned is analyzed and discussed.

5.1 Displacement Approach

Here, the deformations of soil mass in all models for IAE and IAEP analyses are presented and discussed. Also, two types of geometry are adopted while modeling soil mass in the mentioned models. So, vertical deformations are plotted along the depth of soil mass to study the variation of displacements. Also, it is not possible to check deformation at every meter width of soil mass, so a unique approach is used, in which deformation is plotted along with the depth for mid-width of soil mass as shown in Fig. 5.

- As the depth of soil, mass is taken according to the literature available, i.e., 15 m (assuming there is bedrock below this depth), so the bottom boundary is restrained against translations in both directions, and hence, at 15 m depth, displacement must be zero regardless of soil stiffness.
- The main reason behind switching 15 m depth in models 3 and 4 is that there should not be bedrock at such shallow depth and 15 m, decided on the basis of significant depth criteria in which depth is taken up to which the stress increment due to applied loads can produce a significant settlement and shear stress. Hence, it is assumed that there should not be a significant settlement and shear stress below this depth, which is practically wrong. Hence, in order to produce the exact volume of soil mass required to model SSI problem, the shear wave velocity concept in Eurocode 8 is used to model layered soil mass. Thus, results that are more

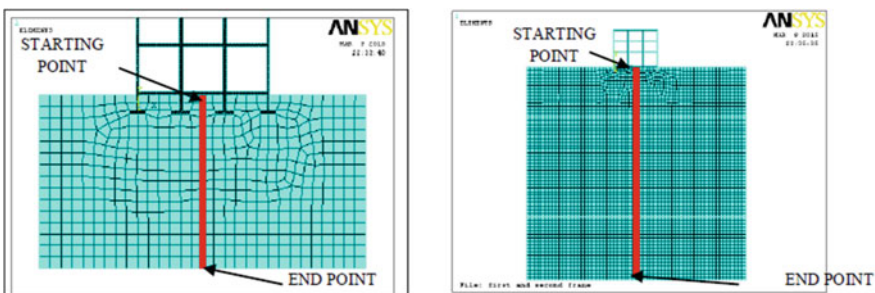


Fig. 5 Single-Layered and Multilayered Soil mass height consider for comparing vertical displacements

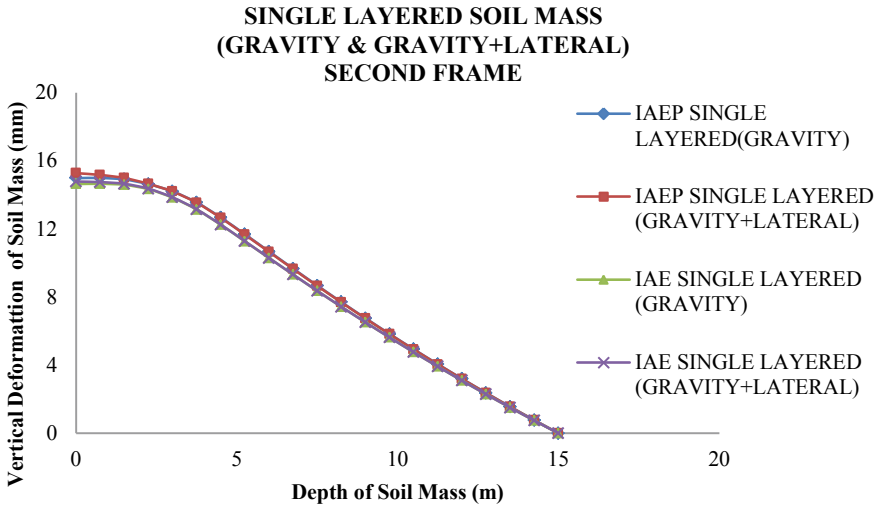


Fig. 6 Variation in vertical deformation along with mid-width depth of soil mass for single-layered soil mass (Second frame)

exact are found for these three-layered soil mass with increasing stiffness than single-layered soil mass with the same stiffness as the top layer of multilayered.

As in gravity load models, the deformation is maximum at the central width of soil mass and in Gravity + Lateral load model, due to uplifting the maximum deformation of soil mass shifted towards the last footing. Hence, to show the variation of deformation in soil mass for both these loading, this path is adopted. As discussed earlier, frames 2 and 4 show the worst results, so a comparison is also done for these two frames only. Following Figs. 6, 7, 8, and 9 show the variation of vertical deformation along the above-mentioned path for single-layered and multilayered soil masses.

Thus, from the above curves, followings points are concluded:

- In single-layered soil mass, depth is 15 m, and elastic and elastoplastic soil properties are used. Thus, Figs. 6 and 7 show that there is a gradual decrease in deformation for elastic and elastoplastic soil mass.
- In single-layered soil mass, IAEP (gravity + lateral) shows maximum deformation than IAEP (gravity); hence, it concluded that after applying lateral loading, mid-width deformations increase than gravity loading.
- For IAE, the same variation in results is found in single-layered soil mass.
- In multilayered IAEP soil mass, deformation suddenly decreases as layer changes and becomes stiffer. But, for IAE, variation in displacement is again gradual and deformations are less than IAEP.
- As discussed earlier in horizontal deformation of the frame and vertical displacement of footing, footings get uplifted after applying lateral load, so at mid-width, the displacement in IAEP due to gravity loading is more than displacement due to gravity + lateral loading. Hence, Figs. 8 and 9 show the same.

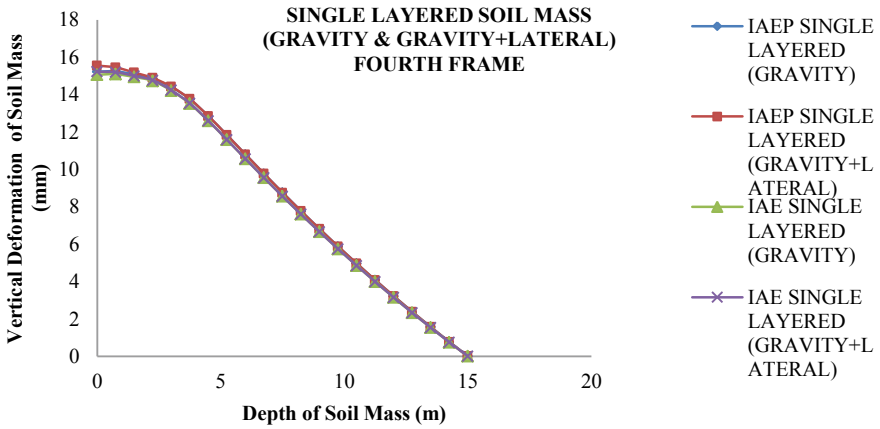


Fig. 7 Variation in vertical deformation along with mid-width depth of soil mass for single-layered soil mass (Fourth frame)

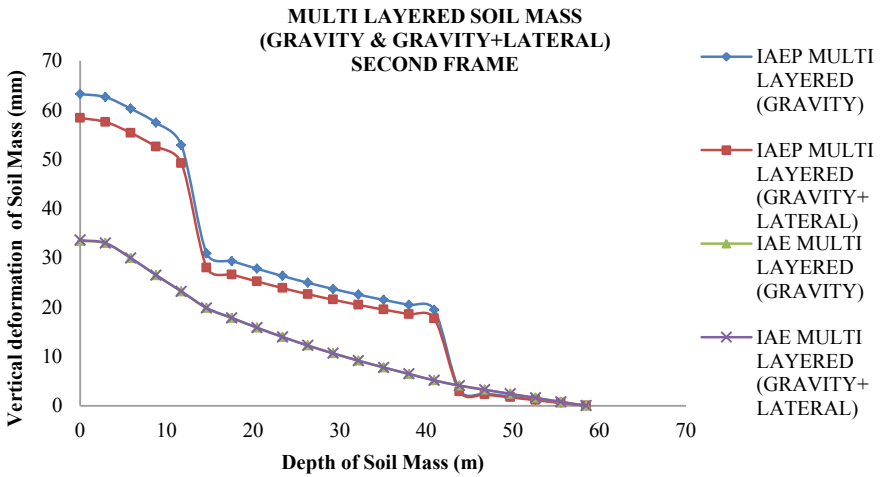


Fig. 8 Variation in vertical deformation along with mid-width depth of soil mass for multilayered soil mass (Second frame)

- In single-layered soil mass, the same frame is come out safe, but in multilayer, the frame tilted. Hence, if a more practical approach is used, then more practical results are found.

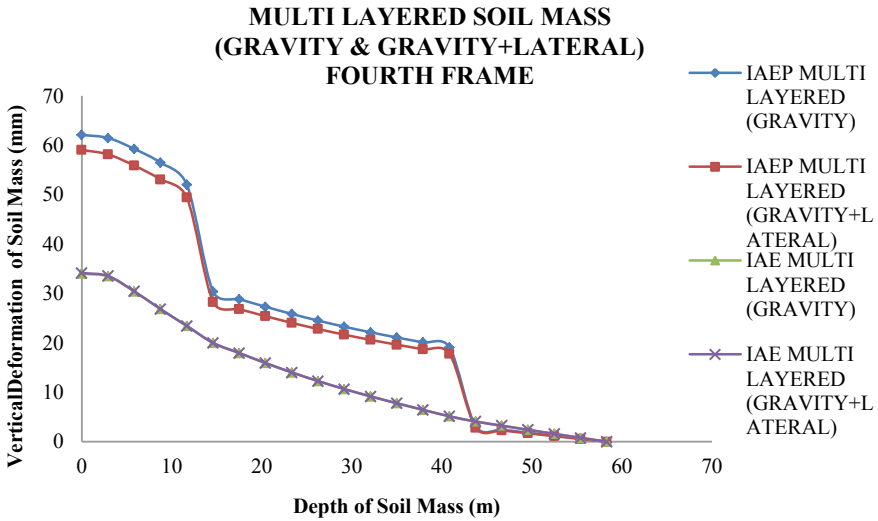


Fig. 9 Variation in vertical deformation along with mid-width depth of soil mass for multilayered soil mass (Fourth frame)

5.2 Stress Approach

In order to understand the distribution of stress in soil mass, the graphs are plotted between the width of soil mass and stress intensity. The width of soil mass at mid-depth of each layer is considered for multilayered model and width at 1/3 rd depth and 2/3 rd depth is considered for single-layered soil mass model. The exact location of layers along which the stress is plot is shown in Fig. 10a, b.

Thus, stress is a plot at above-mentioned location for IAE and IAEP in single- and multilayered (Gravity and Gravity + lateral loading) models and presentation of stress is done in following Figs. 11 and 12.

Thus, from above curves, the following points are concluded:

- From all the curves, it shows that stress is distributing on soil mass considered. Also, as it go dipper in soil mass, the distribution curve become more flat; thus, it shows that stresses are distributing and gets vanished after suitable depth. Of course, such depth is adopted in all models. Hence, SSI model must be correct if this stress distribution follows soil mass in correct way. As it is observed that, if depth is 15 m, then stress intensity increases than 58.34 m depth; hence, it is necessary to take proper depth for analysis.
- As in single-layered soil mass, the depth is less than multilayered soil mass, thus for this shallow depth in single-layered, stress-induced due to structural load also more. So distribution space required for distribution of stress is also limited; hence, if it considers actual depth regardless significant depth, then stress distribution also

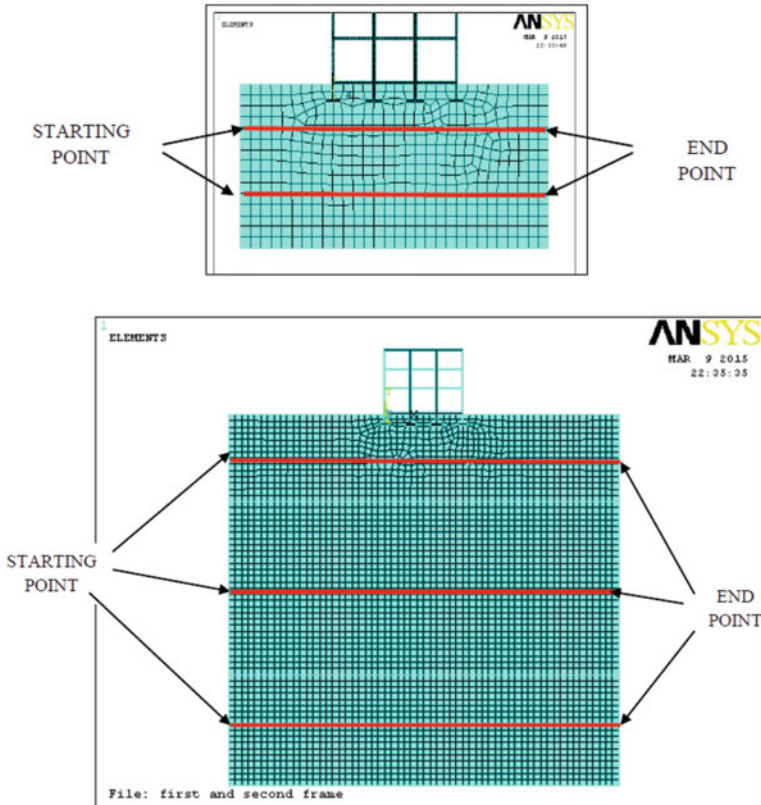


Fig. 10 a Location width at 1/3rd and 2/3rd depth for single-layered soil. b Location width at mid-depth of each layer for multilayered soil

shows best result and value of stress in multilayered model is also less than 15.0 m single-layered model.

- In single-layered soil mass, Frames 2 and 4 show maximum stress, but in multilayered soil mass, it doesn't show result like this.
- If we compare stress in IAE and IAEP side by side, then it shows that the stress value is almost the same but the response of soil changes from IAE to IAEP for the upper layer of all models. Thus, soil behaves as plastic keeping stress value nearly the same, but response after loading majorly changes. Hence, plasticity of soil must be considered for accurate analysis.
- In multilayered models, stress in IAEP under exterior footings increases slightly than IAE and, for inner footings, the stress values slightly decrease than IAE. Thus, exact response can be found out.
- Also in lateral + gravity loading, the peak value of stress slightly shifted in the opposite direction of application of lateral load. Of course, layer nearer to footings

1.Single layered (Gravity + Lateral)

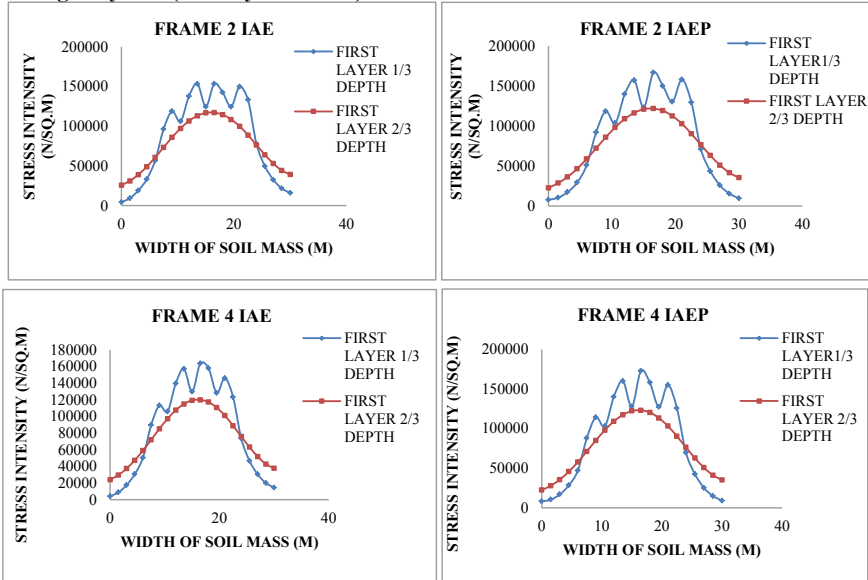


Fig. 11 Distribution of stress along width for soil mass of single-layered (gravity + lateral) IAE and IAEP models

2Multi layered (Gravity + Lateral)

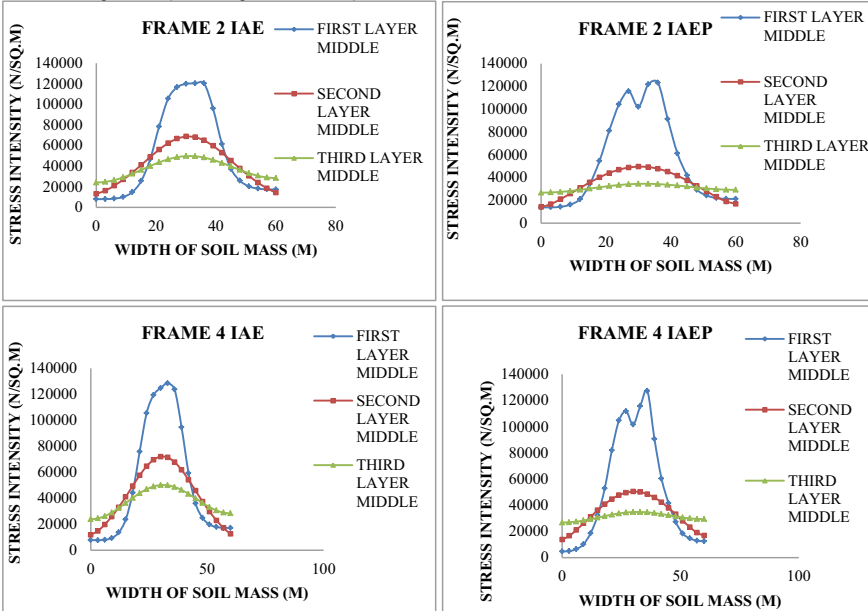


Fig. 12 Distribution of stress along width for soil mass of multilayered (gravity + lateral) IAE and IAEP models

shows drastic effect, but the dipper layer shows a slight change in behavior but a shifting of peak can easily be seen.

- Also after checking the upward soil pressure on footing, the maximum value in single-layered soil mass is found to be 3295 kN/m^2 and, for multilayered soil mass, it is 2607 kN/m^2 . Both values are greater than 200 kN/m^2 (SBC of soil is same for single-layer and top layer of multilayered models). Hence, footings are in tension and structure may fail.
- Thus, designers may switch to other types of footing but they have to check design again for SSI effect or they may increase the stiffness of soil mass by any soil stabilization technique.
- As from the stress analysis, the stress just below the footings is so high that soil fails its strength and that is the basic reason for increasing the vertical displacement.
- Therefore, both stress and displacement are out of limit after considering actual stiffness; hence, while designing in addition to SBC, the stiffness of soil mass must be considered.

6 Conclusion

Soil mass modeling and analysis have been done for Soil–Structure Interaction for getting the results for vertical deformation and stress distribution in the soil mass. The displacements are plotted along with the mid-width depth and stresses are plotted along the width of soil mass. The result shows increased values of displacements and stresses than permissible. Thus, following points are concluded based on the above results.

1. Stress in soil mass is distributing in nature. As it goes dipper, stresses try to vanish, but the intensity of those stresses just below footing is so high that soil fails its strength and excessive deformation occurs.
2. Maximum stress value in single-layered soil mass is more than multilayered soil mass; hence, it can be suggested that for proper distribution of stress, depth, and finite soil mass must be considered properly.
3. Tension is introduced in footing due to drastically increased in upward soil pressure just below footings.
4. Both the stress and vertical deformation are beyond limit after considering actual stiffness of soil; hence, while analyzing, in addition to safe bearing capacity, the stiffness of soil mass must be taken into consideration.
5. Finite element method becomes useful to incorporate the effect of material nonlinearity, non-homogeneity, and interface modeling of soil and foundation.

References

1. Shah SG, Solanki CH, Desai JA (2011) Soil structure interaction analysis methods—State of art-Review. *Int J Civ Struct Eng* 2(1) (2011). ISSN 0976-4399
2. Jancy F, Rajagopal A, Umashankar B, Madhav MR (2011) Finite element modeling of ground—structure interaction considering non-linear response of the ground. In: *Proceedings of Indian Geotechnical Conference Kochi* (Paper No N-281)
3. Garevski M et al (2012) Effect on soil medium on response of base isolated multistory frame structures. In: *15th WCEE conference Lisboa*
4. Rajashekhar Swamy HM (2012) Non-linear dynamic analysis of soil structure interaction of three dimensional structure for varied soil conditions. Doctor of Philosophy in Civil Engineering Thesis, Department of Civil Engineering, Manipal Institute of Technology Manipal
5. Eldin MS, El-Helloty M (2014) Effect of opening on behavior of raft foundations resting on different types of sand soil. *Int J Comput Appl* (0975 – 8887), 94(7)
6. Jain DK, Hora MS (2014) Interaction analysis of space frame-shear wall-soil system to investigate foundation forces under seismic loading. *ARNP J Eng Appl Sci* 9(8). ISSN 1819-6608
7. Garg V, Hora MS (2012) Interaction effect of space frame-strap footing-soil system on forces in superstructure. *ARNP J Eng Appl Sci* 7(11). ISSN 1819-6608
8. Dhadse GD, Mohod MV (2014) Importance of soil structure interaction for framed structure. In: *Proceedings of international conference on advances in civil and mechanical engineering systems (ACMES 2014)*, 23–24 December 2014, Government College of Engineering, Amravati. (C-25), pp 18–27
9. Dhadse GD (2016) Effect of soil structure interaction for framed structure resting on multilayered soil mass. *Int J Eng Res* 5, Issue Special 1:99–105. ISSN: 2319-6890 (online), 2347-5013 (print)
10. Dhadse G (2016) Effect of soil structure interaction on vertical irregularity in framed RC structure. In: *Proceedings of “The sixth international congress on computational mechanics and simulation” at IIT Mumbai on 27 June to 01 July*
11. IS 456 (2000) Indian Standard Criteria for plain and reinforce structure, ICS 91.100.30 New Delhi
12. IS 1893 – (Part 1) (2002) Indian Standard Criteria for earthquake resistant design of structures (ICS 91.120.25)
13. Krishnamoorty CS (2010) *Finite element analysis*, 2nd edn. Mc Graw Hill, New Dehli

Analysis of Moment and Torsion in Skew Plates Using ABAQUS



Anjani Kumar Shukla , Vishal Koruthu Philip , and P. R. Maiti 

Abstract The increased utilization of skew plates in thin-walled structural components of aircrafts, submarines, automobiles, and other high-performance application areas have necessitated a strong need to understand their characteristics. This paper presents the bending analysis of isotropic skewed plates using the finite element software ABAQUS Simulia. Modeling was done in ABAQUS Simulia using the SC8R element as it gave better results for shell structures. An analysis is done on skew plates of various skew angles and aspect ratios with all end clamps subjected to uniform pressure and the results are generated. The effect of skew angle, aspect ratio, and thickness of the plate on various parameters like bending and torsional moments, support shear, and deflection are separately presented which may serve as a benchmark for further research. From the results, it is observed that the maximum central deflection decreases with an increase in skew angle. The negative reaction was found to develop at the acute angle corners and it increased as the skew angle increased. Bending moments were found to decrease and torsion was found to increase with an increase in skew angle.

Keywords Skew plates · Finite element · Uniform pressure · Plate analysis using Abaqus

1 Introduction

Plates and shells are extensively used as structural parts in civil, aerospace, automotive, and marine engineering structures. Specific application of isotropic skew plates includes aircraft wings and aircraft tail fins. The edges of these plates are often so mounted that their boundaries can be assumed to be equivalent to various classical flexural boundary conditions. Due to the rapid development of aviation and aerospace programs, the analysis of plates of different skew angles and with different loading has become necessary.

A. K. Shukla (✉) · V. K. Philip · P. R. Maiti
Department of Civil Engineering, Indian Institute of Technology (IIT-BHU), Varanasi, India
e-mail: akshukla.rs.civ16@iitbhu.ac.in

Experience showed that such structures may fail in many cases not on account of high stresses, surpassing the strength of the material but owing to insufficient stability of slender members. Due to its significance in structural mechanics, a large number of references in the published literature deal with vibration and static stability behavior of plates subjected to uniform in-plane stresses.

A general theory about the bending of skew plates and shells is given in the book of Timoshenko [1]. Das et al. analyzed the large deflection static behavior of isotropic skew plates under uniform pressure loading using appropriate domain mapping technique [2]. Girish et al. studied the buckling behavior of skew plates using the finite element method using HyperMesh as pre- and post-processor and MSC/NASTRAN as solver [3]. Srinivasa et al. studied the buckling behavior of laminated composite skew plates and obtained time history for the nonlinear free vibration of composite skew using Newmark's time integration technique [4]. Naghsh and Azhari employed the element-free Galerkin (EFG) method to analyze the large amplitude-free vibration of point supported laminated composite skew plates [5]. Singha and Daripa studied the large amplitude-free flexural vibration behavior of symmetrically laminated composite skew plates using the finite element method [6]. Dey and Singha investigated the dynamic stability characteristics of simply supported laminated composite skew plates subjected to a periodic in-plane load using the finite element approach with a four-noded shear flexible high precision plate-bending element [7]. Farag and Ashour developed a fast converging semi-analytical method for assessing the vibration effect on thin orthotropic skew (or parallelogram/oblique) plates [8]. Chun and Lim derived analytical solutions for the problem of skewed thick plates under transverse load on a Winkler foundation [9].

Although much research has been done on the behavior of skew plates, very little insight have been obtained about the variation of parameters like moments, shear, and torsion with skewness which may be useful for understanding the behavior of skew slabs and bridges. The objective of this study is to investigate the bending behavior of skew plates using finite element method. The behavior with respect to three parameters (skew angle, aspect ratio, and thickness) is analyzed in detail.

2 Mathematical Formulation

The governing equation for a plate subjected to uniform load is given by (Fig. 1)

$$\frac{\partial^4 w}{\partial x^4} + 2 \frac{\partial^4 w}{\partial x^2 \partial y^2} + \frac{\partial^4 w}{\partial y^4} = \frac{q}{D}$$

where

w is the deflection of the plate

q is the intensity of the uniform load

D is the flexural rigidity of the plate $D = \frac{Eh^3}{12(1-\nu^2)}$.

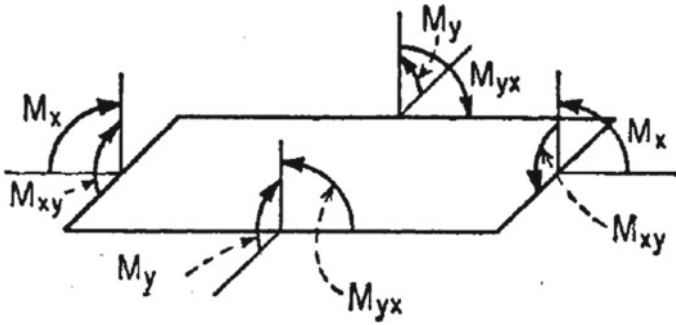


Fig. 1 Diagram showing moments acting on the plate

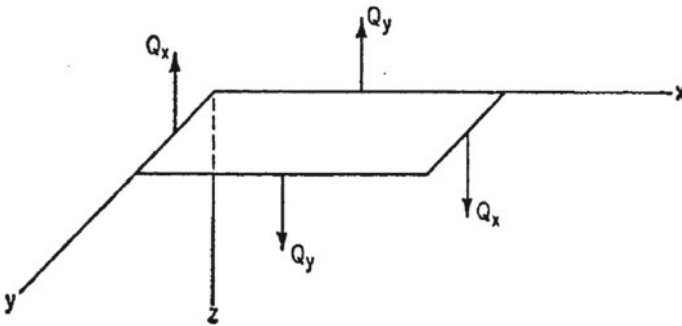


Fig. 2 Diagram showing shear forces acting on the plate

The moments in x and y direction twisting moments are given by (Fig. 2)

$$M_x = -D \left(\frac{\partial^2 w}{\partial x^2} + \nu \frac{\partial^2 w}{\partial y^2} \right) \quad M_y = -D \left(\frac{\partial^2 w}{\partial y^2} + \nu \frac{\partial^2 w}{\partial x^2} \right)$$

$$M_{xy} = -M_{yx} = -D(1 - \nu) \frac{\partial^2 w}{\partial x \partial y}.$$

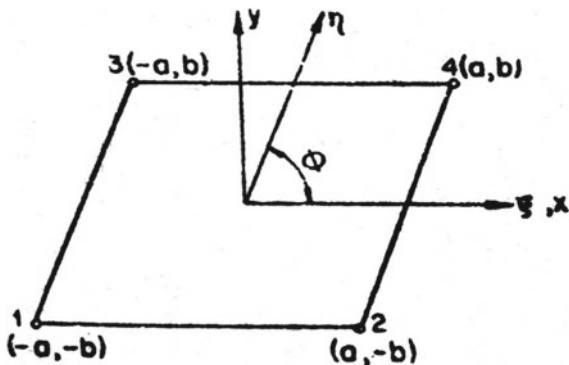
The shear force in x and y directions are given by (Fig. 3)

$$Q_x = \frac{\partial M_{yx}}{\partial y} + \frac{\partial M_x}{\partial x} = -D \frac{\partial}{\partial x} \left(\frac{\partial^2 w}{\partial x^2} + \frac{\partial^2 w}{\partial y^2} \right).$$

$$Q_y = \frac{\partial M_y}{\partial y} - \frac{\partial M_{xy}}{\partial x} = -D \frac{\partial}{\partial x} \left(\frac{\partial^2 w}{\partial x^2} + \frac{\partial^2 w}{\partial y^2} \right)$$

In view of skew geometry of the plate, it is convenient to use the transformation to oblique coordinate system ξ, η such that

Fig. 3 Schematic diagram of skew plate



$x = \xi + \eta \cos \Phi$ and $y = \eta \sin \Phi$ where Φ is the skew angle.

There are three degrees of freedom at each node—the unknown rotations are assumed along with the skew coordinate system, as such, the displacements at node 1 are $\{w_1 \theta_{\xi 1} \theta_{\eta 1}\}$. The complete displacement and the force vectors for this element are

$$X_e^T = \{w_1 \theta_{\xi 1} \theta_{\eta 1} w_2 \theta_{\xi 2} \theta_{\eta 2} w_3 \theta_{\xi 3} \theta_{\eta 3} w_4 \theta_{\xi 4} \theta_{\eta 4}\}$$

$$P_e^T = \{P_1 M_{\xi 1} M_{\eta 1} P_2 M_{\xi 2} M_{\eta 2} P_3 M_{\xi 3} M_{\eta 3} P_4 M_{\xi 4} M_{\eta 4}\}$$

In fig, two coordinate systems have been shown

$$\begin{Bmatrix} x \\ y \end{Bmatrix} = \begin{bmatrix} 1 & \cos \Phi \\ 0 & \sin \Phi \end{bmatrix} \begin{Bmatrix} \xi \\ \eta \end{Bmatrix} \tag{1}$$

Inverting Eq. (1),

$$\begin{Bmatrix} \xi \\ \eta \end{Bmatrix} = \begin{bmatrix} 1 & -\cot \Phi \\ 0 & \operatorname{cosec} \Phi \end{bmatrix} \begin{Bmatrix} x \\ y \end{Bmatrix} \tag{2}$$

Performing the necessary differentiation to Eq. (2), the following results are obtained

$$\frac{\partial \xi}{\partial x} = 1, \quad \frac{\partial \xi}{\partial y} = -\cot \Phi, \quad \frac{\partial \eta}{\partial x} = 0, \quad \frac{\partial \eta}{\partial y} = \operatorname{cosec} \Phi \tag{3}$$

By chain rule,

$$\begin{aligned} \frac{\partial w}{\partial x} &= \frac{\partial w}{\partial \xi} \cdot \frac{\partial \xi}{\partial x} + \frac{\partial w}{\partial \eta} \cdot \frac{\partial \eta}{\partial x} \\ \frac{\partial w}{\partial y} &= \frac{\partial w}{\partial \xi} \cdot \frac{\partial \xi}{\partial y} + \frac{\partial w}{\partial \eta} \cdot \frac{\partial \eta}{\partial y} \end{aligned} \tag{4}$$

Substituting the values of the differentiated quantities of Eq. (8) into Eq. (9) yields

$$\frac{\partial w}{\partial x} = \frac{\partial w}{\partial \xi} \tag{5}$$

$$\frac{\partial w}{\partial y} = -\cot \theta \frac{\partial w}{\partial \xi} + \operatorname{cosec} \theta \frac{\partial w}{\partial \eta} \tag{6}$$

Equation (10) reveals

$$\frac{\partial}{\partial x} = \frac{\partial}{\partial \xi}$$

Hence,

$$\frac{\partial^2}{\partial x^2} = \frac{\partial^2}{\partial \xi^2} \tag{7}$$

Similarly, the second equation of Eq. (8) yields in terms of the operator

$$\frac{\partial}{\partial y} = -\cot \theta \frac{\partial}{\partial \xi} + \operatorname{cosec} \theta \frac{\partial}{\partial \eta} \tag{8}$$

Hence,

$$\frac{\partial^2}{\partial y^2} = \cot^2 \theta \frac{\partial^2}{\partial \xi^2} + \operatorname{cosec}^2 \theta \frac{\partial^2}{\partial \eta^2} - 2\cot \theta \operatorname{cosec} \theta \frac{\partial^2}{\partial \eta \partial \xi} \tag{9}$$

Similarly,

$$\frac{\partial^2}{\partial x \partial y} = -\cot \theta \frac{\partial^2}{\partial \xi^2} + \operatorname{cosec} \theta \frac{\partial^2}{\partial \eta \partial \xi} \tag{10}$$

Substituting the above equations in the general equation of plate, we can obtain equations for skew plates.

3 Finite Element Modeling

In the present study, ABAQUS Simulia software is used for the analysis. Skew plates of different skew angles are modeled using continuum shell-type element SC8R Fig. 4. The analysis of the plates was done with all ends clamped subjected to a uniform pressure of 20 kPa for different aspect ratios and thicknesses. The material properties of the plate modeled were that of mild steel. (Young’s Modulus $E = 2 \times 10^{11} \text{ N/m}^2$, Poisson’s ratio $\mu = 0.3$.) [10]

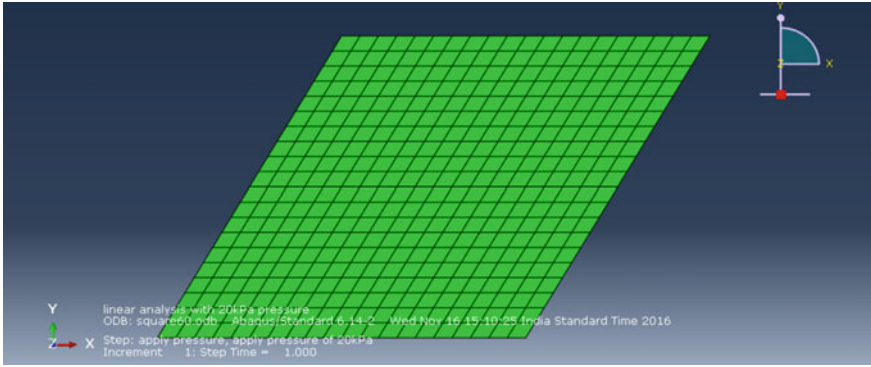


Fig. 4 Finite element model of the plate in ABAQUS

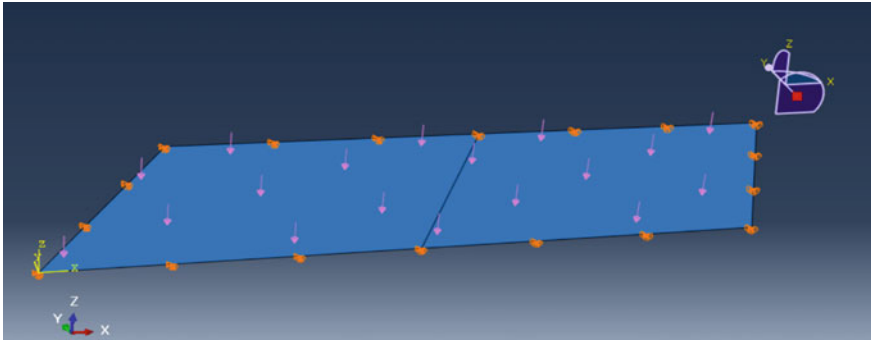


Fig. 5 Applied load on the plate model

For a constant plate thickness (6 mm), the skew angle Φ was varied from 0° to 75° for different aspect ratios, and variation of different parameters like maximum deflection, moments, and shear force at the supports are analyzed. To understand the effect of thickness, an analysis was done for a square skew plate by varying the thickness from 1 to 10 mm for different skew angles (Fig. 5).

4 Analysis of the Plate Model

4.1 Relation Between Maximum Deflection and Sides of Plates

The chart of deflection versus Skew angle for maximum deflection describes that deflection will be reduced, as the size of both sides of the plate will tend to equality

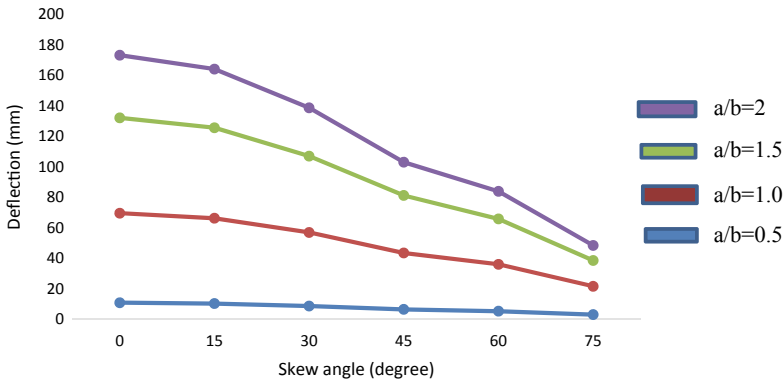


Fig. 6 Variation of maximum deflection with for different aspect ratios

in the case of skew angles, i.e.; with increment in skew angle, deflection is reducing for every aspect ratio (Fig. 6).

4.2 Variation of Longitudinal Moment M_x and M_y

When Moment versus Skew angle chart was analyzed, it can be observed that the aspect ratio of $a/b = 2.0$ shows the lower moment than the aspect ratio 1.0 and 1.5, respectively (Figs. 7 and 8).

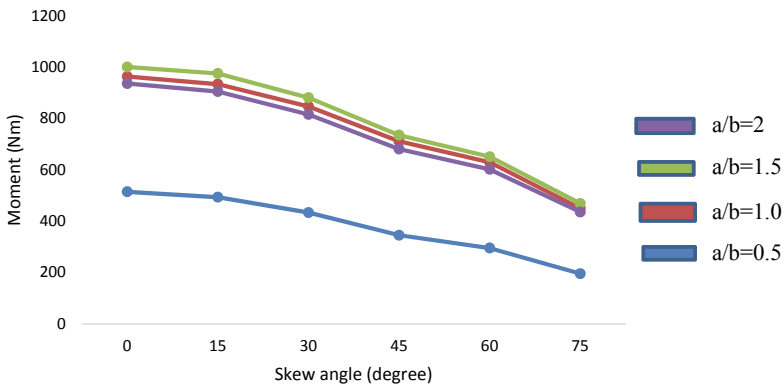


Fig. 7 Variation of longitudinal moment M_x for different aspect ratios

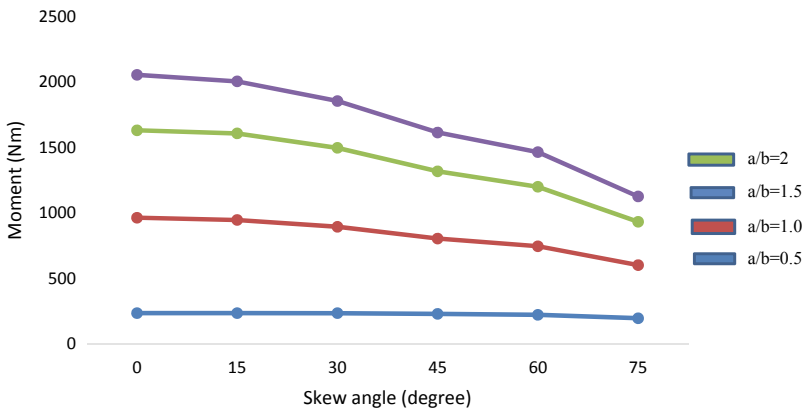


Fig. 8 Variation of longitudinal moment M_y for different aspect ratios

4.3 Variation of Torsional Moment M_{xy} , Maximum Positive and Negative Reaction Force

When the torsion versus skew angle chart was analyzed, it has been observed that $ab = 1.0$ and $a/b = 1.5$ have alternatively defeated each other at 0, 15, 30, 45, 60, 75 degree of skew angles, while $a/b = 2$ is leading in torsion up to 300 Nm to $a/b = 0.5$ at every interval of skew angle (Fig. 9). While torsion increases to 2000–14000, the $a/b = 1.5$ and 2.0 defeated each other at a regular interval, while $a/b = 1.0$ leads $a/b = 0.5$ throughout (Fig. 10). And, it inverse when torsion is in Negative Zone (Fig. 11).

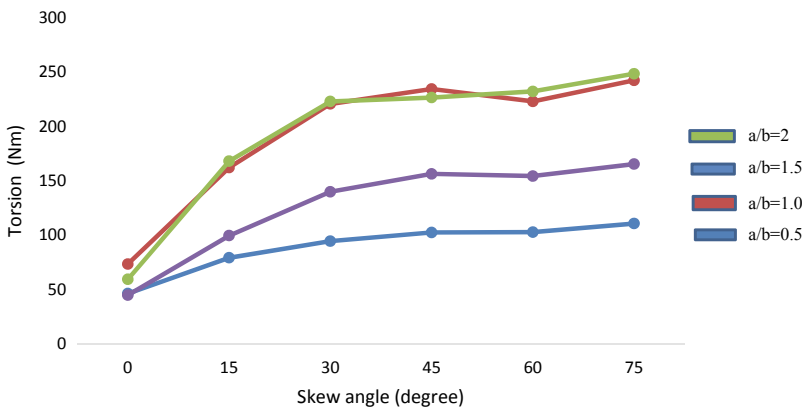


Fig. 9 Variation of torsional moment M_{xy} for different aspect ratios

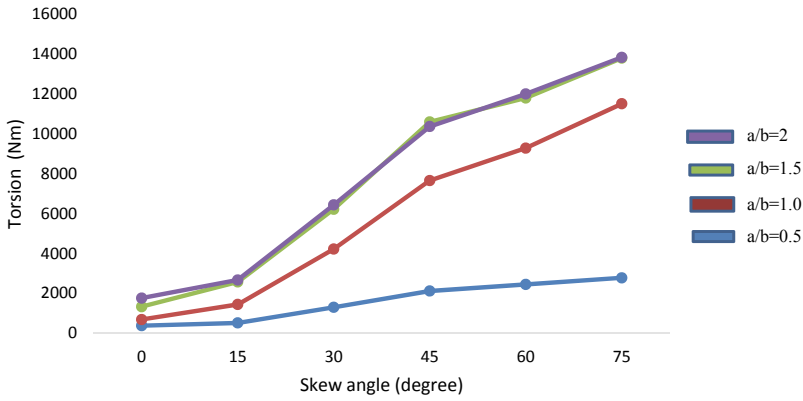


Fig. 10 Variation of maximum positive reaction force for different aspect ratio

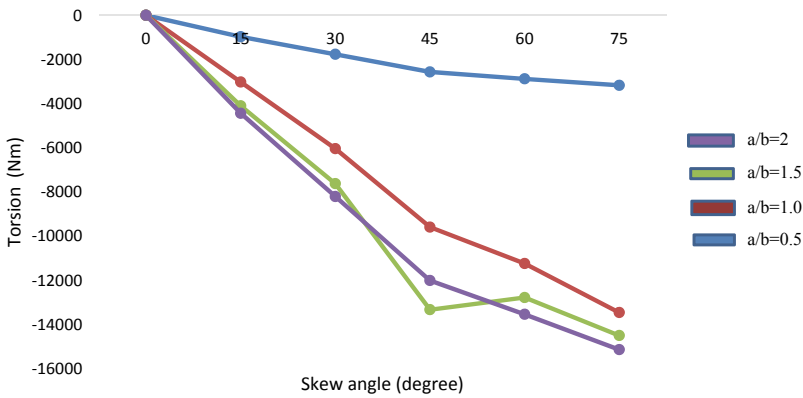


Fig. 11 Variation of maximum negative reaction force for different aspect ratios

5 Result and Discussion

The results obtained from the analysis in ABAQUS are tabulated below (Tables 1, 2, 3 and 4). The results are also graphically plotted to understand the variation in different parameters.

It can be seen in all the tables below that with the increment of aspect ratio (i.e., a/b length ratio) with an increase in skew angle, both maximum negative and maximum positive reaction force is increasing.

Table 1 Variation of parameters for aspect ratio $a/b = 0.5$

Skew angle (degree)	Max deflection (mm)	M_x (Nm)	M_y (Nm)	M_{xy} (Nm)	Max negative reaction force (N)	Max positive reaction force (N)
0	10.84	513.7	235.2	46.1	-381.5	172.8
15	10.27	492.7	235.3	79.05	-970.8	510.7
30	8.68	432.9	234.7	94.32	-1765	1295
45	6.46	344.6	229.3	102.3	-2562	2113
60	5.26	294.6	222.3	102.6	-2876	2442
75	3.044	194.8	196.2	110.5	-3169	2774

Table 2 Variation of parameters for aspect ratio $a/b = 1$

Skew angle (degree)	Max deflection (mm)	M_x (Nm)	M_y (Nm)	M_{xy} (Nm)	Max negative reaction force (N)	Max positive reaction force (N)
0	69.56	962.9	962.9	73.23	-1075	281.5
15	66.24	933.1	945.9	162	-3018	1438
30	56.94	846.3	893.7	220.6	-6036	4220
45	43.46	710.6	804.4	234.3	-9592	7658
60	36	628.7	745.5	222.9	-11,240	9285
75	21.59	449.2	601.5	242.3	-13,460	11,510

Table 3 Variation of parameters for aspect ratio $a/b = 1.5$

Skew angle (degree)	Max deflection (mm)	M_x (Nm)	M_y (Nm)	M_{xy} (Nm)	Max negative reaction force (N)	Max positive reaction force (N)
0	132.1	1000	1630	59.2	-1418	327.7
15	125.6	974.6	1606	167.9	-4098	2568
30	107	880.6	1496	222.8	-7624	6217
45	81.18	734.4	1317	226.4	-13,330	10,600
60	65.79	650.4	1199	232.1	-12,780	11,800
75	38.52	468.2	932.4	248.3	-14,500	13,800

5.1 Variation of Parameters with Skew Angles for Different Aspect Ratios

If the skew angle is increasing on a particular aspect ratio, the Maximum deflection is decreasing with a similar pattern of M_x , M_y , while M_{xy} , maximum negative reaction force, and maximum positive reaction force were increasing (follow Table 1).

Table 4 Variation of parameters for aspect ratio $a/b = 2$

Skew angle degree)	Max deflection (mm)	M_x (Nm)	M_y (Nm)	M_{xy} (Nm)	Max negative reaction force (N)	Max positive reaction force (N)
0	173.2	935.5	2053	44.62	-1638	756.3
15	164.1	904.4	2003	99.41	-4437	2666
30	138.7	815.1	1853	139.7	-8205	6434
45	103	680.1	1613	156.2	-12,010	10,370
60	83.86	601.2	1463	154.2	-13,540	12,000
75	48.37	435.1	1125	165.2	-15,140	13,840

After increasing the aspect ratio by 0.5 (i.e., $a/b = 1$) and increasing skew angle, a similar pattern (as in Table 1) has been observed in Table 2.

When further aspect ratio was increased to 1.5 and 2 with increasing skew angle, then again similar pattern continues (Tables 3 and 4).

5.2 Variation of Parameters with Thickness

If the thickness of the plate is increasing with keeping skew angle at 0° , the maximum deflection along with maximum positive reaction force is decreasing, rest all the moment like M_x , M_y and M_{xy} are also decreasing continuously. In Table 5 and in the chart, it can be observed.

When the skew angle Φ increased by 15° , the same pattern was observed in Tables 6, 7, 8, 9 and 10 as in Table 5.

In Fig. 12, the deflection versus thickness for different skew angle, i.e., 0, 15, 30, 45, 60, and 75 is presented. Here, it can be clearly observed that, with the increase in thickness, the deflection was reduced at each skew angle.

Table 5 Variation of different parameters with thickness for skew angle $\Phi = 0^\circ$

Thickness (mm)	Max deflection (mm)	M_x (Nm)	M_y (Nm)	M_{xy} (Nm)	Max negative reaction force (N)	Max positive reaction force (N)
1	292.6	233.89	513.1	10.03	0	226.7
2	86.6	233.9	513.2	11.16	0	189.1
4	20.84	234	513.7	15.51	0	172.8
6	5.217	234.42	514.3	17.72	0	170.2
8	3.36	234.93	514.9	18.74	0	169.3
10	1.12	234.55	515.6	19.21	0	165.8

Table 6 Variation of different parameters with thickness for skew angle $\Phi = 15^\circ$

Thickness (mm)	Max deflection (mm)	M_x (Nm)	M_y (Nm)	M_{xy} (Nm)	Max negative reaction force (N)	Max positive reaction force (N)
1	250.6	213.79	493.34	21.03	-256.02	436.97
2	76.6	212.9	492.78	22.49	-230.5	418.81
4	15.84	213	493.59	24.34	-200.34	400.28
6	4.217	213.95	494.3	29.27	-187.05	370.82
8	2.96	213.49	493.29	30.47	-157.8	349.36
10	1.03	213.59	493.6	32.12	-146.68	321.59

Table 7 Variation of different parameters with thickness for skew angle $\Phi = 30^\circ$

Thickness (mm)	Max deflection (mm)	M_x (Nm)	M_y (Nm)	M_{xy} (Nm)	Max negative reaction force (N)	Max positive reaction force (N)
1	241.6	200.64	458.51	40.15	-416.02	659.54
2	68.6	203.9	456.28	44.61	-409.5	635.1
4	11.84	201	458.47	46.15	-381.5	614.98
6	3.62	201.52	457.93	47.62	-352.2	601.76
8	2.56	202.3	458.19	50.74	-325.8	582.15
10	0.98	200.85	458.06	53.81	-302.8	565.48

Table 8 Variation of different parameters with thickness for skew angle $\Phi = 45^\circ$

Thickness (mm)	Max deflection (mm)	M_x (Nm)	M_y (Nm)	M_{xy} (Nm)	Max negative reaction force (N)	Max positive reaction force (N)
1	228.6	189.9	427.81	70.86	-569.28	816.7
2	55.6	187.17	426.2	74.28	-548.95	784.41
4	10.24	190.74	426.7	76.98	-532.15	752.98
6	3.12	189.92	427.76	79.2	-500.65	723.62
8	2.16	188.3	428.9	81.4	-487.98	709.13
10	0.91	190.75	426.46	85.56	-479.41	695.28

The moment M_x versus thickness for different skew angles, i.e., 0, 15, 30, 45, 60, and 75 is presented. Moment M_x at $\Phi = 30$ and 45° were deviated (not much) after increasing the thickness. Rest at all skew angles, the moment was observed constantly (Fig. 13).

The moment M_y versus thickness for different skew angles, i.e., 0, 15, 30, 45, 60, and 75 is presented. Moment M_y was constant at every angle when thickness increases (Fig. 14).

Table 9 Variation of different parameters with thickness for skew angle $\Phi = 60^\circ$

Thickness (mm)	Max deflection (mm)	M_x (Nm)	M_y (Nm)	M_{xy} (Nm)	Max negative reaction force (N)	Max positive reaction force (N)
1	212.6	173.16	395.15	94.32	-800.02	1021.57
2	48.6	175.79	396.2	96.16	-776.4	1000.91
4	9.44	173.79	395.47	100.51	-746.39	972.38
6	2.82	174.52	395.3	107.72	-721.53	945.9
8	1.56	173.93	397.69	110.74	-688.95	926.31
10	0.85	173.5	396.36	119.21	-676.19	897.46

Table 10 Variation of different parameters with thickness for skew angle $\Phi = 45^\circ$

Thickness (mm)	Max deflection (mm)	M_x (Nm)	M_y (Nm)	M_{xy} (Nm)	Max negative reaction force (N)	Max positive reaction force (N)
1	182.6	155.84	359.71	120.6	-1040.54	1325.97
2	38.6	155.9	358.42	127.81	-1016.97	1267.1
4	8.74	154.46	359.37	135.51	-991.25	1239.28
6	2.12	153.2	359.3	137.72	-965.82	1197.42
8	1.24	154.83	357.09	145.49	-942.38	1153.79
10	0.69	154.95	359.66	150.42	-908.68	1105.08

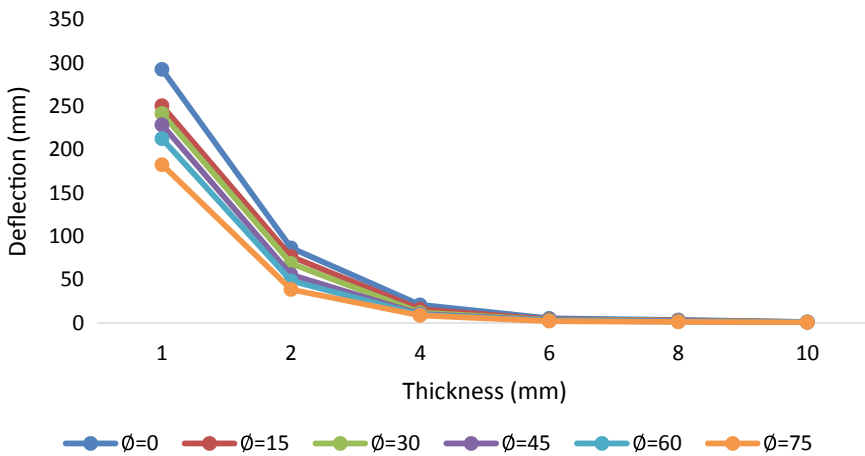


Fig. 12 Variation of maximum deflection with thickness

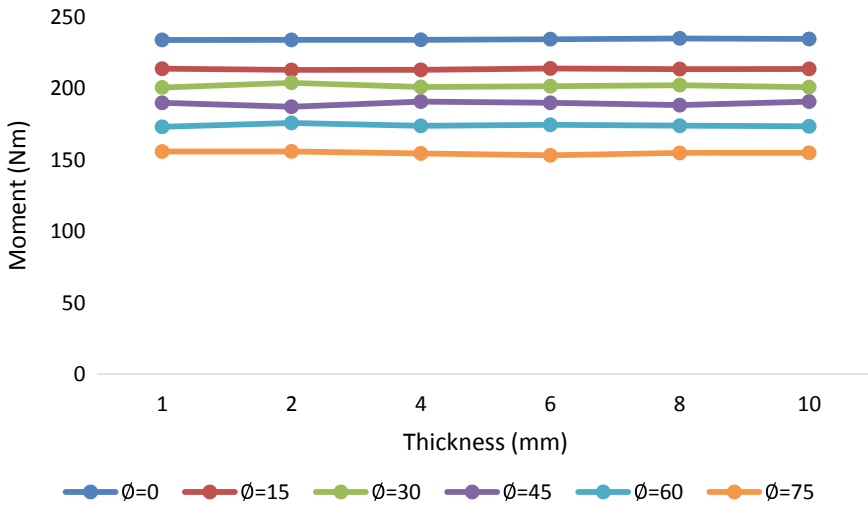


Fig. 13 Variation of moment M_x with thickness

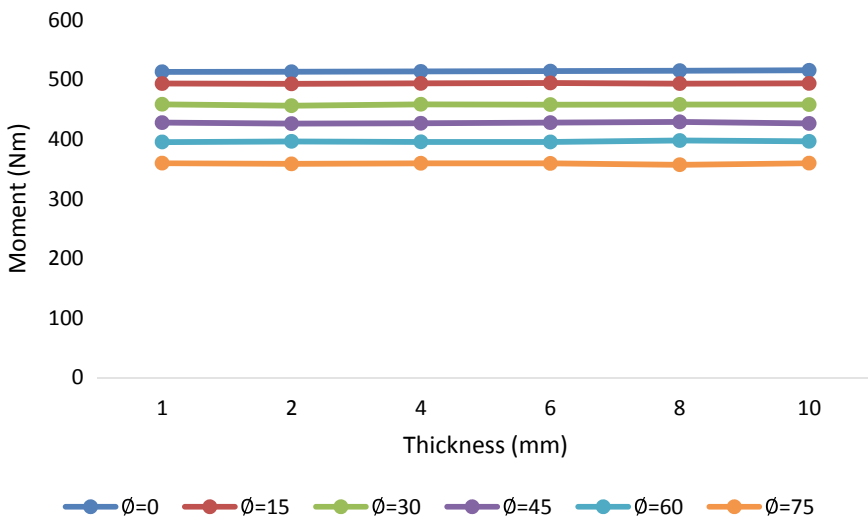


Fig. 14 Variation of moment M_y with thickness

In Fig. 15, the torsional moment M_{xy} versus thickness for different skew angles, i.e., 0, 15, 30, 45, 60, and 75 is presented. Here, in this figure, it can be observed that torsional moment M_{xy} was increasing at every skew angle.

In Fig. 16, the negative reaction versus thickness graph is presented. Here, it can be concluded that except skew angle of 60° , almost all skew angles presented gains in terms of negative reaction when thickness increases.

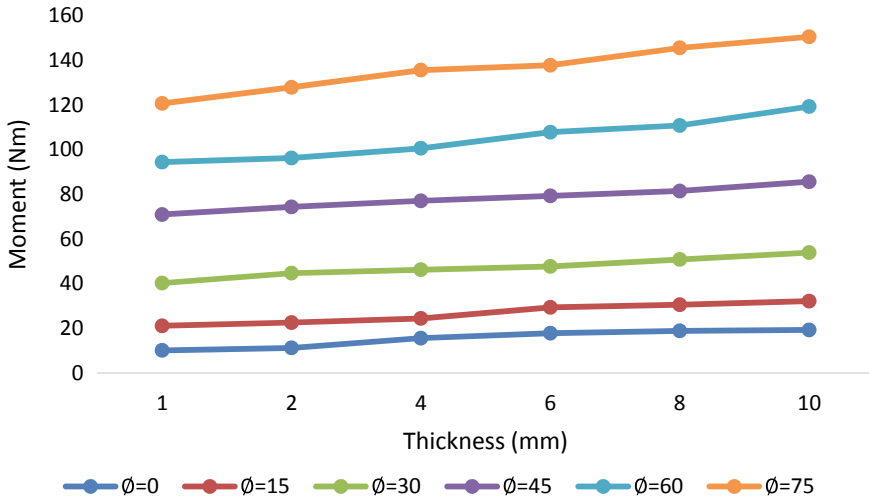


Fig. 15 Variation of torsional moment M_{xy} with thickness

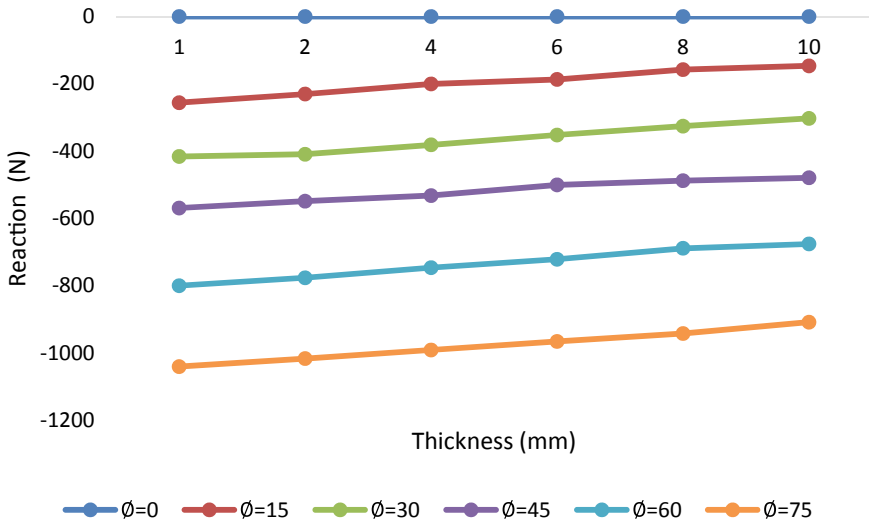


Fig. 16 Variation of negative support reaction with thickness

In Fig. 17, the positive reaction versus thickness graph is presented. Here, it can be concluded that, at all skew angles, it shows a loss in terms of positive reaction when thickness increases.

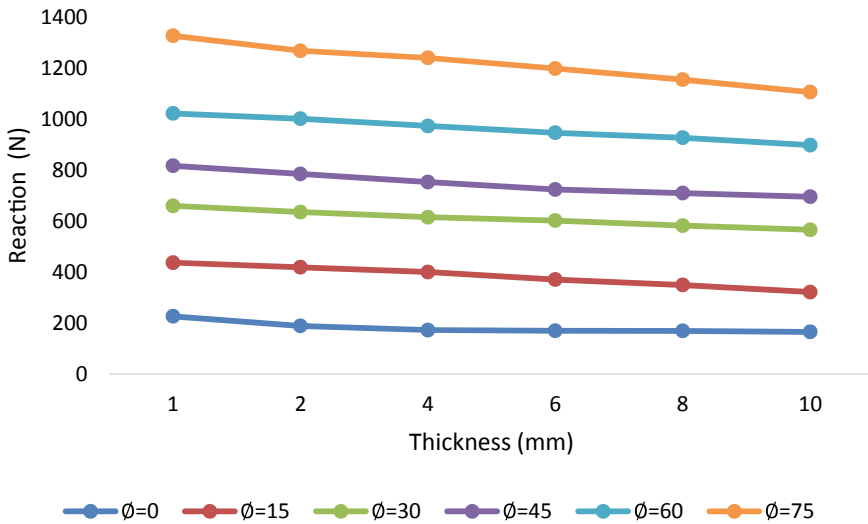


Fig. 17 Variation of positive support reaction with thickness

In Fig. 18a, b, c, d, e, and f, we can observe the principal stress contours at different skew angles show the point of maximum and minimum stress locations on the plate, and this can be used at the time of designing the plate at a particular skew angle and load.

6 Conclusion

In the present work, an effort has been made to analyze the behavior of skew plates with material properties $E = 2 \times 10^{11} \text{ N/m}^2$, Poisson's ratio $\mu = 0.3$ under uniform pressure of 20 kPa. From the results, it is observed that the maximum deflection at the center of skew plates decreases with an increase in skew angle for any fixed value of aspect ratio and this behavior is consistent for all aspect ratios. Observation made based on results obtained is

1. The maximum deflection is found to increase with an increase in the aspect ratio of the plate.
2. The moments M_x and M_y at the mid-span of the plate decreases with an increase in skew angle for any fixed value of aspect ratio.
3. The torsional moment M_{xy} increases with an increase in skew angle for a fixed value of aspect ratio and this behavior is consistent for all aspect ratios.
4. A negative reaction force is found to develop at the obtuse corners of the plate. Both positive and negative reaction forces are found to increase with an increase in skew angle for all values of aspect ratios.

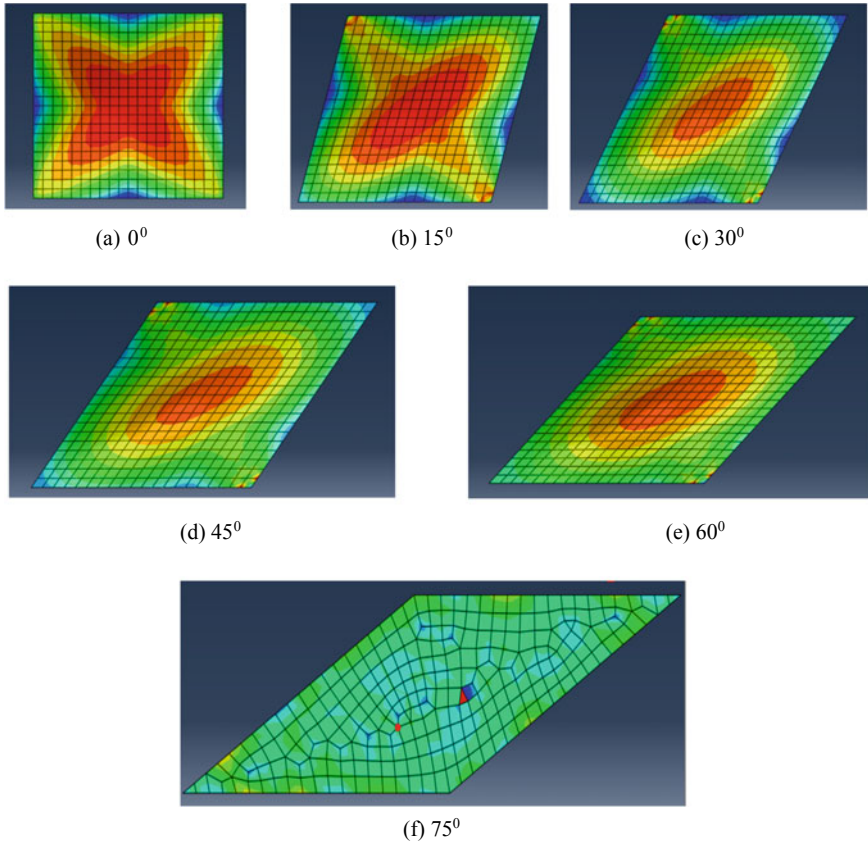


Fig. 18 Principal stress contours for different skew angles

Variation in different parameters with thickness of the plate is also analyzed in the present work. Deflection at the center was found to decrease rapidly with an increase in the thickness of the plate. With an increase in the thickness of the plate, torsional moment M_{xy} was found to increase marginally, but the longitudinal moments M_x and M_y were found to remain fairly constant. The reaction forces at the supports were found to decrease with the increase in the thickness of the plate.

References

1. Timoshenko S, Woinoswksy-Kreiger S (1959) Theory of plates and shells. Mc Graw hills Publication
2. Das D, Sahoo P, Saha K (2010) Large deflection analysis of skew plates under uniformly distributed load for mixed boundary conditions. Int Eng Sci Technol 2(4):100–112

3. Girish GB, Srinivasa CV, Suresh YJ (2011) Buckling of skew plates subjected to linearly varying in-plane edge load using finite element method. In: Proceedings of international conference on advances in robotic, mechanical engineering and design 2011. 02.ARMED.2011.01.18
4. Srinivasa CV, Suresh YJ, Kumar WPP (2012) Buckling studies on laminated composite skew plates. *Int J Comput Appl* (0975 – 8887) 37(1):35–47
5. Naghsh A, Azhari M (2015) Non-linear free vibration analysis of point supported laminated composite skew plates. *Int J Non-Linear Mech* 76:64–76
6. Singha MK, Daripa R (2007) Nonlinear vibration of symmetrically laminated composite skew plates by finite element method. *Int J Non-Linear Mech* 42:1144–1152
7. Dey P, Singha MK (2006) Dynamic stability analysis of composite skew plates subjected to periodic in-plane load. *Thin-Walled Struct* 44:937–942
8. Farag AM, Ashour AS (2000) Free vibration of orthotropic skew plates. *J Vib Acoust* 122:313–317
9. Chun PJ, Lim YM (2011) Analytical behavior prediction for skewed thick plates on elastic foundation. In: *Mathematical problems in engineering*, Article ID 509724, 19 pages
10. Lu P, Shao C (2012) Simplified analysis of a skew-plate bridge based on grillage analogy model. *IES J Part A Civil Struct Engi* 5(4):253–262. <https://doi.org/10.1080/19373260.2012.695251>

Behavior of Liquid Storage Tank Under Multidirectional Excitation



Sourabh Vern, Mahendra Kumar Shrimali, Shiv Dayal Bharti,
and Tushar Kanti Datta

Abstract By revoking the effect of vertical component in the analysis of different response quantities of LST may differ from the true response of structure during a seismic event. This paper aims to study the effect of the vertical component of an earthquake on various response quantities, namely tank wall displacement, surcharge at the free surface of the water, overturning moment, and base shear. The study is compiled with the help of nonlinear time history analysis in an explicit finite element module on ABAQUS platform. For illustration, a 10-m long-rectangular liquid storage tank has been modeled by using a solid element with fluid medium modified by the arbitrary Lagrangian and Eulerian (ALE). Investigation for response is done first with bidirectional and then with the vertical component is considered. Some notable conclusions of the study include vertical component alone, which increases the responses to an order of about 30%.

Keywords FEM · Liquid storage tanks · ALE · FSI

1 Introduction

An important civil structure must be able to keep functioning or should be partially able to work even after an earthquake hazard because the complete collapse in any life-supporting structures can be very damaging for the recovery of a nation from the disaster. One such important structure are liquid storage tanks (LST): the omnipresent

S. Vern (✉) · M. K. Shrimali · S. D. Bharti
National Centre for Disaster Mitigation and Management, MNIT Jaipur, Jaipur, India
e-mail: sourabh.vern@gmail.com

M. K. Shrimali
e-mail: shrimalimk@gmail.com

S. D. Bharti
e-mail: sdbharti@gmail.com

T. K. Datta
Department of Civil Engineering, IIT Delhi, Delhi, India
e-mail: tushar_k_datta@yahoo.com

application and implementation rivet extra attention than that of normal load-bearing structures. There are several historical evidence that show that failures of LST are proven deadly, and their repercussions can last from a few months to more than a decade. Few such examples in which LST are witnessed to collapse are 1933 Long Beach Earthquake, California, USA; 1960 Chile Earthquake, Chile; 1964 The Great Alaska Earthquake, Alaska, USA; 1978 Miyagi Prefecture Offshore Earthquake, Japan; and 2003 Tokachi Offshore Earthquake, Japan. As most of these tanks are used to store liquefied gases and fluids which have a lower flash point a simple spark developed by contact between tank roof and wall can set a full surface fire in the tank.

Authors in the past have taken different approaches to tackle analysis of this problem. Housner [1] represented more defined and exact analyses in which pressure can be subdivided into two major parts, Convective and Impulsive. Impulsive pressure is exerted by the inertial response of the fluid which is because of the inertial response of the tank walls. Whereas the convective response is produced due to the oscillation of the liquid. The author presented a simplified procedure which has been prescribed by API standard 650 [2]. Additional information for measuring the sloshing height, the impact forces due to the sloshing on the columns of the roof is given along with the change in the magnitude of the hoop tension due to the earthquake ground motion. the shift in the design approach is observed from the Housner's rigid tanks in which pseudo-acceleration's spectral value is taken instead of maximum ground acceleration.

Taken up the fluid–structure interaction inside a liquid storage tank by finite element method with emphasis on dynamic and buckling analyses [3]. Lagrangian–Eulerian kinematical description for modeling fluid subdomains in fluid–structure interaction problems, the finite rotation effects in the numerical integration of constitutive rate equations arising in large deformation analysis and the implicit-explicit finite element techniques for transient analysis. Disarray is reported while extracting response for high Reynolds number flows and complex shell buckling. Malhotra et al. [4] explained the design criteria for the simplified cylindrical ground support liquid storage tank. While examining the design criteria, impulsive and convective part of the liquid in flexible steel or concrete tanks fixed to rigid foundations is considered. Virella et al. [5] extracted the sloshing natural periods and their modal pressure distributions by the influence of nonlinear wave theory for two-dimensional behavior rectangular tanks. Cao et al. [6] studied the paralleled SPH codes are programmed to study the liquid sloshing in both two-dimensional and three-dimensional tanks of single and multi-degrees of freedom. A dynamic response analysis of vertically excited liquid storage tanks including both liquid-tank and liquid-soil interaction [7]. The ground excited tank-liquid-soil system is transformed by the generalized-coordinate approach' I and then it is analyzed by the complex frequency response method.

Evaluate dynamic response of an elastic circular cylindrical tank having a rigid base under a vertical excitation taking into consideration the interaction with the foundation soil, a more representative solution for the problem in the frequency domain is obtained where the soil is appropriately modeled by frequency-dependent

parameters [8]. The effects of vertical excitations have shown that significant hoop stresses can be developed in the walls of liquid storage tanks, and for intense motion, these cannot be ignored in comparison with the hydrostatic hoop stresses used in the design of such tanks. Presented a technique for evaluating the dynamic response of an upright circular cylindrical liquid storage tank to a vertical component of ground shaking, considering the flexibility of the supporting medium [9]. It is shown that soil-structure interaction reduces the hydrodynamic effects and that the consequences of such interaction may be approximated with good accuracy by a change in the natural frequency of the tank-liquid system and by an increase in damping. Investigated the method for analyzing the earthquake response of elastic, cylindrical liquid storage tanks under vertical excitations [10]. Tank response under the simultaneous action of both vertical and lateral excitations is calculated to evaluate the relative importance of the vertical component of ground acceleration on the overall seismic behavior of liquid storage tanks. It should be noted that vertical excitation is important in the seismic analysis of reinforced concrete tanks since these structures are more susceptible to the increase in hoop stresses.

Kianoush and Chen [11] conducted the study to determine the response of concrete rectangular liquid storage tanks subjected to vertical ground acceleration is investigated. The maximum response due to vertical acceleration can be as high as 45% of that due to the horizontal component. It is concluded that the effect of the vertical component of ground motion should be considered in the analysis of rectangular tanks for liquid containing structures. This is especially of significance for the near-field zones which require further investigation. Ghaemmaghami and Kianoush [12] developed the finite-element method is used to investigate the seismic behavior of rectangular liquid tanks in two-dimensional space. The method can consider both impulsive and convective responses of the liquid-tank system. Also, applying the vertical excitation will lead to an increase in the convective response of the system. However, it does not affect the impulsive behavior significantly. This increase is more noticeable in tall tank mode. Morris et al. [13] reported a baseline of the percentage increase when switching to the vertical response period and an understanding of how each of the different code's provisions can impact the design forces. As other codes move to adopt the design vertical response spectrum the provisions used to predict the demand should also be reviewed for accuracy.

For controlling the responses of the liquid storage tank, there are several techniques that are being employed in the tanks. Common approach witnessed by several authors is to construct various types of obstruction inside the tank or along the wall to prevent or completely stop the sloshing of the inertial mass of the fluid due to earthquake ground motion. Stricklin and Baird [14] surveyed the Miles' method for determining the damping produced by ring baffles in cylindrical tanks was conducted. O'Neill's modification of Miles' equation which eliminates free surface wave height from this equation is determined. The potential of baffles in increasing the hydrodynamic damping of sloshing in circular-cylindrical storage tanks is investigated, the ability of baffles in reducing the sloshing effects in storage tanks that are especially broader than fuel containers were under question [15]. A numerical model has been developed to study three-dimensional (3D) liquid sloshing in a tank with

baffles [16]. The numerical model solves the spatially averaged Navier–Stokes equations. Systematic numerical simulations are carried out to investigate the sloshing dynamics of liquid in a storage tank, subjected to seismic excitation [17]. To suppress the free surface fluctuations and the associated slosh force, two types of baffles viz., ring and vertical baffle are examined. Spectral analysis of free surface displacement and temporal variation of pressure demonstrate dominant contribution from the fundamental sloshing mode.

Another method which seems to have high reliability and a longer lifespan is the isolation of the structure. The isolation of superstructure can be developed by use of a passive device commonly referred to as base-isolator at the base. There are several base isolation techniques, but due to their large area of applications only two stands out. First being the lead rubber bearing (LRB) and the second is the frictional pendulum system (FPS) which is a sliding type of isolator. A parametric study is conducted to study the effects of important system parameters on the effectiveness of seismic isolation of the liquid storage tanks [18]. It has been found that the bi-directional interaction of frictional forces has noticeable effects and if these effects are ignored, then the sliding base displacements will be underestimated which can be crucial from the design point of view. The seismic response of liquid storage tanks isolated with variable friction pendulum system is investigated under six recorded near-fault ground motions [19]. To improve the safety of concrete RLSS under earthquake action, an energy dissipation method of sliding isolation and limiting devices for concrete RLSS is proposed, the dynamic responses of sliding isolation concrete RLSS under bidirectional earthquake are studied [20].

The present study aims to investigate the effect of the tri-directional earthquake motion on a liquid storage tank and compare the response quantity of interest with that of the bi-directional earthquake. Thus, by concluding the change in the response quantities by the vertical component of the earthquake. The effect of vertical component is studied for two strong ground motion and one little weaker ground motion, to conclude the vertical component will result in an increase of response quantities in both cases.

2 Methodology

The analysis of the liquid storage tank under the earthquake motion involves different physical phenomena. In the sloshing motion, the major part of the interaction is the motion of the container. Apart from the interaction between the two different states namely, liquid and solid, there is the interaction of the fluid media with itself which causes the ripple effect which in effect increases the sloshing height.

For a nonlinear solution, a method for analysis required for extracting response quantities must be able to handle the non-linearity effect along with fluid–structure interaction (FSI). Thus, a robust finite element application method is adopted for long duration nonlinear time history analysis.

The non-linearity is solved in ABAQUS by the help of explicit central-difference integration rule. The simplicity in solving the problem doesn't provide the necessary computational efficiency which is involved with the explicit dynamic procedure. The input of the diagonal mass matrix at initial of the time step increment are resulted from the Eq. (1)

$$\ddot{u}_{(i)}^N = (M^{NJ})^{-1} (P_{(i)}^J - I_{(i)}^J) \tag{1}$$

Here M_{NJ} is the mass matrix, P_J is the load vector, and I_J is the force vector. As given in the Eq. (2) the inverse of the lumped mass matrix is first solved, the number of iterations requires for the solution is equal to the number of degrees of freedom which is obtained by the multiplication between the inverse of the mass matrix and the inertial force.

$$\dot{u}^{(i+\frac{1}{2})} = \dot{u}^{(i-\frac{1}{2})} + \frac{\Delta t^{(i+1)} + \Delta t^{(i)}}{2} \ddot{u}^{(i)} \tag{2}$$

$$\dot{u}^{(i+1)} = \dot{u}^{(i)} + \Delta t^{(i+1)} \ddot{u}^{(i+\frac{1}{2})} \tag{3}$$

The equation of motion for the solution is integrated using the central difference integration rule as stated in Eq. (2), where \dot{u} and \ddot{u} are the velocity and acceleration values respectively. The superscript (i) indicates the incremental series number and ($i - 1/2$) and ($i + 1/2$) refers as mid incremental series number.

2.1 Modelling of Liquid Storage Tank

The finite element modeling for the liquid storage tank is defined. The analysis needs to be compatible with the fluid part of the storage tank which also accounts for the fluid–structure interaction. The tank is modeled with a solid element which is an eight noded linear brick element with reduced integration and hourglass control (C3D8R). The second part of the assembly is the fluid that is modeled with the solid element and the combined hourglass control, which smoothens the analysis as fluid is imparted to a higher level of distortion. The fluid element is refined with the powerful feature, i.e. Arbitrary Lagrangian and Eulerian (ALE). The tank taken in the analysis is flexible so that the inertial effect of the fluid media due to the ground motion can be measured. To extract result of higher accuracy, a mesh convergence is taken up, and convergence is reported at a mesh size of 0.05 m for the fluid media and 0.1 m for the tank elements.

To stimulate an Earthquake ground motion in a liquid storage tank earthquake time history in the form of acceleration time history is given and applied at the base of the tank. A single dynamic explicit step is defined for the earthquake motion, the value of period is taken differently for respective ground motion. While considering

the effect of the union of two different media the need of an interaction property is necessary. A surface to surface contact is defined between the fluid and inner tank surface. The advantage of defining the surface to surface contact is that, it takes into the consideration of the sharp edges which develops an issue of geometry cumbersome that prolongs the computational time.

For the comparative study, the ground motion is applied in the base concerning the X, Y and Z axis. The explicit procedure involves the use of many small-time increments. It uses the central difference operator which is conditionally stable. The value of stable time increment is given by Eq. 4. The presence of high-frequency oscillations increases the stable time increment thus, to mitigate the effect of these oscillations of minuscule order of damping is added into the operator.

$$\Delta t \leq \frac{2}{\omega_{max}} \left(\sqrt{1 + \xi^2} - \xi \right) \quad (4)$$

During the analysis progress, a global estimation program in the explicit module finds out the maximum frequency which is the maximum of the whole system. In the nonlinear problems, the frequency of the system is subjected to changes which in turn changes the stability limit.

The modeling of the fluid media is taken care by the aid of Mie-Gruneisen equation of state in Abaqus explicit module. The equation of state provides a media characteristic of hydrodynamics with respect of volumetric strength. Its ability to calculate the pressure as a function of the mass density and the specific energy makes it a robust tool in dealing with the fluid media.

The Mie-Gruneisen Equation of State represented in first-order form of polynomial Eq. (5).

$$p - p_H = \Gamma_\rho (E_m - E_H) \quad (5)$$

Here, p_H and E_H are Hugoniot pressure and specific energy as a function of density, whereas Γ is known as Gruneisen ratio and is equals to the value given in Eq. (6)

$$\Gamma = \Gamma_o \frac{\rho_o}{\rho} \quad (6)$$

The above equation is then simplified into the Eq. (7)

$$p = p_H \left(1 - \frac{\Gamma_o \eta}{2} \right) + \Gamma_o \rho_o E_m \quad (7)$$

To fit the Hugoniot equation in a linear form, a common Hugoniot equation then becomes as Eq. (8)

$$p_H = \frac{\rho_0 c_0^2 \eta}{(1 - s\eta)^2} \quad (8)$$

In the Eq. (9), c_0 and s represents the single order relationship between the linear shock velocity, U_s and particle velocity, U_p in the form of

$$U_s = c_0 + sU_p \quad (9)$$

By considering the above equation of state $U_s - U_p$ Hugoniot form is presented in the Eq. (10) given below.

$$p_H = \frac{\rho_0 c_0^2 \eta}{(1 - s\eta)^2} \left(1 - \frac{\Gamma_o \eta}{2} \right) + \Gamma_o \rho_0 E_m \quad (10)$$

The ALE is an adaptive meshing tool which gives the advantage to maintain the integrity of the original mesh. A result of the unaffected topology of the fluid media is observed which is allowed due to the independent motion of the mesh nodes, therefore even the during the high scale deformation, the analysis doesn't lose its stability and a steady flow of analysis is maintained. The fluid mass is given the adaptive mesh properties in the present problems. The movement of the mesh covers the same domain of material in the direction which is normal to the motion of the material boundary. Adaptive meshing proved to be pragmatic in this analysis as the fluid media is expected to be deformed severely which leads to termination of the simulations. Not only the ALE posses the property to solve the dramatic change in the material mesh but also it provides results of faster and higher accuracy as compared to the pure Lagrangian approach. Due to the plethora amount of the element distortion and convolution of the mesh, which induces a loss in computational precision and augments the size of the stable time step.

3 Numerical Study

For the present study, a flexible rectangular tank is taken with ground support. To study the vertical effect of earthquake component in the liquid storage tank, different earthquakes are taken into the consideration with different peak ground acceleration (PGA) values. The tank is taken as a steel tank with a thickness of 0.2 m and with a cross-sectional size of 10 m by 10 m. The steel structure is provided with 3% damping. The height of the fluid stored in the tank is of 7.5 m. The sundry properties of the tank and fluid media are given in the Tables 1 and 2.

To develop a lucid conclusive study for the effects of vertical components of earthquakes, various response quantities are extracted. The response of the liquid storage tank is represented with respect to the period of the earthquakes. The paramount study of the interaction between the fluid and tank structure surface with first only the bi-directional horizontal components and then after with tri-directional interactions

Table 1 Material properties for the tank and Fluid media

STEEL	FLUID
Modulus of Elasticity, $E_s = 200 \text{ GPa}$	Density, $\rho_w = 983.204 \text{ Kg/m}^3$
Density, $\rho_s = 7900 \text{ Kg/m}^3$	Equation of state: $c_0 = 1450, s = 0, \gamma_0 = 0$
Poisson's ratio, $\nu = 0.3$	Dynamic Viscosity = 0.001 N-sec/m^2

Table 2 Earthquake record data taken for the analysis

Name of earthquakes	Recording station	Time interval (s)	PGA in x-direction (g)	PGA in y-direction (g)	PGA in z-direction (g)
Bhuj Earthquake (2001)	IIT-R	35	0.69	0.64	0.6
Tabas Earthquake (1978)	Iran	40	0.41	0.35	0.32
Taiwan Earthquake (1986)	Hualien	35	0.195	0.2	0.17

along with vertical components of various ground motions are taken. The impact of material flexibility in tank walls in the analysis of the present study is included while extracting the responses. The responses which are taken for the comparative study are the top board displacement of the tank wall, sloshing height of the fluid media, base shear, overturning moment of the liquid storage tank, shear stress and hoop stress in the tank wall. The development of the time histories of the various response quantities are first extracted and are then are put are in a juxtaposition. The sloshing height of the fluid is extracted at the corner of the tanks. The top board displacement of the tank wall is computed at the right side of the wall in the y-direction. Various stresses which are shear stress and hoop stresses are calculated for the tank wall. To get a profound detail of the tank overall stability and behaviour under the given interactions both the shear force and overturning moment of the tank at the base are provided.

It can be observed from the Fig. 1a for the bi-directional interaction alone that motion of the fluid mass tends to increase first as the time history of the earthquake is proceed. The motion of the sloshing height in the tri-directional scenario can be observed somewhat same, but as the analysis is progressed towards the ends, it can be seen that magnitude of the sloshing height is more than that of the bi-directional interaction.

The top board displacement is discovered for the Bhuj earthquake in Fig. 1b to fold the relative pattern in both the bi-directional and tri-direction interaction.it can be seen from the graph that the peak values here is by the tri-directional interaction of the ground motion. In the case of the tank structural stability, the time history of

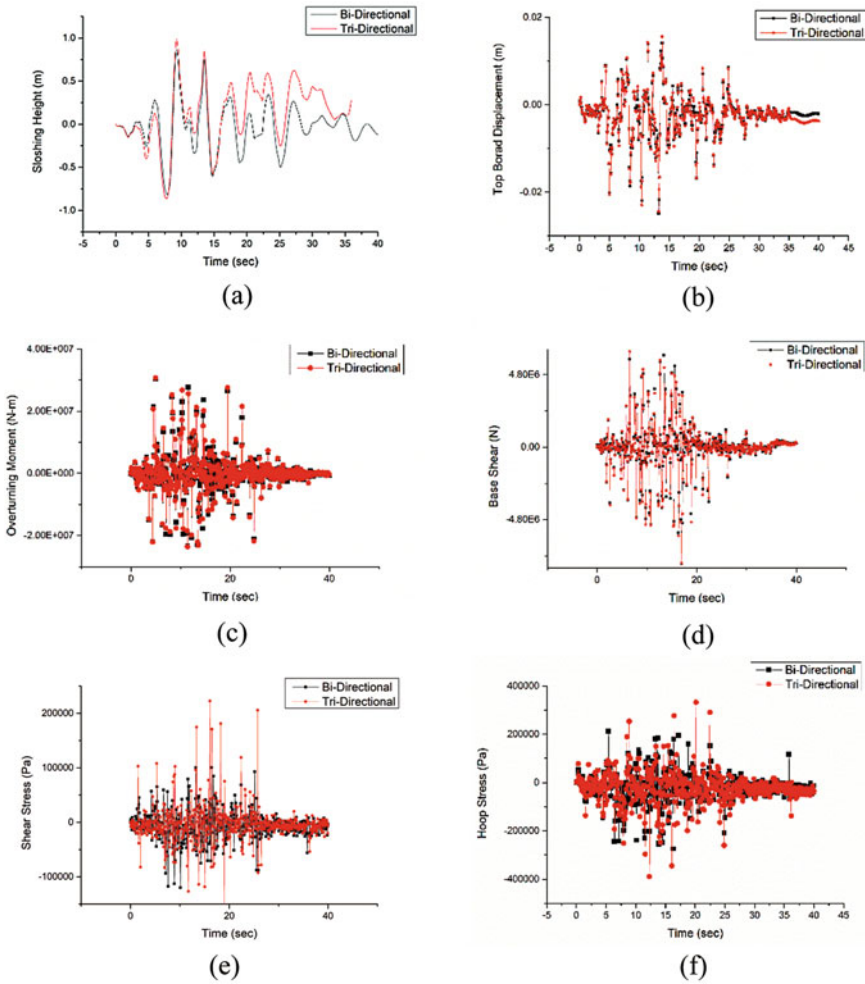


Fig. 1 Various response quantities for the Bhuj Earthquake, **a** sloshing height **b** top board displacement **c** overturning moment **d** base shear **e** shear stress and **f** hoop stress

the overturning moment and base shear shows the peak values at the relatively the nascent stage of the time history. A lucid bifurcation can be marked between the peak values of the tri-directional and bi-directional earthquake interaction. The evidence in the literature review supports the response quantities for the present study are in synchronization, as the vertical component of the ground motion has weakened the stable phase of the liquid storage tank. By examining the stresses time history of the tank wall, it can be clearly justified that due the third component of the ground motion a hike in the sloshing height is observed which in turn impact the tank walls and that results in augmentation in the shear stress and hoop stress as described by the Fig. 1 e, f.

For the case of the Tabas Earthquake, one of the highlighted properties is that the PGA level of the ground motion is considerably lower than that of the Bhuj ground motion. The response quantities seem to be dormant by a change in PGA level and display the same trend as that of the higher PGA ground motion. The various response quantities show an unbalance in the peak values. The absolute peak values of the Tri-directional interaction seem to be the dominant one. Although the tri-directional interaction leads the peak values at almost every increment, in case of the top board displacement of the tank wall the difference is small. The effect of the light vertical contribution in the tri-directional response can be seen for the overturning and base shear time history plot. The peak values the stability variables, i.e., overturning moment, and base shear are achieved between the initial and mid-interval of their time history as shown in Fig. 2c, d. The peak values of these response quantities are observed at the somewhat same location as that of the sloshing height. It can be evidently because of the unbalanced inertial force that is generated by the sloshing mass. Thus, to mitigate this unbalanced mass an energy ameliorating obstruction need are demanded. While determining the shear and hoop stresses in the tank wall, the response displayed peak values at a prolonged time. The values are found near the latter stage of the time history. The peak values are of order twice of that are observed at the initial passage of the time. A significant change in time history values is seen before the half interval of the hoop stress time history as given Fig. 2e, f. The response graph reaches a maximum low value. The order of the difference between both interactions is seen of the highest order here.

The results obtained by the Taiwan ground motion holds the trends, as observed in the above couple of ground motion. In Fig. 3a the time history response of the sloshing in the fluid media is plotted. The maximum value in the sloshing height is marked by the tridirectional interaction. The PGA level taken in this ground motion analysis is the lowest. The value of the sloshing height in the initial stage of the program has developed a crescent look in the tri-directional part. After that on somewhat every peak developed in the response are shadowed by the tri-directional response. The value uncovered in the top board displacement of the tank wall seems to be the quite small it may be because of the elastic strength of the steel. The top board displacement is achieving its zenith value at the nearly same position when the sloshing in the tank is at its highest coordinate. The values in the stability parameters follow the quite a similar path as shown in the Fig. 3c, d. The increase in these values suggests that to get a realistic value while describing the behavior of the liquid storage tank under earthquake ground motion, we cannot ignore the vertical component. The nature of the stresses in the tank due to the unbalanced mass of the fluid media is a complex phenomenon driving from the combined effects of the fluid–structure interaction and the inertial behavior of the fluid media. Here also the maximum values are achieved at the relatively the same time interval as in the various time responses reported for this ground motion.

From Table 3, the maximum absolute values of the various output extracted are shown. For the present study is concluded with the help of the three different earthquakes having different peak ground acceleration magnitude. To comprehend the change in the output values for the various interaction for the ground motion under

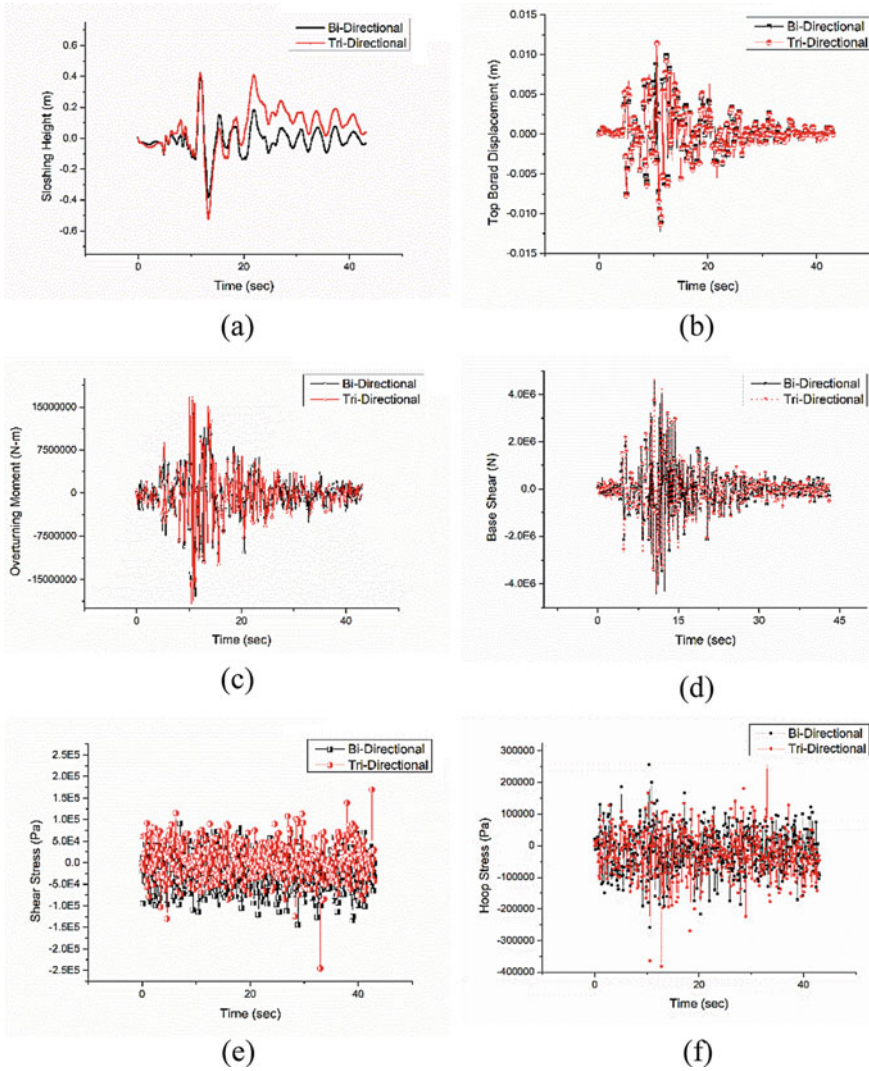


Fig. 2 Various Response Quantities for the Tabas Earthquake, **a** sloshing height **b** top board displacement **c** Overturning moment **d** base shear **e** shear stress and **f** hoop stress

consideration are shown in Table 4. It can be seen that a considerable amount of the imbalance is present between the values of bi-directional and tri-directional interaction for the various values responses.

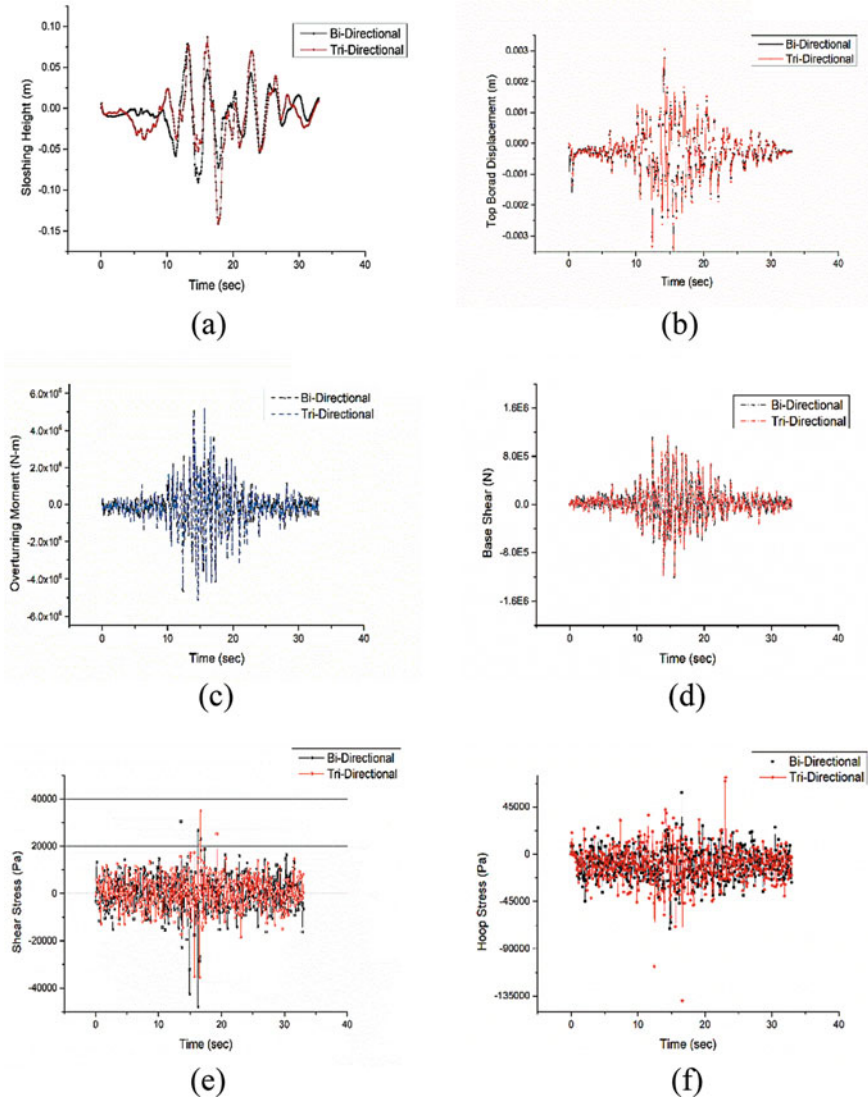


Fig. 3 Various Response Quantities for the Taiwan Earthquake, **a** sloshing height **b** top board displacement **c** overturning moment **d** base shear **e** shear stress and **f** hoop stress

4 Conclusions

The behavior of the liquid storage tank resting on the ground is taken up for the analysis in a finite element modeling software ABAQUS. A rectangular tank having both sides of equal length is taken as a model with fluid capacity at 75 percent. The nonlinear time history analysis is done for the conclusive remarks for the impact of

Table 3 Peak values of the various quantities taken under study represented along with their respective ground motion

Name of Earthquakes	Type of interaction	Sloshing height (m)	Top board displacement (m)	Overturning moment (N-m)	Base shear (N)	Shear stress (Pa)	Hoop stress (Pa)
Bhuj Earthquake (2001)	Bi-Direction	0.853	0.014	1.61e07	6.09e06	1.00e05	2.080e05
	Tri-Direction	0.980	0.0159	1.81e07	6.35e06	2.25e05	3.37e05
Tabas Earthquake (1978)	Bi-Direction	0.36	0.011	1.62e07	4.40e06	8.084e4	2.66e05
	Tri-Direction	0.41	0.010	1.75e07	4.71e06	1.680e5	3.26e05
Taiwan Earthquake (1986)	Bi-Direction	0.083	0.0028	4.92e06	1.05e06	2.55e04	6.24e04
	Tri-Direction	0.090	0.0030	5.26e06	1.75e06	3.65e4	7.78e4

Table 4 Percentage change recorded between the tri-directional and bi-directional interactions for the various extracted response outputs

Name of earthquakes	Sloshing height	Top board displacement	Overturning moment	Base shear	Hoop stress
Bhuj Earthquake	14.9	13.6	12.4	4.3	62.0
Tabas Earthquake	13.9	9.1	8.0	7.0	22.6
Taiwan Earthquake	8.4	7.1	6.9	66.7	24.7

the vertical acceleration in the contribution for the various structural failures during the ground motions. Three types of ground motion are taken up, with different PGA values. The following conclusions can be drawn from the numerical study:

1. The pattern of the tri-directional ground motion follows bi-directional interaction, but in every case, the peak values of tri-directional interaction seem to surpass that of the bi-directional interaction.
2. The small-scale change can be seen in the response case of top board displacement.
3. The sloshing response seems to hold the most changed response in graphical form for the tri-directional interaction than that of the bidirectional interaction.
4. The values of the peak are generally developing when the height of the sloshing fluid is at maximum. Thus, it gives the physical sense of various stresses that are resulted due to the complex FSI and increase in the inertial force of fluid media during seismic activity.

5. The dramatic increase can be seen for the shear stress due to the tri-directional interaction case. The value shows to increase with higher PGA levels and lowers with lesser PGA levels. The hoop stress holds a relatively stable change in the values a maximum percentage change is reported for the Bhuj earthquake.

References

1. Housner GW (1957) Dynamic pressures on accelerated fluid containers. *Bull Seism Soc Am* [Internet] 47(1):15–35. <https://www.bssaonline.org/cgi/content/abstract/47/1/15>
2. Wozniak RS, Mitchell W (1978) Basis of seismic design provisions for welded steel oil storage tanks. In: *Advances in storage tank design*. American Petroleum Institute, Washington, USA
3. Liu WK (1981) Finite element procedures for fluid-structure interactions and application to liquid storage tanks. *Nucl Eng Des* 65(2):221–238
4. Malhotra PK, Wenk T, Wieland M (2000) Simple procedure for seismic analysis of liquid-storage tanks. *Struct Eng Int* [Internet] 10(3):197–201. <https://www.tandfonline.com/doi/full/10.2749/101686600780481509>
5. Virella JC, Prato CA, Godoy LA (2008) Linear and nonlinear 2D finite element analysis of sloshing modes and pressures in rectangular tanks subject to horizontal harmonic motions. *J Sound Vib* 312(3):442–460
6. Cao XY, Ming FR, Zhang AM (2014) Sloshing in a rectangular tank based on SPH simulation. *Appl Ocean Res* [Internet] 47:241–54. <https://dx.doi.org/10.1016/j.apor.2014.06.006>
7. Fischer FD, Seeber R (1986) Dynamic response of vertically excited liquid storage tanks considering liquid-soil interaction 1988(16):329–342
8. Haroun MA, Abdeihafiz EA (1986) A simplified seismic analysis of rigid base liquid storage tanks under vertical excitation with soil- structure interaction 5(4):217–225
9. Veletsos BAS, Asce M, Tang Y (1986) Dynamics of vertically excited liquid storage tanks 112(6):1228–1246
10. Haroun MA, Tayel MA (1984) Response of tanks to vertical seismic excitations 1985(13):583–595
11. Kianoush MR, Chen JZ (2006) Effect of vertical acceleration on response of concrete rectangular liquid storage tanks. *Eng Struct* 28(5):704–715
12. Ghaemmaghami AR, Kianoush MR (2010) Effect of wall flexibility on dynamic response of concrete rectangular liquid storage tanks under horizontal and vertical ground motions. *J Struct Eng* [Internet] 136(4):441–51. <https://ascelibrary.org/doi/10.1061/%28ASCE%29ST.1943-541X0000123>
13. Morris J, Almanzar L, Chu R (2016) Seismic analysis of ground-supported tanks using the vertical response spectrum. In: *Geotechnical and structural engineering congress*, pp 1404–1413
14. Stricklin GP, Baird JA (1996) A survey of Ring baffle damping in Cylindrical Tanks, vol 38
15. Maleki A, Ziyaeifar M (2008) Sloshing damping in cylindrical liquid storage tanks with baffles. *J Sound Vib* 311(1–2):372–385
16. Liu D, Lin P (2009) Three-dimensional liquid sloshing in a tank with baffles. *Ocean Eng* 36(2):202–212
17. Sanapala VS, Velusamy K, Patnaik BSV (2016) CFD simulations on the dynamics of liquid sloshing and its control in a storage tank for spent fuel applications. *Ann Nucl Energy* [Internet] 94:494–509. <https://dx.doi.org/10.1016/j.anucene.2016.04.018>
18. Shrimali MK, Jangid RS (2002) Seismic response of liquid storage tanks isolated by sliding bearings. *Eng Struct* 24(7):909–921

19. Panchal VR, Jangid RS (2008) Variable friction pendulum system for seismic isolation of liquid storage tanks. *Nucl Eng Des* 238(6):1304–1315
20. Jing W, Cheng X, Shi W (2018) Dynamic responses of sliding isolation concrete rectangular liquid storage structure with limiting devices under bidirectional earthquake actions. *Arab J Sci Eng* 43(4):1911–1924

Osdag: A Software for Structural Steel Design Using IS 800:2007



Siddhartha Ghosh, Danish Ansari, Ajmal Babu Mahasrankintakam, Dharma Teja Nuli, Reshma Konjari, M. Swathi, and Subhrajit Dutta

Abstract This paper discusses the research and development undertaken to develop a free and open-source software called Osdag® (Open Steel Design and Graphics) for the design and detailing of steel structures, at the Indian Institute of Technology Bombay. Osdag is a model-based platform-independent software having several modules of structural steel design following the specifications of IS 800:2007 and other relevant standards. It is being developed on interpreted, high-level, general-purpose object-oriented programming (OOP) language Python, and other Python-based tools. An interactive graphical user interface (GUI) is provided with proper validations of user input and maintenance of log files. The log messages provide the user with valuable information on the failure of trial design and suggest required modification(s). The software also features the inclusion of graphics for real-time 3D visualization of the structural component details. The CAD files developed from Osdag can be exported to conventional CAD manipulation software. Osdag generates a design report, showing details of all the inputs, design considerations, fabrication drawings, and—most importantly—details of each design and detailing checks according to the Indian Standards with reference to the appropriate clause number. The current version of Osdag (Release: 2018-06-21) contains connection design modules for shear connections (fin plate, end plate, cleat angle, and seated angle) and beam-to-beam moment connections, namely cover plate and extended end plate connections.

Keywords Osdag · Steel design · Free and open-source · Python · IS 800 · CAD

Osdag® and its logos are registered trademarks of IIT Bombay.

S. Ghosh (✉) · D. Ansari · A. B. Mahasrankintakam · D. T. Nuli · R. Konjari · M. Swathi
Indian Institute of Technology Bombay, Mumbai 400076, India
e-mail: sghosh@civil.iitb.ac.in

S. Dutta
National Institute of Technology Silchar, Silchar 788010, India

1 Introduction: Why Osdag

1.1 *Steel in Construction*

Over the past one and half centuries, steel has emerged as probably the most trusted building material. Modern architectural marvels make significant use of steel as the primary building material. Of these, many bridges, buildings, stadia, etc. are built with what is known as ‘structural steel’ in the domains of the construction industry, structural engineering, and building architecture. The Forth Bridge near Edinburgh, Scotland [1], is one of the earliest examples of such technical marvels, which has been serving rail traffic from 1890 till date. From pre-World War II skyscrapers (such as the Chrysler Building [2] and the Empire State Building in New York, USA) to modern technologically advanced masterpieces (such as the “Gherkin” in London, UK [3]), structural steel has been valued for the necessary qualities it provides: the high strength to weight ratio, durability, sustainability, and ductility. Steel also allows a designer the flexibility to use it in versatile ways. Construction with structural steel is significantly faster—and with better quality control—than most common building materials. Steel buildings can be modular and can efficiently adapt to changes in the use pattern during a building’s life cycle. At the end of the cycle, with about 90% or more of steel being fully recyclable [4], steel appears to be the best choice for the sustainable design of structures.

Even with all these advantages, we hardly see steel structures in India, except for industrial sheds, railway bridges, and transmission towers. India is currently the third largest country in terms of production of crude steel (India produced 101.4 metric tonne steel in the year 2017 [5]), but on the other hand, it is far behind in terms of domestic steel consumption. The per capita consumption of steel in India is as low as 65.2 kg against the world average of 214.5 kg [5]. Also, the steel-to-cement ratio in India is 0.32 [6], which is very less as compared to other developed countries like the USA which has a steel-to-cement ratio of about 1.0 [6]. In the fast-growing construction sector of India, reinforced concrete structures outnumber steel structures by a very large margin. The reasons for this disparity are diverse; here is a quick look at the technological and (technical) education-related aspects.

1.2 *Indian Standard for Steel Design*

The Indian Standard IS 800 provides general guidelines and the standard specifications for the design and detailing of structures using structural steel. It was first published in 1956 [7] to achieve “economy in the use of structural steel.” This was last revised in 2007, shifting the design philosophy from the Working Stress Method (WSM) [8] to the Limit State Method (LSM) [9] and bringing our design specifications closer to those of the modern steel design standards.

After the release of the 2007 revision, the Institute for Steel Development and Growth (INSDAG) [10] along with academics and experienced professionals conducted training programs for college teachers and design engineers across the country. Although this has resulted in some confidence building in the academia and in the industry, to date most college teachers and design professionals are not comfortable in steel design. Also, experienced professionals resist the transition from a design code they are already very familiar with to a new one. Besides, there are complaints against too many specifications to learn and implement and too few helpful resources to make use of.

1.3 Motivation for Osdag

The industry and academia's adaptation to revised British and American steel design codes were eased by making design software/tools available for the new standards. Availability of such design tools has been too few and too late for IS 800:2007 [9]. Commercial software are costly and beyond the affordable range of many design professionals and young practicing students. This results in piracy of the licensed software, both in the industry and the academia, without the user many a time realizing that he/she is committing a criminal offense. Those who stay away from the piracy route rely on in-house (handed down) spreadsheet-like solutions or hand calculations that are not validated and/or are very tedious. The issue of non-validated solutions is most evident in the design of steel connections. Many of the common structural design software do not include modules for steel connection design, for which one typically relies on specialized connection design and detailing software, such as RAM Connection [11]. These are costly software. For example, a single license of a single-connection (beam-to-column shear connection using a fin plate) design module of the Praxis software [12] costs Euro 150.00 (approximately INR 12,110.00, as per the current exchange rates, as on 2018) exclusive of taxes.

Considering this state-of-practice, the Osdag project was initiated in 2014 for developing a software dedicated to structural steel design and detailing as per the Indian Standard(s), which does not make a big dent in the user's pocket and can be one simple and effective solution to bring forth the necessary confidence among steel designers, college teachers, and students of civil engineering.

2 About Osdag

Osdag is a cross-platform, free, and open-source software for the design (and detailing) of steel structures, primarily following the Indian Standard IS 800:2007 [9]. It also adheres to the other relevant standards of structural steel design in India. It allows the user to design steel connections, members, and systems in the form of design modules using an interactive graphical user interface. The design modules

in Osdag are categorized as per design logic for the ease of the user. The interactive GUI provides a 3D visualization of the designed component and creates images for construction/fabrication drawings. The design is typically optimized following industry best practices.

The beta version of Osdag is released under the terms and conditions of the GNU lesser general public license (LGPL) Version 3 [13].

2.1 Osdag GUI

Osdag has an interactive and easy to use graphical user interface (Fig. 1). The GUI is designed to be user-friendly and almost all the operations have an assigned shortcut key. The design modules in Osdag, which are categorized and listed systematically in the opening window of the GUI can be selected by the user by simply clicking on radio buttons. Each radio button is associated with a design module and has a graphical representation of the module to ensure that the user has selected the correct or desired module. Once the user selects the module, Osdag prompts to select or create a ‘workspace directory,’ where all the design files would be saved for further reference. The design window GUI (Fig. 1) is mainly divided into four parts: Input Dock, Output Dock, CAD Window, and Message Window (along with a menu bar and a quick access bar).

The Input Dock on the left side of the design window GUI collects all the input data from the user, validates, stores, and sends it to the design and detailing algorithm. The Input Dock window is dynamic, and whenever a data is entered as an input, it

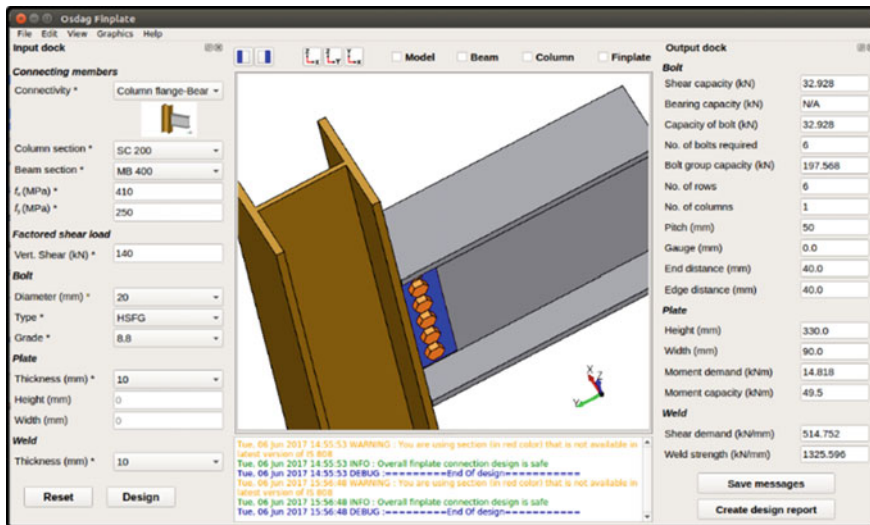


Fig. 1 Design Window of Osdag GUI

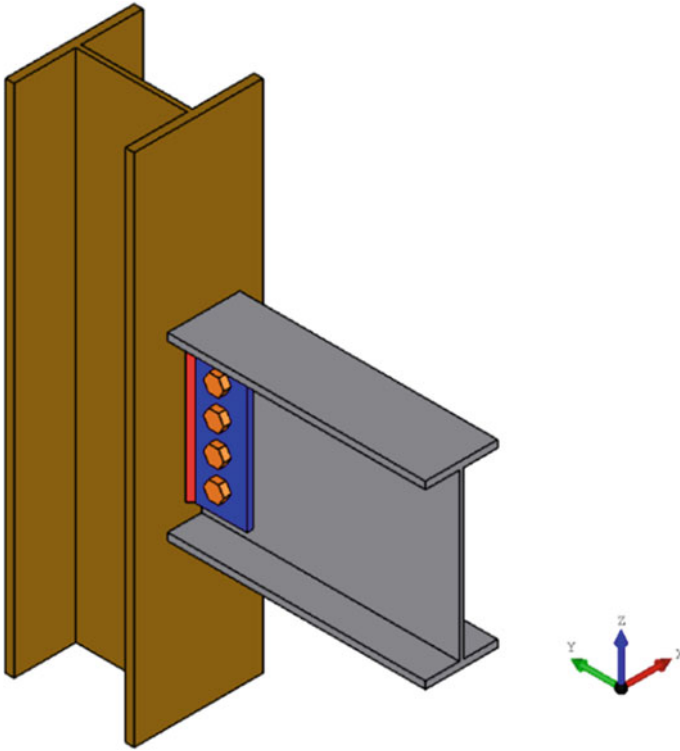


Fig. 2 3D CAD model created automatically in Osdag

is validated by a specially designed algorithm at the backend of the software. The algorithm designed for input data validation is based on the guidelines provided by the relevant standards and industry best practices. ‘Error’ or ‘Warning’ windows pop up when the user input does not satisfy these validations. The feature of input data validation in Osdag enables the user to create a more realistic design and also assists in self-learning. The input data can also be saved into a file (with the ‘.osi’ extension) for recreating the design, proof checking or sharing with clients/students.

The Output Dock on the right side of the Design Window GUI gets populated with design results upon the successful completion of a design. Osdag generates these results from a uniquely written ‘design and detailing algorithm’ which performs each check as per the codal provisions. All the necessary parameters associated with the design are displayed in the form of a checklist into the Output Dock.

A menu bar is provided at the top of the design window GUI which has the following menu options: File, Edit, View, Graphics, and Help. The ‘File’ menu consists of various options for saving and managing the files (including the 3D CAD model, 2D drawings, and design reports) associated with the design. The ‘Edit’ menu has an option for setting ‘Design Preferences’ which can be used by an advanced user to specify special preferences for the design. The ‘View’ menu has an option

for setting the font size, type, and style along with options to dock and undock the Input Doc and the Output Dock. The ‘Graphics’ menu has various options associated with the 3D CAD model. The ‘Help’ menu is loaded with video tutorials to assist a novice user on how to use the software and design examples to learn sample problems with structural steel design. The user can also ask/report queries related to the software or design to the Osdag team using the ‘Ask us a question’ option from the Help menu.

A ‘quick access bar’ is provided at the top of the 3D CAD window. This bar has an option for docking and undocking the input and output docks, viewing and saving the 2D drawings and viewing the sub-components of the design individually.

2.2 CAD Model

An interactive ‘CAD Window’ present at the center of the Design Window GUI displays a 3D CAD model (Fig. 2), which provides a clear visualization of the designed component. You can pan, zoom and rotate the model or view each of the sub-components separately. The sub-components in the CAD model, like the connecting member, connected member, connector, bolt, and weld are color-coded in order to distinguish them individually. The created CAD model can be saved into various formats such as IGS, STL, STEP, and BREP. This CAD model can be later imported to other CAD manipulation software such as AutoCAD [14] or FreeCAD [15].

2.3 Message Log

A text window for message(s) known as the ‘Message Log’ (Fig. 3) displays the status of the design; but more importantly, it also suggests necessary changes if a trial design is found unsafe. This message window at the bottom of the Design Window GUI displays color-coded error/warning/info messages and also suggests

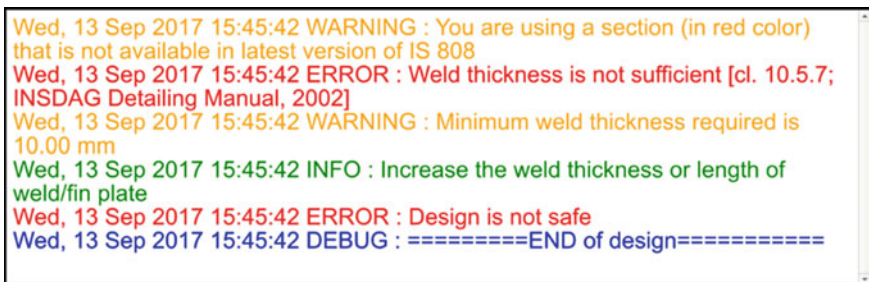


Fig. 3 Osdag Message Log

possible rectifications, all of which can be saved for a design session. Warning, error, and information are displayed in orange, red, and green colors, respectively, for the understandability of the user. These messages also refer to the relevant clause or a design guideline which helps in the self-learning capability of the user to a great extent.

2.4 Structural Drawings

The conventional practices of design require a detailer or a draftsman to create fabrication drawings. This adds to the cost and duration of the project. Also the human involvement is likely to introduce new errors. Osdag readily creates 2D views (Fig. 4) of the designed component in the format of typical good-for-construction drawings. These drawings follow the standard detailing practices adopted by expert

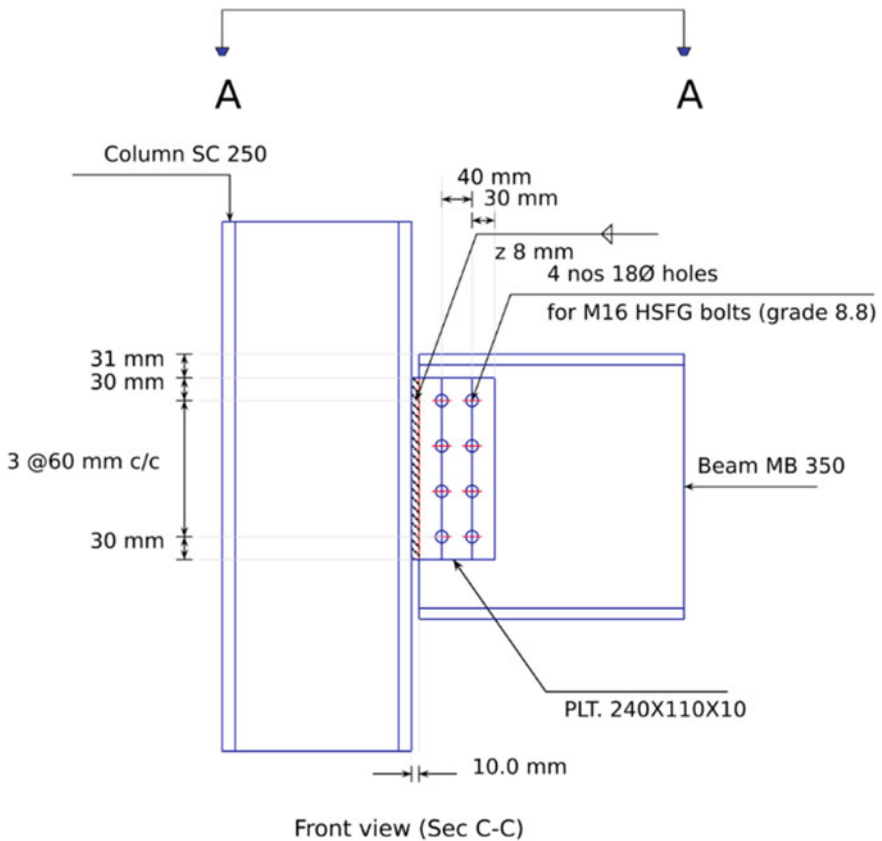


Fig. 4 A structural drawing created automatically in Osdag

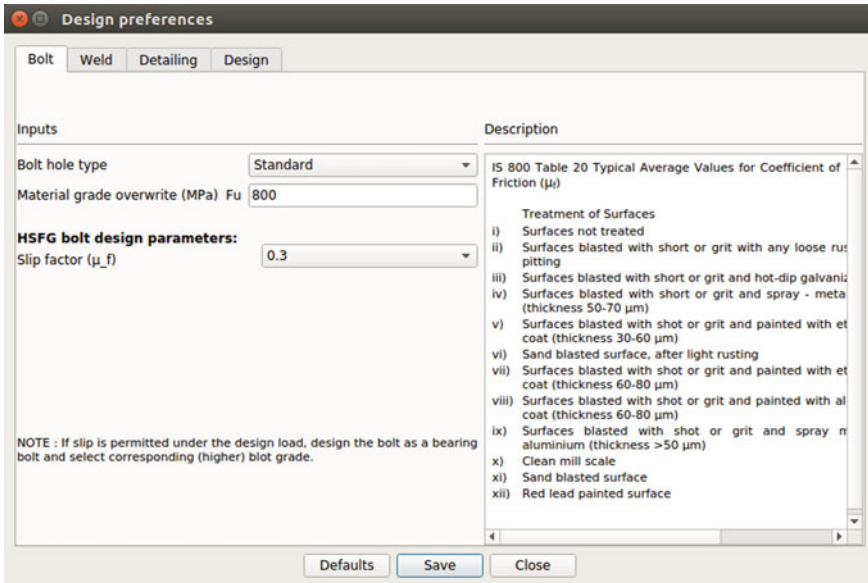


Fig. 5 Osdag design preferences toolbox

consultants, designers, erectors, and fabricators. The views can be saved in vector (SVG) and raster (PNG) formats. The 2D images can also be used by design engineers to submit reports or by teachers as teaching aids.

2.5 Design Preferences

Detailed design preferences (user choices or specific design-based requirements) can be set using the ‘Design Preference’ toolbox (Fig. 5). For a novice user, default values can be used in the design process in lieu of these preferences. The experienced user can set preferences for bolt, weld, detailing, and other design aspects.

2.6 Design Report

Osdag creates a professional and very comprehensive ‘Design Report’ (Fig. 6 and Fig. 7) which can be viewed and saved in the PDF format. The design report compiles all the necessary information, like the company/designer profile, detailed list of checks, 2D drawings, and CAD model. The salient feature of the design report is the inclusion of all the design and detailing checks as per IS 800:2007 [9] and other relevant standards into the design report. In each check, the ‘provided’ value is



		 Created with	
Company Name	IIT Bombay	Project Title	Connection Design Examples
Group/Team Name	Osdag	Subtitle	Fin Plate shear connection
Designer	Engineer #1	Job Number	1.1.1.1.1
Date	18 /06 /2017	Client	Manas M. Ghosh, INSDAG, Kolkata
Design Conclusion			
Fin Plate		Pass	
Fin Plate			
Connection Properties			
Connection			
Connection Title		Single Fin Plate	
Connection Type		Shear Connection	

Fig. 6 Design report created in Osdag: Header showing user and job details

Design Check			
Check	Required	Provided	Remark
Bolt shear capacity (kN)		$V_{dsf} = \frac{((0.3 \times 1 \times 1.0 \times 47.208) / (1.25))}{11.32992}$ [cl. 10.4.3]	
Bolt bearing capacity (kN)		N/A	
Bolt capacity (kN)		11.32992	Pass
No. of bolts	$140 / 11.32992 = 12.4$	14	Pass
No. of column(s)	≤ 2	2	
No. of bolts per column		7	
Bolt pitch (mm)	$\geq 2.5 \times 12 = 30, \leq \text{Min}(32 \times 10.2, 300) = 300$ [cl. 10.2.2]	40	Pass
Bolt gauge (mm)	$\geq 2.5 \times 12 = 30, \leq \text{Min}(32 \times 10.2, 300) = 300$ [cl. 10.2.2]	30	

Fig. 7 Design report created in Osdag: Details of design checks

compared against its ‘required’ value and a remark is provided against the check, where, ‘Pass’ indicates a safe design and ‘Fail’ indicates an unsafe design. Unlike other commercial software, the design report created in Osdag gives information on the reference of the check, which is a very useful tool not just for a student/learner but also for an expert proof-checker/design reviewer.

3 Osdag Architecture

The block diagram (Fig. 8) depicts the architecture of the code(s) and its functioning in Osdag. All the design modules in Osdag follow this architecture in order to create a successful design along with a 3D CAD model, 2D drawings, and design report. The design data is collected in the form of input from the user through an interactive ‘Input Dock’ from the design window GUI. Other inputs, like the section properties, are collected from the Osdag database present at the backend of the software. The database contains properties of the standard Indian steel sections as per IS 808:1989 [16] (rolled sections) and globally used parallel flange sections [10]. The data is collected and stored in the ‘Main File’ of Osdag in an appropriate form only after its validation by uniquely written functions and conditional statements. If the input data is found to be ‘inappropriate’ in terms of design or programming sense, then Osdag pops up errors and suggestions to correct the user input. The Main File is the core of the architecture as it integrates all the supporting files into it, which enables the functioning of the module. The input data is then called into the ‘Calculation File’ where all the design and detailing checks are made. These checks are written in an algorithmic way and include appropriate ‘log message(s).’ When a check does not satisfy a certain design or detailing criterion, the log message associated with this check is displayed in the message window of the GUI. All the calculated parameters in the ‘Calculation File’ are stored in the form of a dictionary as an ‘output dictionary.’ This dictionary is called into the ‘2D Drawing Generator’, ‘3D CAD Model Generator’ and the ‘Design Report Generator’ from the Calculation File. The 2D Drawing Generator file creates 2D views (‘front’, ‘side’, and ‘top’) of the designed component, the 3D CAD Model Generator creates the 3D CAD model and the Design Report Generator creates the design report by echoing the inputs and compiling all the checks, views and the CAD model. These outputs are sent back

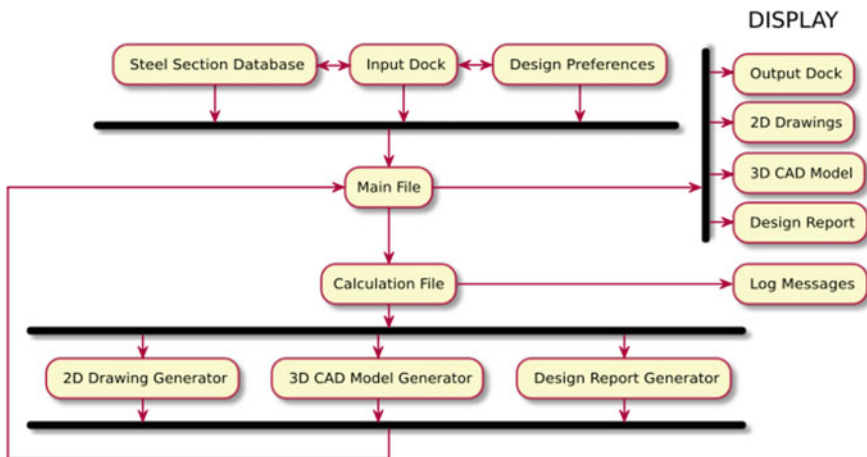


Fig. 8 The software architecture of Osdag

to the Main File where it connects the output to the ‘Display’ unit. The display unit populates the output results into the Output Dock, sends 2D views and 3D CAD model to its display window, loads design reports, and displays respectively. In case of an ‘Unsafe’ design, only the Output Dock and a partial design report are shown.

4 Development Process

The development process in Osdag begins with identifying the most common and widely used design module. The Osdag team, along with its industrial and academic collaborators, decides the modules to be incorporated into Osdag through a review process. Based on a thorough review of existing Indian design standards, design guidelines, detailing guidelines, and standard textbook examples, the ‘Design and Detailing Checklist’ (DDCL), and the ‘Design and Detailing Query’ (DDQ) are prepared. These documents include a list of checks to be carried out for a particular module in an algorithmic way and the queries associated with the design. Using a web-based interface, feedback on DDCL and DDQ are collected from the ‘Expert Reviewers.’ The feedbacks received are analyzed/discussed by the team and then incorporated into the design and detailing algorithm. During the review process, the team works on writing the Python code for the Main File, Calculation File, 3D CAD Model Generator, 2D Drawing Generator, Design Report Generator, etc. The code management and continuous integration (CI) are done using version control systems like Git and GitHub (<https://github.com/osdag-admin/Osdag>). Once the module is integrated into Osdag, it goes through the necessary checks and tests before being compiled into the installer. The Osdag team also works on creating self-learning and e-learning materials such as design examples and video tutorials. The installers and the learning materials are made available to its users free of cost through the Osdag website (<https://osdag.fossee.in/>). The team also takes feedback and resolves user queries through the FOSSEE [17] discussion forum (<https://forums.fossee.in/accounts/login/>).

5 Resources

Adhering to today’s learning/education techniques, Osdag provides a variety of self-learning tools and contents through its website: <https://osdag.fossee.in>. Besides Osdag installers (Fig. 9) for different operating systems (<https://osdag.fossee.in/resources/downloads>), these web pages come with diverse user tools, video tutorials (on different aspects of installing and operating the software, <https://osdag.fossee.in/resources/videos>), design examples (<https://osdag.fossee.in/resources/sample-design>), discussion forum (<https://osdag.fossee.in/forum>), developer tools etc. The video tutorials are also available on Osdag’s YouTube channel: <https://tinyurl.com/OsdagV>

1. Installer [Release: 2018-06-21]

Ubuntu 14.04 and above - 64-bit



- Installation instructions for Ubuntu
- Installer - Linux 386 MB

Windows 7,8 and 10 - 32-bit & 64-bit



- Installation instructions for Windows
- Installer - Windows 304 MB

Fig. 9 Osdag installers available online on the Osdag Resources page

[ideos](#). While these videos and design examples are excellent self-learning materials, these can also be used in conducting training programs on Osdag efficiently.

6 Summary

In this paper, the authors have described the various salient features of a free and open-source software called Osdag. Osdag is used for design and detailing of steel structures as per the relevant Indian Standards (IS 800:2007, primarily). Currently, Osdag is the only Free and Open-Source Software (FOSS) in India for the design of steel structures as per the latest provisions of the Indian Standards. The architecture of the software and its development process have been briefly discussed. The various learning/resource materials and tools available for students, teachers, and design professionals have been highlighted, as well.

Acknowledgements Funding provided by the Ministry of Human Resources and Development (MHRD), Government of India through the (FOSSEE) [17] project under the National Mission on Education through Information and Communication Technology (NMEICT) [18] is used for the Osdag project. The authors acknowledge the contribution of Expert Reviewers of Osdag from academia and industry. The authors also would like to acknowledge the FOSSEE team [19] from IIT Bombay for its continued support. Most importantly, the authors would like to acknowledge the contribution of Deepa Chaudhary, Jayant Patil, Hashmi S. S. Ahmed, Jeffy Jaffar, Aravind P., Sasir Pentyala, Siddhesh Chavan and the advice from Prof. Kannan Moudgalya and Prof. Prabhu Ramachandran.

References

1. The Forth Bridges. <https://www.theforthbridges.org> Last accessed 14 December 2018
2. Massey K (2018) History of Walter P. Chrysler and the Chrysler Building. Allpar. <https://www.allpar.com/history/chrysler-building.html>. Last accessed 14 December 2018
3. Gherkin London. <https://www.30stmaryaxe.com>. Last accessed 16 December 2018
4. World Auto Steel . <https://www.worldautosteel.org>. Last accessed 7 November 2018
5. World Steel Association report, Steel Statistical Yearbook 2018, worldsteel.org. Last accessed 21 December 2018
6. Statista website. <https://www.statista.com>. Last accessed 9 August 2019
7. IS 800 (1956) General Construction in Steel—Code of Practice. Bureau of Indian Standards, New Delhi
8. IS 800 (1984) General Construction in Steel—Code of Practice. Bureau of Indian Standards, New Delhi
9. IS 800 (2007) General Construction in Steel—Code of Practice. Bureau of Indian Standards, New Delhi
10. Institute for Steel Development and Growth—INSDAG. <https://www.steel-insdag.org>. Last accessed 23 November 2018
11. RAM Connection Standalone V8i 7.0, Bentley Systems, Inc (2010). <https://www.bentley.com/en/products/product-line/structural-analysis-software/ram-connection>. Last accessed 13 December 2017
12. EC—PRAXIS 3J. <https://www.gsi-eng.eu>. Last accessed 4 October 2018
13. GNU Lesser General Public License version 3. <https://opensource.org/licenses/lgpl-3.0.html>. Last accessed 7 January 2018
14. AutoCAD: a computer-aided design and drafting software, Autodesk, Inc. <https://www.autodesk.in>. Last accessed 18 December 2018
15. FreeCAD—An open-source parametric 3D CAD modeler. <https://www.freecadweb.org>. Last accessed 18 December 2018
16. IS 808 (1989) Dimensions for Hot Rolled Steel Beam, Column, Channel and Angle Sections. Bureau of Indian Standards, New Delhi
17. Free and Open Source Softwares for Education. <https://fossee.in>. Last accessed 19 December 2018
18. National Mission on Education through Information and Communication Technology. <https://www.worldautosteel.org>. Last accessed 19 December 2018
19. Ghosh S (2018) FOSSEE News, vol 1, issue 3. IIT Bombay, Mumbai

Experimental and Analytical Investigations on Two-Way Flexural Capacity of Biaxial Voided Slab



R. Sagadevan and B. N. Rao

Abstract The rise in urbanisation and subsequent demand for infrastructure accelerates the use of concrete as a construction material. Conventional design practices need large member sizes to fulfil architectural and structural requirements. Hence, the size of structural members such as slab, beam, column, etc., significantly affects the quantity of concrete used. This calls for the need to optimise the use of concrete to reduce the self-weight of structure. The present study explores the possibility of biaxial voided slabs as a substitute for conventional reinforced concrete slabs. A typical biaxial voided slab eliminates concrete from the middle of the floor slab by introducing voids and it leads to a significant reduction in self-weight, about 30–50%. However, these voids reduce the sectional area of slab concrete, which leads to a reduction in flexural stiffness and shear resistance. The behaviour of the biaxial voided slab subjected to two-way flexure is discussed. Experiments are carried out to determine two-way flexural behaviour of the two-way slab with sphere shape voids by adopting 16-point loads. The obtained experimental results of strength and serviceability criteria are compared for slabs with and without voids. It is found that the flexural capacity of the two-way slab with biaxial voids is the same as a solid slab, with a minor reduction in its flexural stiffness. Furthermore, an analytical study is carried out based on the yield line analysis to predict the flexural capacity of the slab and compared with experimental results. It is evidenced that 16-point load is equivalent to 89% of uniformly distributed load and the flexural capacity of void slabs can be predicted by using yield line analysis as used in the conventional solid slab.

Keywords Biaxial voided slab · Flexural capacity · Flexural stiffness · Sixteen-point load · Yield-line analysis

R. Sagadevan (✉) · B. N. Rao
Structural Engineering Laboratory, Department of Civil Engineering, Indian Institute of Technology Madras, Chennai, Tamil Nadu 600036, India
e-mail: sagadevan.ceg@gmail.com

B. N. Rao
e-mail: bnrao@iitm.ac.in

Notations

The following symbols are used in this paper

$A_{st,b}$	Area of bottom reinforcement;
$A_{st,t}$	Area of top reinforcement;
C	Force in concrete per unit width of slab;
d	Overall depth of slab;
d_e	Effective depth to bottom reinforcement;
d'	Effective depth to top reinforcement;
f_{cm}	Mean concrete cube compressive strength;
$f_{st,b}$	Stress in bottom reinforcement;
$f_{st,t}$	Stress in top reinforcement;
l	Overall length of slab;
l_e	Effective length of slab;
m	Ultimate moment capacity per unit width of slab;
m_x	Ultimate moment capacity per unit width of slab in x -direction;
m_y	Ultimate moment capacity per unit width of slab in y -direction;
P_u	Theoretical or experimental ultimate load (16-point load);
T_b	Force in bottom reinforcement;
T_t	Force in top reinforcement;
x_u	Neutral axis depth at ultimate;
\bar{x}	Depth of resultant compressive force in concrete;
W_n	Theoretical ultimate load (UDL) of solid slab based on YLA;
W_{u1}	Equivalent UDL of ultimate load without considering self-weight of slab;
W_{u2}	Equivalent UDL of ultimate load inclusive of self-weight of slab;
δ_u	Mid-span deflection of slab corresponds to ultimate load.

1 Introduction

Reinforced concrete (RC) structures being constructed across the world to overcome the increase in the demand of urbanisation and infrastructure development. It rises the usage of concrete as a construction material. The demand in architectural and structural requirements, such as aesthetic, number of stories, span, etc., increases the size of structural members which further increases the requirement of concrete. In the past, many researchers, structural and design engineers came up with many types of slab systems to overcome the structural and non-structural requirements. One-way voided slab system is one among them which reduces the considerable quantity of concrete without significant change in its structural performances. However, the demand for a two-way slab system was not fulfilled. In the early 2000s, the two-way voided slab system was introduced with plastic void formers having various shapes

such as spherical, donut, cuboid, etc. It leads to the reduction in self-weight up to 50% [1–11]. The biaxial voided slab reduces self-weight by 44% with the same flexural capacity of the solid slab [1]. The one-way flexural capacity of the biaxial voided slab was studied by various researchers [1, 4, 11–15]. These investigations showed that the capacity of RC voided slab is the same as RC solid slab with slightly lower stiffness. Similarly, the two-way flexural behaviour of voided RC slab system was investigated [6, 16]. These studies showed that the flexural stiffness of voided slabs was 25% lower than that of an RC solid slab, however, the flexural capacity remains the same.

In the past, various types of loading configuration were adopted to study the two-way flexural capacity of RC slabs, such as single point load at the centre of slab [17, 18], 5-point load in small-scale specimens [6], 12-point load in full-scale specimens [16]. These tests resulted in premature localised punching shear failure and the load was concentrated at the central region of the slab. A methodology to design and analyse the biaxial voided slab needs to be studied for practical application. Suitable loading configuration, which overcomes the premature failure and load concentration, needs to be verified.

In this study, the flexural behaviour of biaxial RC voided slabs was studied through experiments and compared with analytical expressions. Experiments on three full-scale specimens were conducted, (i) solid slab (SP 1), (ii) slab with 90 mm diameter sphere voids (SP 2) and (iii) slab with 180 mm diameter sphere voids (SP 3). The uniformly distributed load (UDL) was simulated by adopting a 16-point load. The obtained experimental results are compared with theoretical calculations which are based on the yield line analysis (YLA) in conjunction with Indian code IS 456: 2000 [19] provisions. In addition to that, the flexural behaviour of RC solid and biaxial voided slab having identical dimensions and reinforcement details was compared.

2 Experimental Study

The two-way flexural behaviour of slab systems was expressed in terms of the ultimate load-carrying capacity, flexural stiffness and overall load versus deflection plot. The void formers manufactured by recycled polypropylene were used in the slab specimens to create voids. These sphere shape void formers were fabricated with 3 mm wall thickness and it ensures any unintended change in shape while handling, placing the concrete and using a vibrator for compaction. The details of test specimens, materials' properties, load configurations and test methodology are summarised below.

Table 1 Details of specimens

Specimen	Depth (mm)	Reinforcement in both directions			Self-weight (kN)	Mean cube strength (N/mm ²)
		Top (mm ² /m)	Bottom (mm ² /m)	Spacing (mm)		
SP 1	150	343	343	80	39.6	31.2
SP 2	150	343	343	80	36.0	31.0
SP 3	250	257	257	105	54.8	29.4

2.1 Details of Specimens

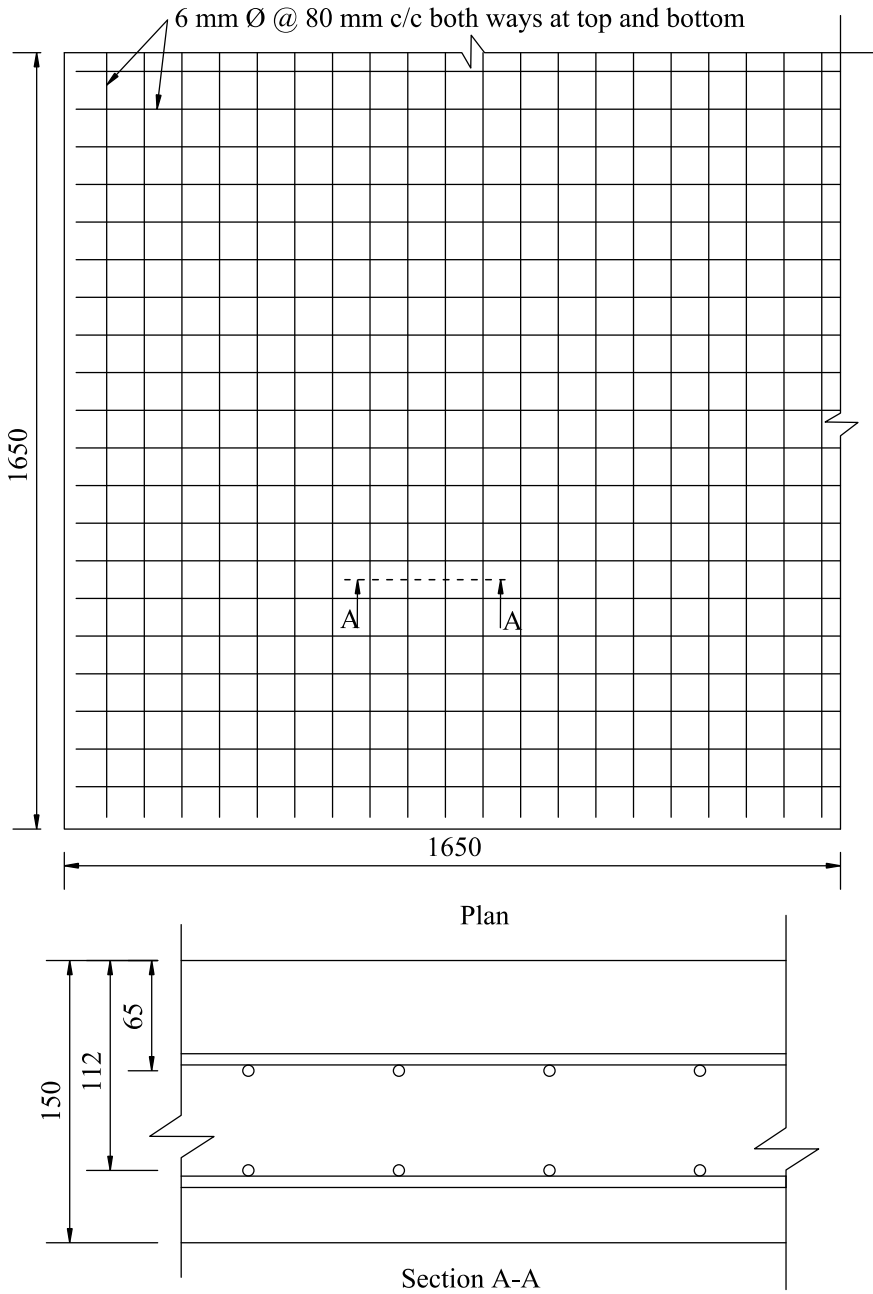
Three full-scale slab specimens were tested. The plan dimensions of test specimens were 3300 × 3300 mm. The minimum reinforcement ratio was provided to ensure flexure failure dominating shear failure as voided slabs are vulnerable to shear. In longitudinal and transverse direction reinforcements were arranged in the form of mesh. The size of reinforcement bars was restricted to 6 mm. The specifications of the specimens are summarised in Table 1. The details of slab specimens are shown in Figs. 1, 2, and 3.

The M 25 grade concrete conforming to IS 456 [19] was used to cast the test specimens with the mix proportion of 1:2.25:4.5 (cement:fine aggregate:coarse aggregate) and the water-cement ratio of 0.55. Concrete cubes were cast and cured under similar exposure conditions as that of slab specimens. The compression test on cubes was carried at the time of the flexure test on the companion slab specimen. The observed mean strength is summarised in Table 1. The reinforcements of grade Fe 500D conforming to IS 1786 [20] was used. The properties of reinforcements were obtained by conducting tensile tests which are summarised in Table 2.

2.2 Experimental Test Set-Up and Instrumentation

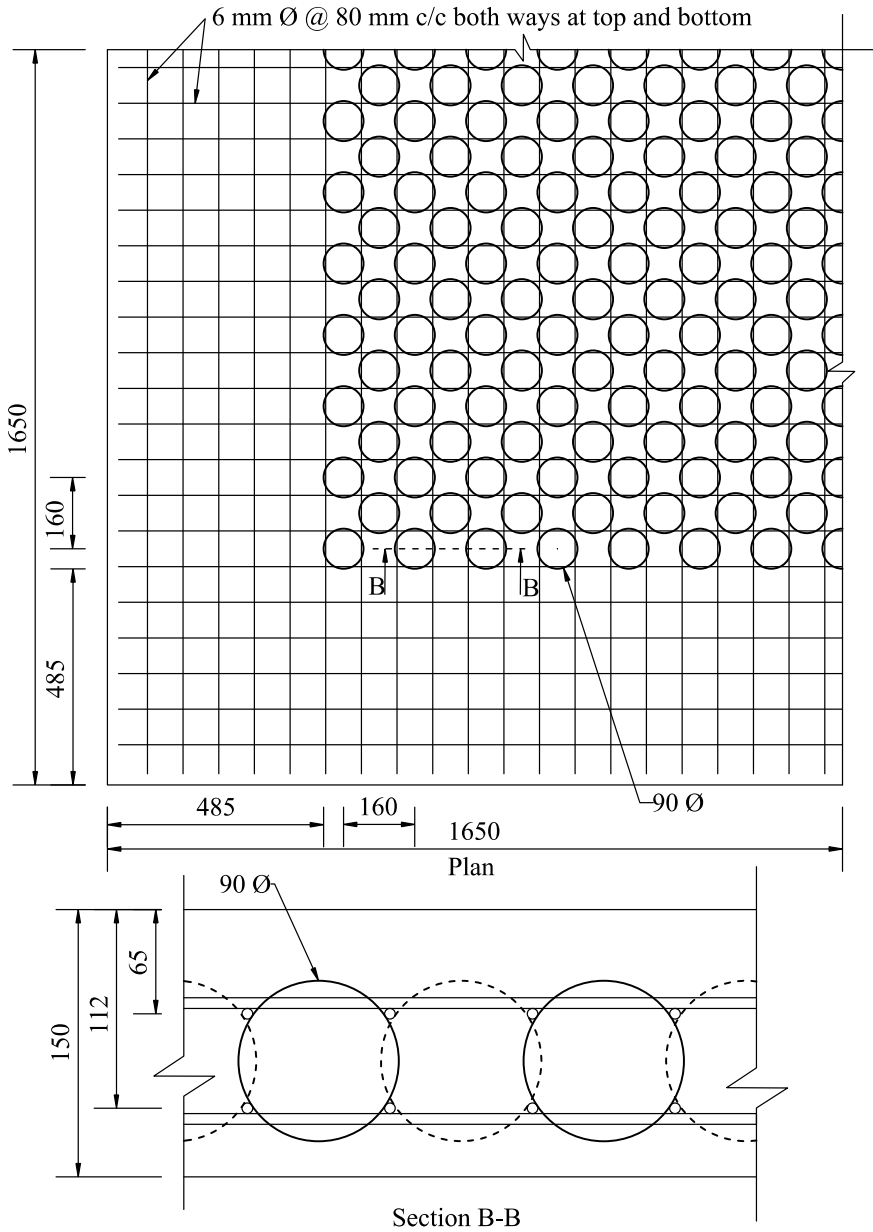
2.2.1 Test Setup

The flexural behaviour of the slab was studied through a sixteen-point load test. Figure 4 shows the actual test set-up. The localised pre-mature punching shear failure was avoided by applying the point load as patch load through a steel plate of size 170 × 170 × 12 mm as shown in Fig. 5. A pair of hydraulic jacks of capacity 1500 kN, each was used to apply the load. The load was transferred through hot rolled steel sections to the slab specimens. The steel sections were allowed to rotate freely with the specimen's deformation by providing the rollers at its ends. The line-type reaction hinge of length 2800 mm was provided at its all four sides at 150 mm from specimen edges to simulate simple support conditions. The experimental errors from the support condition such as stress concentration and generation of fixed end moments were minimised by the support discontinuity at the corner [16].



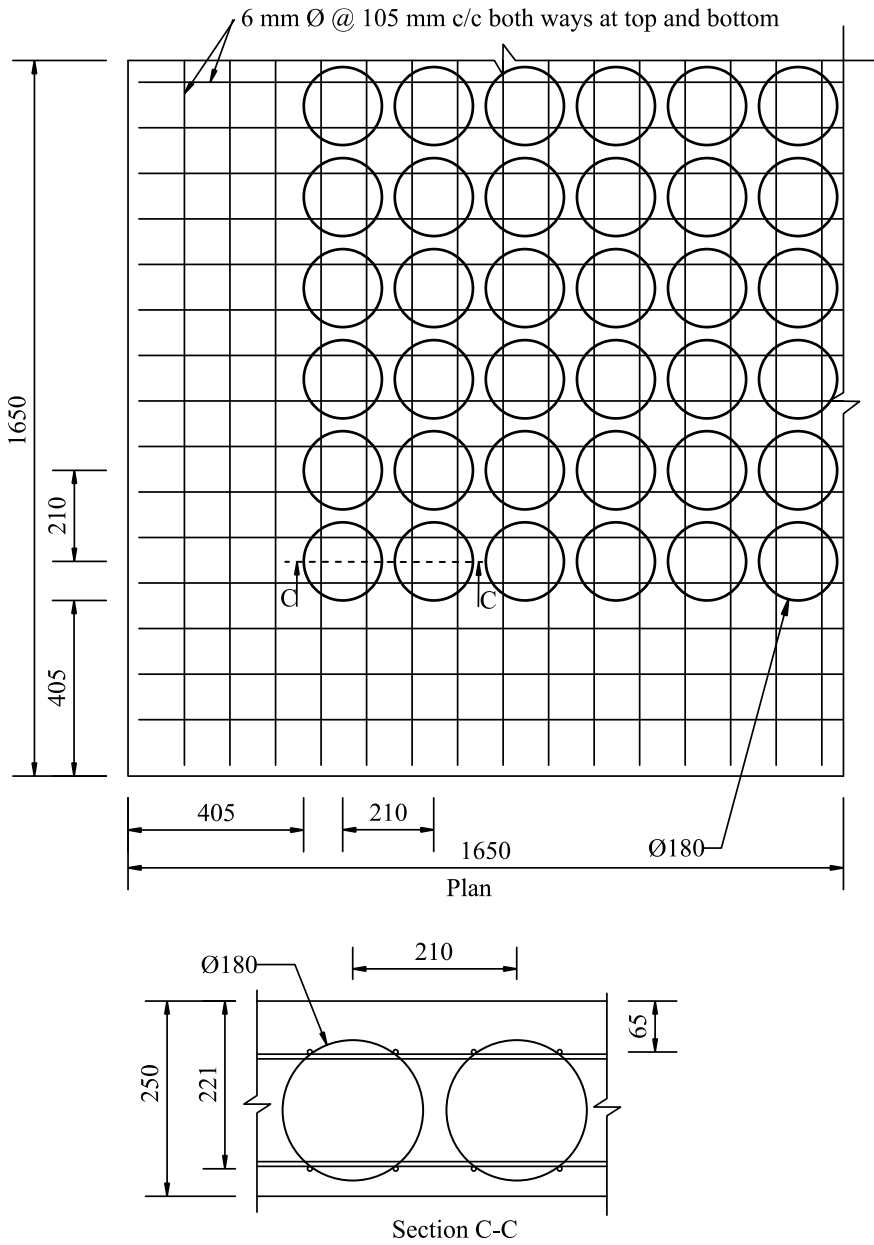
All dimensions are in mm

Fig. 1 Details of test specimen SP 1 (one-quarter of the slab)



All dimensions are in mm

Fig. 2 Details of test specimen SP 2 (one-quarter of the slab)



All dimensions are in mm

Fig. 3 Details of test specimen SP 3 (one-quarter of the slab)

Table 2 Mechanical properties of reinforcement

Diameter (mm)	Strength (N/mm ²)			Strain	
	Nominal	Yield	Ultimate	Yield	Ultimate
6	500	560	650	0.0033	0.0591

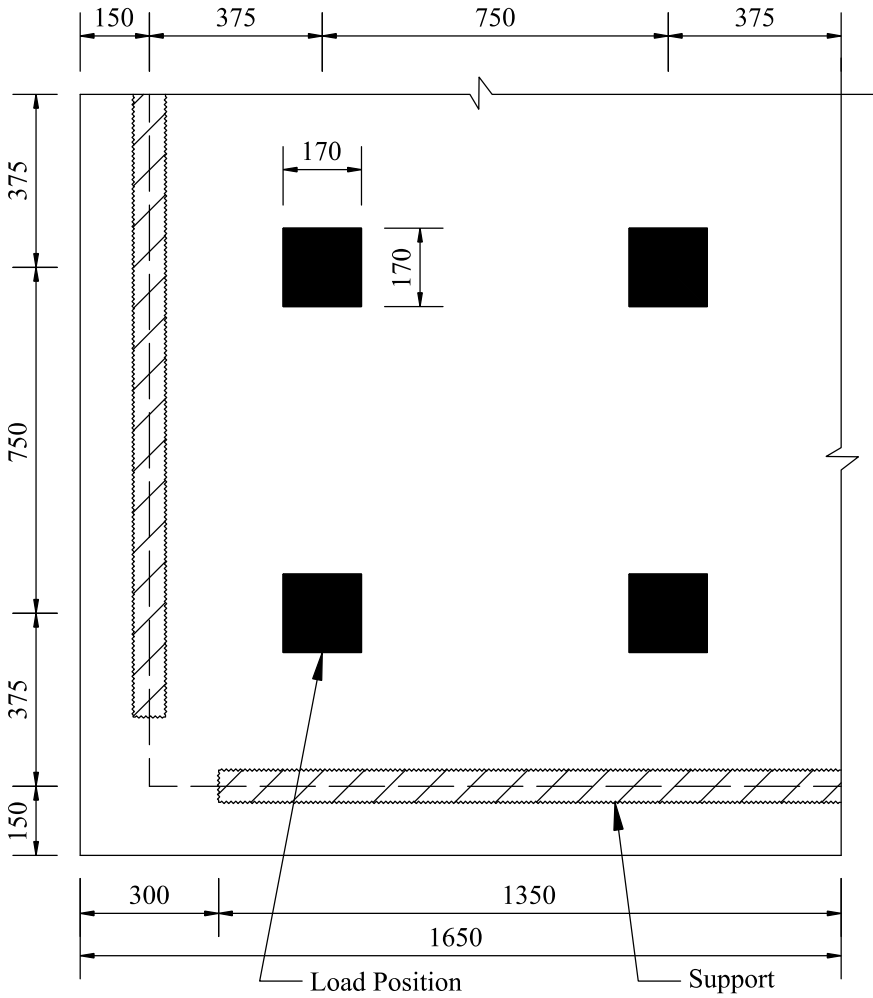
**Fig. 4** Two-way flexural test set-up (16-point load)

2.2.2 Instrumentation

Instruments were provided to measure the applied load, deflection and strain in reinforcements. The applied load was measured by a pair of load cells of capacity 1000 kN each. The deflection was measured at mid-span using the linear variable differential transformer (LVDT) with a measuring range of ± 100 mm. The strain was obtained using strain gauges of 10 mm gauge length in longitudinal and transverse directions of the bottom reinforcements located at the centre of slab specimens. A data acquisition system, having the facility to record load, deflection and strain at the same instance was used.

2.2.3 Test Procedure

Load-controlled monotonic test was performed with a pair of hydraulic jacks. The jacks were synchronised and operated using a single master control system to ensure



All dimensions are in mm

Fig. 5 Position of 16-point (patch) load (one-quarter of the slab)

equal load distribution across each jack. The loading was paused at every 50-kN interval to perform the visual inspection, mark cracks and take photographs. The test was terminated immediately after observing a major drop in applied load; it ensures the safety of measuring and loading devices and avoids any permanent damage to load transfer members.

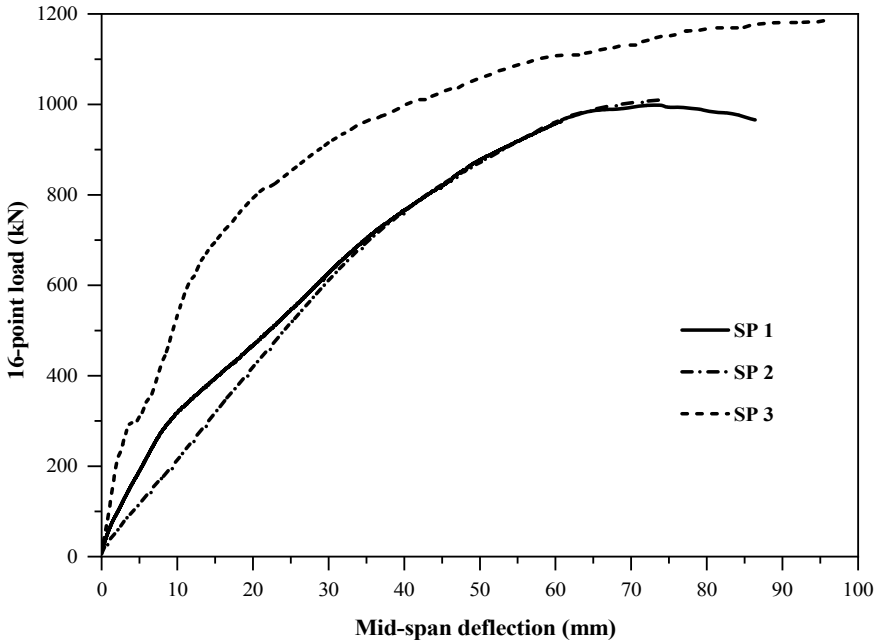


Fig. 6 Load versus mid-span deflection plot of tested specimens

2.3 Test Results and Discussions

2.3.1 Load Deflection Behaviour

All three slab specimens showed typical flexural behaviour. Initially, all specimens remained elastic until cracking, after that inelastic actions started, i.e. yielding of bottom reinforcements at bottom of slab and crushing of concrete at top of the slab. The load versus the mid-span deflection plot is shown in Fig. 6. It can be observed that the behaviour of the solid slab (SP 1) and voided slab (SP 2) specimens show identical load–deflection behaviour after cracking. It implies that the presence of void is not affecting the load-carrying capacity of the slab but the initial stiffness is influenced by the voids. The initial stiffness of SP 1 is 37% more in comparison with the SP 2; however, the secant stiffness corresponding to yield load of voided and solid slab specimens were comparable.

2.3.2 Load-Carrying Capacity

The load-carrying capacity of solid and voided slabs was observed to be equal. The ultimate load and corresponding mid-span deflection are summarised in Table 3.

Table 3 Results based on the experimental study

Specimen	Sixteen-point load		Equ. UDL (kN)	
	P_u (kN)	δ_u (mm)	LL, W_{u1}	DL + LL, W_{u2}
SP 1	997.5	73.64	1121	1160
SP 2	1008.7	74.08	1133	1169
SP 3	1184.9	95.88	1331	1386

Note P_u is the observed ultimate load; δ_u is the mid-span deflection corresponding to P_u

3 Analytical Study

3.1 Moment Capacity of Slab Section

The stress distribution across the depth of the slab is shown in Fig. 7 which corresponds to linear strain variation. Based on the forces in concrete and reinforcements, the equation to estimate the ultimate moment capacity of a slab section per unit width is given in Eq. (1). The contribution from the top and bottom reinforcements was considered for the estimate of capacity.

$$m = T_b(d_e - \bar{x}) + T_t(d' - \bar{x}) \tag{1}$$

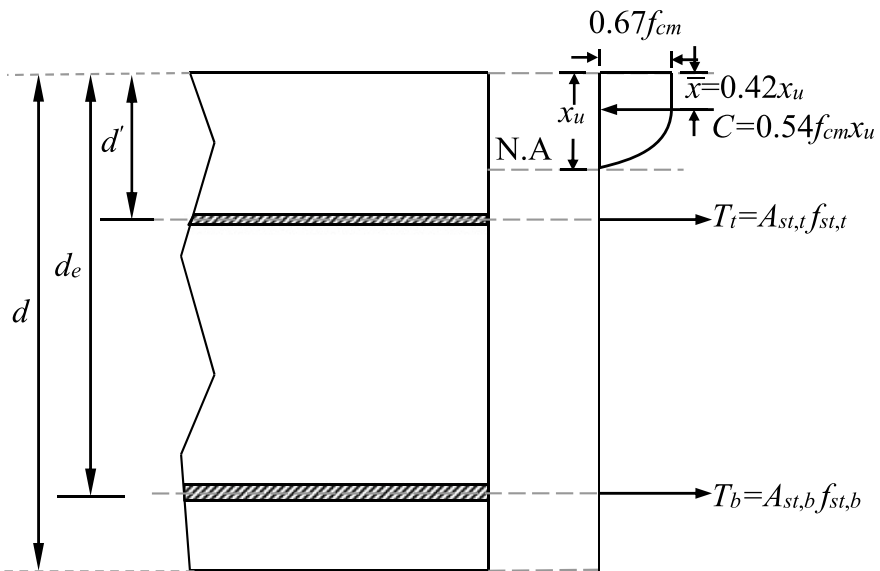


Fig. 7 Stress and force in slab at ultimate

Table 4 Theoretical capacity of slab specimens

Specimen	Moment capacity (kNm/m)		Capacity by YLA (kN)
	m_x	m_y	UDL (W_n)
SP 1	23.96	24.17	635.3
SP 2	23.94	24.15	634.8
SP 3	31.51	31.12	826.7

The moment capacity of tested slab specimens is estimated and given in Table 4. It can be observed that the moment capacity in orthogonal direction remains the same. This is primarily because of the orientation and position of the reinforcements.

3.2 Load-Carrying Capacity of Slab

The theoretical load-carrying capacity of slab specimens was estimated based on YLA. The capacity of the slab was calculated based on the suitable crack pattern at the ultimate stage. In this study, the square shape of the slabs, under two-way flexural action was tested. Therefore, the yield line was assumed to form X-shape along the diagonals; it results in dividing the slabs into four equal triangular parts as shown in Fig. 8. The expression for collapse load was derived based on the equilibrium of slab parts.

The ultimate load carrying capacity (P_u) of the slab specimen subjected to a 16-point load is calculated and given by Eq. (2).

$$P_u = \frac{64 ml}{3l_e} \quad (2)$$

Similarly, the ultimate load-carrying capacity (W_n) of the slab specimen subjected to UDL is calculated and given by Eq. (3).

$$W_n = \frac{24 ml}{l_e} \quad (3)$$

By comparing Eqs. (2) and (3), it is observed that the ratio of the ultimate load-carrying capacity of the slab with 16-point load (P_u) and UDL (W_n) is 89%. The estimated theoretical ultimate load-carrying capacity of slab specimens by YLA is summarised in Table 4.

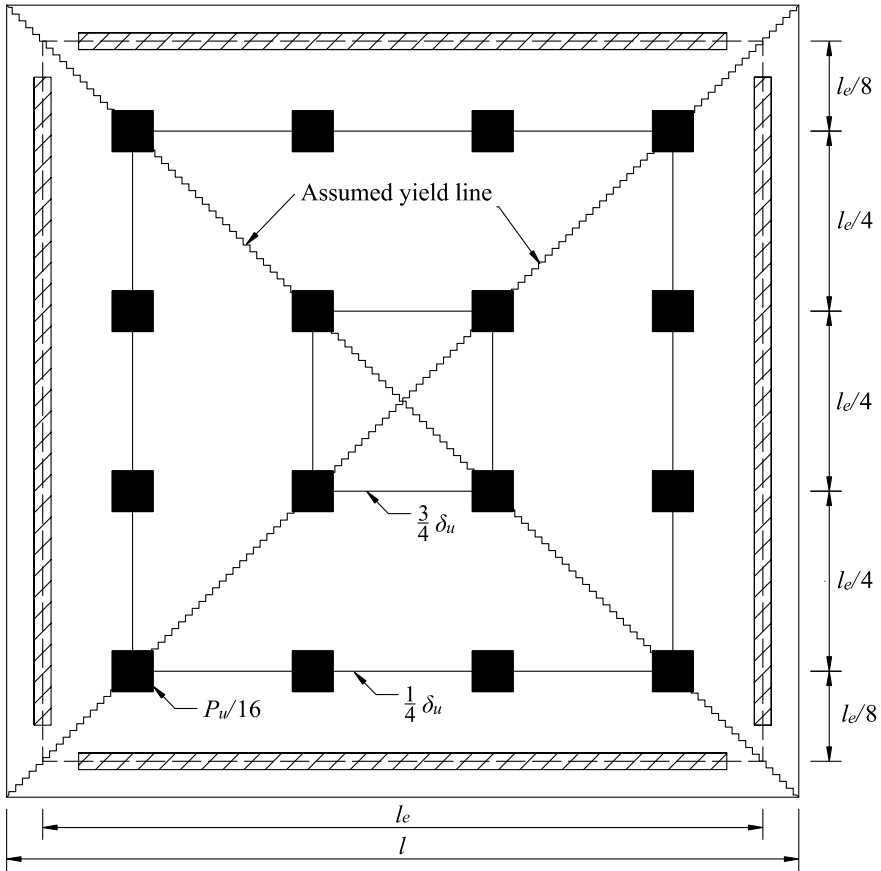


Fig. 8 Assumed yield line pattern with deformation contour

4 Summary and Conclusions

From Table 5, it can be observed that the ratio of experimentally obtained ultimate load capacity of slab specimens and theoretically estimated ultimate load of a solid slab is in the range of 1.68–1.84. Experimentally obtained ultimate load capacity

Table 5 Comparison of experimental and theoretical capacity

Specimen	Capacity—UDL (kN)		Ratio W_{u2}/W_n
	Experimental (W_{u2})	Analytical (W_n)	
SP 1	1160	635.3	1.83
SP 2	1169	634.8	1.84
SP 3	1386	826.7	1.68

is the same for the solid and voided slab. The same was observed in theoretical estimation as well. Thus, the ultimate capacity of the voided slab can be estimated by yield line theory similar to a conventional solid slab.

Based on the experimental and analytical investigations of the biaxial voided slab under two-way flexure, the following conclusions are drawn.

1. The solid and voided slab specimens showed typical two-way flexure behaviour with major cracks in the form of X, similar to assumed yield line pattern.
2. The experimentally observed ultimate load-carrying capacity of solid and voided slab specimens remained the same. The ratio of experimentally obtained ultimate load capacity of slab specimens and theoretically estimated ultimate load of a solid slab is in the range of 1.68–1.84.
3. The analytical investigation by yield line analysis showed that the ratio of the ultimate load-carrying capacity of the slab with a 16-point load and uniformly distributed load is 89%.
4. The analytical estimation of the ultimate load-carrying capacity by yield line analysis in congestion with IS 456 of the solid and voided slab are equal. Thus, the ultimate capacity of the voided slab can be estimated by yield line theory similar to a conventional solid slab.
5. The initial stiffness of solid slab specimen is 37% more in comparison with the voided slab specimen; however, the secant stiffness corresponding to yield load of voided and solid slab specimens were comparable.
6. The ratio of experimentally observed and estimated ultimate capacity of slab specimens was observed to be in the range of 1.68–1.84. The influence of the orientation and ultimate tensile strength of reinforcements on the enhancement of the capacity of slab need to be investigated, as researchers reported that these factors are influencing the ultimate load-carrying capacity of solid slabs [21, 22].
7. The strength enhancement due to tensile membrane action at large deflection in the solid slab was studied by various researchers [21, 23–25]. A similar kind of enhancement in the voided slab need to be verified.

Acknowledgements This work was supported by the Department of Science & Technology, India (SR/S3/MERC/0040/2012). The authors wish to acknowledge the assistance and facilities offered by the technical staff, Structural Engineering Laboratory, IIT Madras.

References

1. BubbleDeck Technology (2008) BubbleDeck voided flat slab solutions—technical manual & documents. UK
2. Chung JH, Park JH, Choi HK, Lee SC, Choi CS (2010) An analytical study on the impact of hollow shapes in bi-axial hollow slabs. In: FraMCoS-7. Korea Concrete Institute, pp 1729–1736
3. Churakov AG (2014) Biaxial hollow slab with innovative types of voids. *Constr Unique Build Struct* 6:70–88
4. Cobiax Technologies (2010) Cobiax engineering manual. Switzerland

5. Daliform Group (2014) U-Boot Beton® system study: lightened concrete slab by using U-Boot Beton®. Italy
6. Ibrahim AM, Ali NK, Salman WD (2013a) Flexural capacities of reinforced concrete two-way Bubbledeck slabs of plastic spherical voids. *Diyala J Eng Sci* 06:9–20
7. Kim BH, Chung JH, Choi HK, Lee SC, Choi CS (2011) Flexural capacities of one-way hollow slab with donut type hollow sphere. *Key Eng Mater* 452–453:773–776. <https://doi.org/10.4028/www.scientific.net/KEM.452-453.773>
8. Kim SH (2011) Flexural behavior of void RC and PC slab with polystyrene forms. *Key Eng Mater* 452–453:61–64. <https://doi.org/10.4028/www.scientific.net/KEM.452-453.61>
9. Sagadevan R, Nageswara Rao B (2019) Numerical study on flexural capacity of biaxial hollow slab. In: Rao ARM, Ramanjaneyulu K (eds) *Recent advances in structural engineering*, vol 1. Springer, Singapore, pp 97–105
10. Taskin K, Peker K (2014) Design factors and the economical application of spherical type voids in RC slabs. In: *International scientific conference people, buildings and environment 2014*, an international scientific conference. Kroměříž, Czech Republic, pp 448–458
11. Valivonis J, Jonaitis B, Zavalis R, Skuturna T, Šneideris A (2014) Flexural capacity and stiffness of monolithic biaxial hollow slabs. *J Civ Eng Manag* 20:693–701. <https://doi.org/10.3846/13923730.2014.917122>
12. Chung JH, Bae BI, Choi HK, Jung HS, Choi CS (2018) Evaluation of punching shear strength of voided slabs considering the effect of the ratio b_0/d . *Eng Struct* 164:70–81. <https://doi.org/10.1016/j.engstruct.2018.02.085>
13. Daliform Group (2012) U-Boot Beton® Disposable formworks for lightened structures in reinforced concrete cast on site. Italy
14. Sagadevan R, Nageswara Rao B (2017) Analytical studies on flexural capacity of biaxial hollow slab. In: *Proceedings of the international conference on composite materials and structures (ICCMS)*. Hyderabad, India
15. Ibrahim AM, Ali NK, Salman WD (2013b) Finite element analysis of reinforced concrete slabs with spherical voids. *Diyala J Eng Sci* 6:15–37
16. Chung JH, Jung HS, Bae BI, Choi CS, Choi HK (2018) Two-way flexural behavior of donut-type voided slabs. *Int J Concr Struct Mater* 12. <https://doi.org/10.1186/s40069-018-0247-6>
17. Fall D, Shu J, Rempling R, Lundgren K, Zandi K (2014) Two-way slabs: experimental investigation of load redistributions in steel fibre reinforced concrete. *Eng Struct* 80:61–74. <https://doi.org/10.1016/j.engstruct.2014.08.033>
18. Matešan D, Radnić J, Grgić N, Čamber V (2012) Strength capacity of square reinforced concrete slabs. *Mater Sci Eng* 43:399–404. <https://doi.org/10.1002/mawe.201200972>
19. IS 456 (2000) Plain and reinforced concrete—code of practice. Bureau of Indian Standards, New Delhi
20. IS 1786 (2008) High strength deformed steel bars and wires for concrete reinforcement—specification. Bureau of Indian Standards, New Delhi
21. Wood RH (1961) *Plastic and elastic design of slabs and plates*. Thames and Hudson, London
22. Taylor R, Maher DRH, Hayes B (1966) Effect of the arrangement of reinforcement on the behaviour of reinforced concrete slabs. *Mag Concr Res* 18:85–94. <https://doi.org/10.1680/mac.1967.19.58.58>
23. Sawczuk A, Winnicki L (1965) Plastic behavior of simply supported reinforced concrete plates at moderately large deflections. *Int J Solids Struct* 1:97–111. [https://doi.org/10.1016/0020-7683\(65\)90019-3](https://doi.org/10.1016/0020-7683(65)90019-3)
24. Taylor R (1965) A note on a possible basis for a new method of ultimate load design of reinforced concrete slabs. *Mag Concr Res* 17:183–186. <https://doi.org/10.1680/mac.1965.17.53.183>
25. Kemp KO (1967) Yield of a square reinforced concrete slab. *Struct Eng* 45:235–240

A Comparative Study of Seismic Response of Structure Isolated with Triple Friction Pendulum Bearing and Single Friction Pendulum Bearing Under Different Hazard Levels of Earthquake



Ankit Sodha, Sandip Vasanwala, Devesh Soni, and Shailendra Kumar

Abstract The Triple Friction Pendulum (TFP) bearing is highly adaptive in nature that contains three effective pendula with four spherical sliding surfaces. By considering desirable displacement capacity with effective damping and period, TFP systems are to be designed. A comparative response of the building isolated by the Single Friction Pendulum (FPS) and Triple Friction Pendulum (TFP) with same effective damping, effective time period, and displacement capacity under different hazard levels of earthquake along with its mathematical models. It shows that the performance of TFP is superior over the FPS. Owing to its multiple sliders, which dissipate seismic energy and distribute sliding displacement over the multiple surfaces. It is also found that the TFP bearing stiffens at low level of input, softens with increasing input, and then stiffens again at higher levels of input. Hence, it behaves adaptively in nature under different hazard levels of earthquake.

Keywords Seismic isolation · Multi-hazard level earthquake · Triple friction pendulum system · Friction pendulum system

1 Introduction

The sliding isolation system is based on the concept of sliding friction [1]. The sliding bearings such as Electric de France system [2], resilient-friction base isolator system were first introduced [3], and further Friction Pendulum System (FPS) was developed [4]. To divulge adaptive behavior of friction pendulum system, a concept of multiple friction pendulum system has been introduced [5]. Further, isolator with two sliders

A. Sodha (✉) · S. Vasanwala · S. Kumar
Applied Mechanics Department, Ichchhanath Circle, Sardar Vallabhbhai National Institute of Technology, Surat 395007, Gujarat, India
e-mail: aankitsodha@gmail.com

D. Soni
Department of Civil Engineering, SardarVallabhbhai Patel Institute of Technology, 388 306
Anand District, Gujarat, India

namely Double Concave Friction Pendulum (DCFP) system [6] and with four sliders Triple Friction Pendulum (TFP) system were introduced [7, 8]. The DCFP and TFP offer the designer extra design parameters to optimize the performance in terms of radius of curvature and coefficients of friction for difference sliding surfaces. The multi frictional pendulum systems like DCFP and TFP are more effective compared to FPS [9, 10].

2 TFP Bearing and Its Mathematical Model

The Triple Friction Pendulum (TFP) system is comprised of four hardened steel curved surfaces with Teflon covering settled by a slider. The displacement capacity represented by d_i , coefficient of friction μ_i , and radius of curvature R_i are shown in Fig. 1a.

The TFP can be modeled as a series model [7]. As shown in Fig. 1b, three FP elements connected in series include friction element, μ_i , representing the surface friction parallel arrangement with gap element, d_i , representing the finite displacement capacity, and linear elastic spring element with stiffness, $1/R_{\text{eff}}$, representing the restoring force provided by the spherical sliding surface. The effective radius of curvature and coefficient of friction are represented by

$$\bar{R}_{\text{eff}1} = R_{\text{eff}2} + R_{\text{eff}3} \quad (1)$$

$$\bar{R}_{\text{eff}2} = R_{\text{eff}1} - R_{\text{eff}2} \quad (2)$$

$$\bar{R}_{\text{eff}3} = R_{\text{eff}4} - R_{\text{eff}3} \quad (3)$$

$$\bar{\mu}_1 = \mu_2 = \mu_3 \quad (4)$$

$$\bar{\mu}_2 = \mu_1 \quad (5)$$

$$\bar{\mu}_3 = \mu_4 \quad (6)$$

3 Ground Motions

Different hazards of levels including Service Level of Earthquake (SLE) having 50% of probability of occurrence in 50 years, for Design Bases Earthquake (DBE) having probability of 10% in 50 years, and Maximum Considered Earthquake (MCE) having

Table 1 Multiple hazard level ground motions

Record lable	Name	Amplitude scale factor	Duration (sec)	PGA (cm/sec ²)
SLE				
LA 41	Coyote Lake, 1979	2.28	39.38	578.34
DBE				
LA 03	Imperial Valley, 1979	1.01	39.38	386.04
MCE				
LA 21	Northridge, 1994	1.15	59.98	1258.00

2% in 50 years. The set of time histories is taken from the developed as a part of SAC steel project followed by ASCE 7. A set of three-time histories, one from each of the three bins: SLE, DBE, and MCE is presented in Table 1 [12].

4 Governing Equation of Motion and Its Solution

The governing equations of motion for the N story superstructure model are expressed in matrix form as

$$[M]\{\ddot{u}\} + [K]\{\dot{u}\} + [C]\{u\} = -[M]\{r\}(\ddot{u}_b + \ddot{u}_g) \quad (7)$$

where $[M]$ is N sized square matrices of the superstructure for mass, $[K]$ is for stiffness, and $[C]$ is for damping.

The structure with isolation containing highly nonlinear force–deformation behavior. For the solution of governing equation of motion, Newmark’s step-by-step method is used with an assumption of linear variation for acceleration over a 1×10^{-6} s time interval. Further, fourth-order Runge–Kutta method is used for hysteretic model analysis.

5 Properties of the Isolation System

To compare FPS and TFP, the effective damping ratio, time period, and design displacement are kept same as $\xi_{\text{eff}} = 10\%, 15\%, 20\%$; $T_{\text{eff}} = 4 \text{ sec}, 5 \text{ sec}, 6 \text{ sec}$; and $D = 1 \text{ m}$, respectively, so that the energy dissipated in each cycle, E_{loop} remain same for all the three systems. The effective period, T_{eff} and damping ratio, ξ_{eff} are given by

$$T_{\text{eff}} = 2\pi \sqrt{\frac{W}{K_{\text{eff}}g}} \quad (8)$$

$$\xi_{eff} = \frac{E_{loop}}{2\pi K_{eff} D^2} \tag{9}$$

where energy dissipation is represented by E_{loop} for the isolator displacement; W is the total weight on the isolator; K_{eff} is the effective stiffness and maximum displacement is represented by D , respectively.

For the FPS effective stiffness, K_{eff} is obtained from the geometry of force-deformation curve and the energy dissipated in each cycle, E_{loop} is calculated from the area enclosed by the hysteresis loop (refer Fig. 2a, c) as given by

$$K_{eff} = \frac{\mu + \frac{1}{R_{eff}}(D - D_y)}{D} W \tag{10}$$

$$E_{loop} = 4\left(\mu - \frac{D_y}{R_{eff}}\right)(D - D_y)W \tag{11}$$

Similarly, for the TFP, the K_{eff} and E_{loop} in each cycle are given by (refer Fig. 2b, d)

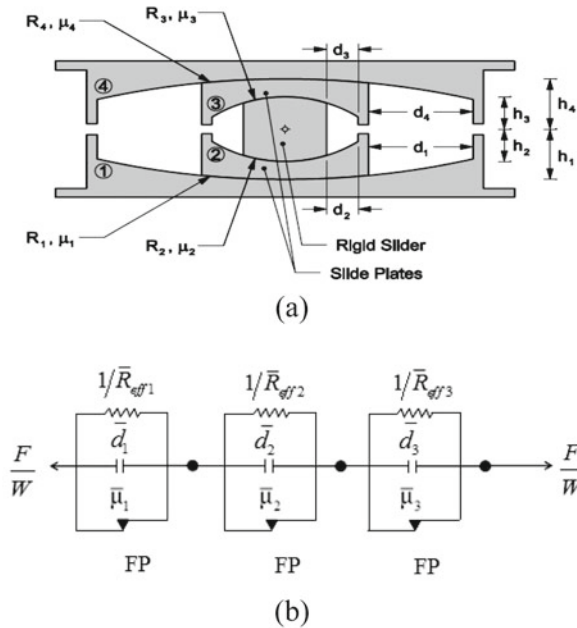


Fig. 1 a Cross section and b series model of TFP

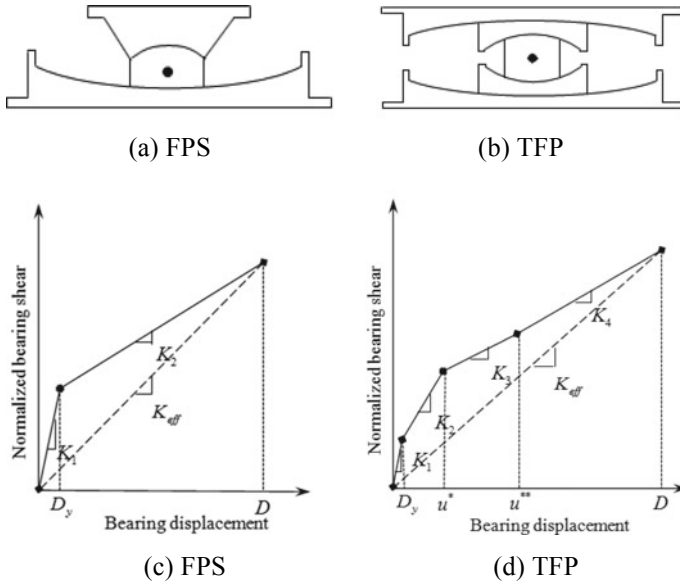


Fig. 2 Schematic diagram of **a** FPS **b** TFP and hysteretic force–displacement relationship of **c** FPS **d** TFP

$$K_{\text{eff}} = \frac{K_1 D_y + K_2 (u^* - D_y) + K_3 (u^{**} - u^*) + K_4 (D - u^{**})}{D} W \quad (12)$$

$$E_{\text{loop}} = 4(u^*)^2 (K_2 - K_3) W + 4D D_y (K_2 - K_1) W + 4u^* D (K_3 - K_2) W + 4u^{**} D (K_4 - K_3) W + 4(u^{**})^2 (K_3 - K_4) W + 4D_y^2 (K_1 - K_2) W \quad (13)$$

where

$$K_1 = \frac{1}{R_{\text{eff}2}}; K_2 = \frac{1}{R_{\text{eff}2} + R_{\text{eff}3}}; K_3 = \frac{1}{R_{\text{eff}3} + R_{\text{eff}1}} \quad (14)$$

$$\text{and } K_4 = \frac{1}{R_{\text{eff}1} + R_{\text{eff}4}}$$

$$u^* = (\mu_1 - \mu_2) R_{\text{eff}2} + (\mu_1 - \mu_3) R_{\text{eff}3} \quad (15)$$

$$u^{**} = u^* + (\mu_4 - \mu_1) (R_{\text{eff}1} + R_{\text{eff}3}) \quad (16)$$

Here, D_y is the isolator displacement to initiate the surface sliding. The D_y is taken as 0.025 cm in this study [11].

For the FPS, radius of curvature and coefficient of friction are calculated using Eqs. (10) and (11). And, for the TFP, radius of curvature and coefficient of friction of

Table 2 Series model parameters for TFP and FPS

	ξ_{eff}	T_{eff}	$D(\text{m})$	\bar{R}_{eff1}	\bar{R}_{eff2}	\bar{R}_{eff3}	$\bar{\mu}_1$	$\bar{\mu}_2$	$\bar{\mu}_3$
FPS1	10	4	1	4.8			0.04		
TFP1	10	4	1	0.6	2.7	2	0.01	0.05	0.03
FPS2	15	5	1	8.27			0.039		
TFP2	15	5	1	0.9	5.05	0.45	0.01	0.038	0.058
FPS3	20	6	1	13			0.035		
TFP3	20	6	1	1.2	6.4	5.4	0.01	0.035	0.045

different sliding surfaces are calculated using Eqs. (12)–(16), respectively, through iterative process. The series model parameters for TFP and FPS are presented in Table 2.

6 Numerical Study

In this study, shear building with a five-storeys is considered. The mass, stiffness, and modal damping ratio of each floor are kept constant in each mode of vibration for simplicity in analysis. The time period of superstructure can be kept fixed at the base by selecting such a value of stiffness. The characterization of base-isolated system is done by the parameters like the ratio of base mass to the superstructure floor mass, mb/m , damping ratio of the superstructure, ξ_s , and the fundamental time period of the superstructure, T_s . The numerical values are kept constant as $T_s = 0.5$ s, $\xi_s = 0.02$, $mb/m = 1$, and $msi/m = 0.0005$ in this study. To achieve desirable fundamental period of 0.5 s, the storey stiffness, $K = 115,740$ kN/m and floor mass, $m = 59,378$ kg have been taken and along with bay width 3.0 m and storey height 5.0 and 3.0 m. To study seismic response, all three response quantities, i.e., displacement of isolator, u_b , base shear of the building normalized by total weight, F_b/W , and top floor absolute acceleration, $A(g)$ are considered.

6.1 Seismic Behavior of FPS and TFP

The displacement under time variation under LA 21 (MCE) for TFP1 of the three FP elements, x_1, x_2, x_3 and total isolator displacement, u_b is shown in Fig. 3. Further, Fig. 4 represents hysteretic behavior for each of FP elements along with TFP isolator under LA 21 (MCE).

To study adaptive behavior of TFP over a FPS, three different design configurations are considered under ground motions of LA 41 (SLE), LA 03 (DBE), LA 21 (MCE) as shown in Table 2. The hysteresis behavior and Time histories of response of TFP and FPS under LA 41 (SLE) are shown in Fig. 5. The hysteresis behavior and

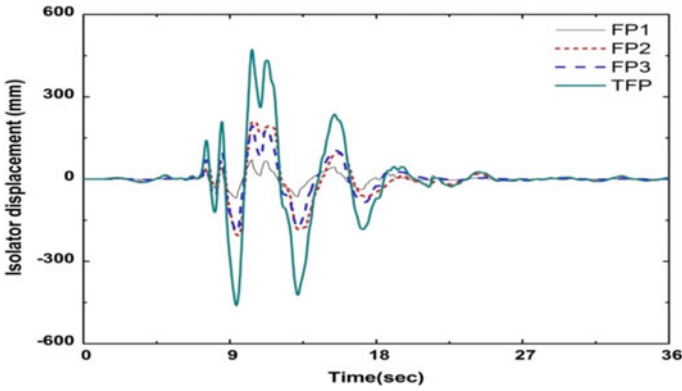


Fig. 3 Displacement variation under LA 21 (MCE) for individual FP elements and TFP1

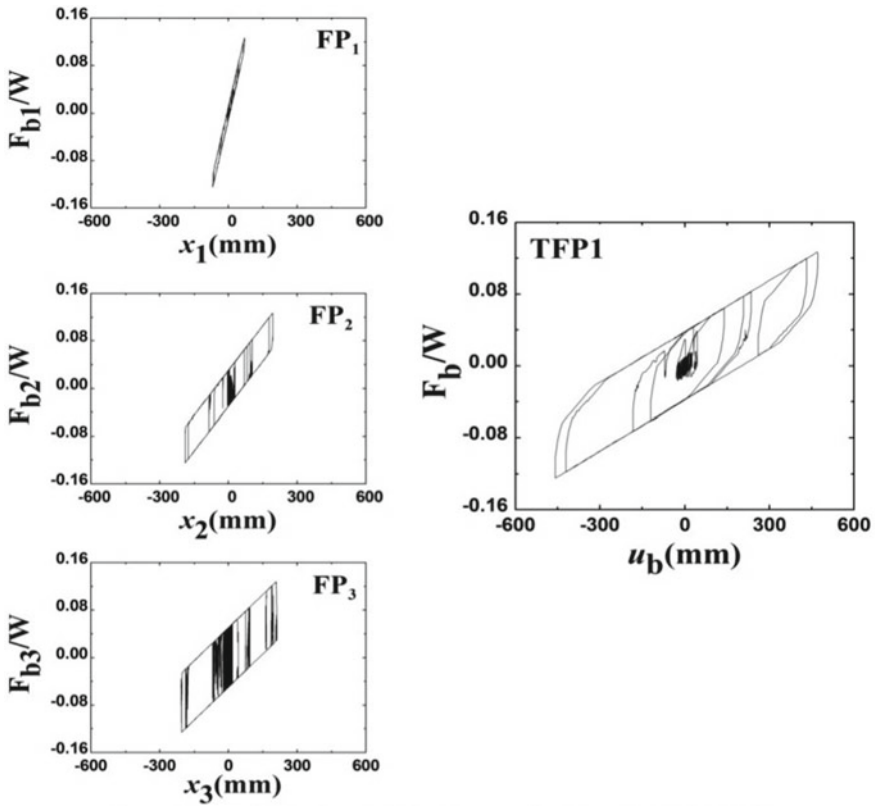


Fig. 4 Hysteretic behavior under LA 21 (MCE) for individual FP elements and TFP1

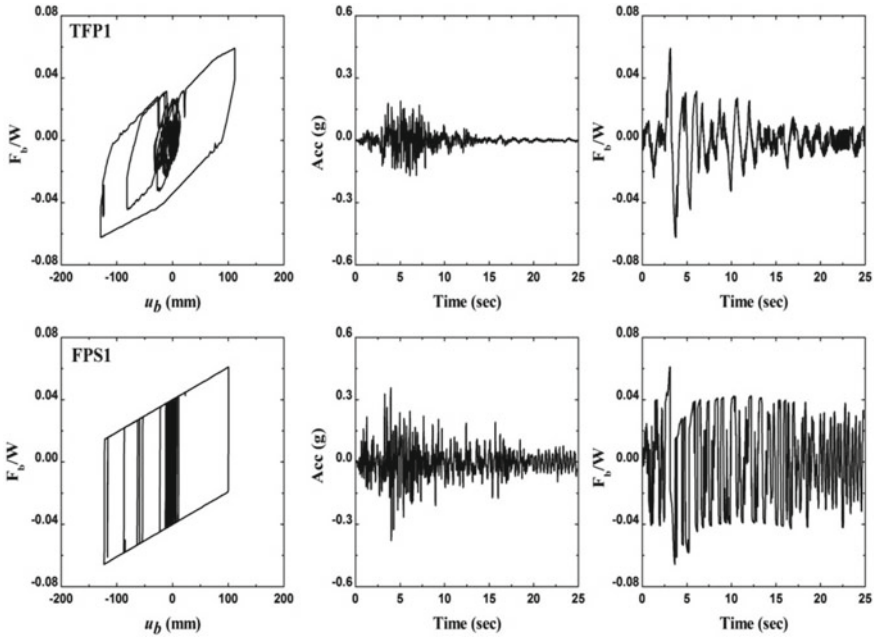


Fig. 5 Hysteretic behavior, acceleration, and base shear of TFP1 and FPS1 under LA 41 (SLE)

Time histories of response of TFP and FPS under LA 03 (DBE) are shown in Fig. 6, and the hysteresis behavior and Time histories of response of TFP and FPS under LA 21 (MCE) are shown in Fig. 7. Here, TFP system stiffens at SLE (low input), at DBE it gets softens and again it gets stiffens at MCE (higher input).

Peak values of top floor acc, g, bearing disp, mm, and base shear, F_b/W of three different configurations for FPS and TFP under MCE, DBE, and SLE, respectively are shown in Table 3.

Here for the effective damping ratio $\xi_{eff} = 10\%$, time period $T_{eff} = 4$ sec, reduction in a peak response of TFP compared to FPS for the top floor acceleration under SLE, DBE, and MCE is 20%, 12%, and 50%, respectively, and the reduction in a peak response of base shear under SLE, DBE, and MCE is 10%, 5%, and 5% under SLE, DBE, and MCE, respectively.

For the effective damping ratio $\xi_{eff} = 15\%$, time period $T_{eff} = 5$ sec, reduction in a peak response of TFP compared to FPS for the top floor acceleration under SLE, DBE, and MCE is 30%, 35%, and 60%, respectively, and the reduction in a peak response of base shear under SLE, DBE, and MCE is 10%, 5%, and 8%, respectively.

For the effective damping ratio $\xi_{eff} = 20\%$, time period $T_{eff} = 6$ sec, reduction in a peak response of TFP compared to FPS for the top floor acceleration is 35%, 35%, and 60% under SLE, DBE, and MCE, respectively, and for the reduction in a peak response of base shear is 15%, 10%, and 5% under SLE, DBE, and MCE, respectively. Here there is no significant change in bearing displacement.

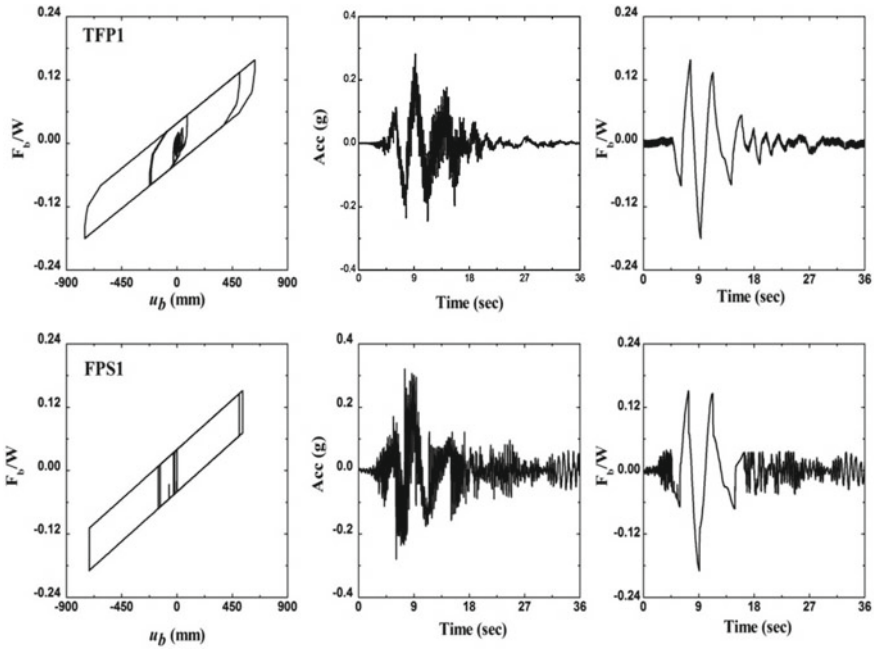


Fig. 6 Hysteretic behavior, acceleration, and base shear of TFP1 and FPS1 under LA 03 (DBE)

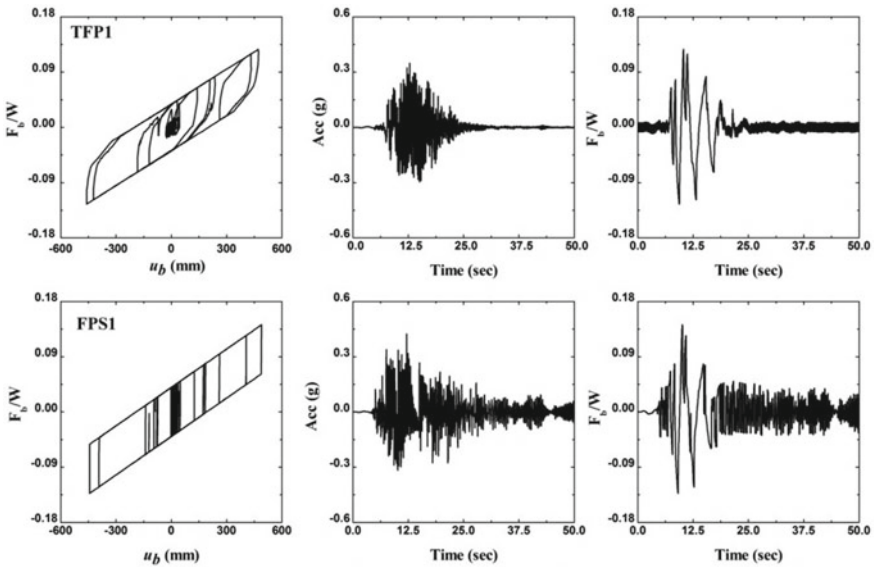


Fig. 7 Hysteretic behavior, acceleration, and base shear of TFP1 and FPS1 under LA 21 (MCE)

Table 3 Peak values of top floor acc, g , bearing disp., and base shear, F_b/W

EQ	Model	Top floor acc, g	Bearing disp. (mm)	Base shear F_b/W
		$\xi_{\text{eff}} = 10\%, T_{\text{eff}} = 4 \text{ sec}$		
MCE (LA 21)	FPS	0.424	489.38	0.142
	TFP	0.347	472.00	0.127
		$\xi_{\text{eff}} = 15\%, T_{\text{eff}} = 5 \text{ sec}$		
	FPS	0.469	471.68	0.096
	TFP	0.339	472.60	0.087
		$\xi_{\text{eff}} = 20\%, T_{\text{eff}} = 6 \text{ sec}$		
	FPS	0.413	480.19	0.072
	TFP	0.277	470.39	0.063
		$\xi_{\text{eff}} = 10\%, T_{\text{eff}} = 4 \text{ sec}$		
DBE (LA 03)	FPS	0.321	714.86	0.189
	TFP	0.281	750.88	0.180
		$\xi_{\text{eff}} = 15\%, T_{\text{eff}} = 5 \text{ sec}$		
	FPS	0.325	616.24	0.114
	TFP	0.214	646.93	0.107
		$\xi_{\text{eff}} = 20\%, T_{\text{eff}} = 6 \text{ sec}$		
	FPS	0.275	634.04	0.084
	TFP	0.182	626.79	0.075
		$\xi_{\text{eff}} = 10\%, T_{\text{eff}} = 4 \text{ sec}$		
SLE (LA 41)	FPS	0.378	122.63	0.066
	TFP	0.190	128.90	0.062
		$\xi_{\text{eff}} = 15\%, T_{\text{eff}} = 5 \text{ sec}$		
	FPS	0.405	110.62	0.052
	TFP	0.172	113.87	0.048
		$\xi_{\text{eff}} = 20\%, T_{\text{eff}} = 6 \text{ sec}$		
	FPS	0.346	112.19	0.044
	TFP	0.147	116.89	0.042

7 Conclusions

To achieve a wide range variation in frequency and intensities, The multi-degree of freedom system is analyzed for TFP and FPS under multi-hazard levels of earthquakes. The following conclusions can be derived from the study:

1. For the different design configurations, it gives greater flexibility for TFP due to its three sliding surfaces compared to FPS. Hence, TFP is very effective to control the parametric response of structure.

2. The TFP shows highly adaptive behavior compared to FPS for various types of ground shaking, despite being a passive system. It stiffens at SLE (low input), at DBE it gets softens and again it gets stiffens at MCE (higher input).
3. As effective damping ratio increases, time period leads to more reduction in a peak response of TFP compared to FPS for peak response of top floor acceleration and base shear. Here there is no significant change in bearing displacement.

References

1. Mostaghel N, Tanbakuchi J (1983) Response of sliding structures to earthquake support motion. *Earthq Eng Struct Dynam* 11(6):729–748
2. Gueraud R, Noel-Leroux JP, Livolant M, Michalopoulos AP (1985) Seismic isolation using sliding-elastic bearing pads. *Nucl Eng Des* 84(3):363–377
3. Mostaghel N, Khodaverdian M (1987) Dynamics of resilient-friction base isolator (R-FBI). *Earthq Eng Struct Dynam* 15(3):379–390
4. Zayas VA, Low SS, Mahin SA (1990) A simple pendulum technique for achieving seismic isolation. *Earthq spectra* 6(2):317–333
5. Tsai CS, Lin YC, Su HC (2010) Characterization and modeling of multiple friction pendulum isolation system with numerous sliding interfaces. *Earthq Eng Struct Dynam* 39(13):1463–1491
6. Fenz DM, Constantinou MC (2006) Behaviour of the double concave friction pendulum bearing. *Earthq Eng Struct Dynam* 35(11):1403–1424
7. Fenz DM, Constantinou MC (2008) Modeling triple friction pendulum bearings for response-history analysis. *Earthq Spectra* 24(4):1011–1028
8. Becker TC, Mahin SA (2013) Approximating peak responses in seismically isolated buildings using generalized modal analysis. *Earthq Eng Struct Dynam* 42(12):1807–1825
9. Dhankot MA, Soni DP (2016) Seismic response of triple friction pendulum bearing under multi hazard level excitations. *Int J Struct Eng* 7(4):412–431
10. Dhankot MA, Soni DP (2017) Behaviour of triple friction pendulum isolator under forward directivity and fling step effect. *KSCE J Civ Eng* 21(3):872–881
11. Constantinou M, Mokha A, Reinhorn A (1990) Teflon bearings in base isolation II: modeling. *J Struct Eng* 116(2):455–474
12. Somerville P, Anderson D, Sun J, Punyamurthula S, Smith N (1998) Generation of ground motion time histories for performance-based seismic engineering. In: *Proceedings 6th national earthquake engineering conference*. Seattle, Washington
13. Shome N, Cornell CA (1991) Probabilistic seismic demand analysis of nonlinear structures. Department of Civil Engineering, Stanford University, Stanford, California; Rep. No. RMS-35
14. Panchal VR, Jangid RS (2008) Variable friction pendulum system for seismic isolation of liquid storage tanks. *Nucl Eng Des* 238(6):1304–1315

Assessment of Important Parameters for Seismic Analysis and Design of Confined Masonry Buildings: A Review



Bonisha Borah , Vaibhav Singhal , and Hemant B. Kaushik 

Abstract Confined masonry (CM) building is emerging as a popular building construction system in many earthquake-prone countries including India. This building type has performed really well in several destructive earthquakes, even though it started as an informal construction. A finished CM building looks like a reinforced concrete (RC) infilled structure, however, the structural behavior of both the systems is quite different. Apart from excellent performances in seismic events, it is very cost-effective and easier to construct. But the design methodology for CM buildings is yet to be standardized for Indian conditions due to lack of research. Therefore, it is important to study the various factors affecting the performance of CM building in comparison to other building types. The objective of this study is to identify the parameters influencing the seismic performance of CM buildings. The dependency of seismic response of CM buildings on different key parameters such as material and geometric properties, gravity loads, amount of longitudinal steel present in tie-columns, and aspect ratio of the wall is discussed in this paper.

Keywords Confined masonry · Seismic response · Seismic analysis · Design parameters

1 Introduction

A systematic and methodical structural analysis and design to construct structure or building ensure a safe, stable, and durable structure capable of resisting all the probable loads during its intended life. Buildings should be adequately designed,

B. Borah · H. B. Kaushik (✉)

Department of Civil Engineering, Indian Institute of Technology Guwahati, Assam, India
e-mail: hemantbk@iitg.ac.in

B. Borah

e-mail: bonisha@iitg.ac.in

V. Singhal

Department of Civil and Environmental Engineering, Indian Institute of Technology Patna, Bihar, India

e-mail: singhal@iitp.ac.in

© Springer Nature Singapore Pte Ltd. 2021

S. Adhikari et al. (eds.), *Advances in Structural Technologies*, Lecture Notes in Civil Engineering 81, https://doi.org/10.1007/978-981-15-5235-9_20

built, and maintained to minimize the seismic risks associated with it. However, embracing new technologies to build structures is a sine qua non in today's age and hence these technologies have been and are being adopted worldwide. Especially in seismic-prone regions, different construction methodologies have emerged over the past few decades as alternatives to seismically vulnerable unreinforced masonry (URM) building and improperly designed and constructed infilled reinforced concrete (RC) frame building. Among them confined masonry (CM) is an attractive building construction technology for low-tech construction in seismic regions. Though this building system started as an informal construction, it showed very good resistance to past seismic events [1, 2]. As a result, the CM structure has attracted considerable interest in the research field. Several guidelines and country codes were developed in the past years for the construction of a CM structure, however, most of these guidelines were determined subjectively on the basis of experience, and are primarily applicable for only one- to two-storey buildings [3]. Therefore, a systematic research is required for developing a detailed engineered design instead of a prescriptive approach. In this regard, it is very important to know the main governing design parameters, which affect the response of this building system under any lateral loads. In the next section, the behaviour of CM structure under gravity and lateral earthquake loads is discussed.

2 Load Transfer Mechanism in CM Building

Confined masonry is a composite construction system, where masonry structural walls are first constructed and after that small-sized RC tie-elements (tie-columns and tie-beams) are built at the walls' perimeter and some other salient locations. The RC tie-elements are not intended to carry either vertical or horizontal loads, and are consequently not designed to behave as a moment-resisting frame. These are mainly provided to confine the masonry wall to engage it under gravity and lateral loading and provide ductility. Even though, at a glance, CM building looks similar to an infilled RC frame building, its behaviour under gravity and lateral loading and the load distribution mechanism are quite different as shown in Fig. 1 [3]. In infilled RC frame, usually there exists a small gap between beam soffit and masonry panel and the frame is relatively very stiffer compared to flexible confining frame of CM wall (Fig. 1a). Therefore under gravity loading, the load transferred to the infill panel is

Fig. 1 Comparison of
a infilled RC frame wall and
b CM wall

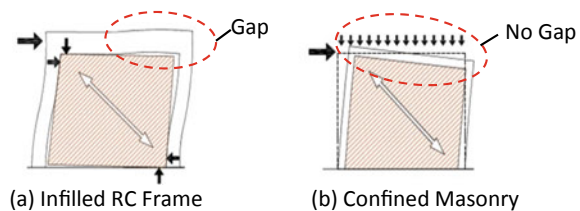
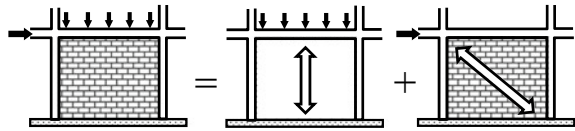


Fig. 2 Load transfer mechanism in confined masonry building



almost negligible, whereas in CM wall as the beam is cast after the construction of the panel, continuity in gravity load transfer occurs from tie-beam to CM panel as shown in Figs. 1b and 2.

From the investigation of experimental test studies and past earthquake damage reports, the general modes of failure of CM structures can be broadly categorized into in-plane failure, out-of-plane failure, failure of diaphragm, connection and non-structural elements [4]. Because of the monolithic action developed between the masonry panel and confining frame, the out-of-plane strength of CM structure is better as compared to that of URM and infilled RC frame structure. Therefore, the in-plane load–displacement behaviour of CM wall has attracted considerable interest in seismic research. Under in-plane lateral loading, masonry may fail under diagonal compression mode or by bed joint sliding or diagonal stepped cracking. In case of CM wall, generally diagonal stepped cracking is the most common type of failure. Therefore, under lateral loading, masonry walls act as diagonal struts subjected to compression, while RC confining members act in tension and/or compression, depending on the direction of lateral earthquake forces [5]. The load transfer mechanism of a CM wall subjected to gravity and lateral load is shown in Fig. 2 [6]. The detailed in-plane behaviour of CM wall under lateral loading and the effects of different parameters are discussed in the next section.

3 Important Parameters for Seismic Analysis and Design of CM Building

A particular structural system greatly influences the analysis and design principle. However, there are some basic parameters that should be considered in design of a seismic-resistant building and these are seismic zone, soil condition, number of stories, building configuration, etc. Building configuration (i.e., size and shape) determines the way of seismic force distribution within the structure. Generally, irregular configurations are avoided for their problematic stress concentration and torsion. A symmetrical arrangement of mass and balanced stiffness against either direction is necessary to keep torsion within a manageable range. The seismic design of structures highly depends on their characteristic force–deformation relationship, which is defined as a function of the three most important design parameters—strength, stiffness and deformability or ductility. For adequate seismic performance, strength and deformation capacities of a structure must be greater than the demand imposed by a design earthquake. The strength of a structure assures the ability to resist applied

forces within a safe limit. Stiffness of a structure determines the degree of resistance to deflection or drift. Ductility assures that the structure is able to deform beyond the elastic range and dissipate seismic energy through plastic deformations. Structural and architectural detailing and construction quality control are very important to ensure ductility and natural damping of the structure and to keep damages to a limited and repairable range.

An idealized load–deformation envelope curve developed in a past study [3] for a CM wall subjected to lateral load is described in Fig. 3. Until the first visible diagonal cracks, the behaviour can be assumed linearly elastic (point A). At higher drift excursion level, the inclined shear cracks extend towards the tie-columns and result in a significant decrease in the wall stiffness (point B). This post-cracking behaviour is directly influenced by the friction and brick interlock in the masonry panel and by the shear resistance of tie-columns. With further loading (point C), the confined wall experiences strength deterioration due to the crushing of bricks and shearing of tie-column ends. The post-peak behaviour (descending branch B–C) and stiffness of the panel at large deformation are mainly governed by the cross section and reinforcement details of tie-columns [3, 7]. Therefore, a properly designed and constructed CM wall can attain significant lateral deformation and ductility before the failure.

The parameters—stiffness, strength, and deformation capacity—of a CM building are functions of different variables, which are generally related to the material properties, geometric characteristics, reinforcement detailing, opening area, loading condition, overburden pressure, etc. In the following section, some important parameters

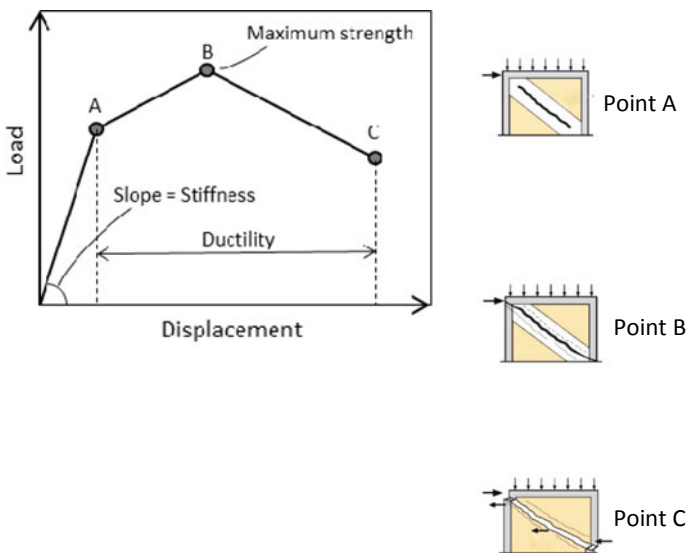


Fig. 3 Idealized load–deformation envelope curve for a CM wall subjected to lateral load

for seismic analysis and design of CM structure are discussed and their effects on the lateral load–displacement behaviour are studied.

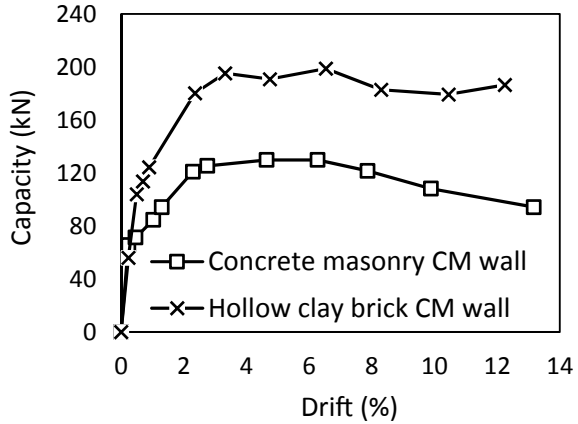
3.1 Wall Density

Wall density is a ratio of cross-sectional area of all walls in one direction to the total floor area. It is an important factor for deciding the required adequate wall area of a CM building. The lateral load resistance at a floor level can be determined as the sum of the wall resistances projected in the direction where seismic loading is being considered. The required wall density in each orthogonal direction of a building to resist the given seismic base shear force can be determined by applying a simplified method, which is based on Mexican practice [3, 8]. As recommended in the guideline, for buildings with different types of masonry, soil condition, and storey level, the minimum value of wall density for each direction of the building plan should range from 1 to 2% for low hazard level ($PGA \leq 0.08$ g), 1 to 5% for medium hazard level ($PGA \leq 0.25$ g) and 1.5 to 9.5% for high hazard level ($PGA \leq 0.4$ g) [3]. After deciding the wall density and thereby the wall area, the thickness and length should be finalized for the individual wall to resist the probable gravity and lateral forces. Individual wall capacity depends on many parameters which are discussed below.

3.2 Masonry Properties

Masonry is a nonlinear, nonhomogeneous, and anisotropic material consisting of two primary materials, masonry units such as bricks, blocks etc., and mortar, which can be cement or lime-based with sand, soil and water. Both materials are different in their behaviour with quite different properties. Compressive strength and elastic modulus of unit and mortar are the basic indicators of material quality. Bricks are relatively stiffer than mortar with much higher compressive strength as compared to mortar. Hence, generally, it is believed that strength and stiffness of masonry would lie within mortar and unit. Depending upon the availability of material, cost, climatic condition, living habits and tradition, different types of unit and mortar combinations are adopted in different parts of the world. However, as per the guidelines, natural stone masonry or adobe masonry and masonry units with horizontal perforations are not recommended for CM construction. The minimum compressive strength of masonry unit should be 4 MPa for hand-made clay bricks, 5 MPa for solid and hollow concrete blocks and 10 MPa for hollow clay units, machine-made and multi-perforated clay bricks [3]. Furthermore, CM walls built using unreinforced low-strength hollow concrete blocks are generally more prone to brittle failures as compared to the walls built using solid concrete and clay units [3]. Yáñez et al. tested 16 specimens of solid and perforated CM walls built with concrete masonry and hollow clay brick [9]. The stiffness and strength obtained for the solid CM walls were 49 kN/mm and

Fig. 4 Effect of type of masonry on lateral load–deformation behaviour of CM wall [9]



130 kN using concrete block masonry units, whereas, large strength and stiffness, i.e., 82 kN/mm and 199 kN were obtained using hollow clay brick masonry units as shown in Fig. 4. By observing the behaviour of all the test specimens, it was concluded that the hollow clay brick masonry unit specimens present larger strength and stiffness degradation than the concrete masonry unit specimens, although the former specimens provide larger maximum horizontal load and energy dissipation capacity.

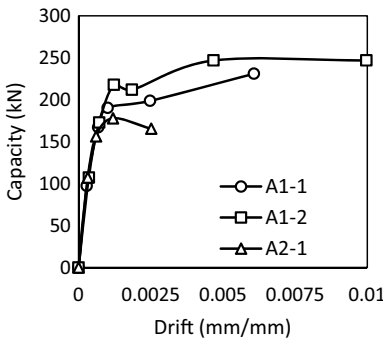
3.3 Confinement Effect

The deficiencies in URM in seismic events are improved by providing RC elements at the outer periphery of the masonry panel in the form of tie-beam and tie-column. Masonry is a composite element with many joint interfaces. It performs fairly well under compression but is weak in tension. Tensile damage is observed even at small displacement levels causing premature failure of wall. The confinement prevents the disintegration of masonry, which reduces stiffness degradation and enhances the ductility characteristic of wall. This further improves the energy dissipation characteristics and capacity of the wall [10]. The effectiveness of confinement depends on various factors such as size, grade of concrete, grade of steel, percentage reinforcement, location, etc.

Confining elements used in CM masonry are relatively small in cross-section compared to a moment-resisting RC frame. Even joints are not treated as fully rigid joints that do not provide effective frame action. The minimum dimension is generally recommended as 150×150 mm with 15 MPa as the minimum compressive strength of concrete [3]. Even though the role of confining element is to confine the masonry wall to avoid premature failure, certain minimum reinforcement is required to avoid sudden failure of members. Use of four 10 mm dia. deformed steel bars with a yield

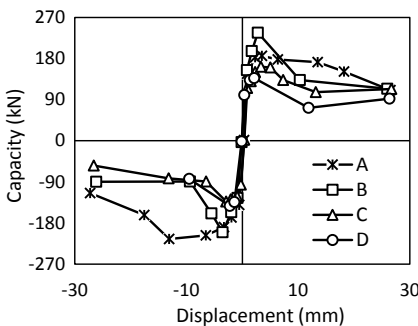
strength of 400 MPa is recommended as longitudinal reinforcement in tie-elements [3]. Also, low-grade reinforcement can be used with suitable modifications. During a seismic event, maximum damage concentrates at the ground floor level due to the high seismic load [11, 12]. It is obvious that an increase in percentage reinforcement will result in increasing lateral capacity substantially as shown in Figs. 5 and 6 [13, 14], therefore it is a wise choice to provide more reinforcement in the confining elements of the ground floor. From the experimental study of Quiroz et al. [14], it was observed that specimens with high tie-column reinforcement, (Wall Id: A1-1 and A1-2) exhibited higher lateral strength as shown in Fig. 5.

Although axial reinforcement increases the lateral load-carrying capacity, the tie-columns and tie-beams are also required to be provided with lateral ties to prevent brittle shear failure mode. Therefore, lateral ties also play a vital role in the behaviour of CM wall. After the initial diagonal crack, when load increases the crack gets propagated to tie-column leading to shear concentration at the ends of the tie-column. Adequate transverse reinforcement is needed to achieve the desired deformation



Wall Id	Axial Reinforcement in	
	Tie - column	Tie - beam
A1-1	0.734 %	0.473 %
A1-2	0.734 %	0.845 %
A2-1	0.411 %	0.473 %

Fig. 5 Effect of tie-column and tie-beam reinforcement on lateral load–deformation behaviour of CM wall [14]



Wall Id	Reinforcement in tie-column	
	Axial	Shear
A	3.8% (Rich)	1.28% (Rich)
B	3.8% (Rich)	0.3% (Poor)
C	0.99% (Poor)	1.28% (Rich)
D	0.99% (Poor)	0.3% (Poor)

Fig. 6 Effect of tie-column reinforcement on lateral load–deformation behaviour of CM wall [13]

and energy dissipation characteristics [13]. It is evident from Fig. 6 that high axial reinforcement increases lateral capacity and high shear reinforcement enhances the ductility of the wall by preventing early shear failures. Mild steel bars of minimum 6 mm diameter at a maximum spacing of 200 mm are recommended with reduced spacing at column ends for the regions of high seismicity [3].

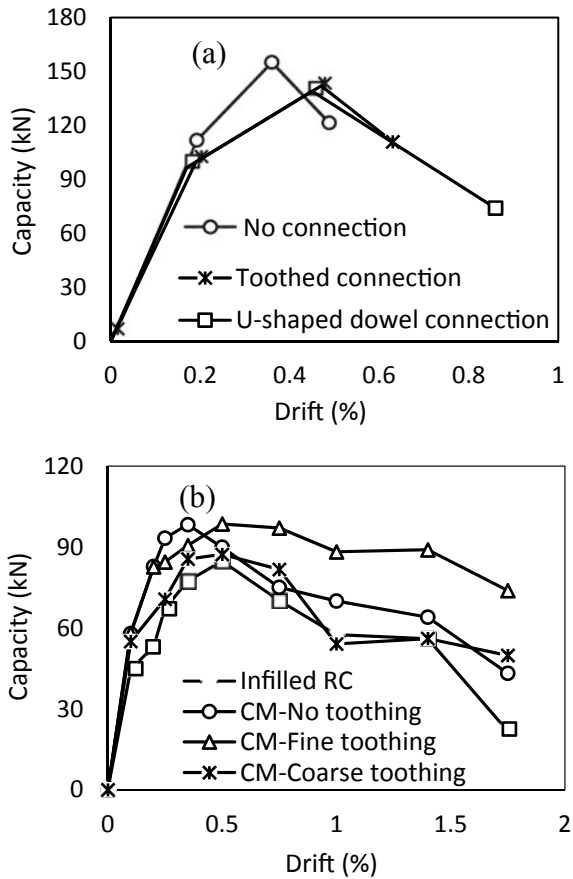
3.4 Interface Between Wall Edge and Tie-Column

The bonding between a masonry wall and RC tie-elements is important for satisfactory earthquake performance and for delaying undesirable cracking and separation at the wall-to-tie-column interface. Generally, masonry units are staggered using tothing or shear-key at the tie-column locations to achieve good bonding between a masonry wall and adjacent RC tie-columns. Good bonding can also be achieved by providing dowels anchored into RC tie-columns. A comparison study was performed by Matošević et al. [15] to study the in-plane response of CM walls with different connection details—toothed connection, U-shaped dowel connection, and no connection. The test results showed that the connection details did not influence the initial stiffness or the maximum lateral resistance significantly, but they did improve the nonlinear wall behaviour and hysteretic energy dissipation. Wall with toothed or U-shaped dowel connectors exhibited more ductile behaviour compared to the one with no connection (Fig. 7a). The connection not only improves in-plane behaviour but also improves the out-of-plane stability of wall. Singhal and Rai [16] tested half-scaled CM wall specimens with a different density of toothed connection and considered the successive applications of out-of-plane and in-plane loading. The seismic performance of CM wall in comparison with that of a typical infilled RC frame wall was also studied. It was observed that the CM walls with or without tothing exhibited improved in-plane and out-of-plane responses in comparison to infill masonry panels. The increased density of tothing caused significant improvement in post-peak behaviour under in-plane loads as shown in Fig. 7b, however, it did not have a significant effect on out-of-plane behaviour [16].

3.5 Aspect Ratio

Depending on the aspect ratio (AR), i.e. height to length ratio of masonry panel, different failure modes can occur in the CM wall. The walls with a low aspect ratio (length of the wall is larger than the height) mainly fail in shear mode, however, the walls with a large aspect ratio (length of wall is much less than the height) are more susceptible to flexural mode of failure due to excessive bending [4, 8]. Therefore, squat CM walls exhibit a mixed shear failure mode with a combination of diagonal tension and sliding along one or more horizontal joints [17]. For slender walls, the typical damage includes horizontal tensile cracks in mortar and tie-columns at the

Fig. 7 Effect of wall to tie-column interface on lateral load behaviour of CM wall: **a** specimens tested [15], **b** specimens tested [16]



tension end of the wall and crushing of bricks in the compression zones [4, 18]. Though shear strength of CM wall increases with a decrease in aspect ratio, the drift corresponding to the ultimate load decreases. Therefore, a sudden and brittle failure is observed in squat walls as shown in Fig. 8 [17].

3.6 Overburden Pressure

It is one of the influencing parameters on the lateral strength of the CM wall. When a masonry panel is subject to lateral load, layers of masonry units tend to slide over one another. The resistance offered against sliding is developed by friction and adhesion between bricks and mortar. As frictional resistance is directly related to normal stress applied, the axial load improves lateral capacity and energy dissipation characteristics of the CM wall. Figure 9a shows the load–deformation behaviour of CM walls (with

Fig. 8 Effect of aspect ratio on lateral load–deformation behaviour of CM wall [17]

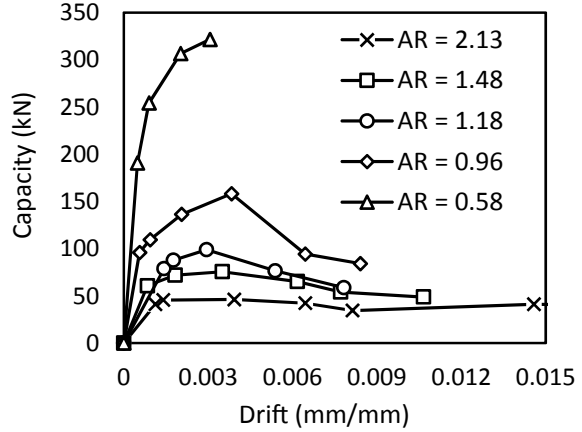
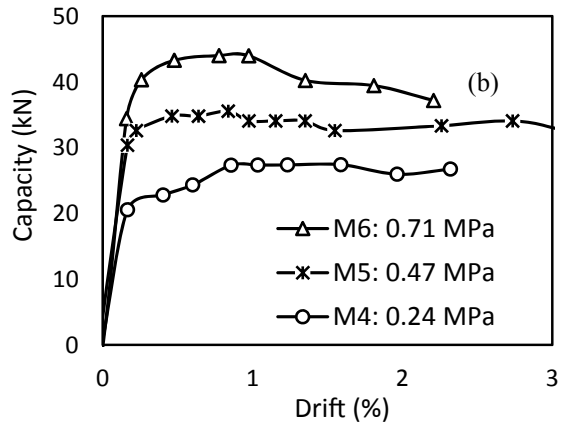
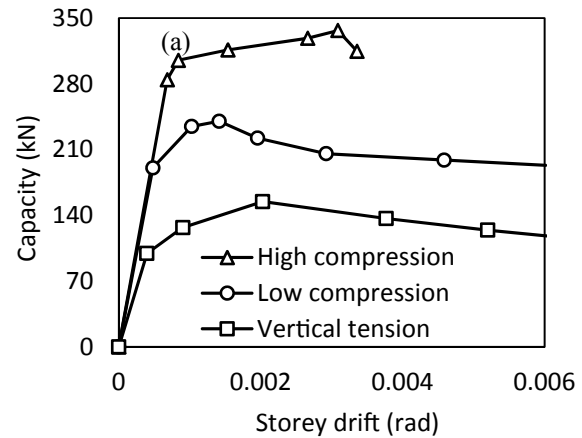


Fig. 9 Effect of overburden pressure on lateral load–deformation behaviour of CM wall: **a** specimens tested [19], **b** specimens tested [20]



no wall reinforcement and low height of repeated lateral forces) tested by Yoshimura et al. [19]. Similarly, Fig. 9b shows the load–deformation behaviour of AAC CM walls tested by Varela-Rivera et al. [20]. From the figures, it can be concluded that shear strength of the CM wall increases with an increase in vertical axial load, though the failure occurs at a lower drift.

3.7 Wall Reinforcement

Though the placing of horizontal wall reinforcement within the mortar joints is an option to improve the seismic response of CM wall, it is not a much popular choice. As masonry is weak in tension, when a wall panel is subjected to lateral load diagonal cracks get developed in the direction perpendicular to the principal tensile stress. This cracking governs the lateral capacity, stiffness degradation and energy dissipation characteristics of the wall. With the provision of horizontal wall reinforcement, the process of crack initiation and propagation gets delayed as reinforcements help in resisting tensile stresses. Moreover, improved lateral load, deformation and energy dissipation capacity is achieved with a more uniform distribution of inclined cracking [18, 21, 22]. Figure 10a shows the behaviour of single-paneled CM wall with and without horizontal reinforcement tested by Aguilar et al. [21]. For the CM walls with horizontal reinforcement, 2-high strength deformed wires at a spacing of 280 mm c/c with reinforcement ratio 0.071 and 0.190% are used. Figure 10b shows the bilinear load–deformation behaviour of CM wall with light bed joint reinforcement, anchored to the confining elements in comparison to no horizontal reinforcement [23, 24].

3.8 Opening

The opening present in a typical masonry wall has negative effects on the capacity when subjected to seismic load [9, 16, 21, 25]. Under the action of lateral loading, stress concentration is observed at the corners of openings causing shear cracks, which makes wall panel unstable and leads to failure of CM wall. For a CM wall with an opening size up to 10% of the wall area has the same in-plane behaviour under lateral load as a solid wall [3]. Beyond this opening size, strength and stiffness reduce drastically. The deficiencies due to openings can be overcome by the provision of confining elements around the openings [25]. Confining elements prevent shear cracks at corners of openings and maintain the stability of wall. It also allows strut formation in the wall, which improves strength and ductility significantly.

Many standards and manuals suggest different locations and arrangements of confining elements around the opening. There are some disagreements on the detailing and arrangement of confining elements. Experiments showed that the provision of continuous sill and lintel beam is a better alternative in terms of ductility of CM wall panel as shown in Fig. 11 [16, 26]. In-plane capacity of continuous tie-

Fig. 10 Effect of horizontal reinforcement on lateral load–deformation behaviour of CM wall: **a** specimens tested [21], **b** specimens tested [23, 24]

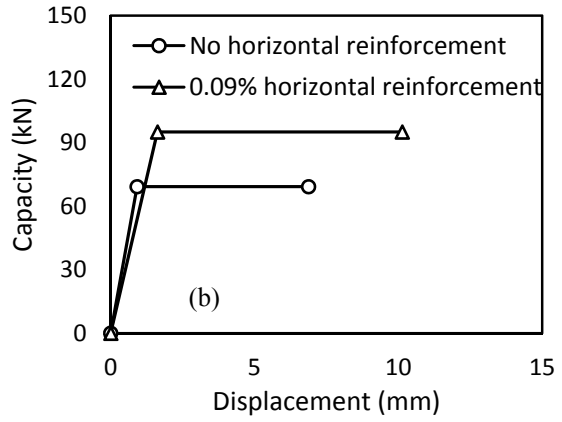
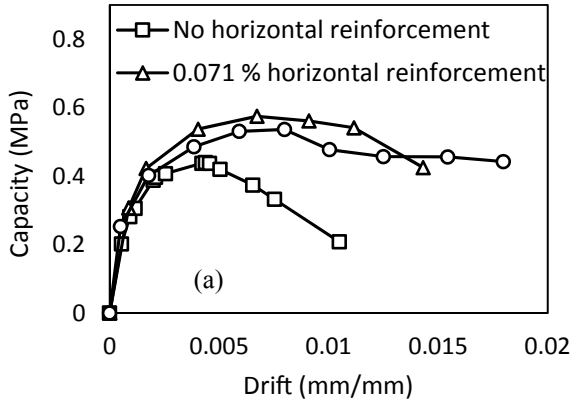
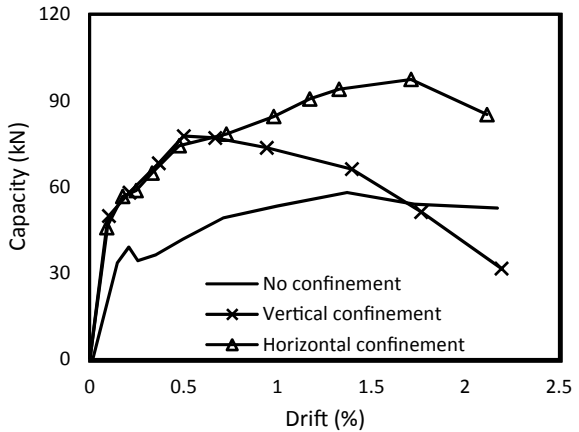


Fig. 11 Effect of confinement around opening on the lateral load–deformation behaviour a CM wall [16, 26]



column and continuous sill and lintel beam arrangement is almost the same but the latter system is more ductile as the beam divides the wall into smaller panels with low aspect ratio ensuring well-distributed diagonal shear cracks throughout the wall.

4 Conclusion

In the age of RC constructions, around 80% of buildings in India are unreinforced masonry structures. With almost 54% of geographical area vulnerable to earthquakes, unreinforced masonry buildings impose great risks because of their poor seismic performance. Confined masonry is one of the most suitable and economical building typologies for a low-to-medium rise low-cost construction practices. The article identifies some of the important parameters which affect the seismic performance of CM building and these are wall density, masonry wall properties, confining element properties, interface between wall-to-confining frame, aspect ratio of wall, overburden pressure, wall reinforcement, opening area, etc. Among them, parameters like masonry strength, aspect ratio, etc., are the strength-dependent parameters, whereas, tie-column reinforcement ratio, wall reinforcement, etc., are mainly ductility dependent parameters. Salient conclusion which can be drawn from this study are briefly discussed in the following:

- Masonry characteristics are mainly responsible for the strength and stiffness of CM structure.
- Confining frame does not have a significant contribution to lateral strength, however, it improves in-plane ductility and reduces stiffness degradation of the wall.
- Wall-to-tie-column interface, in the form of tothing or U-shaped dowels, improves out of plane stability.
- Wall with confined opening, in the form of continuous horizontal beam at lintel and sill, performs better than other alternative confining schemes.
- Aspect ratio, though not widely studied, controls failure modes and initial stiffness and strength of CM wall.
- Wall reinforcement delays crack initiation and improves the ductility of the wall.

It is observed that a lot of attention has been given in the literature to tie-column and masonry properties in understanding the in-plane behaviour of CM wall, whereas less attention has been given to study the behaviour of wall with openings. Interface connection between wall and tie-columns and wall and tie-beams also need to be investigated to understand the out-of-plane behavior of CM wall. Systematic experimental studies are required to be conducted to understand the influence of various parameters on lateral load response of CM buildings to prepare a unified design protocol for such buildings.

References

1. Borah B, Singhal V, Kaushik HB (2009) Sustainable housing using confined masonry buildings. *SN Appl Sci* 1(9):983. <https://doi.org/10.1007/s42452-019-1020-4>
2. Marques R, Lourenço PB (2019) Structural behaviour and design rules of confined masonry walls: review and proposals. *Constr Build Mater* 217:137–155
3. Meli R, Brzev S, Astroza M, Boen T, Crisafulli F, Dai J, Farsi M, Hart T, Mebarki A, Moghadam AS, Quinn D, Tomazevic M, Yamin L (2011) Seismic design guide for low-rise confined Masonry buildings. EERI-WHE, World Housing Encyclopedia
4. Matthews T, Riahi Z, Centeno J, Charlet A, Garcia HJ, Hoffman C, Safaie S, Elwood K (2007) Evaluation of confined Masonry guidelines for earthquake-resistant housing. University of British Columbia (UBC) EERI Student Chapter Committee on Confined Masonry Construction
5. Brzev S, Gavilán JP (2016) Application of strut-and-tie model for seismic design of confined Masonry shear walls. In: Proceedings of the 16th international brick and block Masonry conference (16 IBMAC). Padova, Italy
6. Borah B, Singhal V, Kaushik HB (2018) A simplified approach to analytical modeling of confined Masonry buildings. In: 16th symposium on earthquake engineering, paper no. 247. Roorkee, India
7. Ishibashi K, Meli R, Alcocer SM, Leon F, Sanchez TA (1992) Experimental study on earthquake-resistant design of confined Masonry structures. In: 10th world conference on earthquake engineering. Madrid, pp 3469–3474
8. Brzev S (2008) Earthquake-resistant confined Masonry construction. National Information Center for Earthquake Engineering, Kanpur, India
9. Yáñez F, Astorza M, Holmberg A, Ogaz O (2004) Behavior of confined masonry shear walls with large openings. In: Proceedings of the 13th world conference of earthquake engineering, paper no. 3438. Vancouver, Canada
10. Tomažević M, Klemenc I (1997) Seismic behavior of confined masonry walls. *Earthq Eng Struct Dynam* 26(10):1059–1071
11. Alcocer S, Arias JG, Vazquez A (2004) Response assessment of Mexican confined Masonry structures through shaking table tests. In: Proceedings of the 13th world conference on earthquake engineering, paper no. 2130. Vancouver, Canada
12. Tomažević M, Bosiljkov V, Weiss P (2004) Structural behaviour factor for masonry structures. In: 13th world conference on earthquake engineering
13. Kato H, Goto T, Mizuno H (1992) Cyclic loading tests of confined masonry wall elements for structural design development of apartment houses in the third world. In: Proceedings of the 10th world conference on earthquake engineering. Balkema, Rotterdam
14. Quiroz LG, Maruyama Y, Zavala C (2017) Experimental assessment of the cyclic behavior of Peruvian confined masonry walls and numerical modeling using genetic algorithms. In: 16th world conference on earthquake engineering
15. Matošević Đ, Sigmund V, Guljaš I (2015) Cyclic testing of single bay confined masonry walls with various connection details. *Bull Earthq Eng* 13(2):565–586
16. Singhal V, Rai DC (2016) In-plane and out-of-plane behavior of confined masonry walls for various tothing and openings details and prediction of their strength and stiffness. *Earthq Eng Struct Dynam* 45(15):2551–2569
17. Pérez Gavilán JJ, Flores LE, Alcocer SM (2015) An experimental study of confined masonry walls with varying aspect ratios. *Earthq Spectra* 31(2):945–968
18. Zabala F, Bustos LJ, Masanet A, Santalucia J (2004) Experimental behavior of Masonry structural walls used in Argentina. In: 13th world conference on earthquake engineering, paper no. 1093. Vancouver, B. C., Canada
19. Yoshimura K, Kikuchi K, Kuroki M, Liu L, Ma L (2000) Effect of wall reinforcement, applied lateral forces and vertical axial loads on seismic behavior of confined concrete Masonry walls. In: 12th world conference on earthquake engineering, paper no. 0984

20. Varela-Rivera J, Fernandez-Baqueiro L, Gamboa-Villegas J, Prieto-Coyoc A, Moreno-Herrera J (2019) Flexural behavior of confined Masonry walls subjected to in-plane lateral loads. *Earthq Spectra* 35(1):405–422
21. Aguilar G, Meli R, Diaz R, Vazquez-del-Mercado R (1996) Influence of horizontal reinforcement on the behaviour of confined Masonry walls. In: 11th world conference on earthquake engineering, paper no. 1380. Acapulco
22. Kumazawa F, Ohkubo M (2000) Nonlinear characteristics of confined Masonry wall with lateral reinforcement in mortar joints. In: Proceedings of the 12th world conference on earthquake engineering, paper no. 0743. Auckland, New Zealand
23. Medeiros P, Vasconcelos G, Lourenço PB, Gouveia J (2013) Numerical modelling of non-confined and confined masonry walls. *Constr Build Mater* 41:968–976
24. Gouveia JP, Lourenço PB (2007) Masonry shear walls subjected to cyclic loading: influence of confinement and horizontal reinforcement. In: 10th North American Masonry conference. Missouri, pp 838–848
25. Kuroki M, Kikuchi K, Nonaka H, Shimosako M (2012) Experimental study on reinforcing methods using extra RC elements for confined Masonry walls with openings. In: Proceedings of the 15th world conference on earthquake engineering, paper no. 4967. Lisbon, Portugal
26. Singhal V, Rai DC (2018) Behavior of confined Masonry walls with openings under in-plane and out-of-plane loads. *Earthq Spectra* 34(2):817–841

Design and Performance Criteria for Fire-Resistant Design of Structures—An Overview



Nitant Upasani , Mansi Bansal , Ashirbad Satapathy , Sanket Rawat , and G. Muthukumar 

Abstract Concrete, despite being inherently fire resistant, cannot be considered as a fire-proof material. It undergoes substantial variation in its characteristics during exposure to elevated temperatures. These variations may become hazardous for structural stability and serviceability depending upon the type and extent of exposure. Moreover, high-strength concrete, which is commonly used in tall buildings, may perform poorly against fire due to its high binder content and very low permeability. Despite all the aforementioned factors, fire resistance design of structural members has been given very restricted consideration in the current Indian practice. Although several standards provide guidelines to achieve fire safety in structures, the provisions for high-strength concrete and spalling prevention are not specifically available in the major international and national standards. This paper attempts to compare the provisions corresponding to fire-resistant design in Indian standard with the respective provisions of other country standards, e.g., ACI 216 [3], NZS 3101 [4], EN 1992–2 [8], etc. Comparison parameters primarily include the design requirements for various structural members to improve their fire resistance. Furthermore, suitable recommendations for Indian Codal provisions are attempted in the latter part of the paper to achieve superior performance under elevated temperatures.

Keywords Elevated temperature · Reinforcement cover · Fire resistance rating · Spalling

1 Introduction

In recent decades, India has encountered remarkable urban development. Population explosion and migration to urban areas in the country has put a colossal pressure on the housing and infrastructure needs of the nation. As a result, the development of a substantial number of multistorey buildings in the urban areas has occurred and is on the ascent. Even though there has been such incredible infrastructural development

N. Upasani (✉) · M. Bansal · A. Satapathy · S. Rawat · G. Muthukumar
Department of Civil Engineering, BITS Pilani, Pilani Campus, Pilani, Rajasthan, India 333031
e-mail: nitantupasani@gmail.com

in the nation in recent times, fire safety has not been given proper consideration. Unavailability of proper guidelines and ignorance have caused horrific accidents in the past that took the lives of many and also caused significant monetary losses. Although various Indian standards provide guidelines to enhance structural performance during fire, the provisions available do not seem to cover all the significant parameters. The provisions available in many international standards also restrict the consideration of fire performance in design. In general, all the national and international standards have specified minimum size of member and the cover to the reinforcement corresponding to different fire resistance rating (FRR). FRR for structural elements can be defined as the time, in minutes or hours, that a particular structural member or element can withstand a standard fire exposure. It is generally considered to range from 30 to 240 minutes. The effect of various parameters such as the types of aggregates to be used, cover requirements, design principles for various structural elements, whose integrity forms the prime importance for the safety of the building, with respect to fire resistance has also been studied extensively. Also, though the performance of high-strength concrete is poor when exposed to fire, its use for construction of multistorey structures cannot always be avoided. Hence, it is extremely crucial that special care be taken for the provision of enhancement of fire resistance in multistorey buildings. Moreover, spalling, which is one of the major causes of deterioration of concrete at elevated temperatures, has not been provided due attention by the standards of several countries and no specific provision has been recommended to prevent this phenomenon.

This paper aims at providing a comparative study of the standards of various countries and suggesting additional measures for better design approaches and improved performance of reinforced and prestressed concrete structures under fire exposure. Certain parameters that have been found to have an effect on the fire performance of concrete by various researchers have also been discussed.

2 Indian Specifications for Fire-Resistant Design

Codal specifications for concrete structures in India mainly distinguish between the design for different structural members such as columns, beams, slabs etc., on the basis of FRR and size of the members. The major emphasis in Indian standards for the design of reinforced concrete members when exposed to fire, is on ensuring that the structural members have sufficient thickness or width and cover over the reinforcement. Besides, the occurrence of the spalling phenomenon in high-strength concrete due to fire exposure, has also been accounted in terms of extra cover to reinforcement. On the other hand, Indian codes lack in suggesting any other provisions for improved fire-resistant design of concrete structures. Salient specifications related to fire resistance of concrete structures are discussed in the following sections.

2.1 IS 1642:1989 Fire Safety of Buildings (General)—Details of Construction

Indian standard IS 1642 [1] specifies the minimum dimension and cover to the reinforcement corresponding to different fire resistance periods (Table 1). Separate guidelines are provided for beams, columns, and slabs depending upon the support condition and degree of exposure.

2.2 IS 456:2000 Indian Standard—Plain and Reinforced Concrete—Code of Practice

Indian code IS 456 [2] is widely followed for the construction of concrete structures in India. To incorporate the benefit of inherent fire resistance of concrete, few specifications are highlighted in the standard. The innate fire resistance of concrete is assured by providing minimum overall member dimensions and nominal concrete cover to the steel reinforcement in design. Clause 26.4.3 of the code assures fire resistance by providing minimum nominal cover to the normal weight aggregate concrete. Also, the code has special provisions for an increase in nominal cover in case of structural members with more risk of spalling. The dependency of fire resistance of concrete on type of aggregates, i.e., lightweight aggregates or normal weight aggregates has also been mentioned. However, the minimum dimension and cover to the reinforcement for various concrete structural members have only been provided for normal weight aggregates. The code also emphasizes on detailing of reinforcement being such that both individual and whole structures remain integrated throughout the exposure period. Additional measures to avoid the risk of spalling such as use of fire-resistant finishes for insulation and provision of fire-resistant false ceilings, increase in cover to reinforcements, and provision of sacrificial steel in the tensile zone have also been recommended by the code. Specifications based on minimum cover and member dimensions for normal weight aggregate concrete members for required fire resistance are specified as shown in Table 2.

3 International Provisions

3.1 American Standard (ACI 216.1–07/TMS 0216–07)

The American Standard for fire resistance of reinforced concrete structures provides minimum dimension and cover to the reinforcement specifications, similar to the Indian codes. In addition, the type of aggregate used is also taken into account according to which the minimum size of a member is provided depending on the

Table 1 Minimum dimension of structural elements for different fire resistance ratings as per IS 1642:1989

Minimum Dimension (mm), excluding any finish for a fire resistance of (hours)	Beams				Slabs				Columns					
	Reinforced concrete simply supported		Reinforced concrete continuous		Reinforced concrete simply supported		Reinforced concrete continuous		Fully exposed		50% exposed		One face exposed	
	Width	Cover	Width	Cover	Width	Cover	Width	Cover	Width	Cover	Width	Cover	Width	Cover
0.5 h	80	20	80	20	75	15	75	15	150	20	125	20	100	20
1 h	120	30	80	20	95	20	95	20	200	25	160	25	120	25
1.5 h	150	40	120	35	110	25	110	20	250	30	200	25	140	25
2 h	200	60	150	50	125	35	125	25	300	35	200	25	160	25
3 h	240	70	200	60	150	45	150	35	400	35	300	30	200	25
4 h	280	80	240	70	170	55	170	45	450	35	350	35	240	25

Table 2 Minimum dimension of structural elements for different fire resistance ratings as per IS 456:2000

Minimum Dimension (mm), excluding any finish for a fire resistance of (h)	Beams			Slabs		Columns				
	Cover		Minimum width of beam	Cover		Minimum thickness of slab	Column width/diameter			Nominal cover
	Reinforced concrete simply supported	Reinforced concrete continuous		Reinforced concrete simply supported	Reinforced concrete continuous		Fully exposed	50% exposed	One face exposed	
0.5	20	20	200	20	20	75	150	125	100	40
1	20	20	200	20	20	95	200	160	120	40
1.5	20	20	200	2.5	20	110	250	200	140	40
2	40*	30	200	35*	2.5	125	300	200	160	40
3	60	40*	240	45	35*	150	400	300	200	40
4	70	50	280	55	45	170	450	350	240	40

*Require additional measures to reduce the risks of spalling

fire rating of the building. Member size and cover thickness are given for restrained or unrestrained beams and slabs for prestressed or passively reinforced members. Continuous unrestrained members have longer fire endurance than simply supported members for the reason that the former can redistribute moments, eventually resulting in failure of negative reinforcement over the supports. The code specifies the advantage of better spalling resistance of carbonate aggregates over siliceous aggregates. ACI 216 [3] distinguishes concrete columns on the basis of compressive strength with the threshold for differentiation being 12,000 psi. It is important to note that the American code is more conservative and insists on providing an FRR of at least 1 h for each structural member. Corresponding to a particular FRR, minimum dimension of columns having compressive strength less than or equal to 12,000 psi has been specified in the code. For columns with a compressive strength greater than 12,000 psi, the least dimension should be 24 inches irrespective of the type of aggregate. Furthermore, the minimum cover to the reinforcement specified in the standard does not depend upon the aggregate type and compressive strength and hence, is taken as 2 inches, or 1-inch times the required FRR; whichever is less. Additionally for beams and slabs, the American standard provides specific guidelines for reinforcement detailing to attain a certain rating of fire resistance. The redistributed maximum positive moment must be the primary basis to determine the fire resistance of the bending members. When the continuous beams and slabs are exposed to fire at the bottom, the temperature increases at the bottom and a temperature gradient is established between the top and the bottom surface which causes the expansion of the bottom surface. Consequently, the lift at the ends causes a reduction in positive moments and an increase in negative moments at interior supports. Hence, it is recommended to increase the negative moment carrying capacity of the members.

Furthermore, the maximum reinforcement that has to be provided in the negative moment region is given by.

$$\omega = \rho f_y / f'_c \leq 0.30 \quad (1)$$

where,

$\rho = A_s / bd$, to limit the compressive failure in this region.

A_s is the area of steel reinforcement of yield strength f_y ,

f'_c is the concrete compressive strength,

b and d are the width and depth of the beam or slab strip.

When floors and roofs are made of one layer of normal weight concrete and one layer of lightweight concrete, its fire resistance can be formulated numerically by empirical solutions given below:

- If the layer exposed to fire is of normal weight concrete

$$R = 0.057(2t^2 - dt + 6/t) \quad (2)$$

- If the layer exposed to fire is of lightweight concrete

$$R = 0.063(t^2 + 2dt - d^2 + 4/t) \quad (3)$$

where R is the fire resistance (in hours), t is total slab thickness (in inches), and d is the thickness of the layer exposed to fire (in inches). When the slab is made up of more number of layers of different types of materials, fire resistance may be calculated as:

$$\text{FRR} = (\text{FRR}_1^{0.59} + \text{FRR}_2^{0.59} + \dots + \text{FRR}_n^{0.59} + A_1 + A_2 + \dots + A_n)^{1.7} \quad (4)$$

where FRR_n is the fire resistance rating of n^{th} layer and A_n represents the air factor (0.3) for each continuous air gap.

3.2 *New Zealand Standard (NZS 3101: Part 1: 2006 Concrete Structures Standard)*

New Zealand standard mainly recommends designing a structural member with FRR greater than the required fire resistance and the parameters to judge the fire resistance are defined as—adequacy, integrity, and insulation. The integrity criterion is satisfied if the member meets the requirement of the rest two criteria. The FRR for insulation can be enhanced by providing extra layers of insulating material. In addition, NZS 3101 [4] has also considered a factor “Axis distance” which is defined as the weighted average distance of a group of longitudinal bars from the axis of the bars to the nearest exposed surface.

To achieve the integrity, adequacy, and insulation criteria for slabs, FRR is prescribed from half-hour to 4 h, similar to Indian standards and corresponding to each duration, minimum dimension and axis distance have been detailed. Provisions are specified for columns and walls similar to beams and slabs. In case of columns and walls, an additional parameter has been defined named as “Load value”, and an expression is provided for its calculation which depends on axial load capacities at normal and elevated temperatures. This expression is given by:

$$\eta_{fi} = N_f^*/N_u \quad (5)$$

where,

η_{fi} → load value.

N_f^* → factored design axial load on the column in fire condition. N_u → axial load capacity of column at room temperature.

Load value is either taken as 0.7 or is calculated as per the given formula. Hence, the axis distance and minimum dimensions are stated for columns depending upon FRR, exposure percentage, and load value. Furthermore, different provisions are stated for fire resistance of simply supported and continuous beams and the effect of percentage exposure of beam to fire is also indicated in terms of change in dimensions and cover accordingly in separate clauses. NZS 3101 standard insists on different FRRs for different types of slabs, i.e., solid slabs, flat slabs, and ribbed slabs. Additionally, the axis distance has been listed for different categories of solid slabs (one-way, two-way, and continuous) for each fire durations.

In addition, an alternative to improve insulation is the use of lightweight aggregates. Lightweight aggregates are thermally stable and generally have better fire-resisting capacity in dry building fires because their thermal expansion is almost equal to that of the cement paste.

3.3 Australian Standards AS 3600—2018 for Concrete Structures

The Australian code defines cover to reinforcement in terms of “Average Axis Distance, a_m ” and provides specifications to calculate the same for single layered or multilayered reinforcements of same size or different sizes and characteristic strength, prestressing tendons, or combinations of these. AS 3600 [5] specifies minimum dimensions and cover to the reinforcement for concrete sections to achieve a given fire resistance to a standard fire exposure similar to other standards. The code classifies beams on the basis of support conditions and provides combinations of average axis distance (a_m) and width of beam (b), in tabular form as well as its graphical correlation which signifies that for the same FRR requirement, with an increase in b , the requirement of a_m decreases. AS 3600 [5] has also laid down conditions for beams exposed to fire on all sides. Figure 1 shows the plot for structural adequacy requirements for beams based on support conditions.

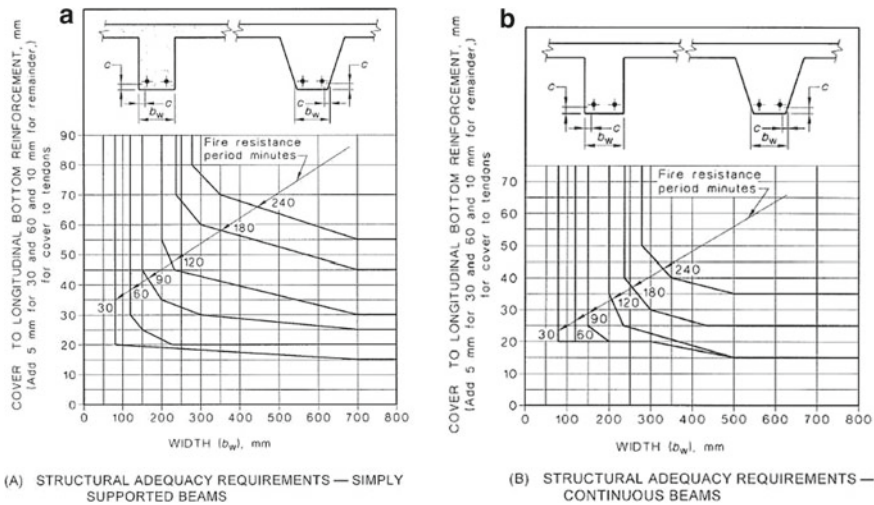


Fig. 1 Structural adequacy requisites for fire resistance of beams: **a** simply supported beams, **b** continuous beams [5]

AS 3600 [5] has prescribed values of dimensions corresponding to various FRRs for satisfying insulation as well as adequacy criteria separately in case of slabs. For adequacy of slabs, the code mentions prescriptive criteria and distinguishes slabs based on core (solid/hollow), ribbed, support condition as well as on the basis of one-way or two-way behavior of slabs. However, the Indian code doesn't specifically mention any difference in values of thickness or cover for one-way and two-way behavior of slabs.

For columns, the Australian Code provides two tabular methods, viz., Restricted Tabular Method and General Tabular Method for determination of dimensions and cover parameters (structural adequacy), both of which are prescribed for braced columns. The restricted tabular method mentions average axis distance (a_s), and smaller cross-sectional dimension (b) requirements with respect to a varying parameter called load level (μ_{fi}), which can be calculated as follows:

$$\mu_{fi} = \frac{N_f^*}{\Phi * N_u} \tag{6}$$

where,

N_f^* = design axial load in the fire situation; Φ = strength reduction factor;

N_u = ultimate strength in compression, or tension, at a cross section of an eccentrically loaded compression or tension member, respectively.

The general tabular method further prescribes combinations of a_s and b with respect to the variation of two more parameters, viz.

$$\omega = 1.3A_s f_{sy} / A_c f_c' \quad (7)$$

' ω ' denotes the mechanical reinforcement ratio at normal temperature conditions and ' η ' which is given by

$$\eta = \frac{N_f^*}{0.7 \left[\left(\frac{A_c f_c'}{1.5} \right) + \left(\frac{A_s f_{sy}}{1.15} \right) \right]} \quad (8)$$

where,

A_s = cross-sectional area of reinforcement;

A_c = smallest cross-sectional area of the concrete strut at any point along its length and measured normal to the line of action of the strut;

f_{sy} = characteristic yield strength of reinforcement;

f_c' = characteristic compressive (cylinder) strength of concrete at 28 days.

3.4 Canadian Code NBC 2010

National Building Code of Canada [6] and the Canadian Commission on Building and Fire Codes (CCBFC) state that low-density aggregate concretes generally perform better under fire action than natural stone aggregate concretes. Furthermore, it segregates the types of concrete on the basis of the nature of the aggregate which is described as follows:

- Type S concrete: Coarse aggregate is granite, quartzite, siliceous gravel/dense materials containing at least 30% quartz, chert, or flint.
- Type N concrete: Coarse aggregate is cinders, broken brick, blast furnace slag, limestone, calcareous gravel, trap rock, sandstone/similar dense material containing not more than 30% of quartz, chert, or flint.
- Type L concrete: All aggregates are expanded slag, expanded clay, expanded shale, or pumice.
- Type L1 concrete: All aggregates are expanded shale.
- Type L2 concrete: All aggregates are expanded slag, expanded clay, or pumice.
- Type L40S concrete: The fine portion of the aggregate is sand and low-density aggregate; sand does not exceed 40% of the total volume of all aggregates
- Type L120S and Type L220S concretes: The fine portion of the aggregate is sand and low-density aggregate; sand does not exceed 20% of the total volume of all aggregates.

The Canadian code prescribes the same minimum cover to principal reinforcement for different types of aggregate concretes in case of reinforced concrete beams. However, for prestressed concrete beams, the minimum thickness of concrete cover

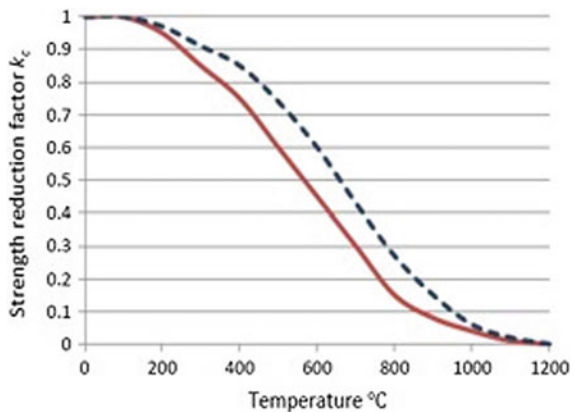
over steel tendons depends on the types of concrete as well as on the cross-sectional area. For minimum dimension criteria, it only stipulates a minimum width of at least 100 mm for reinforced concrete beams.

For reinforced and prestressed concrete slabs, the code prescribes minimum thickness and minimum cover over reinforcement for different types of concrete (Types S, N, and L). In case of reinforced concrete columns, the code mentions a term ‘Overdesign Factor’, which can be defined as the ratio of calculated load-carrying capacity of the column to the strength of the column required to carry a specified load. For various types of aggregate concrete, the minimum dimension (t) of rectangular columns depends upon the fire-resistance rating required (R), the area of vertical reinforcement as a percentage of the column area (p), and a factor ‘ f ’ which varies with the overdesign factor, the effective length factor (k) and the unsupported length of the column (h). The diameter requirement of a circular column can be calculated by adding an increment of 20% to the minimum dimension for a given type of concrete. For the calculation of minimum thickness of concrete cover over the vertical steel reinforcement, the code prescribes empirical formula depending upon the number of hours of fire resistance required.

3.5 Eurocode 2

EN 1992–1-2 [7, 8] incorporates the effect of aggregate on fire resistance of reinforced concrete structural sections by means of providing a factor K to allow for the decrease in the characteristic compressive strength for different types of aggregates, as shown in Fig. 2. The standard primarily specifies this factor for carbonate and siliceous aggregates in both graphical and tabulated form. Eurocode specifies fire resistance of reinforced concrete columns, similar to the Australian standard which depends on exposure level and gives minimum dimension as well as a concrete cover or axis distance. In addition to these factors, Eurocode takes into consideration another

Fig. 2 Variation in coefficient k_c (Θ) with increasing temperature for normal weight concrete with siliceous (solid line) and calcareous aggregates (dashed line)



parameter named as “Degree of utilization in fire situation”, which also plays a significant role in describing minimum member dimension and axis distance. This factor is almost similar to the load value as specified in New Zealand standard and is given by

$$\mu_{fi} = \frac{N_{Ed,fi}}{N_{Rd}} \quad (9)$$

where,

μ_{fi} → Degree of utilization in fire situation; $N_{Ed,fi}$ → Design axial load in fire situation;

N_{Rd} → Design resistance of column at normal temperature.

Additionally, the table provided in this standard for different fire resistance rating of concrete is valid only for certain conditions, unlike all other standards where there is no mention of the validity of the table. The conditions are the following:

The effective length of the column under fire conditions ≤ 3 m.

- first-order eccentricity under fire conditions: $e \leq e_{max}$;
- amount of reinforcement: $A_s < 0.04 A_c$.

Web dimension of the beam depending upon the class of the section as WA, WB, and WC is also presented in Eurocode. It is interesting to note that Eurocode covers the salient provisions in case of high-strength concrete. Unlike every other standard, it has specified the criteria for regulating the spalling phenomenon during fire exposure. For high-strength concrete, reduction in strength is applied and this reduction has been made varying upon the class of concrete. In general, the methodology applied for higher strength concrete is almost the same as that for normal strength concrete, with the additional inclusion of a factor k .

Spalling provisions: Eurocode also suggests limiting the moisture content of concrete to control explosive spalling. The recommended limiting moisture content by mass is 3%. If the moisture content exceeds this, the spalling effect on load bearing may be measured with the assumption of local loss of cover to one reinforcing bar or bundle of bars in the cross section, then calculating the subsequent increase in temperature and the reduced load-bearing function R .

When the cover requirements exceed 40 to 50 mm, the following measures are suggested to prevent the spalling phenomenon.

- Vermiculite being a thermally stable material, its use for plastering can be beneficial.
- To prevent the fire spread to the upper floors, false ceiling made of fire-resistant materials can be utilized.
- Use of lightweight aggregates that perform better at elevated temperatures.
- Use of sacrificial steel.

It is interesting to note that the use of supplementary cementitious material in concrete is highlighted in terms of fire performance. If the fly ash content $>6\%$, and for 80/95 < C grade $< 90/105$, at least one of the following measures must be provided:

- A. A reinforcement mesh with the following:
 - Minimal cover of 15 mm,
 - Wire diameter greater than 2 mm
 - Maximum pitch of 50×50 mm.
 - The nominal cover to the main reinforcement should not be less than 40 mm.
- B. Concrete used must be confirmed that it does not spall when exposed to elevated temperatures using various tests.
- C. Proven protective layers that exhibit the prevention of spalling when subjected to fire conditions must be used.
- D. At least 2 kg/m^3 of monofilament propylene can be mixed with concrete to improve its fire resistance.

Dependency of the frame on the individual member for its stability aids in deciding the provision of spalling protection for that member. Spalling prevention design is usually for the members impinged on flames, or when the temperature of the cover reinforcement is in excess of 100°C .

4 Discussion

It can be analyzed from the above discussion that the guidelines provided by different countries, including India, lack somewhere in taking into account a number of important parameters for the construction of fire-resistant structures. Table 3 provides a concise comparison of the adopted parameters and the corresponding guidelines in the different codes mentioned above, for the enhancement of performance against fire exposure.

4.1 Type of Aggregates

The type of aggregates exceptionally influences thermal performance as it constitutes 70–80% of the volume of concrete. Studies have found that silica, the major constituent of siliceous aggregates, causes a significant loss in the strength of concrete beyond 600°C . According to Ma et al. [9], the use of siliceous aggregates, such as granite, demonstrates unfavorable mechanical properties at high temperatures as compared to the performance of calcareous aggregates such as dolomite and limestone. As observed by Cheng et al. [10], concrete made of calcareous aggregates attains larger ultimate strain than that made from siliceous aggregate, thus rendering

Table 3 Comparison of parameters specified in different standards related to fire performance of concrete

Codes	IS 1642 [1] and IS 456 [2]	ACI 216 [3]	NZS 3101 [4]	AS 3600 [5]	NBCC [6]	Eurocode 2 [7, 8]
Measures	Minimum dimension, concrete cover	Minimum dimension, concrete cover	Minimum dimension, axis distance	Minimum dimension, concrete cover (axis distance)	Minimum dimension, reinforcement cover	Minimum dimension, axis distance
Depending parameters	Support condition, degree of exposure	Aggregate type, Restrained/unrestrained beams, exposure	Exposure (%), load value	Exposure, support condition	Type of concrete (depending on type and volume of aggregates used), overdesign factor	Aggregate type, support condition, exposure, strength of concrete, degree of utilization
Special features		FRR 1–4 h		Graphical correlations	Overdesign factor	Spalling provisions such as use of insulating materials or fibres

better ductility at elevated temperatures. Moreover, calcareous aggregates decompose at a higher temperature than siliceous aggregates. However, both of these aggregates portray greater resistance to fire than usual river aggregates. On the other hand, several codes have also discussed the suitability of the use of lightweight aggregates in concrete and have found that they perform better under fire exposure [1, 3–5] as their coefficient of thermal expansion is almost equal to that of cement paste, which results in effective bonding and stability at high temperatures [4]. These are generally the by-product of incineration or volcanic eruption, and therefore have high resistance to heat as well as low heat conductivity. Thus, concrete manufactured using lightweight aggregates shows better mechanical as well as insulating properties under fire as compared to normal weight aggregates.

4.2 Structural Elements—Hollow Steel Columns

It has been observed that the formation of cracks in a normal concrete column triggers at a temperature of 300 °C and the phenomenon of spalling is observed at around a temperature of 500 °C causing the concrete to relinquish its compressive strength by 70–85% [11]. Concrete with bars of smaller diameter offers greater resistance to fire than that with bars of larger diameter. Whenever steel hollow columns are used as structural members, the fire resistance can be improved significantly by filling them with concrete [12]. Further, the hollow steel columns filled with normal strength concrete offers greater resistance to fire than the one filled with high-strength concrete.

4.3 Spalling

The availability of free water and moisture in the concrete accelerates the phenomenon of explosive spalling when concrete is subjected to higher temperatures. The occurrence of this phenomenon is not possible without moisture availability. If the concrete member is dehydrated to a distance of 200–300 mm from the surface exposed to fire, the member becomes less vulnerable to spalling action. Moreover, by the addition of fibers and improving tie configuration, spalling can be abated to a significant extent and fire performance of concrete can be improved [13]. Existing literature suggests the use of polypropylene fibers as one of the most effective methods to improve the fire resistance. The melting of polypropylene inside concrete takes place at around 170 °C. This melting of fibers facilitates the formation of discontinuous reservoirs or a network of pores in concrete. Hence, the steam generated inside the material vaporizes off through these networks of pores. This process makes steam evacuation easier, thus contributing to the reduction of internal pore pressure which is one of the causes of spalling. Therefore, similar special provisions may be developed to reduce the spalling on fire exposure [14].

4.4 *Supplementary Cementitious Materials*

Several studies have been conducted on the possibility of improvement in the fire resistance of concrete on the addition of supplementary cementitious materials. Research suggests that the use of clinoptilolite, zeolite, fly ash materials has improved the fire performance by an appreciable amount [15, 16]. Temuujin et al. [17] suggested that metakaolin-based geopolymer-type coatings prepared using industrial sodium silicate solution when applied on steel substrate show excellent thermal resistance. This is possibly due to the fact that these coatings have high adhesive strength to the substrate which is required for better fire resistance properties. On the other hand, geopolymers are emerging as alternative binding materials. According to Sarker et al. [18], low-calcium fly ash has been extensively used and found to be the most effective source material suitable for concrete applications. They also studied the influence of fire exposure on low-calcium fly ash based geopolymer concrete and observed that the heat transfer is faster in the geopolymer concrete than in ordinary portland cement (OPC) concrete. This leads to a reduced temperature gradient in fly ash based geopolymer concrete, thus resulting in only minor surface cracking and improved spalling resistance at around temperatures of 800–1000 °C. Therefore, suitable guidelines may also be developed to facilitate the use of various supplementary cementitious materials.

5 Recommendations for Improvement in Indian Standard

Although the Indian codes have discussed the dependency of performance of concrete under fire exposure on the types of aggregates, viz., lightweight aggregates and normal weight aggregates, it has laid down provisions for normal weight aggregate concretes only. Therefore, specific provisions and recommendations may be developed to assimilate the behavior of aggregates on the basis of density, i.e., lightweight or normal weight and nature of material, i.e., siliceous or calcareous aggregates.

IS 456 [2] has only highlighted the role of cover to reinforcement for enhancing the resistance against spalling. It is essential to incorporate the addition of certain materials such as polypropylene fibers, basalt fibers, etc., which can enhance the resistance of concrete against spalling, as discussed in the previous sections. Detailed specific guidelines must be laid down especially for high-strength concrete used in multi-storey buildings, similar to Eurocode which includes methods for spalling prevention; strength reduction factor in high-strength concrete at elevated temperatures, characteristic strength reduction as per aggregates type, etc.

Additional recommendations may also be provided to monitor the use of supplementary cementitious materials such as zeolite, fly ash, vermiculite for plastering, and for additional coatings and finishes to enhance the fire resistance of concrete.

6 Conclusions

Indian, the USA, New Zealand, Australian, Canadian, and European standards related to fire have been briefly studied in this paper and the difference in their criteria are properly indicated. It has been observed that all the standards for structural design during the fire have a prescriptive method, in which the minimum dimension of the member and cover to the reinforcement is prescribed for a given fire resistance rating. Redistribution of moments in continuous members, superior requirements in design for high-strength concrete and spalling resistance are found to be among the primary concerns which have not been extensively addressed in several country standards. Besides, some of the standards also make use of special parameters, e.g., load value, degree of utilization, aggregate effect, etc. for defining minimum member dimension and cover to the reinforcement. IS 1642 does not provide guidance on high-strength concrete or design to resist spalling, whereas IS 456 recommends increasing cover in certain fire situations to avoid the risk of spalling. Therefore, it is suggested that Indian code provisions for spalling of concrete, especially high-strength concrete, needs to be developed and the provided recommendations may be followed as preliminary guidelines for the same.

References

1. IS 1642 (1989) Indian standard—Fire safety of buildings (General) —Details of construction, Bureau of Indian standard, New Delhi, India
2. IS 456 (2000) Indian standard—plain and reinforced concrete—code of practice. Bureau of Indian standard, New Delhi, India
3. ACI 216.1-07/TMS 0216-07 (2007) Standard specifications for fire resistance of concrete and masonry assemblies. American concrete Institute, MI, USA
4. NZS 3101: Part 1 (2006) New Zealand standard concrete structures standard Part 1—the design of concrete structures. Wellington, New-Zealand
5. AS-3600 (2018) Australian standard—Concrete structures. Standards Australia International, Sydney, Australia
6. National Research Council Canada (2010) National Building Code of Canada 2010 (NBCC), Division B, Appendix D, Fire performance rating. Institute of Research in Construction, Ottawa, ON, Canada.
7. EN 1991-1-2 (2002) Eurocode 1: Actions on structures—Part 1-2: General actions on structures exposed to fire, European committee for standardization, Brussels, Belgium
8. EN, 1992-1-2 (2004) Design of concrete structures. Part 1-2: general rules—structural fire design, Eurocode 2, European Committee for Standardization, Brussels, Belgium
9. Ma Q, Guo R, Zhao Z, Lin Z, He K (2015) Mechanical properties of concrete at high temperature—a review. *Constr Build Mater* 93:371–383

10. Cheng F, Kodur VK, Wang TC (2004) Stress-strain curves for high-strength concrete at elevated temperatures. *J Mater Civ Eng* 16(1):84–94
11. Romero ML, Moliner V, Espinos A, Ibañez C (2011) Hospitaler A (2011), Fire behavior of axially loaded slender high strength concrete-filled tubular columns. *J Constr Steel Res* 67:1953–1965. <https://doi.org/10.1016/j.jcsr.2011.06.012>
12. Kodur VR (1999) Fibre-reinforced concrete for enhancing structural fire resistance of columns. *Fibre-Structural Applications of Fibre-Reinforced Concrete*, ACI SP-182, pp 215–234
13. Shorter GW, Harmathy TZ (1961) Discussion on the fire resistance of prestressed concrete beams. *Proc Inst Civil Eng* 20:313
14. Naik TR (1983) Temperature effects on concrete, a symposium sponsored by ASTM committee C-9 on concrete and concrete aggregates. ASTM special technical publication, Kansas City, MO
15. kçaözog̃lu K, Fener M, Akçaözog̃ S, Öcal R (2014) Microstructural examination of the effect of elevated temperature on the concrete containing clinoptilolite. *Constr Build Mater* 72:316–325. <https://doi.org/10.1016/j.conbuildmat.2014.09.023>
16. Canpolat F, Yılmaz K, Köse MM, Sümer M, Yurdusev MA (2004) Use of zeolite, coal bottom ash and fly ash as replacement materials in cement production. *Cem Concr Res* 34:731–735
17. Temuujin J, Van Riessen A, Williams R (2009) Influence of calcium compounds on the mechanical properties of fly ash geopolymer pastes. *J Hazard Mater* 167:82–88. <https://doi.org/10.1016/j.jhazmat.2009.09.063>
18. Sarker PK, Kelly S, Yao Z (2014) Effect of fire exposure on cracking, spalling and residual strength of fly ash geopolymer concrete. *Mater Des* 63:584–592. <https://doi.org/10.1016/j.matdes.2014.06.059>

Wear Behavior of Marble Dust Filled Aluminum Metal Matrix Structural Composite



Hariom Tripathi and Sandeep Kashyap

Abstract In the present work, the stir-casting method for the preparation of Al-6063 composites was adopted. Samples were prepared with the reinforcing different weight % of marble dust (2%, 4%, 6%wt) and fixed wt % of graphite (Gr) (2%wt), glass fiber (2%wt), and boron carbide (B₄C) (4%wt) by stir casting setup. The present work has provided the descriptions of the wear characteristics of the marble dust filled Al-6063 composites. A series of erosion experiments were conducted on the composites under various test conditions using an air jet erosion machine. It was seen that with the incorporation of marble dust powder, the wear resistance property of composites was significantly improved.

Keywords Aluminum metal matrix structural composite · Stir casting technique · Erosion wear · Graphite · Glass fiber · Boron carbide · Marble dust

1 Introduction

The manufacturing of materials which are used in engineering applications should be durable, high strength, and light in weight [1–3]. These types of materials are more popular for the purpose of research and industries. Aluminum-based composites (AMCs) fulfill these conditions because they have low density, design flexibility, better specific strength, good wear properties, etc. [4, 5]. AMCs consist of two parts; the first one is aluminum base and the second part consists of different reinforcement materials that are used for enhancing the properties of the base material [3, 5]. The reinforcements are generally those materials which have superior properties than the matrix materials and they are embedded in the Al matrix in Al-based composite system. It has been found that the AMCs demonstrate better design flexibility, mechanical, physical, and tribological properties compared to without reinforced aluminum base materials [2–6].

H. Tripathi (✉) · S. Kashyap
Material Science and Engineering, MNNIT Allahabad, Prayagraj 211004, India
e-mail: hariom.tripathi7@gmail.com

The performance of Al-based composites can be further enhanced by embedding more than one type of reinforcement particles [6–9], these types of composites in which there are more than one reinforcement particle is present are known as the hybrid composites [8, 16]. Nowadays hybrid aluminum-based composites are getting popularity in many engineering field applications because they can alter the mechanical as well as the physical properties (thermal conductivity, friction coefficient, density, wear resistance, etc.) which are desired for the composite system. The main reason for incorporating more than one reinforcement particle is to increase the wettability between the matrix and reinforcement medium, enhancing the mechanical properties, wear resistance, etc. [8, 16, 18–20].

The addition of graphite as a reinforcement particle in this hybrid composite system reduces the heat buildup because coefficient of friction decreases with the addition of graphite [10–15]. However, the addition of graphite decreases the mechanical properties like hardness, tensile strength [10–15]. Hence, for enhancing the mechanical properties hard particles like boron carbides (B_4C) (4%) are added in the matrix material. B_4C has lower density than other available commercial ceramic materials (TiC, SiC, Al_2O_3 , TiB_2 , etc.), higher specific strength, high hardness, good chemical inertness, good thermal stability, etc., that is why boron carbide is the ideal candidate as the reinforcement in aluminum matrix [6–10]. However as the cost of B_4C is more, for economical purpose in this research for further increase in the mechanical properties composites are prepared by reinforcing different weights % of marble dust (2%, 4%, 6%wt) and fixed wt% of graphite (Gr) (2%wt), glass fiber (2%wt), and boron carbide (B_4C) (4%wt) by, stir casting setup.

The most important factor for the preparation of particles reinforced composites is the wettability of particles with the matrix material. In particle-reinforced Al-based hybrid composite, for enhancing the wettability 1–1.1% of magnesium powder is added in the composite during the casting.

In general hybrid composites of aluminum are fabricated by powder metallurgy method, semisolid processing (friction stir processing) [17], and liquid state processing (squeeze casting, stir casting, etc.). Among all the fabrication techniques, casting is very popular for fabricating composite in bulk.

The objective of this research work is to fabricate an advanced series of Al6063-based MMCs reinforced with and without marble dust particles and observe the effect of reinforcement particles on the erosion wear properties.

2 Experiments

2.1 Matrix and Reinforced Materials

In this research work, 6063 series of aluminum alloy having specific gravity 2.7 was used as the matrix material and varying % of marble dust powder (0, 2, 4, 6%) and fixed % of glass fiber (2%) (0.005–0.01 mm dia.), graphite powder (2%), and B_4C

Table 1 Chemical composition of Al 6063

Elements	Al	Mg	Si	Fe	Others
Wt. %	Max	0.45–	0.2–	Max	~0.65
	97.5	0.90	0.6	0.35	

(4%) were added as the reinforcement in the matrix material for the development of aluminum-based hybrid composite. Marble dust having specific gravity 2.8 is an industrial waste that is utilized in this research work; it contains oxides of silicon, magnesium, calcium, and iron. Graphite powders of avg. size 30 μm , boron carbide particles of avg. size 25 μm , and marble dust of avg. size 40 μm were used. At the time of casting, 1–1.1 weight percentage of mg powder was also added in the molten aluminum to increase the wettability between the different reinforcement particles with the aluminum 6063 matrix. The compositions of alloy which is used in this research as the matrix in the composite are shown in Table 1. The melting point of Al 6063 is 650–660 $^{\circ}\text{C}$.

2.2 Casting of AMC's

To produce marble dust reinforced hybrid AMCs, the billet of Al 6063 alloys was melted in the electrical resistance furnace and stir casting technique was used for the preparation of hybrid composite (shown in Fig. 1).

Matrix material billet (aluminum 6063) was placed inside the graphite crucible and was melted inside the electrical furnace in the inert atmosphere and when the temperature of liquid metal reached at 770–790 $^{\circ}\text{C}$ (heating rate 25 $^{\circ}\text{C}/\text{min}$), then magnesium powder was added for enhancing the bonding between the aluminum and reinforcement particles.

Fig. 1 Stir casting setup

Fig. 2 Sand mold with casted wear test specimen



After that preheated (350–400 °C) reinforced particles (glass fiber (2%), graphite (2%), B₄C (4%), and varying % of marble dust powder (0, 2, 4, and 6% weight)) were added and the mixture of melted metal and reinforcement particles were stirred at 450–550 rpm for 15–20 min for uniform distribution of particles in the matrix. After that, the liquid mixture of hybrid composite was poured into the sand mold (as shown in Fig. 2) and the melted composites were allowed to cool. And in this way, four different grades (0, 2, 4, and 6 weight% of marble dust) of AMCs were prepared.

2.3 Particle Erosion Test (Wear Test)

In order to find out the wear resistance of different AMCs, test specimens were prepared according to ASTM rule.

Samples were polished like mirror for performing erosion wear test. The setup used in this test was proficient of generating duplicatable erosive condition for performing wear resistance capability of prepared composites. The pictorial view of the Air-Jet Erosion Test machine (at Mechanical System Design Lab, Mechanical Engineering Department, MNNIT, Allahabad) is shown in Fig. 3. The erosion wear test rig contains air dryer unit, particle mixer, particle feeder, air compressor, and accelerating chamber units (Table 2).

In this research work, preheated sand (silica) of different particle sizes 75, 125, 150, and 250 μm were utilized as the erodent medium. The compressed and dried air is mixed with the sand particles in the mixing chamber (feed rate of erodent 5g/min). The mixture of air with silica particles was accelerated with the help of nozzle (convergent tungsten carbide) of dia. 1.5 mm. During the time of impact testing with the help of erodent, the samples were held at different angles with respect to erodent flow direction. The stand-off distance is kept constant (10 mm) between specimen and nozzle. The sample size for erosion test specimen (25 mm \times 25 mm \times 10 mm)

Fig. 3 Erosion testing machine



Table 2 Designation of samples

Code	Composition (wt%)
A0	Al 6063+ GF(2%) + Gr(2%) + B ₄ C(4%)
A1	Al 6063+GF(2%) + Gr (2%) +B ₄ C(4%)+ MD (2%)
A2	Al 6063+ GF(2%) + Gr(2%) + B ₄ C(4%)+ MD(4%)
A3	Al 6063+GF(2%) + Gr(2%) + B ₄ C(4%)+ MD(6%)

was well polished by using emery paper of 2000 grades and cloth polishing. Erosion test specimens were weighed before and after the test (particle erosion test) using the electronic balance (accuracy ± 0.01 mg). The losses of weight were recorded and with the help of subsequent calculation, erosion rate was measured.

3 Results and Discussion

The erosion wear rates of marble dust filled Al 6063 metal matrix composites under various conditions were investigated.

3.1 Influence of Impingement Angle

In this type of testing, erosion tests were performed at different impingement angles while the other parameters remained constant (impact velocity = 60 m/sec, and erodent size = 250 μ m). The results were plotted in between the wear rate (mg/kg) and the impingement angle (in degree) as shown in Figs. 4 and 5 shows the surface of composite after the wear test at different impingement angles.

It was observed that the erosion rates were maximum at an angle of 60° for all the samples irrespective of particulate content because removal of materials (micro-plowing) for beyond 60° impingement angle, collision between return particles and forward particles can also reduce the impact momentum resulting in a decrease in erosion rate. This showed the semi-ductile erosion nature of the metal matrix composite. It is evident from Fig. 4 that 5% boron carbide and 0% marble dust reinforced in Al 6063 metal matrix composite(A0) exhibits maximum erosion rate and 5% boron carbide + 6% marble dust reinforced in Al 6063 metal matrix composite

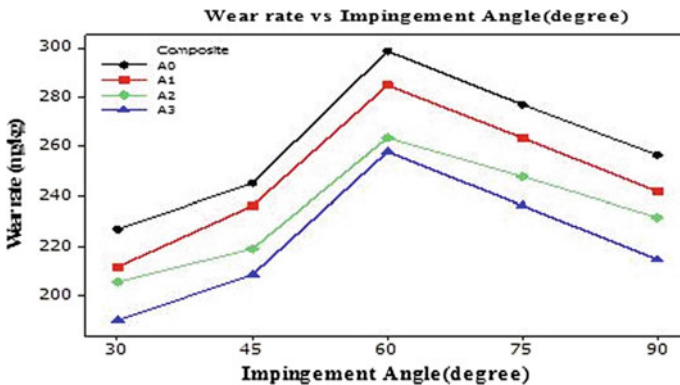


Fig. 4 Wear rate versus impingement angle

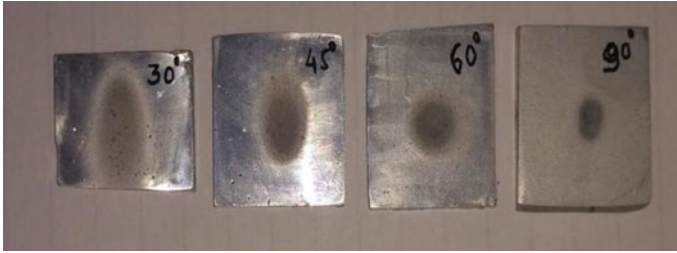


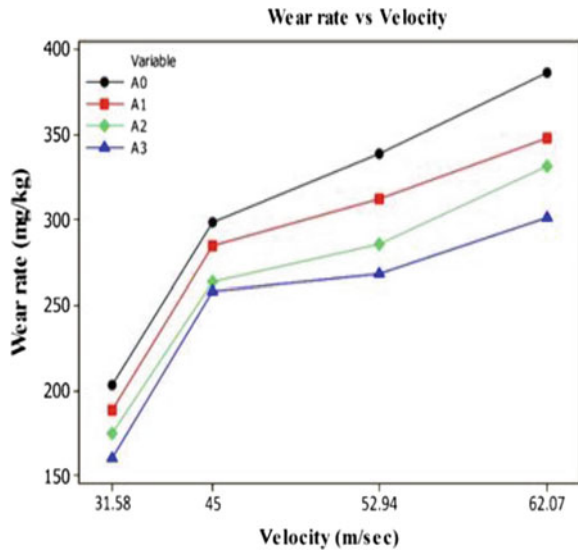
Fig. 5 Surface of composite after the wear test on the variation of impingement angles

(A3) shows the minimum erosion rate irrespective of the impingement angle. It is because of the presence of marble dust, and proper mixing of particulate and matrix, i.e., the matrix covers the whole filler materials in the composites and it exhibits along the bonding between all of them. Figure 5 shows the wear pattern of metal matrix irrespective of different impingement angles. When the silica sand particles were struck on the surface of composites at various angles, they primarily interact with the matrix of the composites. After sufficient loss of materials, they interact with the reinforced particulates. As the hardness value of B_4C and marble dust is much higher than the aluminum matrix material the rate of erosion decreased. Due to the presence of hard particles in the aluminum metal matrix.

Figure 5 also indicates the erosion propagation relevant to each of the impingement angles. When solid particles impact at an angle, the hard particles penetrate the surface leading to the removal of materials mostly by micro-plowing. When the removal of particles starts, there is the formation of the passage from the place of removed particles on the surface of the base material, resulting in a more efficient removal of base material. In case of impact at an angle 30° , the penetration range of solid particle into the matrix was very minimum and passing passage was very high, resulting in less removal of the matrix material.

With further increase in impingement angle up to 60° , the penetration range of the hard particle into matrix material slightly increases with sufficient passage for flow out of the eroded particles. In other terms, the impact angle also determines the magnitude and direction of impact velocity. It mainly resolves the impact velocity into two main components. Firstly, the normal component to the surface, which determines how much the impact and the load are. Secondly, the component of tangential velocity determines how much sliding takes places and shear loading (addition to the normal load) on the surface. From the above, it is signified that the change in the impingement angle leads to change in magnitude and nature of stress.

Fig. 6 Impact velocity influence on erosion rates on different AMC's



3.2 Impact Velocity Influence

The erosion rate variation with respect to impact velocity is shown in Fig. 6. Erosion test were performed at four different velocities and all other variables were kept constant (Impingement angle = 60° and erodent size = $250 \mu\text{m}$).

It is quite clear from Fig. 6 that erosion rate of the aluminum-based metal matrix composites increases with the increase in the velocity of impact. It was also observed that the composite (A3) shows minimum erosion rate followed by the composites (A0, A1, A2). If the velocity is very low (31.58 m/s) then the stresses induced due to impact are not sufficient (for the occurrence of the plastic deformation) and wear proceeds due to the surface fatigue.

However, with the increase in velocity of impact (45 to 62.07 m/s), the erosion rate significantly increases because at higher impact velocity the erosion rate occurs due to plastic deformation and the increase in penetration of erodent particles due to the impact. These effect causes dissipation of more amount of energy to the composite surface. This leads to increase in the crack growth and the erosion rate increases.

4 Concluding Remarks

This chapter has provided the experimental investigation into the erosion behavior of marble dust filled Al 6063 composites leading to the following major conclusions:

1. Industrial waste like marble dust was successfully utilized to produce low-cost metal matrix composites.

2. Erosion resistance of the developed composites is increasing with filler content and A3 (6wt% marble dust) composite has shown least erosion rate than others.
3. With the increase in velocity of impact (45–62.07 m/s), the erosion rate significantly increases.
4. In ductile material, maximum erosion takes place at 30–45° due to micro-plowing action, and in brittle material maximum erosion takes place at 90° due to brittle fracture. However, in the present work, maximum erosion takes place at 60° which depicts the semi-ductile nature of composite. Also least erosion occurred in A4 containing 6% marble dust which shows that marble dust can be used to make erosion resistance composite.

References

1. Mathews FL, Rawlings RD (1994) Composite materials, engineering and science. Chapman and Hall
2. Park BG (2001) Material characterization and mechanical properties of Al₂O₃-Al metal matrix composites. *J Mater Sci* 36:2417–2426
3. Stolarski TA (1990) Tribology in machine design. Heiman Newnes, UK
4. Kivikytö-Reponen P (2006) Correlation of material characteristics and wear of powder metallurgical metal matrix composites. Doctoral Theses, Materials and Earth Sciences, Helsinki University of Technology, Laboratory of Materials Science, Espoo
5. Budinski KG (1998) Surface engineering for wear resistance. Prentice Hall, New Jersey
6. Robinowicz E (1965) Friction and wear of materials. Willey, New York, USA
7. Kosel TH (1992) Solid particle erosion. ASM Handbook, ASM International, vol 18, pp 199–213
8. Ranganath G, Sharma SC, Krishna M (2001) Dry sliding wear of garnet reinforced zinc/aluminium metal matrix composites. *Wear* 251(1):408–1413
9. Kumar MP (2006) Dry sliding wear behaviour of garnet particles reinforced zinc-aluminium alloy metal matrix composites. *Mater Sci-Medziagotyra* 12(3):1392–1420
10. Rohatgi PK (2013) Metal matrix composites. *Defence Sci J* 43(4):323–349
11. Bandyopadhyay NR, Ghosh S, Basumallick A (2007) New generation metal matrix composites. *Mater Manuf Process* 22(6):679–682
12. Chou TW, Kelly A, Okura A (1985) Fibre-reinforced metal-matrix composites. *Composites* 16(3):187–206
13. Avila AF, Tamma KK (1998) Analysis of laminate metal matrix composites. *J Thermal Stres* 21(9):897–917
14. Pramanik A, Zhang LC, Arsecularatne JA (2007) An FEM investigation into the behavior of metal matrix composites: tool–particle interaction during orthogonal cutting. *Int J Mach Tools Manuf* 47(10):1497–1506
15. Shoukry SN, Prucz JC, Shankaranarayana PG, William GW (2007) Microstructure modeling of particulate reinforced metal matrix composites. *Mech Adv Mater Struct* 14(6):499–510
16. Jayamathy M et al (2005) Influence of reinforcement and processing on the wear response of two magnesium Alloys. *Mater Manuf Process* 20(2):255–271
17. Melgarejo, Humberto Z, Marcelo OS, Kumar S (2008) Microstructure and properties of functionally graded Al-Mg-B composites fabricated by centrifugal casting. *Compos A Appl Sci Manuf* 39(7):1150–1158
18. Bharti A, Tripathi H (2019) Enhancement of fatigue life of TIG-welded joint by friction stir processing. *Renew Energy Innovat Technol* 1:51–59. https://doi.org/10.1007/978-981-13-2116-0_5

19. Patnaik A (2010) Solid particle erosion characteristics of fibre and particulate filled polymer composite: a review. *Wear* 268(1):249–263
20. Mishra SK, Biswash S, Satapathy A (2014) A study on processing, characterizations & erosion wear behaviour of silicone carbide particle filled ZA-27 metal matrix composite. *Mater Des* 55:958–965

Quantifying Uncertainty in Structural Responses of Polymer Sandwich Composites: A Comparative Analysis of Neural Networks



R. R. Kumar, T. Mukhopadhyay, K. M. Pandey, and S. Dey

Abstract The manufacturing and fabrication of complex polymer sandwich composite plates involve various processes and parameters, and the lack of control over them causes uncertain system parameters. It is essential to consider randomness in varying parameters to analyse polymer sandwich composite plates. The present study portrays uncertainty quantification in structural responses (such as natural frequencies) of polymer sandwich composite plates using the surrogate model. The comparative study of artificial neural network (ANN) and polynomial neural network (PNN) for uncertain structural responses of the sandwich plate is presented. The proposed ANN as well as PNN algorithm is found to be convergent with intensive Monte Carlo simulation (MCS) for uncertain vibration responses. The predictability of PNN is observed to be more efficient than that of ANN. Typical material properties, skew angle, fibre orientation angle, number of laminate and core thickness are randomly varied to quantify the uncertainties. The use of both the surrogate models (PNN and ANN) results in a significant saving of computational time and cost compared to that of full-scale intensive finite element-based MCS approach.

Keywords Polymer sandwich plate · Artificial neural network · Polynomial neural network · Monte carlo simulation · Randomness

1 Introduction

In the present scenario, speed and efficiency are the most important parameter for any system (either machine or structure). It results in a continuously increasing demand for a better material. Scientists and researchers are continuously trying for

R. R. Kumar (✉) · K. M. Pandey · S. Dey
Department of Mechanical Engineering, NIT Silchar, Silchar, India
e-mail: ravinits2014@gmail.com

T. Mukhopadhyay
Department of Aerospace Engineering, IIT Kanpur, Kanpur, India

a better and efficient material according to its applications such as aerospace, automobile, submarines and other task-defined functions. Therefore, the material developed needs to be highly task-specific and withstand in any service condition. That is why lightweight robust structures are highly preferred, predominantly in structural applications, where a high amount of vibration is suspected to produce due to dynamic loads. Sandwich plates are one of them which is widely used in the design and construction of aerospace structures. Sandwich plates are more widely used in cost-sensitive than that of weight-sensitive applications with respect to monolithic panels [1]. The cost-effective sandwich panel requires a sandwich core of low-cost material which exhibits better weight sensitiveness as well. The development and automation in production processes make possible the production of low-cost sandwich panels. Sandwich panels may be categorised as thin-walled structure which consists of two face sheets separated by core and some adhesive. The inherent superior properties of the sandwich panel are forcing design engineers for their extensive applications. The free vibration is one of the most important design parameters for plate structure. The natural frequency and damping concepts are properly taken into consideration for designing sandwich structures (more sensitive than that of conventional material under dynamic load condition) to avoid resonance. The inevitable effect of uncertainty can affect the vibrational response of such structures significantly. Therefore, it is essential to consider the material and geometric uncertainty to include the variability and inaccuracies occurring during manufacturing and operating conditions. In general, a surrogate-based uncertainty quantification approach [2–15] can be adopted in case of problems, where efficient solutions [16–24] are not available. In this chapter, we aim to present a comparative performance of ANN [25–27] and PNN [28] for the uncertainty quantification of sandwich panels.

2 Governing Equation for Natural Frequency

In the case of structural deformation, relation for strain–displacement [29] is articulated as follows:

$$\{\bar{\varepsilon}(\varpi)\} = \left[\frac{\partial U(\varpi)}{\partial x} \frac{\partial V(\varpi)}{\partial y} \frac{\partial W(\varpi)}{\partial z} \frac{\partial U(\varpi)}{\partial x} + \frac{\partial V(\varpi)}{\partial y} \frac{\partial U(\varpi)}{\partial z} + \frac{\partial W(\varpi)}{\partial x} \frac{\partial V(\varpi)}{\partial z} + \frac{\partial W(\varpi)}{\partial x} \right] \quad (1)$$

If $[H]$ is unit step function, then Eq. (1) can also be expressed as follows:

$$\text{i.e. } \{\bar{\varepsilon}(\varpi)\} = [H(\varpi)]\{\varepsilon(\varpi)\}$$

The generalised displacement vector at any point can be articulated as follows:

$$\{S(\varpi)\} = \sum_{i=1}^n N_i(\varpi) S_i(\varpi) \quad (2)$$

where $\{S\} = \{u_o \ v_o \ w_o \ \theta_x \ \theta_y \ u_u \ v_u \ w_u \ u_l \ v_l \ w_l\}^T$.

With the help of Eq. (2), strain vector can be articulated as follows:

$$\{\varepsilon(\varpi)\} = [A(\varpi)]\{S(\varpi)\} \tag{3}$$

where $[A]$ is the Cartesian strain–displacement matrix.

If stochastic free vibration frequency is expressed by $[R(\varpi)]$ and global mass matrix by $[M(\varpi)]$ then as per Hamilton’s principle, for free vibration analysis, dynamic equilibrium equation can be articulated as follows:

$$[R(\varpi)]\{\bar{S}\} = \lambda^2[M(\varpi)]\{\bar{S}\} \tag{4}$$

If the random mass density of k -th order is written as $\rho_k(\varpi)$, shape function matrix as $[N]$ and $[J]$ is the matrix of an order of 3×11 containing Z terms and some constant, then global mass matrix $[M(\varpi)]$ can be articulated as follows:

$$[M(\varpi)] = \sum_{k=1}^{n_u+n_l} \iiint \rho_k(\varpi)[N]^T[J]^T[N][J]dx dy dz = \iint [N]^T[K(\varpi)][N]dx dy \tag{5}$$

The stiffness matrix $[K(\varpi)]$ can be articulated as follows:

$$[K(\varpi)] = \sum_{k_l}^{n_u+n_l} \rho_k(\varpi)[J]^T[J]dz \tag{6}$$

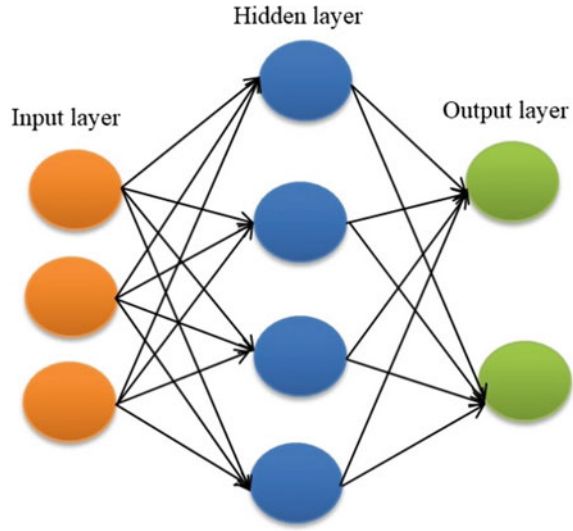
The natural frequencies can be obtained by solving an eigenvalue problem of the mass and stiffness matrices as described above [29].

3 Artificial Neural Network

An artificial neuron, similar to the biological neuron, is the basic processing unit of ANN which receives input from other sources and outputs the final result by combining and performing a non-linear operation on the result [26, 27]. ANN is having good predictability to diagnose and beget the cause–effect relationships. This is performed by training multiple input–output systems which enables ANN an efficient surrogate model to represent the complex system. The performance of ANN is statistically measured by following equations:

$$\text{Root mean squared error (RMSE)} = \sqrt{\frac{1}{m} \sum_{j=1}^m (X_j - X_{jd})^2} \tag{7}$$

Fig. 1 Architecture of ANN



$$\text{Coefficient of determination } (R^2) = 1 - \frac{\sum_{j=1}^m (X_j - X_{jd})^2}{\sum_{j=1}^m (X_{jd} - X_n)^2} \quad (8)$$

$$\text{Absolute average deviation (AAD)} = \left[\frac{1}{m} \sum_{j=1}^m \left| \frac{(X_j - X_{jd})}{X_{jd}} \right| \right] \times 100 \quad (9)$$

where m = Number of points,

X_j = Predicted value,

X_{jd} = Actual value and

X_n = Average of the actual values

The architecture of ANN is shown in Fig. 1. It consists of input layer, hidden layer and output layer.

4 Polynomial Neural Network

An input–output data in optimal PNN structure [27, 28, 30] can be expressed as follows:

$$(X_i, Y_i) = (x_{1i}, x_{2i}, x_{3i}, \dots, x_{ni}, y_i) \quad (10)$$

where $i = 1, 2, 3, \dots, n$.

Let Y is the output of the system which required to model. Polynomial regression equation is computed as follows:

$$Y = A + Bx_i + Cx_j + Dx_i^2 + Ex_j^2 + Fx_ix_j \tag{11}$$

where x_i and x_j is the pair of input variable, whereas Y is the output, $i, j = 1, 2, 3, \dots, n$, and coefficient of the polynomial equation is represented as A, B, C, D, E, F .

If \hat{Y}_i is the estimated output, then it can be expressed as follows:

$$\begin{aligned} \hat{Y}_i = \hat{f}(x_1, x_2, x_3, \dots, x_n) = & A_0 + \sum_{i=1}^n B_i x_i + \sum_{i=1}^n \sum_{j=1}^n C_{ij} x_i x_j \\ & + \sum_{i=1}^n \sum_{j=1}^n \sum_{k=1}^n D_{ijk} x_i x_j x_k + \dots \end{aligned} \tag{12}$$

where $i, j, k = 1, 2, 3, \dots, n$.

$X(x_1, x_2, \dots, x_n)$ = input variable vector (its component can be of finite-difference terms, functional forms or it may be independent variables).

$P(A_0, B_i, C_{ij}, D_{ijk}, \dots)$ = vector of coefficients or weight of lvakhnenko polynomials.

This algorithm provides model structure and model system output on the value of the most noteworthy inputs of the system. The basic taxonomy for the architecture of PNN structure is given in Fig. 2. The methodology of stochastic natural frequency analysis of the sandwich plate by using the surrogate model is presented in Fig. 3.

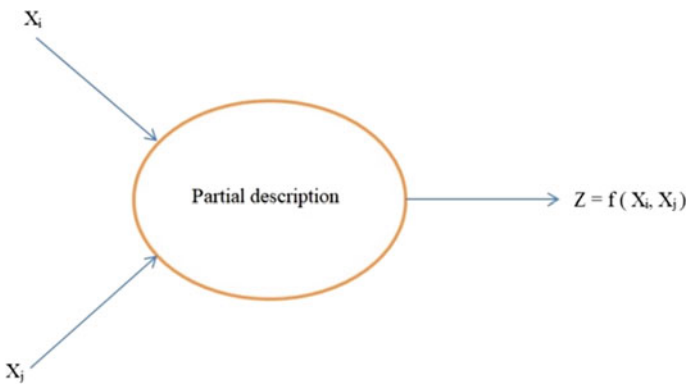


Fig. 2 Taxonomy for the architecture of PNN

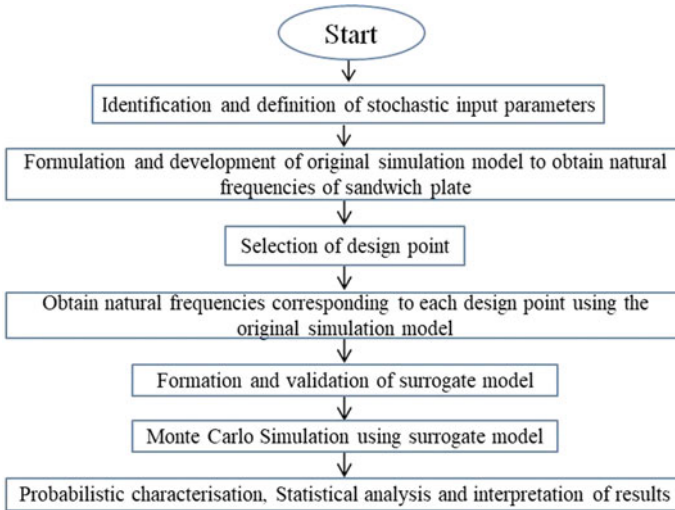


Fig. 3 Flow diagram of stochastic analysis using surrogate model

5 Results and Discussion

The comparative analysis for predictability of ANN and PNN models for uncertainty quantification of natural frequencies (first five) of simply supported skewed (30°) sandwich plate considering a compound variation of all input parameters is presented in this study until otherwise mentioned. The sandwich plate is considered to be 10 cm long (l), 10 cm wide (b) and 1 cm thick (t). The ratio of core and face sheet thickness is considered as 10. Both upper and lower face sheets are having four laminates of $90^\circ/0^\circ/90^\circ/0^\circ$ orientation angle. Stochasticity in skew angle is taken as $\Delta = 5\%$, whereas $\Delta = 10\%$ is taken for core thickness, core material properties, face sheet thickness, face sheet material properties and ply-orientation angle. The deterministic FE code is validated by the authors in a previous study [29] and the same code is used for the current analysis. The material properties [31] considered in this paper is as follows:

(a) Face sheet:

$$E_1 = 131 \text{ GPa}, E_2 = E_3 = 10.34 \text{ GPa}, G_{12} = G_{13} = 6.895 \text{ GPa}, G_{23} = 6.205 \text{ GPa}, \nu_{12} = \nu_{13} = 0.22, \nu_{23} = 0.49, \rho = 1627 \text{ kg/m}^3.$$

(b) Core:

$$E_1 = E_2 = E_3 = 0.00689 \text{ GPa}, G_{12} = G_{23} = G_{31} = 0.00345 \text{ GPa}, \nu_{12} = \nu_{13} = \nu_{23} = 0 = \nu_{21} = \nu_{31} = \nu_{32}, \rho = 97 \text{ kg/m}^3.$$

To check the predictability of the surrogate model probability density function (PDF) plot, scatter plot and mean percentage error plot is presented. The predictability of ANN and PNN models is verified in Fig. 4 by using PDF plot of the first five natural frequencies for different sample sizes. Thereafter, negligible deviation of

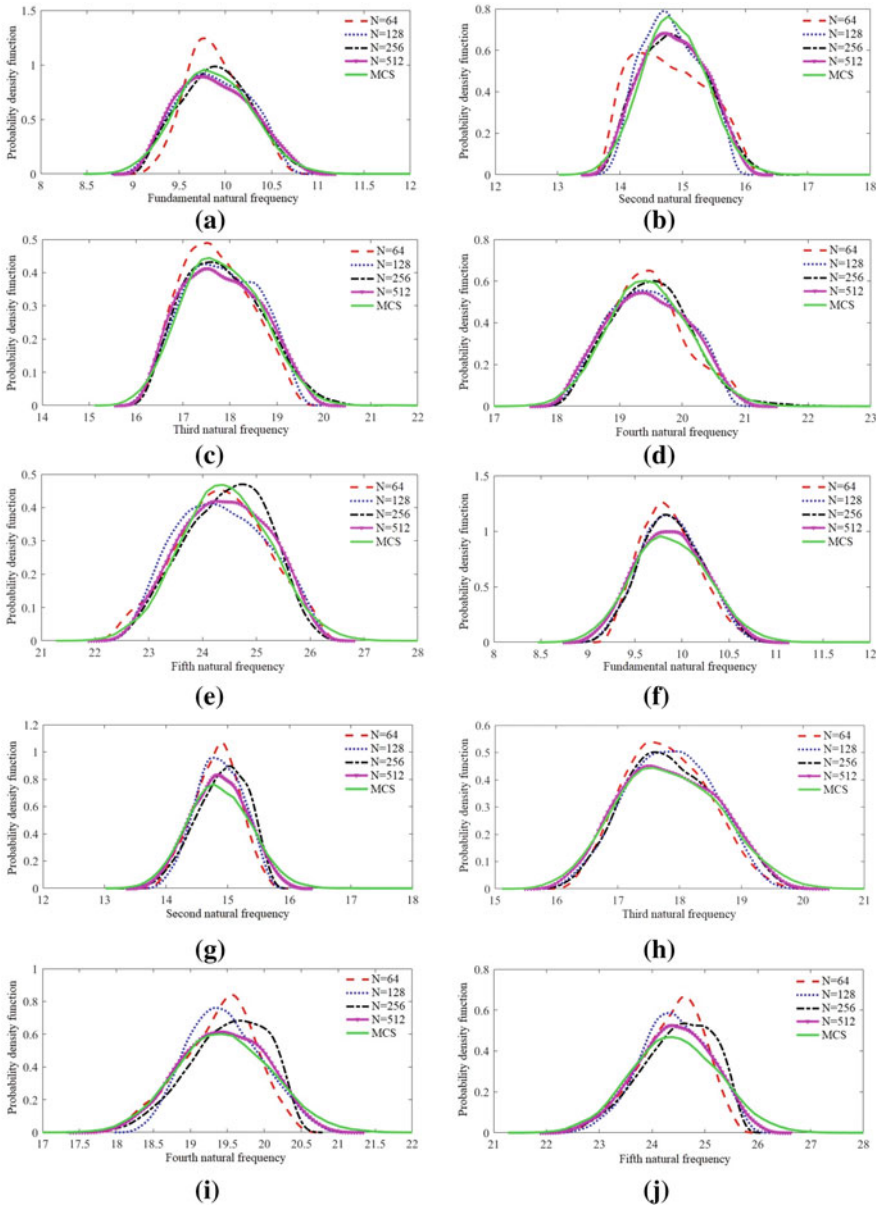


Fig. 4 Probability density function of first five natural frequencies **a–e** for ANN model of different samples with MCS and **f–j** for PNN model of different samples with MCS, of simply supported composite sandwich plates considering the combined variation

the scatter plot from diagonal line confirms the prediction ability of the surrogate model. However, the efficiency of the model depends upon the number of sample sizes required to get a result equivalent to that of MCS as presented in Fig. 5. Mean percentage error is calculated for equivalent MCS results obtained from ANN and PNN model by using 64, 128, 256, 512 samples run with respect to original FE-based MCS result. The sample size of 512 is observed to be optimum for the ANN model, whereas the sample size of 128 is found to be optimum in the case of PNN model on considering the first five natural frequencies which are depicted in Fig. 6. Both

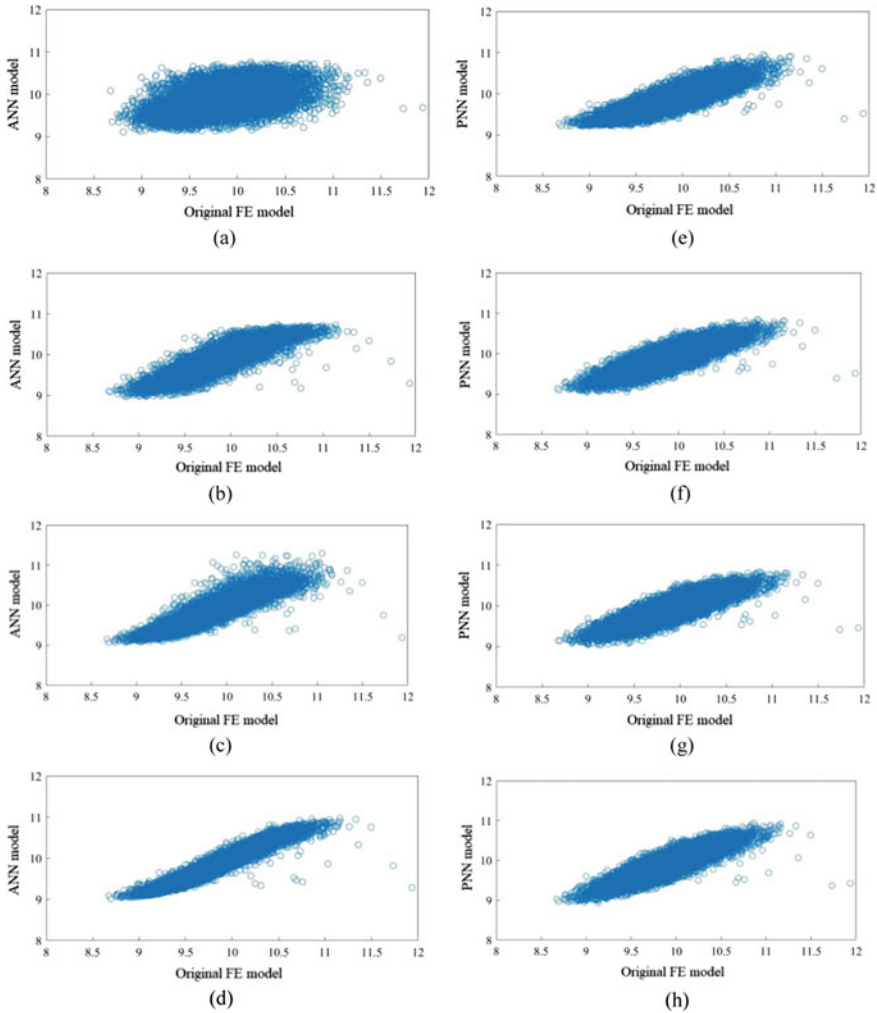


Fig. 5 Scatter plot of ANN model with original FE model for simply supported composite sandwich plates (first natural frequency) for **a** 64, **b** 128, **c** 256, **d** 512 samples, PNN model and original FE model for **e** 64, **f** 128, **g** 256, **h** 512, samples, considering the combined variation

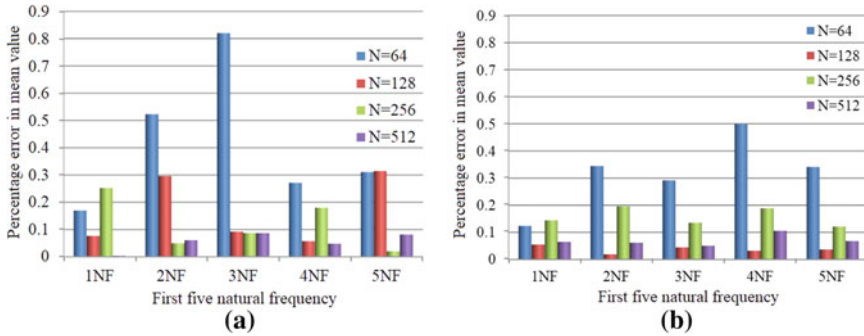


Fig. 6 Percentage error in the mean value of natural frequencies (NF) (first five) between **a** MCS and ANN results, **b** MCS and PNN results with respect to different sample size considering the combined variation of all input parameters

the model gives the efficient result to that of the result obtained through direct MCS as it requires only 128 (in case of PNN) and 512 (in case of ANN) sample-sized Monte Carlo simulations to get a result equivalent to 10,000 sample Monte Carlo simulation.

6 Conclusion

Novelty of the present study includes the assessment of a comparative prediction ability of artificial neural network and polynomial neural network for the first five uncertain natural frequencies of sandwich plate considering a combined variation of all random input parameters. To check the predictability of ANN and PNN as a surrogate model, error analysis is carried out in addition to probability density function. The scatter plot of the result is also obtained through ANN model as well as PNN model with respect to the original finite element model. PNN is observed to deliver better prediction than ANN compared to conventional MCS. In general, it is observed that natural frequencies remarkably deviate from their respective deterministic values. Hence it is required to consider the effect of stochasticity of input parameters in the analysis of sandwich plates for a practical design.

Acknowledgements The first author would like to acknowledge the financial support received from MHRD, Government of India during this research work.

References

1. Pflug J, Verpoest I (2006) Sandwich materials selection charts. *J Sandwich Struct Mater* 8(5):407–421
2. Mukhopadhyay T, Chowdhury R, Chakrabarti A (2016) Structural damage identification: a random sampling-high dimensional model representation approach. *Adv Struct Eng* 19(6):908–927
3. Dey TK, Mukhopadhyay T, Chakrabarti A, Sharma UK (2015) Efficient lightweight design of FRP bridge deck. *Proc Inst Civil Eng—Struct Build* 168(10):697–707
4. Mahata A, Mukhopadhyay T, Adhikari S (2016) A polynomial chaos expansion based molecular dynamics study for probabilistic strength analysis of nano-twinned copper. *Mater Res Express* 3:036501
5. Mukhopadhyay T, Mahata A, Dey S, Adhikari S (2016) Probabilistic analysis and design of HCP nanowires: an efficient surrogate based molecular dynamics simulation approach. *J Mater Sci Technol* 32(12):1345–1351
6. Metya S, Mukhopadhyay T, Adhikari S, Bhattacharya G (2017) System reliability analysis of soil slopes with general slip surfaces using multivariate adaptive regression splines. *Comput Geotech* 87:212–228
7. Dey S, Mukhopadhyay T, Sahu SK, Adhikari S (2018) Stochastic dynamic stability analysis of composite curved panels subjected to non-uniform partial edge loading. *Eur J Mech/A Solids* 67:108–122
8. Dey S, Mukhopadhyay T, Khodaparast HH, Adhikari S (2016) A response surface modelling approach for resonance driven reliability based optimization of composite shells. *Periodica Polytechnica—Civ Eng* 60(1):103–111
9. Karsh PK, Mukhopadhyay T, Dey S (2018a) Spatial vulnerability analysis for the first ply failure strength of composite laminates including effect of delamination. *Compos Struct* 184:554–567
10. Naskar S, Mukhopadhyay T, Sriramula S (2018) Probabilistic micromechanical spatial variability quantification in laminated composites. *Compos B Eng* 151:291–325
11. Maharshi K, Mukhopadhyay T, Roy B, Roy L, Dey S (2018) Stochastic dynamic behaviour of hydrodynamic journal bearings including the effect of surface roughness. *Int J Mech Sci* 142–143:370–383
12. Naskar S, Mukhopadhyay T, Sriramula S, Adhikari S (2017) Stochastic natural frequency analysis of damaged thin-walled laminated composite beams with uncertainty in micromechanical properties. *Compos Struct* 160:312–334
13. Mukhopadhyay T, A multivariate adaptive regression splines based damage identification methodology for web core composite bridges including the effect of noise. *J Sandwich Struct Mater*. <https://doi.org/10.1177/1099636216682533>
14. Kumar RR, Mukhopadhyay T, Pandey KM, Dey S (2019) Stochastic buckling analysis of sandwich plates: the importance of higher order modes. *Int J Mech Sci* 152:630–643
15. Kumar RR, Karsh PK, Vaishali Pandey KM, Dey S (2019) Stochastic natural frequency analysis of skewed sandwich plates. *Eng Computations*. <https://doi.org/10.1108/EC-01-2019-0034>
16. Mukhopadhyay T, Adhikari S (2017a) Stochastic mechanics of metamaterials. *Compos Struct* 162:85–97
17. Mukhopadhyay T, Adhikari S (2016) Free vibration analysis of sandwich panels with randomly irregular honeycomb core. *J Eng Mech* 142(11):06016008
18. Mukhopadhyay T, Adhikari S (2017b) Effective in-plane elastic moduli of quasi-random spatially irregular hexagonal lattices. *Int J Eng Sci* 119:142–179
19. Mukhopadhyay T, Mahata A, Adhikari S, Asle ZM (2018) Probing the shear modulus of two-dimensional multiplanar nanostructures and heterostructures. *Nanoscale* 10:5280–5294
20. Mukhopadhyay T, Mahata A, Adhikari S, Asle ZM (2017) Effective mechanical properties of multilayer nano-heterostructures. *Nat Sci Rep* 7:15818
21. Mukhopadhyay T, Mahata A, Adhikari S, Asle Zaeem M (2017) Effective elastic properties of two dimensional multiplanar hexagonal nano-structures, *2D Materials*, 4:025006

22. Mahata A, Mukhopadhyay T, Probing the chirality-dependent elastic properties and crack propagation behavior of single and bilayer stanine. *Phys Chem Chem Phys*. <https://doi.org/10.1039/C8CP03892A>
23. Mukhopadhyay T, Adhikari S, Batou A, Frequency domain homogenization for the viscoelastic properties of spatially correlated quasi-periodic lattices. *Int J Mech Sci*. <https://doi.org/10.1016/j.ijmecsci.2017.09.004>
24. Kumar RR, Mukhopadhyay T, Naskar S, Pandey KM, Dey S (2019) Stochastic low-velocity impact analysis of sandwich plates including the effects of obliqueness and twist. *Thin-Walled Struct* 145:106411
25. Karsh PK, Mukhopadhyay T, Dey S (2018b) Stochastic dynamic analysis of twisted functionally graded plates. *Compos B Eng* 147:259–278
26. Dey S, Mukhopadhyay T, Spickenheuer A, Gohs U, Adhikari S (2016) Uncertainty quantification in natural frequency of composite plates—an artificial neural network based approach. *Adv Compos Lett* 25(2):43–48
27. Dey S, Mukhopadhyay T, Adhikari S (2018) Uncertainty quantification in laminated composites: a meta-model based approach. CRC Press, ISBN, p 9781498784450
28. Dey S, Naskar S, Mukhopadhyay T, Gohs U, Sriramula S, Adhikari S, Heinrich G (2016) Uncertain natural frequency analysis of composite plates including effect of noise—a polynomial neural network approach. *Compos Struct* 143:130–142
29. Dey S, Mukhopadhyay T, Naskar S, Dey TK, Chalak HD, Adhikari S, Probabilistic characterisation for dynamics and stability of laminated soft core sandwich plates. *J Sandwich Struct Mater*. <https://doi.org/10.1177/1099636217694229>
30. Dey S, Mukhopadhyay T, Adhikari S (2017) Metamodel based high-fidelity stochastic analysis of composite laminates: a concise review with critical comparative assessment. *Compos Struct* 171:227–250
31. Chalak HD, Chakrabarti A, Iqbal MA, Sheikh AH (2013) Free vibration analysis of laminated soft core sandwich plates. *J Vib Acoust* 135(1):011013

Buckling Analysis of Braced Frames under Axial and Lateral Loadings: The Effect of Bracing Location



Narayan  and Krishna Kant Pathak 

Abstract In this study, buckling analyses of two-dimensional steel frames are carried out considering various combinations of 3 bays and 3 stories, with and without braces under lateral and vertical loads separately. The main objective of the study is to investigate the effect of a particular bracing location on the overall buckling behavior of frames incorporating a single diagonal brace or an X (cross) brace in either of the bays of first story or in the other closed loops of the frame, individually. The effects are compared for bare frames, fully braced frames, one other bracing type and for the diagonal braces having the same slenderness as that of beams and columns. Such type of analysis is useful for the safe design of framed structures against buckling.

Keywords Frame buckling · Brace · Eigenmodes · Eigenvalues · Critical load

1 Introduction

The braced frames are used to provide strength and stability to the structures. Researches have been done to improve the buckling behavior of braced frames using various arrangements and techniques. Buckling is an event which does not depend on the strength of the structure. Under compressive loading, the slender members are prone to buckling. As long as the load is small, axial shortening of the member is observed and once the certain critical load (P_{cr}) is crossed, a sudden out-of-side ways bowing of the member occurs giving rise to large deformation [1]. The critical load, P_{cr} is the limiting load under which axial compression in an unbent configuration is possible. The transition from straight to bent configuration takes place because at the buckling load straight configuration ceases to be stable. So the buckling load marks the limit of stability. Stress and strains are assumed to obey hooks law; therefore the

Narayan (✉) · K. K. Pathak
Department of Civil Engineering, IIT (BHU), Varanasi 221005, India
e-mail: narayan.rs.civ17@itbhu.ac.in

K. K. Pathak
e-mail: kkpathak.civ@itbhu.ac.in

nonlinearity is purely geometrical [2]. Ascertaining the working of the structure by preventing buckling of its members need to be taken up very seriously in analysis and design.

Popov [3] using a graphical figure illustrated that major component of story drift in MRFs is majorly contributed by rotation of floor beams, and to achieve the desired drift limitation the size beam has to be increased. Therefore for functional reasons use of diagonal bracing becomes a more economical and safe option. If for moderate loads such braces behave in the elastic range, they provide an economical solution. Popov [4] suggested employing concentric braces when moment resisting frames (MRFs) cannot be designed sufficiently stiff economically for resisting wind forces. In the study, the main focus was on the importance of links used in eccentric braces compared to the influence of link length on the stiffness of braced frames. MRFs are found to have minimum stiffness, and concentrically braced frames (CBFs) are found to have maximum stiffness but as the behavior of CBFs is unreliable under cyclic loadings so eccentric braces with short links were appreciated. Rafael Sabelli [5] gave an equation of frame behavior based on statical relations to estimate brace deformation demand. Gengshu et al. [6] explained about the criteria for discriminating the weakly braced frame. Eghtesadi [7] selected 3, 6, 9, and 12 stories each having 4 bays wide and 2 corner bays braced. X, CBF, and EBF chevron and diagonal bracing types were considered for examining the weight of structure, top story displacement, and energy absorption. X-brace showed maximum energy absorption but this system is considered to have only one lateral force-resisting member in each span which implies that in comparison to other bracing systems it was found to have the lowest rigidity, so required stronger beams and columns which would result in heavy weight of structure. Whereas high energy absorption, less amount of steel, and lower total weight were found to be achieved by chevron CBF system. Amini et al. [8] considered multi-storied buildings using concentric X, V, and chevron braces for two bracing patterns. One pattern is throughout bracing of 2 central bays (*adjacent*) and the other is of 2 end corner bays (*non-adjacent*). Modeling was done using RAM-perform 3D software. For all braces, non-adjacent bays were found to have lower stiffness but higher strength in comparison to adjacent bays configuration. Choi et al. [9] reviewed the design requirements of beams and columns in braced frames, considering inverted V (chevron) braced and suggested to use bigger sized columns to prevent weak stories at lower stories in ordinary CBFs (OCBFs).

The subject matter of this article is the effect of bracing location on the buckling behavior of steel braced frames. The behavior is examined in terms of Pcr values obtained from numerical analysis using linear perturbation buckling analysis method which is based on Eigenvalue problem. Software Abaqus CAE 6.14 [10] has been used to model the frames and to obtain the Pcr values. The frames are subjected to compressive loads in vertical and horizontal (*lateral loading*) direction separately. To validate the method of numerical analysis, a bar with various end restraints was cross-verified with classical Euler critical buckling load results. The results were found to be very much in acceptance with classical method results. As this study is purely based on buckling behavior of braces and the draft NBC of India [11] emphasizes so much on braces and demanded some suggestions and comments, this

study can be considered as a suggestive report for better design and provisioning of braces.

2 Modeling and Methodology

2.1 Modeling

Rigid jointed 2D frames are considered having end supports fixed. All beams and columns are of length 3 m. The braces are concentric. Design of connections is not done here as they are considered as ideal rigidly connected joints. Steel is used as the material for construction of all the members of the frame. Elastic properties used are Young’s modulus, $E = 2e8 \text{ kN/m}^2$, and the Poisson’s ratio = 0.3, and the self-weight is neglected. Homogeneous sections are used with sectional properties as $E = 2e8 \text{ kN/m}^2$, Shear modulus, $G = 7.7e7 \text{ kN/m}^2$.

Firstly, to study the effect of location of brace on the buckling behavior of braced frames, 45 frames made from various combinations of 3 bays and 3 stories have been analyzed. A single diagonal brace (*oriented at 135° angle with x -axis*) or a single X brace in either of the bays of first story or in the upper closed loops/spaces of the frame at each bracing level (story designaton) has been placed individually at a particular location (bay number). For defining nomenclature to the bracing locations, they are numbered as shown in Fig. 1, where Br represents brace. To denote the number of bays and stories, abbreviations B_n, S_n are used (n is the varying number for various bays (B) and stories (S)), respectively. All other abbreviations are given in their context itself.

For comparison, fully braced frames using diagonal or X braces, braces having same slenderness as that of beams and columns and one other bracing type (chevron) have been considered, as shown in Fig. 2. Also, the combinations of single story with bays varying from 1 to 4 have been analyzed to access the best location of multiple braces and to get the best combination of inserting braces at particular locations.

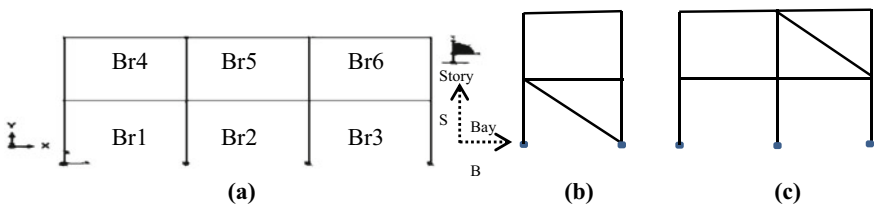


Fig. 1 a Numbering of bracings in rigid frame with fixed supports; b One bay-two stories frame (B1S2 with Br1 brace); c Two bays-two stories frames (B2S2 with Br3 brace)



Fig. 2 Types of braces used are, diagonal brace, cross (X) brace and chevron brace, from left to right

2.2 Methodology

The parameter of concern here is Critical load, P_{cr} under vertical and lateral loadings (from both sides). In linear perturbation method, a unit load is applied on selected nodes and based on them Eigenvalues that refer to critical load are obtained for various Eigen buckling modes. To get the required result, nearly 9 to 18 Eigenmodes were requested for various cases. The first positive Eigenvalue has been chosen to be the P_{cr} value for each frame case. As this is a comparative study, so the P_{cr} values that are obtained higher in comparison to other case are most likely to be obtained as higher in any other buckling analysis method also; so the linear perturbation method is expected to fulfill the purpose of this study. Abaqus software has been used for analyzing the frames considering two-node cubic beam element.

As it is known, strong-column weak-beam is ideal in the case of ductile behavior under the influence of seismic loading. It is also found that in the case of braced frames a strong beam is good for handling the unbalanced forces that come in presence after the post-buckling condition. But the inclusion of strong beam throughout the frame causes weak story problem in lower stories resulting in a brittle failure. To prevent other such design complexities in the present study, for all the members, circular cross-section has been considered for simplicity and ease of understanding. Radius of 0.05 m is used for all structural members including braces. Radius of 0.071 m is used for a comparison case of braces having slenderness equal to that of beams and columns. Concentrated vertical loads are provided at all the nodes connecting beams and columns. Concentric lateral loads are provided at open end corner nodes only (either side). The loadings are shown in Fig. 3 and also it is shown that the results of brace placed at 135° angle orientations can be followed for the corresponding bracing location having orientation 45° which is the mirror image of brace placed at 135° .

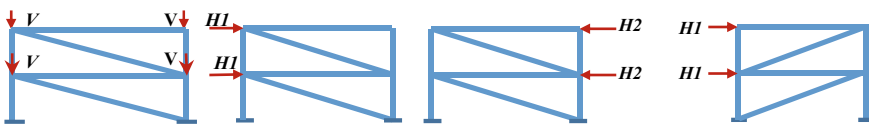


Fig. 3 Vertical force V , lateral force $H1$ and lateral force $H2$, from left to right, for B1S2 frame; lateral force $H1$ for 45° oriented brace corresponds to lateral force $H2$ for 135° oriented brace

3 Results and Discussion

3.1 Effect of Location of Brace on Pcr Value of Steel Frames

Single brace placed at a bracing location individually contribute to one frame case. Unit of the load is in kN. Pcr values $H1$ and $H2$ are lateral (*Horizontal*) loads, and V is vertical load as shown in Fig. 3. H is the lower value among $H1$ and $H2$.

Effect of location of brace introducing a single brace individually in the specific location or space as shown in Fig. 1 for the single storied frames with varying number of bays is given in terms of Pcr values in Table 1.

Effect of location of brace introducing a single brace individually in the specific location or space as shown in Fig. 1 for the two storied frames with varying number of bays is given in terms of Pcr values in Table 2.

Effect of location of brace introducing a single brace individually in the specific location or space as shown in Fig. 1 for the three storied frames with varying number of bays is given in terms of Pcr values in Table 3.

Remark for All Considered Cases of Frames Singly Braced by Diagonal Brace

With the increase in the number of bays for the same number of stories, both vertical and horizontal critical loads increase except for the first story of no brace condition where horizontal Pcr value decreases. With the increase in the number of stories for the same number of bays both horizontal and vertical critical loads get reduced (*i.e.*,

Table 1 Bucking loads (kN) for the single storied frames with a single brace individually

Brace no	Load direction	Diagonal brace			Cross brace		
		Number of bays, B			Number of bays, B		
		1	2	3	1	2	3
No brace	H	3340.130	3250.880	2961.450	3340.130	3250.880	2961.450
	V	804.617	829.638	854.520	804.617	829.638	854.520
Br1	$H1$	1323.730	1329.790	1333.200	5989.060	6172.900	6177.220
	$H2$	2445.050	2115.050	1994.900	5989.060	2665.640	2174.980
	H	1323.730	1329.790	1333.200	5989.060	2665.640	2174.980
	V	2936.390	2940.360	2941.470	4514.540	3049.600	2960.880
Br2	$H1$	-over-	1343.480	1349.150	-over-	2665.640	2668.440
	$H2$		2610.510	2166.730		6172.900	2668.440
	H		1343.480	1349.150		2665.640	2668.440
	V		2937.500	2940.260		3049.600	3044.950
Br3	$H1$		-over-	1350.530		-over-	2174.980
	$H2$			2616.270			6177.220
	H			1350.530			2174.980
	V			2938.410			2960.880

Table 2 Buckling load (kN) for two storied frames with a single brace individually

Brace no	Load direction	Diagonal brace			Cross brace		
		Number of bays, <i>B</i>			Number of bays, <i>B</i>		
		1	2	3	1	2	3
No brace	<i>H</i>	1386.560	2469.360	2614.520	1386.560	2469.360	2614.520
	<i>V</i>	378.228	401.593	415.398	378.228	401.593	415.398
Br1	<i>H1</i>	590.560	607.401	616.721	1856.080	3059.270	2873.010
	<i>H2</i>	1128.110	1270.990	1295.470	1855.760	2165.270	1757.030
	<i>H</i>	590.560	607.401	616.721	1855.760	2165.270	1757.030
	<i>V</i>	671.486	707.964	733.934	706.937	722.725	745.707
Br2	<i>H1</i>	793.410	613.084	623.578	1612.630	2165.290	2321.350
	<i>H2</i>	1199.150	1641.510	1638.350	1612.630	3059.300	2321.350
	<i>H</i>	793.410	613.084	623.578	1612.630	2165.290	2321.350
	<i>V</i>	445.769	702.163	729.906	470.687	722.725	738.889
Br3	<i>H1</i>	-over-	854.428	620.070	-over-	2057.280	1757.030
	<i>H2</i>		1396.420	1634.430		1931.500	2873.010
	<i>H</i>		854.428	620.070		1931.500	1757.030
	<i>V</i>		448.382	729.789		463.202	745.707
Br4	<i>H1</i>		849.064	869.440		1931.500	1978.630
	<i>H2</i>		1407.010	1486.180		2057.280	1859.540
	<i>H</i>		849.064	869.440		1931.500	1859.540
	<i>V</i>		454.538	455.513		463.202	466.821
Br5	<i>H1</i>		-over-	894.403		-over-	2293.060
	<i>H2</i>			1599.900			2293.060
	<i>H</i>			894.403			2293.060
	<i>V</i>			455.732			460.111
Br6	<i>H1</i>			874.188			1859.540
	<i>H2</i>			1335.780			1978.630
	<i>H</i>			874.188			1859.540
	<i>V</i>			459.312			466.821

increase of stories is detrimental). *H1* value is less than *H2* value as there is no tension brace available against *H1* loading. Considering bracing condition alone, mostly the braces with minimum vertical Pcr value give maximum horizontal Pcr value vice-versa. With the rise in the locations of brace in the same configuration of frame, horizontal Pcr value increases and vertical Pcr value decreases. Against the buckling due to the vertical load, braces at the bottom story corner bay are preferable. Bracing at top stories has more horizontal Pcr value but it is not enough to resist buckling in comparison to bare frame. For horizontal load single diagonal brace has been found to be detrimental, whereas for the vertical load it is quite beneficial.

Table 3 Critical load (kN) for three storied frames with a single brace individually

Brace no	Load direction	Diagonal brace			Cross brace		
		Number of bays, <i>B</i>			Number of bays, <i>B</i>		
		1	2	3	1	2	3
No brace	<i>H</i>	657.001	1256.340	1755.950	657.001	1256.340	1755.950
	<i>V</i>	233.663	252.234	263.112	233.663	252.234	263.112
Br1	<i>H1</i>	375.212	388.554	396.061	805.894	1880.280	1837.530
	<i>H2</i>	566.004	719.650	778.346	805.894	1229.470	1309.370
	<i>H</i>	375.212	388.554	396.061	805.894	1229.470	1309.370
	<i>V</i>	327.279	351.102	364.405	340.416	356.969	369.235
Br2	<i>H1</i>	397.025	391.151	399.457	750.600	1229.470	1902.580
	<i>H2</i>	556.975	1060.780	1115.200	750.600	1880.280	1902.580
	<i>H</i>	397.025	391.151	399.457	750.600	1229.470	1902.580
	<i>V</i>	295.722	348.468	362.627	313.214	356.969	366.295
Br3	<i>H1</i>	649.610	435.625	398.490	664.898	1102.230	1309.370
	<i>H2</i>	649.993	677.719	1039.400	664.898	925.805	1837.530
	<i>H</i>	649.610	435.625	398.490	664.898	925.805	1309.370
	<i>V</i>	241.458	297.813	362.579	244.268	308.122	369.235
Br4	<i>H1</i>	-over-	427.760	445.735	-over-	925.805	1071.510
	<i>H2</i>		789.960	738.024		1102.230	1014.030
	<i>H</i>		427.760	445.735		925.805	1014.030
	<i>V</i>		301.832	302.682		308.122	310.531
Br5	<i>H1</i>		790.840	455.639		135.546	1235.900
	<i>H2</i>		920.392	901.090		951.571	1236.050
	<i>H</i>		790.840	455.639		951.571	1235.900
	<i>V</i>		256.781	302.804		258.133	305.973
Br6	<i>H1</i>		779.729	442.009		951.571	1014.030
	<i>H2</i>		1169.020	754.851		135.546	1071.510
	<i>H</i>		779.729	442.009		951.571	1014.030
	<i>V</i>		256.955	305.236		258.133	310.531
Br7	<i>H1</i>		-over-	814.825		-over-	1422.740
	<i>H2</i>			1067.530			1118.830
	<i>H</i>			814.825			1118.830
	<i>V</i>			266.587			267.458
Br8	<i>H1</i>			839.150			1610.550
	<i>H2</i>			1384.620			1610.550
	<i>H</i>			839.150			1610.550
	<i>V</i>			266.652			267.363

(continued)

Table 3 (continued)

Brace no	Load direction	Diagonal brace			Cross brace		
		Number of bays, <i>B</i>			Number of bays, <i>B</i>		
		1	2	3	1	2	3
Br9	<i>H1</i>			815.929			1118.830
	<i>H2</i>			1164.520			1422.740
	<i>H</i>			815.929			1118.830
	<i>V</i>			266.688			267.458

Remark for all Considered Cases of Frames Singly Braced by X Brace

The behavior of *X* brace is very much different from diagonal brace, because of the symmetry of the brace. With increase in the number of bays for the same number of stories, both vertical and horizontal critical loads increase. With the increase in the number of stories for the same number of bays both horizontal and vertical critical loads get reduced. In comparison to diagonal brace, cross braces have higher resistance to buckling under both vertical and horizontal loads. Here, braces at bottom stories are more beneficial.

Remark for all Considered Singly Braced (using either diagonal or the X brace) Frames

For in-plane loadings, any kind of single brace in a frame individually is not enough for restraining the buckling due to lateral loading. What to speak of increasing the buckling resistance, under lateral load, in some cases it is detrimental for the stability of the structure as it degrades the buckling resistance of the frame. If a single ordinary brace is introduced in the frames in any of the configurations of bay and stories, it is for sure that the stability under lateral load is either going to reduce or not going to increase substantially, except for B1S1 configuration (*gets fully braced*), where *X* brace is found beneficial for a considered profile, which has more buckling resistance than that of the bare frame. If talking about the strength gain against buckling due to axial (*vertical*) load even a single brace provides substantially high restraint against buckling. The braces having cross-section same as that of beams and columns resulting into slenderness ratio more than that of beam and columns make them more prone to buckle early. A single brace does not resist the buckling substantially and also because of stiffness related issues, in general practice, a bay braced throughout its stories.

Comparison Between the Fully Braced Cases and the Cases of Frame Braced with One Single Brace, for Each Frame Configuration

In tables, *S1*, *S2*, *S3* refer to the number of stories, and values under them are for the cases of singly braced frames, giving maximum *Pcr* value; ‘*Nbr*’ represents the bare frame cases and ‘*Full*’ represents the fully braced configurations.

Story-Wise Variation for a Particular Number of Bays [B1 (*S1*, *S2*, *S3*); B2 (*S1*, *S2*, *S3*); B3 (*S1*, *S2*, *S3*)]

Considering diagonal brace as shown in Table 4, for vertical loading, in all cases fully braced frame is more stable than singly braced frame and singly braced is more stable than bare frame, but under lateral loading, in case of single bay with increase in number of stories, fully braced frame shows less stability in comparison to best of singly braced frame cases, both being less than bare frame condition due to premature buckling. For two and three bays the fully braced frame has higher stability than singly braced frame (*except for B2S3 configuration*) both having stability less than bare frame condition.

Considering X brace as shown in Table 5, for B1 with stories varying from 1 to 3, it is found that under lateral loading, the best case of singly braced frame gives buckling resistance nearly similar to that of a fully braced case, that is more than bare frame case. For two and three bays with stories varying from 1 to 3, fully braced frame is more stable in comparison to singly braced and the bare frame but the frame singly braced shows stability even less than the bare frame (*except for B3S3 configuration*) because of premature buckling. For vertical loading, in all cases fully braced frame is more stable than the singly braced frame and singly braced is more stable than the bare frame. Similarly, bay-wise variation for a particular number of stories can be found from Tables 1, 2, and 3.

4 Diagonal Braces Having Same Slenderness as that of Beam and Column

The P_{cr} values of frames using diagonal brace having the same cross-section as that of beams and columns (D) are compared with the P_{cr} values of frames using brace having same slenderness as that of beams and columns, (D_{SS}), as given in Table 6.

Considering the fully braced frame, D_{SS} frames have more stability against both the vertical and lateral loadings in comparison to D frames. Under the lateral loading both the cases have less stability in comparison to bare frame condition and under vertical load both have higher stability in comparison to bare frame condition. For considering per bracing level, using a single brace in B1S3 configuration, the numerical analysis results are given in Table 7. For these cases, both single braced D frames and single braced D_{SS} frames have nearly equal stability against vertical loading. With single brace, against lateral loading, D_{SS} has a higher value at lower stories but at the third story D frame configuration has more stability than D_{SS} frame.

Except for the first story, for other considered cases, column buckles first in case of D_{SS} whereas brace buckles in case of D . To access the effects of braces per bracing level B1S3 configuration frame is used.

Table 4 Maximum Per for single location braced and fully braced frames using diagonal brace

Lateral loading (kN)											
H	S1	S2	S3	Nbr S1	Nbr S2	Nbr S3	Full S1	Full S2	Full S3		
B1	1323.730	793.410	649.610	3340.130	1386.560	657.001	1323.730	699.189	610.302		
B2	1343.480	854.428	790.840	3250.880	2469.360	1256.340	2309.540	1267.030	774.168		
B3	1350.530	894.403	839.150	2961.450	2614.520	1755.950	2591.670	2034.270	1162.320		
Vertical loading (kN)											
B1	2936.390	671.486	327.279	804.617	378.228	233.663	2936.390	1618.850	1037.860		
B2	2940.360	707.964	351.102	829.638	401.593	252.234	3003.320	1664.850	1069.990		
B3	2941.470	733.934	364.405	854.520	415.398	263.112	3010.350	1670.450	1076.050		

Table 5 Maximum Per for single location braced and fully braced frames using X brace

Lateral loading (kN)											
H	S1	S2	S3	Nbr S1	Nbr S2	Nbr S3	Full S1	Full S2	Full S3		
B1	5989.060	1855.760	805.894	3340.130	1386.560	657.001	5989.060	1968.540	857.207		
B2	2665.640	2165.290	1229.470	3250.880	2469.360	1256.340	4953.470	4731.260	1990.910		
B3	2668.440	2321.350	1902.580	2961.450	2614.520	1755.950	4744.430	4449.750	3541.930		
Vertical loading (kN)											
B1	4514.540	706.937	340.416	804.617	378.228	233.663	4514.540	2393.950	1552.600		
B2	3049.600	722.725	356.969	829.638	401.593	252.234	4468.670	2541.160	1662.490		
B3	3044.950	745.707	369.235	854.520	415.398	263.112	4396.480	2540.050	1699.740		

Table 6 Comparison with diagonal having same slenderness as that of beams and columns (*Full bracing*)

Stories	D_SS		No brace		D	
	H (kN)	V (kN)	H (kN)	V (kN)	H (kN)	V (kN)
B1S1	2773.330	3049.350	3340.130	804.617	1323.730	2936.390
B1S2	1283.320	1865.070	1386.560	378.228	699.189	1618.850
B1S3	640.445	1227.780	657.001	233.663	610.302	1037.860

Table 7 For B1S3, per brace Pcr (kN) for single bracing per story

Braces	D_SS		D	
	H	V	H	V
Br1	609.901	334.765	375.212	327.279
Br2	530.273	303.784	397.025	295.722
Br3	547.660	242.873	649.610	241.458

4.1 Comparison of Considered Braced Frames with Braced Chevron (Ch) Brace

The results of Pcr values obtained using fully braced diagonal and X braced are compared with chevron brace for one to five stories, as given in Table 8.

Evaluating Story-wise, for both the load types the Pcr value decreases with increase in the number of stories but the rate of decrement varies in both the conditions. For vertical load all braced frames have nearly similar patterns of reduction in Pcr. In the case of lateral loading after fifth story, the effect of bracing is negligible for the frames braced with the braces having the profile as that of columns and beams. Story-wise variation of fully braced frames under lateral loading is shown in Fig. 4.

For vertical loading, the buckling load capacities are found to be more than bare frame conditions. Considering X Brace, for lateral loading there is an abrupt reduction

Table 8 Comparison of Pcr (kN) with fully Braced Chevron up to five stories

Bracing	Loading direction	B1S1	B1S2	B1S3	B1S4	B1S5
No brace	H	3340.130	1386.560	657.001	320.815	231.757
	V	804.617	378.228	233.663	164.549	125.409
Diagonal	H	1323.730	699.189	610.302	336.254	223.053
	V	2936.390	1618.850	1037.860	744.676	541.909
X brace	H	5989.060	1968.540	857.207	475.604	300.986
	V	4514.540	2393.950	1552.600	1128.370	894.775
Chevron	H	2812.400	1419.690	941.974	572.641	346.046
	V	3399.200	1818.780	1181.290	861.855	673.011

Fig. 4 Pcr values under lateral loading

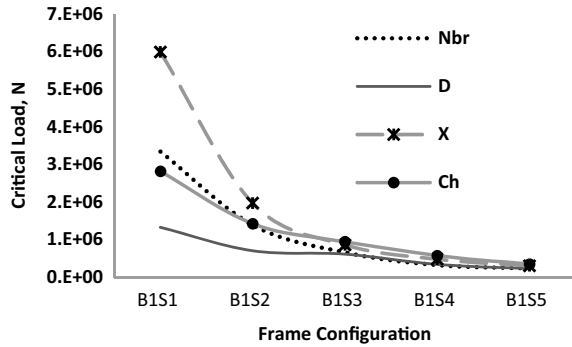
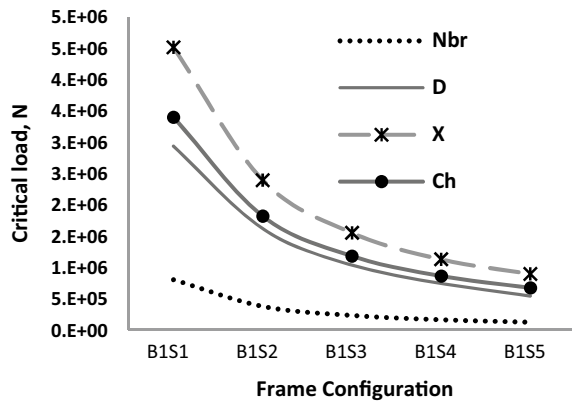


Fig. 5 Pcr values under vertical loading



in buckling load capacity of X braced frame with respect to other bracing conditions but for vertical loading, it is best. Story-wise variation of fully braced frames under vertical loading is shown in Fig. 5. Being unsymmetrical and more slender, diagonal brace could buckle at lesser lateral loads. Considering Chevron brace, for both lateral and vertical loadings rate of decrement is small; and under lateral loading up to two stories, the value of Pcr is less than that of X brace and bare frame but for the higher stories (*except B1S5*), Pcr values are higher than other bracing types. A single story alone does not give complete information about the stability characteristics of a particular brace.

Evaluating Bay-wise (*Single story with a varying number of bays*), under lateral loads, among all considered types of braces, diagonal brace has lowest Pcr values, chevron has Pcr value less than bare frame for first story and has higher Pcr than X brace (*has Pcr values higher than bare frame for all cases*) for three and four stories. Under vertical load, all braces have Pcr higher than bare frame and among them, X brace has maximum Pcr for all considered cases. The comparison of Pcr values using various braces is given in Table 9.

Table 9 Pcr (kN) for fully braced frames configuring single story and multiple bays

Bays	Load	X	Ch	D	Nbr
B4S1	H	4705.860	5809.680	2582.660	2670.500
	V	4357.000	3450.050	3010.970	867.350
B3S1	H	4744.430	5551.050	2591.670	2961.450
	V	4396.480	3449.750	3010.350	854.520
B2S1	H	4953.470	4756.960	2309.540	3250.880
	V	4468.670	3445.790	3003.320	829.638
B1S1	H	5989.060	2812.400	1323.730	3340.130
	V	4514.540	3399.200	2936.390	804.617

To find the best bay-wise arrangement of braces in terms of Pcrs (kN), from various arrangements for the same number of braces in a particular frame, the best arrangements are listed here in Table 10.

For B4S1 and B3S1 configurations, for all considered bracing types, the Pcr values of the arrangements having one brace less than the full bracing have been found to be approximately equal to that of fully braced cases under vertical loads; and for the same arrangement having X braces, Pcr values higher than its fully braced case under both vertical and lateral loads are obtained. For B4S1 configuration, under lateral loading, X brace has maximum Pcr value by bracing just two end corner bays. So, it is suggested to have braces at both corners bays on either side of the frame. For B2S1 configuration, fully braced cases have higher Pcr value; but for B1S1 configuration, different behavior in comparison to more number of bays has been observed as for the same cross-sectional area, only X brace is found to be effective in vertical and lateral/horizontal loading both; whereas chevron and diagonal brace are found to work better than bare frame condition only under vertical load. It can be concluded

Table 10 Best arrangements giving higher Pcr (location-wise bracing, 1 means brace and 0 means no brace)

B4S1 3 Brace	X brace 1101	Chevron 1101	Diagonal 1101	Diagonal 1110
H	4817.110	4820.230	2593.350	2154.070
V	4418.790	3442.680	3005.480	2955.890
B4S1 2 Brace	X brace 1001	Chevron 1001	Diagonal 1001	Diagonal 0110
H	5285.640	4101.420	2152.800	2033.150
V	3416.970	3357.960	2954.430	3003.400
B3S1 2 Brace	X brace 101	Chevron 101	Diagonal 101	Diagonal 110
H	5117.640	4356.880	2147.890	2158.130
V	4479.790	3438.020	3003.420	2954.770

that on the basis of single story results, the character of a brace cannot be decided for higher stories and more number of bays.

4.2 H/V Ratio

The ratio of Pcr value under lateral loading to the corresponding vertical load value for same braced frame configuration is denoted as H/V ratio. It is the ratio which indicates uniformity in increase or decrease of either loading in comparison of others with an increase in the number of bays or stories. When compared with bare frame case ratios, it indicates the change in the behavior of the frame under various loadings on introducing braces. In simple words, it is a representative of optimized increase in stability of frame against both lateral and vertical loading on introducing braces. This ratio is useful for comparing the optimized increase in stability for the type of braces having very similar Pcr values provided both provide stability more than bare frame case under both lateral and vertical loading in all required cases. Some researchers consider only single story to estimate the performance of brace, the behavior of which may not be followed for higher stories or for the more number of bays. Comparison of the H/V ratio of fully braced frames using various braces is given in Table 11.

For Chevron, except for the first story, all values of Pcr under lateral and vertical loadings are higher than bare frames. So if considering stories more than one, it can be seen from Table 11, chevron has less deviation in values of H/V ratio so we can say that it provides optimized stability with increasing stories.

The comparison of H/V ratio for fully braced frames and bare frame are given in Table 12. The table has two parts first one showing bay-wise variation, with three stories and varying bays, where it can be seen that with an increase in the number of bays H/V ratio increases. And the second part shows story-wise variation, with three bays and varying stories where for symmetric braces like X brace and chevron the H/V ratio increases with an increase in the number of stories but for unsymmetric bracing like diagonal brace it can be inconsistent.

Including one more kind of ratio that is the ratio of Pcr values under lateral and vertical loadings of the braced frame to the Pcr values of their respective bare frame. Let, $H_r = H/H_{nbr}$ be the ratio of Pcr value under lateral load and $V_r = V/V_{nbr}$ be the ratio of Pcr values under vertical loading. H_r ratio and V_r ratios are independent of H/V ratio. Both H_r and V_r ratios are higher for X brace (Table 13).

Table 11 Comparison of H/V ratio for fully braced frames

Brace	B1S1	B1S2	B1S3	B1S4	B1S5
No brace	4.15	3.67	2.81	1.95	1.85
Diagonal	0.45	0.43	0.59	0.45	0.41
X brace	1.33	0.82	0.55	0.42	0.34
Chevron	0.83	0.78	0.80	0.66	0.51

Table 12 H/V ratio comparison for 3 stories with varying number of bays and for 3 bays with varying number of stories ('Full' refers to the bracing at all stories in each bay)

Bays	Diagonal	X brace	No brace	Stories	Diagonal	X brace	No brace
Full	H/V	H/V	H/V	Full	H/V	H/V	H/V
B1S3	0.59	0.55	2.81	B3S1	0.86	1.08	3.47
B2S3	0.72	1.20	4.98	B3S2	1.22	1.75	6.29
B3S3	1.08	2.08	6.67	B3S3	1.08	2.08	6.67

Table 13 Hr and Vr ratio comparison for 3 stories with varying number of bays and for 3 bays with varying number of stories

Bays	Diagonal		X brace		Stories	Diagonal		X brace		No brace
Full	Hr	Vr	Hr	Vr	Full	Hr	Vr	Hr	Vr	
B1S3	0.93	4.44	1.30	6.64	B3S1	0.88	3.52	1.60	5.14	1
B2S3	0.62	4.24	1.58	6.59	B3S3	0.78	4.02	1.70	6.11	1
B3S3	0.66	4.09	2.02	6.46	B3S3	0.66	4.09	2.02	6.46	1

5 Conclusion

All the considered braces have been found to improve stability against vertical loading. In most of the cases, a symmetric brace with a symmetric arrangement of bracing is expected to work well against both vertical and lateral load and avoids premature buckling to some extent. Fully braced X braces have been found to increase stability under both vertical and horizontal loads. For diagonal braced frame, under lateral load, in most of the cases the brace buckles prematurely. When the load is applied in the lateral direction, and the diagonal brace is in tension then also in many cases the overall stability of structure has been found to be less than that of bare frame due to premature buckling of beam or column.

It has been observed that the lateral buckling resistance is mostly influenced by very few braces at few lower stories; but here, for the diagonal braces (*having the same cross-section as that of beams and columns*), the braces have been found to buckle prematurely at very low Pcr value, when placed in lower stories. Against lateral buckling, the inclusion of tension brace along with compression brace provides stability to the structure. For vertical load, in general, the bottom braces are more significant in resisting buckling and also reducing brace size at higher stories is not expected to influence the overall stability of structure much; but for the substantial buckling resistance increase and for no significant change in stiffness of stories, bracing every story is significant. As the stories increase, the effect of Pcr values reduces drastically for X braced frames, but in the case of chevron braced, the reduction is minor.

For the frames made from the various combinations of 3 bays and 3 stories, considering the effect of a particular bracing location under applied in-plane loadings, except some cases like B1S1 configuration frame braced (*which is a fully braced*

configuration) using single X brace where substantial increase in buckling load value is observed; for most of the cases, a single brace in the frame is not enough for restraining the buckling due to lateral loading. It has been found that when the slenderness ratio equal to beam and column is provided to the diagonal brace, even then the stability against lateral loading doesn't increase significantly, for both, the singly braced frame having a maximum value at any particular bracing level and for the fully braced frame (for the considered BIS3 frame configuration).

Many researchers suggest bracing central bays portion for both strength and stability against lateral and transverse loading. In general, bracing central bay throughout all stories gives better results in comparison to others for the multi-storied single bay braced frame but when it comes to bracing more than one bay, central bay bracing is not always better. In this study, it has been found that for more than one bay bracing, bracing at least both side's corner bays gives higher buckling load capacity and is found to be the crucial elements for increasing the buckling load resistance of frame. In the arrangements not having corners braces, the beams of un-braced end corner bay tend to buckle at a low buckling load. Regarding stability, it is not necessary that more braces will resist more buckling load for every bracing type and configuration. Story-wise, it is supposed to brace every story to prevent stiffness related issues but to brace throughout bay-wise is not a compulsion. So the best bracing arrangement found after analysis should be selected. For bay-wise bracing, in some cases it has been found that even bracing half the bays provided nearly equal or sometimes more buckling resistance in comparison to full bracing.

As most of the researchers use single story frame to ascertain the buckling resistance of brace type and based on that they conclude the competent behavior of that brace. But it is not necessary that the brace providing better resistance against buckling for low-rise structure would show the same pattern of resistance for high rise structures also. A particular type of brace can be more effective at a particular location in the structure but as a combined effect of whole braced frame its effect may be significantly changed. In a frame, the effect of the particular type of brace in restraining buckling in lower stories may be lesser or higher in comparison to the brace being in upper stories. So concluding based on single storied frame might not show the actual behavior of a braced frame as it might give misleading results. According to this study, it is suggested to go for at least 3 variations of bays and 3 variations of story levels as low, medium, and higher stories to approximately access the characteristic behavior of a bracing type.

References

1. Chajes A (1974) Principles of structural stability theory. Prentice-Hall Civil Engineering and Engineering Mechanics Series, New Jersey
2. Brush DO, Almroth BO (1975) Buckling of bars, plates, and shells, vol 6. McGraw-Hill, New York
3. Popov EP (1983) Recent research on eccentrically braced frames. Eng Struct 5:3-9

4. Popov EP, Kasai K, Engelhardt MD (1987) Advances in design of eccentrically braced frames. *Bull New Zealand Nat Soc Earthq Eng* 20(1)
5. Sabelli R (2001) Research on improving the design and analysis of earthquake-resistant steel-braced frames. EERI, NEHRP Professional Fellowship in Earthquake Hazard Reduction, Final Report, Oakland
6. Gengshu T, Zuyuan S (2001) The stability of weakly braced frames. *Adv Struct Eng*, Sage J 4(4)
7. Eghtesadi S, Nourzadeh D, Bargi K (2011) Comparative study on different types of bracing systems in steel structures. World Academy of Science, Engineering and Technology
8. Amini A, Majd M, Hosseini M (2012) A study on the effect of bracing arrangement in the seismic behavior buildings with various concentric bracings by nonlinear static and dynamic analyses. 15th WCEE, Lisbon, Portugal
9. Choi K-S, Park J-Y, Kim H-J (2017) Numerical investigation on design requirements for steel ordinary braced frames. *Eng Struct* 137:296–309. <https://doi.org/10.1016/j.engstruct.2017.01.066>
10. Abaqus V (2014) Abaqus 6.14 Documentation. Abaqus User's Manual
11. BIS (2015) Draft National Building Code of India: Part 6 Structural Design, Section 6 Steel, Third Revision of SP7 (Part 6/Section 6), CED 46 (8041) WC, New Delhi

A Study on Moment–Curvature Relationships for REINFORCED CONCRETE BEAMS with Varying Fire Loading Conditions



Ankit Borgohain and Sriman Kumar Bhattacharyya

Abstract In this paper, a numerical study by three-dimensional modeling is done for reinforced concrete beam exposed to fire conditions with various boundary conditions. Both geometric and material properties are taken into account in this formulation because of the changes in material properties and the large variations experienced in fire. The three stages associated with the numerical procedure for evaluating fire resistance of RC beams, namely fire temperature calculation, thermal analysis, and strength analysis are modeled using a finite element (FE) model. The FE model is prepared in ABAQUS software to study the response of an RCC beam under fire during loading conditions. The RCC beams are analyzed for different end conditions and fire loading surfaces. Initially, it is kept at 25 °C. Then the uniform loading of one-third of the compressive strength of concrete is applied as a pressure loading in the beam (3D solid element). The other faces of RCC beam have temperature boundary conditions. The temperature boundary condition is governed by temperature–time curve as per ASTM E119. The moment–curvature (M–k) relationships are developed for the beam at few critical positions of the RCC beam for various end conditions as well as temperature boundary conditions. These M–k relationships may be used to carry out the strength analysis of the beam member and draw significant conclusions.

Keywords M–k relationships · Fire temperature calculation · Thermal analysis

A. Borgohain (✉)

UG student, Department of Civil Engineering, NIT Silchar, Silchar 788010, India

e-mail: ankitjeesu@gmail.com

S. K. Bhattacharyya

Professor, Department of Civil Engineering, IIT Kharagpur, Kharagpur, West Bengal 721302, India

1 Introduction

Fire safety of structures has been of tremendous interest in the last few decades particularly after the September 11 attacks on Twin Towers, New York in 2001. This has led to varied research in the field of evaluation of the response of buildings and other structural systems under fire. Fire is one of the most severe risks to buildings and structures. A limited range of relevant research has been reported previously, especially for high-performance concrete. In this paper, a numerical study by three-dimensional modeling is developed for reinforced concrete beam exposed to fire conditions. Fire is one of the most severe design situations as it not only affects the strength of concrete but also the structural stiffness and stability. A reinforced concrete beam, compared to other structural members, has most often to cope with vertical forces and bending moments. In addition, the use of high-strength concrete (HSC) is becoming more popular due to the improvements in structural performance such as higher strength and durability that it can provide compared to conventional Normal Strength Concrete (NSC). This paper presents the development of a computer model for predicting the fire behavior of RC beams under realistic fire loading scenarios. The model is based on a macroscopic finite element approach and a series of moment–curvature relationships for tracing the response of the beam.

2 Literature Review

Kodur et al. [1] prepared batches of concrete with NSC, HSC (siliceous aggregate), HSC (carbonaceous aggregate), HSC (steel reinforcement), HSC (polypropylene), and found that deformation in beams is due to three factors, namely load, thermal expansion, and creep. NSC has a higher deformation rate than HSC due to the fact that HSC has higher young's modulus. Carbonate aggregate has less spalling than siliceous aggregates due to its higher specific heat value.

Lau et al. [2] studied concrete after being subjected to different elevated heating temperatures, ranging between 105 and 1200 °C. The compressive strength, flexural strength, elastic modulus, and porosity of concrete reinforced with 1% steel fiber (SFRC) and changes of color to the heated concrete, etc., were studied. For maximum exposure temperatures below 400 °C, the loss in compressive strength was relatively small. Significant reductions in compressive strength are observed when the temperature exceeds 400 °C. When steel fibers are incorporated at 1%, an improvement of fire resistance and crack development was observed.

Chung [3] developed a finite-difference model that simulates coupled heat and mass transport phenomena in reinforced concrete structures exposed to rapid heating conditions such as fires. A mathematical and computational model for simulating the multidimensional, thermo-hydrological response of reinforced concrete structural elements is developed and used to study the effects of steel reinforcement on

thermodynamic state variables. The effects of steel reinforcement on heat and mass transfer in the surface region of an R/C beam are found.

3 Experimental Program

A reinforced concrete beam of 3-m length and cross-sectional area 250 mm × 350 mm used for the study. An attempt is made to compute the moment versus curvature relationship at various locations of the beam when the fire loading is applied in various faces of the beam. In the present study, a roller–pinned support condition is considered and is subjected to a constant pressure load of 1.333E7 N/m².

The beam is constrained by the boundary conditions applied at both the ends: one end hinged and another end roller having axial DOF. The beam is exposed to ASTM E119 standard fire for different exposure times at different faces. M40 grade of concrete and Fe 415 grade of steel have been used and geometric parameters of the considered beam are described in given in Table 1. The beam instances are constrained as embedded in the concrete solid instance.

3.1 Reinforced Concrete Beam Model

For the numerical analysis, on three faces of the referred RCC beam, model temperature boundary conditions are applied. Investigations are done for the temperature, stress, strain, curvature distribution pattern as field output, and at specific points as history output to characterize the beam exposed to fire. The number of elements created were (a) Concrete beam block 264 elements and (b) Longitudinal reinforcement bar 33 elements. The concrete beam block used the coupled temperature–displacement elements 8-node trilinear displacement and temperature, reduced

Table 1 Geometric parameter of RCC beam

Beam length (mm)	3000
Concrete cross section (mm ²)	350 × 250
Reinforcement diameter (mm)	20
Percentage reinforcement	1.795%
Transverse reinforcement (mm)	12 nos. of 2-legged 8 mm dia. @ 250 mm c/c
Concrete cover (mm)	40
Support conditions	Roller–pinned
Fire exposure method	ASTM E119 Standard fire
Exposure time in hours	0.5, 1, 2, 3, 3.5

integration with hourglass control. The truss elements used as the longitudinal reinforcements and the stirrups are truss elements: three-dimensional, 2-node temperature–displacement truss element. The central element was a beam linear element in space (B31). One side of the beam is fixed by selecting the surfaces of the B31 elements and applying zero translational components in three directions.

The opposite face in the other support is also constrained in the global Y and global Z directions.

3.2 Thermal Conductivity

The thermal conductivity for siliceous concrete is a function of temperature and is expressed by equation (ENV 1992-1-2, 1995). The upper limit of thermal conductivity is given as follows:

$$\lambda_c = 2 - 0.2451(\theta/100) + 0.0107(\theta/100)^2 \text{ W/mK for } 20^\circ\text{C} \leq \theta \leq 1200^\circ\text{C}.$$

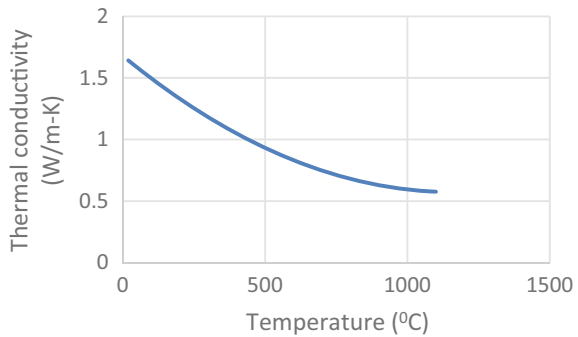
The lower limit of thermal conductivity is given as follows:

$$\lambda_c = 1.36 - 0.136(\theta/100) + 0.0057(\theta/100)^2 \text{ W/mK for } 20^\circ\text{C} \leq \theta \leq 1200^\circ\text{C}.$$

where λ_c is thermal conductivity in (W/m–K),
 θ is the concrete temperature in (°C).

The thermal conductivity versus temperature curve is presented in Fig. 1.

Fig. 1 Thermal conductivity as a function of temperature (ENV 1992-1-2, 1995)



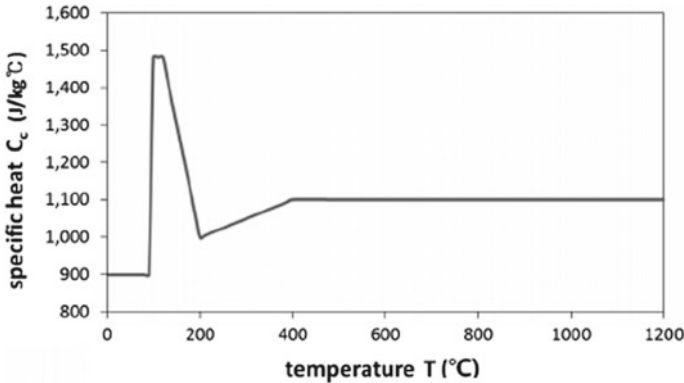


Fig. 2 Specific heat as a function of temperature for ordinary siliceous concrete (ENV 1992-1-2, 1995)

3.3 Specific Heat

The specific heat is a function of temperature and according to the Eurocode, it is valid to both siliceous and calcareous concrete (ENV 1992-1-2, 1995). The specific heat versus temperature curve is presented in Fig. 2.

3.4 Thermal Properties of Steel

Steel is considered an isotropic material in temperature calculations and its thermal properties could be described by three different material properties: thermal conductivity, specific heat, and thermal expansion coefficient, and respective graphs are presented in Figs. 3, 4, and 5.

Fig. 3 Thermal conductivity as a function of temperature for steel (ENV 1993-1-2, 1995)

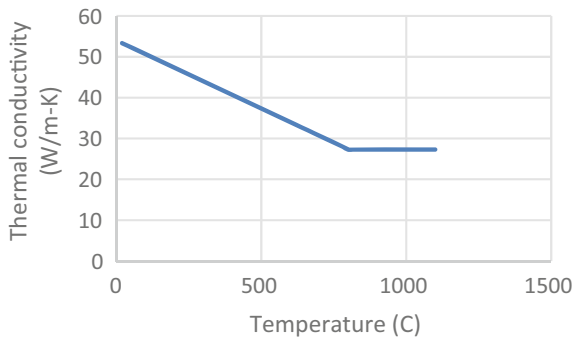


Fig. 4 Specific heat as a function of temperature for steel (ENV 1993-1-2, 1995)

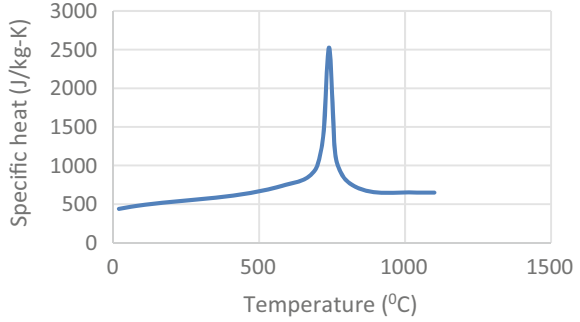
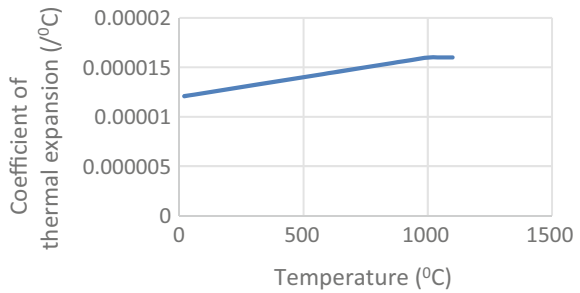


Fig. 5 Thermal expansion coefficient versus temperature



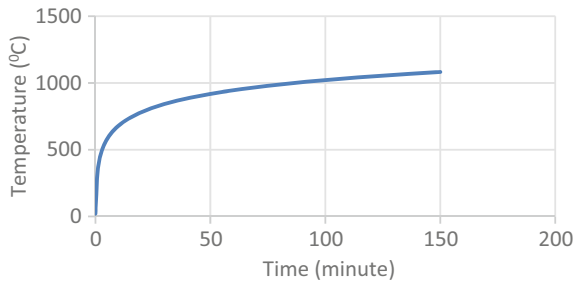
Specific heat of steel is a function of temperature and expressed by Fig. 4 given below(ENV 1993-1-2, 1995).

The density of steel and ordinary siliceous concretes is considered a constant value 7850 kg/m³ and 2400 kg/m³, respectively.

3.5 Fire Exposure Methods

In this analysis, ASTM E119 Standard fire method is considered (Fig. 6).

Fig. 6 Temperature–time curve for the standard fire (ASTM E119, 2007)



The temperature–time relationship on the boundary member is defined by the equation.

$$T_f = T_0 + 750(1 - \exp(-3.79553t_h^{1/2})) + 170.41t_h^{1/2}$$

where

t_h , time (h);

T_0 , initial temperature ($^{\circ}\text{C}$); and

T_f , fire temperature ($^{\circ}\text{C}$).

4 Results and Discussion

4.1 Overview of the Analysis

It is observed that initially the reinforced concrete beam is experienced a simultaneous contraction (at top fibers) and expansion (at bottom fibers) due to constant pressure load at the topmost surface. But when it is exposed to fire, it experienced an expansion in elements and strain is developed. Due to the heating, the curvature of the entire beam configurations changes and varies accordingly with time. Due to the cost of computation, only data for some selected elements of the beam is calculated such as 16 (mid-span), 8, 25 (quarter span), etc. All these elements are beam elements with two nodes. Figure 7 shows a reinforced concrete beam of 3-m length subjected to a constant pressure load of $13,333.33 \text{ kN/m}^2$ on the X–Z surface and exposed to fire according to the fire curve ASTM E119 Standard fire (Transient) with varying exposure condition to fire. The three other surfaces of the beam are kept at a constant temperature at 25°C .

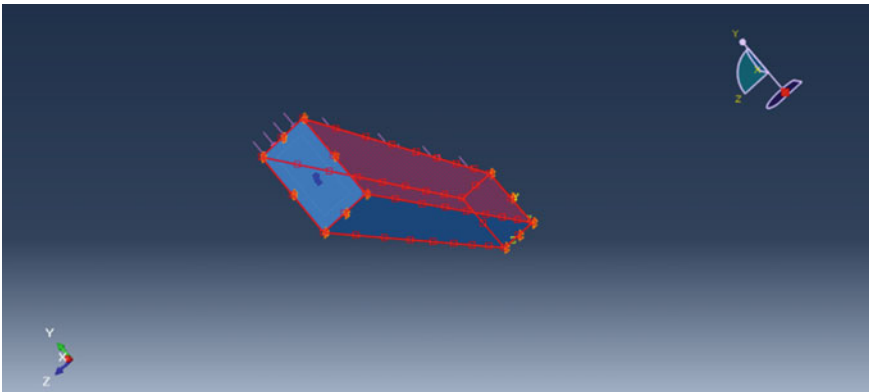


Fig. 7 Temperature boundary conditions (Fire load on 1 surface) applied for the RCC beam

The equivalent section for the reinforced concrete beam is calculated and the area moment of inertia is calculated for the section. The curvatures obtained from the central beam element are tabulated. The various modulus of elasticities of concrete at various temperatures are tabulated and the product of these three quantities is tabulated as the section moment at that particular element. The data for the temperature-dependent mechanical properties for the materials are from the presentation by ROBERT CERIB, Luc DAVENNE, and Iuliana STOIAN: Fire resistance assessment of concrete structures [4] (Figs. 8, and 9).

Fire Loading on One Face (Single Room Under Fire)

Element 8 (One-Fourth of Length)

See Fig. 10.

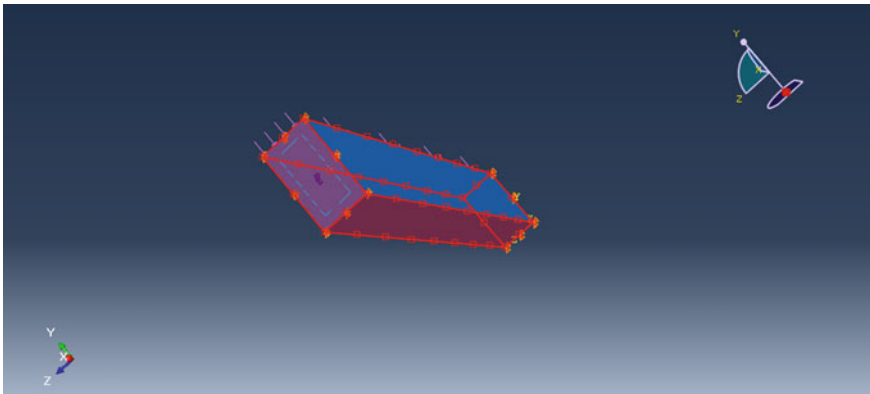


Fig. 8 Other surfaces of the RCC beam kept under ambient condition (For 1 surface loading)

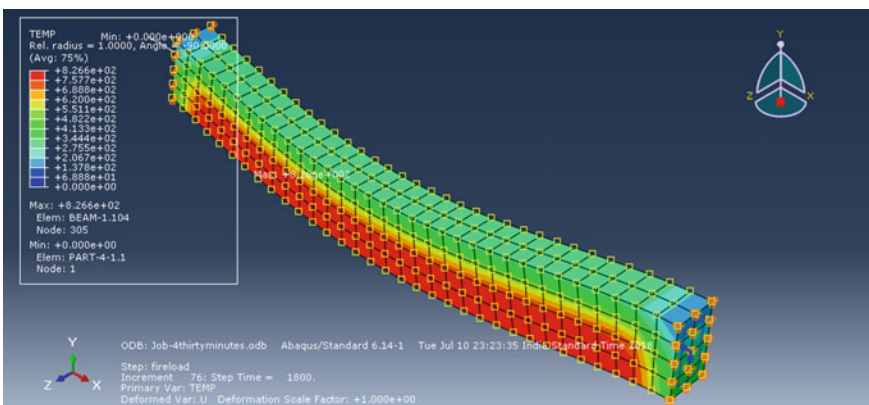


Fig. 9 Fire load applied on three faces

Fig. 10 Moment versus curvature relations for different durations of fire loading for element 8

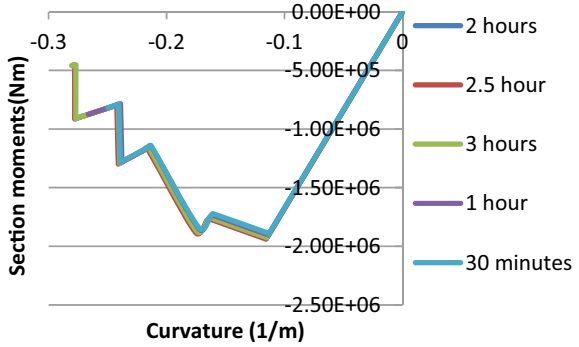
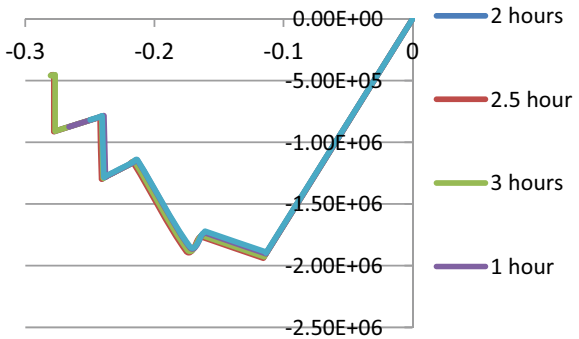


Fig. 11 Moment versus curvature relations for different durations of fire loading for element 16



Element 16 (Mid-point)
See Fig. 11.

Element 25 (Three-Fourth of Length)
See Fig. 12.

Fire Loading on Two Opposite Faces (Opposite Rooms Under Fire)

Results after 30 min of fire loading

See Figs. 13, 14, 15, and 16.

Results after 180 min of fire loading

See Figs. 17, 18, 19, and 20.

Fire Loading on Three Faces (Overhead Beam in a Room Under Fire)

Results after 30 min of fire loading

See Fig. 21.

Initially, the curvature is constant during the analysis of the loading step as there is no temperature change during the loading step. Temperature changes monotonically

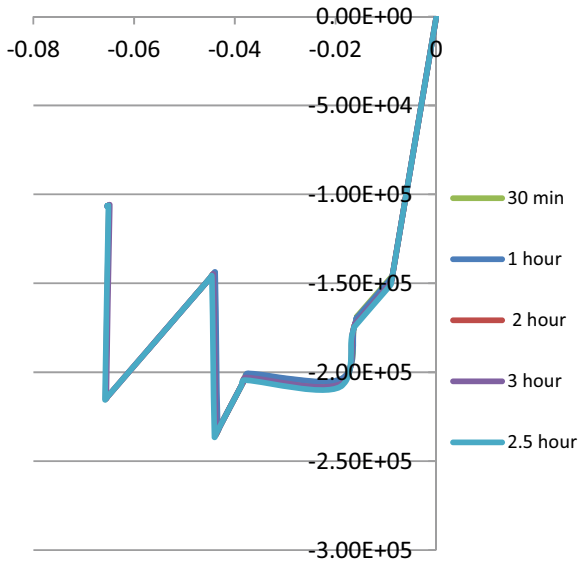


Fig. 12 Moment versus curvature relations for different durations of fire loading for element 25

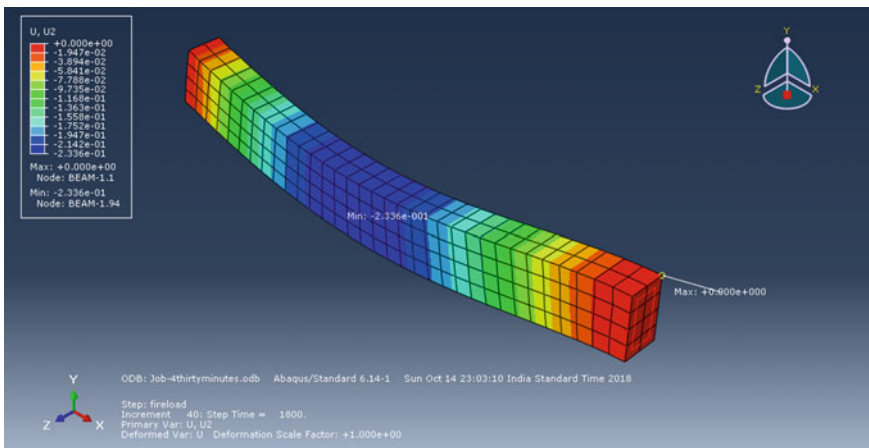


Fig. 13 Deflections in the Y direction under the influence of pressure loading and fire loading for 30 minutes

only in the fire load step and both time and curvature magnitude keep on increasing until heating stops. This is a condition that is observed at all the plots for curvature versus temperature as the static loading step is the same in all cases. Different durations for fire loading exposure for 0.5, 1, 2, 3, and 3.5 h have been tried for. The maximum absolute value for U2 is $2.425e-1$ m at element 1 solid beam part. The

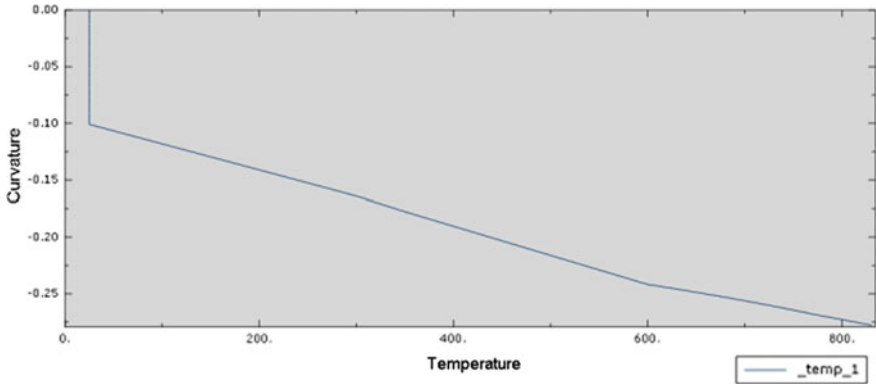


Fig. 14 Curvature versus temperature for element 8 for a fire loading duration of 30 minutes

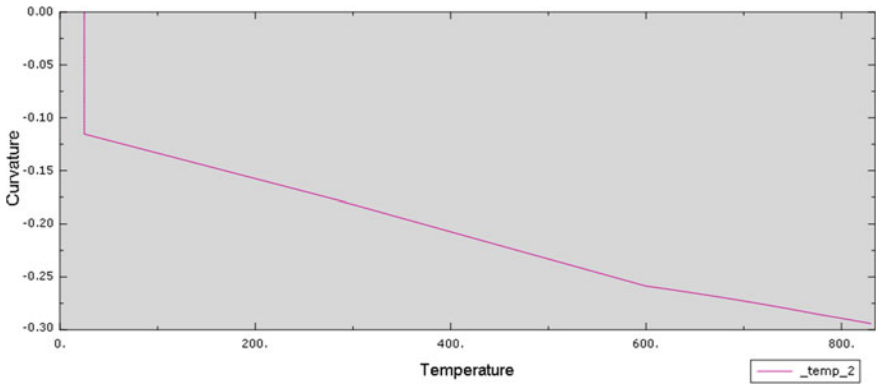


Fig. 15 Curvature versus temperature for element 16 for a fire loading duration of 30 minutes

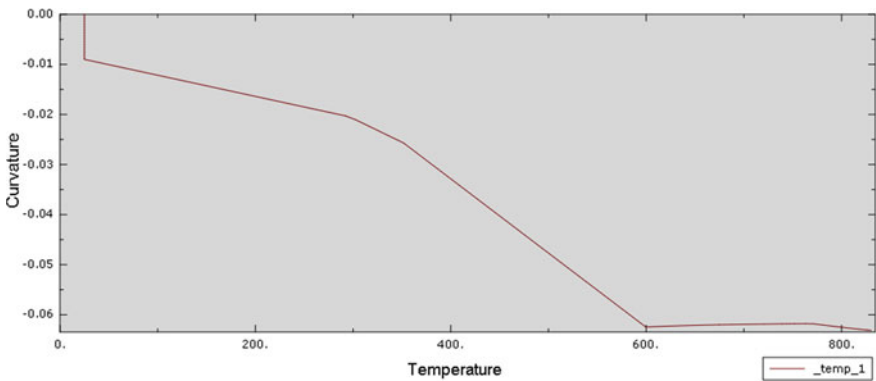


Fig. 16 Curvature versus temperature for element 25 for a fire loading duration of 30 minutes

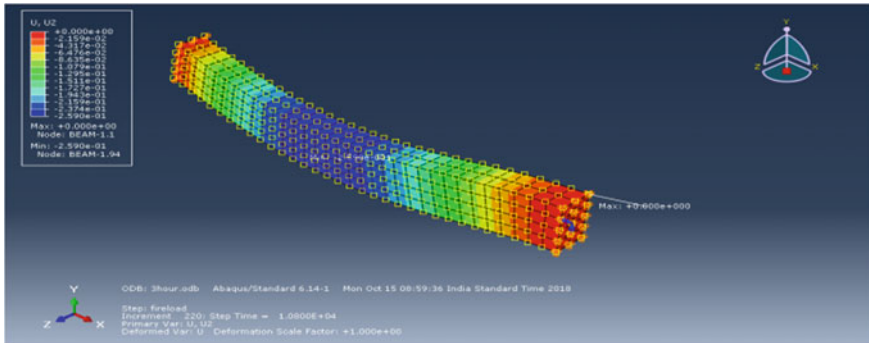


Fig. 17 Deflections in Y direction under the influence of pressure loading and fire loading for 180 minutes

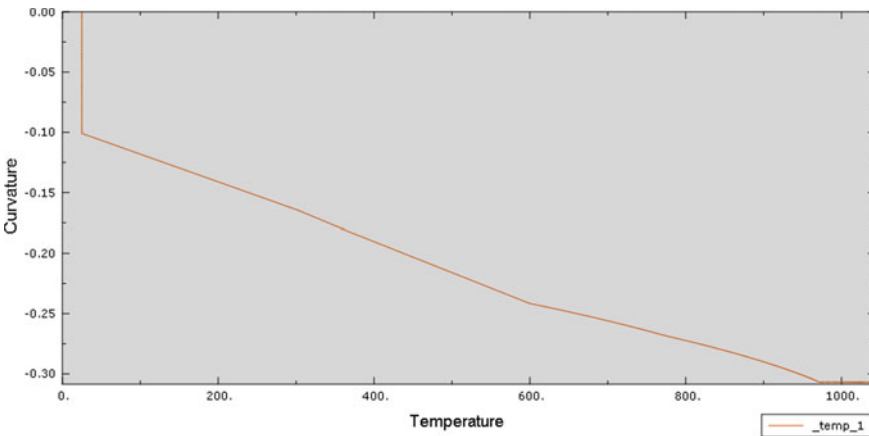


Fig. 18 Curvature versus temperature for element 8 for a fire loading duration of 180 minutes

curvature versus temperature plot for wire beam element for 30-min fire exposure has been presented in Fig. 9 (Fig. 22).

Results for different durations (1, 2, 3, 3.5 h) of fire loading

Analysis has been done for five different conditions of fire loading and deflected shape for all five cases have been extracted. Also, curvature versus temperature curves for all five cases for different elements have been extracted (Fig. 23).

The curvature versus temperature for different exposure durations have been presented in Figs. 10, 11, 12. From these sets of data, moment–curvature relationship has been obtained and presented in Fig. 29 for element 16.

The moment–curvature relationship for all durations was extracted from the FEM software. Figure 16 shows moment versus curvature for 2-h duration (Fig. 29).

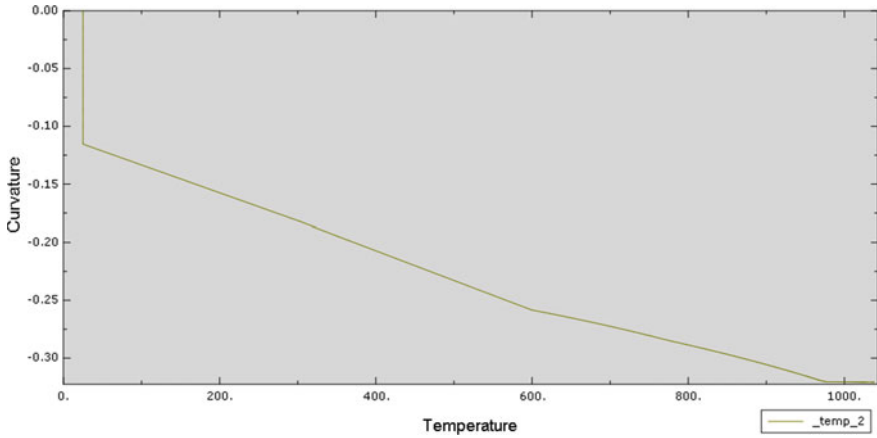


Fig. 19 Curvature versus temperature for element 16 for a fire loading duration of 180 minutes

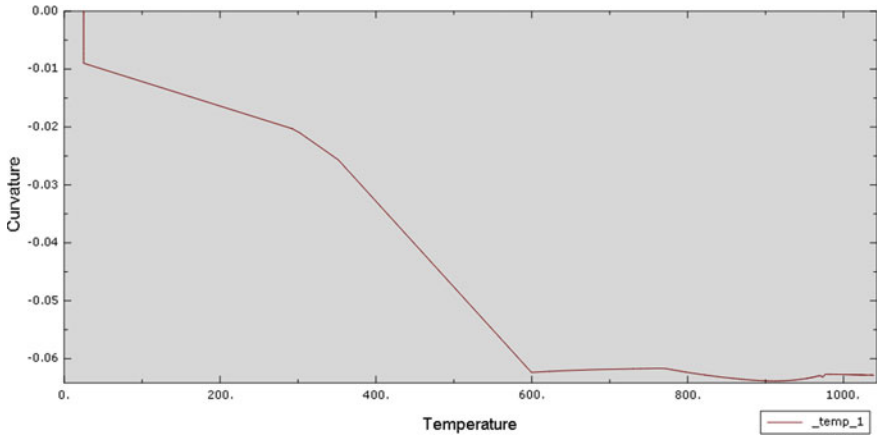


Fig. 20 Curvature versus temperature for element 25 for a fire loading duration of 180 minutes

From the moment–curvature relationships for the three elements, the values of respective moments have been presented in Tables 2, 3, and 4.

5 Conclusion

The moment–curvature values for one face exposure are more than the moment–curvature values for three faces of exposure to fire.

The maximum moment in moment–curvature curve is at location 2 (element 16) at time 150 minutes and is of magnitude 1939.257 kNm at a curvature of 0.1156

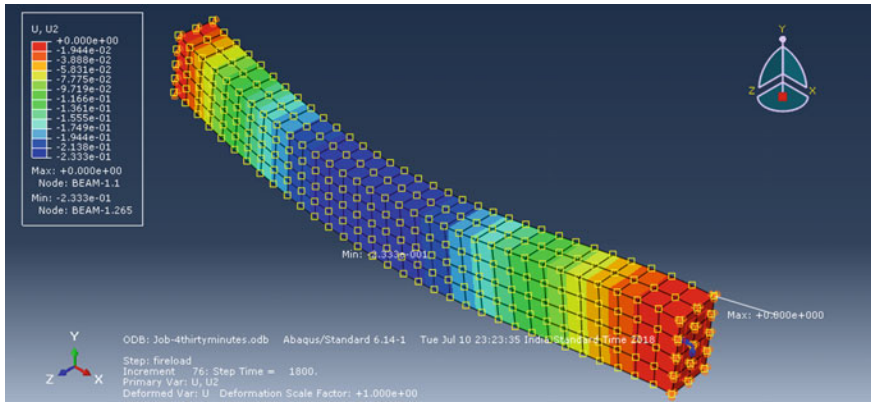


Fig. 21 Displacement U2 (along global Y) contour

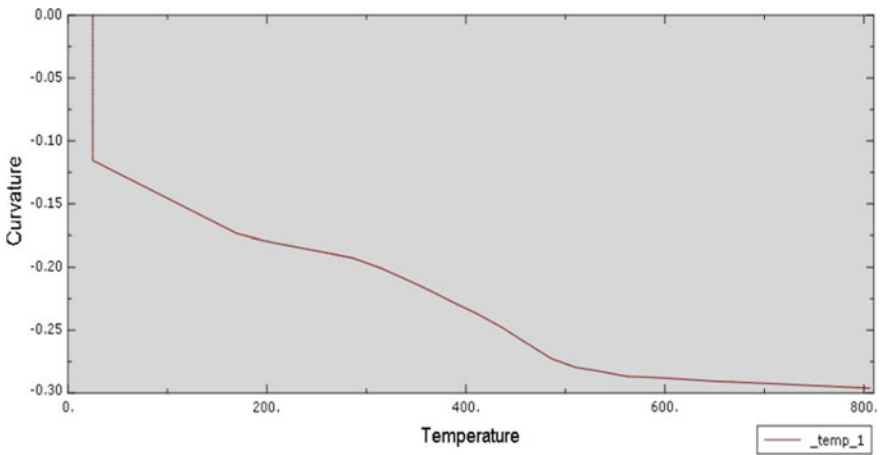


Fig. 22 Curvature versus temperature plot for the central element of the RCC beam (wire-beam element 16)

m^{-1} for one-sided exposure. The next highest moment in moment–curvature curve is at location 1 (element 16) at time 120 min and is of magnitude 1936.96 kNm at a curvature of $0.11553 m^{-1}$ (Table 4).

The moments at location 3 are very small in comparison. It is due to the non-uniform boundary conditions applied at the cross sections: hinge at one cross section and a roller with constraints in any one direction in another direction (Table 2).

The difference in the curves for moment versus curvature for different times of exposure is very small due to the fact that, after 30 min of fire exposure in fire loading step, the increase in temperature is very gradual. Hence, the effect on the moment versus curvature curve is very less making the difference between all the curves seemingly smaller.

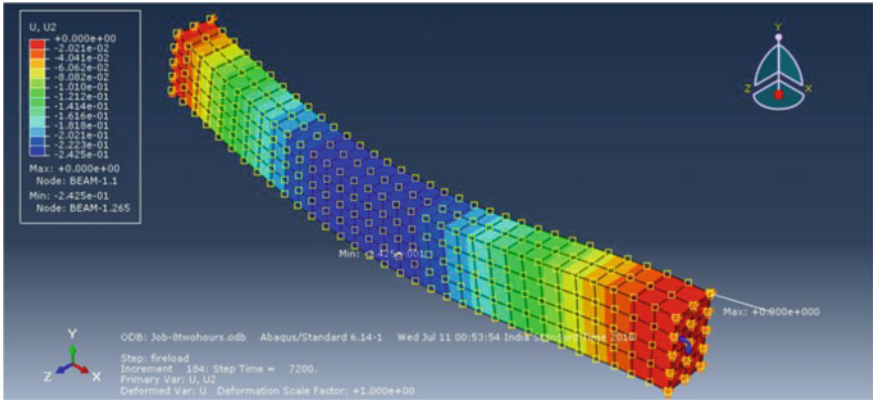


Fig. 23 Displacement U2 (along global Y) contour for the entire beam at the end of 2 h the heating step shown below:

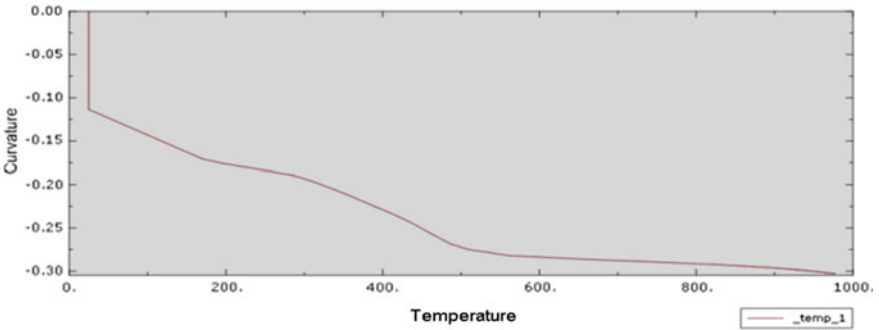


Fig. 24 Curvature versus temperature plot for 120 min

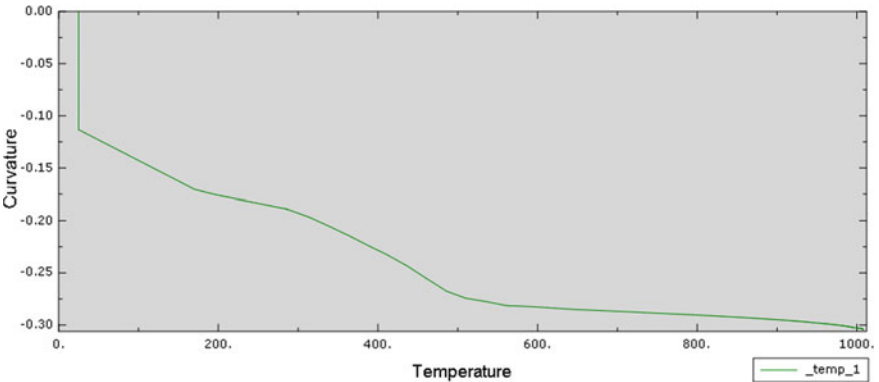


Fig. 25 Curvature versus temperature plot for element 16 (mid-point element) of the central embedded wire-beam element for a duration of 3 hours

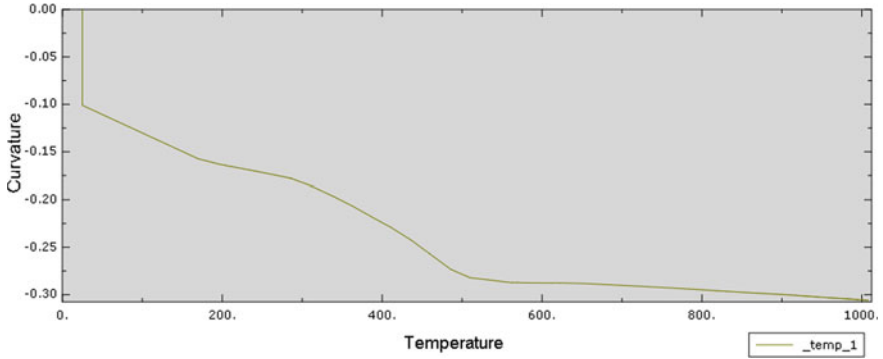


Fig. 26 Curvature versus temperature plot for element 8 (one-fourth length element) of the central embedded wire-beam element for a duration of 3 hours

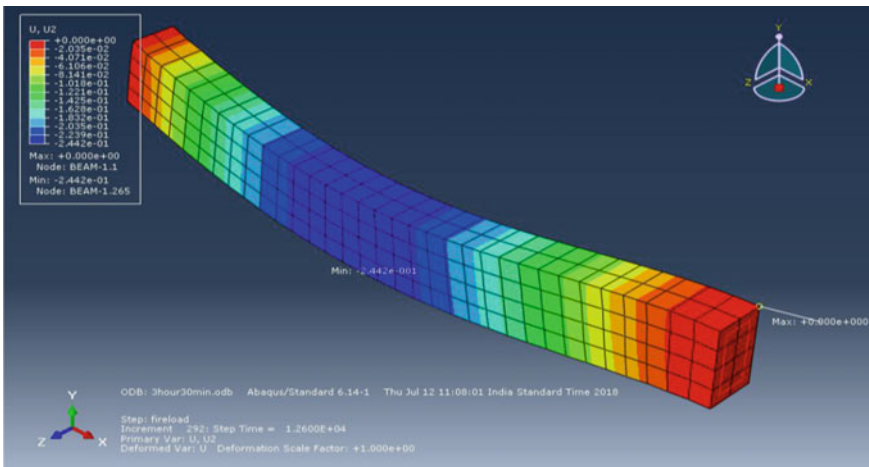


Fig. 27 Displacement U2 (along global Y) contour for the entire beam at the end of the heating step

The curve for lower time of exposure lies above the curve for higher time of exposure.

After exposure to fire for 120 min, the peak moment values and corresponding curvatures are reached for all the three locations elements 8, 16, and 25, respectively in Table 2.

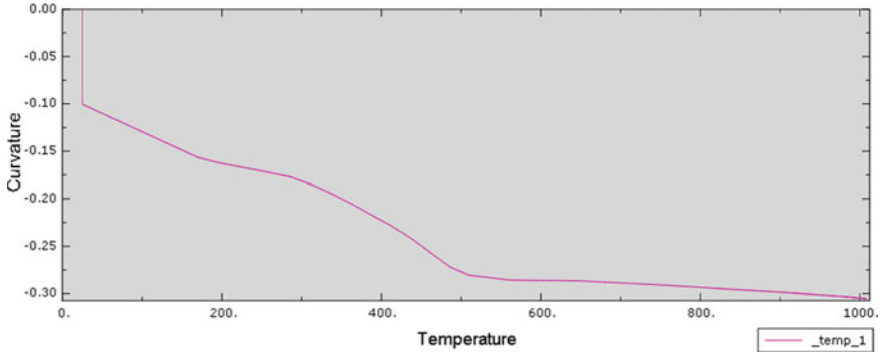


Fig. 28 Curvature versus temperature plot for element 8 (one-fourth element) of the central embedded wire-beam element for a duration of 3 hours and 30 minutes as shown below:

Fig. 29 Moment versus curvature for element 16 (2-hours duration)

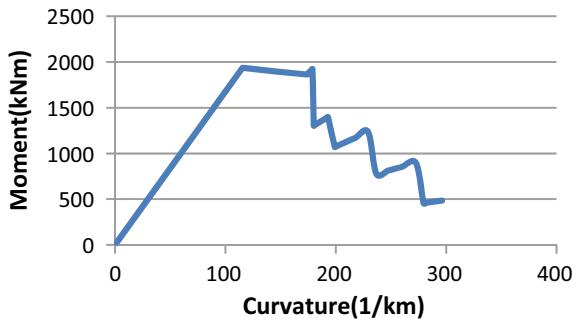


Table 2 Moment and curvatures for salient points for different fire exposures

Sl. no.	Exposure time (min)	Location 1 (Element 8)		Location 2 (Element 16)		Location 3 (Element 25)	
		Moment (kNm)	Curvature (/km)	Moment (kNm)	Curvature (/km)	Moment (kNm)	Curvature (/km)
1	30	1664.293	99.26751	1936.96	115.5308	148.2866	8.844618
2	60	1664.26	99.2659	1903.005	113.505	149.7022	8.929052
3	120	1695.789	101.146	1903.984	113.56	151.2628	9.022137
4	180	1664.3	99.26794	1902.958	113.5028	151.0055	9.006794
5	210	1.66E+03	99.26599	1850.176	110.3546	149.7558	8.932252

Table 3 Moment versus curvature values for element 8 for different exposure conditions and fire loading durations

Element 8		Face 1		Face 3	
Sl. no.	Exposure time (min)	Moment (km)	Curvature (/m)	Moment (kNm)	Curvature (/m)
1	30	1669.264	0.15545	1664.293	0.099.26751
2	60	1664.254	0.1555	1664.266	0.0992659
3	120	1681.789	0.10065	1695.789	0.101146
4	150	1692.404	0.15814	NIL	NIL
5	180	-1679.642	0.10053	1664.300	0.09926794

Table 4 Moment versus curvature values for element 16 for different exposure conditions and fire loading durations

Element 16		Face 1		Face 3	
Sl. no.	Exposure time (min)	Moment (kNm)	Curvature (/m)	Moment (kNm)	Curvature (m)
1	30	1890.46	0.11314	1936.96	0.1155308
2	60	1903.481	0.11353	1903.005	0.1135056
3	120	1930.163	0.1151	1903.984	0.113564
4	150	-1939.28	0.11567	NIL	NIL
5	180	-1927.747	0.11498	1902.958	0.1135028

Acknowledgements I would like to express my special thanks to Prof. Sriman Kumar Bhattacharyya, IIT Kharagpur, for his excellent guidance and encouragement.

I would also like to thank Prof. Arghya Deb, IIT Kharagpur, for his valuable suggestions. I express my sincere gratitude to the Indian Academy of Sciences for offering me this opportunity.

References

1. Kodur VKR, Cheng F-P, Wang T-C, Sultan MA (2003) Effect of strength and fiber reinforcement on fire resistance of high-strength concrete beams. *J Struct Eng [Internet]* 129(2):253–259
2. Lau A, Anson M (2006) (2006) Effect of high temperatures on high performance steel fibre reinforced concrete. *Cem Concr Res* 36(9):1698–1707
3. Chung JH, Consolazio GR (2005) (2005) Numerical modeling of transport phenomena in reinforced concrete exposed to elevated temperatures. *Cem Concr Res* 35(3):597–608
4. https://eurocodes.jrc.ec.europa.eu/doc/2012_11_WS_fire/presentations/06-ROBERT-EC-FireDesign-WS.pdf

Effect of Slab Thickness on Period of the Vibration of Reinforced Concrete Building



Prabhat Kumar Soni , S. K. Dubey , and Prakash Sangamnerkar 

Abstract The fundamental time period of vibration of reinforced concrete (RC) moment resisting frame (MRF) buildings can be calculated using empirical expressions of Indian codes of seismic design to derive design base shear. Indian code IS1893 (Part-1)–2016 provides empirical expression to estimate the approximate natural time period of vibration which widely depend on some basic parameters such as a number of storeys or height of the building. The consideration of the effects of some other parameters of the structures also seems to be required. There is the scope of further improvisation in these equations. It can be observed that there is wide use of fundamental period obtained using these expressions. It is, therefore, in the seismic design of the structures, it is in favour of more accuracy in design to use realistic values of the time period. This study deals with the estimation of the fundamental period of vibration of symmetrical RC MRF buildings which incorporates the parameters like slab thickness, stiffness (referring to column sizes) of the structure in addition to its height. In the paper, different values of the time period have been obtained by performing dynamic analysis on building/structural configurations for different parameters of the building and earthquake zone III as per the provisions are given in the Indian seismic code. The results have been presented with comparative analysis. Computer software STAAD has been used to analyse the building model.

Keywords Nonlinear regression analysis fundamental period number of bay dynamic analysis · Stiffness

P. K. Soni (✉) · S. K. Dubey
Maulana Azad National Institute of Technology (MANIT), Bhopal, India
e-mail: prabhatsoni15@gmail.com

S. K. Dubey
e-mail: dubeysk2000@yahoo.com

P. Sangamnerkar
M.P. Housing Board, Bhopal, M.P, India

1 Introduction

The distribution of mass and stiffness are considered along with the height of the structure/building for analysis of the fundamental natural time period of vibration. For the evaluation of the seismic base shear, the fundamental time period of vibration (T) of the building is required. The approximate time period of vibration (T_a in seconds) of RC building without considerations of brick infill panels can be calculated by following empirical equations of Indian code IS1893 (Part-1)-2016 [5].

$$T_a = 0.075 h^{0.75} \text{ for R.C. frame building} \quad (1)$$

$$T_a = 0.085 h^{0.75} \text{ for steel frame building} \quad (2)$$

$$T_a = 0.09 h / \sqrt{d} \text{ for all other buildings} \quad (3)$$

To evaluate the time period, above-simplified expressions are used in general. Although, the discussion about the scope of further improvement in these equations has been presented in the different research works of Khan and Hoque [4], the expressions in terms of height alone as structural parameter seems inadequate to explain the period evaluation.

Currently, the period of vibration in seismic analysis can be estimated by any of the following methods:

- Observations made by experimental analysis on similar buildings.

- By the use of any rational method (referring to the dynamic analysis).

- By the use of the empirical equations prescribed in the design code.

The simplified expressions of the design codes, which are obtained based on recordings of earthquakes in real buildings, results of laboratory tests and other computations, are used to evaluate the fundamental natural period. From the earlier research work, it can be easily observed that very few buildings are equipped with the vibration measuring instruments and hence actual measured data were also very few in numbers. These data sets were used by various researchers to perform regression analysis. Simple empirical equations were proposed in terms of height as a structural parameter to evaluate the fundamental period, because of the following reasons:

Height of the building/structure is the most influencing parameter which affects the time period. The proposed equation allows the designer to evaluate the fundamental period and hence base shear and other response quantities without going much into the detail for the sizes of structural elements.

Primarily, the basic parameters such as building height or a number of storeys are used in the expressions provided by the technical codes.

2 Literature Study

For the requirement of the design of RC structures, a simplified equation relating the period to the height or number of the storey of the building has been used for many years to evaluate the fundamental period of vibration.

Verderame et al. [8] suggested that global parameter (e.g. plan area) can be incorporated in the simplified equations for rapid and easy period evaluation and pointed out that the formula having height alone as parameter seems inadequate to evaluate period variability. Therefore, they incorporated the base area in an expression of the following equation

$$T = \alpha H^\beta S^\gamma \quad (4)$$

where, $S = L_x \cdot L_y$; principal plan dimensions of the building.

Nyrko et al. [5] developed seven different relations for evaluation of the time period more accurately; they considered seven basic expressions for the elastic period considering different parameters such as the ratio between the number of bays including both the directions, the product of the number of bays including both (longitudinal and transversal) directions in addition to the consideration of the number of floors. Following expressions have been developed to propose for evaluation of the period:

$$T = C_1 N^{C_2} \quad (5)$$

$$T = C_1 N^{C_2} B^{C_3} \quad (6)$$

$$T = C_1 N^{C_2} + C_3 B^{C_4} \quad (7)$$

$$T = C_1 N^{C_2} \left(\frac{B_x}{B_y} \right)^{K C_3} \quad (8)$$

$$T = C_1 N^{C_2} (B_x \cdot B_y)^{C_3} \quad (9)$$

$$T = C_1 N^{C_2} + C_3 (B_x \cdot B_y)^{C_4} \quad (10)$$

$$T = C_1 N^{C_2} + C_3 \left(\frac{B_x}{B_y} \right)^{C_4} \quad (11)$$

where N = number of storeys, B_y and B_x are considered as a number of bays in the transversal direction and longitudinal direction, B = number of bays of the

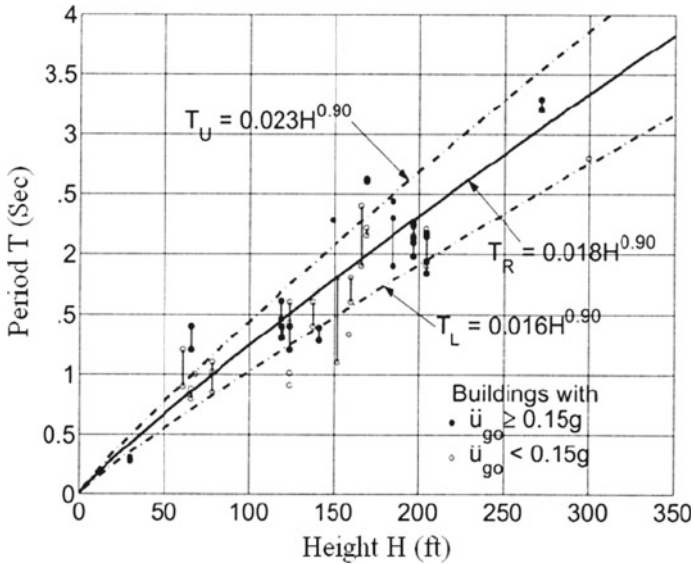


Fig. 1 Shows the results of RC MRF using eigenvalue analysis [Figure considered from Goel and Chopra, 1997 (3)]

building parallel to the direction considered, and C_1 , C_2 , C_3 and C_4 are considered as (unknown) factors.

Goel and Chopra [3] showed that code formula generally underestimates the periods of vibration on the basis of the collected data recorded from different earthquakes and measured the period from 27 RC frames. They proposed different formulae from the semi-empirical analysis (Fig. 1).

3 Analysis

Different values of the time period have been obtained by performing dynamic analysis on building/structural configurations for different parameters of the building and earthquake zone III, as per the provisions given in the Indian seismic code. Computer software STAAD [7] has been used to analyse the building model. The general arrangement of beams and columns are depicted as the Fig. 2 (Table 1):

It can be observed from Tables 2, 3, and 4 and Fig. 3 that the time period varies on the higher side of its values with the increase in the slab thickness, which is obvious due to increment in mass but its effect on time period is considerable due to the difference between the time period calculated by the period formula of IS1893 and the values obtained from the analysis of the buildings having different slab thickness.

It can be observed from Table 2, the period variation for 200 mm slab thickness is 18.66% higher in comparison to slab 100 mm having height considering ground floor

Fig. 2 Example of plan for two—bay square-shaped building for dynamic analysis

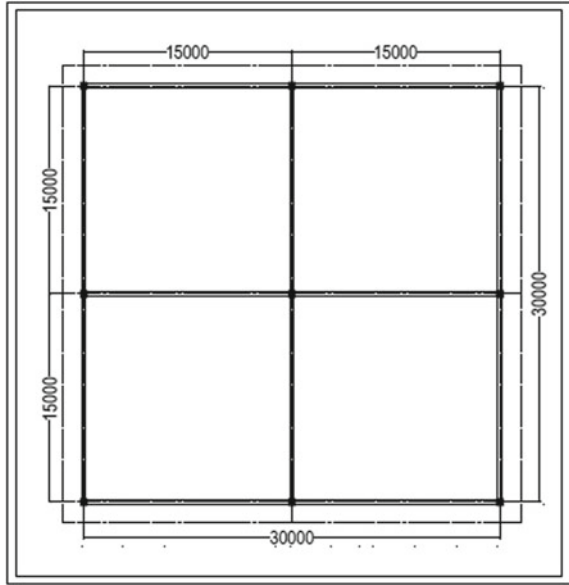


Table 1 Details of building configuration, material used and structure

Building configuration		Material specification		Structural details	
Structure-type	Multi-storey rigid jointed plane frames	Material	Concrete M-25, Reinforcement Fe-415	Size of columns (m × m)	0.7 × 0.7 0.6 × 0.6 0.5 × 0.5 0.4 × 0.4 0.3 × 0.3
No. of storey	GF to G + 5, G + 6 to G + 10	Soil type	Medium soil (type-II)	Slab thickness (mm)	100,150 200,250
Floor height	3.6 m	E_c	$5000\sqrt{f_{ck}}$ N/mm ²	Imposed load	4.00 kN/m ²
				Floor finish	1.00 kN/m ²
Base dimension	30 m × 30 m 36 m × 36 m 48 m × 48 m	F_{cr}	$0.7\sqrt{f_{ck}}$ N/mm ²	Waterproofing	2.5 kN/m ²
				Specific weight of R.C.C	25 kN/m ³

Table 2 Period values (s) for column size 500 × 500 mm—2 bays

Building height (m)	Time period as per IS 1893	Slab thickness		
		100.00 mm	150.00 mm	200.00 mm
3.60	0.273	0.75	0.83	0.89
7.20	0.396	1.35	1.47	1.58
10.80	0.447	1.96	2.13	2.28
14.40	0.554	2.55	2.75	2.95
18.00	0.709	3.15	3.39	3.62
21.60	0.803	3.85	4.12	4.38

Table 3 Period values (s) for column size 400 × 400 mm—2 bays

Building height (m)	Time period as per IS 1893	Slab thickness		
		100.00 mm	150.00 mm	200.00 mm
3.60	0.273	0.93	1.02	1.01
7.20	0.396	1.61	1.76	1.89
10.80	0.447	2.30	2.49	2.66
14.40	0.554	2.95	3.18	3.40
18.00	0.709	3.60	3.88	4.14
21.60	0.803	4.38	4.69	4.99

Table 4 Period values (s) for column size 300 × 300 mm—2 bays

Building height (m)	Time period as per IS 1893	Slab thickness		
		100.00 mm	150.00 mm	200.00 mm
3.60	0.273	1.29	1.42	1.54
7.20	0.396	2.16	2.35	2.53
10.80	0.447	3.01	3.26	3.49
14.40	0.554	3.84	4.14	4.42
18.00	0.709	4.68	5.04	5.37
21.60	0.803	5.68	6.08	6.46

only. But the same variation is 13.76% having building height 21.6 m. This variation is less but when the time period value for 200 mm slab is compared with the period value calculated by the formula of IS 1893, the increment is 445%. Similar results can be observed in Tables 3 and 4 (Fig. 4).

Tables 5 and 6 show the values of the time period for the slab thickness 150 mm and 200 mm, respectively. Time period obtained by considering the different structural parameters of the building are much higher than the value obtained by the period

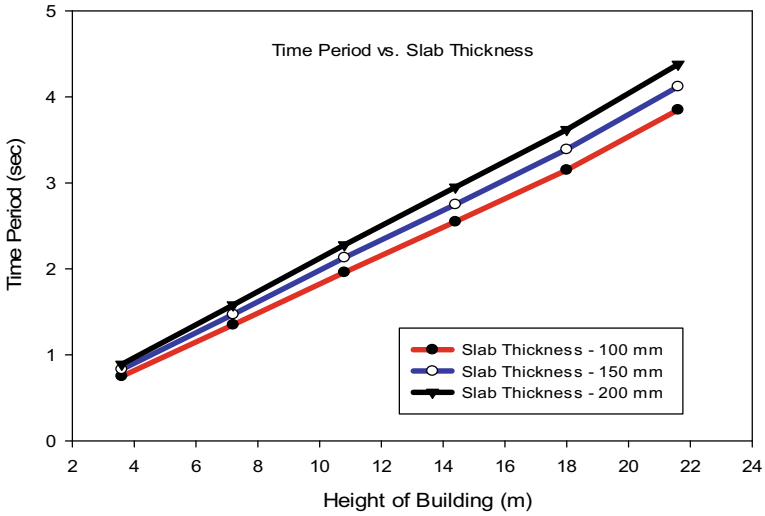


Fig. 3 Variation of period values (s) for column size 0.5×0.5 m—2 bays. Height of the building is in metre

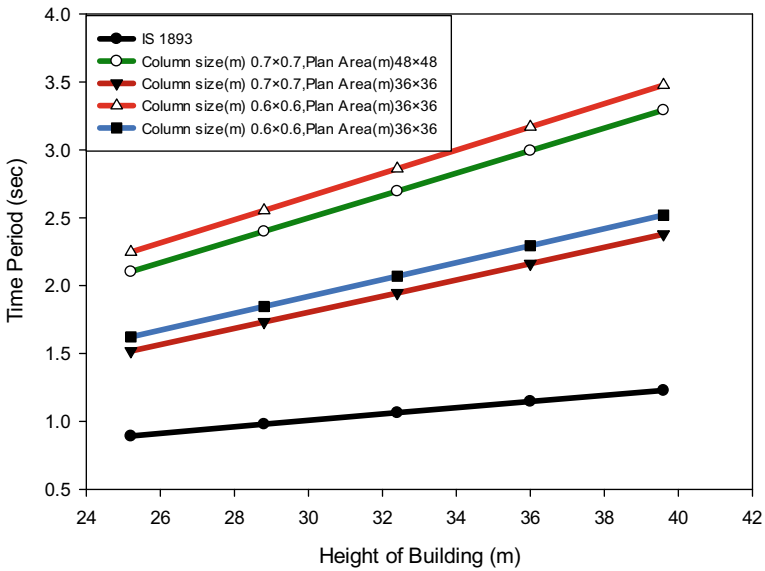


Fig. 4 Comparison of the time period (sec) calculated by the formula of IS 1893 and obtained by analysis of buildings of different configurations having slab thickness 150 mm, bay size 6×6

Table 5 Time period (t): bay size 6 × 6, slab thickness = 150 mm

Floors/Height	Time period as per IS 1893	Columns size (m)			
		0.7 × 0.7		0.6 × 0.6	
		Bay length(m)		Bay length(m)	
		8	6	8	6
		Plan area (m)			
		48 × 48	36 × 36	48 × 48	36 × 36
		T (s)	T (s)	T (s)	T (s)
G + 10 (39.6 m)	1.229	3.293	2.379	3.477	2.520
G + 9 (36 m)	1.148	2.995	2.162	3.169	2.294
G + 8 (32.4 m)	1.065	2.697	1.946	2.861	2.070
G + 7 (28.8 m)	0.981	2.400	1.732	2.554	1.846
G + 6 (25.2 m)	0.893	2.104	1.518	2.248	1.623

Table 6 Time period (T): bay size 6 × 6, slab thickness = 250 mm

Floors/Height	Time period as per IS 1893	Columns size (m)			
		0.7 × 0.7		0.6 × 0.6	
		Bay length (m)		Bay length (m)	
		8	6	8	6
		Plan area (m)			
		48 × 48	36 × 36	48 × 48	36 × 36
		T (s)	T (s)	T (s)	T (s)
G + 10 (39.6 m)	1.229	3.591	2.593	3.845	2.753
G + 9 (36 m)	1.148	3.288	2.358	3.505	2.507
G + 8 (32.4 m)	1.065	2.980	2.123	3.166	2.262
G + 7 (28.8 m)	0.981	2.653	1.890	2.827	2.019
G + 6 (25.2 m)	0.893	2.326	1.657	2.489	1.776

formula of IS1893; such as its value is 212% higher in case of 250 mm slab, G + 10 building and column size 0.6 m × 0.6 m, in comparison to the time period obtained by the code formula.

4 Conclusion

It can be observed from Tables 2, 3, 4, 5, and 6, with the variation of slab thickness, the time period is also showing variation in its values. The difference of time period obtained by the formula of IS1893 and analysis of buildings having different structural parameters is much high. Hence the effect of the same should not be ignored.

Therefore, to evaluate the period of vibration, the formula in terms of height alone seems inadequate. The result of this study highlights that the thickness of the slab along with the stiffness of the structure also affect the time period of vibration. Hence these factors should also be incorporated in simplified relationships given in IS 1893, for evaluation of time period of vibration in seismic analysis.

References

1. BUREAU OF INDIAN STANDARDS. Criteria for Earthquake resistant design of structures- Part-1: General Provisions and Buildings, IS 1893(Part 1):2016, Bureau of Indian Standards, New Delhi
2. BUREAU OF INDIAN STANDARDS. Code of practice for structural safety loadings standards IS 875-1987 Part-1, 2 Bureau of Indian Standards, New Delhi
3. Goel RK, Chopra AK (1997) Period formulas for moment-resisting frame buildings. *Struct Eng Div ASCE* 123:1454–1461
4. Khan MA, Hoque E (2006) A rationale for determining the natural period of RC building frames having infill. *Eng Struct*, Elsevier 28:495–502
5. Nyrko MH, Morie D, Draganic H, Nyarko EK (2012) New direction based (Fundamental) periods of RC frames using Genetic Algorithms. In: 15th world conference on earthquake engineering, Lisboa
6. Sangamnerkar P, Dubey SK (2017) Equations to evaluate fundamental period of vibration of buildings in seismic analysis. *Struct Monit Maint* 4(4):351–364
7. STAAD Pro-V8i –Structural analyses and designing software by Bentley
8. Verderame GM, Iervolino I, Manfredi G (2009) Elastic period of existing RC-MRF buildings, Eurocode 8 Perspectives from Indian standpoint Workshop. Italy, Napoli, pp 79–94

Sampling-Based Techniques for Finite Element Model Updating in Bayesian Framework Using Commercial Software



Ayan Das and Nirmalendu Debnath

Abstract Finite element (FE) model updating in Bayesian framework, using sampling-based techniques like Markov chain Monte carlo (MCMC), is observed to be investigated by many researchers. The present work is focussed on FE model updating using MCMC techniques where modelling is performed using commercial FE software to avoid the difficulties with writing computer program for FE modelling. In this present work, two prominent MCMC techniques based on Metropolis–Hastings (MH) algorithm, viz. enhanced-MCMC and transitional MCMC are primarily used, while FE modelling is performed using a well-known FE software, viz. SAP2000. A reasonably complex structure in the form of a cantilever plate is considered in this study and modelled using shell elements. Besides, damage is simulated in this plate structure by decreasing the Young’s modulus of few of the elements of the discretized plate structure. Modal data in the form of frequencies and incomplete mode shapes, evaluated from the damaged structure, are taken as the measured modal data. The technique of error localisation and an improved parameter selection method are adopted for limiting the number of updating parameters to facilitate better performance. Moreover, Gibbs sampling which is an effective algorithm of MCMC technique is also demonstrated using SAP2000. All the MCMC techniques for FE model updating are performed using a computational framework based on interactions between MATLAB and SAP2000 with the help of SAP2000 open application programming interface (OAPI). It is observed that level of performances in FE model updating is most satisfactory while using enhanced-MCMC in comparison with others.

Keywords Bayesian updating · Enhanced-MCMC · Transitional MCMC · Gibbs sampling · SAP2000

A. Das · N. Debnath (✉)

Department of Civil Engineering, National Institute of Technology, Silchar, Assam, India

e-mail: nirmalendu.debnath@gmail.com

A. Das

e-mail: das.ayan53@gmail.com

© Springer Nature Singapore Pte Ltd. 2021

S. Adhikari et al. (eds.), *Advances in Structural Technologies*, Lecture Notes in Civil Engineering 81, https://doi.org/10.1007/978-981-15-5235-9_27

363

1 Introduction

Finite element (FE) model updating is one of the most widely used technique as a means to bridge the gap between the experimental modal properties of a structure and the predictions of a numerical model. Due to various types of errors such as modelling errors, the analytical/FE model predicted results are different from the experimental/actual results. Hence, FE model updating is a very significant application in this regard to reduce such errors. The fundamental idea of FE model updating is to update/refine the initial numerical model so that the modal properties of the updated model are highly correlated with that of the experimental/real structure. Thus, the updated FE model can more accurately predict the behaviour of the real-structural system. A concise presentation of the review of literature regarding model updating techniques is discussed next.

An elaborate discussion on various FE model updating techniques has been presented in Friswell and Mottershead [1] where direct updating techniques, iterative techniques and frequency response function (FRF) based techniques are explained. Ewins [2] explained various types of errors in relation to the creation of an FE model. Moreover, works by Mottershead and Friswell [3, 4] presented a basic explanation of the model updating techniques. Direct updating techniques where the system matrices are directly updated can be understood from many works [5–13].

Another class of model updating is the sensitivity technique [14] which has gained much significance in the recent years. A comparison between direct and iterative techniques for model updating can be observed from the work of Yang and Chen [15]. Besides, FRF-based FE model updating technique can be observed from a few works [16, 17].

One of the most effective techniques of model updating in recent times is the technique of model updating in Bayesian framework. One such class of model updating is the Bayesian probabilistic updating by maximizing the posterior PDF known as maximum a posteriori (MAP). Many such works [18–20] can be observed where Bayesian statistical framework is utilized not only for system identification but also for identification of updating parameters. Yuen [21, 22] developed a technique of Bayesian model updating based on MAP where matching of mode shapes between the measured and analytical models is not required which is of prime significance in case of large structures. Besides, a book by Yuen [23] elaborately describes Bayesian FE model updating techniques, model class selection and various topics related to it. Similar work can be observed in [24] where a real-life bridge is updated utilizing incomplete modal data. Lastly, Das and Debnath [25] proposed a technique of updating in Bayesian framework based on MAP where the non-negative nature of the updating parameters is taken into consideration by assuming lognormal distribution for the structural parameters.

The method adopted in this paper belongs to the class of sampling based FE model updating in Bayesian probabilistic framework, where MCMC technique is primarily used in the process of maximizing the posterior PDF. Many researchers have successfully adopted modified versions of MCMC techniques, namely adaptive MCMC [26],

transitional MCMC (TMCMC) [27], hybrid MCMC [28], enhanced-MCMC [29–32] in FE model updating. In the present work, two prominent MCMC techniques, viz. enhanced-MCMC and TMCMC which adopt Metropolis–Hastings (MH) algorithm [33, 34] have been used for FE model updating employing a well-known FE software viz, SAP2000 [35]. The need for commercial FE software arises due to the fact that it is not always easy to write computer program for FE modelling of complex structures. The example considered in this paper is a reasonably complex structure in the form of a cantilever plate and its numerical model is created in SAP2000 using shell elements. Also, the damage is simulated in the structure by decreasing the Young’s modulus of a few of the elements of the discretized plate structure. The eigenvalues and incomplete mode shapes corresponding to selected DOFs (degrees of freedom) for the first few modes of the plate structure are evaluated and these serve as the measured modal data. Apart from these, 1% noise is added to the actual modal data to form noisy modal data used in model updating. In order to limit the number of updating parameters in the updating procedure, the technique of error localisation [36] is employed. Besides, an improved updating parameter selection method [37] is also adopted in this paper for improved performance in updating. It may be mentioned that Gibbs algorithm [38], which is also an efficient algorithm of MCMC technique has been demonstrated in this example in spite of difficulties in sub-structuring of structural matrices while using commercial FE software. Various researchers [39–41] have successfully employed Gibbs sampling in successful updating of a structure which do not require the procedure of mode matching. The model updating procedure using all these sampling techniques is performed using a computational framework where interactions between MATLAB [42] and SAP2000 is performed using SAP2000 open application programming interface (OAPI). A comparison has been performed among all the three MCMC techniques in updating the plate structure employing SAP2000 and it has been observed that level of performance is most satisfactory for enhanced-MCMC followed by TMCMC and Gibbs sampling while employing commercial FE software for model updating.

2 Theoretical Background of Bayesian Model Updating

2.1 Formulation of Posterior PDF

The Bayes’ theorem [43] for FE model updating utilizing continuous valued updating parameters may be expressed as in Eq. (1).

$$p(\theta|D) = \frac{p(D|\theta)p(\theta)}{p(D)} \quad (1)$$

where θ represents the unknown structural parameter and \mathbf{D} represents the actual/measured observed data. Besides, $p(\theta|D)$ is the posterior probability density

function (PDF) of the parameter θ given the observed data \mathbf{D} , $p(\theta)$ is the prior PDF of the unknown structural parameter, $p(\mathbf{D}|\theta)$ is the likelihood function of the observed data \mathbf{D} given the parameter θ and $p(\mathbf{D})$ is the normalizing constant. The observed data \mathbf{D} in this paper consists of measured frequencies \hat{f} and mode shapes $\hat{\Psi}$. Assuming the prior PDF to follow uniform distribution, Eq. (1) can be again expressed as shown in Eq. (2).

$$p(\theta|\hat{f}, \hat{\Psi}) = k_1 p(\hat{f}, \hat{\Psi}|\theta) \tag{2}$$

where k_1 is a normalizing constant.

Assuming the modal parameters from different modes to be independent of each other, the likelihood function $p(\hat{f}, \hat{\Psi}|\theta)$ can be expressed as shown in Eq. (3).

$$\begin{aligned} p(\hat{f}, \hat{\Psi}|\theta) &= p(\hat{f}|\theta) p(\hat{\Psi}|\theta) \\ &= \prod_{r=1}^{N_m} p(\hat{f}_r|\theta) \prod_{r=1}^{N_m} p(\hat{\Psi}_r|\theta) \end{aligned} \tag{3}$$

The PDF of the measured eigenvalues for the r th mode $p(\hat{f}_r|\theta)$ can be shown in Eq. (4).

$$p(\hat{f}_r|\theta) = \frac{1}{\sqrt{2\pi}k} \exp\left[-\frac{1}{2k^2} \left(\frac{\hat{f}_r - f_r(\theta)}{\hat{f}_r}\right)^2\right] \tag{4}$$

where k represents the standard deviation of the PDF based on the fractional error between the measured frequency \hat{f}_r and the uncertain parameter θ dependent frequency $f_r(\theta)$. On the other hand, the PDF of the measured mode shape for the r th mode can be shown in Eq. (5).

$$p(\hat{\Psi}_r|\theta) = \frac{1}{\sqrt{2\pi}k} \exp\left[-\frac{1}{2k^2} (1 - \text{MAC}(r))\right] \tag{5}$$

where k is the measure of uncertainty of the fractional error between measured mode shapes $\hat{\Psi}_r$ and calculated mode shapes $\Psi_r(\theta)$ for the r th mode and $\text{MAC}(r)$ is the modal assurance criteria between the measured and calculated mode shapes for the r th mode and is given in Eq. (6).

$$\text{MAC}(r) = \frac{|\hat{\Psi}_r \Psi_r(\theta)|^2}{(\hat{\Psi}_r^T \hat{\Psi}_r)(\Psi_r^T(\theta) \Psi_r(\theta))} \quad (6)$$

Considering unit Euclidean norm of the mode shapes, Eq. (5) can be shown as in Eq. (7).

$$p(\hat{\Psi}_r|\theta) = \frac{1}{\sqrt{2\pi}k} \exp\left[-\frac{1}{2k^2}\left(1 - |\hat{\Psi}_r \Psi_r(\theta)|^2\right)\right] \quad (7)$$

Hence, using Eqs. (4) and (7), the likelihood function is shown in Eq. (8).

$$p(\hat{f}, \hat{\Psi}|\theta) = \exp\left[-\frac{1}{2k^2}J(\theta)\right] \prod_{r=1}^{N_m} \frac{1}{2\pi k^2} \quad (8)$$

where $J(\theta)$ is given as in Eq. (9).

$$J(\theta) = \sum_{r=1}^{N_m} \left[\left(\frac{\hat{f}_r - f_r(\theta)}{\hat{f}_r} \right)^2 + \left(1 - |\hat{\Psi}_r \Psi_r(\theta)|^2 \right) \right] \quad (9)$$

The final expression for the posterior PDF is shown in Eq. (10).

$$p(\theta|\hat{f}, \hat{\Psi}) = k_2 \exp\left[-\frac{1}{2k^2}J(\theta)\right] \quad (10)$$

where k_2 is a normalizing constant.

2.2 Sampling Technique for Model Updating

In this work, MCMC technique is used to sample from the posterior PDF for model updating. Conventionally, Metropolis–Hastings (MH) algorithm [33, 34] is used to sample from the posterior PDF but as described in [26], owing to narrow concentration of parameters space of interest corresponding to the important region of the posterior PDF; it is not trivial to simply apply MH algorithm to draw samples from posterior PDF in FE model updating. Also, further problem arises in case of multimodal (multiple peaks) posterior PDF leading to non-ergodic Markov chain [27]. In such cases, modified versions of MH algorithm, viz. enhanced-MCMC [29–32] and transitional MCMC or TMCMC [27] are employed in this paper for successful model updating of a structure. A detailed explanation of enhanced-MCMC and TMCMC are

seen in [29–32] and [27], respectively. It may be mentioned that both the MCMC techniques employ MH algorithm and the technique of mode matching is required as can be evident from the expression of likelihood shown in Eq. (10). Hence, another important algorithm of MCMC known as Gibbs sampling [38] has been adopted where no mode-matching procedure is required. The basic principle of Gibbs sampling technique can be well understood from [38] where formulation for the conditional PDF of unknown parameters, given value of other parameters, are utilized for sampling. Though uniform distribution for the prior PDF of the updating parameters is assumed in case of enhanced-MCMC and TMCMC; normal distribution is assumed in case of Gibbs sampling as adopted in [38]. Also, it is to be noted that the prior PDF of updating parameters following normal distribution with large variances or prior PDF following uniform distribution is observed to yield quite similar results for MCMC techniques adopted in this paper. One important quality of Gibbs sampling technique is the full acceptance of all samples generated unlike the usual MH algorithm where samples are accepted based on an acceptance/rejection criterion. In model updating using Gibbs sampling [39–41], sub-structuring of the structural matrices corresponding to each of the updating parameters is required. Sub-structuring of matrices is difficult to perform in case of model updating using commercial software especially when the structural matrices are non-linear functions of the updating parameters. Hence in this paper, updating parameter is selected in such a way that the structural matrices are linear functions of the updating parameter so that the sub-structuring structural matrices are constant and less complicated to obtain.

3 Numerical Validation Using Commercial FE Software

3.1 Description of the Structure

In the present work, a complex structure in the form a cantilever plate consisting of 12 shell elements is considered. Computer programming for the FE modelling of such structures is not easy to generate. Thus, use of commercial FE software can be very much helpful in FE model updating of any complex structure. In this paper, FE model of the plate structure is created using SAP2000 version 15, which is one of the most popular and commercially used FE software. The plate considered in this example is a cantilever rectangular plate consisting of 96 DOFs. As shown in Fig. 1., the plate consists of 12 shell elements each having a thickness of 4 mm, Young's modulus of 2.1×10^{11} N/m² and density 7800 kg/m³. To simulate the experimental data, damage is simulated in the structure and it is performed by discretizing one of the shell elements into 100 shell elements and reducing the Young's modulus of 9 elements to 1.2×10^{11} N/m² as shown in Fig. 2. First, five modes corresponding to the damaged structure are considered for model updating. A total of 16-DOFs along z-direction or out of plane directions associated with all joints corresponding to all the unrestrained joints of the analytical model are considered as measured DOFs. It may be mentioned that

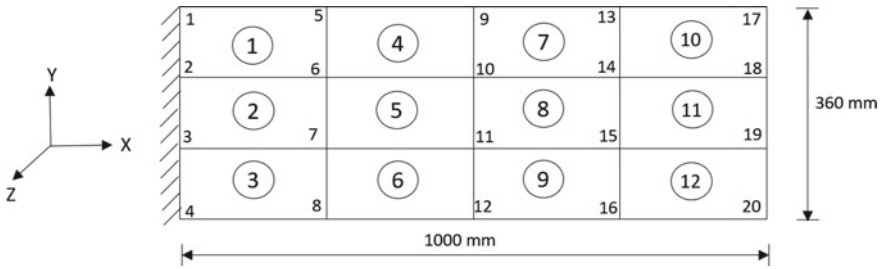


Fig. 1 Analytical model of the plate structure

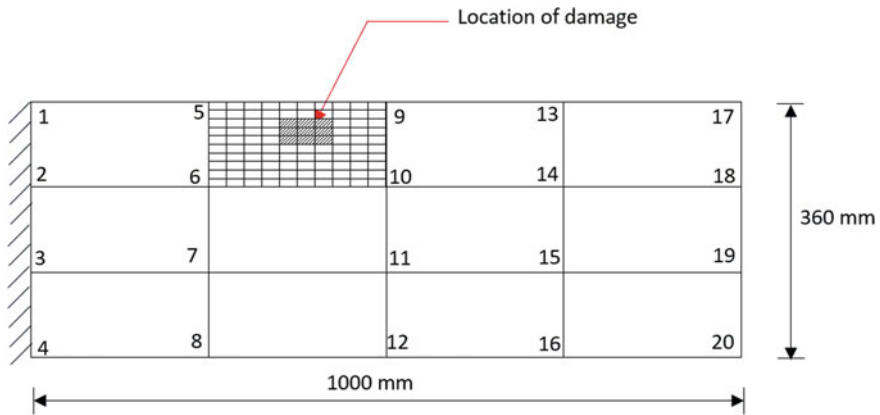


Fig. 2 Simulation of damage in the plate structure

zero mean 1% Gaussian noise has been added to the actual frequencies and mode shapes of the damaged model to implement realistic modal data. Comparison of modal properties of the analytical and damaged structure in terms of frequencies and modal assurance criterion (MAC) values are shown in Table 1. The process of model updating discussed in Sect. 2 in Bayesian framework using both enhanced-MCMC and TMCMC employing MH algorithm and also Gibbs sampling is performed using

Table 1 Comparison of modal properties of damaged plate and undamaged (analytical) plate

Mode no.	Frequencies (Hz)			MAC values
	Experimental (damaged)	Analytical (undamaged)	Error (%)	
1	3.14	3.32	5.56	0.9999
2	17.02	17.41	2.23	0.9979
3	18.35	19.45	5.97	0.9948
4	47.65	51.65	8.41	0.6199
5	51.04	52.14	2.15	0.7821

a computational framework based on interactions between MATLAB and SAP2000 using SAP OAPI, where the structural matrices are extracted from SAP2000 and imported into MATLAB for its further usage in the updating procedure.

3.2 Selection of Updating Parameter

The updating parameters considered in this example initially is the Young’s modulus (E) of the shell elements, making a total of 12 updating parameters. The updating procedure starts by detection of location of modelling errors by performing error localisation technique using a force balance method [36]. In this technique, an error vector is obtained for each mode as shown in Eq. (11).

$$[K_a - \hat{\lambda}^{(r)}M_a]\Phi_e^r = [e_r] \tag{11}$$

where M_a , K_a are the analytical mass and stiffness matrices, $\hat{\lambda}^{(r)}$ is the r th experimental eigenvalue, Φ_e^r is the r th experimental eigenvector and e_r is the error vector for r th mode. It may be mentioned that the measured mode shape is limited to fewer DOFs due to limitation in number of sensors in ideal situations. Hence, the experimental mode shape shown in Eq. (11) is obtained by expanding the actual measured mode shape corresponding to all DOFs of the analytical model using system equivalent reduction expansion process (SEREP) [44]. The average of the error vector for all the measured modes and corresponding to only the measured DOFs is calculated and shown schematically in Fig. 3. From careful evaluation of the figure of error localisation shown in Fig. 3, it shows that dominant errors in the analytical model are located around the simulated damaged plate element location. It is a known fact that the performance of updating procedure is satisfactory if the number of updating parameters is small. Considering this issue, a sensitivity study as described in [37] is performed on the updating parameters, where sensitivity of an objective function

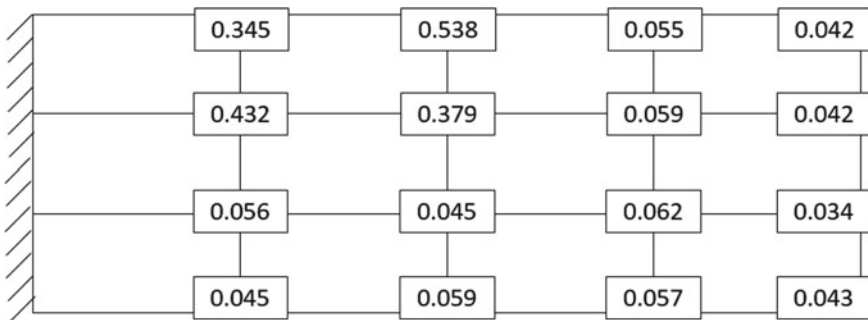


Fig. 3 Error localisation using force balance method



Fig. 4 Schematic diagram of the sensitivity study (blue colour indicates positive value of sensitivity value and white colour indicates negative value)

with respect to each updating parameter is calculated. Two neighbouring parameters are merged into one if the sign of their sensitivities are same. The objective function used for this example is the expression of $J(\theta)$ shown in Eq. (9). The schematic diagram of the sensitivity study is shown in Fig. 4 where elements showing positive and negative sensitivities are presented.

After examining the results shown in Figs. 3 and 4, the updating parameter considered in this example is Young’s modulus corresponding to fourth plate element as shown in Fig. 1. It may be mentioned that Gibbs sampler demands sub-structuring of stiffness matrix for performing parameterization procedure. Typical parameterization of a stiffness matrix is shown as in Eq. (12).

$$K(\theta) = K_0 + \sum_{l=1}^{N_\theta} \theta_l \times K_l \tag{12}$$

where the symbols have usual meanings as already discussed in [1]. However, in our example, Eq. (12) can be written as shown in Eq. (13).

$$K(\theta) = K_0 + E_4 K_S \tag{13}$$

where E_4 is the updating parameter, i.e. Young’s modulus (E) of the fourth plate element and K_S is the sub-matrix of the stiffness matrix associated with E_4 . Usually, K_S is obtained as $K_S = \frac{\partial K}{\partial E_4}$ but this procedure is not likely to be possible while employing commercial software as in SAP2000. In this example, K_S is obtained using a technique as shown in Eq. (14).

$$K_S = K(E_S) \tag{14}$$

where $E_S = (E_1, E_2, \dots, E_{12})$ and E_i is the Young’s modulus of the i th plate element such that $E_l = 0$ for all values of l except $l = 4$ and $E_4 = 1$. On the other hand, the

non-parameterized part of the stiffness matrix K_0 is obtained as in Eq. (15).

$$K_0 = K(E_0) \tag{15}$$

where $E_0 = (E_1, E_2, \dots, E_{12})$ such that $E_l = 2 \times 10^{11} \text{ N/m}^2$ for all values of l except $l = 4$ and $E_4 = 0$. The technique of obtaining the sub-matrix K_S is possible due to the fact that the stiffness matrix is linear function of the updating parameter E_4 . It is not likely to obtain the sub-matrix using commercial software like SAP2000 if the stiffness matrix is non-linear function of the updating parameters because in such situations the sub-matrix K_l associated with the updating parameter θ_l can be obtained only using $K_l = \frac{\partial K}{\partial \theta_l}$ unlike the procedure shown in Eq. (14).

4 Results and Interpretation

The model updating of the plate structure described in Sect. 3 is performed using the sampling techniques of MCMC incorporating MH algorithm, viz. enhanced-MCMC and TCMC and another incorporating Gibbs sampling algorithm as presented in Sect. 2. Apart from this basic difference of employing sampling algorithm, another difference in requirement of mode matching is noteworthy. In this paper, out of the three sampling techniques employed in updating the structure, enhanced-MCMC and TCMC require mode-matching procedure while Gibbs sampling method does not require mode matching between the experimental and analytical modes.

Updating performance of natural frequencies for the damaged plate structure using enhanced-MCMC, TCMC and Gibbs sampling is shown in Fig. 5. As may

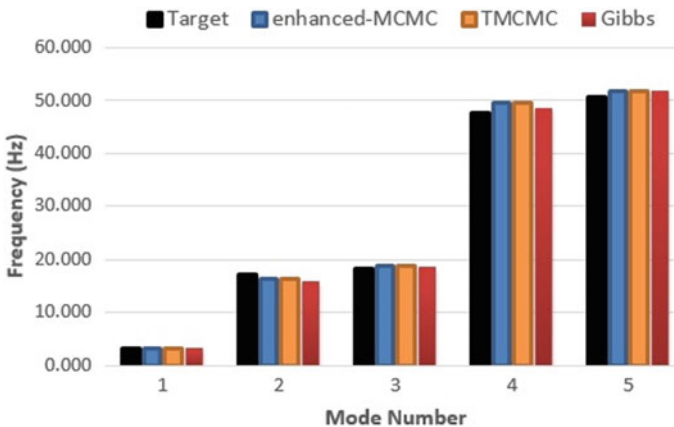


Fig. 5 Comparison of target and updated frequencies using enhanced-MCMC, TCMC and Gibbs sampling

Table 2 MAC values after updating using enhanced-MCMC, TCMCM and Gibbs sampling

Mode no.	Enhanced-MCMC	TCMCM	Gibbs sampling
1	0.9999	0.9999	0.9998
2	0.9979	0.9982	0.9894
3	0.9974	0.9980	0.9846
4	0.9792	0.9786	0.9755
5	0.9841	0.9837	0.9822

Table 3 Updated values of stiffness parameter and its COV after updating using enhanced-MCMC, TCMCM and Gibbs sampling

	Enhanced-MCMC	TCMCM	Gibbs sampling
Young’s modulus (E) ($\times 10^{11}$ N/m ²)	0.7826	0.7722	0.3978
Updated COV	0.092	0.1777	1.1648

be observed from Fig. 5, performance in matching of frequencies is quite similar to enhanced-MCMC and TCMCM and slightly better in comparison to Gibbs sampling for first two modes while Gibbs sampling perform better for the last three modes. On the other hand, performance in updating of mode shapes (modal assurance criteria (MAC) values between initial and target mode shapes) is also shown in Table 2. It may be mentioned that the MAC values are closer to unity in case of enhanced-MCMC and TCMCM in comparison to Gibbs sampling. Also, the updated values of the stiffness parameter or Young’s modulus (E) of the damaged plate element and also their updated COV values are shown in Table 3 for all the three sampling techniques, where the COV values are smallest for enhanced-MCMC followed by TCMCM and Gibbs sampling. It may be mentioned that the parameter (A) [29–32] in case of enhanced-MCMC and (β) in case of TCMCM [27] are utilized for controlling the variance of the posterior PDF from one level to another. The value of ‘ A ’ controls the rate at which variance k^2 shown in Eq. (10) of the likelihood function reduces from one level to another with its value equal to unity at first level. On the other hand, the value of ‘ β ’ controls the constant rate at which the power of the likelihood function increases from zero in first level to unity in final level. The updating results are obtained using the values of ($A = 1.1$) and ($\beta = 0.0344$) in case of enhanced-MCMC and TCMCM respectively for model updating of the plate structure. On the other hand, number of samples obtained using Gibbs sampling after disregarding the built-in period is 54,803. Both the MCMC techniques employing multi-level MH algorithm, viz. enhanced-MCMC and TCMCM generate samples multiple times (i.e. multiple levels) instead of generating samples once, where PDF of proposal distribution of a particular level is estimated based on the samples of previous level as explained in [27, 29]. It may be mentioned that the assumption of the initial values of the updating parameters at the start of the MCMC simulation plays a little role in the updating performance. Values quite apart from nominal values tend to have a little larger burn-in period of the Markov chain samples in comparison to that initial

values close to the target values, thereby increasing the required number of samples by little margin. Apart from that, Markov chain samples obtained after disregarding the burn-in samples, through these MCMC techniques have shown similar convergence regardless of the initial assumed values of the parameters. It is to be noted that computation time depends on number of sampling levels in case of enhanced-MCMC and TMCMC and on number of samples (i.e. number of sampling-iterations) in case of Gibbs sampling where the values of algorithmic parameter (A) and (β) influence the performance of enhanced-MCMC and TMCMC. Also, the different values of algorithmic parameter (A) for enhanced-MCMC are considered as 2.5, 2, 1.8, 1.5, 1.2 and 1.1 while different values of algorithmic parameter (β) for TMCMC are considered as 0.25, 0.111, 0.0714, 0.0526, 0.0416 and 0.0344. In such quantification of computational efficiency, a single computer (make: Dell Inc., model: OptiPlex 9020) is used having RAM: 4096 MB and hard disk drive: 500 GB. Computational efficiency of the three MCMC techniques is shown in Fig. 6 based on modal distance

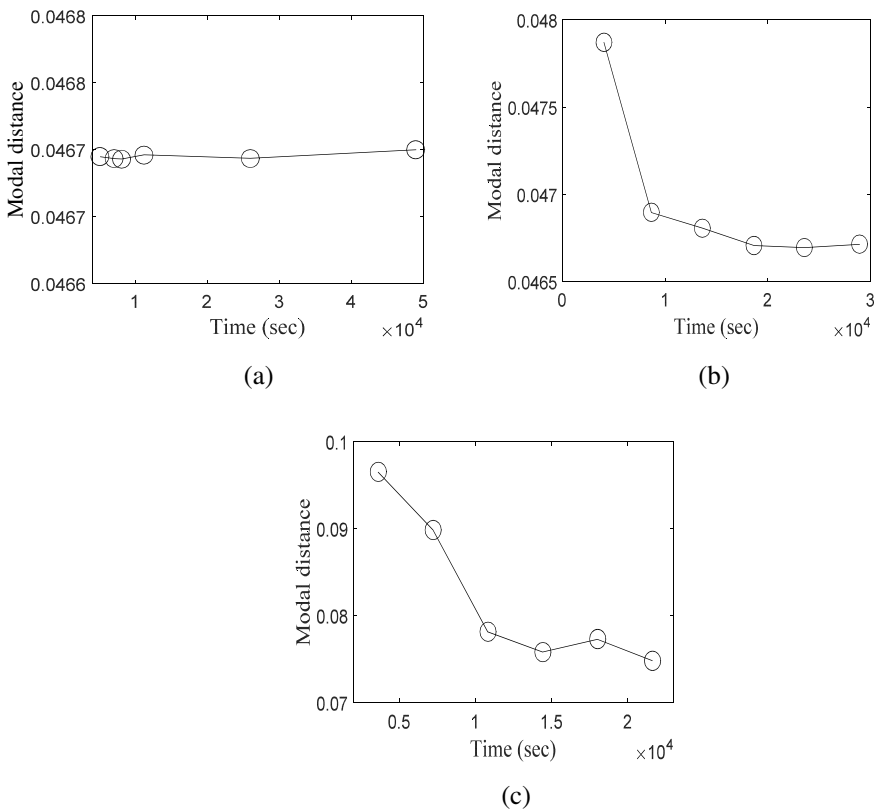


Fig. 6 Evolution of modal distance versus time taken of (a) enhanced-MCMC (b) TMCMC and (c) Gibbs sampling using SAP2000

(shown in Eq. (12)) against the time taken and it has been observed that the enhanced-MCMC and TMCMC perform better in comparison to Gibbs sampling. Additionally, a number of levels of sampling (for enhanced-MCMC and TMCMC) and number of samples generated (for Gibbs sampling) are also plotted (as shown in Fig. 7) against time taken for more lucid observation on computational efficiency. In order to study the final samples obtained using these MCMC techniques, histogram of the final level samples for enhanced-MCMC and TMCMC and all the samples after disregarding the burn-in samples for Gibbs sampling are shown in Fig. 8. From studying the histogram of the final samples in Fig. 8, samples show close to bell shaped normal distribution for enhanced-MCMC, while the samples are slightly more dispersed for TMCMC and samples are skewed similar to lognormal distribution or gamma distribution for Gibbs sampling. Many diagnostic criteria (e.g. the Gelman–Rubin convergence statistic [45]) can be adopted for testing the convergence of the Markov chain samples that are generated. Also, the convergence of the samples obtained can

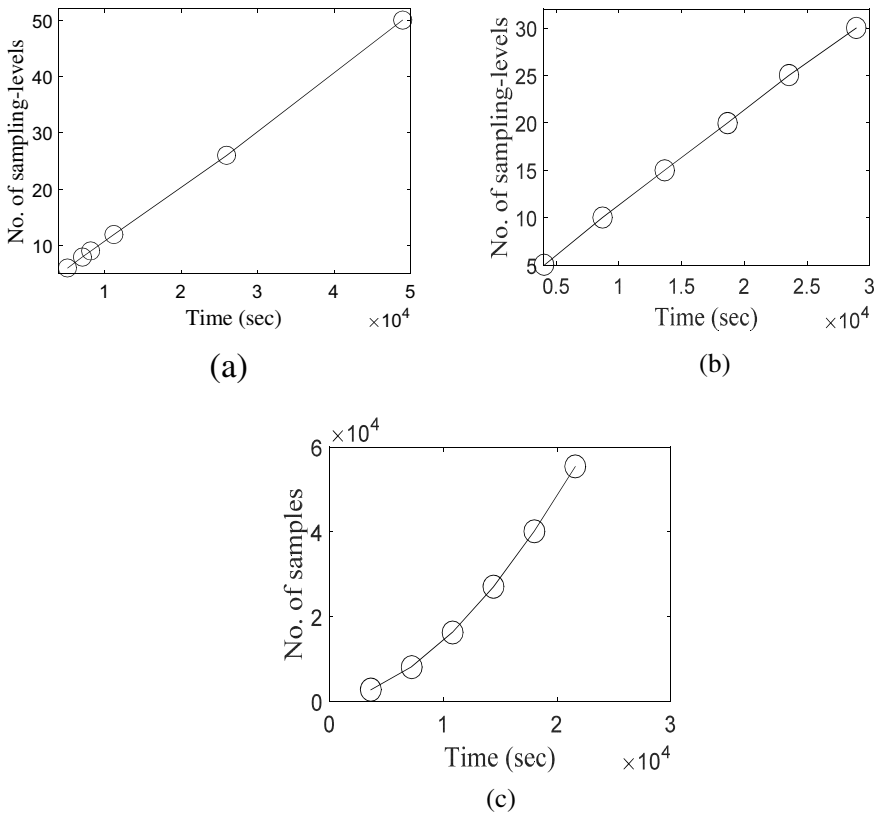


Fig. 7 Number of sampling levels/samples versus time taken of (a) enhanced-MCMC (b) TMCMC and (c) Gibbs sampling

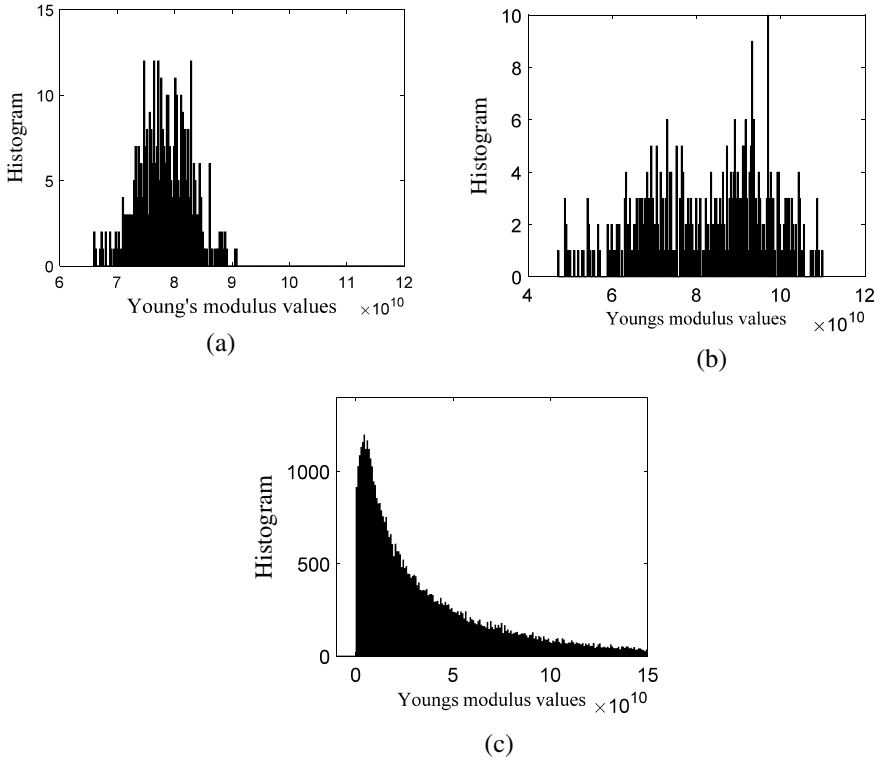


Fig. 8 Histogram of final samples of stiffness parameters using values (a) enhanced-MCMC, (b) TCMC and (c) Gibbs sampling

also be studied from a simple and effective method of visual inspection which is also adopted in this paper.

5 Conclusion

The FE model updating of a reasonably complex structure in the form of a cantilever plate using sampling techniques popularly known as MCMC is performed with the help of a commercially recognized FE software SAP2000 since it is not easy to write a computer program for FE modelling of any complex structure. In this paper, two MCMC techniques which employ MH algorithm in multiple levels, viz. enhanced-MCMC and TCMC are employed in updating the structure which requires mode-matching procedure. Besides, Gibbs sampling is also adopted in updating of the structure which does not require mode-matching procedure but the procedure of sub-structuring of the structural matrices is required. The procedure of sub-structuring of the stiffness matrix in this paper with respect to the updating

parameter is accomplished by employing SAP2000 since this method is required in successfully performing the Gibbs sampling. It may be mentioned that the computational framework of the updating procedure is accomplished by the interaction of SAP2000 and MATLAB using SAP OAPI, which proves to be an effective application programming interface. It may be mentioned that other open-source programs like Python and R can also be utilized in place of MATLAB for this study. Performances of the MCMC techniques for model updating of the structure are studied for a damage scenario which is incorporated by damaging one of the plate elements of the structure. Besides, computational efficiency of all the MCMC techniques is also studied. It has been observed that the technique of enhanced-MCMC performs the best out of the three chosen techniques followed by TMCMC and Gibbs sampling in successfully updating the structure.

References

1. Friswell MI, Mottershead JE (1995) Finite element model updating in structural dynamics. Kluwer Academic Publishers, Boston
2. Ewins DJ (2000) Adjustment or updating of models. *Sadhana* 25:235–245
3. Mottershead JE, Friswell MI (2001) Physical understanding of structures by model updating. In: Proceedings of the international conference on structural identification, Kassel, Germany, pp 81–96
4. Mottershead JE, Friswell MI (1993) Model updating in structural dynamics: a survey. *J Sound Vib* 167:347–375
5. Baruch M (1978) Optimization procedure to correct stiffness and flexibility matrices using vibration tests. *AIAA J* 16:1208–1210
6. Baruch M (1982) Methods of reference basis for identification of linear dynamic structures. In: Proceedings of the 23rd structures, structural dynamics and material conference, New Orleans, Louisiana, May pp 557–563
7. Baruch M (1984) Methods of reference basis for identification of linear dynamic structures. *AIAA J* 22(4):561–564
8. Baruch M, Bar-Itzhack IY (1978) Optimal weighted orthogonalization of measured modes. *AIAA J* 16(4):346–351
9. Berman A, Nagy EG (1983) Improvement of large analytical model using test data. *AIAA J* 21(8):1168–1173
10. Caesar B (1986) Update and identification of dynamic mathematical models. In: Proceedings of the fourth international modal analysis conference, Los Angeles, pp 394–401
11. Caesar B (1987) Updating system matrices using modal test data. In: Proceedings of the fifth international modal analysis conference, London, England, April, pp 453–459
12. Wei FS (1990) Analytical dynamic model improvement using vibration test data. *AIAA J* 28(1):175–177
13. Friswell MI, Inman DJ, Pilkey DF (1998) The direct updating of damping and stiffness matrices. *AIAA J* 36(3):491–493
14. Mottershead JE, Link M, Friswell MI (2011) The sensitivity method in finite element model updating: a tutorial. *Mech Syst Sig Process* 25:2275–2296
15. Yang YB, Chen YJ (2010) Direct versus iterative model updating methods for mass and stiffness matrices. *Int J Struct Stab Dyn* 10:165–186
16. Lin RM, Ewins DJ (1994) Analytical model improvement using frequency response functions. *Mech Syst Sig Process* 8(4):437–458

17. Imregun M, Visser WJ, Ewins DJ (1995) Finite Element model updating using frequency response function data—I theory and initial investigation. *Mech Syst Sig Process* 9(2):187–202
18. Beck JL (1996) System identification methods applied to measured seismic response. In: *Proceedings of the eleventh world conference on earthquake engineering*
19. Beck JL, Katafygiotis LS (1998) Updating models and their uncertainties. I: Bayesian statistical framework. *J Eng Mech* 124(4):455–461
20. Vanik MW, Beck JL, Au SK (2000) Bayesian probabilistic approach to structural health monitoring. *J Eng Mech* 126(7):738–745
21. Yuen KV (2006) An extremely efficient finite-element model updating methodology with applications to damage detection. In: *Proceedings of enhancement and promotion of computational methods in engineering and science X*, Sanya, Hainan, China, August 21–23, pp 166–179
22. Yuen KV, Beck JL, Katafygiotis LS (2006) Efficient model updating and health monitoring methodology using incomplete modal data without mode matching. *Struct Control Health Monit* 13:91–107
23. Yuen KV (2010) *Bayesian methods for structural dynamics and civil engineering*. Wiley (Asia) Private Limited, Chichester, UK
24. Mustafa S, Debnath N, Dutta A (2015) Bayesian probabilistic approach for model updating and damage detection for a Large Truss Bridge. *Int J Steel Struct*
25. Das A, Debnath N (2018) A Bayesian finite element model updating with combined normal and lognormal probability distributions using modal measurements. *Appl Math Model* 61:457–483
26. Beck JL, Au SK (2002) Bayesian updating of structural models and reliability using Markov Chain Monte Carlo simulation. *J Eng Mech* 128(4):380–391
27. Ching J, Chen YC (2007) Transitional Markov Chain Monte Carlo method for Bayesian model updating, model class selection, and model averaging. *J Eng Mech* 133(7):816–832
28. Cheung SH, Beck JL (2009) Bayesian model updating using hybrid Monte Carlo simulation with application to structural dynamic models with many uncertain parameters. *J Eng Mech* 135(4):243–255
29. Lam HF, Yang J, Au SK (2015) Bayesian model updating of a coupled-slab system using field test data utilizing an enhanced Markov chain Monte Carlo simulation algorithm. *Eng Struct* 102:144–155
30. Lam HF, Hu J, Yang JH (2017) Bayesian operational modal analysis and Markov chain Monte Carlo-based model updating of a factory building. *Eng Struct* 132:314–336
31. Lam HF, Alabi SA, Yang JH (2017) Identification of rail-sleeper-ballast system through time-domain Markov chain Monte Carlo-based Bayesian approach. *Eng Struct* 140:421–436
32. Lam HF, Yang JH, Hu Q, Ng CT (2018) Railway ballast damage detection by Markov chain Monte Carlo-based Bayesian method. *Struct Health Monit* 17(3):706–724
33. Metropolis N, Rosenbluth AW, Rosenbluth MN, Teller AH, Teller E (1953) Equation of state calculations by fast computing machines. *J Chem Phys* 21(6):1087–1092
34. Hastings WK (1970) Monte Carlo sampling methods using Markov Chains and their applications. *Biometrika* 57(1):97–109
35. CSI Computer & Structures Inc. (2009) *Three dimensional static and dynamic finite element analysis and design of structures*. SAP2000, Computer & Structures, Inc., Berkeley, CA
36. Fissette E, Stavriniadis C, Ibrahim S (1988) Error location and updating of analytical dynamic models using a force balance method. In: *Proceedings of the 6th international modal analysis conference*, Kimssimnee, FL, pp 1183–1190
37. Kim GH, Park YS (2008) An automated parameter selection procedure for finite-element model updating and its applications. *J Sound Vib* 309:778–793
38. Geman S, Geman D (1984) Stochastic Relaxation, Gibbs Distributions, and the Bayesian Restoration of Images. *IEEE Trans Pattern Anal Mach Intell* 6(6):721–741
39. Ching J, Muto M, Beck JL (2006) Structural model updating and health monitoring with incomplete modal data using Gibbs sampler. *Comput Aided Civ Infrastruct Eng* 21:242–257
40. Bansal S (2015) A new Gibbs sampling-based Bayesian model updating approach using modal data from multiple setups. *Int J Uncertainty Quantif* 5(4):361–374

41. Cheung SH, Bansal S (2017) A new Gibbs sampling based algorithm for Bayesian model updating with incomplete complex modal data. *Mech Syst Sig Process* 92:156–172
42. MATLAB 2015a, The MathWorks, Inc.: 2015.
43. Bernardo JM, Smith AFM (2000) Bayesian theory. Wiley, England
44. O'Callahan J, Avitabile P, Riemer R (1989) System equivalent reduction expansion process (SEREP). *IMAC VII*:29–37
45. Gelman AB, Rubin DB (1992) Inference from iterative simulation using multiple sequences. *Stat Sci* 7:457–472

Stochastic Structural Optimization of Multiple Tuned Mass Damper (MTMD) System with Uncertain Bounded Parameters



Kamalesh Bhowmik and Nirmalendu Debnath

Abstract This study deals with the optimization of parameters of multiple tuned mass damper (MTMD) system for seismic vibration control considering uncertain bounded structural parameters. An approach based on Taylor expansion of objective function along with subsequent interval extension is taken into account in this study. The objective function involving the uncertain bounded parameters is transformed into two independent deterministic sub-problems leading to the lower and upper bound solutions with the help of interval extension. The optimization strategy investigated in this optimization framework is the stochastic structural optimization (SSO) where the root mean square displacement of the primary–secondary coupled system is minimized. A numerical study is performed to observe the effect of uncertainties on the optimization of MTMD parameters where the primary system is coupled with MTMD system with two, three, five and ten mass units. The performance of these MTMD systems is also compared under various levels of uncertainties. Fundamental mode of the system is considered for vibration control, where natural frequency and damping ratio associated with the fundamental mode are found to be nearly 10 rad/s and 0.03, respectively. In this study, natural frequency and damping ratio of the primary system, natural frequency and damping ratio of elastic filter, intensity of the power spectral density of white noise excitation at the bed rock are taken as the uncertain parameters. It is observed that SSO is suitable for higher levels of uncertainties associated with structural parameters. It may be mentioned that such observations are found for various numbers of mass-units of MTMD system.

Keywords Multiple tuned mass damper system · Stochastic structural optimization · Uncertainties

K. Bhowmik · N. Debnath (✉)

Department of Civil Engineering, National Institute of Technology, Silchar, Assam, India
e-mail: nirmalendu.debnath@gmail.com

K. Bhowmik

e-mail: kamaleshbhowmik93@gmail.com

© Springer Nature Singapore Pte Ltd. 2021

S. Adhikari et al. (eds.), *Advances in Structural Technologies*, Lecture Notes in Civil Engineering 81, https://doi.org/10.1007/978-981-15-5235-9_28

381

1 Introduction

The tuned mass damper (TMD) is used as an important passive devices in the area of passive vibration control of structural systems. TMD has been used as dynamic vibration absorber in the investigation of many researchers [1, 2]. It is an interesting area of research at present to examine how tuned mass damper performs under the base-excitation. Multiple tuned mass damper systems are taken in the designing exercise because it performs very well in vibration control [3]. TMD can be designed individually targeting any mode for single degree of freedom (SDOF) system. For multi-degree of freedom (MDOF) system, it can be designed in the same way [4].

In various engineering fields, the standard method to design the vibrating structures is to consider deterministic models and parameters [5]. The uncertainties of different parameters (mechanical characteristics, geometric parameters, external loading) are presented in the designing process for approving the hypotheses. The mean values, extreme values of the parameters can be used for the hypotheses [5]. The analysis of uncertainties is also considered to get optimal design. Tuned mass damper (TMD) has been used [6, 7] in passive vibration control problems to reduce vibrations. Two different processes can be used to define uncertainties: the probabilistic method and the non-probabilistic method [8]. The Monte Carlo simulations [9], the stochastic finite element method, the orthogonal series expansion [8] are under the category of probabilistic method. These methods are used in vibration control problems for various uncertainties. But these methods are not useful, if statistical parameters are not sufficient. Sometimes, parameters are defined in a non-probabilistic process with the help of mean and extreme values. These values are known as uncertain but bounded (UBB) parameters [10]. Interval analysis was introduced in the presence of these kind of parameters for finding the extremum of static response for structures [11, 12]. Nowadays, the extremum of dynamics response is solved by using this process [8, 13]. This interval analysis is also used for the vibration control problems like stochastic structural optimization (SSO) problems [14] and reliability-based optimization (RBO) problems [15]. For these strategies, we have to find the optimal parameters of tuned mass damper for UBB parameters. In stochastic structural optimization problem, the standard deviation of the response of the structure is reduced and for reliability-based optimization problem, a failure probability associated with the response of the structure is reduced. The aim of this investigation is to study and discuss the effectiveness of this strategy for various uncertainty levels associated with the stochastic structural optimization strategy. In this strategy, the optimal values of the MTMD parameters are achieved by reducing the root mean square displacement (rmsd) of the primary–secondary coupled system [R13]. It is observed that SSO is suitable higher levels of uncertainties associated with structural parameters. It may be mentioned that such observations are found for various numbers of mass-units of MTMD system.

2 Structural Model and the Equations

Figure 1 shows the primary system supported by n number of tuned mass dampers which have various dynamic properties. The stiffness, damping constant and mass of the primary system are k_s , c_s , and m_s , respectively. The damping ratio in the primary system is denoted by ξ_s . Similar to the primary system, the stiffness, the damping constant and the mass of the j th TMD are k_j , c_j and m_j , respectively.

The tuning frequency ratio of the MTMD system is expressed by

$$f = \frac{\omega_T}{\omega_S} \tag{1}$$

where ω_s = natural frequency of the primary system.

The natural frequency, ω_j of the j th TMD is expressed by

$$\omega_j = \omega_T \left[1 + \left(j - \frac{n+1}{2} \right) \frac{\beta}{n-1} \right] \tag{2}$$

and

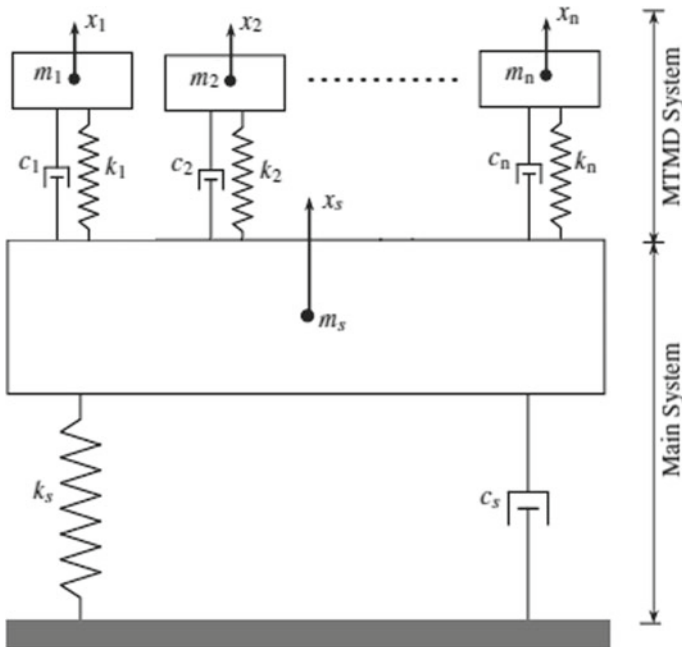


Fig. 1 Structural model of primary system with n numbers of MTMD

$$\omega_T = \sum_{j=1}^n \omega_j/n \tag{3}$$

$$\beta = \frac{\omega_n - \omega_1}{\omega_T} \tag{4}$$

where ω_T = average frequency of all MTMD units; and β = non-dimensional frequency band-width of MTMD system.

The damping constant of the j th TMD is denoted by

$$c_j = 2m_j\xi_T\omega_j \tag{5}$$

where ξ_T is the damping ratio and it is kept constant for all MTMD units.

The mass ratio (μ) of the MTMD system is written as

$$\mu = \frac{\sum_{j=1}^n m_j}{m_s} \tag{6}$$

The equation of motion of the system is

$$[M]\{\ddot{x}\} + [C]\{\dot{x}\} + [K]\{x\} = \{F\} \tag{7}$$

where $[M]$, $[C]$ and $[K]$ are the mass, damping and stiffness matrices, respectively, while $\{F\}$ is force vector.

The matrices, $[M]$, $[C]$ and $[K]$ are expressed as

$$[M] = \text{diag}[m_s, m_1, m_2, m_3, \dots, m_n] \tag{8}$$

$$[C] = \begin{bmatrix} C_S + \sum C_T & -C_T \\ [-C_T]^T & \text{diag}[C_T] \end{bmatrix} \text{ where } C_T = [C_1, C_2, C_3, \dots, C_n] \tag{9}$$

$$[K] = \begin{bmatrix} K_S + \sum K_T & -K_T \\ [-K_T]^T & \text{diag}[K_T] \end{bmatrix} \text{ where } K_T = [K_1, K_2, K_3, \dots, K_n] \tag{10}$$

The state-space covariance matrix R can be solved from the Lyapunov equation [7, 8, 12]:

$$AR + RA^T + B = 0 \tag{11}$$

where the state system matrix A is

$$A = \begin{bmatrix} 0 & I \\ H_K & H_C \end{bmatrix} \tag{12}$$

and where the two sub-matrices H_K and H_C are respectively

$$H_K = \begin{bmatrix} & & & \omega_f^2 & & \\ & & & \omega_f^2 & & \\ & & -(M^{-1}K) & \cdots & & \\ & & & \cdots & & \\ & & & & \cdots & \\ & & & & & \omega_f^2 \\ 0 & \cdots & \cdots & \cdots & \cdots & 0 \end{bmatrix} \tag{13}$$

$$H_C = \begin{bmatrix} & & & 2\xi_f\omega_f & & \\ & & & 2\xi_f\omega_f & & \\ & & -(M^{-1}C) & \cdots & & \\ & & & \cdots & & \\ & & & & \cdots & \\ & & & & & 2\xi_f\omega_f \\ 0 & \cdots & \cdots & \cdots & \cdots & 0 \end{bmatrix} \tag{14}$$

All elements of matrix B are zero except the last element on the main diagonal,

$$B = 2\pi S_0 \begin{pmatrix} 0 & \dots & 0 \\ \vdots & \ddots & \vdots \\ 0 & \dots & 1 \end{pmatrix} \tag{15}$$

Let, the TMD is placed on the primary structure with n_0 degrees of freedom. Then, the root mean square displacement σ_{y_s} (rmsd) and the root mean square velocity $\sigma_{\dot{y}_s}$ (rmsv) of the system are found as follows:

$$\sigma_{y_s} = \sqrt{R(n_0 + 1, n_0 + 1)} \tag{16}$$

and

$$\sigma_{\dot{y}_s} = \sqrt{R(n_0 + n + 2, n_0 + n + 2)} \tag{17}$$

The system matrices (A, B) are considered as uncertain and the parameters of tuned mass damper are optimized for minimizing the objective function. If structural parameters $X = (X_1, X_2, \dots, X_q)$ ($q = \text{no. of uncertain parameters}$) are uncertain but bounded (UBB) parameters, then the better option is to define these parameters using intervals. Let $X = [X_1, X_2, \dots, X_q]$ be the corresponding box and $X_i = [\underline{X}_i, \bar{X}_i]$ be

the corresponding interval. The mean value of X_i is μ_i and the maximum deviation is ΔX_i . Then we can write the UBB parameter as follows:

$$X_i = [\underline{X}_i, \overline{X}_i] = [\mu_i - \Delta X_i, \mu_i + \Delta X_i] = \mu_i + e_\Delta \Delta X_i \quad \text{where } e_\Delta = [-1, 1] \tag{18}$$

If uncertainty level is assumed small, we can extend the response in Taylor series about mean value $\mu = (\mu_1, \dots, \mu_q)$ in the first-order terms of $\delta X_i \in [-\Delta X_i, \Delta X_i]$ as

$$f(X) = f(\mu) + \sum_{i=1}^q \left. \frac{\partial f}{\partial X_i} \right|_{X_i=\mu_i} \tag{19}$$

All derivatives $\partial f / \partial X_i$ are calculated at the mean value of the related uncertain parameter. With the help of interval extension, these UBB parameters are transformed into two functions, one is upper bound function and another is lower bound function. These functions can be written as

$$\overline{f}(X) = f(\mu) + \sum_{i=1}^q \left| \frac{\partial f}{\partial X_i} \right| \Delta X_i \quad \text{and} \quad \underline{f}(X) = f(\mu) - \sum_{i=1}^q \left| \frac{\partial f}{\partial X_i} \right| \Delta X_i \tag{20}$$

The system matrices A and B can be calculated using Taylor expansion. We can obtain the following equations for i th UBB parameter by neglecting the higher order terms:

$$A(\mu)R(\mu) + R(\mu)A(\mu)^T + B(\mu) = 0 \tag{21}$$

$$A(\mu) \frac{\partial R}{\partial X_i} + \frac{\partial R}{\partial X_i} A(\mu)^T + B^u = 0 \tag{22}$$

$$\text{where } B^u = \frac{\partial A}{\partial X_i} R(\mu) + R(\mu) \frac{\partial A}{\partial X_i} + \frac{\partial B}{\partial X_i} \tag{23}$$

3 Optimization Strategies

The TMD optimization problem consists in finding the parameters of TMD such as the optimal natural frequency $\omega_T = \sqrt{k_T/m_T}$ and the damping ratio $\xi_T = c_T/2\sqrt{k_T m_T}$. The mass ratio $\mu = m_T/m_S$ is considered as constant, where m_S = mass of primary system. A common formula [7, 8] of TMD optimization problem is defined as follows:

$$\text{Find } d = (\omega_T, \xi_T) \text{ To minimize OF} \tag{24}$$

where OF is the objective function. This function is correlated to the response of the primary system. In this study, OF is correlated to the displacement response of the primary system say, y_S and the stochastic structural optimization strategy is considered.

The optimal values of the TMD parameters are calculated by reducing the root mean square displacement (rmsd) as defined in Eq. (16). The formulation of the problem can be written as follows [11, 12]:

$$\text{Find } d = (\omega_T, \xi_T) \text{ To minimize } OF_1 = \sigma_{y_s} \tag{25}$$

The objective function OF_1 is UBB parameters' function. This function is approached and extended considering Eqs. (19) and (20) as follows:

$$\bar{\sigma}_{y_s}(x) = \sigma_{y_s}(\mu) + \sum_{i=1}^q \left| \frac{\partial \sigma_{y_s}}{\partial x_i} \right| \Delta x_i \tag{26}$$

$$\underline{\sigma}_{y_s}(x) = \sigma_{y_s}(\mu) - \sum_{i=1}^q \left| \frac{\partial \sigma_{y_s}}{\partial x_i} \right| \Delta x_i \tag{27}$$

$\sigma_{y_s}(\mu)$ can be calculated from Eq. (16) and the sensitivity of rmsd can be calculated as

$$\frac{\partial \sigma_{y_s}}{\partial x_i} = \frac{1}{2} \left(\frac{\partial R(n_0 + 1, n_0 + 1)}{\partial x_i} \bigg/ \sqrt{R(n_0 + 1, n_0 + 1)} \right) \tag{28}$$

The sensitivity of R is found from the solution of Eq. (22). The sensitivity of A and B are found with the help of central finite difference method. The primary SSO problem is transferred into two deterministic independent sub-problems leading to the lower and upper bound solutions. These two sub-problems are as follows:

$$\text{Sub-problem 1 (lower bound) : Find } d = (\omega_T, \xi_T) \text{ To minimize } \underline{\sigma}_{y_s}(x) \tag{29}$$

$$\text{Sub-problem 2 (upper bound) : Find } d = (\omega_T, \xi_T) \text{ To minimize } \bar{\sigma}_{y_s}(x) \tag{30}$$

4 Numerical Study

A numerical study has been considered to examine and discuss the efficiency of the presented technique of optimization strategy. The optimized results for SSO problem are matched with respect to the deterministic optimization. For this investigation, the mean values of the uncertain parameters are taken.

For modelling the base acceleration $\ddot{Y}_b(t)$, the stationary Kanai–Tajimi model [16, 17] is used in this investigation:

$$\begin{aligned} \overline{\ddot{Y}_b(t)} &= \overline{\ddot{Y}_f(t)} + \omega(t) = -\left(2\xi_f\omega_f\overline{\ddot{Y}_f} + \omega_f^2\overline{Y_f}\right) \\ \overline{\ddot{Y}_f(t)} + 2\xi_f\omega_f\overline{\ddot{Y}_f} + \omega_f^2\overline{Y_f} &= -\omega(t) \end{aligned} \tag{31}$$

where $\omega(t)$ = stationary Gaussian zero mean white noise process (its intensity is S_0 which represents the excitation at bed rock), ω_f = frequency of filter, ξ_f = damping ratio of filter.

In this study, natural frequency of primary system, damping ratio of the primary system, natural frequency of elastic filter, damping ratio of elastic filter, intensity of the power spectral density of white noise excitation at bed rock are taken as the uncertain parameters as usually considered by various researchers.

$$X = (\omega_S, \xi_S, \omega_f, \xi_f, S_0) \tag{32}$$

Table 1 shows the mean values of uncertain parameters. Different results of the SSO strategy are shown in Figs. 2, 3, 4, 5, 6, 7, 8, and 9.

The effects of rmsd with respect to different uncertainties are shown in Figs. 2, 3, 4, and 5. The mass ratio is taken as 0.02 and the uncertainty varies from 2.5 to 20%. Four cases of MTMD systems are considered where the primary system is coupled with MTMD system with (i) two mass units (ii) three mass units (iii) five mass units and (iv) ten mass units.

The effects of rmsd with respect to different mass ratios are shown in Figs. 6, 7, 8, and 9. In this case, the mass ratio varies from 0.02 to 1 and the uncertainty is taken as 10%.

From the numerical study, we can see that when the uncertainties are increasing for a fixed mass ratio, the difference between the upper and lower bound of rmsd value is also increasing. But in case of fixed uncertainty, if the value of mass ratio increases, the difference between the upper and lower bound of rmsd value does not increase so much in comparison to the previous case.

Table 1 Mean values of uncertain parameters

Uncertain parameters	ω_S (rad/s)	ξ_S	ω_f (rad/s)	ξ_f	S_0 (m^2S^{-3})
Mean values (μ)	10	0.03	9π	0.04	0.03

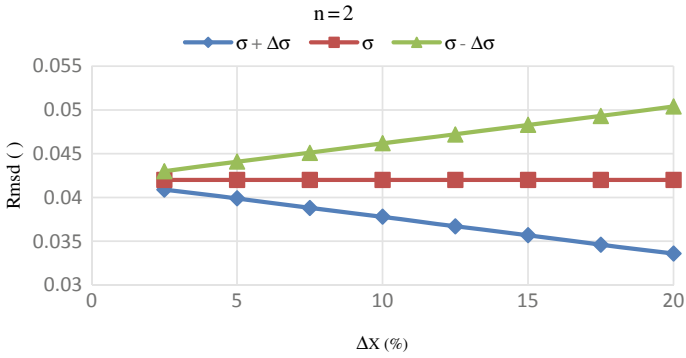


Fig. 2 Optimized root mean square displacement with respect to uncertainty ($n = 2$)

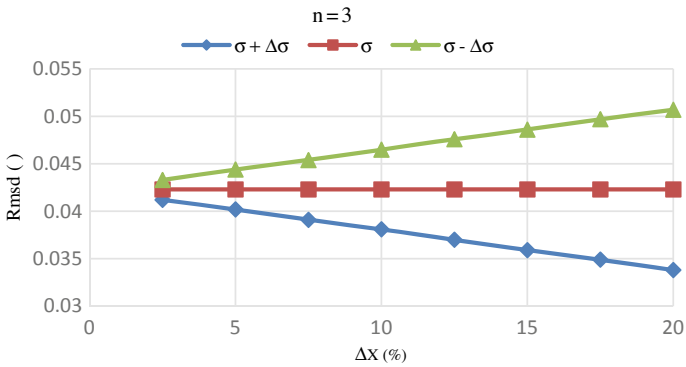


Fig. 3 Optimized root mean square displacement with respect to uncertainty ($n = 3$)

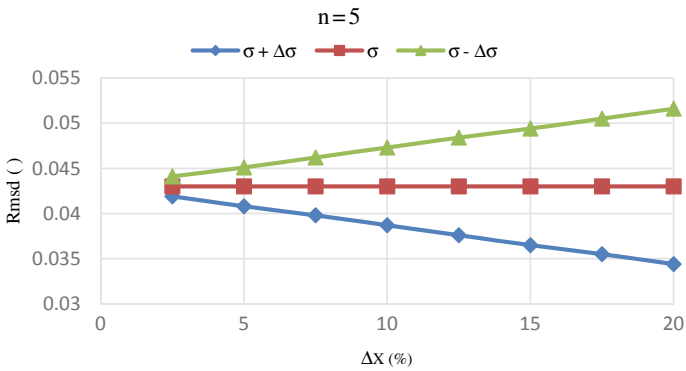


Fig. 4 Optimized root mean square displacement with respect to uncertainty ($n = 5$)

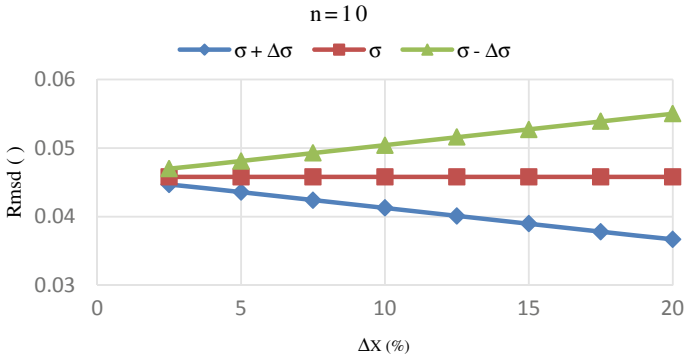


Fig. 5 Optimized root mean square displacement with respect to uncertainty ($n = 10$)

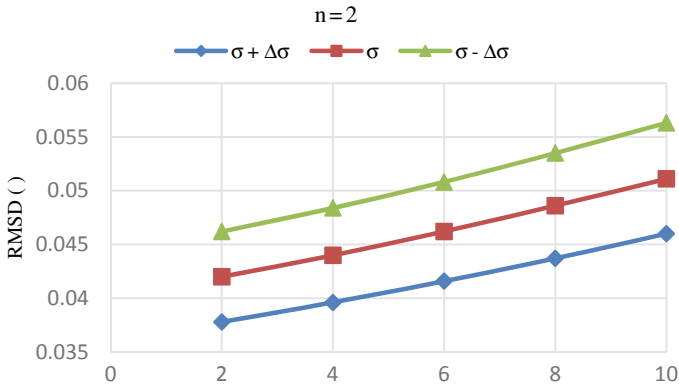


Fig. 6 Optimized root mean square displacement with respect to mass ratio ($n = 2$)

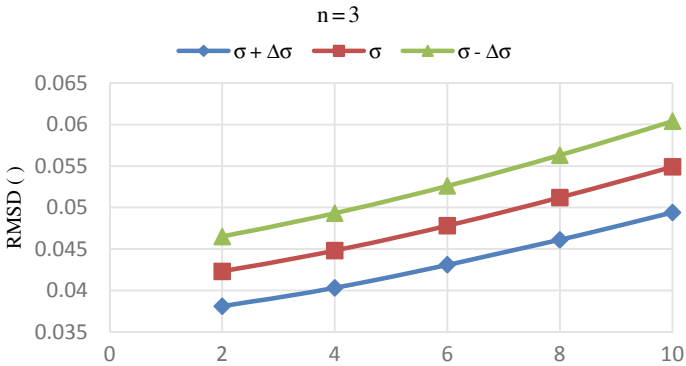


Fig. 7 Optimized root mean square displacement with respect to mass ratio ($n = 3$)

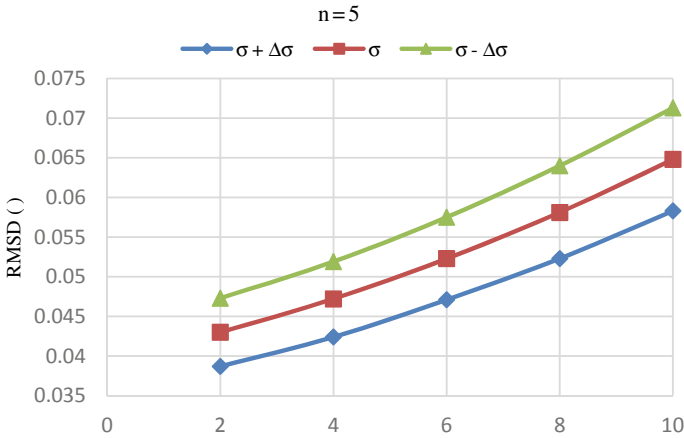


Fig. 8 Optimized root mean square displacement with respect to mass ratio ($n = 5$)

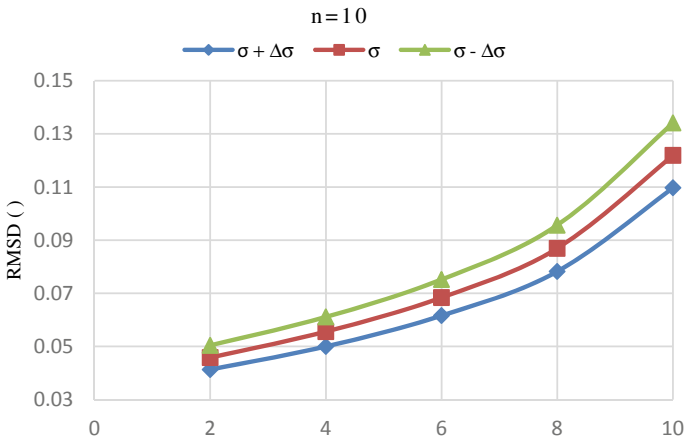


Fig. 9 Optimized root mean square displacement with respect to mass ratio ($n = 10$)

5 Conclusion

In this present work, the stochastic structural optimization of MTMD system considering uncertain bounded structural parameters is studied. The optimum parameters of MTMD system are found in probabilistic framework for different mass ratios and different numbers of MTMD units. The method studied in this paper is about Taylor expansion and it is followed by interval extension. This method has been examined with the stochastic structural optimization strategy. The method allows the primary non-deterministic problem to transfer into two deterministic independent sub-problems in presence of UBB parameters.



From the obtained results, it is observed that when the uncertainties are increasing for a fixed mass ratio, the difference between the upper and lower bound of rmsd value is also increasing. But in case of fixed uncertainty, if the value of mass ratio increases, the difference between the upper and lower bound of rmsd value does not increase so much in comparison to the previous case. So, there is a certain change in the upper and lower bound optimum results, when considering the uncertainties. It is observed that SSO is suitable for higher levels of uncertainties associated with structural parameters. It may be mentioned that such observations are found for various numbers of mass-units of MTMD system.

References

1. Den Hartog JP (1956) *Mechanical vibrations*. McGraw-Hill, New York
2. Ormondroyd J, Den Hartog JP (1928) The theory of the dynamic vibration absorber. *Trans ASME, Appl Mech* 50:9–22
3. Debnath N, Deb SK, Dutta A (2015) Multi-modal vibration control of truss bridges with tuned mass dampers under general loading. *J Vib Control* 22(20):4121–4140
4. Rana R, Soong TT (1998) Parametric study and simplified design of tuned mass dampers. *Eng Struct* 20:193–204
5. Schueller GI, Jensen HA (2008) Computational methods in optimization considering uncertainties—an overview. *Comput Methods Appl Mech Eng* 198:2–13
6. Marano GC, Greco R, Sgobba S (2010) A comparison between different robust optimum design approaches: application to tuned mass dampers. *Probab Eng Mech* 25:108–118
7. Rubio L, Loya JA, Miguelez MH, Fernandez-Saez J (2013) Optimization of passive vibration absorbers to reduce chatter in boring. *Mech Syst Sig Process* 41:691–704
8. Qiu Z, Wang X (2003) Comparison of dynamic response of structures with uncertain-but-bounded parameters using non-probabilistic interval analysis method and probabilistic approach. *Int J Solids Struct* 40:5423–5439
9. Kroese DP, Taimre T, Botev ZI (2011) *Handbook of Monte Carlo methods*. Wiley, Hoboken, New Jersey
10. Muscolino G, Sofi A (2013) Bounds for the stationary stochastic response of truss structures with uncertain-but-bounded parameters. *Mech Syst Sig Process* 37:163–181
11. Liu ZS, Chen SH, Han WZ (1994) Solving the extremum of static response for structural systems with unknown but bounded parameters. *Comput Struct* 50:557–561
12. Qiu Z, Xia Y, Yang J (2007) The static displacement and the stress analysis of structures with bounded uncertainties using the vertex solution theorem. *Comput Methods Appl Mech Eng* 196:4965–4984
13. Qiu Z, Wang X (2009) Vertex solution theorem for the upper and lower bounds on the dynamic response of structures with uncertain-but-bounded parameters. *Acta Mech Sin* 25(3):367–379
14. Mrabet E, Guedri M, Ichchou MN, Ghanmi S (2015) Stochastic structural and reliability based optimization of tuned mass damper. *Mech Syst Sig Process* 60–61:437–451
15. Ranganathan R (1999) *Structural reliability analysis and design*. Jaico publishing house, Mumbai
16. Kanai K (1957) Semi-empirical formula for the seismic characteristics of the ground. *Bulletin of the Earthquake Research Institute, University of Tokyo*. 35:309–324
17. Tajimi, H.: A statistical method of determining the maximum response of a building during earthquake. In: *Proceedings of the of second world conference on Earthquake engineering (1960)*

Hearth Monitoring of Blast Furnace Using Finite Element Analysis and Artificial Intelligence



Debi Prasad Ghosh , Bhaskar Sengupta , and Shyam Krishna Maitra

Abstract Hearth wear profile determines the life of a blast furnace, which is generally monitored by an inverse heat conduction analysis. Numerous thermocouples are embedded in the refractory lining and the temperature readings are used to access the wear profile of the hearth, which provides warnings about the infiltration of liquid iron through the refractory mass to the shell of the blast furnace. Because of the fatal nature of the consequences, accurate predictions about the profile of the inner refractory of the blast furnace are useful for initiating corrective action. This paper describes a method whereby the left out refractory lining profile is estimated as well as the thickness of the protective skull using finite element analysis and artificial intelligence. It serves as a guide to continue the operation of the furnace, to direct repair work to the critical areas, as well as to suggest the replacement of faulty sensors. In the effect, this method serves to increase the working life of blast furnaces.

Keywords Hearth monitoring · Blast furnace · Finite element analysis · Artificial intelligence

Terminologies

- Campaign: The duration of the operation of a Furnace, for one lining.
- Breakout: An accident, when the hot metal infiltrates the refractory layer through to the steel shell of the Furnace.
- Dead Man Zone: An unreactive body of coke at the base of the hearth
- Ramming mass: A refractory mix used to fill gaps
- Hot metal: The metal produced in blast furnaces. Iron with 4%C, at 1450 °C.
- Hearth: The base of the blast furnace holding hot metal formed with refractory material, subject to severe thermal and abrasive wear conditions.
- Tap-hole: An opening through which the hot metal (liquid iron) is extracted.
- Shell: Cylindrical steel lining, which forms a container for the blast furnace.
- Skull: A hard growth of refractory material and charge ore, on the lining.

D. P. Ghosh (✉) · B. Sengupta · S. K. Maitra
Larsen & Toubro Limited, Kolkata, India
e-mail: debiprasadghosh@Intecc.com

- RMS: Root Mean Square of the deviation between calculated and measured temperature values in sensors.
- 1150 °C solidus surface: A temperature contour at 1150 °C, considered to be the solidification location of liquid iron (iron-carbon solidus). Also, considered as the refractory boundary.
- Forward/Inverse Finite Element (FE) problem: Forward refers to the standard FE technique, where the thermal properties are used to solve for the temperature field. Inverse refers to the estimated values of the thermal properties that result in a temperature field that best matches measurements at a few specified locations.

1 Introduction

Blast furnaces are the primary route through which iron is produced. It is a counter current reactor, comprising a vertical steel shell lined internally with refractories. A preheated hot blast of air is forced into the base, hence the name “Blast Furnace”. Raw material as Iron ore together with fuel in the form of coke and fluxes as limestone is charged from the top. Complex reactions in the solid, liquid and gas phases occur, with temperatures in the region of 2000 °C. Liquid iron known as hot metal drips down in the lower third of the furnace at a temperature of 1450 °C, and collects in the lower region known as the hearth, from where it is tapped out through openings called “Tap-holes”.

Typically numerous thermocouples are embedded in the refractories at insertion depths of varying depth (Fig. 1), and temperatures are watched for sudden and unexplained increases. A linear interpolation from dual inline thermocouples is sometimes used to obtain the 1150 °C solidus line (Fig. 2), as 1150 °C is the temperature at which liquid iron solidifies, and can be considered to be the refractory boundary (Fig. 3). The common practice is to derive the remnant refractory thickness based on a linear interpolation of the temperature drop in a pair of inline thermocouples (example: temperatures are 150 and 50 °C in a pair of inline thermocouples placed 100 mm apart, then the linear interpolation would place a point at 1000 mm inline inwards from the inner sensor to be at 1150 °C). This simple method is flawed in that the heat flow in a solid body is a three-dimensional phenomenon, wherein the thermal properties of neighboring bricks influence the heat flux field. It frequently happens that the outer sensor of a pair of thermocouples records, a higher temperature than the inner sensor. Linear interpolation of the pair in such a situation would place the 1150 °C solidus contour line outside the shell of the blast furnace. The liquid hot metal must not touch the steel shell of the blast furnace, where it would melt and pierce the structure, and lead to fatal accidents. This is known as a “Break out”, and is a major concern in the iron-making process.

The finite element analysis [1, 2] is an established method of calculating the flux and temperature fields, and has been employed by many researchers to model the hearth of blast furnaces. A simplified 2D Axis symmetric Mesh (Fig. 4) is considered. The boundary conditions comprise the hot metal temperature (1450 °C) in the interior

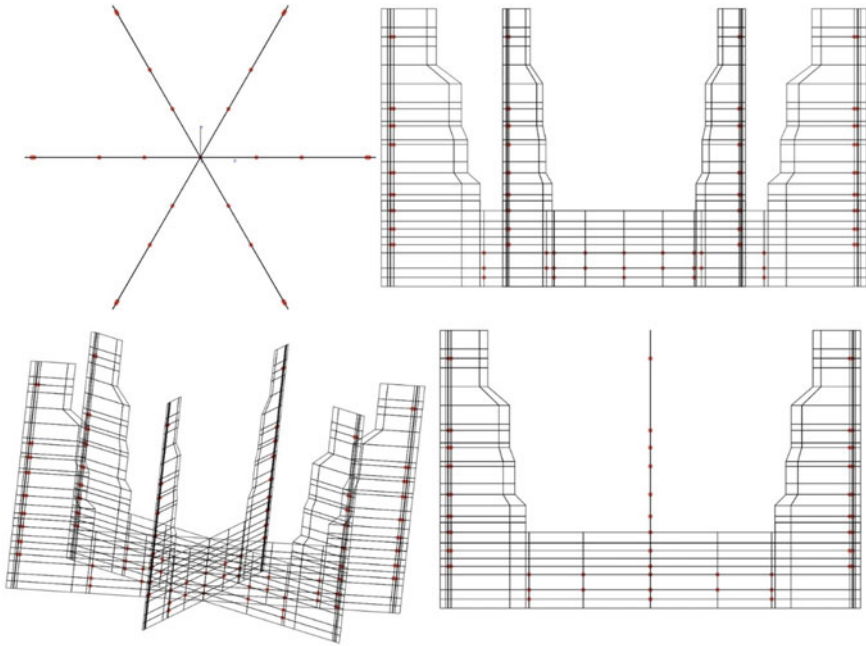


Fig. 1 Typical thermocouple layout in a new blast furnace lining for 6 sectors in different views

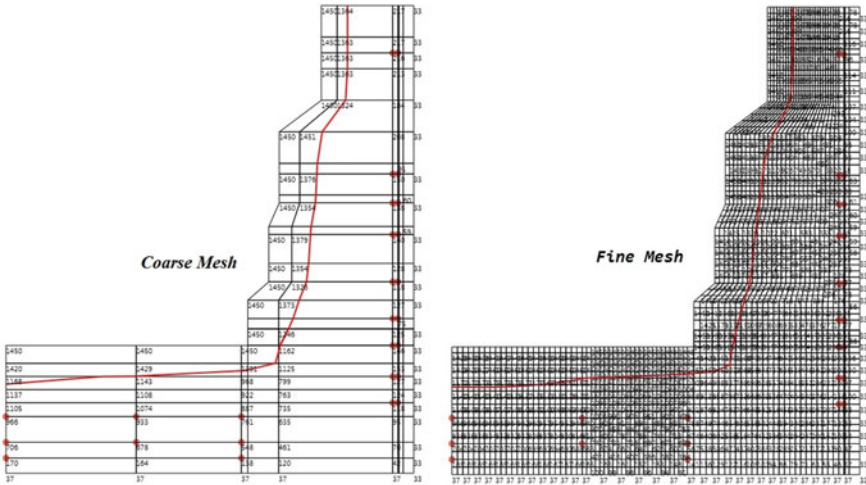


Fig. 2. 1150 °C Isotherm: Computed with Coarse Mesh and Fine Mesh

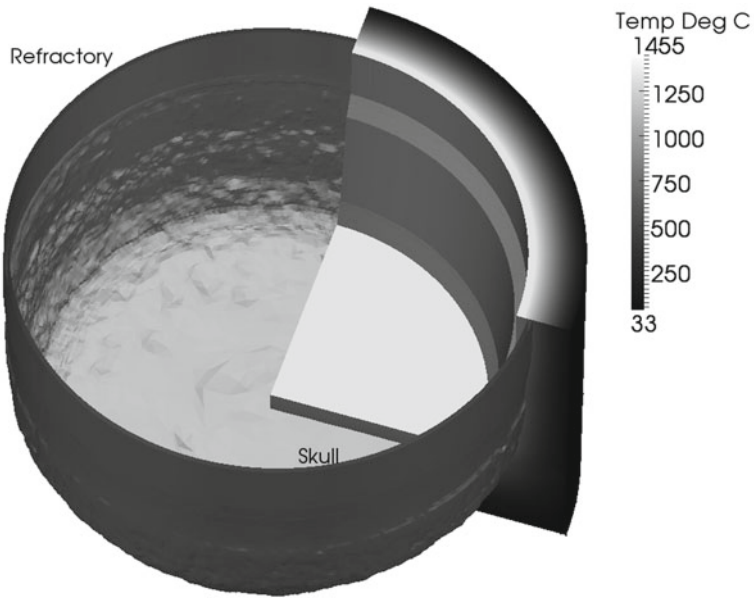


Fig. 3 Refractory boundary and Skull iso-surface 3D rendered. Juxtaposition of the physical picture of an actual hearth

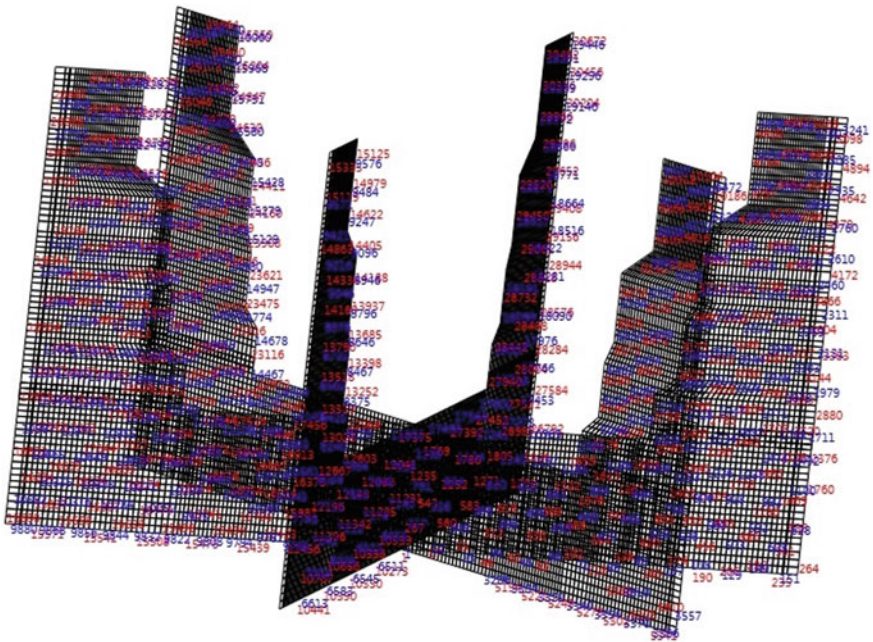


Fig. 4 Fine Mesh of new blast furnace in 6 different sectors

of the furnace, and the ambient temperature (40 °C say) at the exterior of the shell. The temperature and heat fluxes at the mesh are readily computed based on standardized software [3]. In initial conditions, the calculated and the measured temperatures are matched using the model updating from de novo state of blast furnace. But, as time progresses, measured temperatures tend to increase.

The heat in the body of the blast furnace will seek to flow out to the cooler periphery, giving rise to a heat flux. Normally, there would be a smooth gradient of temperatures, assuming isotropic material properties. In practice discrepancies occur. Some of the reasons are as follows:

- Cracks in the refractories: The hot metal enters these spaces. The thermal expansion induces progressive increase in the cracks. The increase in the conductivity causes an increase in the heat flux and so to an increase in temperature.
- Gaps develop between the refractory and the steel shell: The discontinuity provides an impediment to the heat flow, and leads to a rise in the refractory temperature.
- The hot metal fluid flow in the vicinity of the Tap-holes carries an enormous amount of heat flux. This serves to pump up the temperatures where the fluid impinges on the refractory wall.
- The coke body comprising the “Dead Man Zone” influences the metal flow, and directs the fluid stream toward the refractory wall in an unpredictable manner.

Because of these effects, thermocouple temperatures change dynamically, and differ from the static predictions of FE calculations. The problem is to estimate the thermal conductivity of the refractory bricks. As explained above, the properties of the refractories degrade during the course of their service life (Fig. 5).

Cracks in the refractory bricks would impede the heat flow. Conversely, if the interstitial spaces become filled with hot metal which subsequently solidifies, the conductivity would increase. The hot metal is at 1450 °C. At such high temperatures, there is considerable thermal expansion. The outer regions of the furnace being cooled to ambient temperatures would mean that these regions are not subjected to thermal expansion. To compensate for these unequal expansions, a region of about 50 mm is loosely packed with a mixture known as the “ramming mass”. The steel shell would serve to withstand the thermal stresses induced in the inner layers in excess of the compensating ramming mass layers.

While it is theoretically possible to withdraw core samples [4] from the different regions of the refractory bed and experimentally determine the thermal conductivities, such invasive methods would ruin the refractories. The best alternative is to estimate the thermal properties, in a manner that predicts a temperature field that matches the measured values. This is the opposite of the conventional finite element thermal analysis technique, which starts with thermal properties, to deduce a temperature field. In a sense, this is an “Inverse” application [5] of the finite element technique, in that the thermal properties are iteratively searched to provide a matching temperature field. This modified mesh is then used in a 2D axis symmetric FE thermal analysis to derive the refractory wear profile. Zagaria et al. [6] calculated the erosion profile in the hearth lining by combining the online reading of temperatures and historical

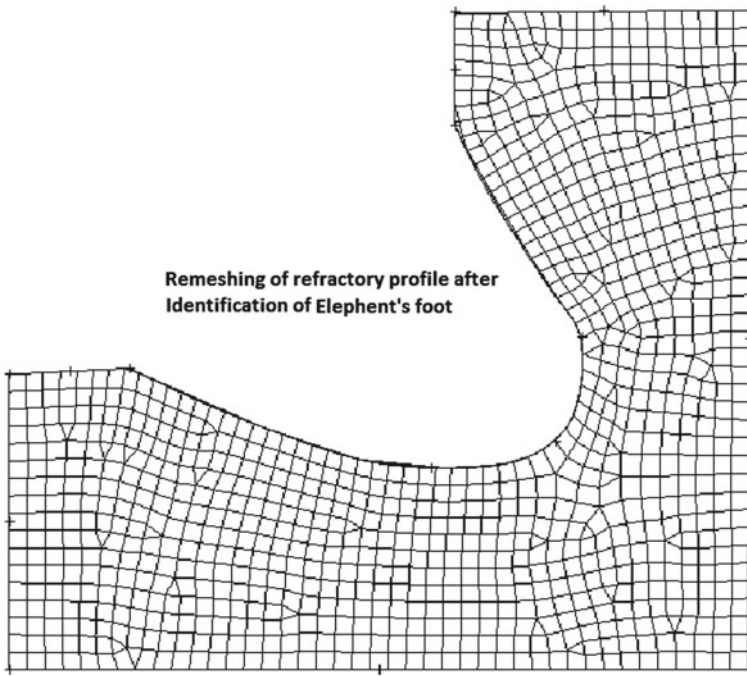


Fig. 6 Re-meshing of refractory profile after knowing size of elephant's foot

2 Methodology

To determine the position of the left out refractory lining in the hearth of a blast furnace, it requires physical measurements of the temperatures inside the refractory lining. The location of these sensors is an input, although the method places no constraints that the thermocouples are to be placed in pair inline. Any arbitrary configuration of thermocouples can be entertained, and equal credence is placed on all the sensors when deriving the refractory profile. Typically about 350 thermocouple sensors are used in hearths of large modern blast furnaces. For this purpose, the structure of the blast furnace hearth is modeled in 6 sectors. The asymmetry introduced by tap-holes is ignored in this description, although it will be apparent that the tap-holes can be readily included in a 3D representation. The 6 sectors are individually analyzed as axi-symmetric 2D FE thermal analysis problems. There are several sensors at the same elevation and insertion depth, spread out circumferentially at different angular locations. In the 3D representation, they can be individually considered, but in the 2D representation, the ones in the same sector at identical height are grouped together and their mean temperature value is taken.

Although, no major iron-making chemical reactions are involved (since the air from the tuyeres enters at a higher level), a complex set of phenomena occur in the hearth of the blast furnace. Several simplifications are made in order to keep the

problem tractable. One of these is that once a refractory means is worn off, it is removed from the model. Since the calculations are based on measured temperatures, this implies that the thermocouples should measure monotonically increasing values. To achieve this, temperatures are stored in a database, and the campaign maxima values are used in the refractory wear calculations. A temporary protective layer forms over the remnant refractory lining, known as the skull. This is also estimated based on the 1150 °C solidus contour line. The difference is that whereas the refractory wear profile is estimated based on the campaign maxima, leading to a monotonically increasing wear profile, the skull is inferred from the current temperatures. If the current temperatures fall, it is reflected in an increased skull layer thickness over the refractory lining. Thus, to calculate the left out refractory thickness, the necessary steps are.

- (a) Determining maximum campaign temperature of the individual sensor of the individual sector;
- (b) Receiving the temperature data from the sensor and recording and storing maximum campaign temperature of an individual sensor of the individual sector in the memory of the computer for providing the stored data when needed during simulation, or optionally recording and storing maximum campaign temperature of an individual sensor of the individual sector in an external memory device, or a repository which when loaded/installed with the computing device for providing the stored data when needed during the simulation;
- (c) Estimating conductivity values of defined refractory bricks from predefined maximum and minimum limit;
- (d) Determining temperature at the location of the sensor using finite element method;
- (e) Selecting conductivity values, whereby the campaign maximum temperature values matches the computed values at the location of the sensor; and
- (f) Determining about 1150 °C isotherm representing the left out refractory lining profile in the hearth of the blast furnace.

The method also estimates the skull profile over left out refractory lining profile in the hearth of an operating blast furnace in the following steps:

- (a) Estimating conductivity values of defined refractory bricks from predefined maximum and minimum limit;
- (b) Determining the temperature at the location of the sensor using finite element method;
- (c) Determining about 1150 °C isotherm representing the skull profile over the left out refractory lining profile in the hearth of the blast furnace.

The initial conductivity values are recorded from the refractory brick manufacturer's specifications. The procedure outlined above has to be executed individually for each of the sectors twice, once with the campaign maxima temperatures to derive the refractory wear profile, and a second time with current temperatures, to derive the skull profile over the worn refractory lining.

Values for conductivity of bricks are initially assumed through a heuristic method. Later artificial intelligence is used to derive the same and improvements in RMS error reduction.

3 Finite Element Formulation

Axis symmetric heat conduction 2D equation is as follows [1, 2]:

$$\frac{1}{r} \frac{\partial}{\partial r} \left(k_r r \frac{\partial T}{\partial r} \right) + \frac{\partial}{\partial z} \left(k_z \frac{\partial T}{\partial z} \right) + Q = 0$$

And the boundary conditions are temperature and temperature gradient (flux) as

$$T|_{bT} = T_{bT}$$

$$n_r k_r \frac{\partial T}{\partial r} + n_z k_z \frac{\partial T}{\partial z} \Big|_{bq} = q_{bq}$$

where

k_r and k_z are thermal conductivities of the material in radial and axial direction, respectively; n_r and n_z are component of boundary in radial and axial direction, respectively; Q is internal heat supply; q_{bq} is flux boundary condition; T_{bT} is temperature boundary condition.

Subsequently, from FEA formulation matrix equation as

$$[C]\{T\} = \{Q\}$$

where

$[C]$ is matrix from conductivity values, similar to stiffness matrix in structural analysis.

$\{Q\}$ is vector coming from heat flux, similar to force vector in structural analysis.

$\{T\}$ are nodal temperatures, which can be obtained by solving the above equation.

4 Artificial Intelligence

Artificial intelligence is used to search the correct value of conductivities of refractories through surrogate models and genetic algorithms. A genetic algorithm [29] is used for global search in the conductivity space and a surrogate model [30] is able to approximate input/output behavior of complex systems.

Genetic algorithm is the population-based, optimization algorithm with mimicking biological evolution on a natural selection process, even for non-differentiable, non-continuous objectives. It is the most successful algorithm among other algorithms in the family of evolutionary computations from single-objective, multi-objective to constrained-optimization problems. The main advantages of genetic algorithm or other evolutionary-based algorithm are its decoupled nature of solution without considering any assumption of the original problem to be optimized. There are many disadvantages in the genetic algorithm, out of which numerical cost of function evaluation for every objective function in every generation in every population is most addressable. Such disadvantages can be removed by Surrogation assisted genetic algorithm, where costly function evaluation is replaced by inference of deep Surrogation.

One of the main motivation behind deep Surrogation is to replace the costly FEA software in the blast furnace operation site, once deep surrogates are trained by training set obtained from the output of FEA software. Out of various types of surrogate model, deep learning [31] based “deep-surrogate” is suitable to explore input vs. output results of FE analysis, which can learn from results without depending on hand-engineering features.

Unlike, support vector machine, in recent development of artificial intelligence, deep learning is gaining importance in the machine learning research today. It works similar to human neocortex, which is capable of transforming the complex input data to learn, and solve different types of complicated tasks efficiently. Specially, if the original domain problem (computational solid mechanics, computational fluid dynamics, computational granular mechanics, computational electro-magnetic, etc.) is computationally expensive such deep-surrogate model can reduce the computational burden through a representative input vs output map of the domain. Many python-based open-source deep learning software are available [32–34]. Input for the model is taken from the conductivity image of the refractory and target is taken as the temperature at the location of sensors. Depending on the mesh, the total of elements for adjustable conductivity differs, hence the input space of the surrogate. But the output space of the surrogate is fixed as the number of temperature sensors used in the model.

Convolutional neural network (CNN) is the main tool behind the recent success of artificial intelligence. Unlike fully connected network, CNN works with share weight architecture through a mathematical operation called convolution. Most of the available deep learning framework works on CNN with square shape input space for 2D convolution. As the 2D-axi-symmetric model is not square in shape (the liquid iron part is out of the FEA model), the use of 2D convolution is difficult. So, 1D convolution [tf.nn.conv1d (input1d, filter)] is used after flattening the conductivity values in one dimension. Although, one-dimensional flattening removes the two-dimensional neighborhood information of the elements, initial layers of successive convolution are responsible for mapping back into the two-dimensional representation internally as a black-box such that overall network can mimic the 2D axi-symmetric heat flow simulation, and temperatures at thermocouples as output of network are similar to FEA calculation.

5 Numerical Experiment

To validate the methodology, the configuration of a typical blast furnace is considered in the numerical experiment. Hearth dimension of the blast furnace is as follows: radius = 7.76 m, total height = 8.89 m, bottom pad thickness = 2.6 m. Conductivity values for steel, ramming mass, and brick are used as 50, 36, and 10 W/ (m K), respectively.

Commercially available finite element analysis software, ANSYS is used for FEA solution. ANSYS input files (APDL) are generated through C#/.NET based in-house program from randomly generated conductivity values of elements near wear front. Conductivity values are taken between iron and refractory, where near iron conductivity means the element is almost eroded. For axi-symmetric thermal analysis PLANE-55 element type (keyopt3 as 1) is used in ANSYS software. Conductivity and temperature tables (required for python-based deep learning software as input) are generated from different ANSYS output files using in-house C#/.NET program.

For checking of finite element mesh convergence, one typical wear/conductivity profile is considered for coarse as well as different fine meshes. Coarse mesh analysis is done with 810 numbers of elements and 887 numbers of nodes. Different fine mesh analyses are performed with gradually increasing the number of nodes and elements. Temperatures at the location of thermocouples are checked for the convergence of meshing. Finally, the convergence of 1150 °C isotherm is also checked (Fig. 2). As modeling of wear through conductivity is indirect, after getting the wear profile, a re-mesh is done considering the identified wear profile. According to 1150 °C isotherm, shape of the wear is similar to “elephant foot”, which is a common occurrence when blast furnace brick is taken down for relining, the excavated hearth bottom shows such wear profile. A new FEA analysis is performed for cross-check as well as to use for the subsequent model update required in the later stage of blast furnace life.

Open-source machine learning software TensorFlow [32] and Scikit-learn [34] are used to create the surrogate model. For numerical validation of the surrogate model, FEA output set is randomly divided into two different sets—training set and testing set. Initially, to check the preliminary mapping between conductivity and temperature, following script is used for the linear model of scikit-learn:

```
import os
import pandas as pd
import numpy as np
from sklearn import linear_model
temFile = os.path.join("C:\\Inverse", "Temperature.csv")
conFile = os.path.join("C:\\Inverse", "Conductivity.csv")
conductivity = pd.read_csv(conFile);
temperature = pd.read_csv(temFile);
exmp = len(conductivity);
def split_train_test(len_data, test_ratio):
    shuffled_indices = np.random.permutation(len_data)
    test_set_size = int(len_data*test_ratio)
    test_indices = shuffled_indices[:test_set_size]
```

```
train_indices = shuffled_indices[test_set_size:]
return train_indices, test_indices
train_indices, test_indices = split_train_test(exmp, 0.2)
train_conductivity = conductivity.iloc[train_indices];
test_conductivity = conductivity.iloc[test_indices]
train_temperature = temperature.iloc[train_indices];
test_temperature = temperature.iloc[test_indices]
clf = linear_model.SGDRegressor(max_iter = 1000, tol = 1e-3)
clf.fit(train_conductivity, train_temperature)
```

Finally, for nonlinear Surrogation, TensorFlow framework is used and a set of thermocouple temperature is considered for identification of the respective 1150 °C isotherms. Checking of mesh convergence with a complete model using genetic algorithm as well as the Surrogation engine (Fig. 2) is performed. Similarly, the calculation of 1150 °C for all 6 sectors is computed to generate 3D representation of 1150 °C iso-surface (Fig. 3).

6 Conclusion

The present paper relates to artificial intelligence for providing estimates and knowledge/status of the condition of the refractories in the hearth region, particularly the left out lining thickness in a blast furnace. The method also determines the temporary protective skull layer thickness over the remnant refractory. This method is applicable to running blast furnaces in the later stages of their operating life. In case, the estimate shows a dangerously thin refractory layer remaining in a specific location, it alerts the operators to take remedial action by directing repairs of the refractories at the relevant areas, to improve cooling arrangements to withdraw heat fluxes, or to close specific tuyeres to run the blast furnace at reduced capacity. Failing these, this method informs the management that the time has come to shut down the blast furnace for relining the refractory layers.

References

1. Bathe KJ (1982) Finite element procedures in engineering analysis. Englewood Cliffs, NJ, Prentice-Hall
2. Zienkiewicz OC, Taylor RL (1991) The finite element method, solids and fluid mechanics, dynamics and nonlinearity. McGraw-Hill, London
3. ANSYS Parametric Design Language: ANSYS Inc.
4. Engl H, Hanke M, Neubauer A (1996) Regularization of inverse problems. Dordrecht, Kluwer Academic Pub. ISBN 978-0-7923-4157-4
5. Shinotake A, Nakamura H, Yadoumaru N, Morizane Y, Meguro M (2003) Investigation of blast-furnace hearth sidewall erosion by core sample analysis and consideration of campaign operation. *ISIJ Int.* 43(3):321–330. <https://doi.org/10.2355/isijinternational.43.321>

6. Zagaria M, Dimastromatteo V, Colla V (2010) Monitoring erosion and skull profile in blast furnace hearth. *Ironmaking Steelmaking* 37(3):229–234. <https://doi.org/10.1179/030192309X12595763237003>
7. Sadri A, Ying W, Chataway D, and Gordon Y (2016) Principles for Blast Furnace Refractory Lining Inspection and Monitoring. AISTECH 2016
8. Zhou D, Cheng S, Zhang R, Li Y, Chen T (2017) Uniformity and activity of blast furnace hearth by monitoring flame temperature of raceway zone. *J-STAGE home/ISIJ Int* 57(9):1509–1516. <https://doi.org/10.2355/isijinternational.ISIJINT-2017-091>
9. Fraser B, Tanzil F, Zulli P, Dwight R (2003) Monitoring the blast furnace hearth refractory with the 1150 °C isotherm and acoustic wave measurements. In: 3rd, International conference on science and technology of ironmaking. METEC Congress, Dusseldorf, Germany, pp 462–470. ISBN: 3514006903
10. Nightingale R, Tanzil F, Beck A, Price K (2001) Blast furnace hearth condition monitoring and tap-hole management techniques. *Metall Res Technol* 98(6). <https://doi.org/10.1051/metal:2001103>
11. Torrkulla J, Saxen H (2000) Model of the state of the blast furnace hearth. *ISIJ Int* 40(5):438–447. <https://doi.org/10.2355/isijinternational.40.438>
12. Takatani K (2001) Inada T and Takata K (2001) Mathematical model for transient erosion process of blast furnace hearth. *ISIJ Int.* 41(10):1139–1145. <https://doi.org/10.2355/isijinternational.41.1139>
13. Kumar S (2005) Heat transfer analysis and estimation of refractory wear in an iron blast furnace hearth using finite element method. *ISIJ Int* 45(8):1122–1128. <https://doi.org/10.2355/isijinternational.45.1122>
14. Mehrotra SP, Nand YC (1993) Heat balance model to predict salamander penetration and temperature profiles in the sub-hearth of an iron blast furnace. *ISIJ Int.* 33(8):839–846. <https://doi.org/10.2355/isijinternational.33.839>
15. Brannbacka J, Saxen H (2008) (2008) Model for fast computation of blast furnace hearth erosion and buildup profiles. *Ind Eng Chem Res* 47(20):7793–7801. <https://doi.org/10.1021/ie800384q>
16. Gonzalez M, Goldschmit M (2006) Inverse geometry heat transfer problem based on a radial basis functions geometry representation. *Int J Numer Methods Eng* 65(8):1243–1268. <https://doi.org/10.1002/nme.1487>
17. Zhao H, Cheng S, Zhao M (2007) Analysis of all-carbon brick bottom and ceramic cup synthetic hearth bottom. *J Iron Steel Res Int* 14(2):6–12, 2007. [https://doi.org/10.1016/S1006-706X\(07\)60019-3](https://doi.org/10.1016/S1006-706X(07)60019-3)
18. Wu L, Cheng H, Su Y, Feng H (2003) Mathematical model for on-line prediction of bottom and hearth of blast furnace by particular solution boundary element method. *Appl Therm Eng* 23(16):2079–2087. [https://doi.org/10.1016/S1359-4311\(03\)00184-4](https://doi.org/10.1016/S1359-4311(03)00184-4)
19. Zhang Y, Deshpande R, Huang D, Chaubal P, Zhou CQ (2008) Numerical analysis of blast furnace hearth inner profile by using CFD and heat transfer model for different time periods. *Int J Heat Mass Transf* 51(1–2):186–197. <https://doi.org/10.1016/j.ijheatmasstransfer.2007.04.052>
20. Radmoser E, Wincor R (1998) Determining the inner contour of a furnace from temperature measurements. Linz, University of Linz
21. Dmitriev A, Chen K (2017) Development and introduction of monitoring system of refractory lining wear in blast furnace hearth. *J Environ Sci Eng B* 6(2017):558–563. <https://doi.org/10.17265/2162-5263/2017.11.003>
22. Shulte M, Klima R, Ringell D, Foss M (1998) Control of blast furnace hearth deterioration by means of heat flux sensors. *Ferrous Met* 4:17–22
23. Pinchuk D, Panchoha G, Kanaev V, Mozharenko N (2005) Modern methods of control of a residual thickness of lining of blast furnace hearth. *Fundam Appl Prob Ferrous Metall* 11(247–53):2005
24. Dmitriev A, Chesnokov Y, Chen K, Ivanov O, Zolotykh M (2014) New monitoring system of firebrick lining deterioration of blast furnace devil in metallurgical plants of China. *Adv Mater Res* 834(939–43):2014. <https://doi.org/10.4028/www.scientific.net/AMR.834-836.939>

25. Dmitriev A, Zolotykh M, Chesnokov Y, Chen K, Ivanov O, Vitkina G (2014) New monitoring system of the refractory lining wear in the blast furnace hearth. *Appl Mech Mater* 670:1274–1284. <https://doi.org/10.4028/www.scientific.net/AMM.670-671.1274>
26. Liu Z, Zhang J, Zuo H and Yang T (2012) Recent progress on long service life design of Chinese blast furnace hearth. *ISIJ Int* 52(10):1713–1723 <https://doi.org/10.2355/isijinternational.52.1713>
27. Almeida B, Neves E, Silva S, Junior F (2017) Blast furnace hearth lining: post mortem analysis. *Mater Res* 20(3):814–818 <https://doi.org/10.1590/1980-5373-MR-2016-0875>
28. Magnago L and Catabriga L (2014) Comparison of methods for solving inverse problems to estimate the wear line in a blast furnace hearth. In: *Blucher mechanical engineering proceedings* May 2014, vol. 1, num. 1. <https://doi.org/10.5151/meceng-wccm2012-19359>
29. Goldberg DE (1989) *Genetic algorithms in search, optimization and machine learning*. Addison-Wesley Longman Publishing Co. ISBN: 0201157675
30. Yaochu J (2011) Surrogate-assisted evolutionary computation: recent advances and future challenges. *Swarm and Evol Comput* 1:61–70. <https://doi.org/10.1016/j.swevo.2011.05.001>
31. LeCun Y, Bengio Y, Hinton G (2015) Deep learning. *Nature* 521:436–444. <https://doi.org/10.1038/nature14539>
32. TensorFlow: An end-to-end open source machine learning platform. <https://www.tensorflow.org/>
33. PyTorch: from research to production. <https://pytorch.org/>
34. Scikit-learn: Machine Learning in Python. <https://scikit-learn.org/>

Fatigue Resistance of Recycled Steel Fibers (Discarded Vehicle Tyre Steel Fibers) Concrete Pavement



M. V. Mohod and K. N. Kadam

Abstract Concrete pavements are exposed to repetitive (cyclic traffic) loads throughout its lifespan resulting in the instigation of cracks. Propagation of cracks implies to permanent damage of rigid pavement owing to fatigue damage. From inception, cause of the creation of cracks in the rigid pavement is less resistance of the rigid pavement against bending, tension, and cracking. Market available (Industrial) steel fibers are incorporated in plain concrete to enhance its post-cracking flexural behavior and fatigue performance. Even though industrially manufactured steel fibers help concrete pavements by restricting cracks, these are not preferred due to the higher cost of material. An alternative to using recycled steel fibers recovered from discarded vehicle tyres is a cheaper fiber solution with notable environmental benefits. Research work aligned to the adaptability of recycled steel fibers has been reported, but there is the lack of studies on exploring fatigue performance of recycled steel fibers reinforced concrete pavement with reference to IRC 58:2015 guidelines. Experimental findings recommend the use of 'Hybrid fibers' a mix of waste tyre steel fiber and industrial steel fiber in a definite proportion which enhances mechanical properties of concrete. Temperature study and fatigue analysis warranty the use of hybrid fibers in pavement construction as it provides cost-effective, environment-friendly solutions.

Keywords Concrete pavement · Temperature gradinet · Cumulative fatigue damage · Recycled steel fibres · Discarded vehicle tyre steel fibres · IRC 58:2015

M. V. Mohod (✉)

Civil Engineering Department, PRMIT&R, Badnera, Amravati, Maharashtra, India
e-mail: mvmohod@gmail.com

K. N. Kadam

Department of Applied Mechanics, GCOEN, Nagpur, Maharashtra, India
e-mail: kadamkshitija7@gmail.com

1 Introduction

Solid waste management and its disposal is a high-time environmental concern all around the globe. A large amount of non-biodegradable materials are annually stock-piled in landmasses due to the unawareness of law enforcement related to recovery or because recycling the same is not cost-effective. The proposed research on concrete technology reinforced with discarded vehicle steel tyre fibers suggests an added advantage to improve sustainable development in concrete construction for rigid pavements. This innovative approach to the concrete technology curtails the quantity of raw materials, reusing the by-products such as recycled aggregates, recycled fibers, marble dust, etc. In addition to this, the evolution of discarded vehicle steel tyre fibers can reduce the demand for traditional steel fibers along with a reduction in the required amount of energy needed for their production. In this context, present research concerns the application of discarded vehicle steel tyre fibers as discreet reinforcement for the concrete matrix in pavement. The research work is focused to perform a comparative study between industrial steel fiber, discarded vehicle steel tyre fibers and mix of the both in described proportion called as 'Hybrid fibers,' identify the optimum dosage of the same to be adopted in construction practices. The final aim is to demonstrate the effectiveness of discarded vehicle steel tyre fibers in pavement construction as it indirectly provides environmental and ecological benefits. In this essence, the abundant availability of waste tyre steel fiber can be utilized as an effective additional or replaceable material for concrete which will be beneficial for all the circumstances.

2 IRC 58 2015—Design Chart for CFD Analysis

The IRC 58 aims at rationalizing the design procedure by aligning it with recent trends in design and analysis by considering cumulative fatigue damage (CFD) due to the dual effect of wheel load and environmental loading (temperature gradient) existing across the depth of the slab. In IRC 58 code, region-wise maximum temperature differentials are recommended for various pavements thicknesses. An analysis is made for cumulative fatigue damage (CFD) by using recommended and experimental temperature differential for PCC and modified concrete.

3 Methodology

The concrete processed out by using recycled wastes such as C and D of concrete which is cost-effective and environmental supportive, Green concrete. Green concrete

is a remarkable benchmark in the history of concrete technology. Quality and notable research have been cited out by researchers on the adaptability of various industrial by-products/wastes and micro-fillers such as marble dust in concrete. The major concern of using pozzolanic wastes was not only the economic point of view but also to enhance the properties of concrete, especially durability. Using the waste products steel tyre fibers, an innovative concrete has been developed to effectively study the improvement in the mechanical properties of the new developed concrete, planning, procedures, and methods must be wisely chosen. The criteria to assess the mechanical properties are based on the activities to plan and preparation, which shall be carried out before the test for mechanical properties of fiber reinforced concrete. These activities are (a) Aggregate and cement testing, (b) Sieve analysis (aggregate grading), (c) Fiber volume dosage rate, (d) Mix Design, (e) Preparation of test specimen, (f) Concrete mixing, Curing, and temperature study.

1. Material Properties/Data:

Details of various materials adopted in the present study are presented below

i. Cement:

The cement used was Pozzolana Portland cement (PCC) grade 53 and confirming to IS 1489-1-1991. The initial and final settling times of cement were 158 min and 345 min, respectively.

ii. Aggregate:

Aggregates are the most important elements in the concrete mix. It forms the major section of the concrete, reduces shrinkage, and economy with reference to material cost. For producing workable concrete, an effective gradation of aggregates is of prime importance.

iii. Fine Aggregate:

Fine aggregates ranging from 4.75 to 150 microns can be termed as fine aggregate. The river sand is washed and screened to reduce deleterious materials and oversized particles in sand. Good quality WARDHA river sand (Fig. 1) was used as a fine aggregate.

Fig. 1 Wardha sand





Fig. 2 Coarse aggregate

iv. **Coarse Aggregate:**

The material whose particles are of size as retained on I.S. Sieve No. 480 (4.75 mm) is termed as coarse aggregate as shown in Fig. 2.

2. **Tyre steel fibers:**

Variation of fibers exists in types, shape, properties, and availability in the construction market. Common types of fibers incorporated in concrete are steel fibers, glass fibers, and polypropylene fibers. Their use differs in concrete as per the application. Selection of fiber is done based on their properties like usefulness, cost-effectiveness, and availability. High tensile strength steel fiber obtained from dismantled scrap tyres is adopted (Fig. 3). The effective waste/disposal management of used/worn-out tyres is of major concern for most of the environmental organization and agencies all over the globe. Tyre production is on clutch every year due to the increase of vehicle purchase from market. The generation, collection, and disposal of waste are dangerous to life and have caused very serious problems/issues to the human habitation all around. Recently, some research has been carried out on the use of recycled



Fig. 3 Tyre steel fibers



Fig. 4 Waste tyre site

steel. Shape and impermeability of tyres retain water for a long course of time thus provide breeding sites for mosquito, etc. (Fig. 4). Waste tyres also have an additional serious problem of a fire hazard since they are easy to ignite and dangerous for living.

3. Superplasticizer

A plasticizer is used for better workability of concrete. During the trial mix, the workability was found to be very less, so we used plasticizer. It reduces the w/c ratio and ultimately enhances the strength parameter of concrete. Plasticizer is added at a rate of 5 ml per liter of water. The plasticizer we used was AC-MENT-BV-430-A3, superPlasticizer for pumpable concrete on PC Base, an Apple chemical industries product.

4. Concrete mix design

Mix design for M30

- (1) Grade designation = M30.
- (2) Type of cement used = Pozzolana Portland Cement 53 Grade.
- (3) Max nominal size of aggregate adopted = 20 mm.
- (4) Minimum cement Content = 240 kg/m^3 .
- (5) Water-Cement Ratio = 0.45.
- (6) Standard deviation = 5 N/mm^2 .
- (7) Crushed Sand confirming to Zone 1.
- (8) Exposure Condition = Moderate.
- (9) Workability = Low (25–75 mm).
- (10) Target mean Strength = 38 N/mm^2 .

After various calculations and corrections of oversize, specific gravity the final quantity of materials is calculated as follows:

- (1) Cement = 377.07 kg.
- (2) Water content = 170.1 kg/cum.
- (3) Fine Aggregate = 1075 kg.
- (4) Coarse aggregate = 20 mm = 671.60 kg/cum
= 10 mm = 193.45 kg/cum.

By using this quantity of material, a mix design of concrete is prepared. This mix design helps in achieving a desired workability, strength, and durability for concrete work. For making the mix design more workable, an admixture is also used. The experimental tests were carried out to obtain the mechanical strength properties of tyre steel fiber added to concrete to use them in the pavements. Effect of replacing the cement by locally available tyre steel fiber on concrete was studied. The replacement of materials considered in the mix was by increasing percentages by weight of cement, respectively. Observation for 7, 14, and 28 days of curing period were recorded and presented in the form of tables and graphs. Cumulative fatigue damage (CFD) was also performed on concrete. In CFD analysis, concrete of size 0.3 m × 0.3 m with varying thicknesses of 150 mm, 200 mm, 250 mm, and 300 mm were prepared. The temperature variations of 24 h were recorded after each hour and temperature differential was calculated. After obtaining the temperature variation, flexural strength, and compressive strength results in CFD data analysis chart available in IRC 58 2015, result regarding safe pavement thickness were obtained.

5. Material testing values

Prerequisite test has been performed on materials adopted in the concrete mix design. Totally 4 tests have been performed which includes specific gravity test, Fineness Modulus test, Moisture Content Test, and Water Absorption Test. Table 1 provides the results of various tests performed on fine aggregate and coarse aggregate both.

Table 1 Material testing results

Sr. no.	Particulars	Fine aggregate	Coarse aggregate (10 mm)	Coarse aggregate (20 mm)
1	Specific gravity	2.63	2.8	2.86
2	Fineness modulus	4.7	6.2	6.2
3	Moisture content	0%	0%	0%
4	Water absorption	1.81%	0.591%	0.591%

4 Mechanical Properties of Concrete

Compressive strength, flexural strength, and split tensile strength results for mix M30 concrete are presented as follows:

1. For conventional concrete mix M30:

Test results pertaining to the normal mix of M30 grade of concrete are presented below,

i. *Compressive strength for conventional mix M30*

From Fig. 5, it can be visualised that the conventional concrete has achieved satisfying results according to days of curing, i.e., at 7 days period of curing, the concrete has achieved above 60% results, at 14 days curing above 80%, and at 28 days achieved 100% results.

ii. *Flexural strength for conventional mix M30*

From Fig. 6, it can be seen that the flexural strength for the M30 mix of 7 14, and 28 days of curing shows a good gain in strength.

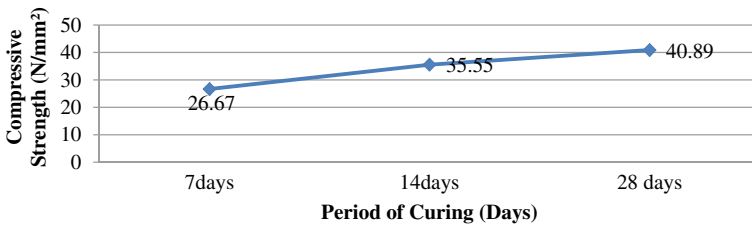


Fig. 5 Compressive strength for conventional mix M30

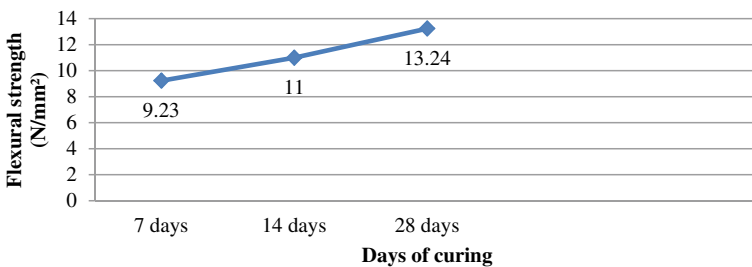
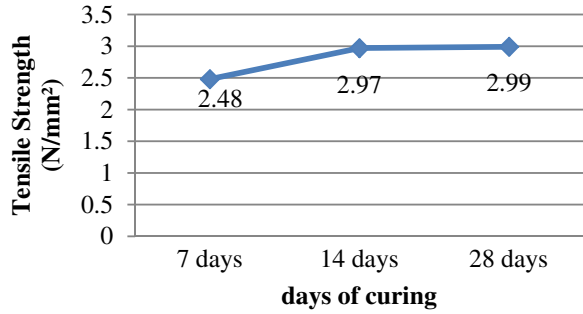


Fig. 6 Flexural strength for conventional mix M30

Fig. 7 Split tensile strength for conventional mix M30



iii. *Split Tensile strength for conventional mix M30*

From Fig. 7, it can be seen that the split tensile strength for 7, 14, 28 days shows satisfying results.

2. For Tyre steel fiber-added concrete (M30 mix)

Tyre steel fiber replacement with cement is done in increasing percentages in concrete and from the test results obtained for compressive strength, flexural strength, and split tensile strength. The percentage replacement was 0, 0.5, 0.1, 0.15, and 0.2% with cement.

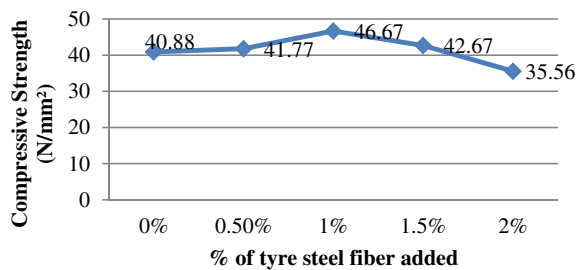
i. *Compressive strength for tyre steel fiber-added concrete*

From Fig. 8 above, plotted graph for the variation in compressive strength for mix proportion M30 with reference to varied tyre steel fiber content (0.5, 1, 1.5, 2%) cites the drop of strength after 1% tyre steel fiber addition. Two percent tyre steel fiber replacing to cement shows the lowest strength. It is observed that the optimum content (dosage) of tyre steel fiber is 1% of replacement of cement for compressive strength.

ii. *Flexural Strength for tyre steel fiber-added concrete*

From Fig. 9, plotted graph for the variation in Flexural strength for mix proportion M30 with reference to varied tyre steel fiber content (0.5, 1, 1.5, 2%) depicts the drop

Fig. 8 Compressive strength for tyre steel fiber-added concrete



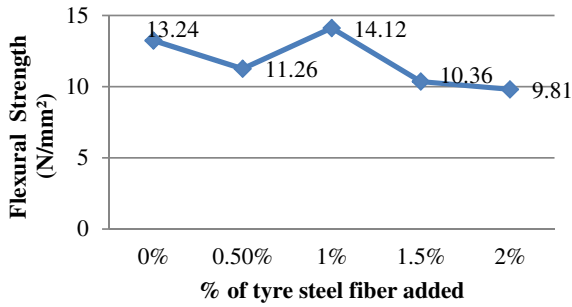


Fig. 9 flexural strength for tyre steel fiber-added concrete

of strength after 1% tyre steel fiber addition. The strength for conventional concrete is less than 1% replacement of fibers. Two percent tyre steel fiber replacing to cement shows the lowest strength. It is understood that the optimum content (dosage) of tyre steel fiber for flexural strength is 1% of replacement of cement.

iii. *Split tensile strength for tyre steel fiber-added concrete*

From Fig. 10, plotted graph for the variation in split tensile strength for mix proportion M30 with respect to varying tyre steel fiber content (0.5, 1, 1.5, 2%) shows the drop of strength after 0.5% tyre steel fiber addition. The strength of conventional concrete is less than 0.5% replacement of fibers. Two percent tyre steel fiber replacing to cement shows the lowest strength. It is observed that the optimum value of tyre steel fiber for flexural strength is 0.5% of replacement of cement.

3. For Industrial steel fiber-added concrete (M30 mix)

Industrial steel fiber replacement with cement is done in increasing percentages in concrete and from the tests results obtained for compressive strength, flexural strength, and split tensile strength. The percentage replacement was 0, 0.5, 1, 1.5, and 2% with cement.

i. *Compressive strength for industrial steel fiber-added concrete*

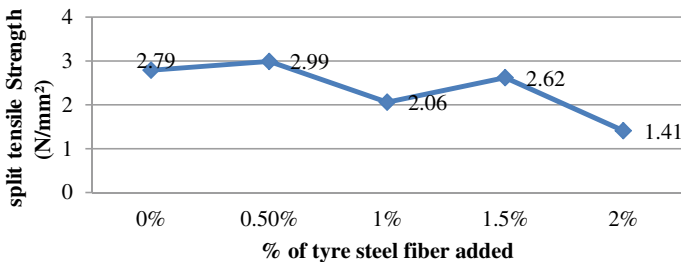


Fig. 10 Split tensile strength for tyre fiber-added concrete

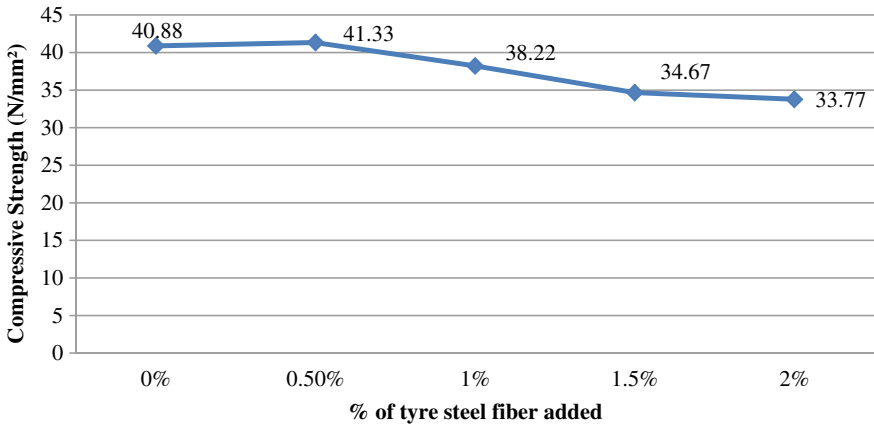


Fig. 11 Compressive strength for industrial steel fiber-added concrete

From Fig. 11, plotted graph for the variation in compressive strength for mix proportion M30 with reference to varied industrial steel fiber content (0.5, 1, 1., 2%) cites the drop of strength after 0.5% industrial steel fiber addition. The strength of conventional concrete is slightly less than the optimum percentage, i.e., 0.5% replacement. Two percent industrial steel fiber replacing to cement shows the lowest strength. It is understood that the optimum content (dosage) of industrial steel fiber is 0.5% of replacement of cement for compressive strength.

ii. *Flexural Strength for industrial steel fiber-added concrete*

From Fig. 12, plotted graph for the variation in Flexural strength for mix proportion M30 with reference to varied tyre steel fiber content (0.5, 1, 1.5, 2%) cites the drop of strength after 0.5% tyre steel fiber addition. The strength of conventional concrete

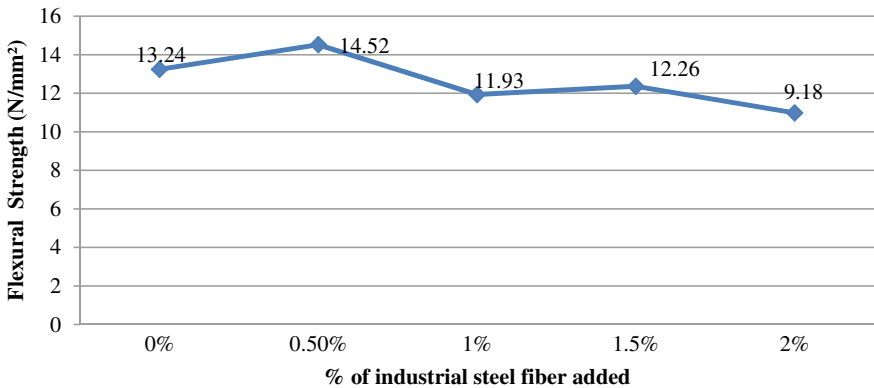


Fig. 12 Flexural strength for industrial steel fiber-added concrete

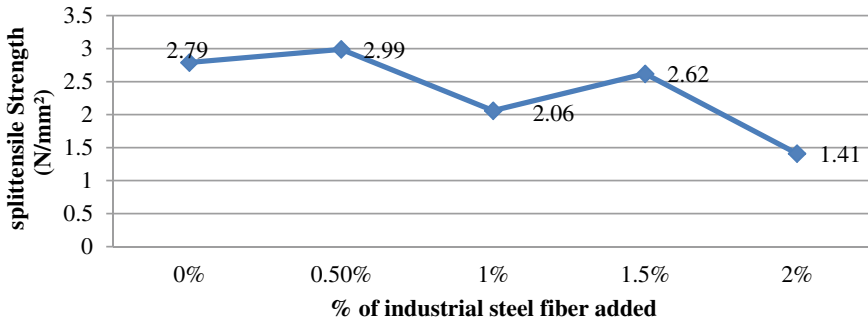


Fig. 13 Split tensile strength for industrial fiber-added concrete

is less than 0.5% replacement of fibers. Two percent tyre steel fiber replacing to cement shows the lowest strength. It is understood that the optimum content of tyre steel fiber for flexural strength is 0.5% of replacement of cement.

iii. *Split tensile strength for tyre steel fiber-added concrete*

From Fig. 13, plotted graph for the variation in split tensile strength for mix proportion M30 with reference to varied industrial steel fiber content (0.5, 1, 1.5, 2%) cites the drop of strength after 0.5% industrial steel fiber addition but also increases at 1% replacement. The strength of conventional concrete is less than 0.5% replacement of fibers. Two percent industrial steel fiber replacing to cement shows the lowest strength. It is understood that the optimum content (dosage) of industrial steel fiber for flexural strength is 0.5% of replacement of cement.

4. **For Hybrid fiber concrete (combined tyre steel fiber and industrial steel fiber added in concrete) M30 mix.**

Combined Industrial steel fiber and Tyre steel fiber replacement with cement is added in increasing percentages (0, 0.5, 1, 1.5, 2%) in concrete and from the tests results obtained for compressive strength, flexural strength, and split tensile strength. The replacement was 50% of industrial steel fibers and 50% of tyre steel fibers for each replacement percentages (0, 0.5, 1, 1.5, 2%) for Industrial steel fiber and tyre steel fiber, respectively.

i. *Compressive Strength for Hybrid Fiber concrete*

From Fig. 14, plotted graph for the variation in compressive strength for mix proportion M30 hybrid fibers replacement with cement is added in increasing percentages (0, 0.5, 1, 1.5, 2%) in concrete and the tests results obtained for compressive strength. The replacement was 50% of industrial steel fibers and 50% of tyre steel fibers for each replacement percentages (0, 0.5, 1, 1.5, 2%) for Industrial steel fiber and tyre steel fiber, respectively. The graph cites the drop of strength after 1% Hybrid fiber content. Here, the 1% shows the highest compressive strength which is more than

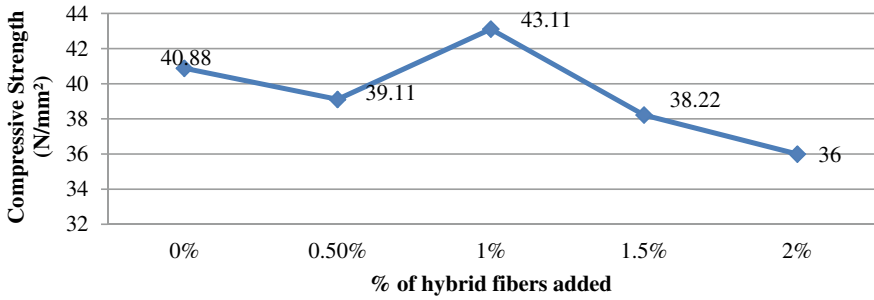


Fig. 14 Compressive strength for combined hybrid fiber-added concrete

the conventional mix. It is understood that the optimum content (dosage) of hybrid fiber is 1% for compressive strength

ii. *Flexural Strength for hybrid fiber-added concrete*

From Fig. 15, plotted graph for the variation in compressive strength for mix proportion M30 hybrid fibers replacement with cement is added in increasing percentages (0, 0.5, 1, 1.5, 2%) in concrete and the test results obtained for compressive strength. The replacement was 50% of industrial steel fibers and 50% of tyre steel fibers for each replacement percentages (0, 0.5, 1, 1.5, 2%) for Industrial steel fiber and tyre steel fiber, respectively. The graph cites the drop of strength after 1% Hybrid fiber content. Here, 1% replacement shows the highest compressive strength which is more than the conventional mix. The lowest flexural strength observed was of 2% replacement. It is understood that the optimum content (dosage) of hybrid fiber is 1% for flexural strength.

iii. *Split tensile strength for Hybrid fiber concrete*

From Fig. 16, plotted graph for the variation in compressive strength for mix proportion M30 hybrid fibers replacement with cement is added in increasing percentages (0, 0.5, 1, 1.5, 2%) in concrete and the tests results obtained for compressive strength. The replacement was 50% of industrial steel fibers and 50% of tyre steel fibers for each

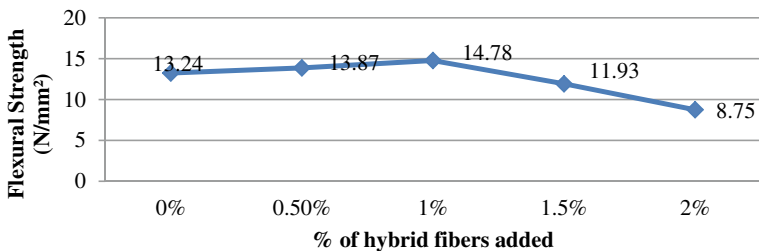


Fig. 15 Flexural strength for combined hybrid fiber-added concrete

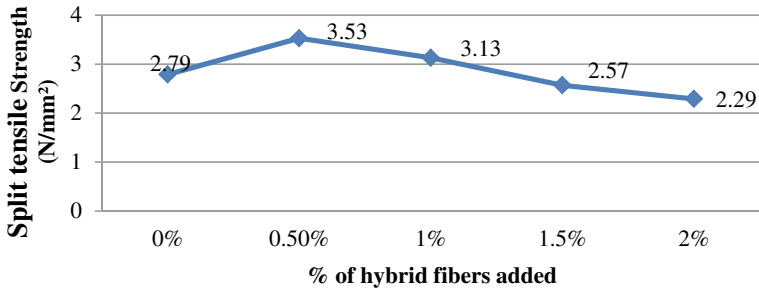


Fig. 16 Split tensile strength for hybrid fiber fiber

replacement percentages (0, 0.5, 1, 1.5, 2%) for Industrial steel fiber and tyre steel fiber, respectively. The graph cites the drop of strength after 1% Hybrid fiber content. Here, 0.5% replacement depicts the highest compressive strength which is more than conventional mix and industrial fiber concrete but less than tyre fiber concrete. The lowest flexural strength observed was of 2% replacement. It is understood that the optimum content (dosage) of hybrid fiber is 1% for flexural strength.

5. Maximum strength (compressive, flexural, tensile) at optimum percentages (dosage) of industrial fiber concrete, tyre steel fiber, Hybrid fiber concrete, and conventional concrete

Comparison of maximum strength parameters such as compressive strength, flexural strength, and split tensile strength is presented below in the graphical form

i. Compressive strengths at optimum percentages

Bar graph from Fig. 17 cites the variation in compressive strength for the type of materials used in the concrete mix. Here, cement replaced with tyre steel fiber shows comparatively good strength than that of industrial fiber, conventional concrete, and

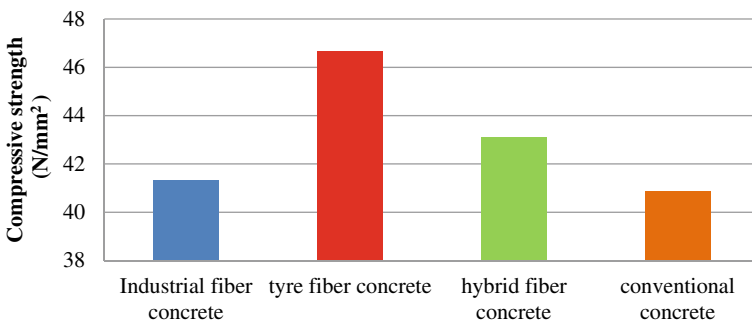


Fig. 17 Compressive strength at optimum percentages

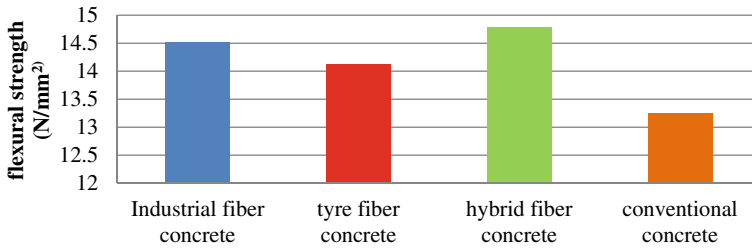


Fig. 18 Flexural strength at optimum percentages

hybrid fiber concrete. The strengths for industrial fiber concrete, tyre steel fiber, and hybrid fiber concrete all of them satisfying the target strength.

ii. *Flexural strengths at optimum percentages*

Bar graph from Fig. 18 depicts the variation in compressive strength for the type of materials used in the concrete mix. Here, cement replaced with hybrid fiber shows comparatively good strength than that of industrial fiber, conventional concrete, and tyre fiber concrete. The strengths for industrial fiber concrete, tyre steel fiber, and hybrid fiber concrete all of them satisfying the target strength

iii. *Split tensile strengths at optimum percentages*

From Fig. 19, split tensile strength for, tyre steel fibers shows the highest results than industrial fiber concrete, hybrid fiber concrete, and conventional concrete.

6. Cumulative Fatigue Damage (CFD) Analysis, Variation of Temperature in Concrete Pavement

Following graphs (Figs. 20, 21, 22, and 23) shows the behavior of temperature gradient at three locations: top, middle, and bottom of pavement slab for 150, 200, 250, 300-mm-thick concrete cast with tyre steel fibers. Temperature data is recorded for 24-hour duration at three levels (top, middle, bottom) by using a digital thermometer. The variation in temperature profile at all levels in plotted and the temperature differential is calculated for a particular thickness of slab, which has been used

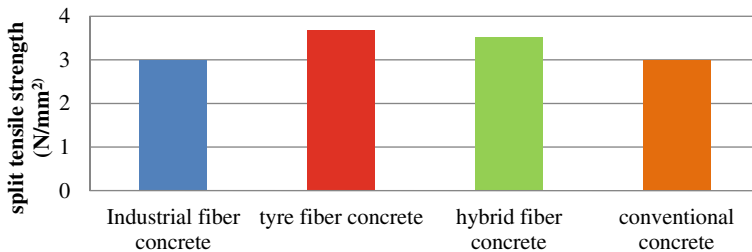


Fig. 19 Split tensile strengths at optimum percentages

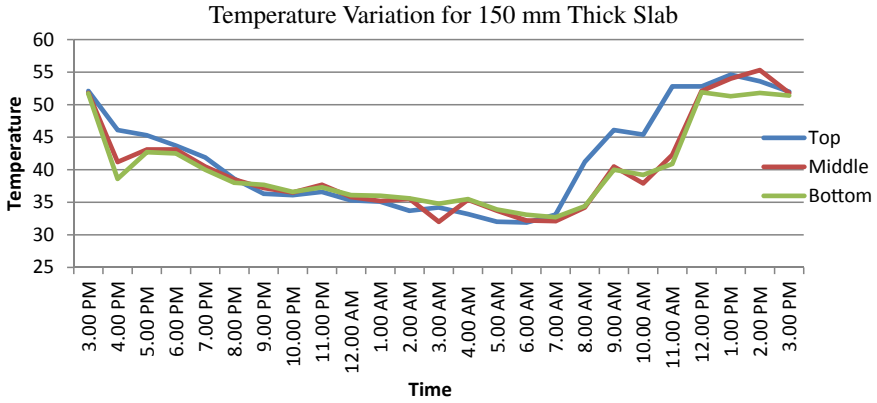


Fig. 20 Temperature variation for 150 mm thick slab

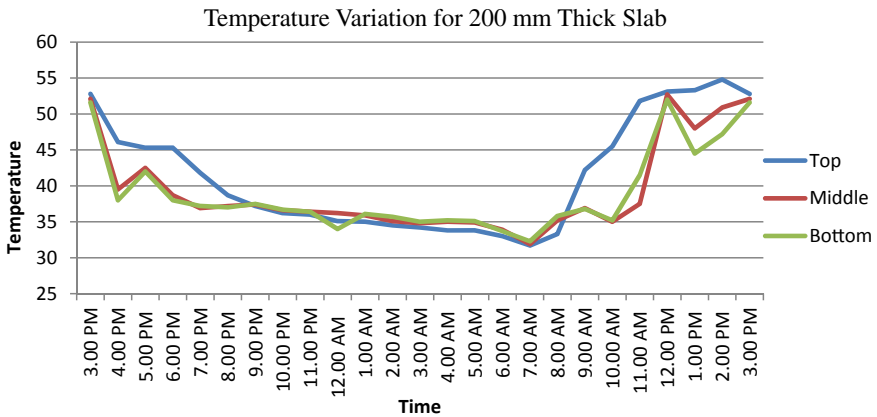


Fig. 21 Temperature variation for 200 mm thick slab

further in cumulative fatigue damage analysis for obtaining safe PQC thickness. The comparison of IRC recommended temperature differential and those obtained through experimental work with a difference between them is presented in Table 2.

Figure 20 is showing temperature results and the temperature gradient is calculated as follows:

- The highest temperature at top for 24 h–Lowest temperature at bottom for 24 h.
- For example: Temperature gradient for 150-mm slab = $54.6^{\circ} - 32.7^{\circ} = 21.9$.
- Temp. gradient = The highest temperature at top for 24 h–the lowest temperature at bottom for 24 h.
- Temperature gradient for 150-mm slab = $54.8 - 32.3^{\circ} = 22.5^{\circ} \text{C}$.
- Temp. gradient = The highest temperature at top for 24 h–the lowest temperature at bottom for 24 h.

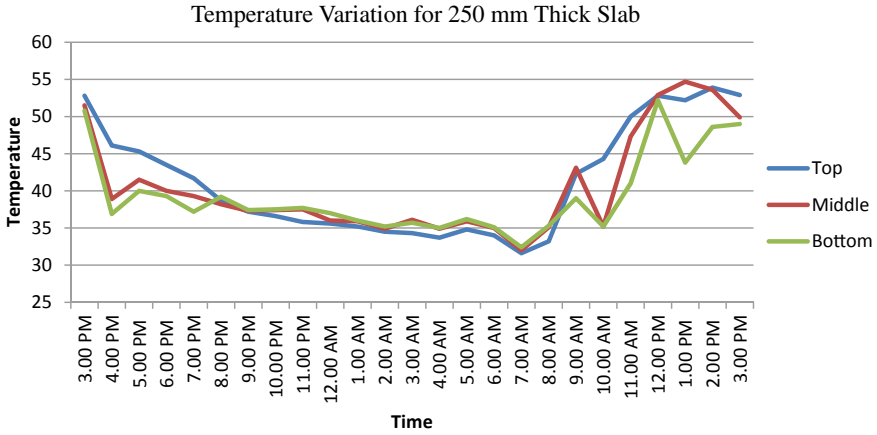


Fig. 22 Temperature variation for 250 mm thick slab

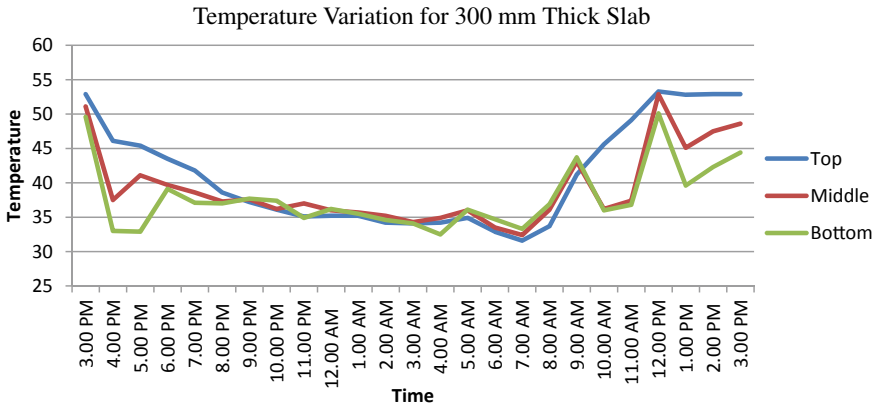


Fig. 23 Temperature variation for 300-mm-thick slab

Table 2 Temperature differentials in °C

Thickness in mm/T °C	150	200	250	300
Exp. data result	21.9	22.5	21.5	20.4
IRC 58-2015	17.3	19	20.3	21
Difference	4.6	3.5	1.2	0.6

Temperature gradient for 150-mm slab = $53.9 - 32.4^\circ = 21.5^\circ\text{C}$.

Temp. gradient = The highest temperature at top for 24 h—the lowest temperature at bottom for 24 h.

Temperature gradient for 150-mm slab = $53.9 - 32.4^\circ = 21.5^\circ\text{C}$.

5 Calculation of Safe PQC Thickness of Concrete Slabs with Reference to Design Charts/Procedure from IRC-58 2015

Safe PQC slab thickness is calculated by adopting design guidelines prescribed by IRC 58-2015. As hybrid fiber has shown appreciable results in terms of strength parameters and temperature, the study revealed a difference in IRC recommended temperature differential, and two varieties of input data are considered for calculating safe PQC thickness by varying concrete (Conventional and Hybrid fiber reinforced) and temperature data (IRC recommended and Experimental data). Initially, CFD results are presented for conventional concrete by considering temperature variation (IRC and Experimental) for calculating safe PQC thickness: later on, CFD analysis for Hybrid fiber reinforced concrete by considering temperature variation (IRC and Experimental). Other relevant data required for CFD analysis have been adopted from the design example from IRC 58-2015. Details of CFD analysis are given below.

1. Cumulative fatigue damage analysis for Conventional Concrete:

From Table 2, the IRC-58 2015 Values and Experimental data result values are observed and CFD analysis is performed for conventional concrete at flexural strength 13.24 MPa and compressive strength 40.89 MPa. The following graphs show the behavior of fatigue damage while calculating safe PQC thickness.

For 0 °C, the slab thickness is safe at 140 mm thickness for conventional concrete at flexural strength 13.24 MPa and compressive strength 40.89 MPa. For 17.3 °C, IRC value of the slab thickness 150 mm is safe at 160 mm thickness for conventional concrete at flexural strength 13.24 MPa and compressive strength 40.89 Mpa, the same be referred from Fig. 24.

For 17.3 °C, experimental value of the slab thickness 150 mm is safe at 160 mm thickness for conventional concrete at a flexural strength 13.24 MPa and compressive strength 40.89 MPa. For 19 °C, IRC value of the slab thickness 200 mm is safe at 170 mm thickness for conventional concrete at flexural strength 13.24 MPa and compressive strength 40.89 MPa, the same be referred from Fig. 25.

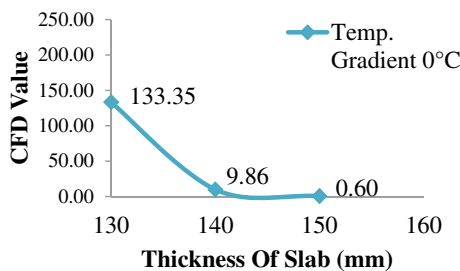


Fig. 24 CFD analysis for 0 °C of conventional concrete

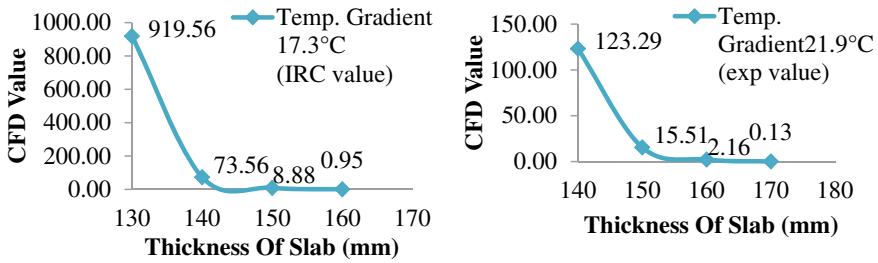


Fig. 25 CFD analysis for 17.3 and 21.9 °C of 150 mm conventional concrete

For 22.5 °C, experimental value the slab thickness 200 mm is safe at 170 mm thickness for conventional concrete at flexural strength 13.24 MPa and compressive strength 40.89 MPa. For 20.3 °C, IRC value of the slab thickness 250 mm is safe at 170 mm thickness for conventional concrete at flexural strength 13.24 MPa and compressive strength 40.89 MPa, the same be referred from Fig. 26.

For 21.5 °C, experimental value of the slab thickness 250 mm is safe at 170 mm thickness for conventional concrete at flexural strength 13.24 MPa and compressive strength 40.89 MPa. For 21 °C, IRC value of the slab thickness 300 mm is safe

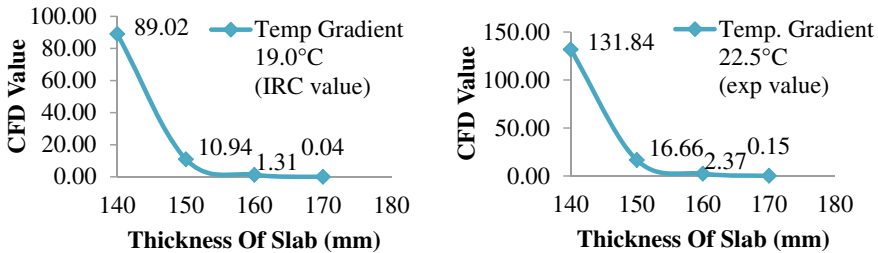


Fig. 26 CFD analysis for 19.0 and 22.5 °C of 200 mm of conventional concrete

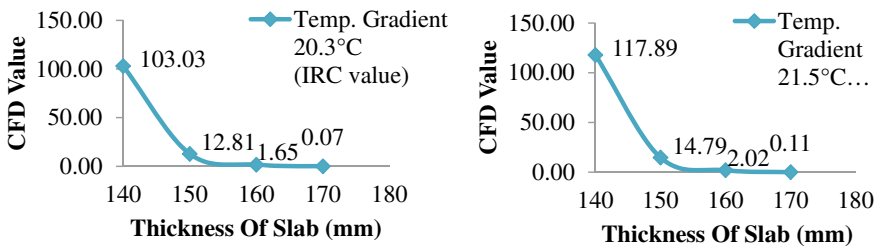


Fig. 27 CFD analysis for 20.3 and 21.5 °C of 250 mm of conventional concrete

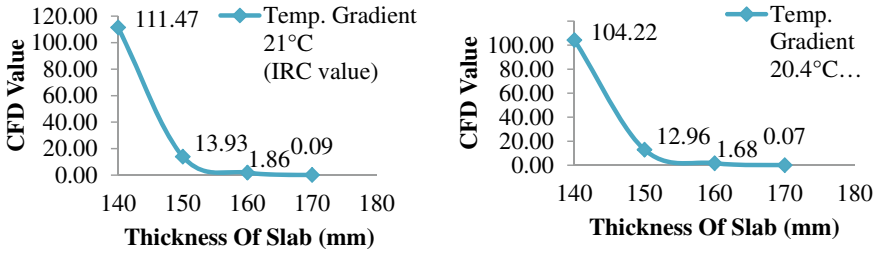


Fig. 28 CFD analysis for 21 and 20.4 °C of 300 mm for conventional concrete

at 170 mm thickness for conventional concrete at flexural strength 13.24 MPa and compressive strength 40.89 MPa, the same be referred from Fig. 27.

For 20.4 °C, experimental value the slab thickness 300 mm is safe at 170 mm thickness for conventional concrete at flexural strength 13.24 MPa and compressive strength 40.89 MPa, the same be referred from Fig. 28.

i. *Cumulative fatigue damage analysis for Hybrid Fiber Concrete*

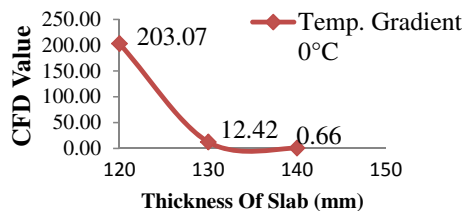
From Table No. 15, the IRC-58 2015 Values and Experimental data result values are observed and CFD analysis is performed for Hybrid fiber concrete at flexural strength 14.78 MPa and compressive strength 43.11 MPa. The following graphs show the behavior of fatigue damage.

For 0 °C, the slab thickness is safe at 140 mm thickness for Hybrid fiber concrete at flexural strength 14.78 MPa and compressive strength 43.11 MPa, the same be referred from Fig. 29.

For 21.9 °C, experimental value of 150 mm thickness the slab thickness is safe at 160 mm thickness for hybrid fiber concrete at flexural strength 14.78 MPa and compressive strength 43.11 MPa. For 19 °C, IRC-58 value of 200 mm the slab thickness is safe at 150 mm thickness for hybrid fiber concrete at flexural strength 14.78 MPa and compressive strength 43.11 MPa, the same be referred from Fig. 30.

For 22.5 °C, experimental value of 200 mm the slab thickness is safe at 160 mm thickness for hybrid fiber concrete at flexural strength 14.78 MPa and compressive strength 43.11 MPa. For 20.3 °C, IRC-58 value of 250 mm the slab thickness is safe

Fig. 29 CFD analysis for 0 °C for hybrid fiber concrete



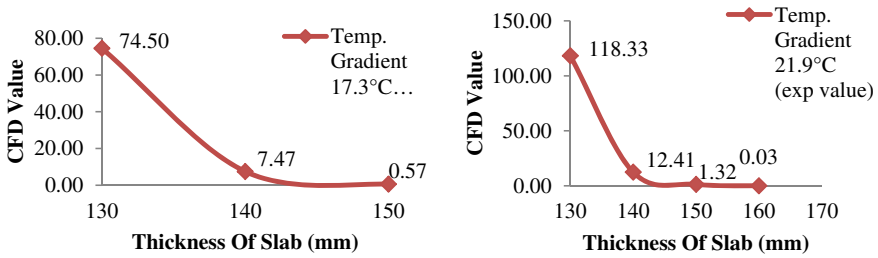


Fig. 30 CFD analysis for 17.3 and 21.9 °C of 150 mm for Hybrid fiber concrete

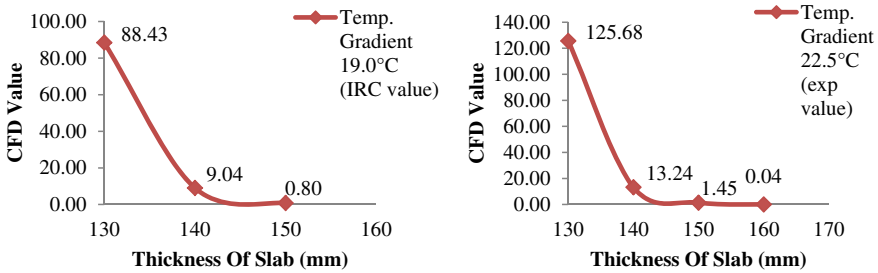


Fig. 31 CFD analysis for 19 and 22.5 °C of 200 mm for Hybrid fiber concrete

at 160 mm thickness for hybrid fiber concrete at flexural strength 14.78 MPa and compressive strength 43.11 MPa, the same be referred from Fig. 31.

For 20.3 °C, experimental value of 250 mm the slab thickness is safe at 160 mm thickness for hybrid fiber concrete at flexural strength 14.78 MPa and compressive strength 43.11 MPa. For 22.5 °C, IRC-58 value of 300 mm the slab thickness is safe at 160 mm thickness for hybrid fiber concrete at flexural strength 14.78 MPa and compressive strength 43.11 MPa, the same be referred from Fig. 32.

For 20.4 °C, experimental value of 300 mm the slab thickness is safe at 160 mm thickness for hybrid fiber concrete at flexural strength 14.78 MPa and compressive strength 43.11 MPa, the same be referred from Fig. 33.

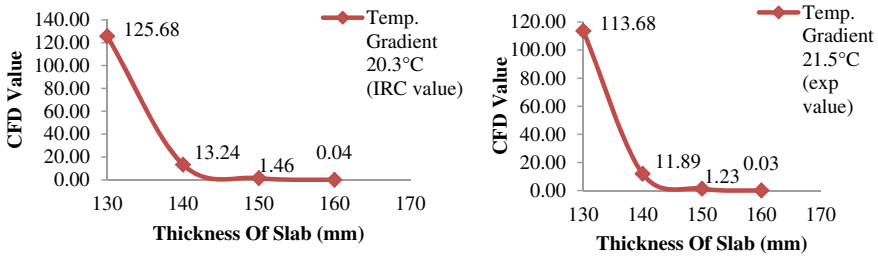


Fig. 32 CFD analysis for 20.3 and 21.5 °C of 250 mm for Hybrid fiber concrete

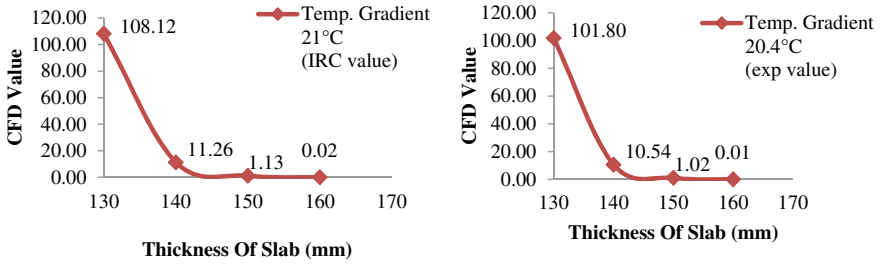
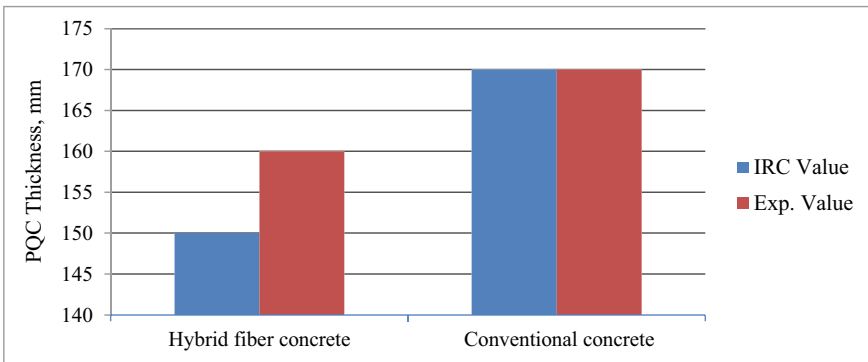


Fig. 33 CFD analysis for 21 and 20.4 °C of 300 mm for hybrid fiber concrete

2. Comparison of safe PQC thickness for Hybrid fiber concrete and conventional concrete



The graph above clearly indicates that the thickness of Hybrid fiber-cast concrete slab is less as compared to the conventional concrete slab. Thus, in the case of hybrid fiber concrete pavement, the thickness will be less as compared to conventionally cast concrete slabs. So ultimately, there is no requirement to provide 200-mm-thick PQC slab. Instead, using hybrid fibers of 170 mm thickness of slab is sufficient. Eventually, 30-mm PQC concrete thickness can be saved.

3. Cost analysis

- For 200-mm conventional concrete slab, 170 mm of Hybrid fiber concrete-cast slab is found safe.
200 – 170 mm = 30 mm saving of concrete.
- According to Current Schedule Rate, cost of concrete/m³ = 7500 Rs/-.
- For Road pavement of 3.75 m wide, 1 km long, 3.75 × 1000 × 0.03 = 112.5 m³.
- Saving of concrete/kilometer = 112.5 × 7500 = 8,43,750 Rs/km.

6 Conclusions

This research paper has proposed the innovative way for the usage of waste Tyre steel fibers their behavior on different mechanical properties and their effects on the concrete, In addition to this, a study on fatigue analysis of cement concrete slabs is performed. The research utilizes waste tyre steel fiber in concrete which enhances the mechanical properties of concrete. The CFD analysis for various temperature differentials of different replacement has been made. By this analysis, the comparison of different thicknesses is made.

- (1) From the experimental results, 1% replacement of discarded/waste/recycled tyre steel fiber by cement shows the highest compressive strength.
- (2) The flexural strength is found to have the highest value for 1% replacement of discarded/waste/recycled tyre steel fiber by cement.
- (3) At 0.5% replacement of discarded/waste/recycled tyre steel fiber by cement, the highest split tensile strength is shown for hybrid steel fibers.
- (4) The optimum percentage (dosage) of replacement of cement with tyre steel fibers comes out to be 1% by weight for compressive and flexural strength, for split tensile strength is 0.5% by weight.
- (5) Using waste tyre steel fiber in concrete mix proved to be very useful to solve the environmental problem and produce green concrete. Therefore, it is recommended to re-use tyre steel fiber in concrete to move toward sustainable development in the construction industry.
- (6) On the other hand for 200 mm thickness of slab, 160 mm is safe thickness against fatigue. i.e. no need to increase the thickness up to 200 mm. Similarly, in the case of 250 and 300 mm thick slabs, 160 mm thickness is safe thickness against fatigue.
- (7) After studying CFD analysis with IRC-58 2015 in the worst condition (as the experimental results were observed at peak of summer), it can be concluded that concrete thickness can be reduced rather than providing higher thickness and which ultimately results in saving of concrete materials, especially natural constituents such as sand, aggregates, and, most importantly, water.